Low-cost, highly efficient, and tunable ultrafast laser technology based on directly diode-pumped Cr:Colquiriites

by

Umit Demirbas

B.Sc. Physics
B.Sc. Electrical and Electronics Engineering
Koc University, Turkey, 2004

M.S. Materials Science and Engineering
Koc University, Turkey, 2006

SUBMITTED TO THE DEPARTMENT OF ELECTRICAL ENGINEERING AND COMPUTER SCIENCE IN PARTIAL FULFILLMENT OF THE REQUIREMENTS FOR THE DEGREE OF

DOCTOR OF PHILOSOPHY IN ELECTRICAL ENGINEERING AND COMPUTER SCIENCE

AT THE
MASSACHUSETTS INSTITUTE OF TECHNOLOGY

June 2010

Signature of Author: _____
Department of Electrical Engineering and Computer Science
May 10, 2010

Certified by: _____
James G. Fujimoto
Professor of Electrical Engineering and Computer Science
Thesis Co-supervisor

Certified by: _____
Franz X. Kärtner
Professor of Electrical Engineering and Computer Science
Thesis Co-supervisor

Accepted by: _____
Terry P. Orlando
Chair, Department Committee on Graduate Students

Low-cost, highly efficient, and tunable ultrafast laser technology based on directly diode-pumped Cr:Colquiriites

Submitted to the Department of Electrical Engineering and Computer Science on May 10, 2010 in Partial Fulfillment of the Requirements for the Degree of Doctor of Philosophy in Electrical Engineering and Computer Science at the Massachusetts Institute of Technology

by

Umit Demirbas

ABSTRACT

This doctoral project aims to develop robust, ultra low-cost ($5,000-20,000), highly-efficient, and tunable femtosecond laser technology based on diode-pumped Cr:Colquiriite gain media (Cr:LiCAF, Cr^{3+}:LiSAF and Cr:LiSGaF). By using inexpensive single-mode diodes ($150) as the pump source, we have obtained continuous-wave (cw) output powers >250-mW with slope efficiencies >50%. Record cw tuning ranges were demonstrated for Cr:LiSAF (775-1042 nm), Cr:LiSGaF (777-977 nm), and Cr:LiCAF (754-871 nm). For femtosecond pulse generation, semiconductor saturable absorber mirrors (SESAMs/SBRs) were developed, which were used to initiate and sustain mode-locking. Typical performance was ~25-100 fs pulses, with an optical spectrum in the 770-920 nm range, with ~1-2 nJ of pulse energies from ~100-MHz repetition rate cavities. Record electrical-to-optical conversion efficiencies of ~10% were demonstrated in the cw mode-locked regime. A mode-locked tuning range of 767-817 nm, with ~130-fs long pulses was obtained by using Cr:LiCAF as gain medium. With the Cr:LiSAF gain medium, using regular SESAMs/SBRs centered around 800 nm, 850 nm, and 910 nm, mode-locked tuning ranges of 803-831 nm, 828-873 nm, and 890-923 nm were demonstrated, respectively. By using a broadband oxidized SESAM/SBR, a record tuning range of 800-905 nm was demonstrated with ~150-fs long pulses. Using an extended cavity Cr:LiCAF laser, pulse energies >15-nJ with peak powers exceeding 100-kW were obtained. We performed the first cavity-dumping experiments with a Cr:Colquiriite laser and demonstrated pulse energies >100-nJ, and peak powers approaching MW level, at repetition rates up to 50-kHz. Cr:LiCAF gain media were also pumped by single-emitter multimode diodes, where we obtained >2-W output power in cw operation, and ~100-fs pulses with 390-mW of average power at a repetition rate of 140 MHz in cw mode-locked operation. As an example application area for this low cost technology, we performed multiphoton microcopy experiments with a single-mode diode-pumped Cr:LiCAF laser. We also performed attosecond-resolution timing jitter characterization experiments of the femtosecond Cr:LiSAF laser, and measured a record-low upper limit for the integrated timing jitter of the Cr:LiSAF laser (137-attoseconds in 10 kHz-10 MHz range).

Thesis Supervisors: James G. Fujimoto and Franz X. Kärtner
Professor of Electrical Engineering and Computer Science

ACKNOWLEDGEMENTS

The research we have performed during this doctoral research was challenging, and it would not have been possible without the help and support from several people.

First and foremost, I would like to thank my research advisors Prof. James Fujimoto and Prof. Franz Kärtner for providing this rare opportunity to conduct research at RLE's Optics and Quantum Electronics group. I appreciate their guidance, support and patience during the last four years. Besides their constant contribution to my research, they have also significantly contributed to my personal development. Prof. Kärtner has been an excellent resource for valuable advice, and his ideas constantly shaped and saved our research program. Prof. Fujimoto has impressed me with his capability to focus on even the smallest details of the experiments, despite his hectic schedule. I have learned several valuable concepts from him that I will remember throughout my life.

I would like to especially thank Prof. Alphan Sennaroglu from Koc University. I have had the opportunity to work with him since my undergraduate years, and I am indebted to him for his constant support over the last 10 years. He has been patient enough to spend hours with us in the lab and in his office, even while we were just undergraduate students. He has also contributed significantly to my PhD work over the last four years. I would like to also thank Adnan Kurt, Prof. Mehmet Somer, Prof. Iskender Yilgor, and Prof. Tekin Dereli from Koc University for their significant contributions to my career. Without the skills that I learned from them during my undergraduate and MS years, my life at MIT would have been much harder.

I would like to also especially thank Ms. Dorothy Fleischer, for her constant help with administrative issues. More important than that, she has been a very good friend, and I thank her for constantly trying to keep the spirit of the group high.

Prof. Leslie Kolodziejski, Dr. Gale Petrich, and Sheila Nabanja from RLE's Integrated Photonics Devices and Materials Research group have significantly contributed to this research. Without the saturable absorber mirrors they have grown and characterized for us, several of the projects we performed during this research would not have been possible.

I would like to thank especially Prof. Erich Ippen for serving on my research qualification and PhD thesis committees. It has been an honor to have him in these committees.

I would like to thank Dr. Sava Sakadžic and Prof. David Boas from the Photon Migration Imaging laboratory at the Athinoula A. Martinos Center for Biomedical Imaging at the Massachusetts General Hospital, for making the multiphoton microscopy experiments with the Cr:LiCAF laser possible.

Andrew Benedick from Prof. Kärtner's group has been a great source of help, and he has contributed to the timing jitter project significantly. Dr. Jonathan Birge from Prof. Kärtner's group designed the Cr:LiSAF mirror set, which was crucial for several of the projects, including the ultra-broad tuning of Cr:LiSAF and the GHz Cr:LiSAF lasers. I would like to also thank Dr. Kyung-Han Kong from Prof. Kärtner's group for his help with the cavity-dumped Cr:LiSAF laser project. I would like to thank Dr. Peter Fendel from Thorlabs, who has provided constant help with the Cr:Colquiriite laser project. I would like to thank Yimin Hu from Thorlabs, for his help with the high-reflector coating of the SESAMs/SBRs. I would like thank Dr. Detlef Klimm and Dr. Reinhard Uecker from the Institute for Crystal Growth of Germany for providing the 5% chromium-doped Cr:LiCAF boule.

I also would like to thank my friends Duo Li and Jing Wang who began working on the Cr:Colquiriite project with me in 2008 and 2009, respectively. I have tried to transfer my skill set on Cr:Colquiriite lasers to them, and they will be quite valuable in continuing our effort to develop low-cost Cr:Colquiriite laser technology. I want to also thank the micromachining part of our group, Josh Chuang and Yu Gu, for sharing the laser lab equipment and for their friendship.

The primary support for our studies has been provided by National Science Foundation (NSF), U.S. Air Force Office of Scientific Research (AFOSR), the National Institutes of Health, and Thorlabs. I am deeply grateful for their support without which this work would not have been possible.

During these years, it has been quite hard to be ~8000 km away from home, both for me and for my family. Hence, last but not least, I wish to thank my family for their constant love and support.

Her Şey Sende Gizli

Yerin seni çektiği kadar ağırsın,
Kanatların çırpındığı kadar hafif..
Kalbinin attığı kadar canlısın,
Gözlerinin uzağı gördüğü kadar genç...
Sevdiklerin kadar iyisin,
Nefret ettiklerin kadar kötü..
Ne renk olursa olsun kaşın gözün,
Karşındakinin gördüğüdür rengin..
Yaşadıklarını kâr sayma:
Yaşadığın kadar yakınsın sonuna; ne kadar yaşarsan yaşa,
Sevdiğin kadardır ömrün..

Can Yücel

This thesis is dedicated to my wife, Meryem, for her endless love and support.

TABLE OF CONTENTS

CHAPTER 1

INTRODUCTION

This thesis is focused on detailed lasing investigation of Cr:Colquiriite gain media (Cr^{3+}:LiCAF [1-3], Cr^{3+}:LiSAF [4, 5] and Cr^{3+}:LiSGaF [6]) both in continuous-wave (cw) and cw mode-locked regime. In this chapter we introduce Cr:Colquiriite gain media to the reader in a relatively smooth and comparative way, starting with a historical review aiming to show where Cr:Colquiriite laser gain media stands amongst thousands of others. In Chapter 2, we will present cw lasing results of diode-pumped Cr:Colquiriite gain media. Chapters 3-5, will discuss cw mode-locked operation of Cr^{3+}:LiCAF, Cr^{3+}:LiSAF and Cr^{3+}:LiSGaF gain media, respectively. Chapter 6 will discuss the extended cavity Cr^{3+}:LiCAF laser results, which we reduced the laser repetition rate to ~10MHz level, aiming to scale pulse energies in cw mode-locked regime. In Chapter 7, we will present the first cavity dumping experimental results with Cr^{3+}:LiSAF gain media. In Chapter 8, multiphoton microscopy imaging results with a Cr^{3+}:LiCAF laser will be presented. Finally, in Chapter 9, we will present timing jitter noise characterization of mode-locked Cr^{3+}:LiSAF lasers. In Appendixes A and B, we will give details about the optics and laser pump diodes we have used during this PhD, respectively. Appendix C will present a list of Cr:Colquiriite crystals that we have used. In Appendix D, we will try to describe how one can design saturable absorber mirrors (SESAMs/SBRs) that can be used in mode-locking Cr:Colquiriite lasers. In Appendix E, we will list the specs of saturable absorber mirrors that were grown during this PhD. Finally, Appendix F will present some new saturable absorber mirror designs that might be useful in future projects.

1.1 Invention of Laser

Light amplification by stimulated emission of radiation (LASER or laser) is a physical mechanism to generate spatially coherent (directional) electromagnetic waves using the stimulated emission process. Although the "laser" term describes the physical mechanism, now it is also used to name the devices that actually produce electromagnetic waves with this mechanism. The underlying idea of lasers is stimulated emission, which was proposed by Albert Einstein in 1917, in his famous paper on "Quantum theory of radiation" [7]. In spontaneous emission, an ion in an excited state relaxes (decays) back to a lower energy level, and releases its energy by emitting a photon in a random spatial direction. Einstein predicted that, the ion in its excited state can be stimulated by an incoming photon. In this case (stimulated emission),

the ion emits a photon that is identical to the incoming photon, which amplifies the incoming light. By generating identical photons, stimulated emission process enables the generation of spatially and temporally coherent electromagnetic wave (the degree of coherence depends on the type of laser).

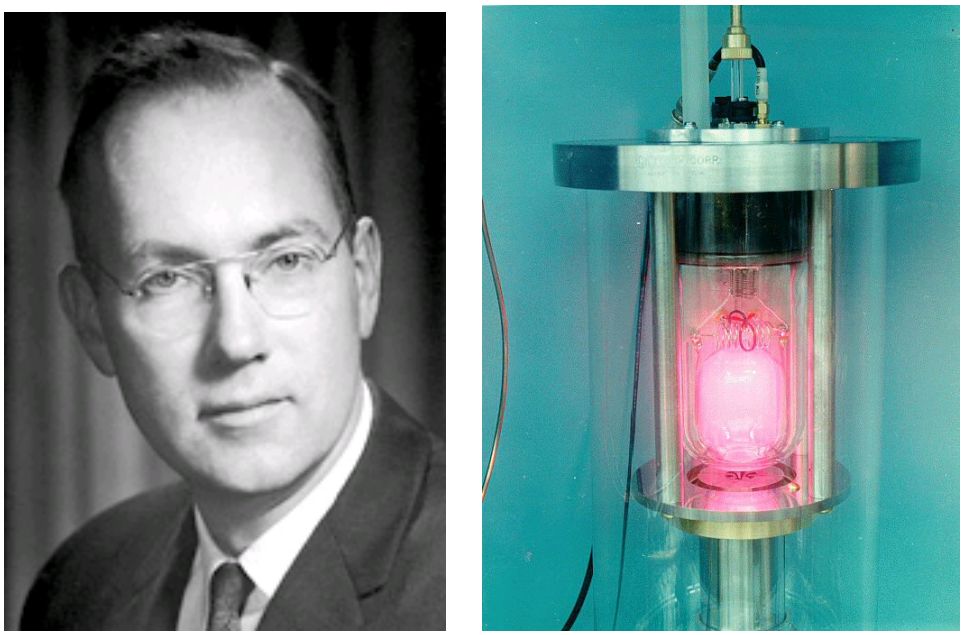

Figure 1.1: (left) Charles Townes, the inventor of the MASER [8]. (Right) Hydrogen maser working at a wavelength of 21.106 cm [9]. Courtesy of NASA/JPL-Caltech.

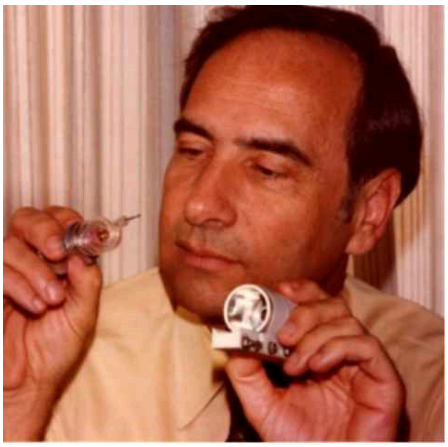

Figure 1.2: (left) Theodore Maiman holding the first ruby laser [10]. This picture is used here under the fair use doctrine of United States copyright law [11].

It took quite a while for physicists to use the idea of stimulated emission in experimental research. In 1947 Willis Lamb and Robert Retherford from Colombia University used stimulated emission to amplify the microwave frequency radiation emitted by hydrogen molecules at a wavelength of 2.74 cm [12]. The amplification process enabled them to measure the frequency of $2^2P_{1/2}$ to $2^2P_{3/2}$ transition with better

accuracy [12]. In 1954, Charles H. Townes, J. P. Gordon, and H. J. Zeiger build the first maser (microwave amplification by stimulated emission of radiation) using the vibrational energy levels of ammonia molecules in a resonant cavity, obtaining only nW level powers at a wavelength of around 1.25 cm (23870 MHz) [13, 14]. C. H. Townes and A. L. Schawlow suggested the extension of maser technology to higher (optical) frequencies, and they proposed the idea of Fabry-Perot resonators for feedback [15]. It took a while to find a suitable gain media and a suitable way for exciting this gain media that could generate enough population inversion [16]. Finally, in 1960, T. Maiman build the first laser operating at 694.3 nm using the ^2E, $^4A_2$ transition of ruby (Cr^{+3} in corundum, crystalline form of Al_2O_3) as the gain medium where flahslamps were used as the excitation mechanism (Fig. 1.2) [17].

Note: Actually, today we know that there are natural masers/lasers that occur in clouds of molecular gases in the universe [18]. For example CO_2 atmosphere at Venus and Mars is known to produce lasing at 10.4 μm wavelength, and H gas at Cygnus MWC349 star produces laser/maser action at wavelengths of 52.5, 88.8, 169.4, 453 and 850 μm [18-20].

1.2 Types of Lasers

While I am writing these lines, in the year of 2010, the world is currently celebrating the 50th year of lasers. Since 1960, lasing has been demonstrated in thousands of different laser gain media, and the Handbook of Laser Wavelengths by M. J. Weber lists more than 15,000 laser lines (most gain media have more than one line) [18, 21]. Among all these available lasers, only a few hundreds of them are used most frequently [21]. One can categorize these lasers in several ways, using their operational wavelength (UV, visible, IR, etc..), operational mode (continuous-wave, q-switched, mode-locked, etc..), excitation mechanism (electrically pumped, flashlamp pumped, diode-pumped, etc..), and their application area. Maybe one of the most convenient ways of categorization lasers is made by differentiating them according to the type of gain media used. In this respect lasers can be categorized as (a) Gas lasers, (b) Liquid lasers, (c) Solid-state lasers and (d) others [18], where others include free electron lasers, inversionless lasers, nuclear pumped lasers, etc..

1.2.1 Gas Lasers

Among the 15000 laser lines listed in Handbook of Laser Wavelengths, about 12000 of them belongs to gas lasers [18, 21]. The lasing lines of gas lasers are quite narrow in general (Doppler, collisional and rotational line broadening effects are present but they are not very strong), and without a tuning element, an individual laser can lase at several different distinct wavelengths simultaneously[18, 22]. The transition involved in the stimulated emission process might be between electronic, vibrational or transitional energy levels, enabling gas lasers to cover a quite wide spectral range [18]. The wavelengths

available from gas lasers start from ~3.9 nm and covers all the vacuum ultraviolet, ultraviolet, visible, infrared, far infrared, and millimeter microwave regions [18]. So the wavelength range of gas lasers actually overlaps with mm wave masers. Nowadays, among the gas lasers, CO_2 laser, short-wavelength (200-350 nm) ion lasers (F2) and the rare gas halide lasers (He, Ne, Ar, Kr, etc) are still used in research labs. As an example commercial He-Ne lasers are quite popular and can provide mW level continuous-wave output power at wavelengths of ~543, 594, 612, 632, 1152, 1523 and 3391 nm. CO_2 lasers can provide kW level powers in cw operation and kJ level pulses at pulsed operation at 10.6 μm[18], and they are mostly used in industrial applications like laser cutting, laser drilling, laser engraving, and laser welding. Commercial Neon (Ne^+), Argon (Ar^+) and Krypton (Kr^+) ion lasers can provide watts of continuous wave output power at ~332, 488, 515, and 647 nm lines (and others) [18]. However, nowadays gas lasers are mostly replaced by all-solid-state lasers especially in the 0.5 μm to 3 μm range [18].

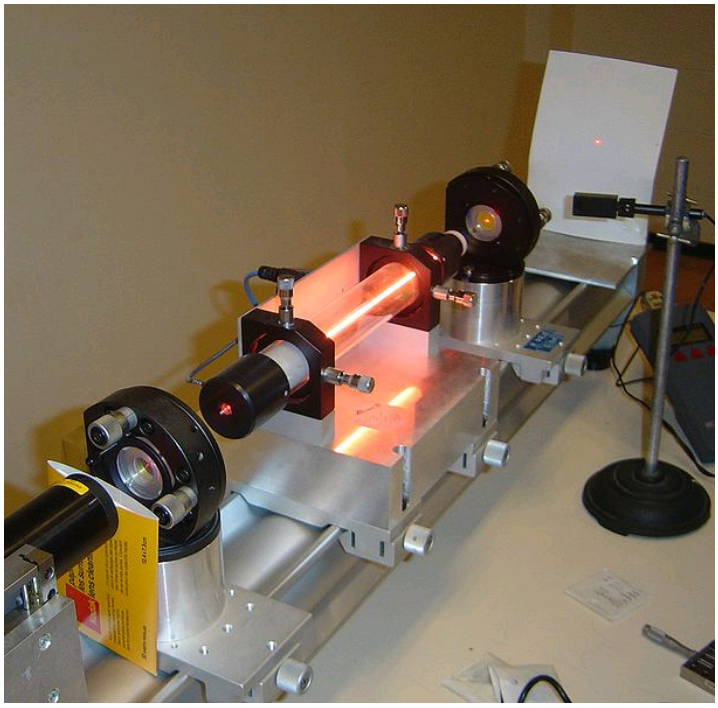

Figure 1.3: Helium-Neon laser demonstration at the Kastler-Brossel Laboratory at Paris VI: Pierre et Marie Curie. The glowing ray in the middle is a discharge tube (akin to that of a neon light), it is not the laser beam. The laser beam crosses the air and marks a red point on the screen to the right [23]. This picture is used here under the Creative Commons Attribution 2.5 Generic license [24].

1.2.2 Liquid Lasers

Liquid lasers are mostly based on organic dye lasers, which are basically dye molecules in an organic solvent [18]. Dye lasers were discovered quite early in 1966, by P. P. Sorokin and F. P. Schäfer around the same time [25, 26]. They have relatively broad absorption and emission bands due to the coupling of

electrons with molecular vibrations. Hence they enable tunable laser operation over 10's of nm's, and also sub-100-fs pulse generation in mode-locked regime (27 fs pulses directly from the oscillator [27] and down to 6 fs pulses with external pulse compression [28]). Using different dye molecules, the laser wavelength range from 330 nm to 1800 nm could be covered [18]. Dye gain media have relatively high gain and their upper-state lifetimes are in the ns range; hence, they don't have the tendency for q-switching instabilities during mode-locked operation [29, 30]. In 1970's and 1980's most of the ultrafast laser technology was based on dye lasers [29, 30]. Unfortunately, the dye lasers have several disadvantages including low output powers, requirement for expensive pump sources in the green or blue region of the spectrum and rapid degradation during laser operation [29]. Moreover, dye gain media and/or the solvents are sometimes highly toxic [29]. Hence, today dye lasers are mostly replaced by solid state laser technology, and mostly with Ti:Sapphire. Besides the organic dye lasers, liquid lasers also include rare-earth chelate lasers and inorganic aprotic solvents, which also had very little practical usage, due to their corrosive and toxic nature [18].

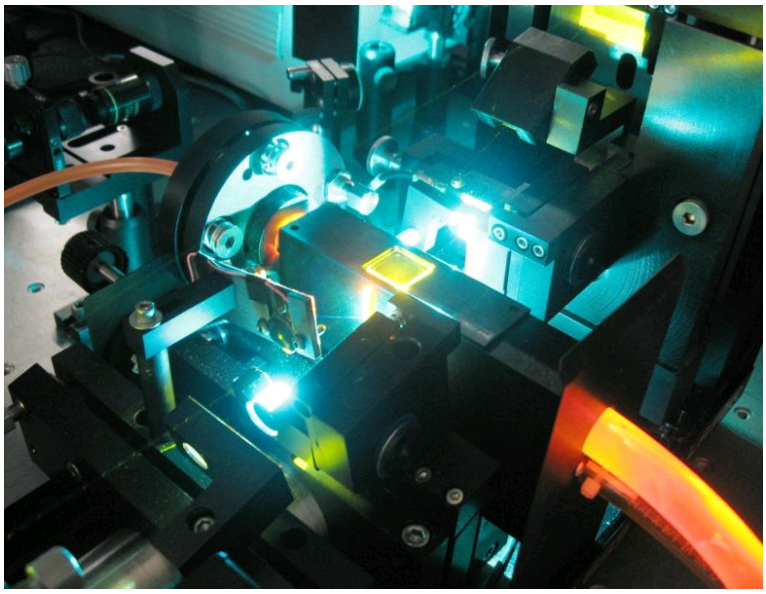

Figure 1.4: Coherent model 899 ring dye laser, with rhodamine 6G dye, pumped with a 514 nm argon laser. The laser is tuned somewhere around 580 nm. Photo taken by Han-Kwang at the AMOLF Institute in Amsterdam, Netherlands [31, 32]. This picture is used here under the Creative Commons Attribution 2.5 Generic license [24].

1.2.3 Solid-State Lasers

Solid state lasers are based on solid-state crystalline or amorphous hosts and have laser transitions originating from the doping of paramagnetic ions (mostly rare-earth and transition-metal ions), organic dye molecules and color centers [18]. The typical doping concentrations of active ions are less than 1 % in general, but can reach to 100 % (stoichiometric lasers) for some specific cases like LiChrom ($LiSrCrF_6$, 100% Cr doped $LiSrAlF_6$) [18, 33]. Semiconductor lasers are also listed under solid-state

lasers, since they are also solid-state devices, but actually they use completely different physics in the generation of laser active centers [18]. Today solid-sate lasers has an important part in laser market, due to their several favorable properties including robustness, reliability, safety, user-friendliness, compactness, and low-cost per performance [34]. They can cover the spectral region from 170 nm to 360 μm, enabling the generation of laser radiation required for many different applications [18].

Color center (or F-center) solid-state lasers are quite interesting sources that could generate laser radiation from 357 nm to 5 μm [33, 35]. The first color center laser was demonstrated in 1965 by Fritz and Menk, which was based on Li^{+}:KCL material and lased around 2.7 μm upon xenon flashlamp pumping [35, 36]. Earlier, they were especially popular as near-infrared lasers (~1-3.5 μm range), since they can have high gain, and large homogeneous emission bandwidths that can enable broadly tunable laser operation or fs pulse generation [35, 37]. For example F^{+}_{2} -like centers in KCl:Na^{+}:O^{-}_{2} crystals has a demonstrated tuning range from 1.71 μm to 2.15 μm, with 100s of mW output power when pumped with a 3-W Nd:YAG laser at 1.3 μm. However, color center lasers are not very convenient to use, since they often require cooling to cryogenic temperatures, and they also have limited operating lifetime (hours to months depending on cooling) [18, 30]. Hence, today they are mostly replaced by other alternatives available at their wavelength range [21].

Dye gain media can also be incorporated into solid-state gain media such as polymers, organic single crystals, and organic and inorganic glasses, and by using different dyes and solid hosts, lasing have been demonstrated from 376 nm to 865 nm [18, 38]. For example, a 671 nm diode pumped solid state dye laser based on Ox 725 in modified PMMA was reported to generate pulsed laser action around 740 nm with about 18% slope efficiency [39]. The main problem limiting their use is photodegragation (degradation of a photodegradable molecule caused by the absorption of photons), however, recent research efforts started to show more durable materials [18, 38].

Semiconductor lasers use population inversion generated by electron and hole pairs to generate gain; hence, they are quite different than other solid state gain media which require an active ion for the lasing action. Moreover, unlike other solid-state gain media, semiconductor lasers don't have distinct sharp laser lines, and their emission wavelength can be engineered by changing their composition. Most of the semiconductor lasers are laser diodes, which are electrically pumped to generate the required population inversion. Semiconductor lasers can also be pumped optically like in the case of vertical–external-cavity surface-emitting laser (VECSELs)[40]. Common materials for semiconductor lasers include Pb salts, GaN, GaAs, AlGaAs, InGaAs, InGaN, InGaAsP and AlGaInP [18]. Different semiconductor materials with varying composition was used to generate laser light ranging from 330 nm to 360 μm [18]. The main advantages of semiconductor lasers compared to other types of lasers include, high efficiency, long lifetimes, reduced cooling requirements, compactness and reduced cost[41]. As an example, nowadays

AlGaInP diodes can provide up to 150 mW of diffraction limited cw power around 650 nm, at a cost of only about $200 [42]. This diode is used in imaging, in projection, in large capacity optical disc memories, such as DVD-RAM, and also in various other types of optical equipment. As we will describe in detail later (Appendix B), we have also used this laser diode for pumping our Cr:Colquiriite lasers.

In the following, we will discuss rare-earth and transition-metal doped solid-state lasers in more detail.

1.3 Rare-Earth Doped Solid-State Lasers

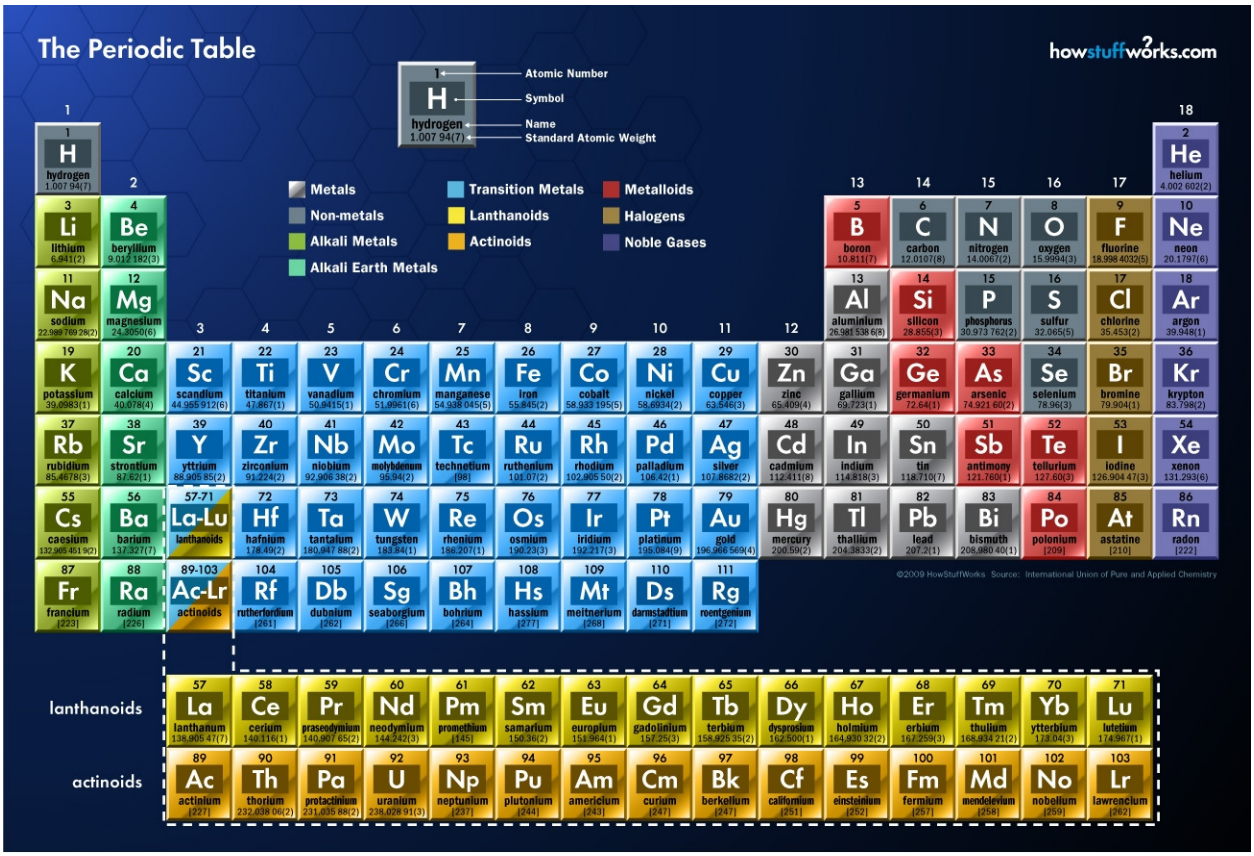

Figure 1.5: Periodic table of elements [43], courtesy of HowStuffWorks [44]. This periodic table is used here under the fair use doctrine of United States copyright law [11].

Rare earth elements/metals are a collection of 17 chemical elements which includes lanthanoids (lanthanides), scandium and yttrium (Fig. 1.5). Scandium and yttrium are included in this group of elements because they have similar chemical properties and they are found in same ore deposits [45, 46]. The term "rare-earth" comes from the rare earth minerals, which rare-earth metals were first isolated [45]. Rare earth minerals were thought to be rare, but actually their concentration in earths crust is relatively high (cerium: 68 parts per million, 25th most abundant element in earths crust, neodymium: 38 ppm, ytterbium: 3.3 ppm, ytterbium: 0.48 ppm) [45, 47]. Actually, to our knowledge lasing action in scandium,

yttrium, and lanthanum have not been reported yet [18]; and in his book "Solid State Engineering", Dr. Walter Koecher names only elements from cerium to lutetium as rare earth elements [16]. We will follow his nomenclature in this short review.

To understand the ground state electronic configuration of rare earth atoms, we will start with noble gas xenon, which has the following electronic configuration:

xenon(54):$1s^2\,2s^2\,p^6\,3s^2\,p^6\,d^{10}\,4s^2\,p^6\,d^{10}\,5s^2\,p^6$: [Xe]

Xenon has all the shells with quantum numbers n=1,2 and 3 are completely filled, and among the n=4 shells all the s, p and d subshells are also completely filled. Than the electrons fills the 5s and 5p subshells leaving the 4f subshell empty [16]. Cesium and barium follows xenon in the periodic table, and they start to fill the 6s subshell:

cesium(55): [Xe] $6s^1$

barium(56): [Xe] $6s^2$

Lanthanum, the first element of lanthanoids has one additional electron in the 5d orbit:

lanthanum(57): [Xe] $5d^1\,6s^2$

Then rare earth elements begin to fill the 4f orbitals, and the electronic configuration of cerium is:

cerium(58): [Xe] $4f^1\,5\,d^1\,6s^2$

If we look at neodymium, which is one of the most common laser elements, it has the following electronic configuration:

neodymium (60): [Xe] $4f^4\,6s^2$

Neodymium's valance electrons are $4f^4\,6s^2$ and its filling orbital is $4f^4$. When neodymium is doped in a solid state gain media, the ionic structure is normally trivalent, where the ion loses its outmost 6s electrons and also one electron from the 4f shell:

Nd^{+3} (57): [Xe] $4f^3$

The lasing lines of rare-earth doped gain media originate mostly from the transitions between the partially filled 4f shells. These states are split by Coulomb interaction, spin-orbit coupling and crystal-field interaction. Coulomb interaction has the strongest effect on the lines which separates the lines by ~10,000 cm^{-1} (~1.24 eV, λ~1000 nm photon), followed by the spin orbit coupling which creates an additional splitting of ~3,000 cm^{-1} (0.37 eV, λ~3350 nm photon). Since the 4f shell is shielded by the outer 5s and 5p electrons, the effect of crystal field is relatively weak, which further splits each manifold by only ~200 cm^{-1} (25 meV, λ~50 μm photon) [48]. The shielding of crystal field results in relatively narrow but strong emission lines in rare-earth doped gain media (σ_{em} is high), and also the position and width of the emission lines does not differ a lot from host to host [16]. Hence, most of the rare-earth doped gain media provide very little tunability and the obtainable pulsewidths in mode-locked regime are relatively long. Moreover, dipole transitions between the 4f shells are parity forbidden, and a mixture of

wave functions with opposite parity is required for a transition [48]. These opposite parity wave functions are generated by the weak crystalline field, hence these transition probabilities are quite weak also [48]. This results in relatively long upper state lifetimes (τ) in rare-earth doped gain media [48]. Hence in general, rare-earth doped gain media has a very high $\sigma_{em}\tau$ value, resulting in low laser thresholds at low concentration values (at high concentrations increased nonradiative decay rates might lower the lifetime) [48].

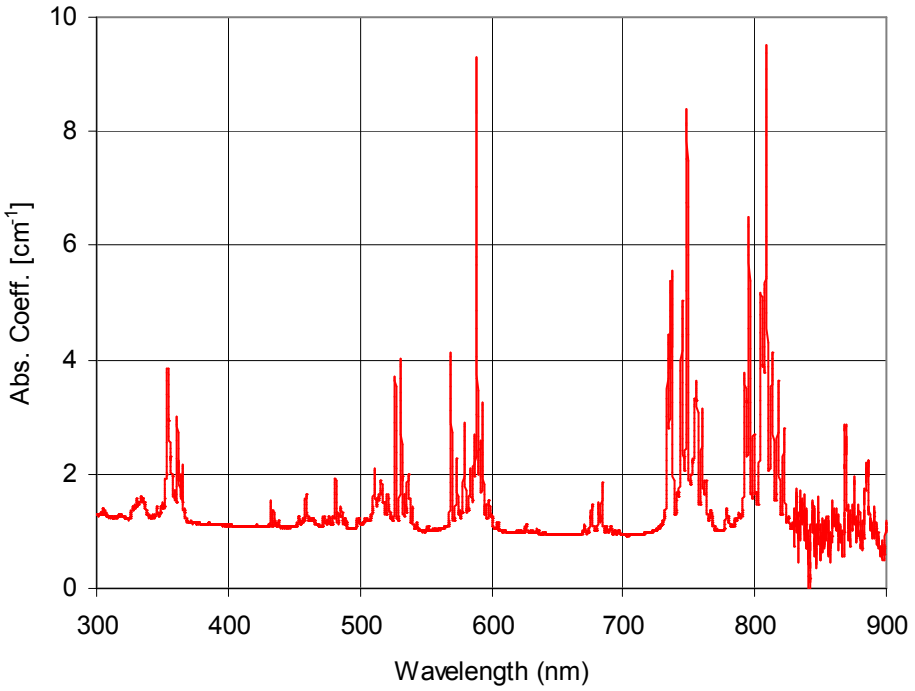

Figure 1.6: Measured absorption spectrum of Nd:YAG gain medium in the spectral range from 300 to 900 nm. Note the sharp and quite strong spectral transition lines, which is quite common in rare-earth doped gain media. The position and width of the transitions does not change a lot from host to host due to the screening of the crystal field by outer electrons. Data is taken using a Shimadzu UV3101PC scanning spectrometer at a resolution of 0.1 nm at Koc University Laser Research Laboratory.

We note hear that, in some cases, rare-earth doped gain media can also have lasing transitions between 4f and 5d shells, and in this case laser lines are quite broad and one can possibly obtain broad tunability and ultrashort pulses (examples are Ce^{+3}:$LiCaAlF_6$ and Sm^{+2}:SrF_2) [18]. This is because unlike the 4f shell, the 5d shell has no shielding and hence it is exposed to the crystalline environment, which broadens the emission lines [22].

Also, one should differentiate rare-earth doped glasses from rare earth doped crystals. Rare-earth doped glasses can take the form of bulk materials, fibers or planar waveguides [18]. In glassy structure the crystalline field surrounding the active ions are not as well defined as crystalline hosts; hence, laser emission lines can be slightly broader [16], enabling relatively broadband tuning and shorter pulses in mode-locked operation. Other advantages of glass hosts include ability to produce large samples for high

energy applications, and ease of fabrication, whereas the drawbacks include lower thermal conductivity, lower emission cross section, and thermally induced birefringence problems [16].

1.4 Transition-Metal Doped Solid-State Lasers

Transition metal elements are elements whose atom has an incomplete d sub-shell, or elements which can give rise to cations with an incomplete d sub-shell [49, 50]. The name "transition" comes from the place they appear on periodic table: they represent transition between group 2 and group 13 elements [49]. So far, lasing have been reported in the transition metal elements of titanium (Ti), vanadium (V), chromium (Cr), manganese (Mn), iron (Fe), cobalt (Co) and nickel (Ni), and gain has been reported in transition metal elements of copper (Cu), silver (Ag) and rhodium (Rh) [18].

For example the chromium atom has the following electronic configuration:

chromium (24): $1s^2\,2s^2\,p^6\,3s^2\,p^6\,d^5\,4s^1$

When doped into different gain media chromium can have several charge states including:

Cr^{+2} (22): $1s^2\,2s^2\,p^6\,3s^2\,p^6\,d^4$

Cr^{+3} (21): $1s^2\,2s^2\,p^6\,3s^2\,p^6\,d^3$

Cr^{+4} (20): $1s^2\,2s^2\,p^6\,3s^2\,p^6\,d^2$

Example gain media doped with chromium ion include Cr^{+2}:ZnSe, Cr^{+2}:ZnS, Cr^{+3}:Al_2O_3 (ruby, first lasers gain media), Cr^{+3}:LiCAF, Cr^{+3}:LiSAF, Cr^{+4}:Mg_2SiO_4(forsterite) and Cr^{+4}:YAG. The most important point here is the d orbitals determine the optical properties of ions, and since the d orbitals are not shielded (as in the case of rare-earth ions), the optical properties are greatly influenced by the host. Moreover, absence of shielding in transition-metal doped gain media enables strong phonon broadening in the absorption and emission lines, which enables ultra broad tuning ranges and ultrashort pulse generation in mode-locked operation. Dipole transitions between the 3d shells are also parity forbidden, however due to the strong crystal field, opposite parity wave functions are generated more easily, resulting in higher transition rates and shorter lifetimes (compared to rare-earth doped gain media) [48]. Compared the RE-doped gain media $\sigma_{em}\tau$ value is an order of magnitude smaller [48]. In closing, we note here that, besides the chromium doped gain media we have listed above, other important transition metal doped gain media include Ti^{+3}:Al_2O_3(sapphire), Co^{+2}:MgF_2, Ni^{+2}:MgF_2, Fe^{+2}:ZnSe and V^{+2}:MgF_2. We will review some of these gain media in more detail in the following sections.

1.5 Solid-state Gain Media for Broadly Tunable Laser Operation

As already mentioned above, Cr^{3+}:Colquiriite lasers belongs to the family of tunable solid-state lasers, also referred to as vibronic lasers due to the role of electron-phonon coupling in the broadening of the absorption and emission bands. In tunable solid-state lasers, the output wavelength can be tuned over a

substantial fraction of the central emission wavelength. As such, the fractional tuning range, defined as $\Delta\lambda/\lambda_0$ ($\Delta\lambda$=full width of the tuning range and λ_0=the central emission wavelength) can be several tens of percent. The broad emission bandwidth of these gain media might also enable ultrashort pulse generation or amplification. Table 1.1 shows some examples of tunable solid-state gain media and their reported fractional tuning range at room temperature. Demonstrated shortest pulsewidths in mode-locked regime is also reported along with the estimated minimum pulsewidth that is supported by the gain bandwidth of the material. Figure 1.7 graphically shows the demonstrated room-temperature cw tuning ranges of selected solid state gain media.

Gain Medium	Short name	Tuning Range (nm)	$\Delta\lambda/\lambda_0$ (%)	Minimum theoretical pulse duration (fs)	Shortest demonstrated pulsewidth (fs)
Ce^{+3}:$LiCaAlF_6$	Ce:LiCAF	280-316 [51]	12	3 [52]	6000 [52]
Ce^{+3}:$LiSrAlF_6$	Ce:LiSAF	288-313 [53]	8	-	-
Ce^{+3}:$LiLuF_4$	Ce:LiLuF	305-333 [54]	9	-	-
Ti^{3+}:Al_2O_3	Ti:Sapphire	660-1180 [55]	57	3.6 [56]	~5 [57]
Cr^{3+}:$BeAl_2O_4$	Alexandrite	701-818 [58]	15	-	-
Cr^{+3}:$LiCaAlF_6$	Cr:LiCAF	720-871 [1, 59]	19	6 [56]	9 [60]
Cr^{+3}: $LiSrGaF_6$	Cr:LiSGaF	777-977 [59, 61]	23	7.2 [56]	14 [62]
Cr^{+3}:$LiSrAlF_6$	Cr:LiSAF	775-1042 [59, 63]	29	7.6 [56]	10 [64]
Nd:GSAG:YSGG	-	-	-	-	260 [65]
Nd^{+3}:glass	-	-	-	53[56]	60 [66]
Nd^{+3}:glass (dual gain media)	-	-	-	-	38 [67]
Cr^{4+}:Mg_2SiO_4	Cr:Forsterite	1130-1367 [68]	19	11 [56]	14 [69]
Cr^{4+}:$Y_3Al_5O_{12}$	Cr:YAG	1309-1596 [70]	20	11 [56]	20 [71]
Yb^{+3}:glass	-	-	-	31 [66]	58 [72]
Yb^{+3}:CaGdAlO4	Yb:CALGO	-	-	14 [56]	47 [73]
Tm,Ho:BaY_2F_8	Tm,Ho:BaYF	2005-2094 [74]	4	-	120000 [74]
Tm:YAG	-	1870-2160 [75]	15	-	35000 [76]
Tm:YLF	-	1910-2070 [77] 2200-2460 [78]	8 11	-	-
Co^{2+}:MgF_2	-	1750-2500 [79]	35	-	-
Cr^{2+}:ZnS	-	1962-3195 [80, 81]	48	12 [56]	-
Cr^{2+}:CdSe	-	2180-3610 [82-84]	49	-	-
Cr^{2+}:ZnSe	-	1880-3349 [81, 85]	56	11 [56]	80 [86, 87]
Fe^{2+}:ZnSe	-	3900-4800 [88]	21	-	-

Table 1.1 Room-temperature tuning ranges and calculated fractional tuning percentage of several broadly tunable transition metal and rare-earth ion-doped solid state gain media. Minimum theoretical pulse durations and demonstrated shortest pulse widths are also included.

In this section we will review a few of the broadly tunable gain media: Ce:LiCAF, Ti:Sapphire and Cr:ZnSe. Note that these are the most promising and/or accomplished gain media in their wavelength region of operation. For a comprehensive review of broadly tunable laser gain media in general, we refer the reader to several excellent review articles on this subject [58, 89-96]. We will review Cr^{3+}-doped solid state gain media in more detail in the next sections.

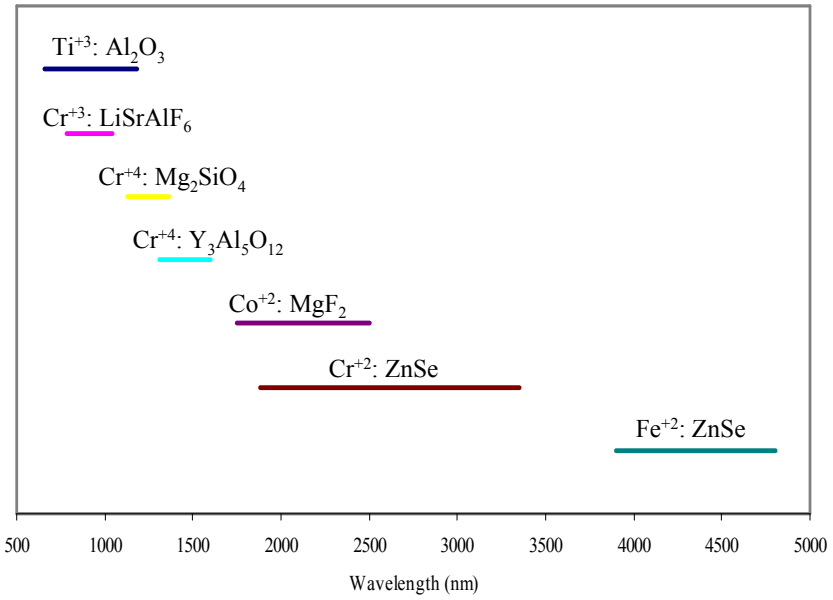

Figure 1.7: Demonstrated room-temperature tuning ranges of selected solid-state gain media in cw or gain-switched operation.

Ce^{+3}: LiCAF (280-316 nm): As mentioned above Ce^{+3}:$LiCaAlF_6$ is an exceptional rare earth doped gain media, where the lasing transitions between 4f and 5d shells can be used to generate broadly tunable laser operation [51, 97, 98]. Ce:LiCAF has a fluorescence lifetime (τ) of only 25 ns, and has an emission cross section (σ_{em}) of 9.6×10^{-19} cm^2; hence, the product $\tau\sigma_{em}$ is only 2.4×10^{-20} $\mu s \times cm^2$ [97], which is about 50 times smaller compared to Ti:Sapphire (131×10^{-20} $\mu s \times cm^2$). This prevents continuous wave lasing operation in this gain media (due to high lasing thresholds), and so far only gain switched operation have been reported with ps to ns pulse durations, upon pumping with the 4th harmonic of pulsed Nd-lasers [97]. The demonstrated tuning range in gain switched operation extends from 280 nm to 316 nm, with ~W level average output powers from ~ns pulses at ~kHz repetition rates [51]. Recently, the first mode-locked operation of Ce:LiCAF has also been reported, where 6 ps pulse durations were demonstrated upon synchronously pumping [52]. Ce:LiCAF gain media has also been used in chirped pulse amplification of ultraviolet femtosecond pulses around 290 nm [99], which is attractive due to its high saturation fluence (115 mJ/cm2) [98]. We note here that the bandwidth of Ce^{+3}:LiCAF is broad enough to support ~3-fs pulses [52]. Other important Ce^{+3} doped solid state gain media include Ce:$LiLuF_4$ (LiLuF) with a tunability from 305 nm to 333 nm [54], and Ce:LiSAF with a tunability from 288 nm to 313 nm [53].

Ti^{+3}: Sapphire (660-1180 nm): $Ti^{+3}:Al_2O_3$ gain media have been discovered by Dr. Peter Moulton in 1982, and with time it has quickly become the working horse of ultrafast laser technology, by replacing the dye lasers [55, 100]. Among solid-state lasers, Ti:Sapphire has the broadest tuning range (660-1180 nm), and can directly generate the shortest possible pulses from a laser oscillator (sub-5-fs) [55, 57, 101]. Ti:Sapphire lasers are commercial standards today, and systems can provide (i) more than 3 W of output power with continuous-wave (cw) tuning from 675 to 1100 nm, and (ii) peak powers of hundreds of kW in mode-locked operation with either ~100 fs tunable pulses (680 to 1080 nm) or ~10 fs pulses around 800 nm. Ti:Sapphire gain media has a relatively weak absorption band centered around 490 nm, with a FWHM of ~ 120 nm (460 to 580 nm) [102]. Due to the absence of high power laser diodes in this wavelength range, efficient direct diode pumping of Ti:Sapphire gain media is not currently possible, which is the main disadvantage of Ti:Sapphire technology. In the absence of direct diode pumping, Ti:Sapphire lasers are typically pumped by frequency-doubled diode-pumped neodymium lasers around 532 nm. Unfortunately, these pump sources are inefficient, bulky and cost $50-100k, making the overall system cost high and limiting wide-spread use.

We note here that there is a relatively recent technology based on optically pumped semiconductor lasers, which can generate high laser output power at the green region of spectrum by intracavity frequency doubling. Compared to the diode-pumped neodymium lasers around 532, this new technology has lower cost of ownership, lower thermal problems and lower intensity noise (due to the short lifetimes of semiconductor gain media), and a smaller footprint [103, 104]. Hence, this newly emerging technology might help to reduce the cost of femtosecond laser technology based on Ti:Sapphire gain media in the near future.

We also note here that, recently direct diode pumping of Ti:Sapphire has been demonstrated using a 1-W multimode GaN laser diode around 450 nm. However, the obtained cw power levels were only ~20 mW, due to the presence of an unforeseen parasitic loss induced by pump, which is not present with ~532 nm pumping [102].

Cr^{+2}: ZnSe (1880-3349 nm): Undoped bulk II-VI semiconductors (also referred to as chalcogenides) such as CdSe, ZnSe, and ZnTe have a wide transparency window in the near infrared and mid infrared regions of the electromagnetic spectrum. If divalent transition metal ions (TM^{2+}) such as Cr^{2+}, and Fe^{2+} are introduced into these materials, crystal field splitting and strong electron-phonon coupling lead to the formation of broad absorption and emission bands in the mid infrared. For example, Cr^{2+}:ZnSe possesses a strong absorption band around 1800 nm and a strong emission band in the mid-infrared between 2 and 3 μm. In their pioneering work (in 1996), De Loach et al. studied the absorption and emission characteristics of various zinc chalcogenides doped with Cr^{2+}, Co^{2+}, Ni^{2+}, and Fe^{2+} and evaluated their

potential as active media in the mid infrared, and they have demonstrated room-temperature lasing in Cr^{2+}:ZnSe and Cr^{2+}:ZnS near 2.4 μm [105, 106]. Since then, tunable room-temperature laser action has also been successfully demonstrated with other chalcogenide hosts doped with Cr^{2+}, including CdSe [82, 107, 108], CdTe [109], ZnS_xSe_{1-x} [110], $Cd_xMn_{1-x}Te$ [111-115], CdZnTe [116], and others.

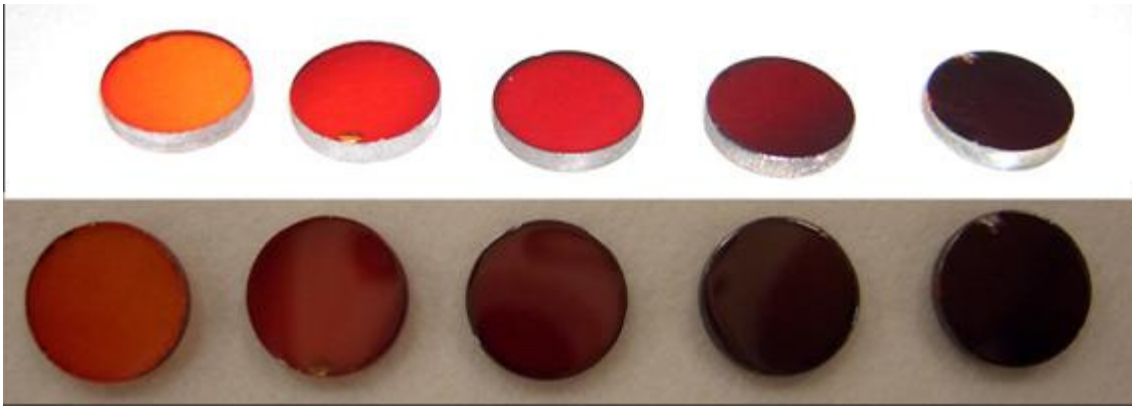

Figure 1.8: Polycrystalline Cr:ZnSe samples prepared by thermal diffusion method (chromium concentration of the samples increase towards right). As the chromium concentration increases, samples get darker due to the presence of an absorption band around 500 nm originating from the $Cr^{2+} + e_{VB} \rightarrow Cr^{1+} + h_{VB}$ transition (where e_{VB} is a valance band electron and h_{VB} is a valance band hole) [117-119]. Cr:ZnSe samples are prepared at Koc University Laser Research Laboratory [120].

Cr^{2+}:ZnSe remains as the most extensively studied member of this class of lasers and, over the last decade, has emerged as a versatile source of broadly tunable laser radiation in the mid-infrared region between 2 and 3 μm. This gain medium possesses many favorable spectroscopic characteristics that enable efficient lasing. These include a 4-level energy structure and absence of excited-state absorption which allow low-threshold continuous-wave (cw) operation, a broad absorption band that overlaps with the operating wavelength of many laser systems for optical pumping, a phonon-broadened emission band that gives rise to wide tunability, and near-unity fluorescence quantum efficiency at room temperature. To date, gain-switched [105, 106], cw [121], diode-pumped [122], mode-locked [123], random-lasing [94], and single-frequency [124] operations have been demonstrated. Broad tunability in the 1973-3349 nm wavelength range in cw operation and in the 1880-3100 nm wavelength range in pulsed operation was also reported [81, 85, 90]. Pulses as short as 80-fs and 95 fs have been demonstrated from saturable absorber mirror and Ker-lens mode-locked Cr:ZnSe lasers[86, 87, 125].

We note in passing that another important TM^{2+}-doped chalcogenide laser is Fe^{2+}:ZnSe in which lasing action was reported in the 4-5 μm wavelength range [88, 126], however Fe:ZnSe requires cooling for continuous wave laser operation [127]. There is a lot of ongoing activity in the investigation of solid-state lasers and saturable absorbers based on Fe^{2+}:ZnSe. We refer the reader to Refs. [88, 126, 128-133] for further discussion on these studies.

1.6 Cr^{+3} Colquiriite Gain Media

As mentioned above, currently Ti:Sapphire lasers are the commercial standards for most of the femtosecond optics applications. However, their high cost sets a strong barrier and limits their widespread usability, slowing down progress in many important areas of science and technology. As an example, multi-photon microscopy is a very powerful tool for biomedical imaging, and it is extensively used in cancer research. However, due to the requirement to use expensive fs Ti:Sapphire technology, the number of research groups that can afford multiphoton microscopy systems is limited, which then limits the progress in cancer research. Hence, lowering the cost of femtosecond technology can have a big impact on society, by accelerating research in basic and applied sciences. Among all the lasing materials, Cr^{3+}-doped Colquiriite crystals are the most attractive low-cost alternative to Ti:Sapphire technology due to (i) their broad absorption bands around ~650 nm which enables direct diode pumping with low-cost diode lasers, and (ii) their broad emission bands around 800 nm enabling down to ~10-fs pulse generation. In this section, we will review Cr:Colquiriite gain media in detail.

Gain Medium	Ti^{3+}:Al_2O_3 (Ti:Sapphire)	Cr^{+3}:$LiSrAlF_6$ (Cr:LiSAF)	Cr^{+3}: $LiSrGaF_6$ (Cr:LiSGaF)	Cr^{+3}:$LiCaAlF_6$ (Cr:LiCAF)
Maximum gain wavelength [nm]	790 [22]	855[22]	~840	780[22]
Tuning range [nm]	660-1180[101]	775-1042[59, 63]	777-977[59, 61]	720-871[1, 59]
Minimum theoretical pulse duration [fs]	3.6[56]	7.6[56]	-	6[56]
Demonstrated shortest pulse length [fs]	~5 [57]	10 [64]	14 [62]	9 [60]
Nonlinear refractive index (n_2) [$x10^{-16}$ cm^2/W]	3.2 [22]	0.8 [22]	1.2 [22]	0.4 [22]
Peak emission cross section (σ_{em}) [$x10^{-20}$ cm^2]	41 [56]	4.8 [56]	3.3 [6]	1.3 [56]
Room-temperature fluorescence lifetime (τ) [μs]	3.2 [56]	67 [56]	88 [6]	175 [56]
$\sigma_{em}\tau$ [μs $x10^{-20}$ cm^2]	131 [56]	322 [56]	290 [56]	228 [56]
Intrinsic slope efficiency [%]	64 [134]	53 [4], 54[59]	52% [6], 60[59]	67 [1], 69[59]
Relative strength of excited-state absorption	0 [55]	0.33 [135]	0.33 [6]	0.18 [135]
Fracture toughness [MPa $m^{1/2}$]	2.2[136]	0.4[136]	-	0.31[136]
Thermal conductivity [W/K.m]	28 [136]	3.1 [136]	3.6 [22]	5.1[136]
$T_{1/2}$, $\tau_F(T_{1/2})=0.5\tau_R$[C]	~100 [55]	69 [137]	88 [138]	255[137], 190 [138]
Lifetime figure of merit	290[139]	105	-	830
Thermal expansion coefficient [$x10^{-6}$/K]	5.3[136]	25 [6]	-	22[6]
Thermal shock resistance [$W/m^{1/2}$]	22[136]	0.4[136]	-	0.5[136]
Auger Rate [10^{16} cm^3/s]	-	6.5 [135]	6.5 [135]	1.65 [135]
Thermal lensing problem	YES	YES[138]	-	NO[138, 140]
Diode Pumping	NO	YES	YES	YES

Table 1.2: Comparison of the spectroscopic and laser parameters of the Ti:Sapphire, Cr:LiSAF, Cr:LiSGaF, and Cr:LiCAF gain media.

Strong electron-phonon coupling in Cr^{+3}:Colquiriite gain media creates three strong and broad absorption bands that are centered around ~275 nm, ~425 nm and ~650 nm (Fig. 1.9). Existence of these broad absorption bands and a relatively long upper state lifetime, which allows reasonable energy storage, enable flashlamp pumping of Cr:Colquiriites. Even though flashlamp pumping is still used for pumping Cr:Colquiriites for some applications, there is a more attractive pump option. The absorption band centered around ~650 nm, has a bandwidth of about ~100 nm (FWHM), and this absorption band enables

direct diode pumping of Cr:Colquiriites by low cost AlGaAs and/or AlGaInP diodes. Direct diode pumping of Cr:Colquiriites allows the construction of compact, efficient and low-cost laser systems. Actually, the total material cost of an entire laser system can be reduced below ~$10k [141], which is a significant advantage over today's femtosecond Ti:Sapphire technology. This has also been the main motivation towards the studies we have performed during this PhD work.

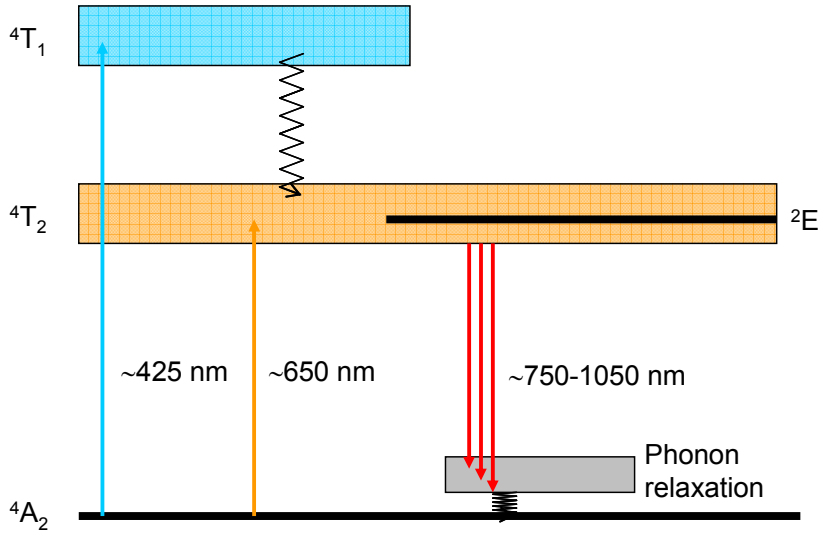

Figure 1.9: Simplified energy level diagram for Cr:LiSAF. Lasing occurs between the vibronically broadened $^4T_2$ and $^4A_2$ levels. Note the presence of the ^2E state which lies within the $^4T_2$ state. The transition between ^2E and $^4T_2$ states is very fast. The lowest energy level of $^4T_2$ state lies below the ^2E state; hence, at equilibrium the $^4T_2$ state is heavily populated, and the ^2E state does not play a role in lasing dynamics. As we will discuss below, in other Cr^{+3}-doped gain media, like ruby and alexandrite, the ^2E energy state can be below the $^4T_2$ state, which then considerably effects the laser properties [16, 48].

Compared to Ti:Sapphire, emission cross section of Cr:Colquiriites is ~8-32 times lower. A lower emission cross section increases the tendency of the laser towards q-switched mode-locking instabilities. Especially for Cr:LiCAF, which has the lowest emission cross section value among Cr:Colquiriites, the stable working range of cw mode-locked lasing is quite narrow for sub-50-fs pulses, and this issue will be discussed in more detail in Chapters 3-5.

However, room temperature upper state lifetime of Cr:Colquiriites is ~21-55 times longer than Ti:Sapphire. Hence, actually for Cr:Colquiriites the product of room temperature upper state lifetime and emission cross section ($\sigma_{em}\tau$) is ~2-2.5 times higher. This product is inversely proportional with the lasing threshold pump power, and provides Cr:Colquiriites lasing thresholds as low as ~5-10 mW (even lower than Ti:Sapphire).

In general a higher $\sigma_{em}\tau$ product also means a higher small signal gain, but unfortunately this is not true for Cr:Colquiriites. This is because small signal gain is proportional to the product of emission cross section and population inversion, and even though Cr:Colquiriites has a quite long upper state lifetime,

they cant achieve high population inversion levels due to the Auger upconversion process. Auger upconversion process exists in all of the Cr:Colquiriites and limits the achievable small signal gain values, and it is one of the biggest drawbacks of Cr:Colquiriites (it does not exists in Ti:Sapphire). More details about this process can be found in Chapter 2, where we will discuss thermal effects in Cr:Colquiriites in detail (Section 2.6). If we compare Cr:Colquiriites within each other, Cr:LiCAF has the lowest gain (smallest $\sim\sigma_{em}\tau$ product), which requires the usage of low-loss optics.

One other advantage of Cr:Colquiriites is their lower quantum defect compared to Ti:Sapphire due to their red shifted pump wavelength (~532 nm versus ~650 nm). A lower quantum defect decreases the thermal load on the crystal and allows higher slope efficiencies. However, Cr:Colquiriites suffer from excited state absorption (ESA) which lowers the obtainable slope efficiencies (Ti:Sapphire does not have ESA). As a result, presence of ESA balances the higher quantum defect observed in Ti:Sapphire gain media, and hence both Cr:Colquiriites and Ti:Sapphire has about ~50-70 % intrinsic slope efficiency. Among Cr:Colquiriites, Cr:LiCAF has the highest intrinsic slope efficiency value (69%), due to its lower excited state absorption and lower quantum defect. The relatively high conversion efficiencies of Cr:Colquiriites, combined with efficient pump diodes, enables electrical-to-optical conversion efficiencies above ~10% in Cr:Colquiriites. This also allows construction of quite compact fs Cr:Colquiriite lasers that can be powered by small batteries.

In terms of thermal and mechanical properties Ti:Sapphire is superior to Cr:Colquiriites. Ti:Sapphire has ~5.5-9 times higher thermal conductivity, about 8 times higher fracture toughness, about 5 times lower thermal expansion coefficient, and about 8 times higher thermal shock resistance. Moreover, as we mentioned above, Ti:Sapphire does not suffer from excited state absorption and Auger upconversion process. Also, thermal quenching of upper state fluorescence lifetime is less significant in Ti:Sapphire compared to Cr:LiSAF and Cr:LiSGaF. Especially, Cr:LiSAF has a critical temperature for thermal quenching of only 69 °C [137], which limits power scaling of laser output power in Cr:LiSAF lasers, or requires careful thermal management (this is true for multi-mode diode pumped systems).

We refer the reader to Section 2.6 for a more detailed discussion of thermal effects in Cr:Colquiriites. However, we want to stress here that among Cr:Colquiriites, Cr:LiCAF stands out with its superior thermal properties, which has the highest intrinsic slope efficiency [142], highest thermal conductivity [142], lowest thermal lensing [138, 140], lowest quantum defect, lowest excited-state absorption [1, 4], and lowest upconversion rate [135]. Most importantly, thermal quenching of fluorescence for Cr^{3+}:LiCAF occurs at a much higher temperature (255 °C) in comparison with Cr^{3+}:LiSAF (69 °C) and Cr:LiSGAF (88 °C) [137]. Finally, the lifetime figure of merit [139], which provides insight about how robust the laser is against thermal effects due to the temperature dependence of the fluorescence lifetime, is about 8

times larger for Cr^{3+}:LiCAF compared to Cr^{3+}:LiSAF (Table 1.2). Due to these superior thermal properties, multimode diode-pumped Cr^{3+}:LiCAF laser systems are capable of producing higher average output powers using standard laser cavities [143]. On the other hand, the currently available pump power levels from single-mode diodes are still relatively low (~1 W in total from 6 diodes); hence, for single-mode diode pumped systems, thermal effects are less significant and output powers from Cr:Colquiriite lasers are limited by the available pump power rather than thermal issues. So, as of today. the superior thermal properties of Cr:LiCAF is an advantage mostly in multimode diode pumped systems.

1.7 Short Literature Review for Cr^{+3}:Colquiriite Lasers

We would like to clearly mention that, several top quality research groups around the world have contributed to the progress of Cr:Colquiriite laser technology, and the work we have done during this PhD would not have been possible without their effort in previous years. It is hard to give a detailed and complete review of earlier contributions, but in the following couple of paragraphs, we will try to summarize some of the main contributions. We apologize in advance for contributions that we could not mention below.

Cr:LiSAF (775-1042 nm): Lasing in Cr:LiSAF gain medium was first demonstrated by Stephan Payne and his coworkers at Lawrence Livermore National Laboratory in 1989 [4]. It is the most extensively studied member of the Cr:Colquiriites, due to its lower scattering losses, higher emission cross section, and broader tunability. The first diode pumping of Cr:LiSAF (and also of other Cr:Colquiriites) was demonstrated by Richard Scheps and his coworkers around 1990 [144-148], who also demonstrated the first diode pumping of alexandrite (Cr^{+3}:$BeAl_2O_4$, first diode pumped Cr^{+3}-doped material) [149]. The first mode-locked operation in Cr:LiSAF is demonstrated in 1992 by Miller et al., using Kerr-lens mode-locking (KLM), from an cw krypton ion pumped laser, where the laser produced ~150 fs long pulses with ~50 mW average power [150]. This was also the first mode-locked operation of a Cr:Colquiriite laser. However, the first work by Miller et al, required the presence of a acousto-optic modulator to initiate and sustain mode-locking [150]. Just a few months later, Evans et al, demonstrated a Ar-ion laser pumped Cr:LiSAF laser that produces 50-fs 150 mW pulses via self-sustaining KLM operation [151], which was the first unambiguous demonstration of mode-locking in KLM mode-locked Cr:Colquiriites. In 1993, Balembois et al, and French et al. demonstrated first mode-locking of multimode diode pumped Cr:LiSAF lasers around the same time, with ps long pulses [152-154]. In 1997, Kopf et al. reported up to 1.42 W of output power in cw operation and 110-fs pulses with 500 mW of average power in cw mode-locked operation from a Cr:LiSAF that was pumped by a 15-W laser diode array [142]. This study required the usage a specialized laser cavity, with cylindrical cavity mirrors and a very thin crystal with

an optimized cooling geometry [142]. These are still the highest average powers obtained from diode pumped Cr^{3+}:LiSAF laser [142].

In 1997, Valentine et al. to the first time demonstrated mode-locked operation of Cr:LiSAF laser that is pumped with inexpensive single-mode (narrow-stripe) diodes [155]. Using a single-mode diode laser providing only ~30 mW of pump power, they have obtained ~200-fs pulses with 230 μJ of pulse energy at a repetition rate of 180 MHz. This initial work demonstrated the feasibility of the idea for low-cost, compact, efficient, battery-powered, diode-pumped femtosecond laser systems based on Cr:Colquiriites [59, 156-161]. In 2000, Sadao Uemura and Kenji Torizuka demonstrated the shortest pulses with Cr:LiSAF gain medium, where they have obtained 10-fs long pulses with 2.3 mW of average power at a repetition rate of 200 MHz, from a multimode diode pumped Cr:LiSAF laser [64, 162]. In 2001, Kemp et al. built the first GHz repetition rate Cr:LiSAF laser, where they have obtained ~146-fs long pulses with 3 mW average power at 1 GHz repetition rate, form a single-mode diode pumped Cr:LiSAF laser [163]. In 2003, Prasankumar et al. has built the first extended cavity Cr:LiSAF laser where they have obtained 39-fs, 0.75 nJ pulses at a repetition rate of 8.6 MHz, from a low-cost Cr:LiSAF laser system pumped by single-mode diodes.

During this PhD work, using recently available higher power single-mode laser diodes as pump sources, we have investigated the cw and cw mode-locked operation of Cr:LiSAF lasers in detail. These studies demonstrated pulse energies of ~2-3 nJ from standard ~100 MHz repetition rate Cr:LiSAF lasers, which was an order of magnitude improvement over earlier results [59]. Using a recently developed broadband oxidized saturable absorber mirror technology, we have demonstrated a record tuning range of 105 nm with ~150-fs long pulses, which we believe is the broadest tuning range ever reported from any saturable absorber mirror mode-locked laser [164]. We have also demonstrated first cavity dumping experiments with a low-cost Cr:LiSAF laser, and obtained nearly transform limited ~120 fs pulses, with pulse energies exceeding 100 nJ at repetition rates of up to 50 kHz [165]. We have also performed attosecond resolution timing jitter characterization of femtosecond diode pumped Cr:LiSAF lasers by using a single crystal balanced optical intensity cross correlator. An integrated timing jitter of less than 137 as in the 10 kHz to 10 MHz range is measured in this study, which is to our knowledge is the lowest reported value of timing jitter for any mode-locked solid-state laser to date [166].

Cr:LiSGaF (777-977 nm): The sister crystal, Cr:LiSGaF, which was discovered by Larry K. Smith and his coworkers at Lawrence Livermore National Laboratory in 1992 [6], has very similar properties with Cr:LiSAF. Cr:LiSGaF has slightly better thermal properties, slightly higher intrinsic slope efficiency and slightly higher nonlinear refractive index as compared to Cr:LiSAF; however, these advantages may not be sufficient to offset the disadvantages due to the lower gain and narrower tuning range. As a result, so

far, Cr:LiSGaF gain medium has not attracted much attention [61, 62, 167-171]. In 1994, Sorokina et al. demonstrated cw mode-locking with Cr:LiSGaF gain medium to the first time, where they have obtained 64-fs pulses with 200 mW of average power from a system pumped by a Kr-ion laser [61, 168, 171]. In 1995, Yanovsky et al. demonstrated the first mode-locked operation of a multimode diode pumped Cr:LiSGAF laser and generated ~100-fs pulses with 35 mW of average output power [167, 172]. In 1997, Sorokina et al. demonstrated 14-fs pulses with 100 mW average power from a Kr-ion pumped Cr:LiSGaF laser, and this is still the shortest pulses reported from the Cr:LiSGaF gain media [62, 169]. In our studies, we have performed the first cw mode-locked laser experiments with a low-cost single-mode diode pumped Cr:LiSGAF laser and obtained record efficiencies, and demonstrated pulse energies of ~2 nJ from standard ~100 MHz repetition rate Cr:LiSGaF lasers [59].

Cr:LiCAF (720-871 nm): Cr:LiCAF gain medium was discovered by Stephan Payne and his coworkers at Lawrence Livermore National Laboratory in 1988 [1, 173]. Even though it is the first Cr:Colquiriite gain media that was discovered, initially it did not attract much attention, and compared to Cr:LiSAF, much less work has been reported using the Cr^{3+}:LiCAF gain media [1-3, 60, 135, 143, 174-184]. This is mostly due to the high level of parasitic losses (~2% per cm) observed in Cr^{3+}:LiCAF during the early years of its production (for Cr:LiSAF passive losses have been around ~0.2% per cm) [136, 180, 185-189]. This high level of passive loss in Cr:LiCAF was caused mostly by micron-sized or smaller precipitates arising during the growth process [185, 188, 189] which prevented efficient laser operation in this low-gain medium [3]. However, with recent advances in crystal growth technology, researchers now claim that, it is now possible to grow Cr:LiCAF with crystal quality approaching that of Cr:LiSAF [187, 190]. The first mode-locked operation in Cr:LiCAF is demonstrated in 1992 by LiKamWa et al., using Kerr-lens mode-locking (KLM), from an Kr ion pumped laser, where the laser produced ~170 fs long pulses with ~1.1 nJ of pulse energy at a repetition rate of 90 MHz [176]. First mode-locked operation of a multimode diode pumped Cr:LiCAF laser was demonstrated by Gabel et al. in 1998 [175]. Using KLM, they have obtained ~52-fs long ~0.7 nJ and ~20-fs ~0.14 nJ pulses at a repetition rate of 95 MHz [175]. In 2002, Wagenblast et al. demonstrated pulses as short as ~9-fs from a KLM mode-locked Cr:LiCAF laser pumped by a Ti:Sapphire laser (2.2 nJ pulse energy at a repetition rate of 97 MHz) [60]. One year later (in 2003), they have also demonstrated ~10-fs ~0.37 nJ pulses form a diode pumped Cr:LiCAF laser system at 110 MHz repetition rate [174].

In 2007, our group has demonstrated first SESAM/SBR mode-locked Cr:LiCAF laser, where we have obtained ~67-fs ~2.5-nJ pulses at 120 MHz from a multimode diode pumped system [143]. In 2008, we have applied single-mode diode pumping to the first time to Cr:LiCAF, and demonstrated ~72-fs ~1.4

nJ pulses at 127 MHz repetition rate [178]. This single-mode diode pumped system has reached electrical-to-optical conversion efficiencies of 12% in cw mode-locked operation [178]. In 2009, we have build the first extended cavity Cr:LiCAF laser, where we have obtained 98 fs pulses with energies of 9.9 nJ and peak powers of ~101 kW at a repetition rate of 9.58 MHz [191].

LiChrom: LiChrom ($LiSrCrF_6$) is 100% Cr doped $LiSrAlF_6$ (LiSAF), which was first demonstrated by Smith et al in 1993[33]. Surprisingly, its physical and optical properties are quite similar to Cr:LiSAF [33]. LiChrom enables direct diode pumping around ~780 nm, where higher power AlGaAs diodes are available [33]. Unfortunately, to our knowledge this crystal is not available commercially.

Applications of Cr:Colquiriite Lasers: Here, we will try to provide a list of demonstrated application areas for Cr:Colquiriite lasers.

- Amplifiers: To our knowledge, In 1992, Perry et al. have built the first Cr:Colquiriite amplifier, using a flash-lamped Cr:LiSAF rod as an amplifier medium, and produced ~150-fs, 8 mJ pulses at a repetition rate of 10 Hz [192]. In 1994, Mellish et al. have demonstrated the first diode-pumped Cr:Colquiriite amplifier system, where they have obtained ~200-fs, ~1 μJ pulses at repetition rates as high as 25 kHz [193, 194].
- Blue generation: Cr:Colquiriite lasers can also be used to generate tunable blue light. In 1995, Falcoz et al, demonstrated tunable blue generation using an intracavity frequency doubled cw Cr:LiSAF laser [195]. In 2002, Agate et al., demonstrated blue generation with electrical-to-optical efficiencies of ~1%, from a $KNbO_3$ crystal pumped by a compact, efficient SESAM/SBR mode-locked Cr:LiSAF laser [196-198].
- White-light generation: In 2001, Holzwarth et al. created broad white light spectrum, spanning more than an optical octave, by using a photonic crystal fiber pumped by a battery powered Cr:LiSAF laser, and showed that its frequency comb is suited for optical frequency metrology applications [199].
- Optical coherence tomography: In 2004, Wagenblast et al. used a diode pumped KLM mode-locked Cr:LiCAF laser for optical coherence tomography application [200].
- Multiphoton microscopy: In 1996, Svoboda et al demonstrated the use of low-cost Cr:LiSAF lasers for multiphoton microscopy to the first time[201]. In 2008, our group have demonstrated the use of Cr:LiCAF laser in multiphoton microscopy [202].
- Low timing jitter Source: In 1999, Hidemi Tsuchida, investigated the timing jitter noise performance of Cr:Colquiriite lasers that is locked to reference electronic oscillators [203-205].

In 2010, we have measured the timing jitter noise of Cr:LiSAF lasers using an optical cross correlator, and found the upper limit for timing jitter to be 137 as in the 10 kHz to 10 MHz range [166].

1.8 Other Cr^{+3} Doped Gain Media

In their fist paper on Cr:Colquiriite lasers, Payne et al. lists 15 laser materials where Cr^{+3} ion has been shown to lase at that time: $BeA1_2O_4$, $Be_3Al_2(SiO_3)_6$, $Gd_3Sc_2Ga_3O_{12}$, $Gd_3Sc_2Al_3O_{12}$, $LaLu_2Ga_3O_{12}$, $Y_3Ga_5O_{12}$, $Y_3Sc_2Ga_3O_{12}$, $Na_3Ga_2Li_3F_{12}$, $KZnF_3$, $SrAlF_5$, $ZnWO_4$, $Al_2(WO_4)_3$, $ScBO_3$, and $La_3Ga_2SiO_{14}$ [1]. However among those only a few of them can generate laser slope efficiencies above 50%, including Cr^{+3}:$BeA1_2O_4$ (alexandrite) and Cr^{+3}:$Be_3Al_2(SiO_3)_6$ (emerald), besides the Cr:Colquiriites, which is the topic of this PhD thesis. Most of these gain media suffer from strong excited state absorption which prevent efficient lasing [1]. So we want to stress here that Cr^{+3}: Colquiriites are among the few Cr^{+3}-doped gain media with rare physical and optical properties, which enable efficient laser operation. In this section, we will review Cr^{+3}: Al_2O_3 (ruby), Cr^{+3}: $BeAl_2O_4$ (alexandrite) and Cr^{+3}:$Be_3Al_2(SiO_3)_6$ (emerald) gain media, due to their historic importance.

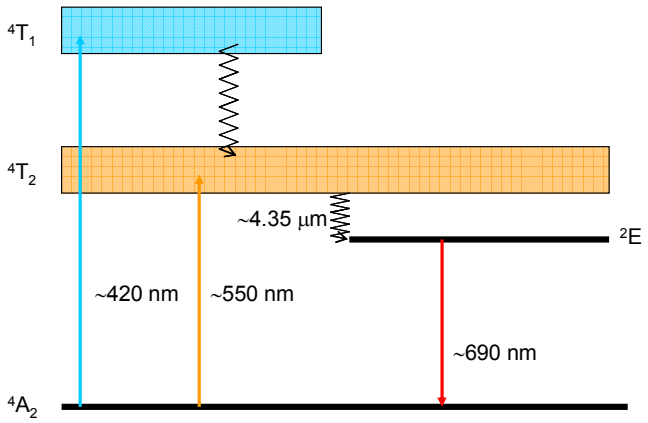

Figure 1.10: Simplified energy level diagram for ruby gain medium.

Cr^{+3}: Al_2O_3 (Ruby): Ruby gain media is the first gain medium where lasing is demonstrated [17]. However unlike Cr:Colquiriites, ruby is not a phonon broadened laser system. Moreover, it is a three level laser systems, as we can see from the simplified energy diagram which is shown in Fig. 1.10 [16, 48]. Similar to Cr:Colquiriites, ruby can be excited either in the blue (~420 nm) or green (~550 nm) regions of the spectrum. However, unlike the Cr:Colquiriites, the ^2E energy level lies well below the $^4T_2$ in ruby (compare with Fig. 1.9). The $^4T_1$ and $^4T_2$ states has very short lifetimes (1 ps), and decay back to the metastable ^2E, which has a lifetime of about 3 ms [16, 48]. Hence, at room temperature, one can assume

that only the ^2E state is occupied in ruby upon optical excitation. Lasing transition occurs between the ^2E and $^4A_2$ states and transitions between these states are not phonon broadened. So ruby lasing line around ~690 nm is quite sharp, enabling only ps pulse generation in mode-locked regime. Also, due to the three level energy structure, high pump powers is required to obtain lasing in ruby; hence, it is in general pumped by pulsed sources [16, 48]. On the other hand, ruby has broad absorption bands that matches the emission spectrum of flashlamps, and has a long upper state lifetime, and a reasonably large emission cross section (~$2.5x10^{-20}$ cm^2), which make ruby lasers quite attractive as a pulsed lasers source in the visible [16, 48]. Nowadays they are mostly replaced by Nd-based laser systems, except for cases where their short emission wavelength is an advantage such as pulses holography [16, 48]. For example, Physical Sciences Inc. offers a pulsed ruby laser with repetition rates up 500 kHz, pulsewidths of ~10 ns, and a pulse energy of ~1-J, for high-speed photography, ballistic impact, flow visualization applications [206].

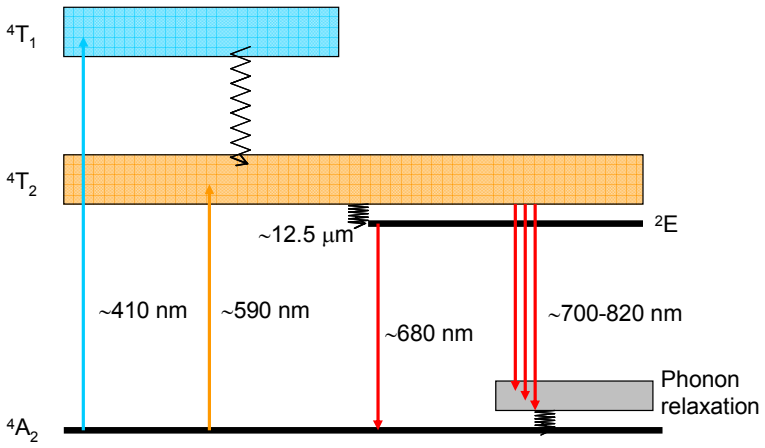

Figure 1.11: Simplified energy level diagram for alexandrite gain medium.

Cr^{+3}: $BeAl_2O_4$ (Alexandrite): Alexandrite was the first broadly tunable ion solid state laser that can be operated at room temperature, and historically it took quite a lot of attention (it has an intrinsic slope efficiency of ~65% at room temperature) [16, 48, 96, 207-210]. Figure 1.11 shows a simplified energy level structure for alexandrite gain medium, which actually looks quite similar to ruby, where the ^2E state lies below the vibronically broadened $^4T_2$ level. However, the energy difference between the ^2E and $^4T_2$ levels is lower in alexandrite (~12.5 μm or ~800 cm^{-1}), which is only a few kT at room temperature (~48 μm). Hence, in thermal equilibrium, upon excitation, a reasonable level of the states in the $^4T_2$ level is populated. Duo to Franck-Condon principle, transitions from the $^4T_2$ level to $^4A_2$ is preferable over transition from the ^2E level to $^4A_2$ level; hence, alexandrite can produce broadly tunable laser radiation in the 700-820 nm wavelength range [16, 48]. To increase the performance of alexandrite lasers, the crystal

is usually held at elevated temperatures (50-70 °C) [16, 48, 211]. Flashlamp pumped alexandrite laser system are capable of generating average power as high as 100 W at low repetition rates (~25 Hz) [16, 48]. In 1990, Scheps et al. demonstrated first diode pumped operation of the alexandrite laser using two 5 mW diodes around 680 nm, which pumped into the narrow transition between the ^2E and $^4A_2$ levels [149]. In 1993, Scheps et al. also demonstrated diode pumped cw operation via pumping into the $^4T_2$ level using 640 nm multimode diodes, where they have also reported slope efficiencies as high as 64% upon pumping with a dye laser [212]. In mode-locking experiments, ~35 ps long pulses were obtained from an actively mode-locked alexandrite laser pumped by a 3W Ar-ion laser [22, 213]. The laser was tunable in a narrow range around 750 nm (~30 nm tunability), with average powers of 7-15 mW at 112 MHz repetition rate [213]. By mode-locking with saturable absorbers dyes, pulses of ~10-ps have been obtained from a flashlamp pumped alexandrite laser [214]. To our knowledge sub-ps pulses have not been demonstrated with alexandrite gain medium yet. Alexandrite lasers are still in use today. For example, pulsed alexandrite lasers with ms pulsewidths find use in medical application areas such as hair removal and treatment of surface vein [215].

Cr^{+3}: $Be_3Al_2(SiO_3)^6$ (Emerald): Emerald is another Cr^{+3} gain media, besides Cr:Colquiriites, that can provide more than 50% slope efficiency. Emerald's emission cross section is four times larger than to alexandrite, but its thermal conductivity is about 6 times lower [216]. Michael L. Shand and John C. Walling introduced the emerald laser in their 1982 paper, where they have demonstrated lasing upon pulsed flashlamp pumping [217]. However, the crystal was quite lossy (11%/cm), and they could only obtain 6.8 mJ pulses with 100-J pump energy [217]. In 1984, Michael L. Shand and S. T. Lai demonstrated a cw Kr-ion laser pumped emerald laser, and demonstrated slope efficiencies as high as 34%, and a tunability from 729 to 809 nm in quasi-cw operation [218]. The slope efficiency was limited by the passive losses of the crystal, which was around 2.4%/cm [218]. In 1987, S. T. Lai demonstrated slope efficiencies as high as 64%, and average output powers as high as 1.6 W, and a tunability from 720 to 842 nm, from a Kr-ion laser pumped quasi cw emerald laser using a lower loss crystal; however, the crystal size they could grow was quite small (4.5cm x 1.5 cm x0.6 cm) [219]. In 2006, Zhenqiang Chen and Ge Zhang reported a cw emerald laser pumped by multimode laser diodes around 660 nm; however, the laser produced only 24 mW of out put power using ~2.5 W of pump power[216]. The progress in emerald laser research seems to be slowed down by the difficulty of growing large size, high optical quality samples [219].

CHAPTER 2

CONTINUOUS WAVE CR:COLQUIRIITE LASERS

Possible diode pumping options for Cr:Colquiriite gain media include multimode laser diode arrays [142], multimode broad-stripe single-emitter diodes [143, 153, 174, 177, 220], and single transverse-mode laser diodes [160, 178, 220]. Laser diode arrays can provide pump powers above 10 W, but are relatively expensive and have poor beam quality (M^2 ~1000 along the axis of the array) [142]. In comparison, broad-stripe multimode, single emitter diodes are cheaper than arrays, have higher beam quality (M^2 ~10 along the junction axis) [143, 174], and can now produce up to 1.5 W at 665 nm (n-Light Photonics). Single mode diodes can only provide about ~150 mW of output (recently ~200 mW), which is quite low compared to others. However, single-mode diode-pumping provides lower cost, ease of operation, better mode-matching, significantly lower lasing thresholds, reduced thermal effects, and higher efficiencies [178, 220]. Moreover, for single-mode diode-pumping, no cooling is needed for the pump diodes or the laser crystal, enabling compact, portable systems (this is true for 130 mW 660 nm diodes, 150 mW 640 nm diodes requires cooling).

In this chapter, we will present continuous wave lasing results with single-mode and multimode single emitter diode pumped Cr:LiSAF, Cr:LiSGaF, and Cr:LiCAF gain media. We have not used laser diode arrays in this research due to their high cost, and poor beam quality. Also, multimode single emitter diode pumping is only applied to Cr:LiCAF gain medium, due to its superior thermal properties.

The chapter is organized as follows: In Section 2.1, we first present cw lasing results for a Ti:Sapphire laser pumped Cr^{3+}:LiCAF laser. This experiment aimed to determine the upper limit of performance for Cr:LiCAF gain medium, since, the Ti:Sapphire laser provides a symmetric and diffraction limited output beam profile. Then, in Sections 2.2-2.4, we will present cw lasing results of single-mode diode pumped Cr:LiCAF, Cr:LiSAF, and Cr:LiSGaF gain media, respectively. In Section 2.5, we will present multimode broad-stripe single-emitter diode pumping performance of a cw Cr:LiCAF laser. Then, Section 2.6 will discuss thermal effects in Cr:Colquiriite gain media. Later in Section 2.7 we will present a quick overview of cw lasing results with the recently available higher power single-mode diodes. Section 2.8 will discuss possible future work with multimode diode pumped Cr:LiCAF lasers, and present some initial motivating experiments. Section 2.9 discusses the self q-switching behavior we have observed in Cr:Colquiriite gain media. Finally, in Sections 2.10, we will compare the cw performance of

Cr:Colquiriites with each other. We refer the reader to Appendix A for more information on the mirrors sets used in this study, and to Appendix B, for specs of the laser diodes that we have used to pump the Cr:Colquiriite lasers.

2.1 CW Operation of the Ti: Sapphire Pumped Cr:LiCAF Laser

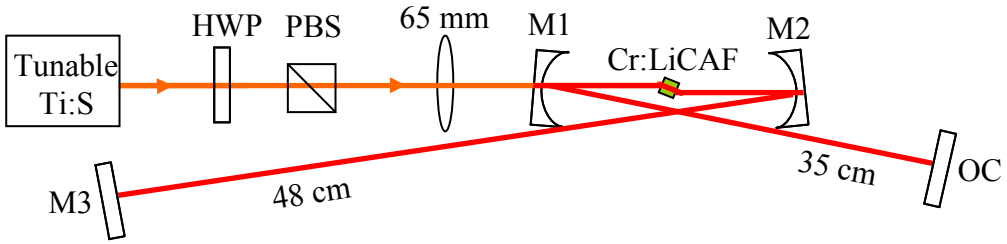

Figure 2.1: Schematic of the tunable Ti:Sapphire-pumped Cr^{3+}:LiCAF laser system. The Ti:Sapphire laser (Tunable Ti:S) was tuned to provide up to 550 mW of pump power at 694 nm. HWP: half wave plate, PBS: polarizing beam splitter cube, M1-M2: curved pump mirrors with R= 75 mm, M3: flat high reflector, OC: output coupler.

In order to determine the optimum performance as a benchmark, studies were first performed using a tunable Ti:Sapphire pump laser with a symmetric and diffraction limited output beam (Fig. 2.2). Figure 2.1 shows a schematic of the Ti:Sapphire pumped cw Cr^{3+}:LiCAF laser. The home-built tunable Ti:Sapphire laser (Tunable Ti:S) is pumped by 5-W of green light from a frequency doubled Nd:Vanadate laser (Coherent, Verdi). The maximum output power from the Cr^{3+}:LiCAF laser was obtained at a pump wavelength of 694 nm (Fig. 2.2 (a)), in agreement with previous reports (693 nm, [60]). At this wavelength, as much as 550 mW of TM polarized pump light was available from the Ti:Sapphire laser. A half wave plate (HWP) and a polarizing beam splitter (PBS) cube was used to adjust the incident pump power, and a 65 mm focal length lens was used to focus the pump beam into the crystal. The Cr^{3+}:LiCAF laser resonator was a standard x-folded, astigmatically compensated cavity, with two curved pump mirrors, each with a radius of curvature (roc) of 75 mm (M1 and M2), a flat end high reflector (M3), and a flat output coupler (OC). Pump mirrors (M1-M2) had a reflectivity bandwidth extending from 750 nm to 850 nm and a transmission >95 % at the pump wavelength 694 nm (Layertec Cr:Colquiriite pump mirror set I, a detailed description is given in section Appendix A3).

Continuous wave laser performance was measured with ten different output couplers (0.5, 0.85, 1.05, 1.2, 1.4, 1.95, 3, 5, 6 and 10 % @ ~800 nm). The gain medium was a 2-mm-long, Brewster-cut, 10 mole % Cr-doped Cr^{3+}:LiCAF crystal (VLOC) [143, 174, 178], which was mounted with indium foil in a copper holder (10 mole % doping corresponds to a chromium concentration of about 9.5×10^{20} ions/cm^3 [1]). The crystal was mounted with indium foil in a copper holder, as shown in Fig. 2.3. The crystal absorbed ~70% of the incident TM polarized pump light at 694 nm, and the maximum total absorbed

pump power was ~360 mW. Water cooling of the crystal was not required at these low absorbed pump power levels. Arm lengths of 35 cm (OC arm) and 48 cm were used to obtain a laser mode size of ~20 μm x 28 μm (sagittal x tangential) inside the Cr:LiCAF crystal, which has a refractive index of n~1.4 [60]).

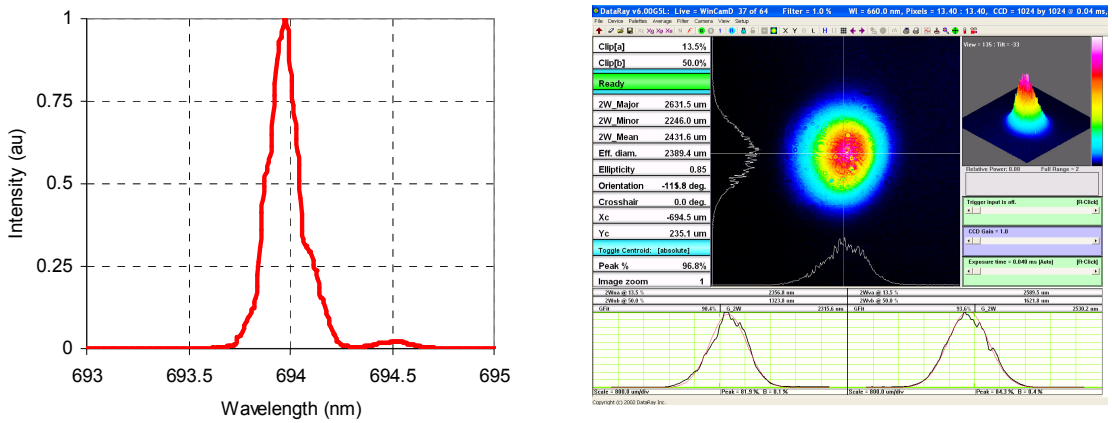

Figure 2.2 (Left) Ti:Sapphire pump laser wavelength, (Right) Shape of the Ti:Sapphire laser output measured by a CCD camera.

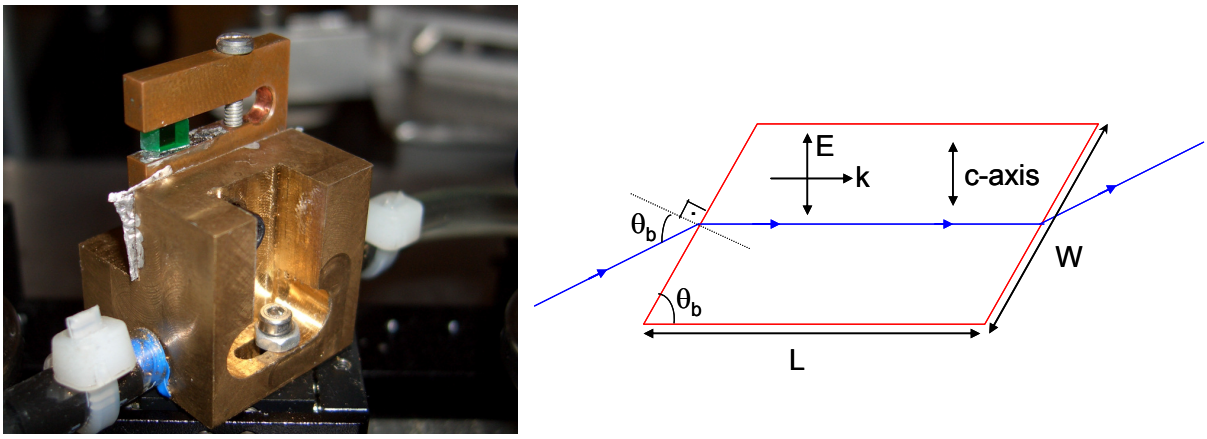

Figure 2.3: (Left) Picture of the Cr^{3+}:LiCAF crystal, and its holder. Crystal holder might be cooled by circulating water from a chiller. Water cooling is not required for single-mode diode pumping. (Right) Top view of the Brewster-Brewster cut Cr:LiCAF crystal with the electric filed parallel to the crystal axis (E//c). Optical path of a TM polarized light is inside the crystal is also shown (blue line). L: Crystal thickness, W: Width of the crystal.

Figure 2.4 shows an example of the measured cw performance of the Ti:Sapphire pumped Cr:LiCAF laser with the 0.5 and 1.95% transmission output couplers. With the 1.95% output coupler, the laser produced up to ~180 mW of output power with ~340 mW of absorbed pump power. The corresponding threshold pump power and slope efficiency with respect to the absorbed pump power were ~40 mW and ~60%, respectively. Threshold pump powers as low as ~11 mW with the 0.5% output coupler and ~6 mW with a high reflector were measured. These, we believe are the lowest threshold absorbed pump powers

reported for Cr^{3+}:LiCAF lasers[145]. The high slope efficiencies and low threshold pump powers can be attributed to the extremely low loss optics used in the laser (R >99.95%).

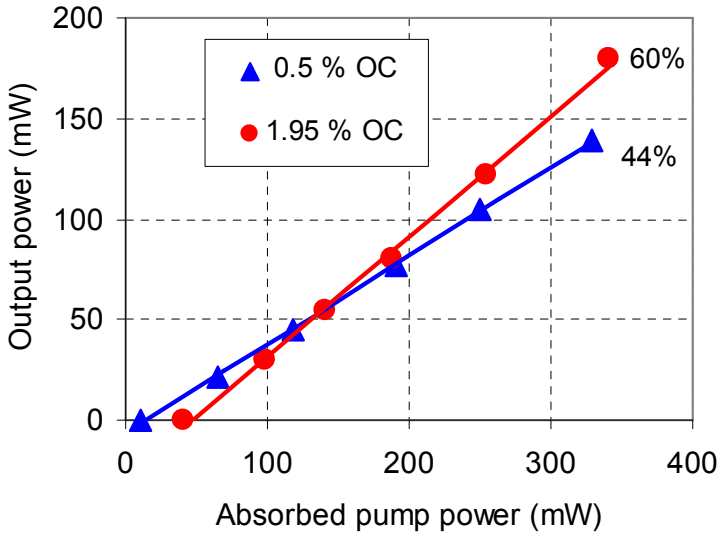

Figure 2.4: Continuous-wave efficiency curves for the Ti:Sapphire pumped Cr^{3+}:LiCAF laser (Fig. 2.1), taken with the 0.5 and 1.95% output couplers. The measured slope efficiencies with respect to absorbed pump power were 44 and 60% for the 0.5 and 1.95% output couplers, respectively.

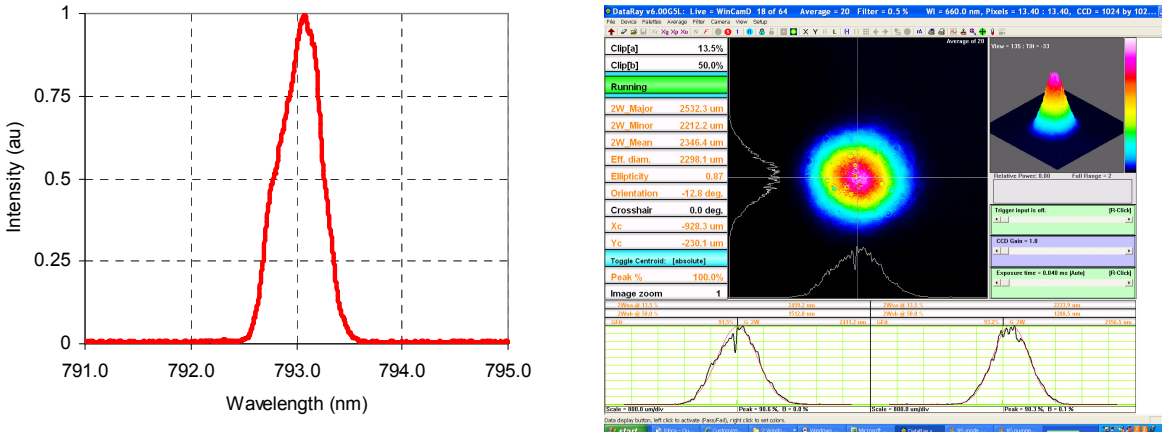

Figure 2.5 (Left) Free running laser wavelength, and (right) laser output mode measured with the 1.4 % OC for the cw Cr:LiCAF laser.

Figure 2.6 shows the measured variation of the maximum obtainable cw output power with output coupler (OC) transmission, taken at the maximum incident pump power of 550 mW. The free-running cw output wavelength was ~790 nm for all output couplers (Fig. 2.5). Figure 2.6 confirms the low gain nature of the Cr^{3+}:LiCAF medium, due to its small emission cross section, and shows that the roundtrip gain is less than 10% [180]. Also, Fig. 2.6 shows that the optimum output coupling for Cr^{3+}:LiCAF gain media lies in the 1-2% range, and for this configuration the highest output power was obtained with the 1.4% OC, which is in good agreement with previously reported values (1.25%) [177].

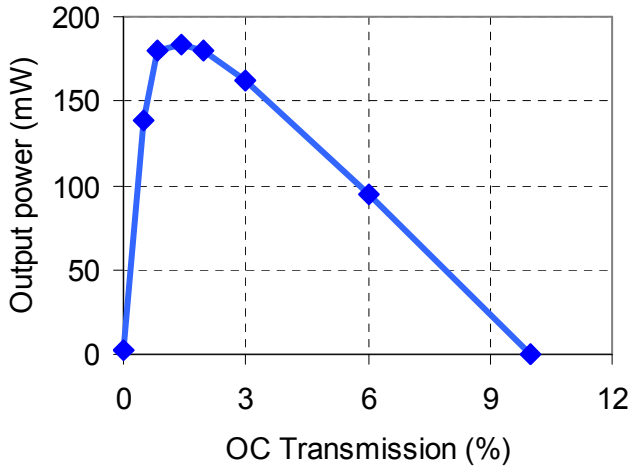

Figure 2.6: Measured variation of the maximum obtainable output power with output coupler transmission taken with full pump power of 360 mW (absorbed). Optimum output coupling is 1-2 %. The data were taken using the Ti:Sapphire-pumped Cr^{3+}:LiCAF laser system shown in Fig. 2.1.

Figure 2.7 shows the variation of the measured lasing threshold pump power with output coupler transmission (circular dots). According to Findlay-Clay analysis [1, 221] the threshold pump power P_{th} required to attain lasing is proportional to the cavity total round trip loss (L) and can be expressed as

$$P_{th} = \frac{\pi\left(w_p^2 + w_c^2\right)h\nu_p}{4\left(\sigma_e - \sigma_{ESA}\right)\tau_f \eta_p}\left(2A_g + T + L\right), \qquad (2.1)$$

where h is Planck's constant, ν_p is the pump photon frequency, w_p and w_c are the pump and cavity beam waists, η_p is the pumping efficiency, σ_e and σ_{ESA} are the emission and excited state absorption (ESA) cross section values at the lasing wavelength, τ_f is the fluorescence lifetime of the upper laser level, A_g is the ground state absorption of the Cr^{3+} ions, and T is the transmission of the output coupler. For the free running laser, the laser wavelength was around ~790 nm, and self absorption losses due to the Cr^{3+} ion (A_g) are negligible at this wavelength. Then, the expression for the incident threshold pump power can be written as $P_{th} = C(T + L)$, where all the parameters in front of (T+L) in Eq (2.1) are combined in a single constant C. Hence, under this approximation, P_{th} shows a linear dependence on the cavity total round trip loss (L). Using Eq. (2.1) and the measured variation of the threshold pump power with output coupler transmission (Fig. 2.7), we determined the cavity total round trip loss (L) to be 0.3 ± 0.1%. The linear solid line in Fig. 2.7 is the theoretical best fit to the experimental data.

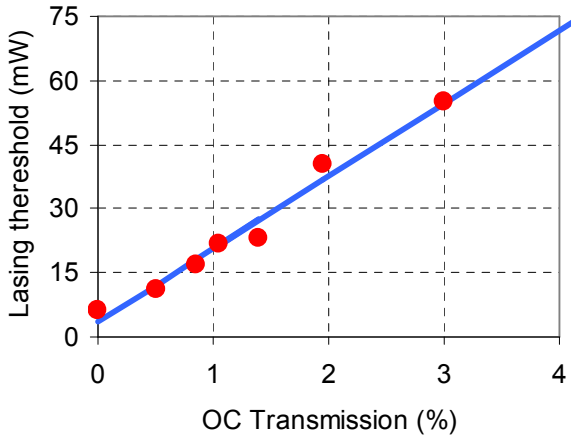

Figure 2.7: Measured variation of the pump power required to attain lasing (P_{th}) as a function of output coupler transmission (T). Using Findlay-Clay analysis, the round-trip passive cavity loss (L) was estimated to be 0.3 ± 0.1 %. Solid line is the best linear fit to the experimentally measured data using Eq. (2.1). The data were taken using the Ti:Sapphire-pumped Cr^{3+}:LiCAF laser system shown in Fig. 2.1.

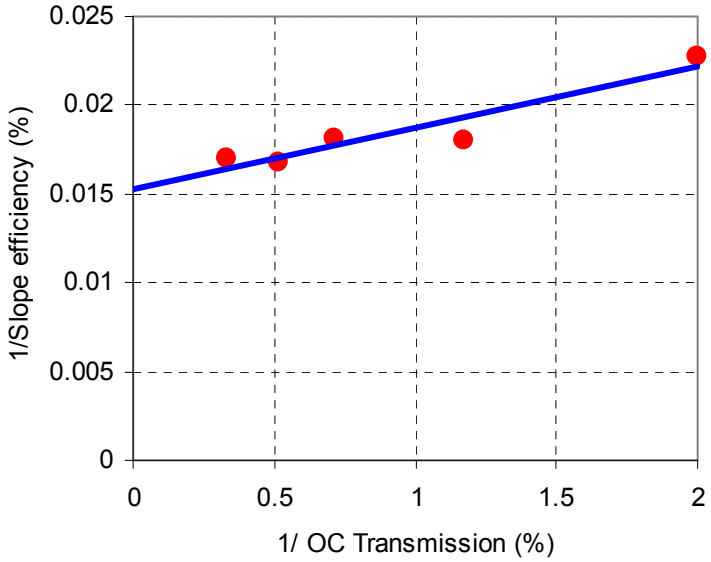

Figure 2.8: Measured variation of 1/η (inverse of slope efficiency) with 1/T (inverse of the output coupling). Using Caird analysis, the round-trip passive cavity loss (L) and intrinsic slope efficiency (η_0) were calculated to be 0.4± 0.2 % and 69 ± 5 %, respectively. Solid line is the best linear fit to the experimentally measured data using Eq. (2). The data were taken using the Ti:Sapphire-pumped Cr^{3+}:LiCAF laser system shown in Fig. 2.1.

Resonator losses at the lasing wavelength can also be estimated by using Caird [1, 222] analysis. In Caird analysis, one uses the fact that the slope efficiency η of the laser can be expressed to a good approximation as

$$\eta = \left[\left(\frac{h\nu_l}{h\nu_p}\right)\eta_p\left(\frac{\sigma_e - \sigma_{ESA}}{\sigma_e}\right)\right]\frac{T}{T+L} = \eta_0\frac{T}{T+L}, \qquad (2.2)$$

where v_l and is the laser photon frequency. The terms in square parentheses can be combined together and could be defined as η_0, which is the maximum (intrinsic) slope efficiency that can be obtained at high output coupling. Figure 2.8 shows the experimentally measured variation of the inverse slope efficiency ($1/\eta$) as a function of the inverse output coupling ($1/T$) for the Cr^{3+}:LiCAF laser (circular dots), which roughly lies on a straight line. The relatively large fluctuation in the data (both in Fig. 2.7 and 2.8) is mainly due to the difference in the passive losses of the output couplers, which become important for this low gain material. Using Eq. (2.2), the best-fit values of L and η_0 were determined to be 0.4± 0.2% and 69 ± 5%, respectively. Again, the linear solid line in Fig. 2.8 is the theoretical best fit to the experimental data.

Within experimental errors, the round trip passive resonator losses (L) estimated using Caird (0.4± 0.2%) and Findlay-Clay (0.3 ± 0.1%) analyses are in good agreement with each other. Since extremely low loss optics were used in the cavity, the dominant source of loss should be from the crystal. For the 2-mm-long crystal, this corresponds to a loss of ~0.8% per cm. Klimm et al. showed that, for Cr^{3+}:LiCAF crystals with low chromium concentration, it is possible to obtain crystals with passive losses below 0.2% per cm [190]. The crystal used in this study had a high chromium concentration (10 mole%), so we believe the measured loss level (~0.8% per cm) is reasonable, and confirms the presence of concentration dependent parasitic losses in Cr^{3+}:LiCAF gain media [177, 223]. However, it is not clear whether further advances in crystal growth technology will reduce the loss level of highly doped samples, since some part of this loss might be due to a parasitic absorption band of the chromium dopant centered around 1040 nm [223].

The best fit value for the intrinsic slope efficiency (69 ± 5%) is quite high, and shows the potential of the Cr^{3+}:LiCAF gain media as an efficient laser source. This value is in very good agreement with the value (67%) reported by Payne et al. for a 1.08% doped Cr^{3+}:LiCAF crystal [1]. The similarities in the reported values show that the excited state absorption in the 10% doped crystal used in this study and the 1.08% doped crystal used in Payne's study are similar (Eq. 2). Hence, one can conclude that despite the early indications [177], the variation of excited state emission cross section with chromium concentration is significantly less than expected, although further detailed investigations are necessary to confirm this [177]. The quantum defect limited value of the slope efficiency for our Cr^{3+}:LiCAF laser was ~88%, ($\eta_p \approx 1$ [1, 4], $\lambda_l \approx 790$ nm and $\lambda_p \approx 694$ nm), and the difference between the quantum defect limited efficiency (~88%) and measured intrinsic slope efficiency (~69 ± 5%) could be attributed to the presence of excited state absorption (ESA) [1]. Using the best fit value of η_0 and Eq. (2.2), we estimated the ESA cross section to be less than 20% of the value of the emission cross section at the lasing wavelength (~790 nm) [6]. This confirms that ESA is relatively insignificant for Cr^{3+}:LiCAF, as several previous studies

have already shown (Table 1.2) [1, 4, 6, 180, 223, 224]. For comparison, the intrinsic slope efficiency of Cr^{3+}:LiSAF is only 53%, which is due to the stronger ESA band at the lasing wavelength of Cr^{3+}:LiSAF (855 nm) [4, 225, 226].

2.2 CW Operation of the Single-Mode Diode Pumped Cr:LiCAF Laser

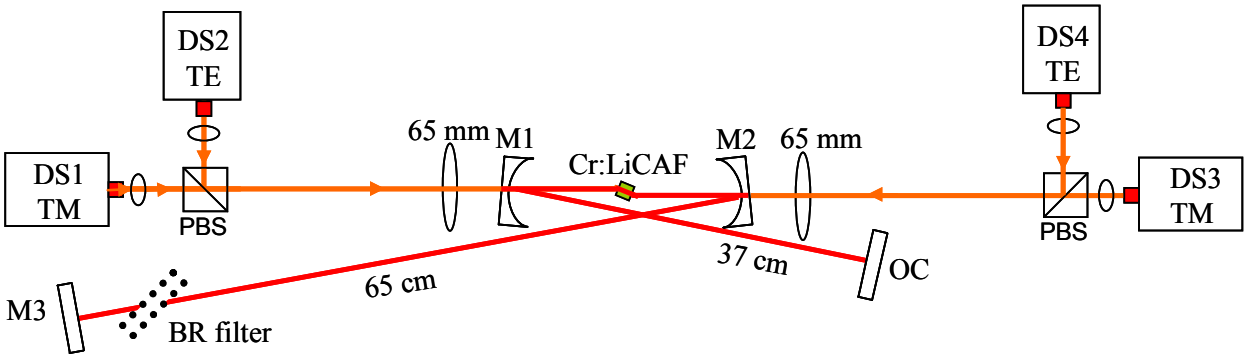

Figure 2.9: Schematic of the single-mode diode pumped Cr^{3+}:LiCAF laser system. The Cr:LiCAF is pumped by four ~150 mW 660 nm single-mode diodes. BR filter: Birefringent filter.

Figure 2.9 shows a schematic of the single-mode diode-pumped Cr^{3+}:LiCAF laser cavity used for cw laser experiments. Four ~660±2 nm AlGaInP single-mode diodes, with circularized output (VPSL-0660-130-X-5-G, Blue Sky Research), each costing only ~$150, were used as the pump source (DS1-DS4). At a drive current of 220 mA (2.6 V), the diodes provided up to ~160-170 mW of output each, with a corresponding electrical to optical conversion efficiency of ~28-30%. At this maximum driving current (220 mA), the four diodes required at total of ~2.3 W and produced ~660 mW of output power. Aspheric lenses with a focal length of 4.5 mm were used to collimate the diode output beams. Since the diodes were linearly polarized, polarization multiplexing using PBS cubes could be employed to couple pairs of diodes from each side of the crystal. Two 65-mm focal length lenses were used to focus the pump beams inside the crystal. The cw laser resonator was similar to what was described earlier (Fig. 2.1) and again same optical elements were used to ensure that the loss level was nearly the same. Cavity arm lengths of 37 cm (OC arm) and 65 cm were used to obtain a laser mode size of ~16 μm x 22 μm (sagittal x tangential) inside the Cr^{3+}:LiCAF crystal. The 10% doped Cr^{3+}:LiCAF crystal absorbed 97.5% and 84% (0.9 x 93.5%) of the incident TM and TE polarized pump lights at ~660 nm, respectively, and the total absorbed pump power was ~570 mW. Similar to the Ti:Sapphire pumped cavity, water cooling of the crystal was not required at these low pump power levels. This is another very important advantage of the single-mode diode pumping configuration. For the cw tuning experiments we have either used a 400 μm thick fused silica birefringent plate or a Brewster cut fused silica prism.

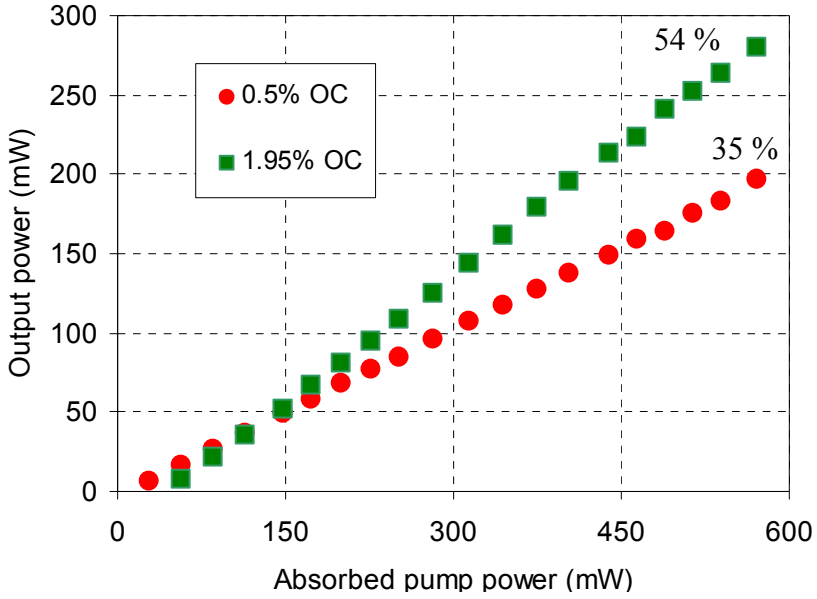

Figure 2.10: CW efficiency curves for the single diode-pumped Cr^{3+}:LiCAF laser (Fig. 2.9), taken with 0.5 and 1.95% output couplers. The measured slope efficiencies with respect to absorbed pump power were 35 and 54% for the 0.5 and 1.95% output couplers, respectively.

Cw performance of the cavity was measured with six different output couplers, with transmission between 0.5 and 10%. The best cw laser power performance was obtained with the 1.95% output coupler. Figure 2.10 shows the cw laser efficiency curves taken using the 0.5 and 1.95% transmitting output couplers. Using the 1.95% output coupler, the laser produced up to 280 mW of output power with 570 mW of absorbed pump power, at a slope efficiency of ~54%. To the best of our knowledge, this is the highest slope efficiency obtained from any diode pumped Cr^{3+}:colquiriite laser [177]. The corresponding optical to optical conversion efficiency was ~42% (280 mW / 660 mW), and the electrical to optical conversion efficiency was around 12.2% (280 mW / 2.3 W). Using the 0.5% OC, lasing could be obtained with record low incident pump power levels of ~10 mW (corresponding absorbed pump power was ~9 mW). This lasing threshold power is even lower than the value obtained with the Ti:Sapphire pumped setup (~11 mW), due to tighter focusing. The maximum slope efficiency obtained with single mode diode pumping (~54%) is close to what was obtained with Ti:Sapphire pumped cavity (~60%). The difference in slope efficiencies is probably due to the aberrations in the pump beam caused by the mode correction optics.

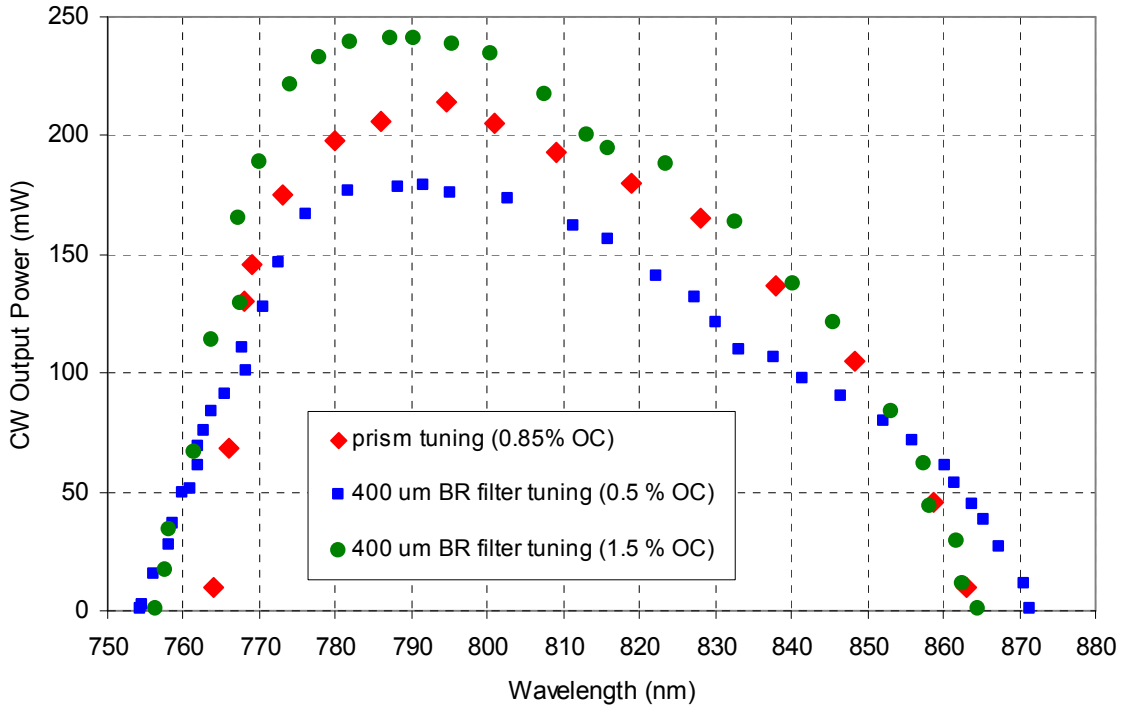

Figure 2.11: CW tuning curves for the single-mode diode pumped Cr^{3+}:LiCAF laser taken with (a) a 0.85% output coupler and a prism for tuning (b) 0.5% output coupler and the 400 μm birefringent plate for tuning, (c) 1.5% output coupler and the 400 μm birefringent plate for tuning. Laser wavelength could be tuned smoothly between 754 and 871 nm. The data were taken at an absorbed pump power of ~570 mW using the single-mode diode-pumped Cr^{3+}:LiCAF laser system shown in Fig. 2.9. Layertec Cr:Colquiriite pump mirror set I is used in all of the tuning data.

We have also studied the cw tuning characteristics of the Cr^{3+}:LiCAF laser. Figure 2.11 shows the measured tuning curves with the prism or with the 400 μm thick BR plate. For tuning with a prism, a Brewster-cut fused silica prism was inserted into the HR arm (~35 cm away from the HR, M3 in Fig. 2.9) to enable tuning. The relatively long distance between the HR and the prism (~35 cm) resulted in narrow-linewidth laser operation (FWHM≈0.2 nm). The laser output could be tuned continuously between 765 and 865 nm, with output powers exceeding 200 mW around 790 nm. Usage of the birefringent plate for tuning enabled a slightly broader tuning range, which might due to an increased modulation depth for wavelength selectivity. Using the BR plate with a 1.5% output coupler, laser could be tuned from 756 to 865 nm. The 0.5% output coupler provided a tuning range from 754 nm to 871 nm. This is the first demonstration of tuning above 840 nm for Cr:LiCAF [1, 220]. Previously, Payne et al. demonstrated tuning between 720-840 nm in quasi cw operation using a 0.32 mol.% doped Cr^{3+}:LiCAF crystal [1]. For our case, tuning below 754 nm could not be achieved due to the overlap of the absorption and emission bands, which caused strong self-absorption losses for the highly doped 10% crystal (self-absorption losses are represented by the term A_g in Eq. 2.1). Measured single pass absorption of the 2 mm long 10%

chromium doped Cr:LiCAF crystal is plotted in Fig. 2.12 along with the normalized cw tuning range and the emission spectrum. For example, the single-pass absorption of the crystal was measured to be 1% and 3.4% at 762 and 750 nm, respectively. For this low gain medium, such a loss level is enough to prevent lasing. The low doping and pulsed excitation (1 ms pulses with 2W of average power) may enable the extended short wavelength tuning in [1].

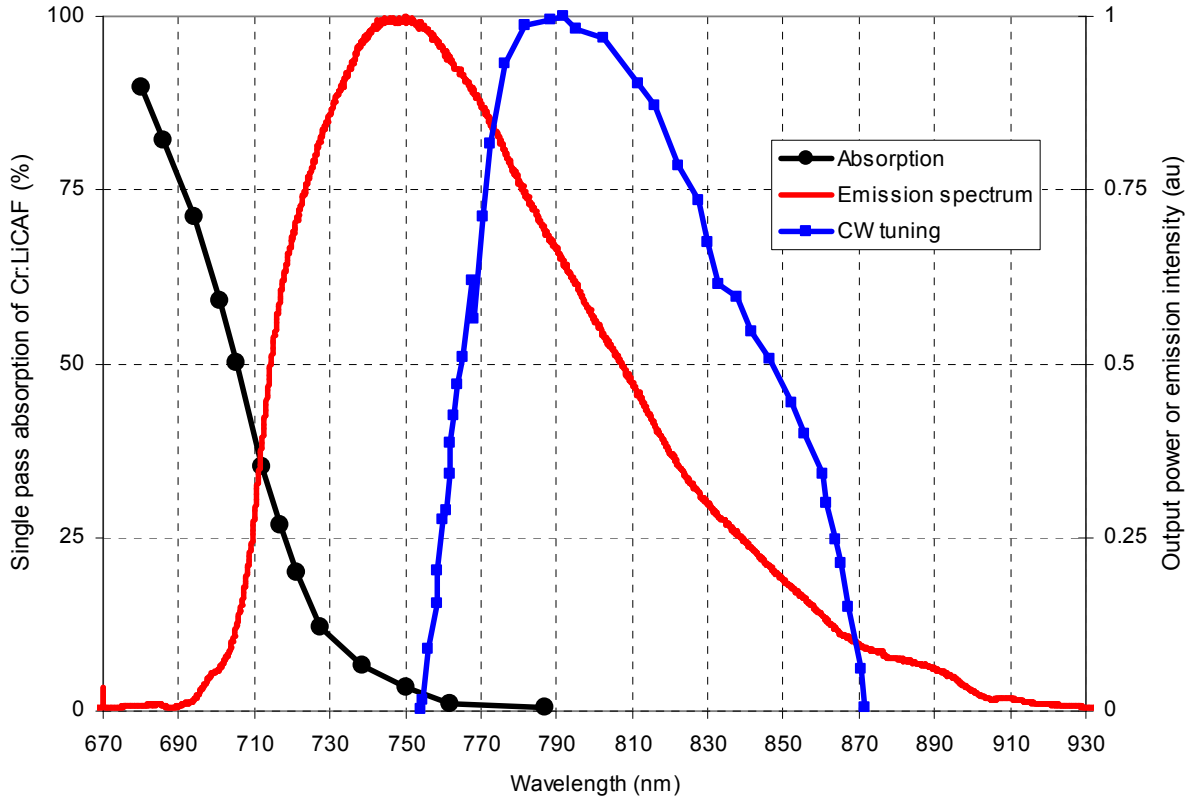

Figure 2.12: Normalized cw tuning range of Cr:LiCAF laser is plotted with normalized un-polarized emission spectrum of Cr:LiCAF and measured single pass absorption loss of the 2 mm long 10% chromium doped Cr:LiCAF crystal for TM polarized light (measured using the output from the tunable Ti:Sapphire laser).

For the long wavelength side, the pump mirror reflectivity range, the presence of excited state absorption (ESA) and also the decreased emission cross section might play a role in limiting the tuning range above 871 nm. The pump mirrors used in this study (M1-M2, Layertec Cr:Colquiriite pump mirror set I, see details in Appendix A.3) have reduced reflectivity above 860 nm. As an example, the pump mirrors had a transmission of about 0.2% at 870 nm, giving an additional loss of 0.8% (four bounces), which may limit tunability. In addition, previous studies showed the existence of strong ESA in Cr^{3+}:LiCAF on the long wavelength side [1]. Furthermore, Beaud et al. showed that, due to the presence of ESA, small-signal gain of Cr^{3+}:LiCAF even becomes negative above 895 nm for π-polarized light (polarized parallel to the c-axis) [180]. The reason for the tuning limit above 871 nm in our studies is not clear, but we believe that it is probably due to the presence of stronger ESA at longer wavelengths.

Further investigation with broader bandwidth optics is required to understand the factors limiting tuning above 871 nm.

We note that, for Cr^{3+}:LiCAF media, combining the results obtained by Payne et al. [1] and this work, the total demonstrated tuning range extends from 720 to 871 nm, corresponding to a fractional tuning bandwidth ($\Delta\lambda/\lambda_0$) of ~0.19.

2.3 CW Operation of the Single-Mode Diode Pumped Cr:LiSAF Laser

The continuous wave laser cavity for the single-mode diode-pumped Cr:LiSAF laser was similar to the Cr:LiCAF laser cavity. A 1.5 mm thick, 5-mm-long, 1.5% Cr-doped Cr:LiSAF crystal was used in the experiments which absorbed ~99% and ~72% (0.9 x 80%) of the incident TM and TE polarized pump light at ~660 nm. Except the laser crystal, same optics were used in the laser experiments to be able to obtain a fair comparison between Cr:LiCAF and Cr:LiSAF gain media (note that Layertec Cr:Colquiriite pump mirror set I reflectivity range is suitable for cw experiments with all the Cr:Colquiriite gain media, a detailed description is given in section Appendix A3). Water cooling was not used during the experiments (except for cases where thermal issues were investigated).

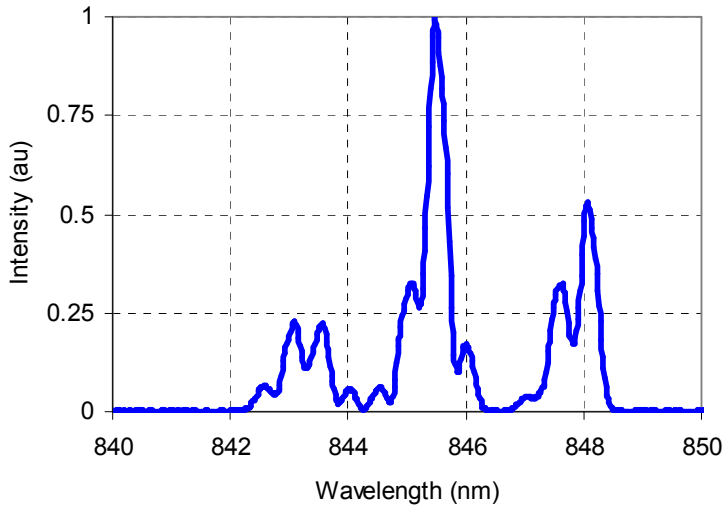

Figure 2.13 Representative free running laser wavelength measured of diode pumped cw Cr:LiSAF laser, taken with the 1.6 % output coupler.

Slope efficiency data for the Cr:LiSAF laser were measured using nine output couplers with transmissions from 0.05 - 25%. Free running cw lasing wavelength was ~835±15 nm. This broad variation in cw lasing wavelength is most probably due to the relatively broad gain bandwidth of Cr:LiSAF gain media, which is somehow flat in this region. Figure 2.13 shows a representative cw laser spectrum taken with the 1.6% output coupler. Figure 2.14 shows representative cw laser efficiency curves for the single-mode diode pumped Cr:LiSAF laser taken with 0.5% and 3.1% output couplers. With the

0.5 % output coupler, the lasing threshold was 12 mW, and up to 240 mW of cw output power is obtained with 555 mW of absorbed pump power, with a corresponding slope efficiency of 45%. The 3.1% output coupler gave up to 265 mW of cw output power, where the corresponding lasing threshold and slope efficiency values were 50 mW and 53%, respectively. With Cr:LiSAF gain media, cw lasing thresholds as low as 5 mW were measured with a 0.05% output coupler. The highest cw output power (271 mW) was obtained using a 1.6% output coupler with a 22 mW lasing threshold and 50% slope efficiency. Figure 2.15 summarizes the cw lasing results which shows the variation of the maximum attainable cw power with output coupler transmission.

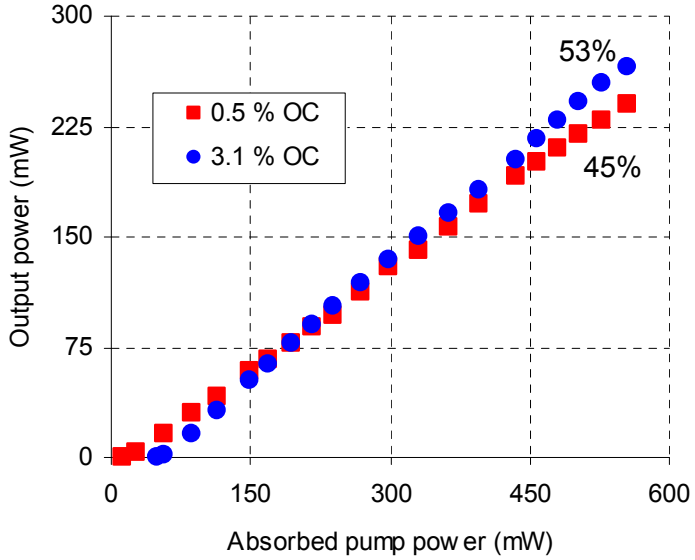

Figure 2.14: CW efficiency curves for the single diode-pumped Cr^{3+}:LiSAF laser, taken with 0.5 and 3.1% output couplers. The measured slope efficiencies with respect to absorbed pump power were 45 and 53% for the 0.5 and 1.95% output couplers, respectively.

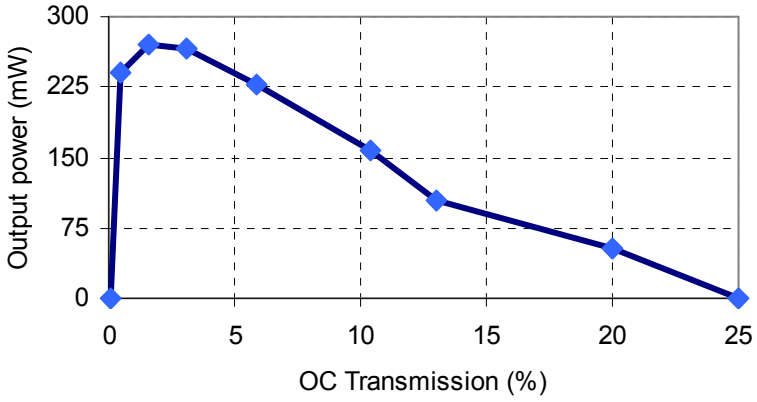

Figure 2.15: Measured variation of the maximum obtainable cw output power with output coupler transmission for the single-mode diode pumped Cr:LiSAF laser. The data is taken at the full pump power of 555 mW (absorbed). Optimum output coupling is around 0.5-4 %.

Using the measured threshold pump power with several different output couplers (Findlay-Clay analysis, Eq. 2.1) [221], a roundtrip cavity loss of 0.25% was estimated (Fig. 2.16). Using the measured slope efficiency with different output couplers (Caird analysis, Eq. 2.2) [222], the intrinsic slope efficiency was estimated to be 54%, with roundtrip cavity losses of 0.1% (Fig. 2.16). Estimated cavity loss levels are in relatively good agreement with each other, considering these are relatively small values, which is hard to measure accurately. This intrinsic slope efficiency (54%) is in good agreement with the previously reported value of 53% [4].

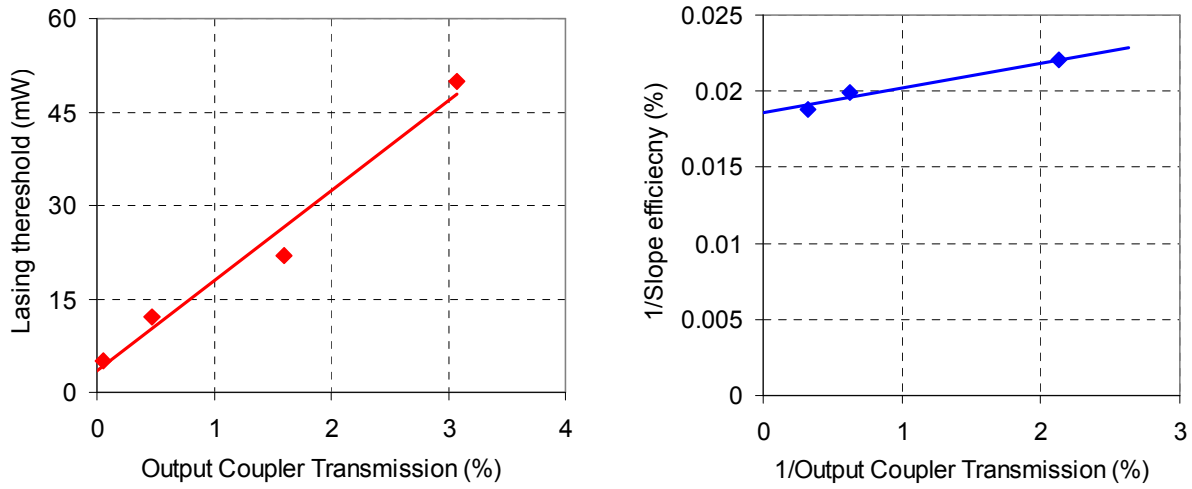

Figure 2.16: Findlay-Clay (left) and Caird analysis (right) for the single-mode diode pumped Cr:LiSAF laser. Roundtrip cavity loss is estimated to be 0.25% and 0.1% using Findlay-Clay and Caird analysis respectively.

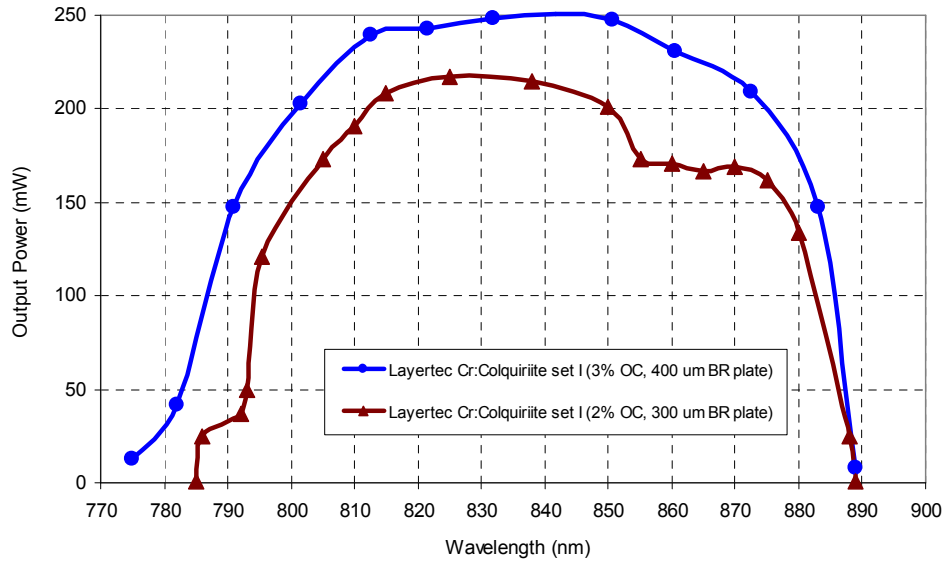

Figure 2.17: Measured cw tuning curves for the single-mode diode pumped Cr^{3+}:LiSAF laser taken with Layertec Cr:Colquiriite pump mirror set I and with (a) a 3% output coupler and the 400 μm birefringent plate for tuning, (b) a 2% output coupler and the 300 μm birefringent plate for tuning. (c) 1.5% output coupler and the 400 μm birefringent plate for tuning. Laser wavelength could be tuned smoothly between 775 and 889 nm.

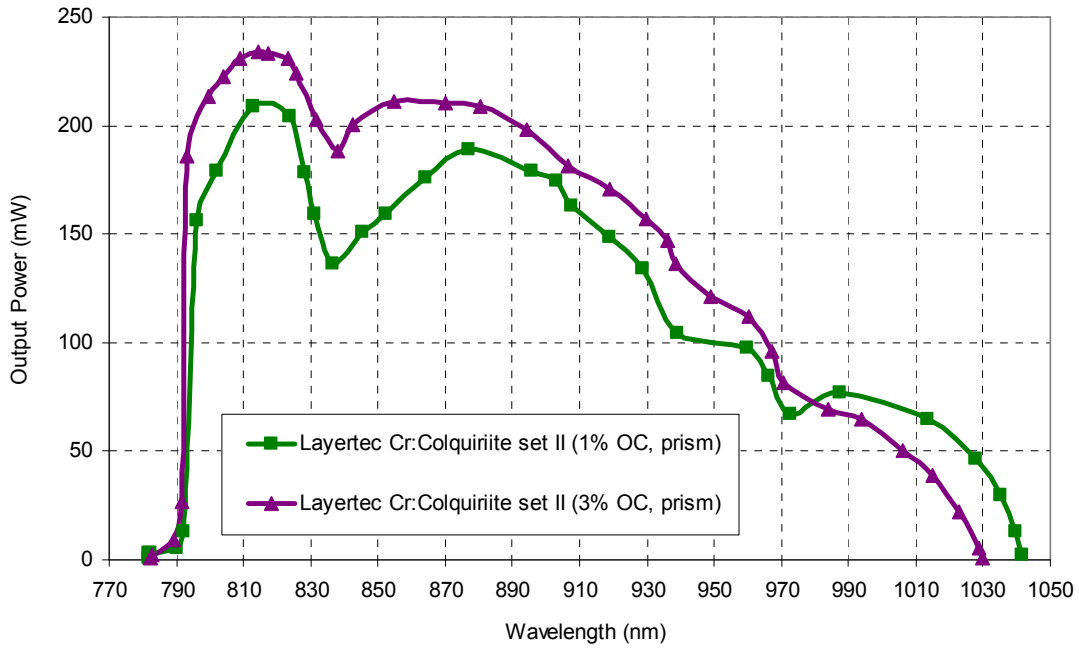

Figure 2.18: Measured cw tuning curves for the single-mode diode pumped Cr^{3+}:LiSAF laser taken with Cr:Colquiriite pump mirror set II and with (a) a 1% output coupler and a fused silica prism for tuning, (b) a 3% output coupler and a fused silica prism for tuning. Laser wavelength could be tuned smoothly between 782 and 1042 nm.

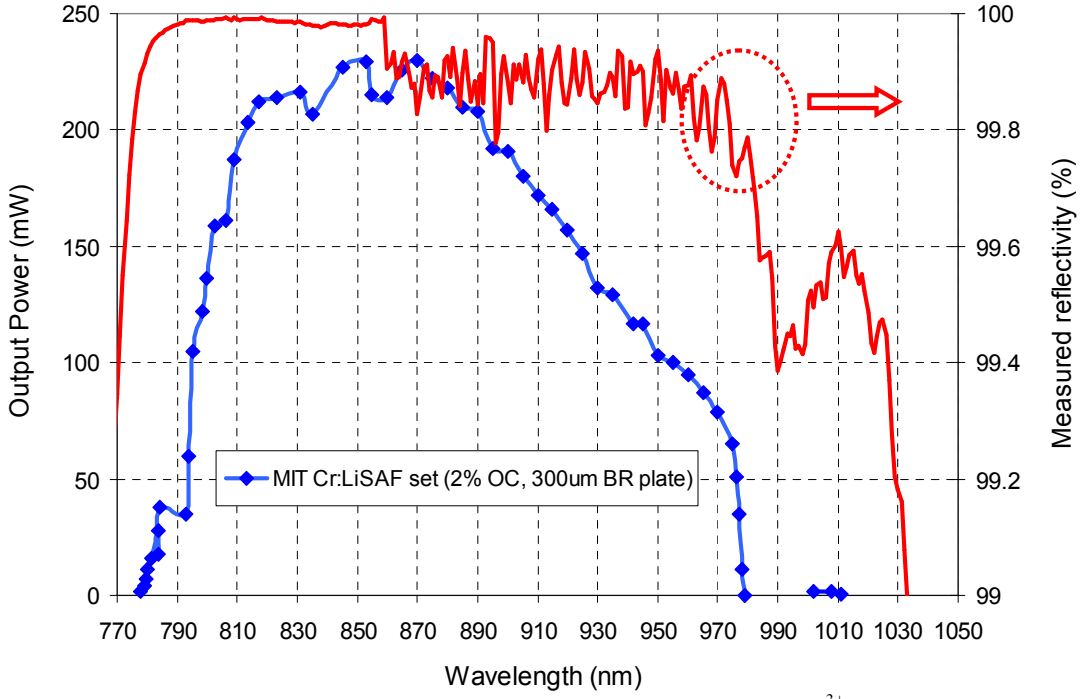

Figure 2.19: Measured cw tuning curve for the single-mode diode pumped Cr^{3+}:LiSAF laser taken with MIT Cr:LiSAF pump mirror set and with a 2% output coupler and 300μm BR tuning plate. Laser wavelength could be tuned smoothly between 778 and 979 nm. Measured reflectivity of the MIT Cr:LiSAF pump mirror set was also shown. The jump in the reflectivity measurement around 850 nm and the decreases signal to noise ratio thereafter is due to a detector change in the spectrometer.

We have also investigated the cw tuning behavior of single-mode diode pumped Cr:LiSAF laser in detail using different mirror sets and different output couplers. Figure 2.17 shows the measured tuning range of Cr:LiSAF with the Layertec Cr:Colquiriite pump mirror set I, where we have obtained a tuning range extending from 775 nm to 889 nm. Tuning is limited above 889 nm due to the reflectivity bandwidth limitation of Layertec Cr:Colquiriite pump mirror set I, which for example leaks about 0.5% around 890 nm. On the short wavelength side, we believe the tuning range is limited by self absorption losses of Cr:LiSAF gain media, since the mirror sets reflectivity range extends up to ~740 nm. More information on Layertec Cr:Colquiriite pump mirror set I can be found in Appendix A3.

To be able to demonstrate the full tuning range of Cr:LiSAF, we have used a different broadband pump mirror set, namely Layertec Cr:Colquiriite pump mirror set II (see Appendix A4 for details). As show in Fig. 2.18, with the Layertec Cr:Colquiriite pump mirror set II set, using a 1% OC, the Cr:LiSAF laser could be tuned between 782 to 1042 nm. A 3% OC enabled a smoother tuning curve with a slightly narrower range (782-1030 nm). Comparing the shape of the tuning curves of 1% and 3% output couplers, we see that the dip around 835 nm is from leakage in the broadband pump mirrors. This is also evident when one compares tuning ranges obtained with Layertec Cr:Colquiriite pump mirror set I and II .

Lastly, we have also taken the cw tuning data with MIT Cr:LiSAF pump mirror set, which was shown in Figure 2.19 along with the measured reflectivity of the mirror set (see Appendix A1 for more details). With this set, using a 2% output coupler we could obtain tuning from 778 nm to 979 nm. Again the long wavelength tuning range is limited by the reflectivity bandwidth of the set.

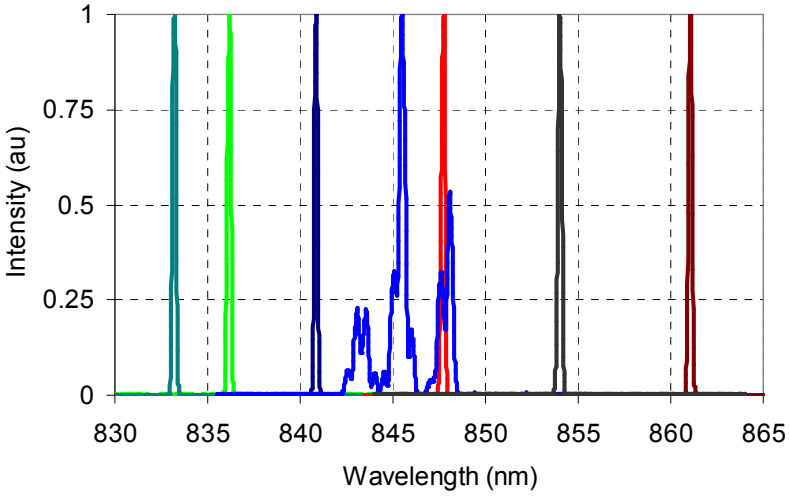

Figure 2.20: Representative optical spectra taken during cw tuning of Cr:LiSAF with the 400 μm thick birefringent plate. For comparison free running laser wavelength measured with the 1.6 % output coupler is also shown. Insertion of a tuning element inside the cavity narrows down the cw laser spectrum width (FWHM) to ~0.2 nm level.

Figure 2.20 above shows example optical spectrum taken during the cw tuning experiments. For comparison, Fig. 2.20 also includes the optical spectra for the cw free running laser with the 1.6% output coupler. Note that insertion of a tuning element into the cavity narrows down the spectrum and allows narrowband operation. Figure 2.21 shows the emission spectrum of the Cr:LiSAF gain medium along with the obtained cw tuning ranges. The total demonstrated tuning range here extends from 775 nm to 1042 nm, and is the broadest tuning range reported for Cr:LiSAF so far (267 nm). This corresponds to a fractional tuning bandwidth ($\Delta\lambda/\lambda_0$) of ~0.29. We believe that tuning below 775 nm is limited by the self absorption losses, where as tuning above 1042 nm is limited by the gain bandwidth of the Cr:LiSAF gain media. This tuning range might possibly be extended by pumping with higher power diodes in the future (or by pulsed pumping).

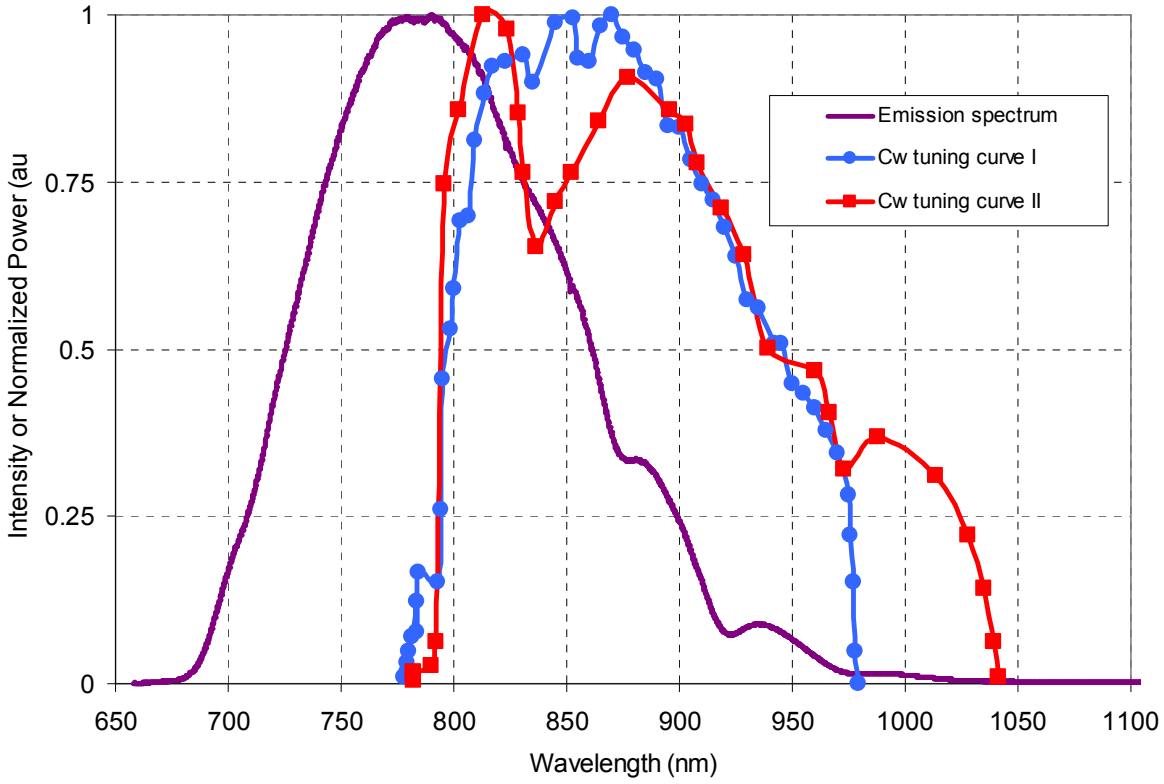

Figure 2.21: Normalized cw tuning range of Cr:LiSAF laser (taken with two different mirror sets) is plotted with measured unpolarized emission spectrum of Cr:LiSAF gain media. The modulations in the emission spectrum is an artifact from the HR we used to collect the light. Also emission spectrum is measured with a silicon CCD detector; hence the decrease in emission strength at longer wavelengths might be partly due to the decreased quantum efficiency of the Si detector.

2.4 CW Operation of the Single-Mode Diode Pumped Cr:LiSGaF Laser

The continuous wave laser cavity for the single-mode diode-pumped Cr:LiSGaF laser was identical to the Cr:LiSAF laser cavity, which was described in Section 2.3. A 1.5 mm thick, 5-mm-long, 3% Cr-doped Cr:LiSGaF crystal was used in the experiments which absorbed ~99.5% and ~86.5% (0.9 x 96%) of the incident TM and TE polarized pump light at ~660 nm. Water cooling was not used during the experiments (except for the case where thermal issues were investigated).

For Cr:LiSGaF, the laser slope efficiency was measured using eight output couplers with transmissions from 0.05 - 17.5%. Figure 2.22 shows representative curves with 0.5%, 3.1% and 5.9% output couplers. Figure 2.23 summarizes the laser cw efficiency results by showing the variation of maximum attainable output power with output coupler transmission. Similar to Cr:LiSAF, the cw lasing wavelength was ~835±15 nm, and thresholds as low as 6 mW were obtained with a 0.05% output coupler. Using the 1.6% output coupler, the highest cw output power (283 mW), a 33 mW lasing threshold and a 55% slope efficiency were measured. Slope efficiencies up to 62% were obtained with a 5.9% output coupler. The roundtrip cavity loss was estimated at 0.35% and 0.1% using Findlay-Clay and Caird analyses (Fig. 2.24). Caird analysis yield a value of 60% for the intrinsic slope efficiency, slightly higher than previously reported (52% [6]).

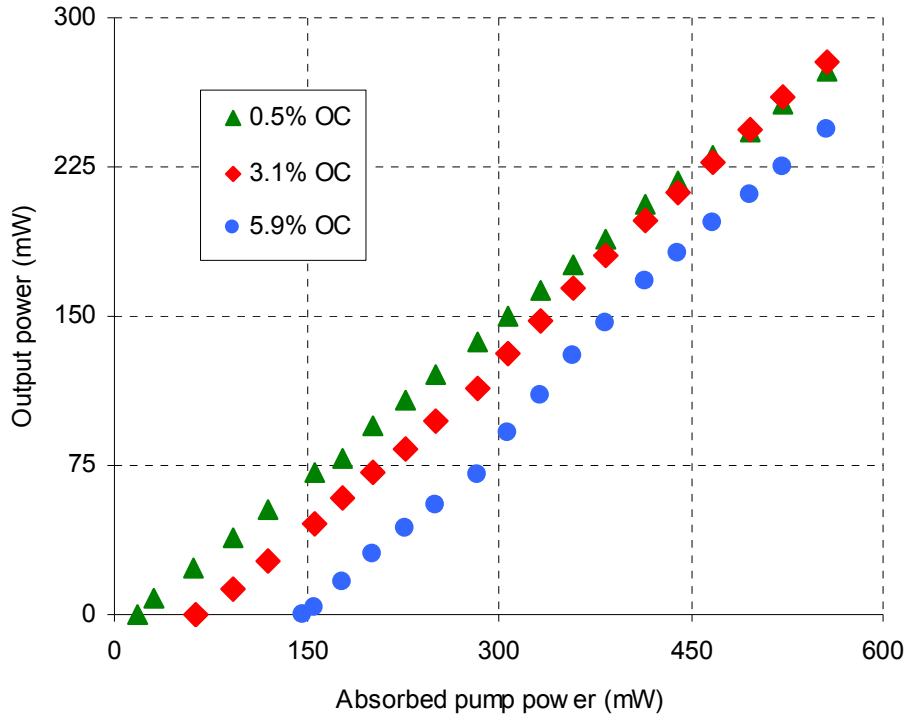

Figure 2.22: CW efficiency curves for the single diode-pumped Cr^{3+}:LiSGaF laser, taken with 0.5, 3.1 and 5.9 % output couplers. The measured slope efficiencies with respect to absorbed pump power were 51%, 58% and 62%, respectively.

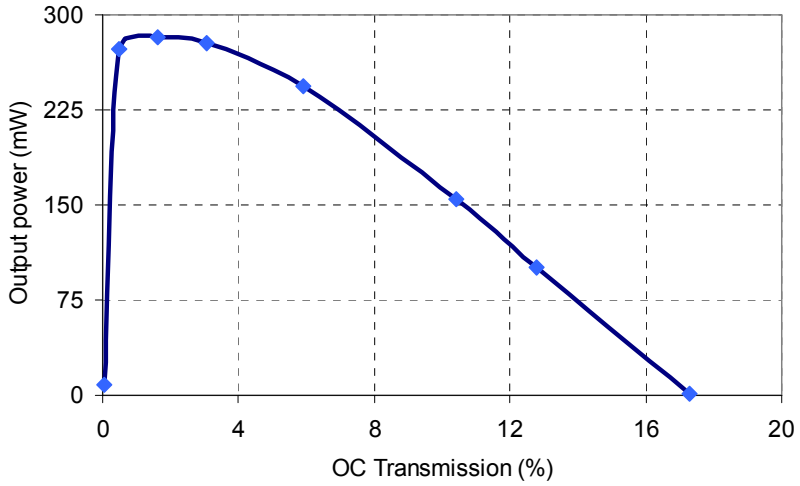

Figure 2.23: Measured variation of the maximum obtainable cw output power with output coupler transmission for the single-mode diode pumped Cr:LiSGaF laser. The data is taken at the full pump power of ~560 mW (absorbed). Optimum output coupling is around 0.5-4 %.

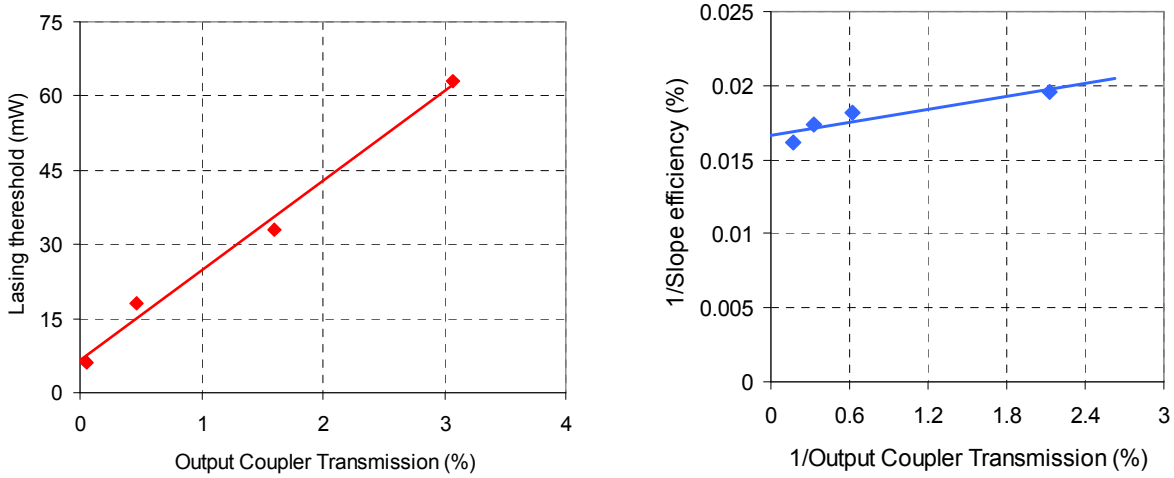

Figure 2.24: Findlay-Clay (left) and Caird analysis (right) for the single-mode diode pumped Cr:LiSGaF laser. Roundtrip cavity loss is estimated to be 0.35% and 0.1% using Findlay-Clay and Caird analysis respectively. Intrinsic slope efficiency was estimated to be and 60 ± 5 %.

Figure 2.25 shows the cw tuning experimental data taken with the Cr:LiSGaF gain media. Using Layertec Cr:Colquiriite pump mirror set I, we have obtained a tuning range extending from 779 nm to 890 nm. Similar to Cr:LiSAF, Layertec Cr:Colquiriite pump mirror set I limits tuning above 889 nm due to its limited reflectivity bandwidth. Layertec Cr:Colquiriite pump mirror set II gave a cw tuning range extending from 777 nm to 977 nm. On the short wavelength side, we believe the tuning range is limited by self absorption losses of Cr:LiSGaF gain media (Figure 2.26).

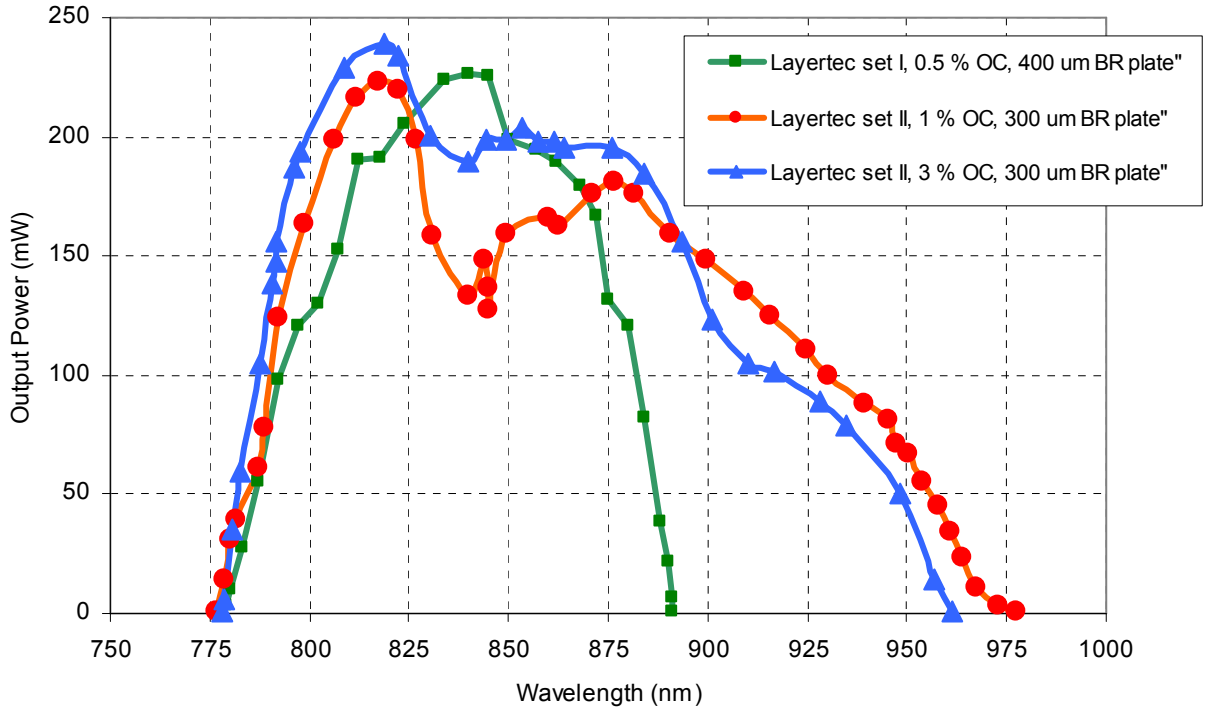

Figure 2.25: Measured cw tuning curves for the single-mode diode pumped Cr^{3+}:LiSGaF laser taken with (a) Layertec Cr:Colquiriite pump mirror set I and with a 0.5% output coupler using the 400 μm birefringent plate for tuning, (b) Layertec Cr:Colquiriite pump mirror set II and with a 1% output coupler using the 300 μm birefringent plate for tuning, (c) Layertec Cr:Colquiriite pump mirror set II and with a 3% output coupler using the 400 μm birefringent plate for tuning. Laser wavelength could be tuned smoothly between 779 and 890 nm with Layertec pump mirror set I, and between 777 and 977 nm with Layertec pump mirror set II.

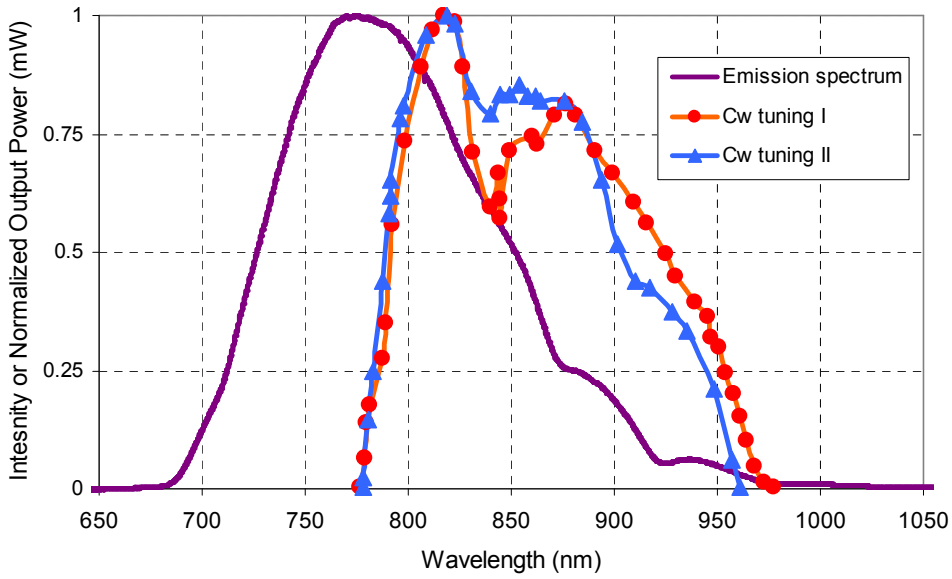

Figure 2.26: Normalized cw tuning range of Cr:LiSGaF laser is plotted with measured unpolarized emission spectrum of Cr:LiSGaF gain media. The modulations in the emission spectrum is an artifact from the HR we used to collect the light. Also emission spectrum is measured with a silicon CCD detector; hence the decrease in emission strength at longer wavelengths might be partly due to the decreased quantum efficiency of the Si detector.

2.5 CW Operation of the Multi-Mode Diode Pumped Cr:LiCAF Laser

Among the Cr^{3+}-doped colquiriite gain media, Cr:LiCAF has several distinct and favorable characteristics. Cr:LiCAF lases in the spectral range from ~720 to ~870 nm, and the ~720 to ~800 nm region is not accessible by the other Cr:Colquiriites. Moreover, compared to other Cr:Colquiriites, Cr:LiCAF has superior thermal properties, which can enable high-power operation. The main disadvantage of Cr:LiCAF is its low emission cross section, which results in low gain (round-trip gain < 10%), requiring extremely low loss optics. Moreover, due to its lower emission cross section, Cr:LiCAF has higher tendency to q-switch. However, despite these disadvantages, 750-800 nm spectral region is important for applications such as amplifier seeding or multiphoton microscopy, and superior thermal properties of Cr:LiCAF can enable power scaling. In this chapter we will provide a detailed summary of cw lasing experiments with single-emitter, multimode diode pumped Cr:LiCAF laser. Multimode diodes provide relatively high power levels (~1.5W) with a multimode output; hence, this pumping is not applied to Cr:LiSAF and Cr:LiSGaF, due to their susceptibility to thermal effects. Cw mode-locked lasing experiments with multimode diode pumped Cr:LiCAF laser will be presented in Chapter 3. More information on properties of single-emitter, multimode diodes can be found in Appendix B.3. Finally, we not here that we have started the multimode pumping experiments with 1-W diodes, and obtained with 1-W multimode diode pumped Cr:LiCAF laser can be found in [143]. In this chapter, we will only present latest results obtained with the 1.5-W diodes; since this is the newest technology, and gave better performance from a simpler setup.

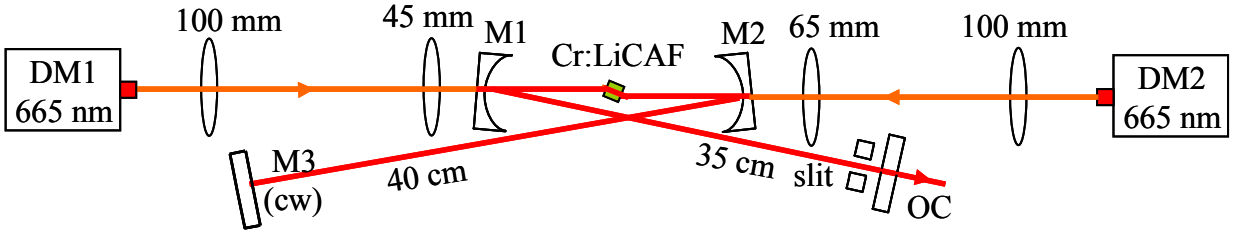

Figure 2.27: Schematic of the multimode diode-pumped Cr^{3+}:LiCAF laser system. Two multimode diodes (DM1-DM2), each providing 1.6 W of pump power at 665 nm, were used as the pump source. A slit near the OC (tangential plane) was used to control the transverse mode structure of the laser beam. M1-M2: pump mirrors with R= 75 mm, M3: flat high reflector, OC: output coupler.

Figure 2.27 shows the schematic of the multimode diode-pumped Cr^{3+}:LiCAF laser cavity used in the cw lasing experiments. Two linearly-polarized, multimode, single-emitter diodes (DM1-DM2) were used as the pump source (see Appendix B.3 for details). The diode outputs were first collimated with 100 mm lenses and then focused inside the crystal using achromatic doublets with focal lengths of 45 mm (left) and 65 mm (right). Figure 2.28 shows the pump focusing characteristics at the position of the crystal. The cw Cr^{3+}:LiCAF laser resonator was a standard x-folded, astigmatically compensated cavity, with two

curved pump mirrors, each with a radius of curvature (roc) of 75 mm (M1 and M2), a flat end high reflector (M3), and a flat output coupler (OC). Pump mirrors (M1-M2) was same as what we have used in single-mode diode pumped Cr:LiCAF laser experiments (Layertec Cr:Colquiriite pump mirror set I). Continuous wave laser performance was measured with ten different output couplers (0.5, 0.85, 1.05, 1.2, 1.4, 1.95, 3, 5, 6 and 10 % @ ~800 nm). Figure 2.29 shows a picture of the cw laser cavity.

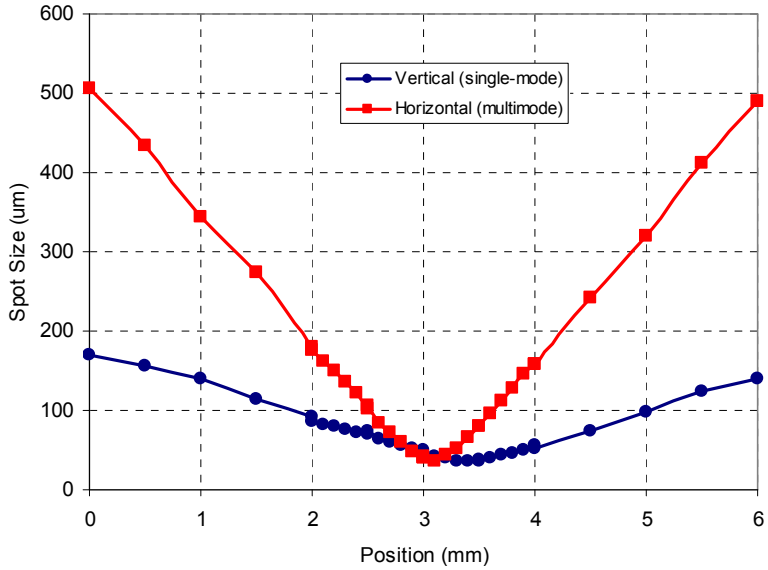

Figure 2.28: Measured variation of the pump beam spot size in both axes. Diode output was first collimated by a 100 mm lens, then focused using a 45 mm focal length lens. The focusing in this measurement should be similar to the pump focusing inside the laser crystal. Note that the beam focuses at different positions for the vertical and horizontal axis. Moreover, due to the multimode nature of the beam in the horizontal axis, smaller Rayleigh range in this axis is a limiting factor in laser experiments. For example, this small Rayleigh range requires the usage of relatively short crystals (~2-4 mm).

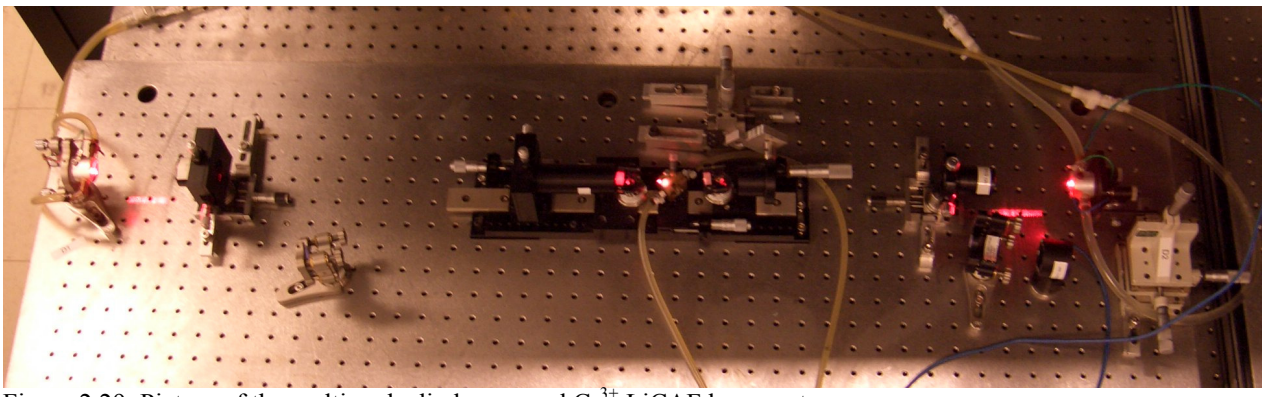

Figure 2.29: Picture of the multimode diode-pumped Cr^{3+}:LiCAF laser system.

We used the same 2-mm-long, Brewster-cut, 10 mole % Cr-doped Cr^{3+}:LiCAF crystal that we have also used in single-mode pumping experiments. The crystal was mounted with indium foil in a copper holder. The crystal absorbed ~97% of the incident TM polarized pump light at 665 nm (FWHM≈ 2 nm), which

resulted in a total absorbed power of 2.9-W at the full drive current of the diodes. To reduce the thermal effects, the crystal holder was water-cooled, and unless otherwise noted, all the cw and cw mode-locked laser data in this section were taken at the crystal holder temperature of 5 °C. Cavity arm lengths of 35 cm (OC arm) and 40 cm were used to obtain a laser mode size of ~22 μm x 31 μm (sagittal x tangential) inside the crystal. Lastly, a slit near the OC (tangential plane) was used to control the transverse mode structure of the laser beam. Without the slit, the laser output was multimode in the tangential direction and single mode in sagittal direction (Fig. 2.30 a). With the slit width adjusted, it was possible to obtain a symmetric, diffraction limited TEM_{00} laser beam (Fig. 2.30 b-c). Figure 2.31 shows the measured free running laser wavelength, when the laser output was multimode (without the slit) and TEM_{00} (with the slit). Having the intracavity slit also enabled narrow linewidth operation in cw regime.

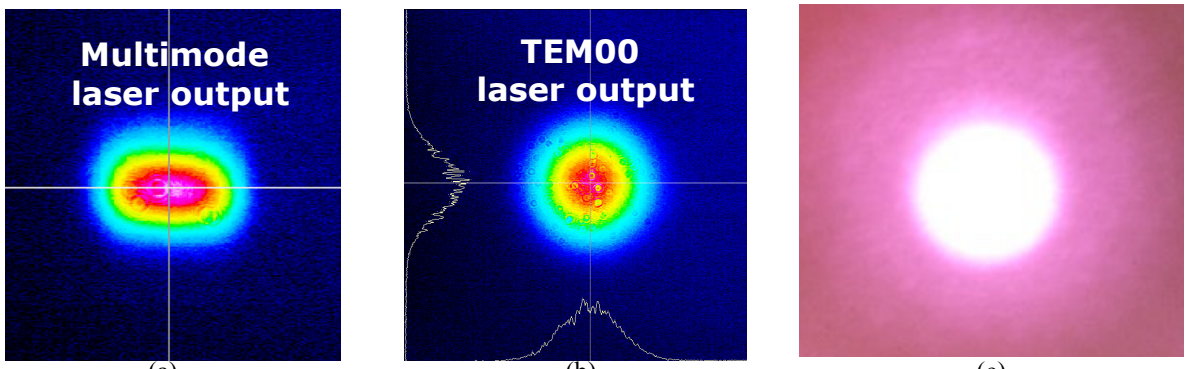

(a) (b) (c)

Figure 2.30: Measured output beam profile of the multimode diode-pumped Cr^{3+}:LiCAF laser (Fig. 2.27) using a CCD camera (a) without the intracavity slit and (b) with the intracavity slit. Adjusting the width of the intracavity slit in the tangential plane enabled TEM00 laser output. (c) Similarly, picture of the output beam, with the intracavity slit.

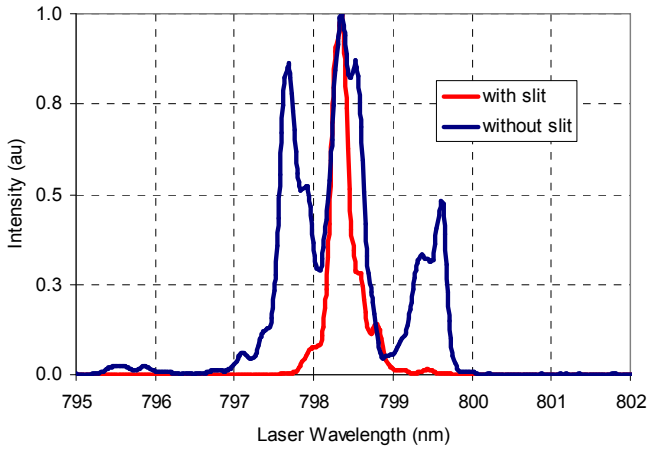

Figure 2.31: Laser wavelength with and without the intracavity slit. The intracavity slit also enabled narrower linewidth operation.

Figure 2.32 shows the measured cw performance of the multimode diode pumped Cr^{3+}:LiCAF laser taken using the 1.4, 3 and 5% output couplers. No intracavity slit was used and the laser output was multimode (Fig. 2.30 (a)). The best power performance is obtained with the 1.4% output coupler. This output coupler enabled output powers as high as 880 mW at 2.9 W of absorbed pump power with a slope efficiency of 32%. The obtained output powers were limited by thermal effects and increasing pump power did not increase the output power levels. The highest slope efficiency obtained from a multimode diode-pumped Cr:LiCAF laser to date is 49.7%; however this high slope efficiency was obtained using a lower doped crystal and a specially designed laser cavity with an asymmetric laser mode [177]. In our standard cavity, a significant mismatch between the laser and the pump modes was present and this limited the slope efficiencies (which will be discussed in more detail later). Also, the lasing threshold measured with the 0.5% OC was ~70 mW (~7 times larger compared to single-mode pumping as will be discussed in next chapter), which also shows the significant mismatch between the cavity and pump beam waists.

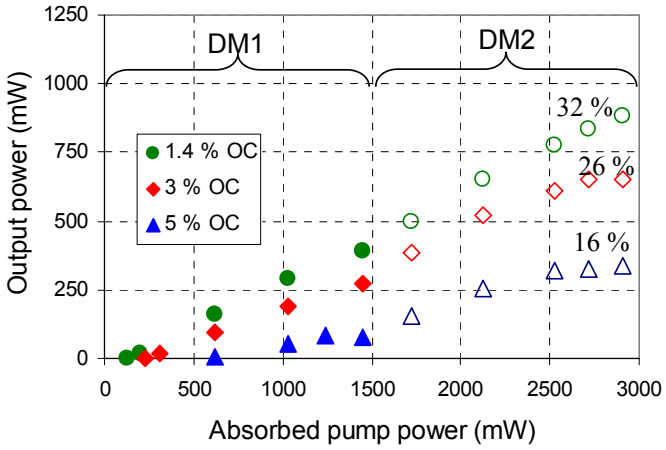

Figure 2.32: CW efficiency curves for the multimode diode pumped Cr^{3+}:LiCAF laser (Fig. 2.27), taken with 1.4, 3 and 5 % output couplers, without the intracavity slit. The laser output was multimode (Fig 2.30-a). Data up to 1.5 W of absorbed pump power was taken using multimode diode 1 only (DM1), then multimode diode 2 (DM2) was also turned on which provided up to 3W of total absorbed pump power. The measured slope efficiencies with respect to absorbed pump power were 32, 26 and 16% for the 1.4, 3 and 5% output couplers, respectively. The observed saturation at high pump power levels and the reduction of the obtainable output power levels with increasing output coupling are due to thermal effects.

With the insertion of the intracavity slit near the output coupler, it was possible to obtain a TEM_{00} laser output (Fig. 2.30 (b)-(c)). In this measurement, the laser output was monitored by a CCD camera and for each output coupler the slit width (in tangential plane) was adjusted to obtain a symmetric circular beam profile. Figure 2.33 shows the cw efficiency curves taken with this configuration. With the slit inside the cavity, the best cw laser performance was obtained with the 0.85% output coupler where the laser generated 590-mW of TEM_{00} output power with 2.9 W of absorbed pump power at a slope efficiency of 19%. The intracavity slit enabled TEM_{00} operation at the expense of lower slope

efficiencies, lower output powers, and increased thermal effects. The optimum output coupling was lower in this case (0.85%), due to the presence of strong thermal effects. Figure 2.34, which shows the variation of the obtained output power levels with output coupling, summarizes the results for the cases with and without the intracavity slit.

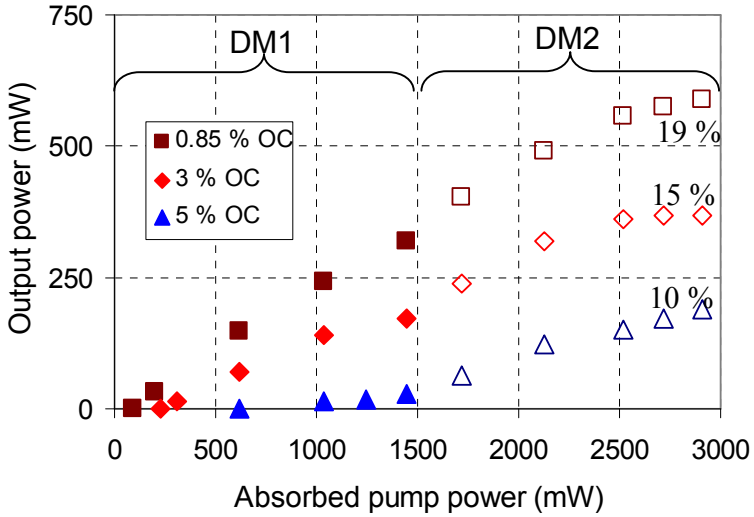

Figure 2.33: CW efficiency curves for the multimode diode pumped Cr^{3+}:LiCAF laser (Fig. 2.27), taken with 0.85, 3 and 5 % output couplers, with the intracavity slit. The laser output was single mode (Fig 2.30-b). The measured slope efficiencies with respect to absorbed pump power were 19, 15 and 10 % for the 0.85, 3 and 5 % output couplers, respectively.

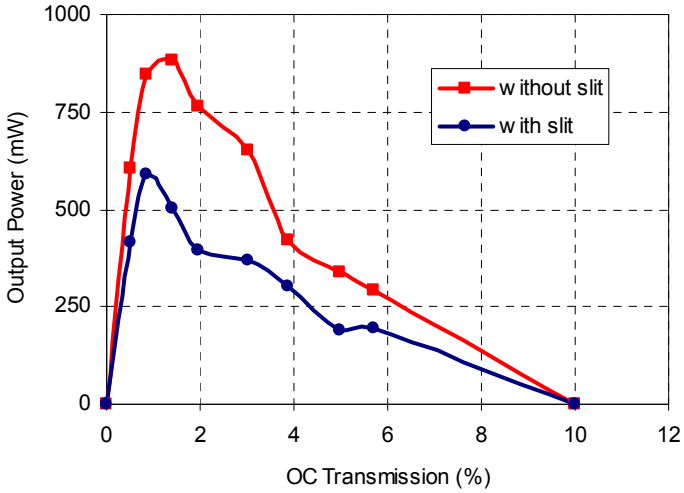

Figure 2.34: Variation of the obtained cw output power levels with output coupler transmission for the multimode diode pumped Cr:LiCAF laser. The case with and without the intracavity slit is shown.

With this multimode diode-pumped system, we also measured the cw performance of several other Cr^{3+}:LiCAF crystals (all from VLOC): (i) a 2 mm long 8.5% chromium doped, (ii) a 1.5 mm long 11% chromium doped (iii) a 2 mm long 11% chromium doped and (iv) a 2.5 mm long 11% chromium doped. In these experiments, two more multimode 1.6-W, 665 nm pump diodes were inserted to the existing

cavity (Fig. 2.27) using polarization coupling, and more than 5 W of incident pump power was available. As an example, Fig. 2.35 shows the measured cw performance of the 2.5-mm-long, 11% crystal along with the 2-mm-long 10% crystal for comparison. The data were taken without an intracavity slit; hence the laser output was multimode. The 11% chromium doped, 2.5-mm-long Cr:LiCAF crystal gave cw output powers as high as 1.01 W at an absorbed pump power of 4 W, with a slope efficiency of 26%. We believe this is the highest cw output power obtained form a Cr^{3+}:LiCAF laser to date [143]. Higher cw output powers could be obtained with this longer (2.5 mm) crystal, because of the reduced thermal effects. Also, compared to the 2 mm long, 10% crystal with 32% slope efficiency, the slope efficiency of the 2.5 mm long, 11% crystal is slightly lower (26%). This is mostly a result of the reduced mode matching between the laser mode and the multimode pump mode, due to the increased crystal length. The output powers and the slope efficiencies with the other crystals were also similar, which shows the uniformity of the optical properties of the Cr^{3+}:LiCAF crystals.

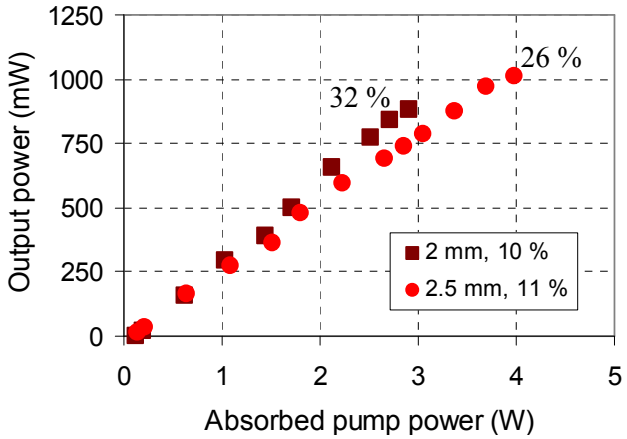

Figure 2.35: CW efficiency curves for the multimode diode-pumped Cr^{3+}:LiCAF laser, taken by using two different Cr:LiCAF crystals (i) a 2-mm-long 10% chromium doped and (ii) a 2.5-mm-long 11% chromium doped Cr:LiCAF crystal. The data were taken with the 1.4 % output coupler, without using intracavity slit, hence the laser output was multimode. For this experiment, two more multimode pump diodes were inserted to the existing cavity (Fig. 2.27) using polarization coupling, which enabled more than 5 W of incident pump power. Due to thermal effects up to ~4 W of the available pump power was used in the experiments.

As mentioned earlier, compared to the 60% slope efficiency obtained in the diffraction limited Ti: Sapphire pumped experiment, even though same optics were used in the laser, the slope efficiencies obtained with multimode diode pumping were relatively low (~32% and 19%). Figure 2.36 shows a rough sketch of the laser and the pump modes inside the crystal for the multimode diode-pumped cavity. Due to the multimode nature of the pump beam along the tangential direction (with an M^2 of ~10), there is a significant mode mismatch between the pump and the laser modes, causing low slope efficiencies. With the insertion of the intracavity slit, the mode mismatch becomes worse and decreases the slope efficiencies even further. We will consider the effect of this mode mismatch on thermal effects in the next

section. In conclusion, we note that multimode diode-pumped Cr^{3+}:LiCAF lasers have the potential of generating up to 3 W of cw output powers (using four 1.6 W diodes as the pump source); however, a carefully designed laser cavity with an asymmetric laser mode must be used for better mode matching [142, 177, 227, 228].

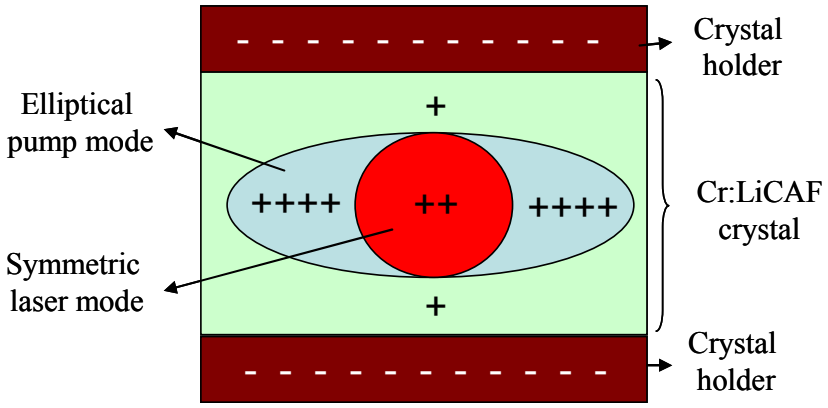

Figure 2.36: Rough schematic of the laser and pump modes inside the crystal for the multimode diode pumped Cr:LiCAF laser. In the experiments crystal holder is water cooled, and the (-) sing indicates the lower temperature. Region shown with (++) is the region where pump and laser modes overlap. (++++) regions are excited by the pump beam, but lacks stimulated emission since it does not overlap with the laser mode, hence suffers from extreme thermal loading due to upconversion. More detailed information is provided in the text.

2.6 Thermal Effects in Cr:Colquiriite Lasers

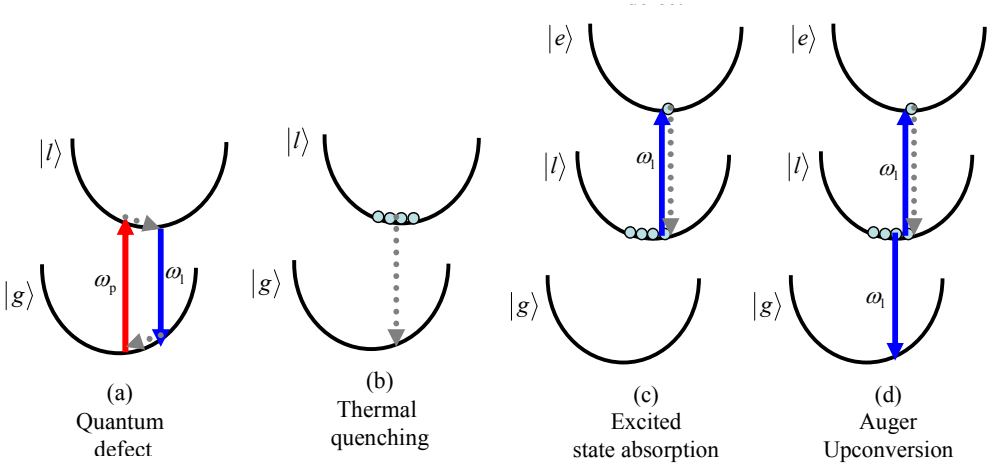

Figure 2.37: Quantum defect, thermal quenching, excited-state absorption and the Auger upconversion effects that cause thermal loading in Cr^{3+}-doped colquiriites. See the text for a detailed explanation of each process.

As evident from the efficiency curves in Figs. 2.32-2.33, thermal effects were significant for the multimode diode-pumped Cr:LiCAF cavity and limited the obtainable output power levels. In order to understand these thermal effects, mechanisms that create thermal loading inside the crystal should be studied [137-140, 180, 223, 229-235]. In chromium-doped colquiriites, there are four main mechanisms that contribute to thermal loading inside the crystal: (a) quantum defect, (b) thermal quenching of the

upper laser level, (c) excited-state absorption, and (d) upconversion (Fig. 2.37). The quantum defect is due to the energy difference between the pump (ω_p) and laser (ω_l) photons and the difference in energy is transferred to the crystal via nonradiative transitions. The thermal load caused by quantum defect is linearly proportional to the pump power, and, in general, is not the major heat source for Cr:Colquiriites since pump and laser wavelengths are very close to each other (~650 nm and ~800-850 nm). Among the Cr:Colquiriites Cr:LiCAF has the lowest quantum defect due to its blue shifted emission spectrum.

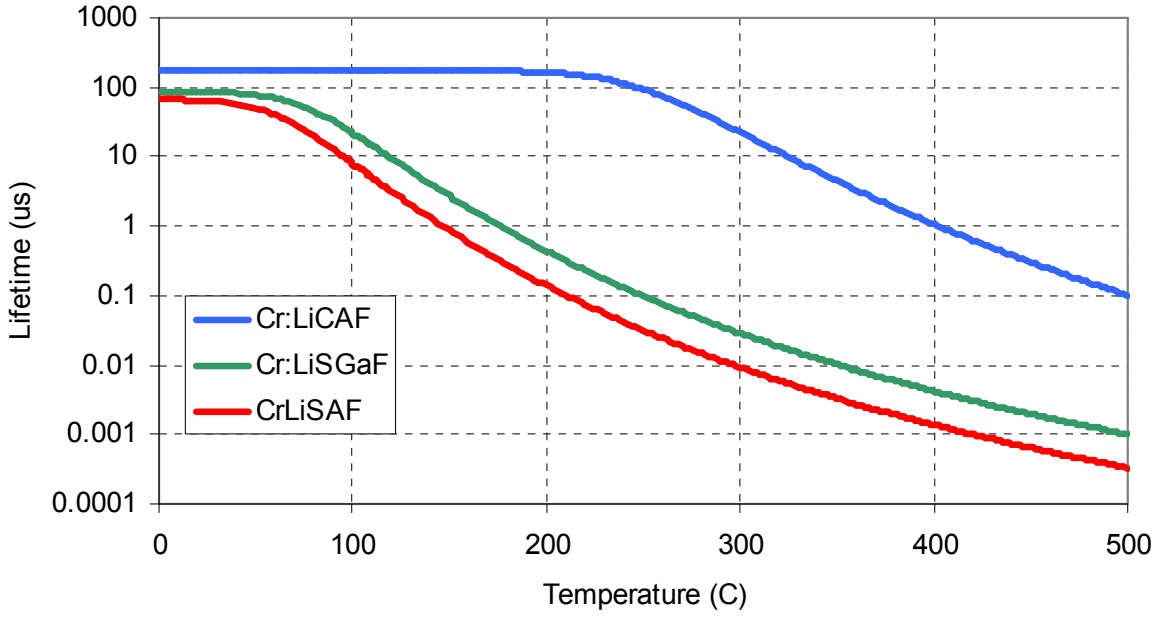

Figure 2.38: Calculated effect of temperature (thermal quenching) on fluorescence lifetimes of Cr:LiCAF, Cr:LiSAF and Cr:LiSGaF gain media.

The second mechanism that creates thermal loading in Cr^{3+}:Colquirrites is thermal quenching of the upper laser level $|l\rangle$. The upper state lifetimes of the Cr^{3+}-doped colquiriites are temperature-dependent and for temperatures above a critical value ($T_{1/2}$ in Table 1.2), thermal quenching starts to cause significant nonradiative decay of the excited-state ions from the upper laser level $|l\rangle$ to the ground state $|g\rangle$ (here the critical temperature, $T_{1/2}$ [137], is the temperature at which the fluorescence lifetime drops to half of the radiative lifetime value). For transition metal ion-doped laser materials, the Mott equation is generally used to describe the strength of temperature-dependent nonradiative relaxation processes[236, 237]. In this model, the temperature dependence of the fluorescence lifetime $\tau_F(T)$ is given by

$$\frac{1}{\tau_F(T)} = \frac{1}{\tau_R} + \frac{1}{\tau_{NR}(T)} = \frac{1}{\tau_R} + \frac{1}{\tau_{NR\,0}} \mathrm{Exp}\left(-\frac{\Delta E}{kT}\right). \qquad (2.3)$$

Here, τ_R^{-1} is the spontaneous radiative decay rate, $\tau_{NR}(T)^{-1}$ is the temperature-dependent nonradiative decay rate, τ_{NR0}^{-1} is the high temperature limit of the nonradiative decay rate, ΔE is the activation energy, k is the Boltzmann's constant and T is the absolute temperature in degrees Kelvin. Figure 2.38 shows the calculated variation of fluoresce lifetime with temperature for Cr:Colquiriites using Equation 2.3 and the required parameters that was listed in Table 1.2 [137, 138].

Amongst all the four heating mechanisms (Fig. 2.37), thermal quenching process, which decreases the gain of the crystal, is the most destructive one. This is because of the cascading nature of this mechanism; the rate of heat generation via thermal quenching is itself temperature-dependent. Once thermal quenching becomes significant, additional heating increases its rate even further in an exponential manner. This finally leads to a rapid decay of all the excited ions to the ground state via thermal quenching, and all of the absorbed pump power is converted into heat. This can even cause permanent damage to the crystal. Therefore, for efficient laser operation, the crystal temperature should be always well below $T_{1/2}$. For Cr^{3+}:LiCAF the critical temperature for thermal quenching is quite high ($T_{1/2}$ =255 °C) [137], and for crystal temperatures below ~150 °C, thermal quenching is not a significant heating mechanism (Figure 2.38). As mentioned earlier, the main drawback of Cr^{3+}:LiSAF and Cr^{3+}:LiSGaF is their low critical temperature ($T_{1/2}$ =69 °C for Cr^{3+}:LiSAF and 88 for Cr^{3+}:LiSGaF) [137, 138], which sets a barrier in laser output power scaling [142, 177, 227, 228]. It is mainly the higher critical temperature of Cr^{3+}:LiCAF that enables multimode diode pumping and hence watt-level output powers even from regular cavities.

The third mechanism that causes thermal loading is excited state absorption (ESA), where an ion in the upper laser level $|l\rangle$ absorbs a laser or a pump photon and gets promoted to a higher lying excited level $|e\rangle$. The ion then relaxes back to the upper laser level $|l\rangle$ via nonradiative decay, and hence heats up the crystal. For Cr^{3+}:Colquirrites, ESA cross section at the lasing wavelength is relatively small (~20-30%) [135] and at the pump wavelength, it is negligible. Hence, ESA mechanism does not create a significant thermal load in Cr^{3+}:Colquirrites.

The last mechanism that creates thermal loading in Cr^{3+}:Colquirrites is the Auger upconversion process, which is similar to the ESA. However unlike ESA, the upconversion process does not require the presence of external photons to occur. In this process, ions at the upper laser level $|l\rangle$ interact with each other, where one of the ions decay to the ground state $|g\rangle$ and the created energy from this decay transfers another neighboring ion to the upper lying excited level $|e\rangle$. Again, the ion in the excited state $|e\rangle$ non-radiatively decays back to the laser level $|l\rangle$ and heats up the crystal. Caused by the interaction of the ions

in the upper laser level, upconversion process scales with the square of the upper state population density, and hence could generate a significant heat load at high pumping intensities. Figure 2.39 shows the calculated variation of fluoresce lifetime with population inversion density for Cr:Colquiriites using the Auger upconversion rates in Table 1.2 [135]. Since Auger upconversion process rate does not depend on temperature, it is quite effective even at low temperatures. The upper state lifetime of Cr:LiCAF decreases to half of its value at a population inversion density of 3.6×10^{19} ions/cm^3. For Cr:LiSAF/Cr:LiSGaF Auger upconversion rate is slightly higher, and the critical inversion density is only 2.3×10^{19} ions/cm^3. Auger upconversion significantly limits the population inversion densities (and hence the small signal gain values) one could obtain in Cr:Colquiriites; hence, it is a very important factor to consider for an efficient laser or amplifier design.

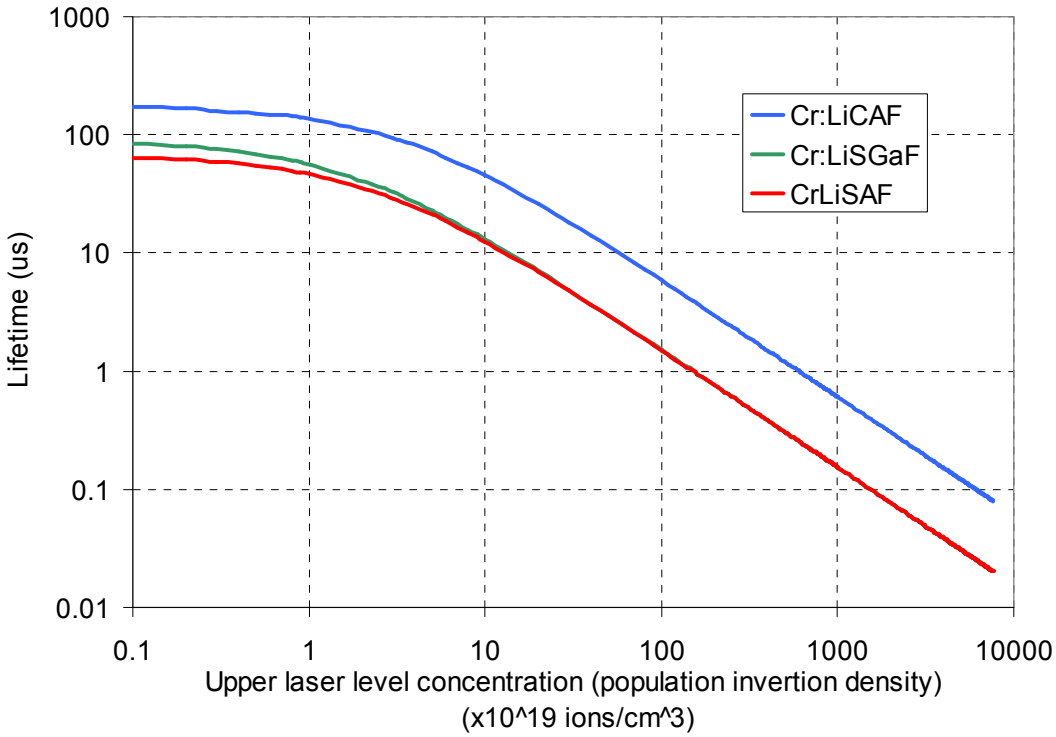

Figure 2.39: Calculated effect of Auger upconversion process on fluorescence lifetimes of Cr:LiCAF, Cr:LiSAF and Cr:LiSGaF gain media.

For the multimode diode pumped Cr:LiCAF laser, in addition to causing the low slope efficiencies, the unmatched pump and laser modes also cause strong thermal loading inside the gain medium via upconversion. As shown earlier in Fig. 2.36, there is a significant mode mismatch between the multimode pump mode and the laser mode. For the matched parts of the pump mode, stimulated emission during lasing depletes the upper state population and hence limits the heat load due to upconversion to a reasonable level (++ regions in the Fig. 2.36). However, for the unmatched parts of the pump volume,

there is no stimulated emission, and hence upper state population densities can be quite high. Therefore, the unmatched pump volume has a high upper laser level population density and the upconversion processes which scale as the square of the population density generate a considerable heat load (++++ regions in the Fig. 2.36). These regions can reach temperatures above 200 °C, which is enough to generate a significant additional heat load via thermal quenching, and hence reduces the obtainable output powers. As mentioned above, this upconversion initiated heat load due to thermal quenching could even cause termination of lasing and permanent damage to the crystal at high pumping intensities.

Based on the above discussion, it is possible to understand the thermal effects observed in Figures 2.32-2.35. First, it is clear from Figs. 2.32 and 2.33 that the thermal effects increase with increasing output coupler transmission and decreases the obtainable output powers. This effect is well known and caused by upconversion, which was also observed in Cr^{3+}:LiSAF lasers [234]. With increasing output coupler transmission, the intracavity laser power decreases and reduces the rate of stimulated emission, which then increases the population of the upper laser level. Since the upconversion process scales with the square of the upper laser level population; this causes stronger thermal effects with increased output coupling and reduces the laser performance. Here, we note that the lower laser performance is due to the increased lasing threshold with decreasing fluorescence lifetime τ_f with temperature. This is not clear from Figs. 2.32 and 2.33, where the decreased laser performance seems to be caused by the decreased slope efficiency. However, the lower slope efficiencies are just side effects of the increased lasing threshold (since slope efficiency is not affected by the variation of fluorescence lifetime). We should also note that, we haven't observed any indication of thermal lensing problem during our experiments, in agreement with previous work [138, 140]

Secondly, for the laser cavity with the intracavity slit (Fig. 2.33), the observed thermal effects are more significant compared to the cavity without mode filtering (Fig. 2.32). As mentioned earlier, the slit decreases the degree of mode matching between the laser and pump modes, since it forces the laser mode to be symmetric. Decreasing mode matching increases the regions of unmatched pump volume inside the crystal (++++ regions in the Fig. 2.36) and increases thermal loading due to upconversion. Hence, lower output powers were obtained for the cavity with the slit.

Also, for the multimode diode-pumped Cr^{3+}:LiCAF laser, rather than pumping from one side of the crystal, we use double-side pumping (Fig. 2.27). This is because double-side pumping enables a more homogeneous distribution of the upper laser level population inside the crystal, and therefore decreases the thermal effects due to upconversion increasing the obtainable output power levels. Lastly, thermal loading effects started at a higher absorbed pump power level (4W) with the 2.5-mm-long, 11% crystal compared to the 2-mm-long, 10% crystal (3 W). Hence, it was possible to obtain higher output powers with the longer crystal (Fig. 2.35). This is because, with the longer crystal, pumped regions on each side

of the crystal were further away from each other, and enabled a better distribution of the heat load inside the crystal.

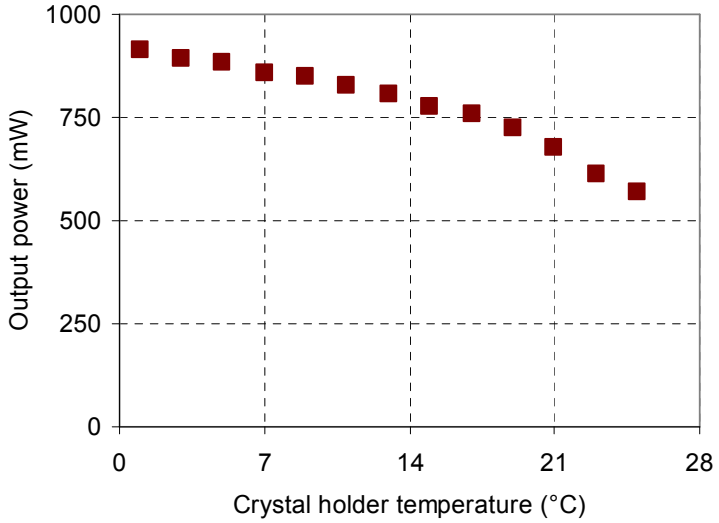

Figure 2.40: Measured variation of the cw output power with crystal holder temperature for the multimode diode-pumped Cr^{3+}:LiCAF laser, taken at an absorbed pump power of 2.9 W. The data were taken with the 1.4% output coupler, without using the intracavity slit. Hence the laser output was multimode.

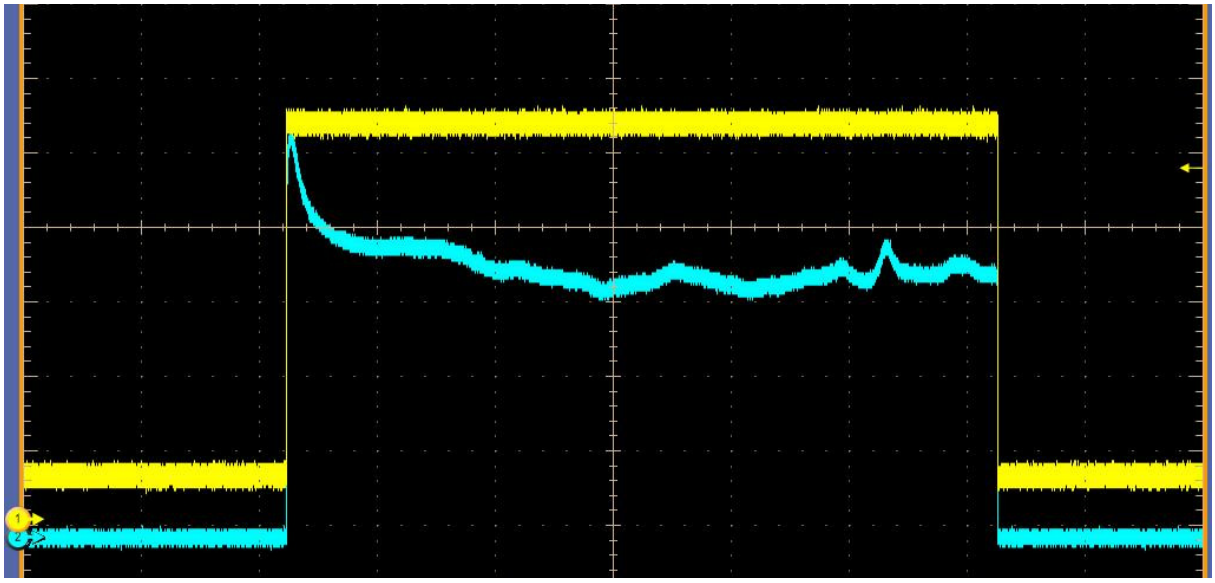

Figure 2.41: Oscilloscope traces for pump (square wave input) and laser output power, measured with a Si detector. Modulation in the pump laser power was created by modulating the diode driver current of the pump laser. The pump light has a duty cycle of 10%, and a FWHM of about 3 s. After the pump is turned on, the laser power first increases, but then starts to decrease due to thermal effects, and finally reaches to a near equilibrium point.

To better understand the thermal effects, we measured the variation of cw laser output power as a function of the crystal holder temperature (Fig. 2.40). The data were taken at an absorbed pump power level of 2.9 W, without the intracavity slit, using the 1.4% OC. Fig. 2.40 clearly shows the presence of strong thermal loading inside the crystal. The obtainable output powers decreased from 915 mW to 570

mW when the crystal holder temperature is increased from 1 °C to 25 °C. The decrease in the output power results from a decrease in the fluorescence lifetime which reduces the gain or increases the lasing threshold (thermal quenching in Fig. 2.37). Thermal quenching in Cr:LiCAF becomes effective for temperatures above 200 °C, so the measured variation in Fig. 2.40 shows that significant local thermal loading is present inside the crystal at these high pumping intensities. Lastly, Fig. 2.41 shows the response of the laser, when the pump light is modulated. Again, transient response of the laser output power, shows the existence of strong thermal effects.

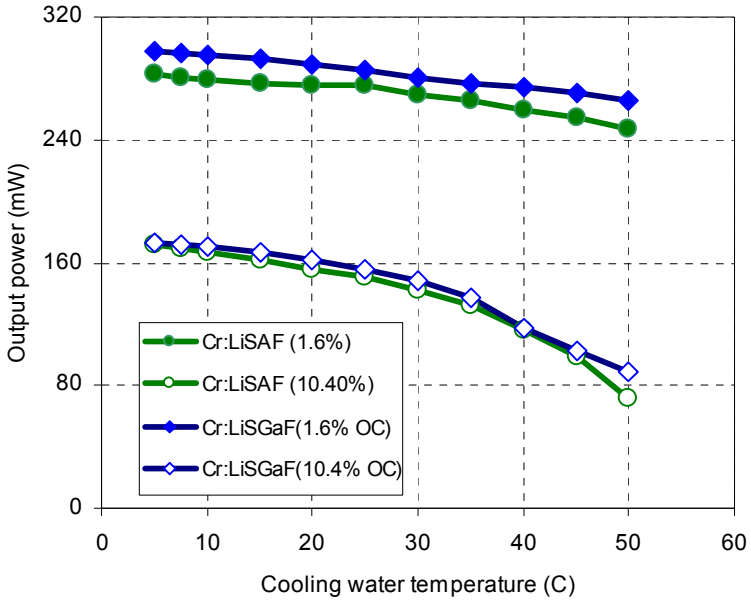

Fig. 2.42 Measured variation of cw output power with crystal holder temperature for Cr:LiSAF and Cr:LiSGaF gain media. Two different output couplers were used, and the absorbed pump power was about 550 mW during the measurements.

We have also investigated the effects of thermal loading on the laser crystals for the single-mode diode pumped Cr:Colquiriite lasers. Compared to multimode pumping, the total power incident on the crystal is 5-10 times lower. Moreover, with single-mode diode pumping we have almost perfect mode matching between the laser and pump modes, which prevents excessive heating due to upconversion. Hence, thermal effects are expected to be much smaller.

To investigate the thermal effects, similar to multimode pumping case (Fig. 2.40), the cw laser performance was measured at several different crystal holder temperatures using a water re-circulator. Figure 2.42 shows the measured cw laser output powers versus crystal holder temperatures for the Cr:LiSAF and Cr:LiSGaF lasers, at an absorbed pump power level of ~550 mW. For each gain medium, the variation of the output power with temperature was measured using two different output couplers to study the effect of output coupling on the thermal load.

Figure 2.42 shows that, as expected, thermal effects are more severe with the higher 10.4% output coupler, due to increased upconversion-induced heating [220]. However, thermal effects are negligible at room temperature with the 1.6% output coupler (comparing the output powers at 5 and 20 °C). Hence, although there is some thermal loading in Cr:LiSAF and Cr:LiSGaF, water cooling was not required (since for operation near the optimum output coupling of 1-3%, cooling the crystal yields only ~5% improvement in output). Also, note that although Cr:LiSGaF has slightly better thermal properties than Cr:LiSAF, thermal effects caused a similar decrease in the output power for both materials. We believe this results from the slightly higher absorption of the 3% chromium doped Cr:LiSGaF crystal that was used in this study ($\alpha \cong 10.5$ cm^{-1}), compared to the 1.5% Cr:LiSAF crystal ($\alpha \cong 9$ cm^{-1}). We therefore believe a 2.5% doped Cr:LiSGaF crystal would exhibit better thermal performance.

Finally, for the Cr:LiCAF gain medium, the thermal effects were measured using the 1.6% output coupler, and the variation in the output power was very small (1-2 mW). This is expected, since Cr:LiCAF has much better thermal properties as compared to Cr:LiSAF and Cr:LiSGaF (higher thermal conductivity [142], lower thermal lensing [138, 140], lower quantum defect, lower excited-state absorption [1, 4], and a lower upconversion rate [135], Table 1.2).

2.7 Recent Work with Single-mode Diode Pumping

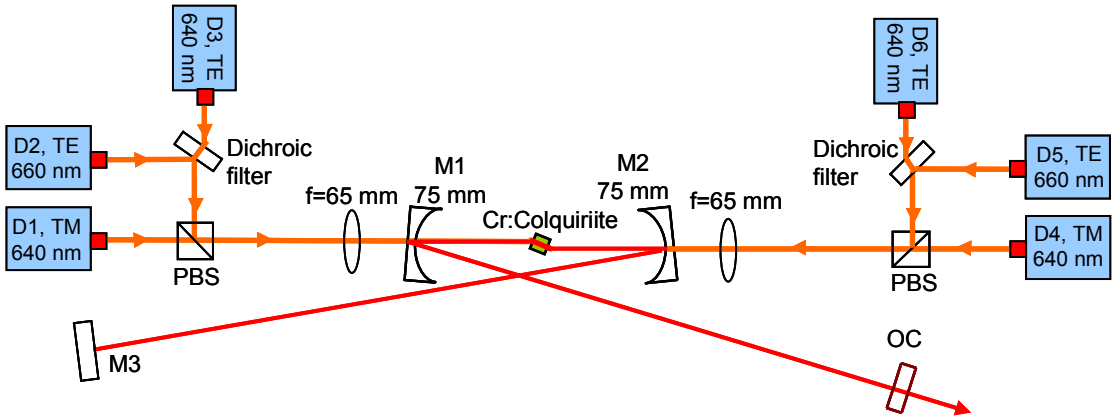

Figure 2.43: Schematic of the cw Cr:Colquiriite laser which is pumped by six single-mode diodes.

When we started the single-mod diode pumping experiments with Cr:Colquiriites in August 2007, HL6545MG (660 nm 130 mW) was the highest power commercial single-mode diode around 650 nm (600-700 nm range). Hence, during this PhD. work most of the data with single-mode diodes have been taken with this 660 nm 130 mW diode. In 2009 HL6385DG (642 nm 150 mW) become available, and we have started using it after July 2009. In this section we will provide some representative data with the

recently available higher power diodes. We note here that red-diode laser technology keeps improving. For example, Optnext just released a 637 nm 170 mW diode in Jan 2010 (HL63133DG) [238]. Also, recently, a 1-W, nearly transform-limited (M^2~1.3) 650 nm diode laser source was demonstrated [239]. It is clear that these advances will have a direct positive impact on the specifications of Cr:Colquiriite lasers in the future. For a more detailed description of the single-mode diodes, we refer the reader to Appendix B.

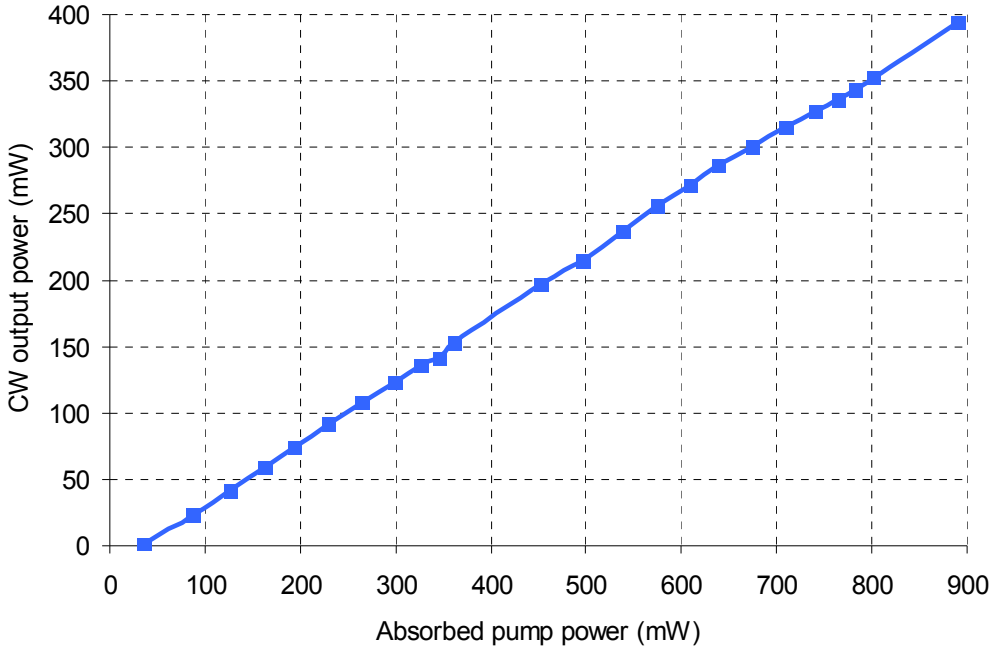

Figure 2.44: CW efficiency curve taken with the six single-mode diode pumped Cr:LiCAF laser using a 1% output coupler. We thank Jing Wang for his help while taking this data.

Figure 2.43 shows schematic of a typical Cr:Colquiriite laser which is pumped by six single-mode diodes. Out of this six single mode diodes four of them is HL6385DG (642 nm 150 mW), and two of them is HL6545MG (660 nm 130 mW). 642 nm and 660 nm are wavelength coupled with each other using a dichroic mirror, then further polarization coupling enabled coupling of three diodes from each side. Each 640-nm laser diode produces about 200 mW of output power when driven at 350 mA (above the typical rating of 150 mW, 280-350 mA, at 25 °C), while each 660-nm laser diode produces about 150 mW output power when driven at 220 mA (above the typical rating of 130 mW, 180-220 mA). The 640 nm diodes were TEC-cooled to 20 °C, whereas no active cooling was applied to the 660 nm diodes. In total, about 1 W of pump power is available on the Cr:Colquiriite crystals. With the six diode pumped system we could generate ~450 mW of pump power from the Cr:LiCAF and Cr:LiSAF lasers (a similar performance is expected from Cr:LiSGaF, bit this not demonstrated experimentally). We have been also

using simper version of this cavity, namely Cr:Colquiriite lasers pumped by four HL6385DG (642 nm 150 mW), where the obtained cw power levels are around ~350 mW.

As an example, Fig. 2.44 shows the measured sloped efficiency of the six single-mode diode pumped Cr:LiCAF laser taken with a 1% output coupler. As much as ~395 mW of cw output power is obtained with about ~900 mW of absorbed pump power, where the lasing threshold and slope efficiency were ~30 mW and 46%, respectively.

2.8 Future Work with Multimode Diode Pumping

For the multimode diode pumped Cr:LiCAF system, our initial results with a 5% Cr:LiCAF 4-mm long crystal have shown that, using a lower chromium concentration will significantly decrease the thermal load on the x-tal (in comparison with a 2-mm 10% chromium doped crystal, with same level of absorption). Moreover, we have seen that one can still get similar slope efficiency (this is not clear in this case since pump is multimode and Rayleigh range is short). In this section, we will give a short summary of the initial results.

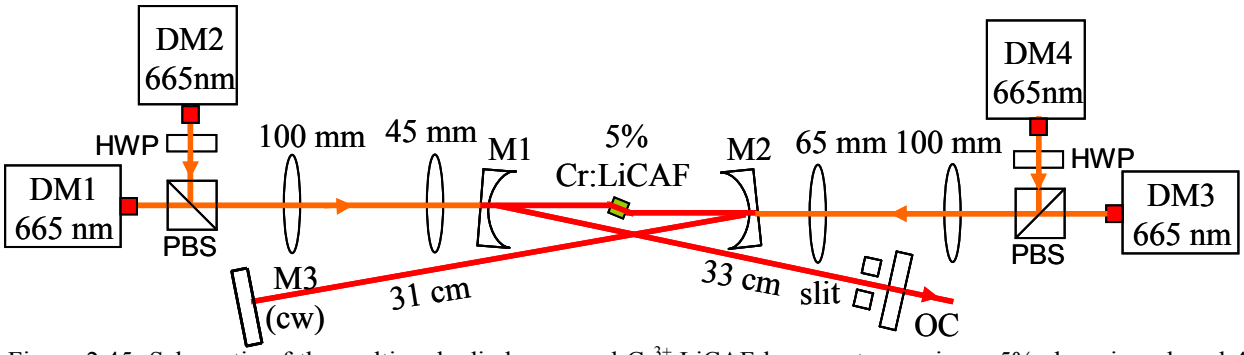

Figure 2.45: Schematic of the multimode diode-pumped Cr^{3+}:LiCAF laser system, using a 5% chromium doped 4-mm long crystal. Four multimode diodes (DM1-DM2), each providing 1.6 W of pump power at 665 nm, were used as the pump source. The diodes were coupled using polarizing beam splitter cubes (PBS). Half-wave plated (HWP) were used to rotate the polarization of the diode lasers. A slit near the OC (tangential plane) was used to control the transverse mode structure of the laser beam.

Figure 2.45 shows the schematic of the multimode diode-pumped Cr^{3+}:LiCAF laser cavity used in the cw lasing experiments. This time, four linearly-polarized, multimode, single-emitter diodes (DM1-DM2) were used as the pump source. Cw laser cavity was similar to what was described earlier. The gain medium was a 4-mm-long, 1.5-mm thick, Brewster-cut, 5 % Cr doped Cr^{3+}:LiCAF crystal which was mounted with indium foil in a copper holder and water-cooled at 15 °C. The absorption of the crystal was larger than 90 % for both TE and TM polarized light at 665 nm. Again, a slit near the OC (tangential plane) was used to control the transverse mode structure of the laser beam.

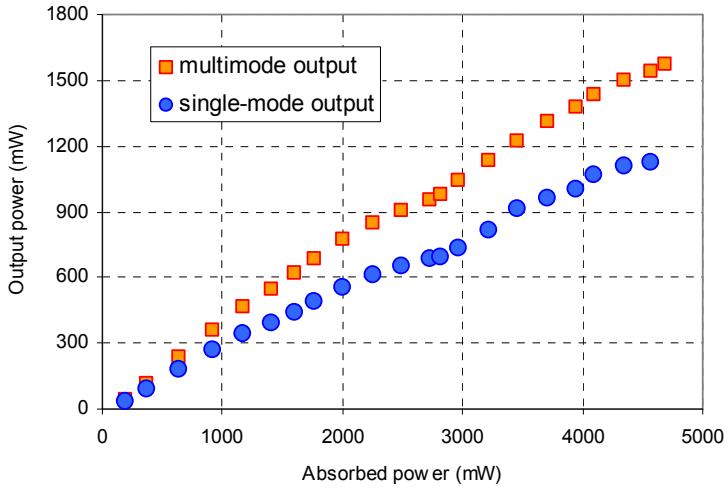

Figure 2.46: Measured performance of multimode diode pumped Cr:LiCAF laser with the 4 mm-long 5 % Cr doped Cr^{3+}:LiCAF crystal.

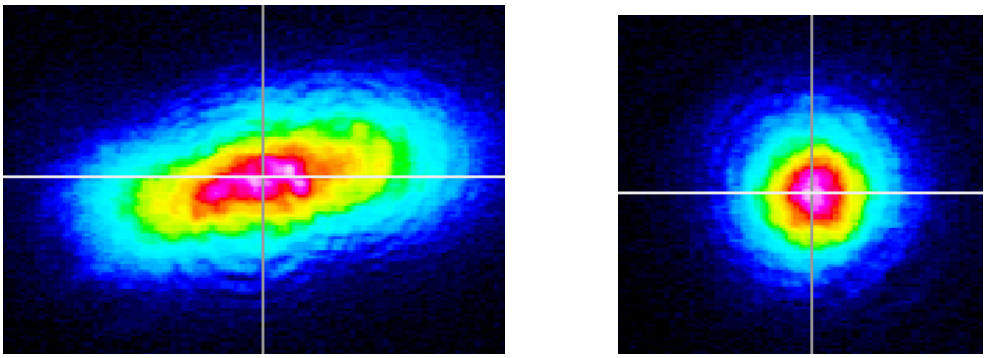

(a) (b)

Figure 2.47: Cr:LiCAF laser output mode structure (a) Without the intracavity slit, where the output power was 1.57 W. (b) With the intracavity slit, where the output power was 1.23 W.

Figure 2.46 shows the measured cw performance of the multimode diode pumped Cr^{3+}:LiCAF laser taken using a 0.85% output coupler. The data is taken for the case with and without the intracavity slit. Without the intracavity slit, the laser output was multimode (Figure 2.47-(a)), and we obtained 1.57 W of laser output, with 4.7 W of absorbed pump power (4.95 W incident power), where the corresponding slope efficiency of the laser was ~34%. With the intracavity slit, we can obtain single-mode laser output (Figure 2.47-(b)), with 1.23 W of output power, using 4.6 W of incident pump power. The slope efficiency for this case was ~25%. We also measured the variation of cw laser output power as a function of the crystal holder temperature (Fig. 2.48). The data were taken at an absorbed pump power level of 4.7 W, without the intracavity slit, using the 0.85% OC. Fig. 2.48 also shows that thermal effects are not very strong for this lowly doped x-tal. Lastly, using a 2% output coupler, we have obtained more than 2 W of output power for the cavity without the slit. Unfortunately, one of the diodes burned while taking this data, hence we don't have an efficiency curve for this case.

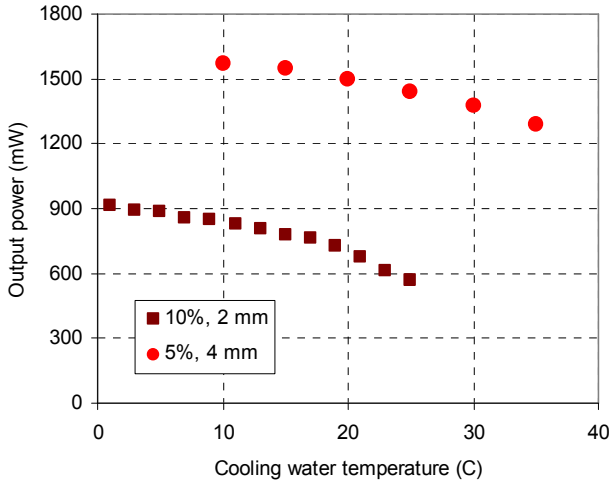

Figure 2.48: Measured variation of the cw output power with crystal holder temperature for the multimode diode-pumped Cr^{3+}:LiCAF laser. The data for the 5% chromium doped 4-mm long Cr:LiCAF crystal was taken at an absorbed pump power of 4.7 W, using a 0.85% output coupler. The data for the 10% chromium doped 2-mm long Cr:LiCAF crystal was taken at an absorbed pump power of 2.9 W, using a 1.4% output coupler. Both cases were taken without using the intracavity slit; hence, the laser output was multimode.

2.9 Self Q-switching Behavior in Cr:Colquiriite Lasers

In this section we would like to briefly describe a somehow unexpected behavior we have observed in Cr:Colquiriite lasers, namely self q-switching behavior. Self q-switched operation in Cr^{3+}:Colquiririte laser occurred with the regular cw cavity (without the SESAM/SBR). The phenomenon was self-starting, observed at several different curved mirror separations (M1-M2 separation) and was repeatable (similar phenomena were observed with multimode and single-mode diode pumping cavities also). At several values of curved mirror separation (not necessarily near the edge of the stability regions), the laser switched from cw operation to q-switched operation with an accompanying decrease in output power (Fig. 2.49). Also at these positions, the laser transverse mode switched from single-mode to a structured multimode (Fig. 2.50), and spectral widening was also observed in some cases (Fig. 2.51). When the laser is forced to operate in single transverse mode with the insertion of an intracavity slit, the effect disappeared and the laser returned back to cw operation. Similar self q-switching phenomenon in Cr^{3+}:CrColquirrite lasers have also been reported earlier, and this behavior is used to produce short (~30 ns), high-energy (~50 nJ) q-switched pulses [240-245]. The phenomenon in Cr^{3+}:LiSAF is attributed to a time-dependent nonlinear lensing effect inside the gain medium [240-245].

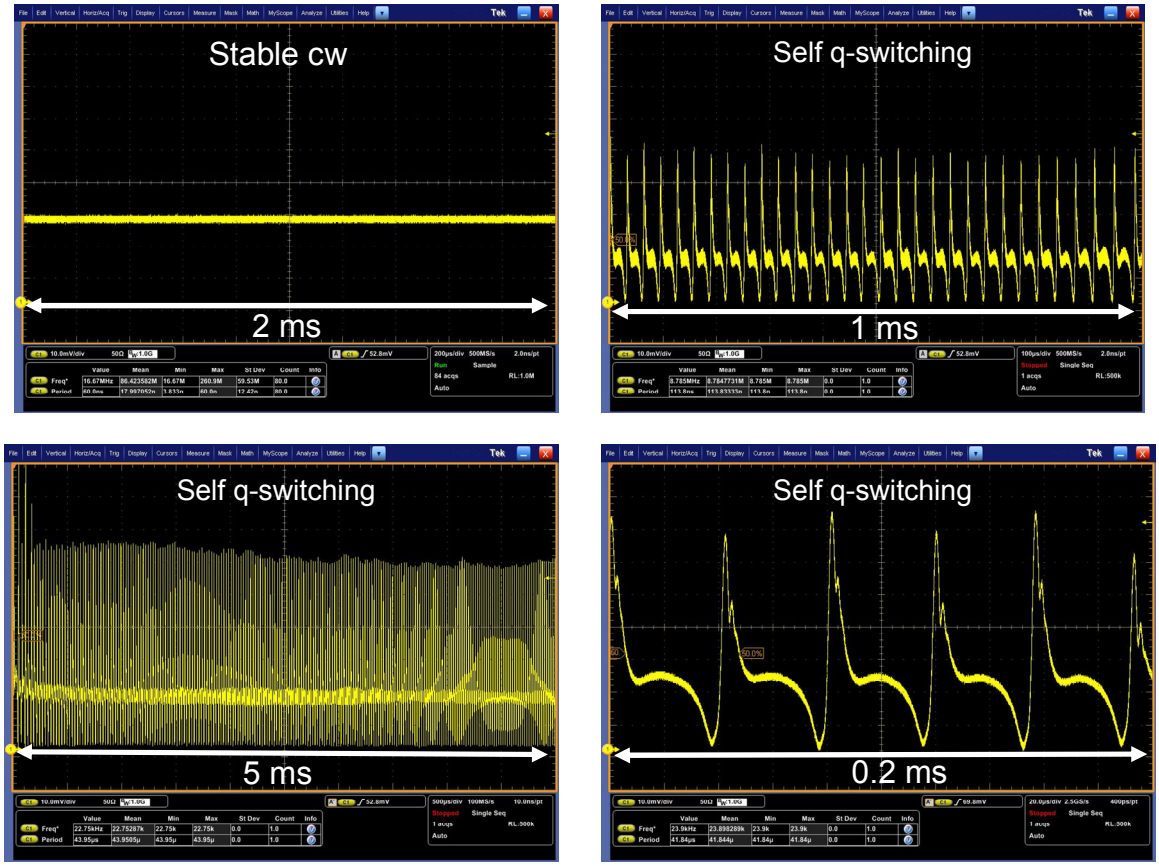

Fig. 2.49 Measured oscilloscope traces for the self q-switching behavior we have observed in single-mode diode pumped Cr:LiCAF laser.

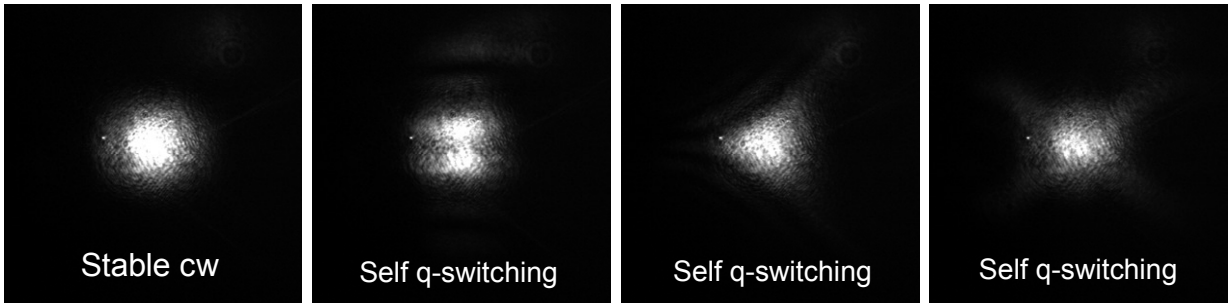

Fig. 2.50 Measured laser output beam profiles for the self q-switching behavior we have observed in single-mode diode pumped Cr:LiCAF laser.

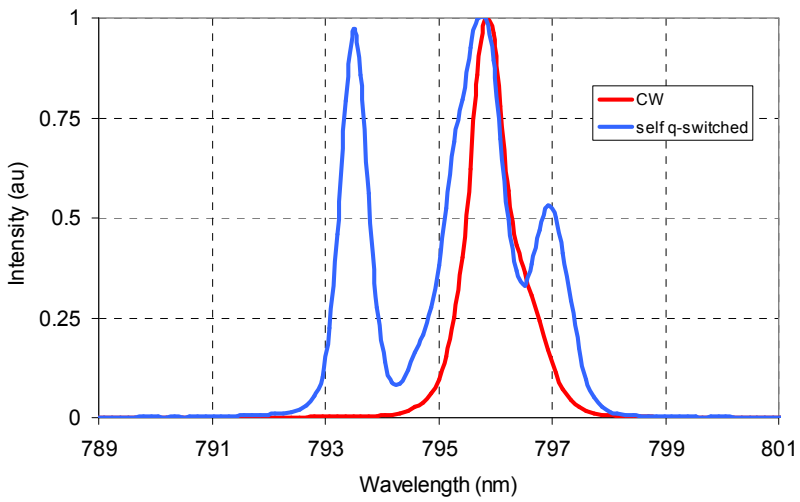

Fig. 2.51 Measured optical spectrum of the laser for during regular cw and self q-switched operation for the single-mode diode pumped Cr:LiCAF laser.

2.10 CW Performance Comparison of Cr:LiCAF, Cr:LiSAF and Cr:LiSGaF Gain Media

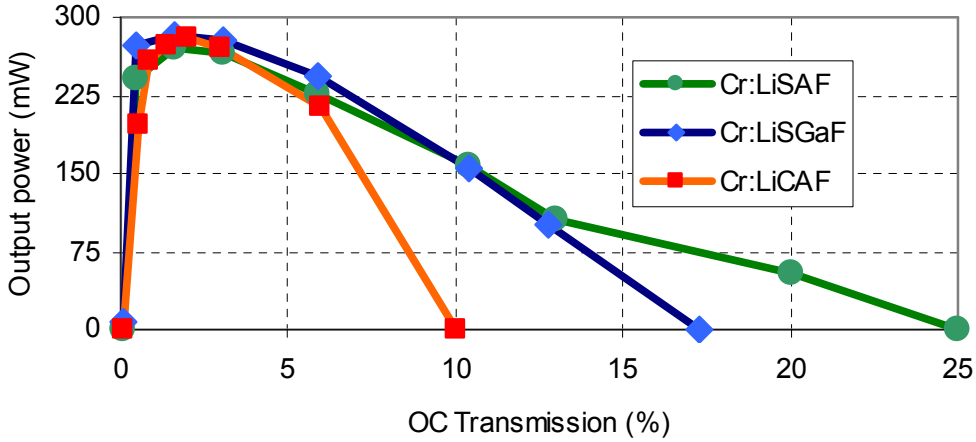

Figure 2.52 Measured variation of cw laser output power with output coupler transmission for Cr:LiSAF, Cr:LiSGaF and Cr:LiCAF gain media, at an absorbed pump power of ~550 mW.

In this section we would like to briefly compare the cw experimental results obtained with Cr:Colquiriite gain media. Figure 2.52 shows the measured cw laser output power variation with output coupler transmission for Cr:LiSAF, Cr:LiSGaF, and Cr:LiCAF lasers together. All of the results were obtained at room temperature with an absorbed pump power level of ~550 mW, using the single-mode diode pumped system which was pumped by four 660 nm diodes. Up to 271, 283 and 280 mW of output power were obtained with Cr:LiSAF, Cr:LiSGaF and Cr:LiCAF lasers, respectively. Hence, the maximum obtained power levels are almost same with each gain media. The optimum output coupling is ~1-3% for all cases, which indicates that the resonator losses are very low. Cr:LiSAF has the highest gain

among the three media, since lasing could be obtained at higher output coupling levels compared to Cr:LiCAF and Cr:LiSAF. This is consistent with its larger emission cross section, fluorescence lifetime product (~$\sigma_{em}\tau$ product, Table 1.2). Cr:LiCAF has the lowest gain and low loss optics (R>~99.99%) are required for efficient lasing operation. We should note here that, some component of the decrease in output power at high output coupling levels is due to the increased role of Auger upconversion process. Rate of Auger upconversion increases for high output coupling due to decreased intracavity power levels (as described in Section 2.6 above). Hence, even though Cr:Colquiriites has a higher $\sigma_{em}\tau$ product than Ti:Sapphire, they cant lase at high output couplings that Ti:Sapphire laser can laser (such as ~30-40 %), which shows the significant effect of Auger upconversion process on small signal gain.

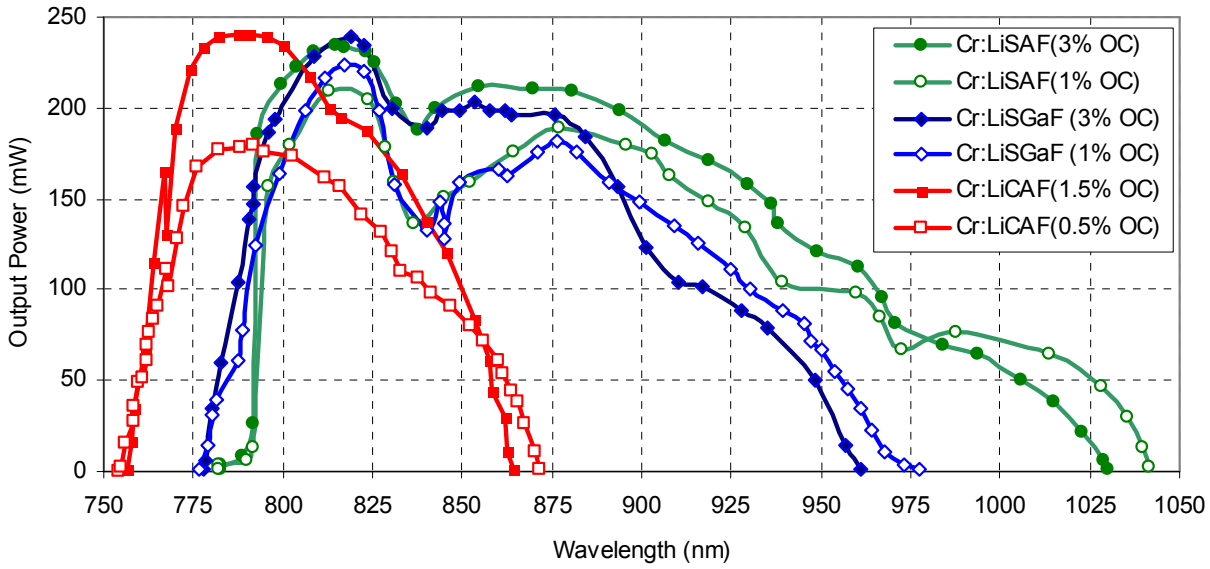

Figure 2.53: CW tuning curves for Cr:LiSAF (782-1042 nm), Cr:LiSGaF (777-977 nm) and Cr:LiCAF (754-871 nm), taken at room temperature, at an absorbed pump power of ~550 mW.

Figure 2.53 shows the measured cw tuning range for the Cr:Colquiriite lasers together, taken at an absorbed pump power of ~550 mW. Record tuning ranges were obtained with all of the materials, which we believe result from increased pump powers, pump beam quality and the availability of low-loss optics, and better quality crystals. Ti:Sapphire has the widest tuning range among solid-state materials, with a fractional tuning range of 0.57 (660-1180 nm, $\Delta\lambda/\lambda_0 \cong 0.57$, where $\Delta\lambda$ is the full width of the tuning range and λ_0 is the central wavelength [55]). The fractional tuning ranges are ~0.29 for Cr:LiSAF (775-1042 nm, $\Delta\lambda/\lambda_0$ = 262/911), ~0.23 for Cr:LiSGaF (777-977 nm, $\Delta\lambda/\lambda_0$ = 200/877) and ~0.19 for Cr:LiCAF (720-871 nm, $\Delta\lambda/\lambda_0$ = 151/795.5). Among the Cr:Colquiriites, Cr:LiSAF has the highest gain and broadest tuning range, making it attractive over Cr:LiSGaF and Cr:LiCAF. The sister crystal, Cr:LiSGaF, has slightly better thermal properties, slightly higher intrinsic slope efficiency and slightly higher nonlinear

refractive index as compared to Cr:LiSAF; however, these advantages may not be sufficient to offset the disadvantages due to the lower gain.

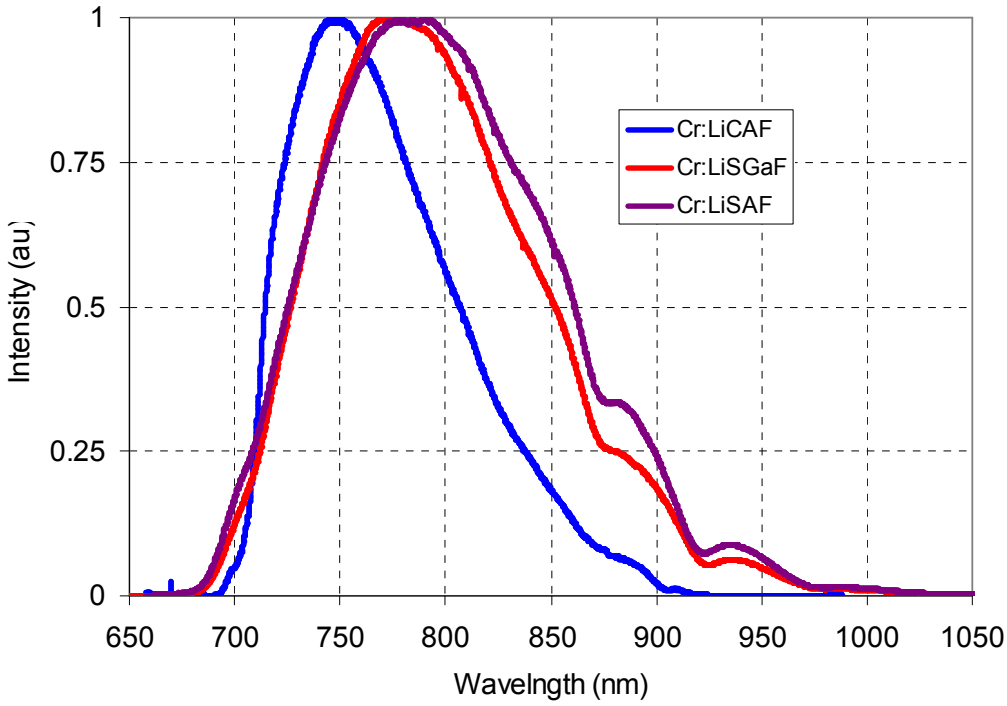

Figure 2.54: Measured unpolarized emission spectrum of Cr:LiCAF, Cr:LiSGaF and Cr:LiSAF gain media at room temperature. The modulations in the emission spectrums is an artifact from the HR we used to collect the light. Also emission spectrum is measured with a silicon CCD detector; hence the decrease in emission strength at longer wavelengths might be partly due to the decreased quantum efficiency of the Si detector.

As mentioned above, Cr:LiCAF is quite distinct from Cr:LiSAF and Cr:LiSGaF gain media. The main advantage of Cr:LiCAF is its blue-shifted emission spectrum, which covers the spectral range from ~750 to ~800 nm (Fig. 2.54). The 750-800 nm spectral region is quite important for applications like Ti:Sapphire amplifier seeding and multiphoton microscopy [202]. Moreover, the thermal properties of Cr:LiCAF is superior to other Cr:Colquiriites; hence it can enable better power scaling. Although Cr:LiCAF has the lowest gain and narrowest tuning range among Cr:Colquiriites, its unique spectral range and thermal properties makes it the material of choice in some applications.

CHAPTER 3

MODE-LOCKED CR:LICAF LASERS

In Chapter 2, we have presented our continuous-wave lasing experimental results with Cr:Colquiriite gain media, which demonstrated their efficient laser operation and their broad gain bandwidths enabling broad tunability in ~750-1000 nm wavelength region. This suggests that Cr:Colquiriite gain media can also be used for efficient generation of ultrashort pulses. Starting from this chapter, we will start to present mode-locking lasing results with Cr:Colquiriite gain media. In this Chapter ,we will present mode-locking results with Cr:LiCAF gain media. Then, Chapter 4 and 5 will discuss the mode-locking experiments with Cr:LiSAF and Cr:LiSGAF respectively.

Cr:LiCAF gain medium is distinct in the Cr:Colquiriite family. Cr:LiCAF lases in the spectral range from ~750 to ~800 nm, which is not accessible by the other Cr:Colquiriites and has better thermal properties, which can enable high-power operation. The main disadvantage of Cr:LiCAF is its low emission cross section, which results in low gain (round-trip gain < 10%), requiring extremely low loss optics. Moreover, due to its lower emission cross section, Cr:LiCAF has higher tendency to q-switch [220]. However, despite these disadvantages, 750-800 nm spectral region is important for applications such as amplifier seeding or multiphoton microscopy [202], and superior thermal properties of Cr:LiCAF can enable power scaling.

Table 3.1 lists some of the key mode-locking results obtained with Cr:LiCAF gain media during this PhD thesis work. Firs of all, note that the total pump power is different for different results. Most of the results were obtained from single-mode diode pumped systems except the last 4 (case 15-18, marked by*), which were obtained from multimode diode pumped systems. With single-mode diode pumping, in the earlier experiments we have used four HL6545MG (~660 nm) diodes to excite the gain media, which provides up to about ~600 mW of total pump power. Later, we have also started to use four HL6385DG (~640 nm) pump diodes, which can provide up to about ~800 mW of pump power. Currently, the highest pump power we could get with single-mode pumping is about ~1W, which we can obtain by using two HL6545MG and four HL6385DG pump diodes together. We note here that HL6545MG diode does not require water cooling, where as the HL6385DG diode and the multimode diode does. Detailed information on the pump diodes we have used during this PhD can be found in Appendix B.

Case	Pulse width (fs)	Output power (mW)	Peak power (kW)	Pulse energy (nJ)	Rep rate (MHz)	Central Wavelength (nm)	Output Coupler (%)	Dispersion compensation method	Pump power (mW)	Section/ Ref
1	72	178	19.5	1.4	127	~800	2	DCMs	~600	3.1, [178]
2	63	144	18	1.13	127	~805	0.85	DCMs	~600	3.1, [220]
3	45	120	20.5	0.92	130	~803	2.4	DCMs	~600	-
4	70	180	25.7	1.8	100	~800	2	DCMs	~600	8.2, [202]
5	90	140	15.6	1.4	100	~808	0.85	GTIs & DCMs	~600	-
6	240	180	5.8	1.38	130	~805	2.4	GTIs & DCMs	~600	-
7	~130	~130	11.6	~1.5	86	785-817 (767-817)	2	GTIs & DCMs	~800	3.4
8	39	125	41.6	1.62	77	~805	2	DCMs	~800	3.3
9	270	253	9.2	2.48	102	~812	2	GTIs & DCMs	~1000	3.2
10	180	265	15.2	2.73	97	~813	2	GTIs & DCMs	~1000	3.2
11	117	245	22.3	2.61	94	~813	2	DCMs	~1000	-
12	170	265	16.6	2.82	94	~807	2	DCMs	~1000	-
13	98	95	101.2	9.92	9.58	783	2.4	GTIs & DCMs	~600	6, [191]
14	310	160	49.1	15.22	10.51	795	2.4	GTIs & DCMs	~600	6, [191]
15*	50	150	25	1.25	120	~800	1	DCMs	~4000	[143]
16*	67	300	37.3	2.5	120	~800	2.4	DCMs	~4000	[143]
17*	60	280	31.1	1.87	150	~800	1	DCMs	~2500	3.5, [220]
18*	97	390	28.7	2.78	140	~795	1.4	DCMs	~2500	3.5, [220]

Table 3.1: Summary of cw mode-locking results obtained with Cr:LiCAF gain media. * Obtained from multimode diode pumped systems. All the results reported in this table have an uncertainty of about ±10%. DCMs: Double-chirped mirrors, GTIs: Gires–Tournois interferometer mirrors.

For dispersion compensation we have used commercially available double-chirped mirrors (DCMs) and/or Gires–Tournois interferometer mirrors (GTIs) from Layertec. The commercial DCMs had a group velocity dispersion (GVD) of only ~ - 40-50 fs^2 per bounce. Sometimes this required the usage of large number of bounces on DCM mirrors, which then produces loss, which is quite bad, for a low gain media such as Cr:LiCAF. On the other hand, GTI mirrors can have high GVD per bounce (~ -500 fs^2), and only 1-2 bounces is required to compensate the cavity dispersion, but they had quite narrow dispersion bandwidth with rapid oscillations. Detailed specs of the Layertec DCM and GTI mirrors can be found in Appendix A.

As mentioned earlier, for initiating and sustaining mode-locking, we have used SESAM/SBR mode-locking. This is because of the low nonlinear refractive index (n_2) of Cr:Colquiriites, which prevents the usage of Kerr-lens mode-locking (KLM). Advantages of using SESAMs/SBRs instead of KLM include self-starting mode-locked operation, immunity to environmental fluctuations and reduced cavity alignment requirements. All of the results in Table 3.1 were obtained using MIT 800 nm quantum well absorber with 2 pairs of high-reflective layer coatings(MIT-800-QW-2HR), which had a modulation depth of about 0.6%. We have listed the specs of this SESAM/SBR in Appendix E7. We have also used several other SESAM/SBRs with Cr:LiCAF laser, and we will compare their laser performance in Section 3.7.

Note that, in mode-locked operation the free running optical spectrum of Cr:LiCAF laser is mostly centered around 800 nm, but sometimes shifted to ~785 nm or ~810 nm region. This shift is mostly caused by a dispersion minimum at those wavelengths, especially for the results obtained with GTI mirrors. The gain of Cr:LiCAF medium is also relatively flat in this region, which allows this shift.

With Cr:LiCAF gain media, pulses as short as 39 fs, and pulse energies as high as 2.8 nJ, and peak powers as high 41.6 kW were obtained from ~100 MHz cavities (Table 3.1). Using an extended cavity Cr:LiCAF laser, pulse energies can be scaled to 15.2 nJ [191], and peak powers exceeding 100 kW were also demonstrated (case 13-14). With multimode diode pumping average powers as high as 390 mW could be obtained. The central wavelength of the mode-locked Cr:LiSAF laser could be tuned from continuously from 785 nm to 817 nm, by just rotation of a birefringent filter element. Initial results suggested that by a proper DCM set, this tuning range can be extended to at least cover the 767 nm-817 nm region.

In the following sections, we will give the details of some of the mode-locking results obtained with Cr:LiCAF gain media. In Section 3.1 we will present typical mode-locked operation results of single-mode diode pumped Cr:LiCAF laser. Here by typical operation we mean operation parameters of the laser such as the pulse width and the repetition rate is chosen at an intermediate level, where the laser operates relatively more stably. This section will also discuss stability issues of SESAM/SBR mode-locked lasers such as q-switching instabilities and multiple pulsing instabilities. In Section 3.2, we will present our recent mode-locking results with higher power single mode diodes. Section 3.3 will describe sub-50-fs pulse generation in Cr:LiCAF gain media. In Section 3.4, we will present our initial tuning results with sub-200-fs pulses. In Section 3.5, we will present mode-locking experiments with multimode diode pumped Cr:LiCAF laser. In Section 3.6, we will compare mode-locking performance our different 800 nm SESAM/SBRs. Section 3.7, will discuss pure q-switched operation of Cr:LiCAF gain media with a SESAM/SBR. Finally in Section 3.8, we will summarize the results during this PhD and compare it with the earlier results in the literature.

3.1 Typical Mode-Locked Operation of Cr:LiCAF Laser

In this section, we will present some typical results from mode-locked Cr:LiCAF laser. Figure 3.1 shows a schematic of the single-mode diode-pumped Cr^{3+}:LiCAF laser cavity used for cw mode-locked laser experiments. The cavity was similar to what was used in cw laser experiments (see Chapter 2). Four HL6545MG (~660 nm) single-mode diodes provided about ~600 mW of pump power. The gain medium was a 2-mm-long, Brewster-cut, 10% Cr-doped Cr^{3+}:LiCAF crystal mounted with indium foil in a copper holder [143, 174]. The crystal absorbed 97.5% and 84% (0.9 x 93.5%) of the incident TM and TE polarized pump lights, respectively, and the total absorbed pump power was ~570 mW. Neither the

crystal nor diodes required water cooling. For mode-locking experiments, two double-chirped mirrors (DCMs) with group velocity dispersion (GVD) of ~ -45±10 fs^2 per bounce were used to provide negative dispersion (see Layertec DCM set II in Appendix A.6). MIT 800-nm SESAM/SBR with quantum well absorber design with two pairs of HR coating was used to initiate and sustain mode locking. This SESAM/SBR has a quite low modulation depth (0.6%), which gives the best performance in low gain Cr:LiCAF media. More details about this SESAM can be found in Appendix E. A 75 mm radius of curvature mirror (M4) was used to focus on the SESAM (from Layertec pump mirror set I). The SESAM mode-locked laser was self-starting, immune to environmental fluctuations and did not require careful cavity alignment, enabling turn-key operation.

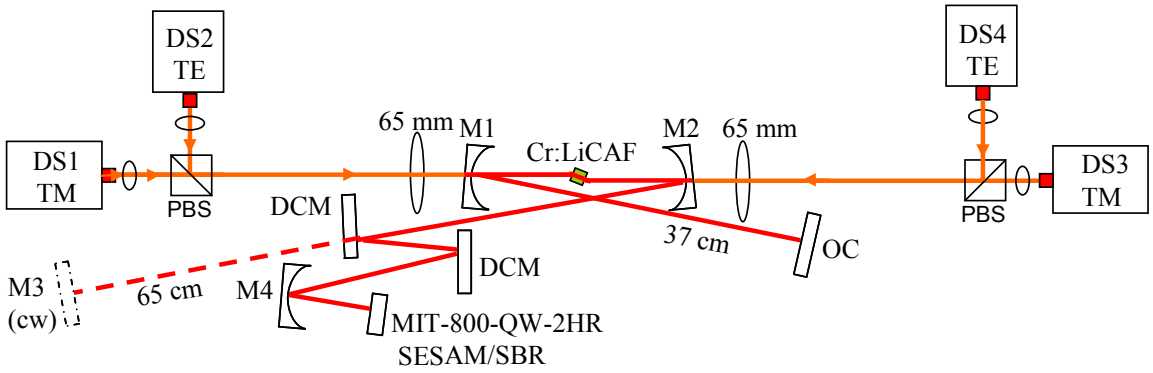

Figure 3.1: Schematic of the single-mode diode-pumped Cr^{3+}:LiCAF laser system. Four single-mode diodes (DS1-DS4) each providing ~150 mW of pump power at 660 nm was used as the pump source. Dashed lines indicate the continuous-wave laser cavity. PBS: polarizing beam splitter cube, M1-M2: pump mirrors from Layertec Cr:Colquiriite pump mirror set I, with R= 75 mm, M3: flat high reflector, M4: curved high reflector with R=75 mm, OC: output coupler, DCM: flat double-chirped mirrors from Layertec DCM set II with ~-45±10fs^2 dispersion per bounce, SESAM/SBR: semiconductor saturable absorber mirror / saturable Bragg reflector.

The estimated total round-trip cavity dispersion was shown in Fig 3.2, which includes the dispersion from the Cr:LiCAF crystal, DCM mirrors, SESAM/SBR and the intracavity air. Dispersion for the output coupler was unknown and we assumed that it has negligible dispersion in the region of interest. The 10% Cr-doped Cr^{3+}:LiCAF crystal has a group velocity dispersion (GVD) of about ~28 fs^2/mm around 800 nm, and produces about 110 fs^2 of dispersion in round trip. Intracavity air also produces a GVD of ~20 fs^2 per meter. Four bounces on DCM mirrors cancels provides about ~ -200 fs^2 and cancels out the positive dispersion from the intracavity air and the Cr:LiCAF crystal. We estimate the total round-trip cavity dispersion to be about ~-40 fs^2 around 800 nm. Note that the relatively narrow GVD bandwidth of the SESAM/SBR disturbs the relatively flat dispersion from the other cavity elements.

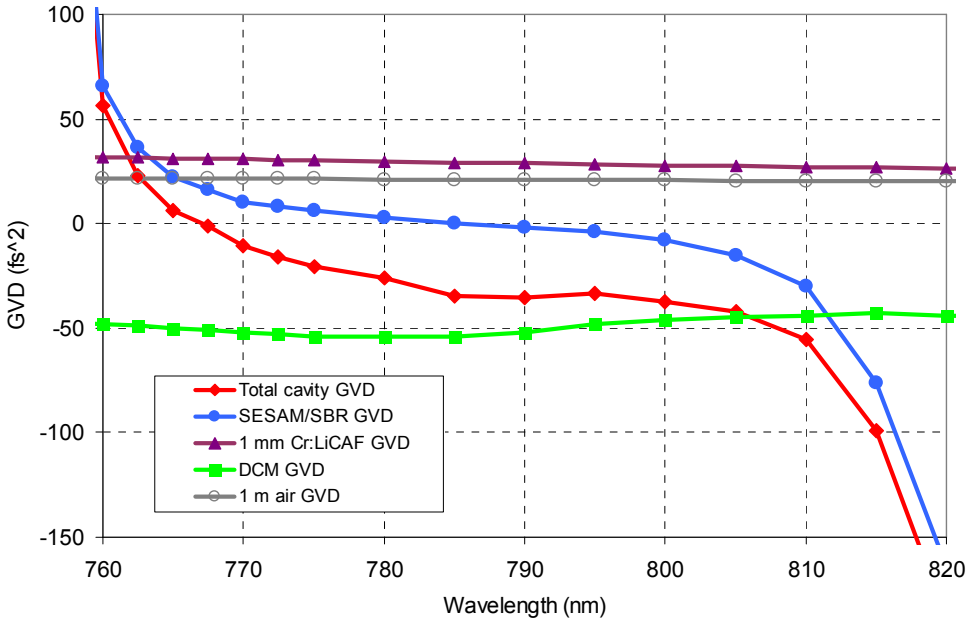

Figure 3.2: Estimated total cavity dispersion for the Cr:LiCAF laser that was shown in Fig 3.1. GDD curves for the Cr:LiCAF crystal, air, DCM, and the SESAM/SBR are also included.

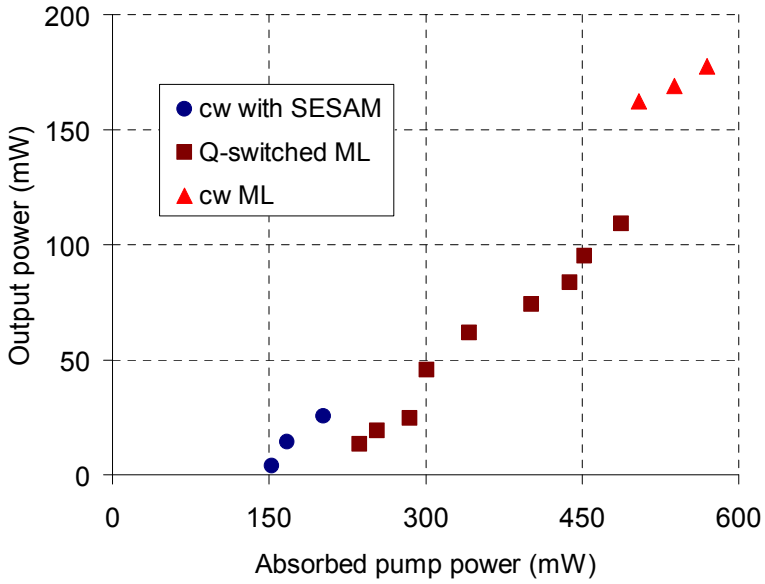

Figure 3.3: Efficiency curve for the mode-locked Cr^{3+}:LiCAF laser in different regimes of operation taken with the 2% output coupler.

In mode locking experiments, different output couplers were tried to optimize the mode-locked performance. Although shorter pulses could be obtained with lower output couplers, a 2% output coupler gave the maximum average output power in mode-locked regime. Figure 3 shows the variation of laser output power and laser dynamics with absorbed pump power, measured using a 2% output coupler. The

laser operated in cw mode for absorbed pump powers up to ~225 mW, and generated Q-switched mode-locked pulses for pump powers between ~225 and ~500 mW (Q-switched ML in Fig. 3.3). For pump powers above ~500 mW we could obtain stable cw mode-locked operation (cw ML). Figure 3.4 shows the pulse trains in cw mode-locked regime for two different oscilloscope settings.

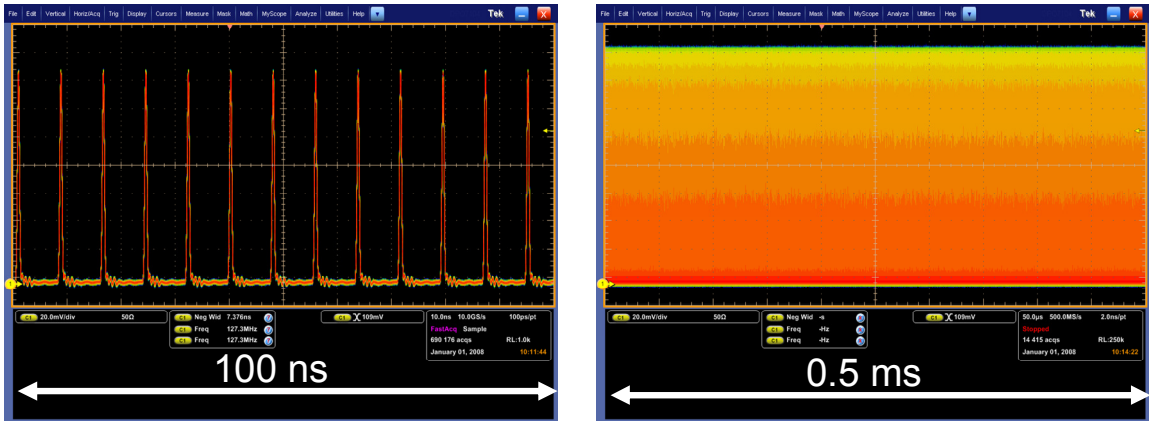

Figure 3.4: Pulse train in stable cw mode-locking regime. Repetition rate is 127 MHz.

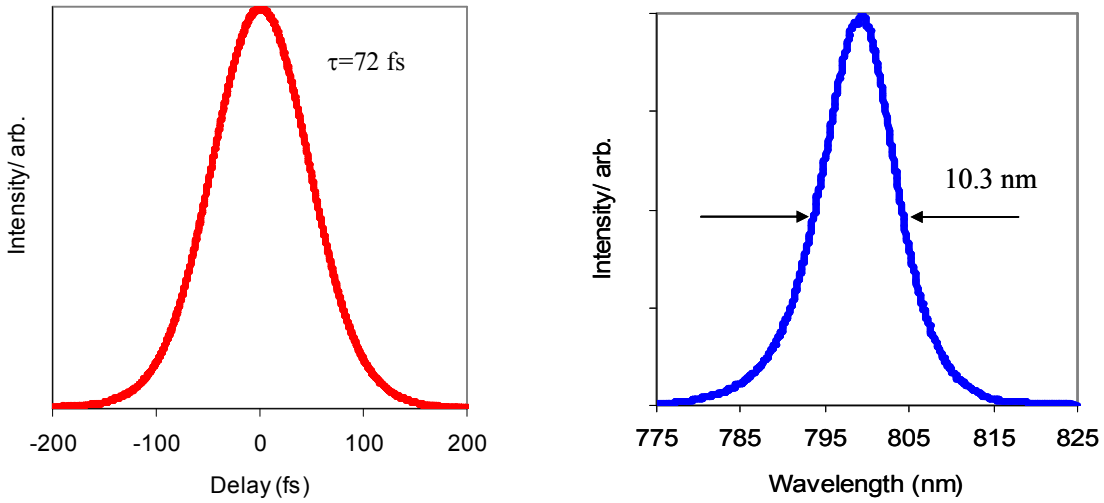

Figure 3.5: Measured spectra and autocorrelation trace for the 72-fs, 1.4 nJ pulses with 178 mW of average output power, taken using the 2% OC.

Figure 3.5 shows the spectra and autocorrelation trace taken with the 1.9% output coupler at the pump power of ~570 mW. The laser produced 72-fs pulses (assuming $sech^2$ pulses) with 178 mW average power and 10.3 nm spectral bandwidth near 800 nm at 127 MHz (~1.4-nJ pulse energy). The time bandwidth product was ~0.35, close to the transform limit of 0.315 for $sech^2$ pulses.

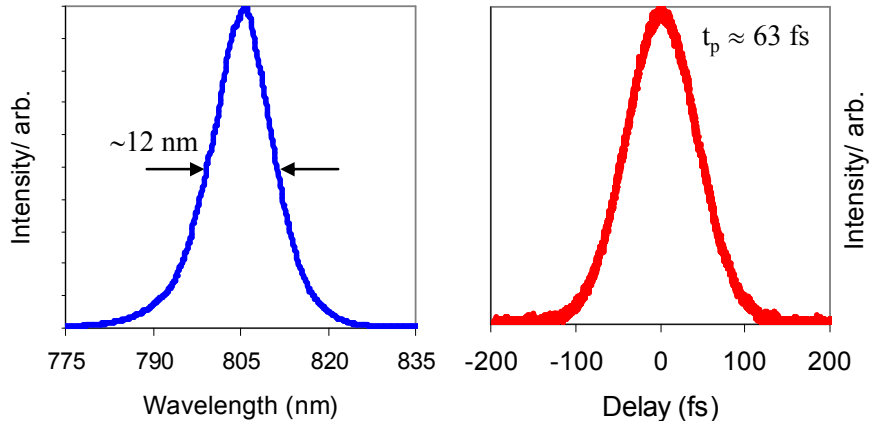

Figure 3.6: Measured spectrum and second harmonic autocorrelation taken with the single-mode diode-pumped Cr^{3+}:LiCAF laser using the 0.85 % output coupler at an incident pump power of ~570 mW. The FWHM of the autocorrelation is 95 fs, corresponding to a 63-fs pulse duration (assuming $sech^2$ pulse shape). The average output power is 144 mW, corresponding to pulse energy of 1.13 nJ for a 127-MHz repetition rate cavity. The spectrum has a bandwidth of ~12 nm (FWHM) centered around ~805 nm. The corresponding time bandwidth product is ~0.35.

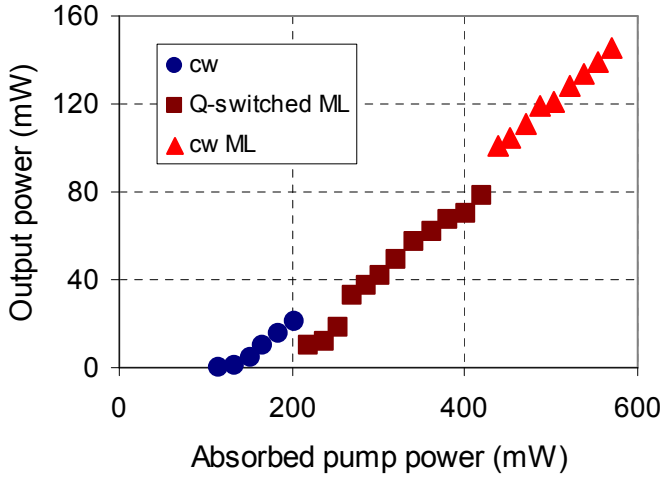

Figure 3.7: Efficiency curve for the single-mode diode pumped mode-locked Cr^{3+}:LiCAF laser in different regimes of operation taken with the 0.85 % output coupler. cw: continuous-wave operation, Q-switched ML: Q-switched modelocked operation, cw ML: continuous-wave modelocked operation.

Using an output coupler with lower transmission (0.85%), 63-fs duration pulses with 144 mW average power at 127 MHz (1.13-nJ pulse energies) were also demonstrated (Fig. 3.6). Lower output coupling enabled shorter pulses due to the increased intracavity pulse energy levels and self-phase modulation. Increased intracavity pulse energies also decreased the pump powers required for stable cw mode-locking from ~500 mW to ~430 mW (Fig. 3.7). However, with the lower output coupler, the laser is more immune to cavity losses, and the average output power is lower.

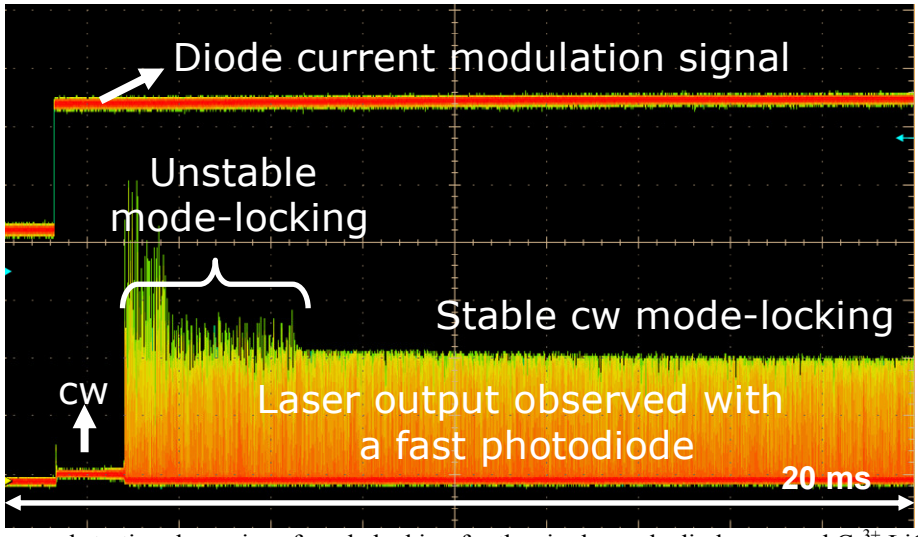

Figure 3.8: Measured starting dynamics of mode locking for the single-mode diode-pumped Cr^{3+}:LiCAF laser taken using the 0.85 % OC.

To understand the mode locking mechanism with SESAM/SBR, we have measured the starting dynamics of mode-locking by modulating the pump diode currents. For this, at first the laser diodes were turned off for a long time, and then turned on with a square wave current input. In the 'on' state, the diodes provided ~570 mW of absorbed pump power. The data were taken using the 0.85 % OC, and the mode locking dynamics were observed by detecting the laser output with a fiber-coupled 2-GHz silicon detector and a 1-GHz oscilloscope. Figure 3.8 is a typically observed oscilloscope trace, which shows both the applied rectangular pump current signal and the laser behavior afterwards. When the pumps were first turned on, the laser typically required 30-50 μs to start lasing. The lasing started with some relaxation oscillation with a relaxation frequency of ~125 kHz, then stable cw operation was observed. In this cw mode, the output powers were quite low (~20-40 mW), due to the high level of losses (~1%) of the SBR/SESAM at low incident fluencies. Then in 0.5 ms to 5 ms, the SESAM/ SBR initiated some pulsing, where the average power levels jumped above 100 mW. In most of the cases, at first the initiated mode locking was unstable and required between 1 ms to 50 ms for the SBR/SESAM to stabilize mode locking (unstable mode-locking in Fig. 3.8). In all the cases, after about 100 ms, stable cw mode-locking with an average power of ~140-150 mW was obtained. For the specific case shown in Fig. 3.8, SBR/SESAM initiated pulsing started in about 2 ms, and stable cw mode locking was obtained after 6 ms. Lastly the observed slight decrease of average mode locked power in Fig. 3.8 is due to the heating of the pump diodes, which caused a decrease in available pump power level. It required about one second for the diodes to reach their thermal equilibrium and then the laser output power was stable.

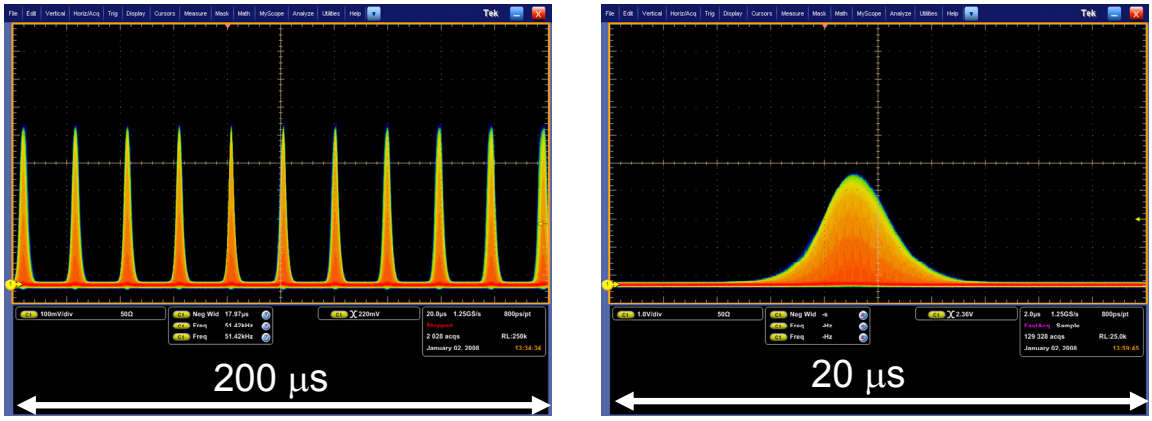

Figure 3.9: Oscilloscope traces for stable q-switched mode-locked operation.

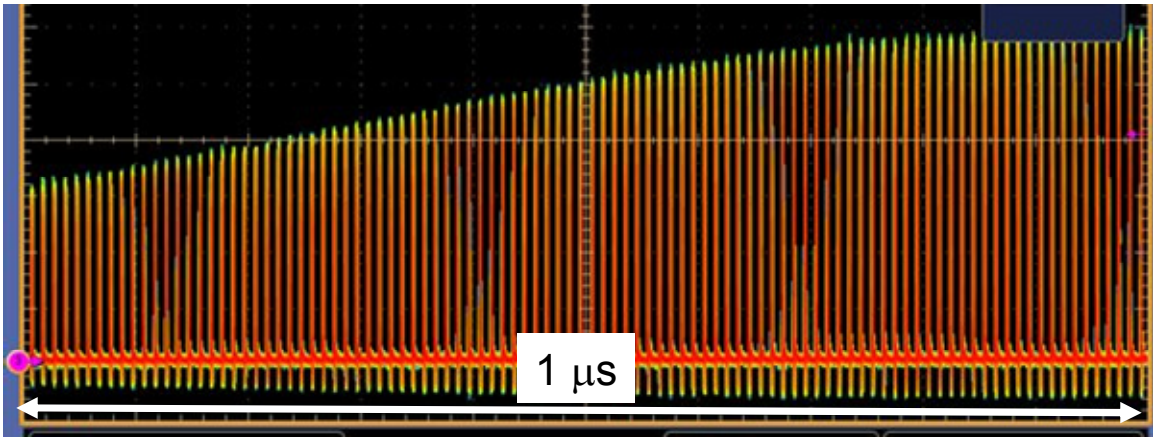

Figure 3.10: Stable mode-locked pulse train under the q-switched laser envelope.

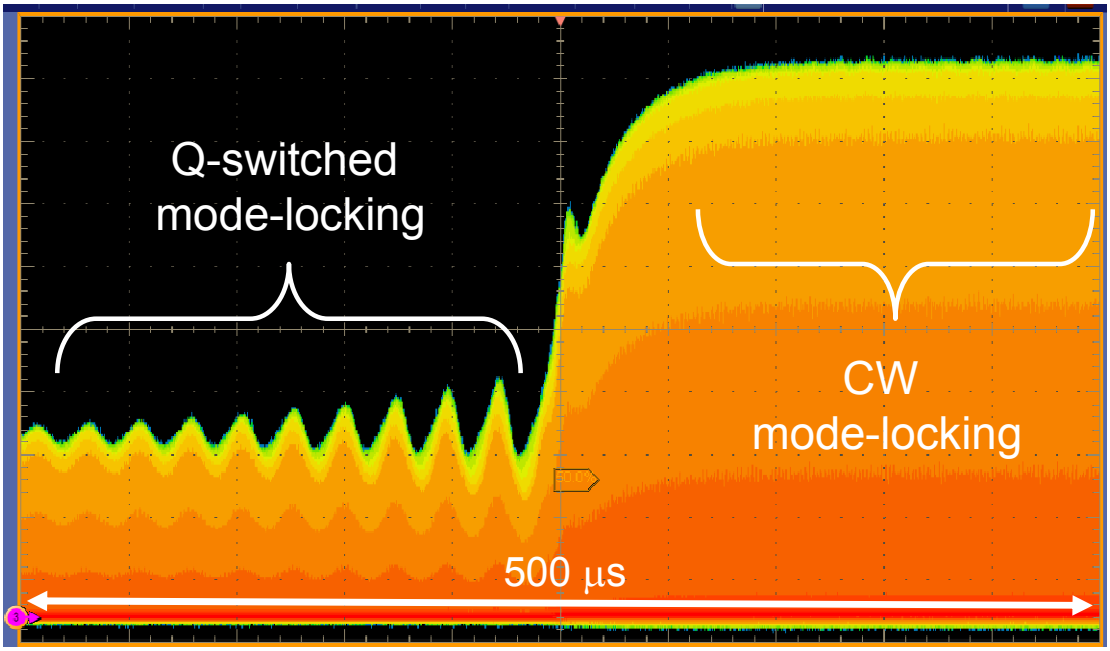

Figure 3.11: Transition of the laser from q-switched mode-locked operation to cw mode-locked operation as the pump power is increasing by modulation of diode current.

We finish this section by discussing the two different mode-locking regimes (Q-switched versus cw mode-locking) observed with the SBR/SESAM mode-locked Cr:LiCAF laser described in this work. The measured variation of laser dynamics of the Cr:LiCAF laser in Figs. 3.3 and 3.7 show that stable cw mode-locking could be obtained after the laser output power reaches a critical value. However below this value the laser operates in Q-switched modelocked regime (Fig. 3.9-3.11). This behavior is well-known in lasers modelocked with an SESAM/SBR [246-248]. Starting from a rate equation analysis and by making several simplifying assumptions, it is possible to show that in order to obtain stable cw mode-locking (without Q-switching), the intracavity pulse energy should be above a critical value ($E_{P,c}$) [246, 247]. This critical intracavity pulse energy ($E_{P,c}$) can be written as [246]:

$$\mathrm{E_{P,c}} = \sqrt{\mathrm{E_{sat,L}}\,\mathrm{E_{sat,A}}\,\Delta R}\,, \tag{3.1}$$

where $E_{sat,L}$ is the saturation energy of the gain medium, $E_{sat,A}$ is the absorber (SBR/SESAM) saturation energy and ΔR is the modulation depth of the absorber. Saturation energy of the gain medium ($E_{sat,L}$) is defined as [246]:

$$\mathrm{E_{sat,L}} = \frac{\mathrm{h}\nu_l}{(\mathrm{m}\sigma_{\mathrm{em}})}\mathrm{A_{eff,L}}\,, \tag{3.2}$$

where σ_{em} is the emission cross section of the gain medium, m is the number of passes through the laser crystal in one round trip, and $\mathrm{A_{eff,L}}$ is the effective laser mode area inside the gain medium. Absorber saturation energy ($E_{sat,A}$) is defined as the product of absorption saturation fluence ($\mathrm{F_{sat,A}}$) and effective laser mode area on the absorber [246]:

$$\mathrm{E_{sat,A}} = \mathrm{F_{sat,A}}\mathrm{A_{eff,A}}\,. \tag{3.3}$$

With these, Eq. (3) could also be written as:

$$\mathrm{E_{P,c}} = \sqrt{\frac{\mathrm{h}\nu_l}{(\mathrm{m}\sigma_{\mathrm{em}})}\mathrm{A_{eff,L}}\mathrm{F_{sat,A}}\mathrm{A_{eff,A}}\Delta R}\,. \tag{3.4}$$

Here, we note that, the critical pulse energy defined by Eq. (3.4) considers a laser mode-locked by SESAM/SBR mechanism only. For the Cr:LiCAF laser described in this work, SESAM/SBR initiated and sustained stable mode locking, however, the pulses were shaped mainly by a soliton mechanism enabling fs pulse generation [246]. The effect of soliton pulse shaping is to lower the critical pulse energy required for stable mode locking even further [246]. For the single-mode diode pumped Cr:LiCAF laser cavity, using Eqs. (3.4), we estimated the critical value of the intracavity pulse energy for stable cw mode locking ($E_{P,c}$) as ~40 nJ (m=2, $\sigma_{em}\approx$ 1.3 x10^{-20} cm^2, $\mathrm{A_{eff,L}} \approx \pi(16)(20)$ μm^2, $\mathrm{A_{eff,A}} \approx \pi(16)(16)$ μm^2,

$F_{sat,A} \approx 280$ μJ/cm^2, $\Delta R \approx 0.006$). The experimentally measured value of the critical intracavity pulse energy ($E_{P,c}$) was ~75 nJ and ~44 nJ for the 0.85 and 1.95 % output couplers, respectively (see Fig 16 for the 0.85 % OC results, and see Fig. 3 in reference [178] for the 1.95 % OC results). We attribute the difference between the measured values and the estimated value of $E_{P,c}$ using Eq. (3.4), to the difficulty of determining the parameters used in Eq. (3.4) accurately.

In general, it is desirable to have a laser with low $E_{P,c}$ in order to obtain stable cw mode locking even with low pumping powers. One challenge with Cr:LiCAF gain medium is its lower emission cross section (σ_{em}). The saturation energy of the gain medium ($E_{sat,L}$) is inversely proportional to the emission cross section (Eq. 3.2). Hence, keeping all the other parameters in Eq (3.4) the same, due to its much higher emission cross section (Table 1.2), a Ti:Sapphire laser has ~6 times lower $E_{P,c}$ than a Cr:LiCAF laser, and this explains why the tendency to Q-switch is less for Ti:Sapphire. In Cr:LiCAF, obtaining stable mode-locked operation, without Q-switching requires careful laser design and selection of operating parameters. Finally, it is important to note that Q-switched modelocked operation of Cr:LiCAF might be advantageous in some applications such as micromachining, surgery, and nonlinear microscopy [246].

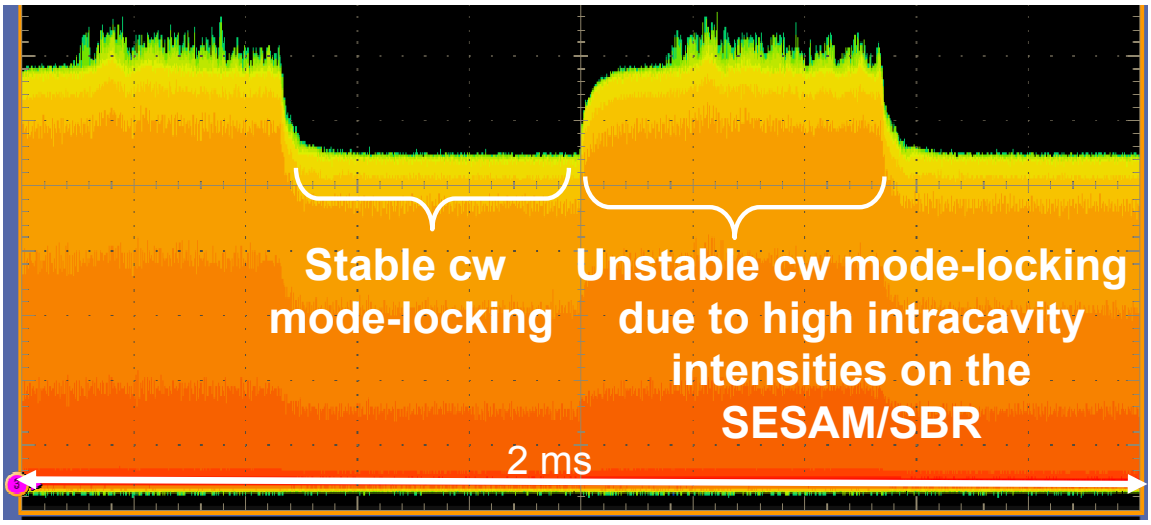

Figure 3.12: Transition of the laser from stable cw mode-locked operation to unstable cw mode-locked operation due to increased pump power. This instability is caused by two photon absorption effects on the SESAM/SBR.

Looking at Eq. 3.4, one might suggest arbitrarily decreasing the effective spot size on the SESAM/SBR or inside the gain medium, to decrease the required critical pulse energy levels. However, in general there is an optimum spot size for the gain medium, and decreasing it in an arbitrary way might lower the laser slope efficiencies or might generate too much self-phase modulation, which would be hard to balance. Also, we cant decrease the spot size on the SESAM/SBR too much. This is because at tighter

focusing and at high intracavity intensity levels, two-photon absorption (TPA) process will start on the SESAM/SBR, which can generate pulse to pulse instability in the mode-locked pulse train (pulse energy and pulse duration might fluctuate). As an example, Fig. 3.12 shows this type of instability in the cw mode-locked laser due to the tight focusing on the SBR. Note that even a small increase in pump power above a certain level is enough for TPA induced laser instabilities. Increasing the focusing on the SESAM/SBR further might even cause multiple pulsing instabilities as shown in Figure 3.13. We note here that TPA effect starting threshold is a function of peak power. Hence, for pulses with same energy, shorter pulses will be more susceptible to TPA effects.

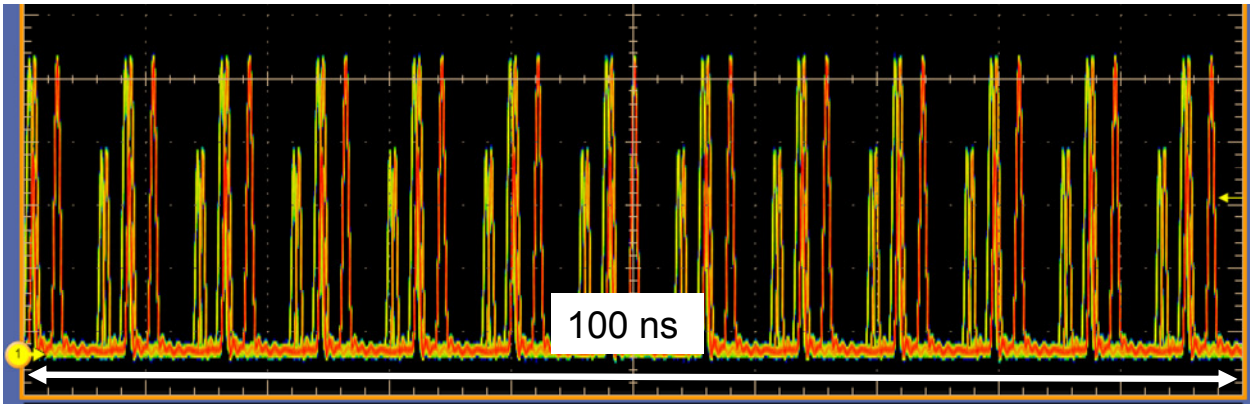

Figure 3.13: Multiple pulsing instability in cw mode-locked regime.

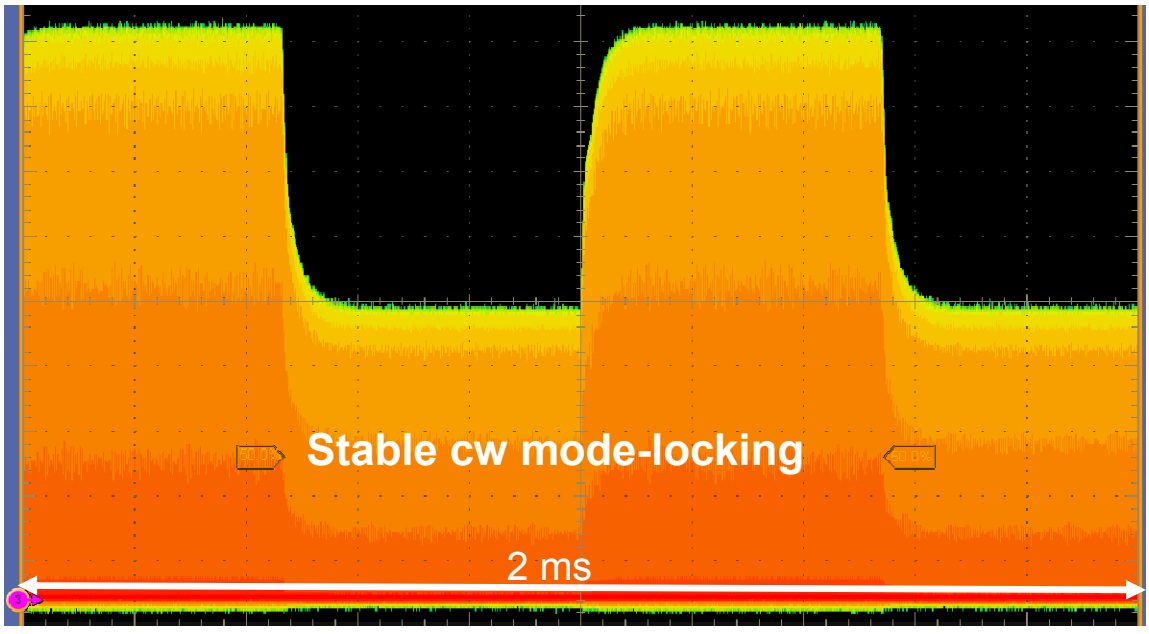

Figure 3.14: Stable cw mode-locking at two different pump powers, demonstrating the working range of SESAM/SBR.

In short, there is a limited working range of a SESAM/SBR, where it produces stable cw mode-locking (Fig. 3.14). Decreasing the focusing on the SESAM/SBR or decreasing the intracavity pulse energy levels too much, might cause q-switched mode-locking instability. On the other hand, focusing too tight on the SESAM/SBR or increasing the intracavity pulse energies too much might cause TPA induced multiple pulsing instabilities. Note that for gain media with higher emission cross section, working range of the SESAM/SBR is broader, since the critical pulse energy for stable cw mode-locking is an inverse function of emission cross section. Also note that, the working range is also broader for longer pulses, because the TPA effects starting threshold will be higher. Due to these facts, it is quite challenging to generate short pulses with high pulse energy from gain media with low emission cross section such as Cr:LiCAF.

3.2 Mode-Locking of Cr:LiCAF Laser with Higher Power Single Mode Diodes

As mentioned earlier, we have started the single-mod diode pumping experiments with Cr:Colquiriites in August 2007, using HL6545MG (660 nm). Then we started using HL63133DG in around Jan 2010. Here, we will give representative mode-locking data of the Cr:LiCAF gain medium with this higher power diodes. For a more detailed description of the single-mode diodes, we refer the reader to Appendix B.

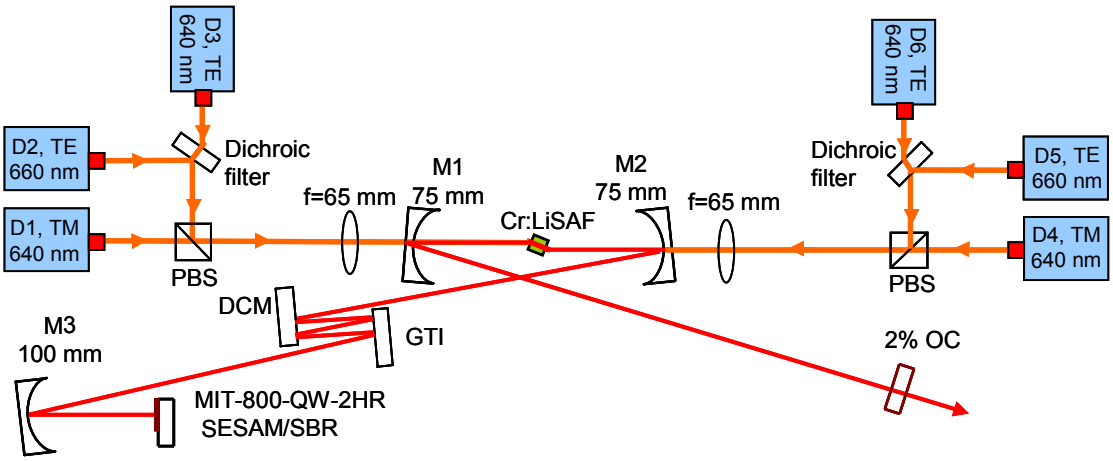

Figure 3.15: Schematic of the cw mode-locked Cr:LiCAF laser which is pumped by six single-mode diodes.

Figure 3.15 shows schematic of the cw mode-locked Cr:LiCAF laser which is pumped by six single-mode diodes. Out of this six single mode diodes four of them is HL6385DG (642 nm 150 mW), and two of them is HL6545MG (660 nm 130 mW). The six diodes provide about 1 W of pump power on the Cr:LiCAF crystals. A 2.5 mm long, 11% chromium doped Cr:LiCAF crystal was used in the experiments. Water cooling was not applied to the crystal. MIT 800 nm SESAM/SBR with quantum well absorber and 2 pairs of HR coating is used to initiate and sustain mode-locked operation. M1-M3 are

regular pump mirrors with ~0 dispersion from Layertec Cr:Colquiriite pump mirror set I. Dispersion compensation is accomplished by use of GTI and DCM mirrors. The GTI mirror provided -550 ± 50 fs^2 dispersion per each bounce (Layertec GTI mirror set I), whereas the DCM mirror provided only -45 ± 10 fs^2 per bounce (Layertec DCM mirror set II). We refer the reader to Appendix A for more information on the specs of the mirrors.

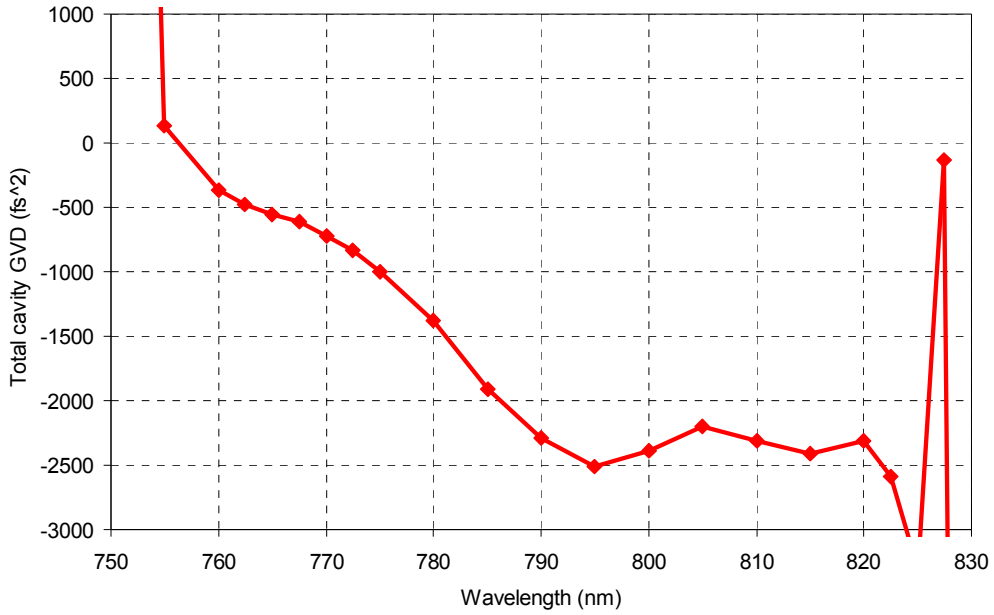

Figure 3.16: Estimated total cavity dispersion. Dispersion estimate includes GVD of laser crystal, intracavity air, DCM mirrors, GTI mirror, and SESAM/SBR.

Figure 3.16 shows the estimated total dispersion of the cavity. Note the large amount of total negative dispersion due to the use of GTI mirrors. When mode-locked the laser produced ~270-fs long pulses with 253 mW of average output power at a repetition rate of 102 MHz, at an absorbed pump power of ~900 mW. The corresponding pulse energy was as high as 2.48 nJ. The optical spectrum was centered around ~812 nm, and had a bandwidth of 2.5 nm. Figure 3.17-3.19 summarizes the obtained mode-locking results. When the number of bounces on GTI and DCM in one round-trip was decreased from 4 to 2, we have obtained ~180-fs pulses with 2.73 nJ of pulse energy at a repetition rate of 97 MHz. Optical spectrum and the estimated cavity dispersion level is shown in Fig. 3.20 for this case. As expected decreased magnitude of total cavity dispersion enabled longer pulses. Note that the optical spectrum in Fig. 3.20 has a spike, which we believe is a result of rapid dispersion oscillations in the GTI mirror.

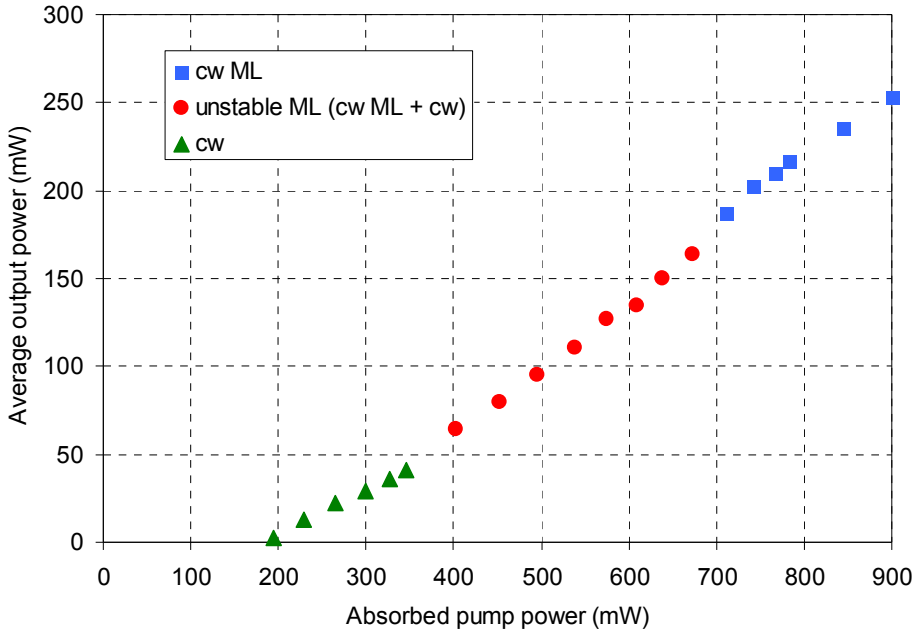

Figure 3.17: Efficiency curve for the mode-locked Cr^{3+}:LiCAF laser pumped by six single-mode diode pumped.

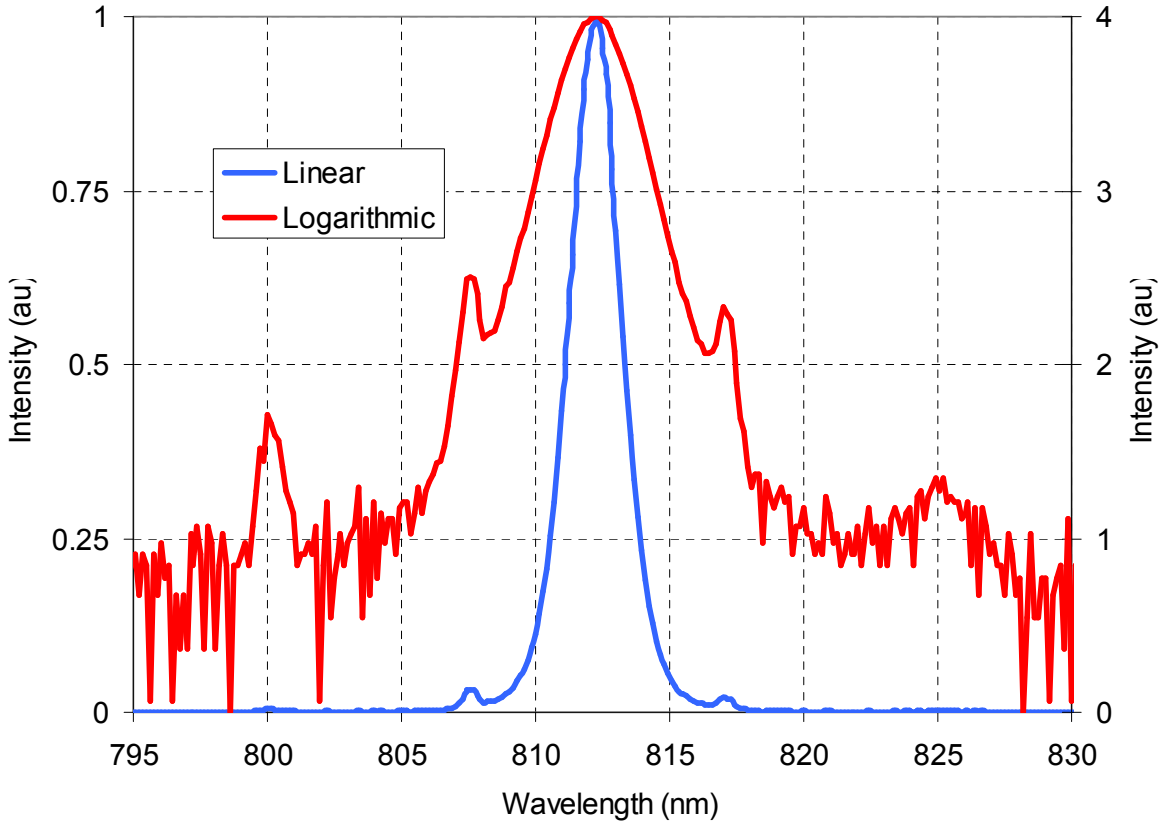

Figure 3.18: Recorded optical spectrum in linear and logarithmic scales for the ~270-fs, 2.48 nJ pulses.

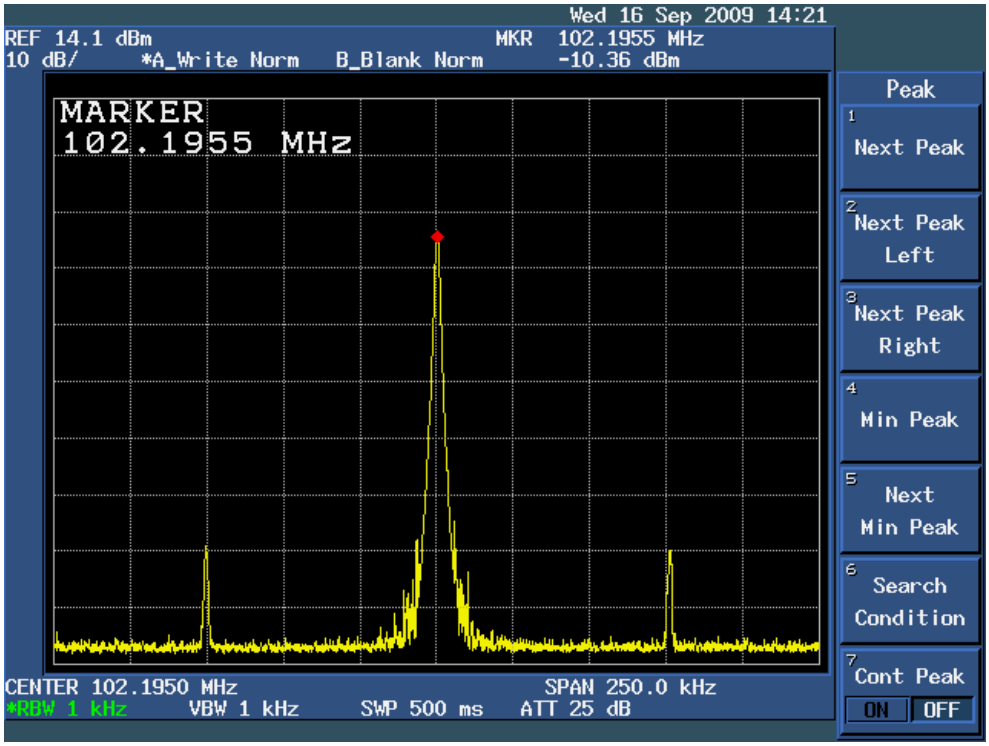

Figure 3.19: Recorded microwave spectrum for the ~270-fs, 2.48 nJ pulses. The repetition rate is measured as 102.1955 MHz.

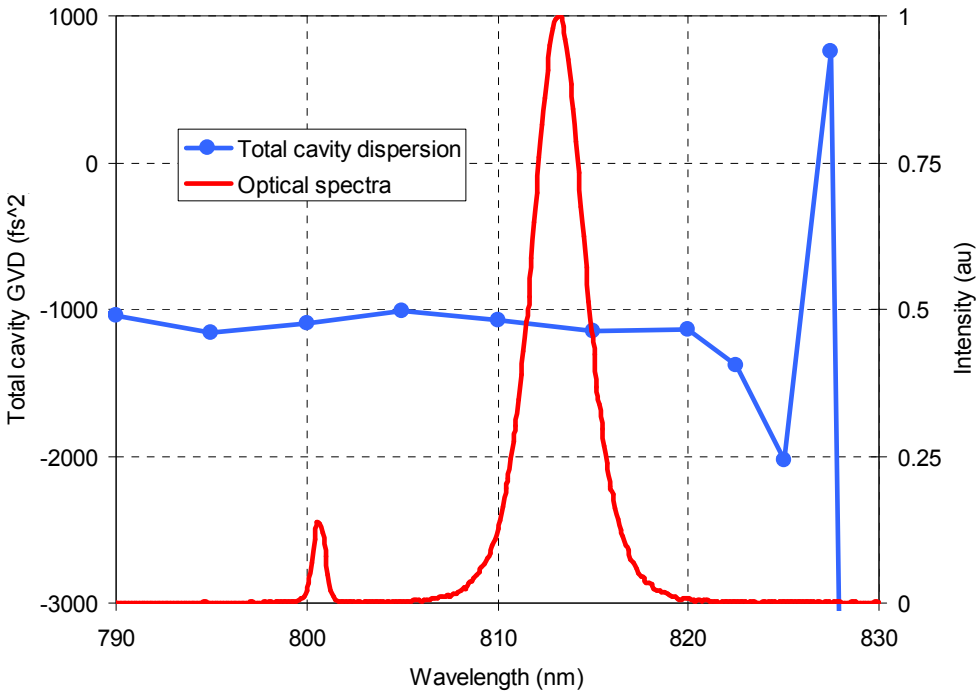

Figure 3.20: Recorded optical spectrum and the estimated total cavity dispersion level for the ~180-fs, 2.73 nJ pulses.

3.3 Sub-50-fs Pulses from Cr:LiCAF Laser

By careful adjustment of intracavity dispersion level, it was possible to obtain sub-50-fs pulses from Cr:LiCAF laser. For fine dispersion adjustment, one can use prism pairs in general. However, it is a better option to use prism free cavities for the long term stability of the system. In this section we will present a Cr:LiCAF laser, which can produce sub-50-fs pulses by using DCMs for dispersion compensation.

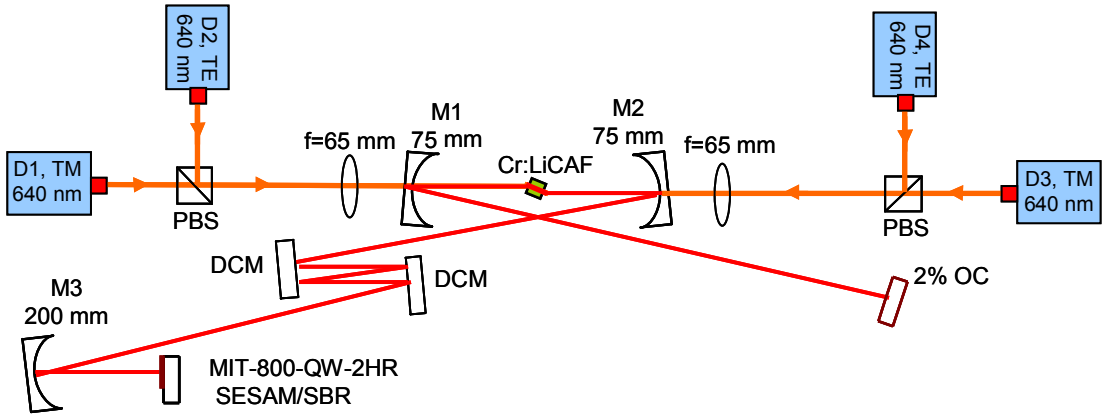

Figure 3.21: Schematic of the cw mode-locked Cr:LiCAF laser which is pumped by four 640 nm single-mode diodes. The laser is used to generate sub-50-fs pulses.

Figure 3.21 shows the schematic of the cw mode-locked Cr:LiCAF laser which is pumped by four 640 nm single-mode diodes (HL6385DG). The four diodes provided about ~800 mW of pump power, and the 2.5 mm long, 11% chromium doped Cr:LiCAF crystal absorbed more than ~700 mW of the incident pump power. MIT 800 nm SESAM/SBR with quantum well absorber and 2 pairs of HR coating is used to initiate and sustain mode-locked operation. Similar to the earlier cavities, M1-M3 are regular pump mirrors with ~0 dispersion from Layertec Cr:Colquiriite pump mirror set I. Dispersion compensation is accomplished by use of DCM mirrors (one mirror from Layertec DCM set I, and one mirror from Layertec DCM set III).

When mode-locked the laser produced ~39-fs long pulses with 125 mW of average output power at a repetition rate of 77 MHz, with an absorbed pump power of ~700 mW. The corresponding pulse energy was 1.62 nJ. Figure 3.22 shows the obtained recorded spectrum as well as the estimated dispersion of the cavity. The optical spectrum was centered around ~805 nm, had a bandwidth of 18.8 nm, and is broad enough to support ~36-fs level pulses. The dispersion of the cavity was around -100 fs^2 at the center of the optical spectrum, and is bended at the corners due to the relatively narrow dispersion bandwidth of the SESAM/SBR. Figure 3.23 show that, the optical spectrum covers a good amount of the SESAM/SBR bandwidth. Finally, 3.24 show the measured autocorrelation trace.

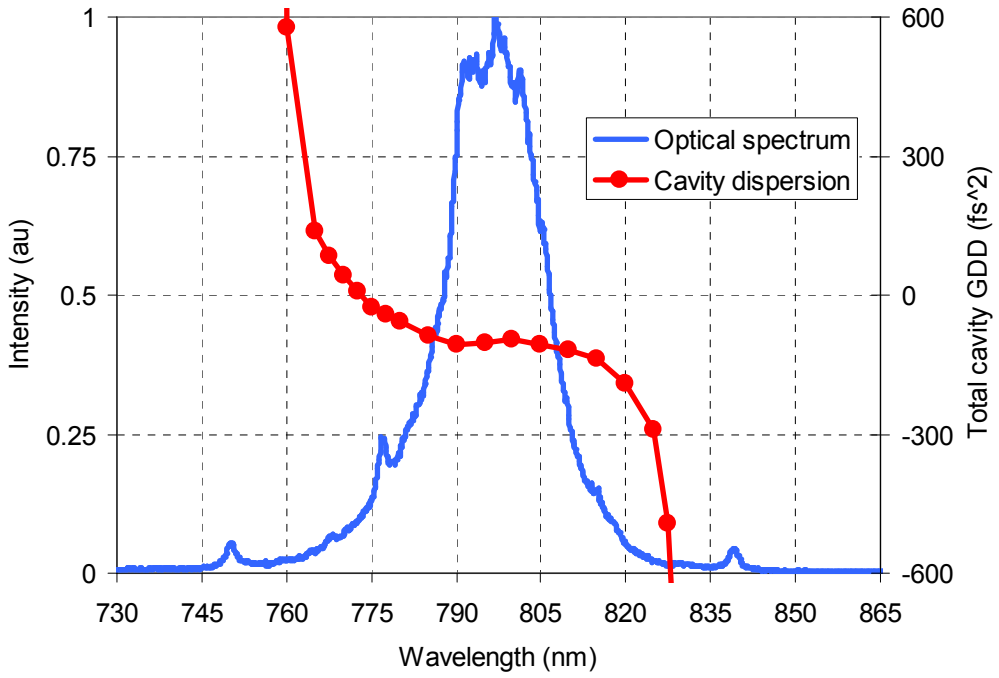

Figure 3.22: Measured optical spectrum for the ~39-fs 1.62 nJ pulses. Estimated cavity dispersion level is also shown.

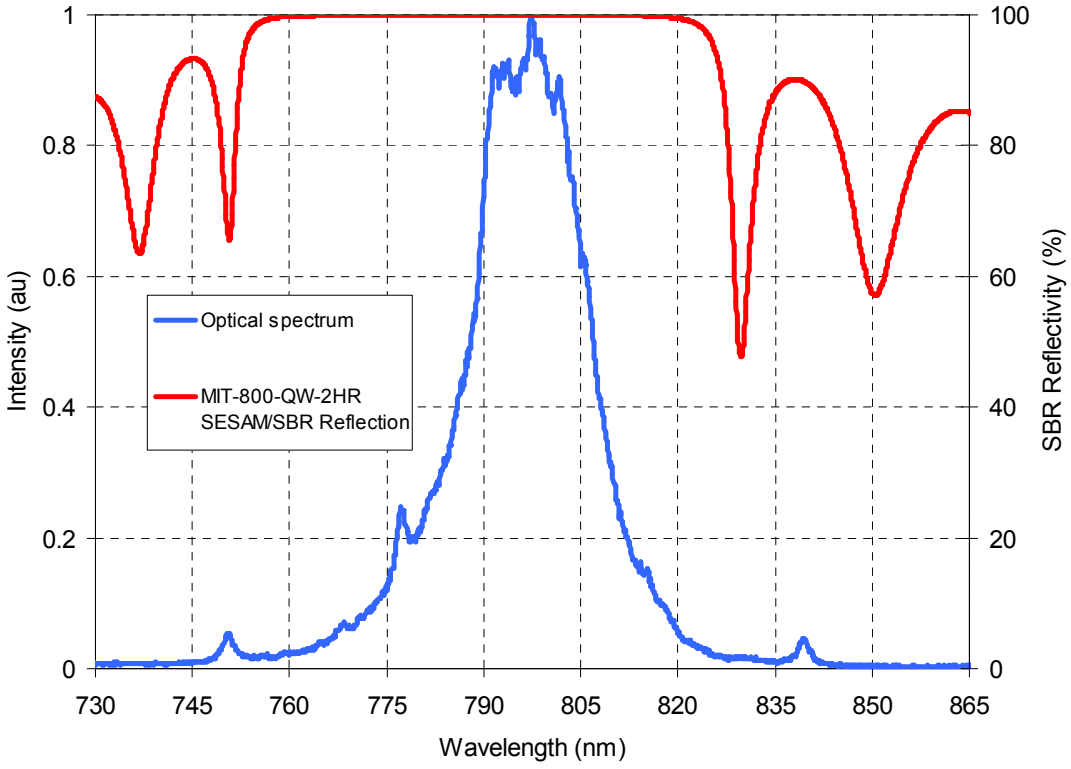

Figure 3.23: Measured optical spectrum for the ~39-fs 1.62 nJ pulses along with the calculated reflectivity curve for the MIT 800 nm SESAM/SBR with quantum well absorber and two layers of HR coating.

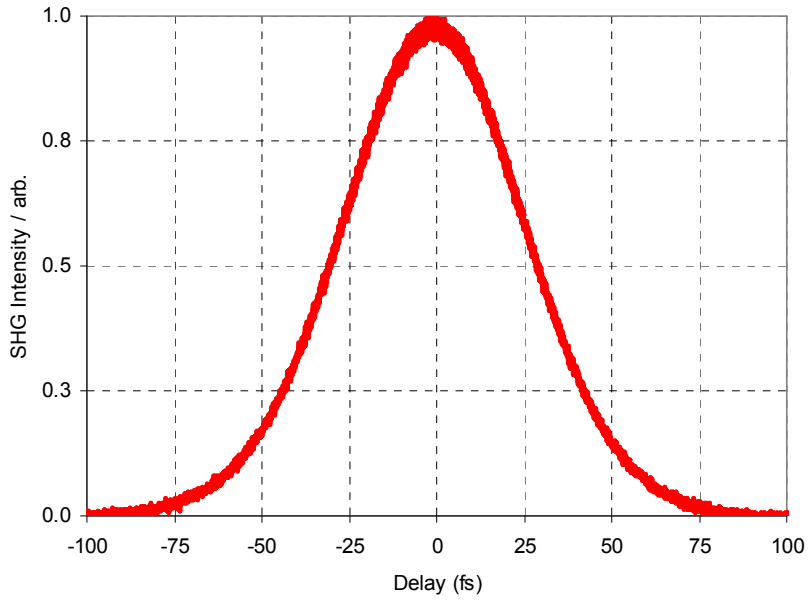

Figure 3.24: Measured background free autocorrelation trace for the ~39-fs 1.62 nJ pulses.

3.4 Mode-locked Tuning Experiments with fs Cr:LiCAF Laser

So far we have looked at free running mode-locked laser operation of Cr:LiCAF laser, and the center of the laser spectra was shifting between 795 nm to 815 nm. However, several applications of fs lasers require femtosecond pulses at a specific wavelength, or they require tunable fs pulses. In this section we will review our fs tuning experiments with the mode-locked Cr:LiCAF laser.

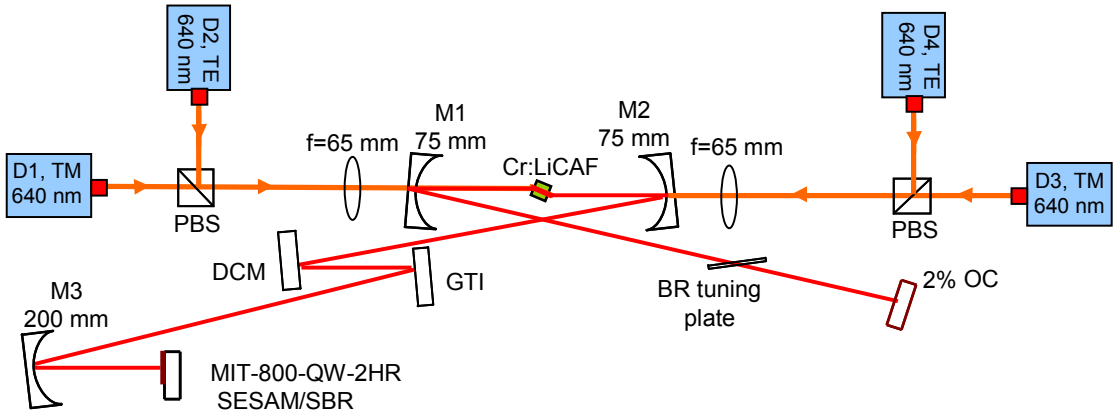

Figure 3.25: Schematic of the cw mode-locked Cr:LiCAF laser that is used in femtosecond tuning experiments.

Figure 3.25 shows the schematic of the cw mode-locked Cr:LiCAF laser that we have used in femtosecond tuning experiments. The cavity is very similar to what was described above. A specially designed, 3 mm thick crystal quartz birefringent filter, with a crystal axis pointing out of the crystal surface, was used to tune the central wavelength of the pulse spectrum. Dispersion compensation is

accomplished by use of GTI and DCM mirrors (Layertec GTI mirror set I and Layertec DCM mirror set II). In tuning experiments, one generally wants a flat dispersion profile to obtain the best possible tuning result. However, in our case, we were forced to use the GTI mirror with a narrow dispersion bandwidth and rapid dispersion oscillations. This is because, otherwise it might require too many bounces on DCM mirrors to cancel out the dispersion from the Cr:LiCAF crystal ~125 fs^2 (5 mm), quartz birefringent filter ~260 fs^2 (~7.3 mm), and the intracavity air ~70 fs^2 (~3.5 m). GTI mirror provides -550 ± 50 fs^2 dispersion per bounce, and effectively cancels out the positive dispersion; however its non-flat dispersion profile limited our tuning as we will describe shortly below.

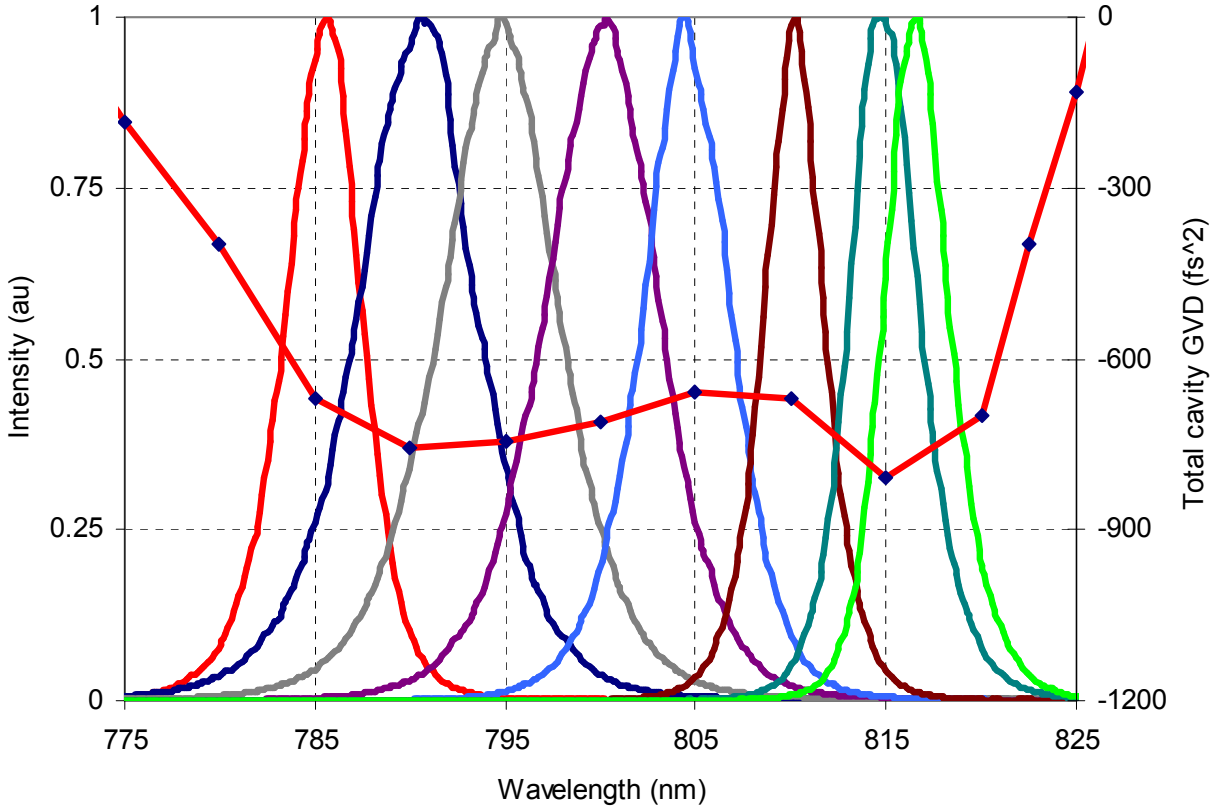

Figure 3.26: Sample spectra taken at discrete wavelengths while tuning the femtosecond Cr:LiCAF laser. Estimated cavity dispersion is also shown. The laser was continuously tunable from 785 nm to 817 nm.

Figure 3.26 shows samples spectra obtained during femtosecond tuning experiments. The laser was continuously tunable from 785 nm to 817 nm (~32 nm), and tuning was obtained by just the rotation of the Birefringent filter. Fig. 3.26 also shows the estimated total dispersion of the cavity. Tuning was limited by dispersion bandwidth of the GTI mirror on the short wavelength side. Figure 3.27 shows the measured variation of pulse width and pulse energy along the tuning range. The average pulse-width was 133-fs and the average pulse energy was 1.48-nJ. The repetition rate of the laser was 86 MHz.

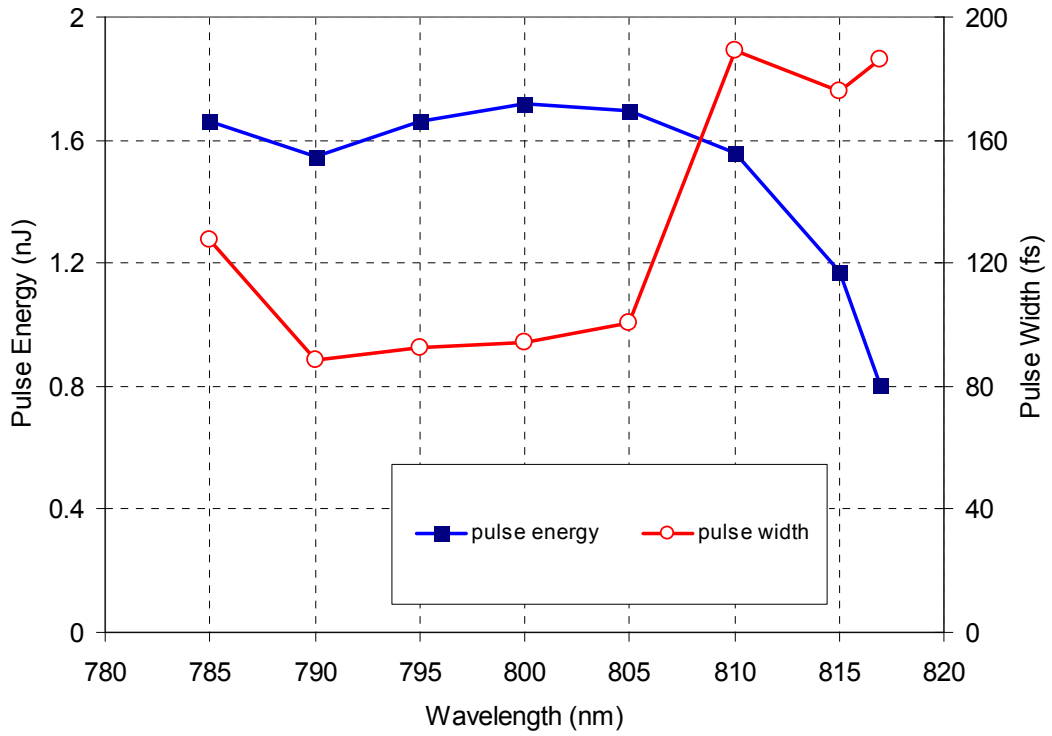

Figure 3.27: Measured variation of output pulse energy and pulsewidth with central wavelength along the tuning range. The laser was continuously tunable from 785 nm to 817 nm.

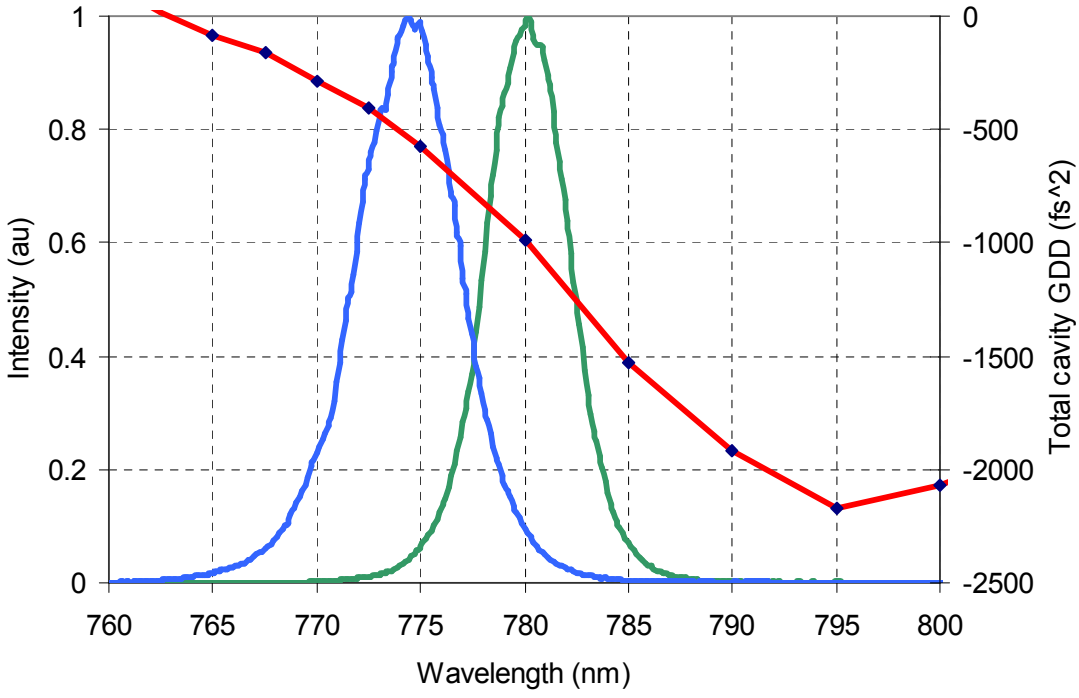

Figure 3.28: By increasing the number of bounces on GTI mirrors from 1 to 2 and making the total cavity dispersion more negative, it was also possible to obtain tuning in the 775-785 nm range. Sample spectra taken at discrete wavelengths are shown with the estimated cavity dispersion level.

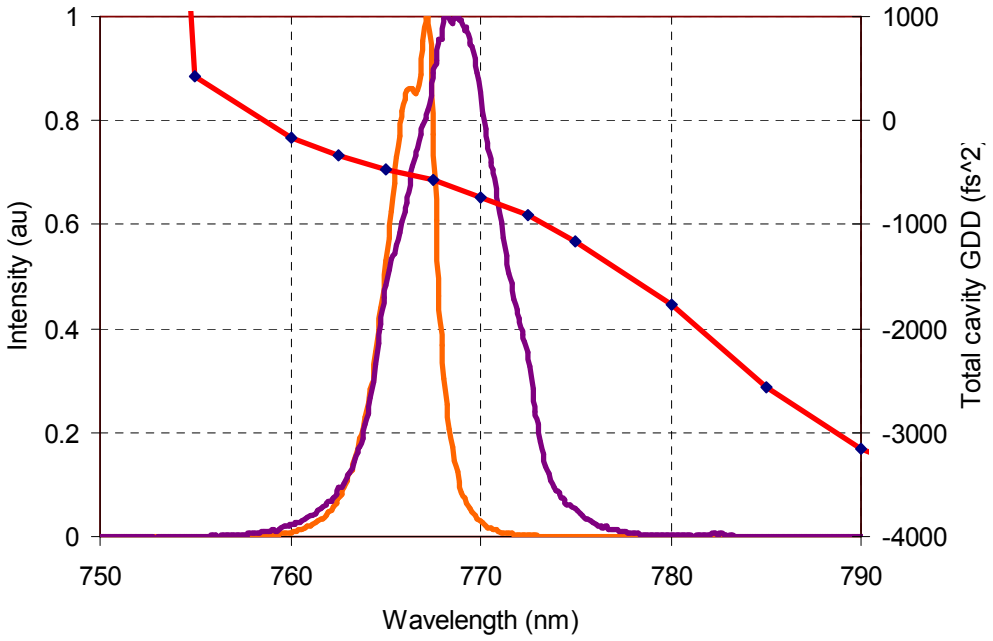

Figure 3.29: By increasing the number of bounces on GTI mirrors to 3, it was possible to extend the lower wavelength tuning limit to 767 nm. Sample spectra are shown with the estimated cavity dispersion for this case.

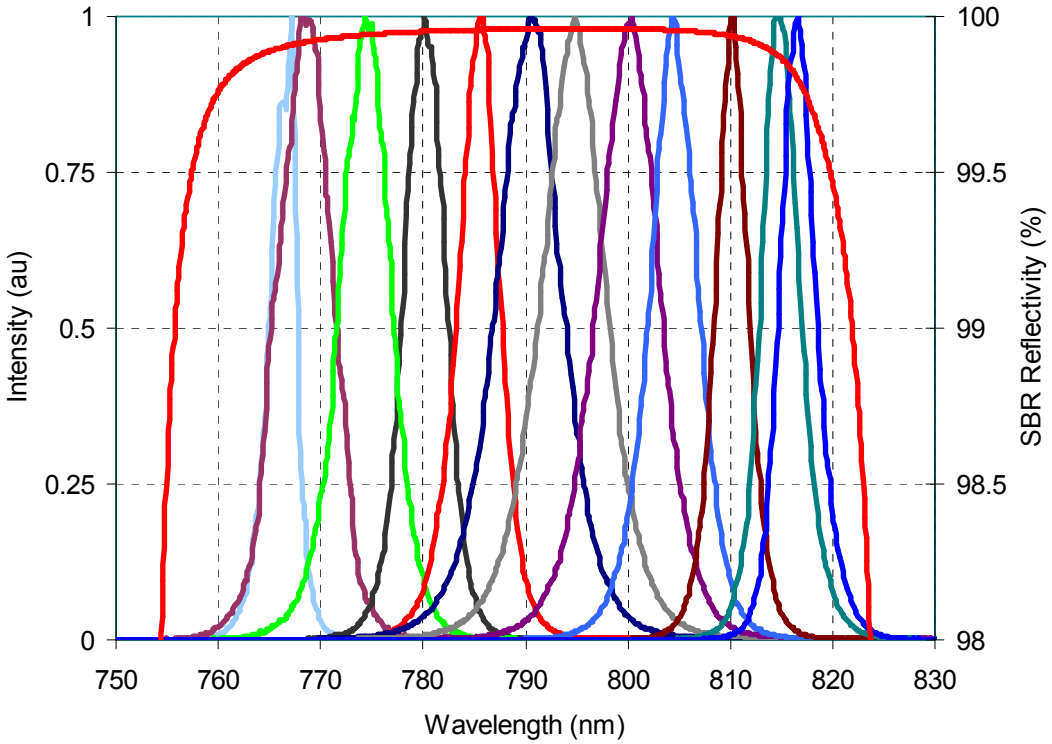

Figure 3.30: Full tuning range we have obtained with the MIT 800 nm SESAM/SBR with a quantum well absorber and 2 layers of HR coating. Calculated reflectivity of the SESAM/SBR is also shown (Note that the reflectivity is shifted ~10 nm to shorter wavelengths, compared to the simulations in Appendix E. This is because grown SESAM/SBR central wavelength was shorter than the design). The total tuning range extends from 767 nm to 817 nm.

To confirm that GTI mirror dispersion bandwidth limited the tuning below 785 nm, we have decreased the cavity dispersion (make more negative) by increasing the number of bounces on GTI mirror. Figure 3.28 and 3.29 show the obtained spectrums for the cases where we have 2 and 3 bounces on the GTI mirror, respectively (4 and 6 bounces in round trip). Figure 3.30 shows all the obtained mode-locked spectrums together along with the reflectivity of MIT-800-QW-2HR SESAM/SBR. Note that, tuning above 817 nm is limited by the SESAM/SBR bandwidth, which was also apparent from the power decrease we have observed (Fig. 3.27). The total tuning range extends from 767 nm to 817 nm (50 nm), but we should remember that this is not taken with a single set of optics. However, this shows that with a proper mirror set with relatively flat dispersion in this range, one can possibly obtain continuous tuning of central wavelength in this region.

Central Wavelength (nm)	Pulse width (fs)	Average output power (mW)	Pulse energy (nJ)
817	186	69	0.80
815	176	101	1.17
810	189	134	1.56
805	100	146	1.70
800	95	148	1.72
795	93	143	1.66
790	89	133	1.55
785	127	143	1.66
-	-	-	-
780	145	143	1.66
775	120	140	1.63
770	126	140	1.63
767	170	118	1.37

Table 3.2: Summary of tuning results obtained with MIT-800-QW-2HR SESAM/SBR. Measured average powers, pulse energies and pulse widths are listed.

3.5 Mode-locked Operation of Multimode Diode Pumped Cr:LiCAF Laser

Figure 3.31 shows the schematic of the multimode diode-pumped Cr^{3+}:LiCAF laser cavity used for cw and cw mode-locked lasing experiments. The cw laser cavity and results have already been discussed in Section 2.5. The DCM mirror had ~-300 fs^2 of GVD per bounce; hence, it was possible to obtain the required negative dispersion levels with only one mirror. However, as we will see, the GVD of this DCM mirror set had rapid dispersion oscillations. Besides providing the required negative GVD, DCM was also used to focus the beam onto the SBR/SESAM to a spot size of ~30 μm. The Cr^{3+}:LiCAF crystal (~25 fs^2/mm), and intra-cavity air produced a total positive GVD of ~150 fs^2. All the other optics used in the setup had negligible second-order dispersion (GVD <20 fs^2). For the cavity shown in Fig. 3.30, the estimated total round trip GVD was approximately -400 fs^2. As mentioned above, with DCM-1 set, the obtained GVD for the total cavity was not smooth, which limited the pulsewidths to ~100 fs level. Figure 3.32 shows the calculated total GVD for the cavity.

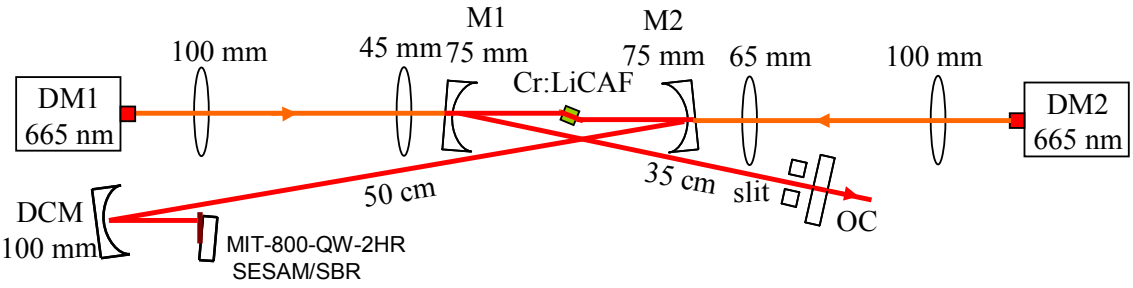

Figure 3:31: Schematic of the multimode diode-pumped cw mode-locked Cr^{3+}:LiCAF laser system. DCM: curved (R=100 mm) double-chirped mirror with ~-300fs^2 dispersion per bounce.

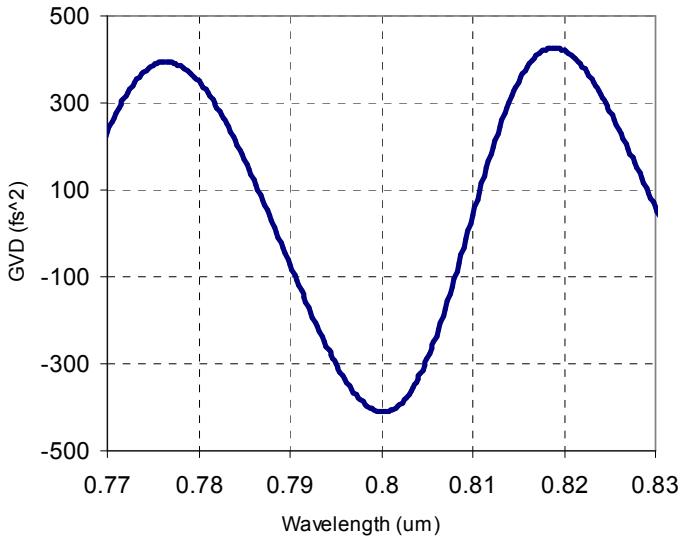

Figure 3.32: Calculated total GVD of cavity (Fig. 3.30): 4 mm of Cr:LiCAF, ~2 m of intracavity air, and 2 bounces on DCM mirror.

The highest average mode-locked power was obtained with the 1.4% output coupler. Figure 3.33 shows the measured variation of laser dynamics and laser output power as a function of absorbed pump power, using the 1.4% output coupler. With the insertion of the DCM mirror and the SESAM, the cw lasing threshold increased from ~120 mW to ~250 mW. For absorbed pump powers up to ~1 W, the laser operated purely cw. Q-switched mode-locked pulses were observed for pump powers between ~1 W and ~1.8 W (Q-switched ML in Fig. 3.32). For pump powers above ~1.8 W, stable and self-starting cw mode-locked operation was obtained (cw ML), where the slope efficiency was about 19%. Again, the obtainable mode-locked average power levels were limited by thermal effects.

Figure 3.34 shows the spectra and background-free autocorrelation trace taken with the 1.4% output coupler at an absorbed pump power of ~2.4 W. The laser produced 97-fs pulses (assuming $sech^2$ pulse shape) with 390 mW average power and 8 nm spectral bandwidth near 800 nm at 140 MHz (~2.8-nJ pulse

energy). The time bandwidth product was ~0.35, close to the transform limit of 0.315 for sech^2 pulses. Figure 3.35 shows the optical pulse train recorded using a fast Si detector with fiber coupling.

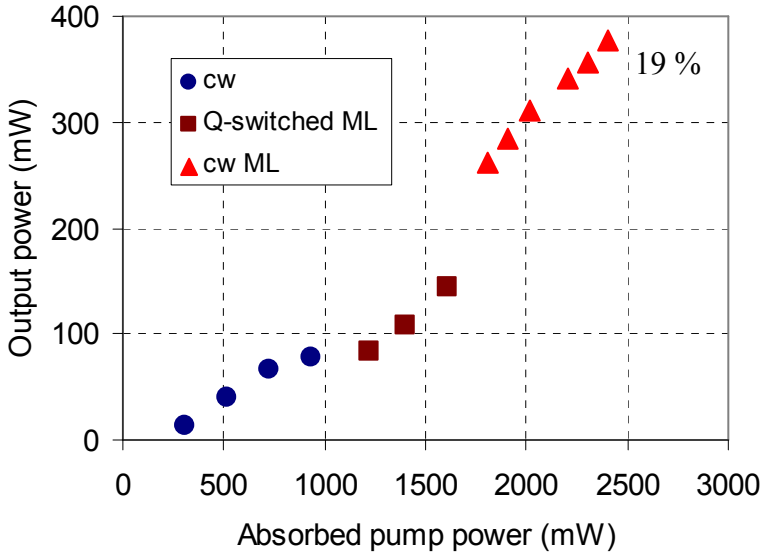

Figure 3.33: Efficiency curve for the multimode diode pumped mode-locked Cr^{3+}:LiCAF laser in different regimes of operation taken with the 1.4 % output coupler. The slit near the OC was used to provide a TEM_{00} laser output. cw: Continuous-wave operation, Q-switched ML: Q-switched modelocked operation, cw ML: Continuous-wave modelocked operation.

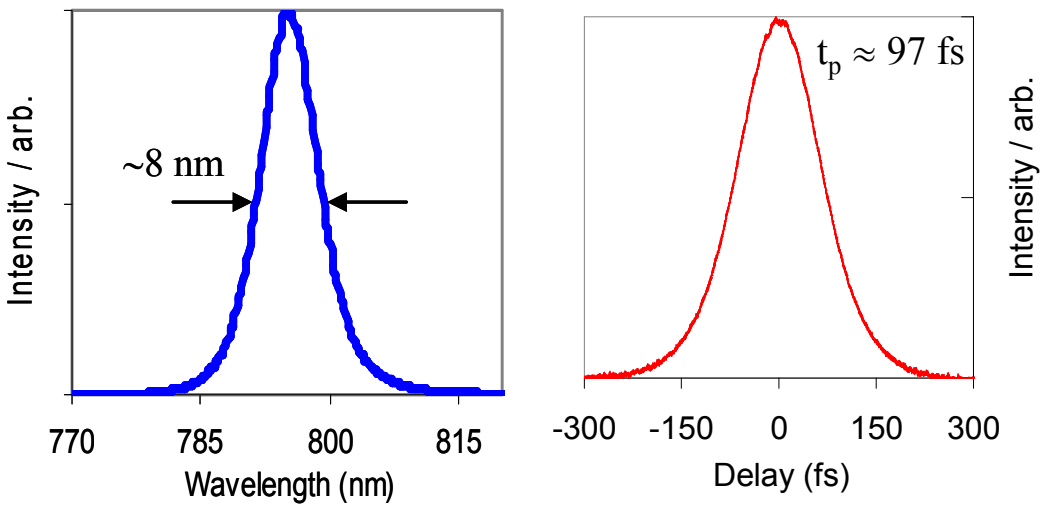

Figure 3.34: Measured spectrum and second harmonic autocorrelation taken with the multimode diode-pumped mode-locked Cr^{3+}:LiCAF laser using the 1.4% output coupler at an absorbed pump power of ~2.4 W. The FWHM of the autocorrelation is 147 fs, corresponding to a 97-fs pulse duration (assuming sech^2 pulse shape). The average output power is 390 mW, corresponding to a pulse energy of 2.8 nJ for a 140-MHz repetition rate cavity. The spectrum has a bandwidth of 8 nm (FWHM) centered around ~795 nm. The corresponding time bandwidth product is ~0.35.

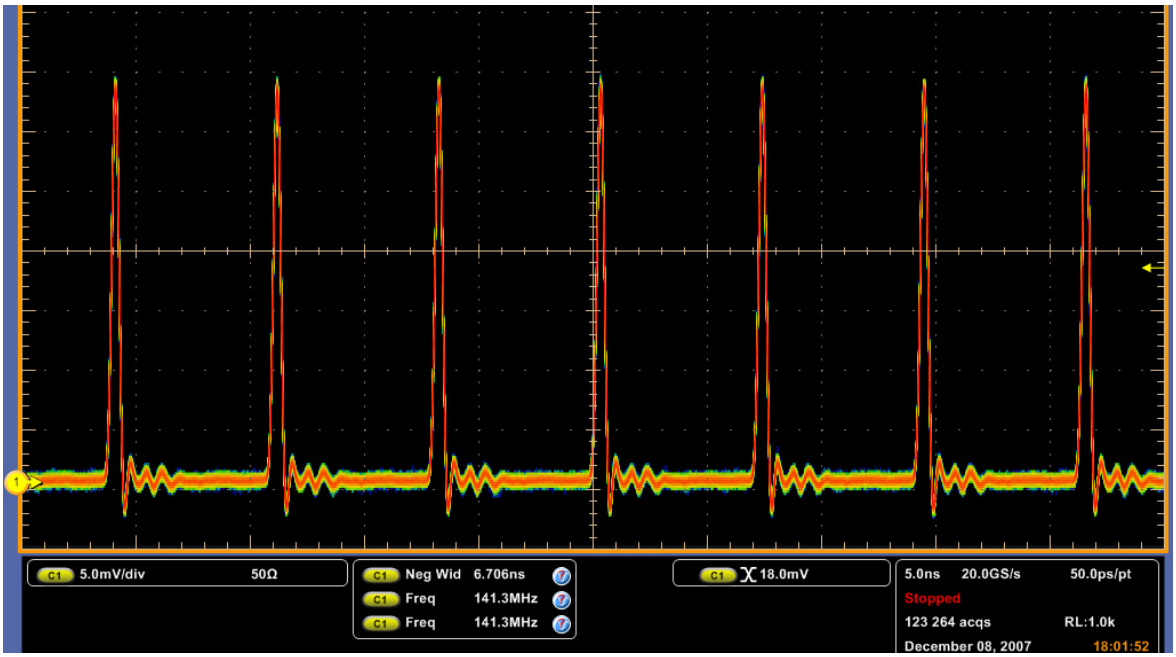

Figure 3.35 Stable pulse train recorded with a fast Si detector, which has a repetition rate of ~140 MHz. Stabilizing the pulse train required adjusting the intracavity slit width (compare with Fig. 2.23).

We note there that, similar to the cw operation, the intracavity slit near the output coupler was necessary for a TEM_{00} laser output in cw mode-locked regime also. Without the slit, the laser output was multimode and interference effects caused pulse instabilities. Figure 3.36 shows the unstable pulse train and the recorded autocorrelation trace for this case. Even though the pulse train was unstable, we haven't observed any instability in the autocorrelation trace or in the measured optical spectra. However, except for a few case, obtaining a stable pulse train required the existence of intracavity slit near the output coupler, with its width adjusted. This caused the obtainable average output powers to decrease from 450 mW to 390 mW.

We have also used DCM mirrors from Layertec DCM mirror set II in the mode-locking experiments with the multimode diode pumped Cr:LiCAF laser. Four bounces on DCMs provided a GVD of about -200 fs^2, and the estimated total round trip GVD was approximately -50 to -100 fs^2 (Fig. 3.37). At this dispersion level the cavity produced ~60 fs long pulses with 280 mW of average output power, at a repetition rate of ~150 MHz. The corresponding pulse energy was 1.9 nJ. Laser dynamics was similar to what was described in the previous section. The slightly shorter pulses obtained with Layertec DCM mirror set II, is due to the ability to control the cavity dispersion more accurately with this mirror set. Similarly, the intracavity slit was necessary to stabilize the pulse train, and to make the laser output beam TEM_{00} (Fig. 3.39).

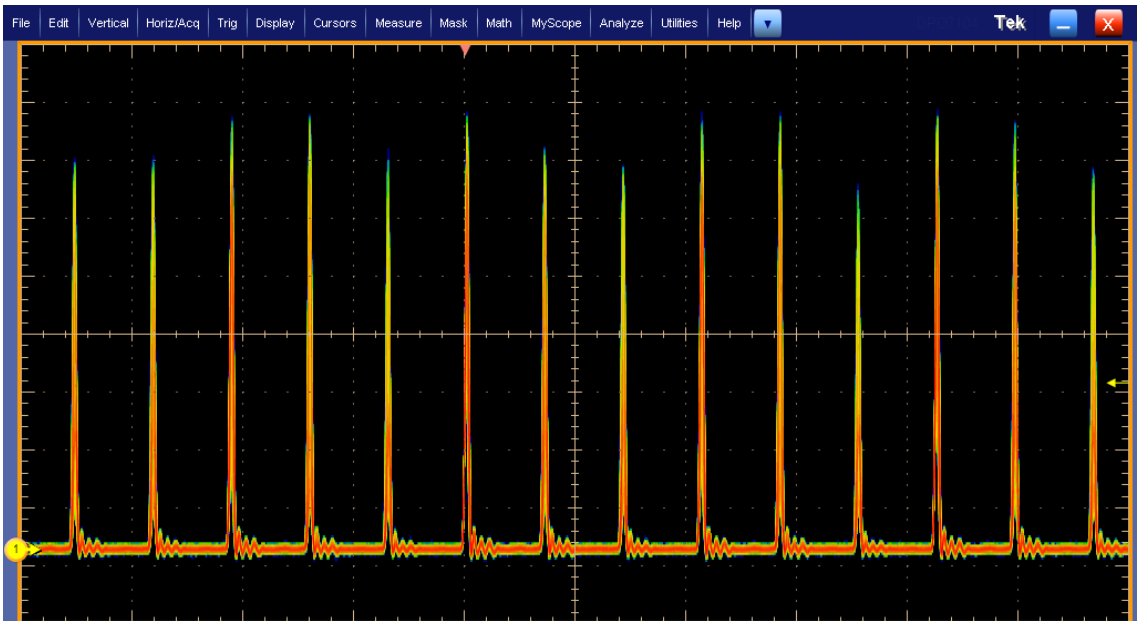

(a)

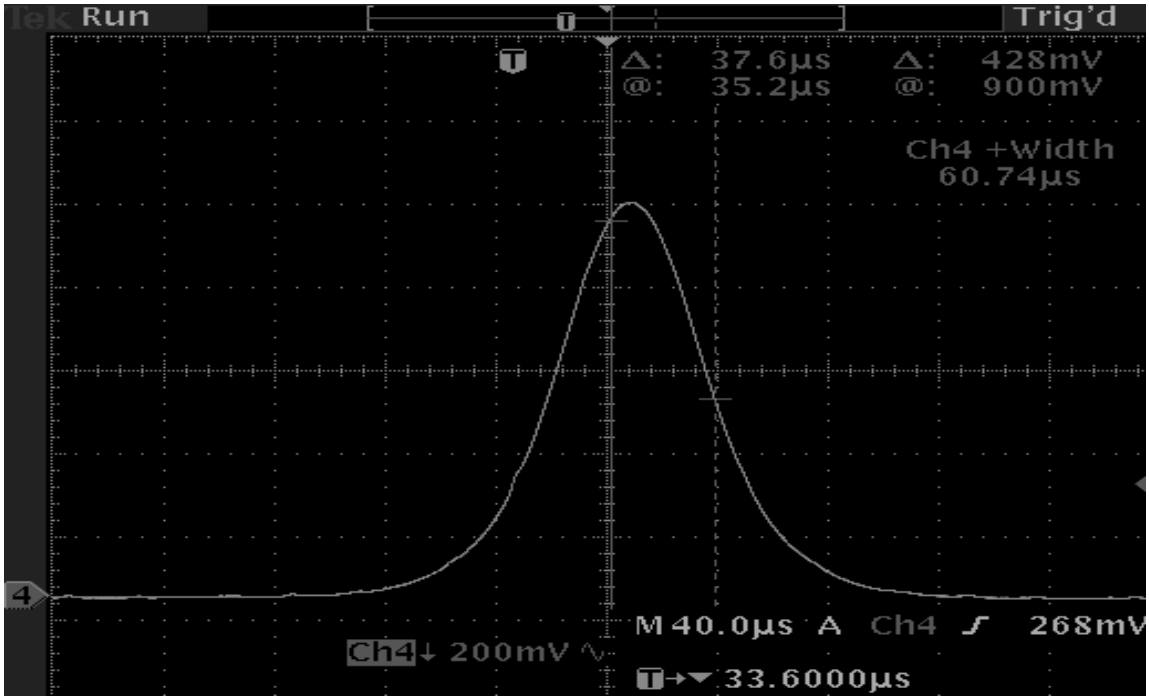

(b)

Figure 3.36: (a) Unstable pulse train observed when the laser was operated without the intracavity slit. The laser was producing ~80 fs pulses with 450 mW of average power. Autocorrelation trace was clean (b). Repetition rate is ~140 MHz. In most cases, the intracavity slit near the output coupler was necessary to obtain a stable pulse train.

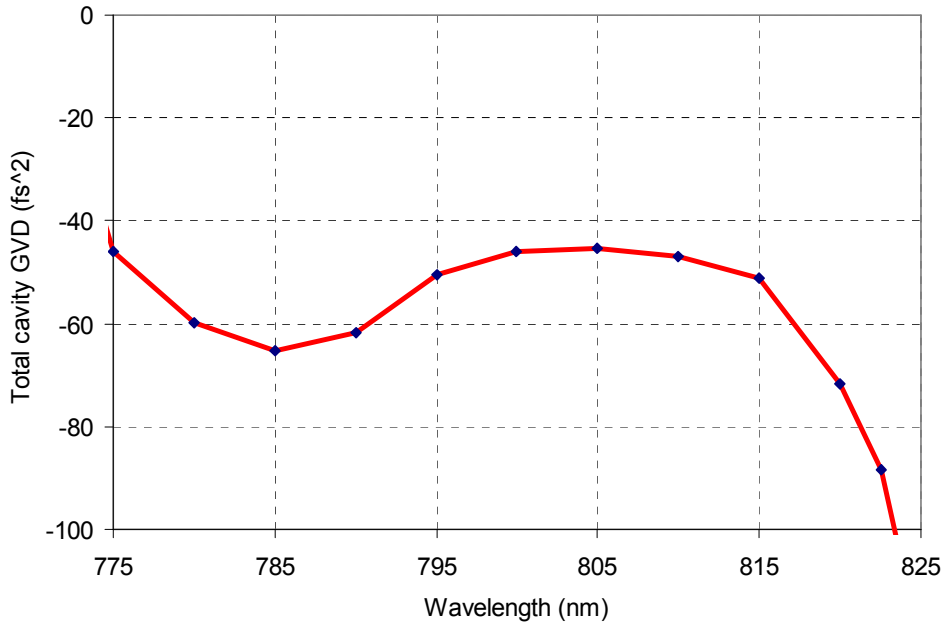

Figure 3.37: Calculated total GVD of the cavity that uses DCM mirrors from Layertec DCM Set II. The dispersion estimate includes: 4 mm of Cr:LiCAF, ~2 m of intracavity air, and 4 bounces on DCM mirrors, and one bounce on SESAM/SBR.

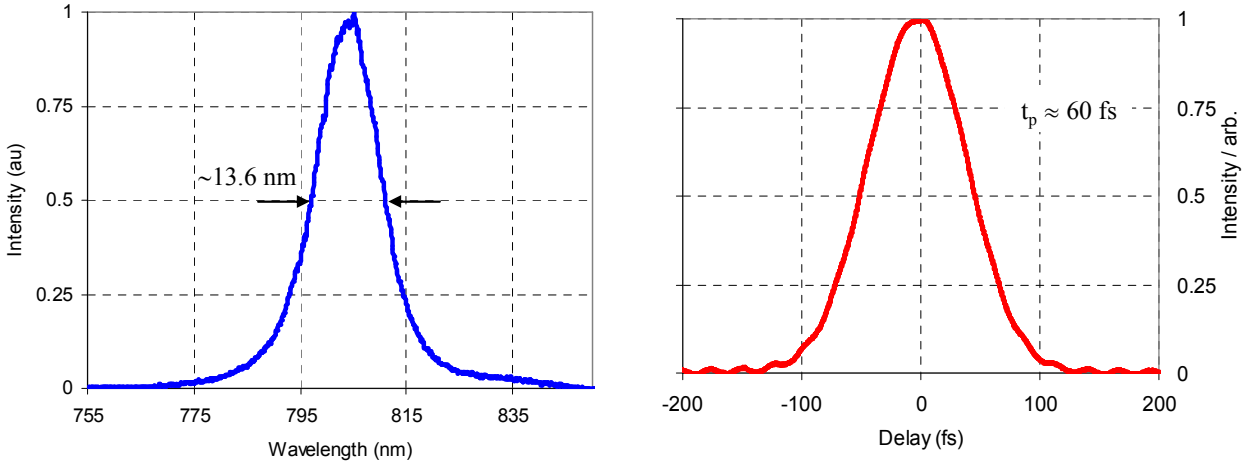

Figure 3.38: Measured spectrum and second harmonic autocorrelation taken with the multimode diode-pumped mode-locked Cr^{3+}:LiCAF laser using DCM2 mirrors for dispersion compensation. The laser generated ~60 fs pulses with 1.9 nJ of pulse energy at a repetition rate of ~150 MHz. The spectrum has a bandwidth of 13.6 nm (FWHM) centered around ~795 nm. The corresponding time bandwidth product is ~0.38.

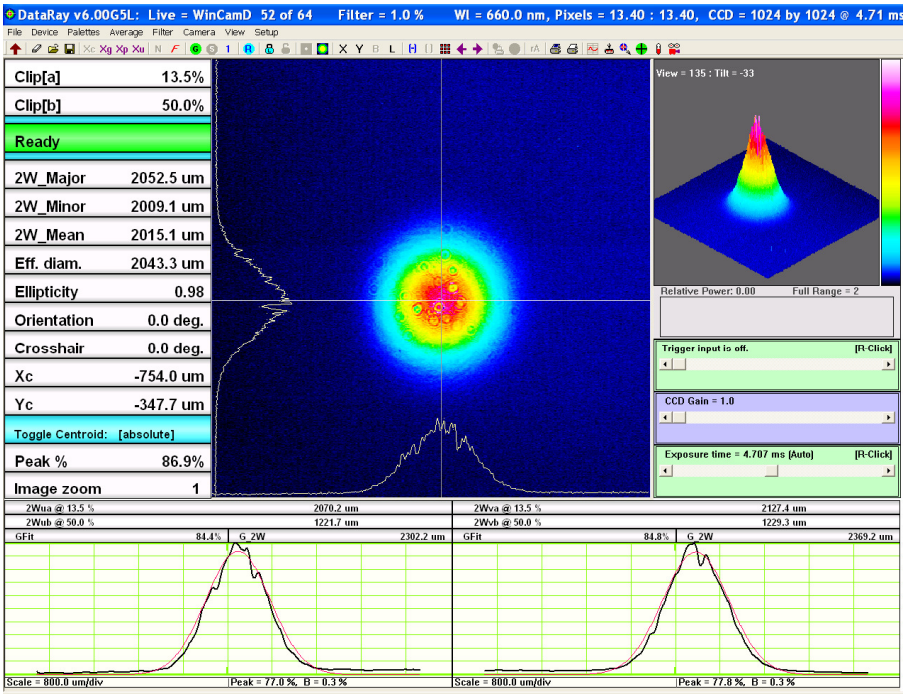

Figure 3.39: Measured profile of the laser output beam using a CCD camera. The slit near the OC was required to obtain a circular output, and stable pulse train.

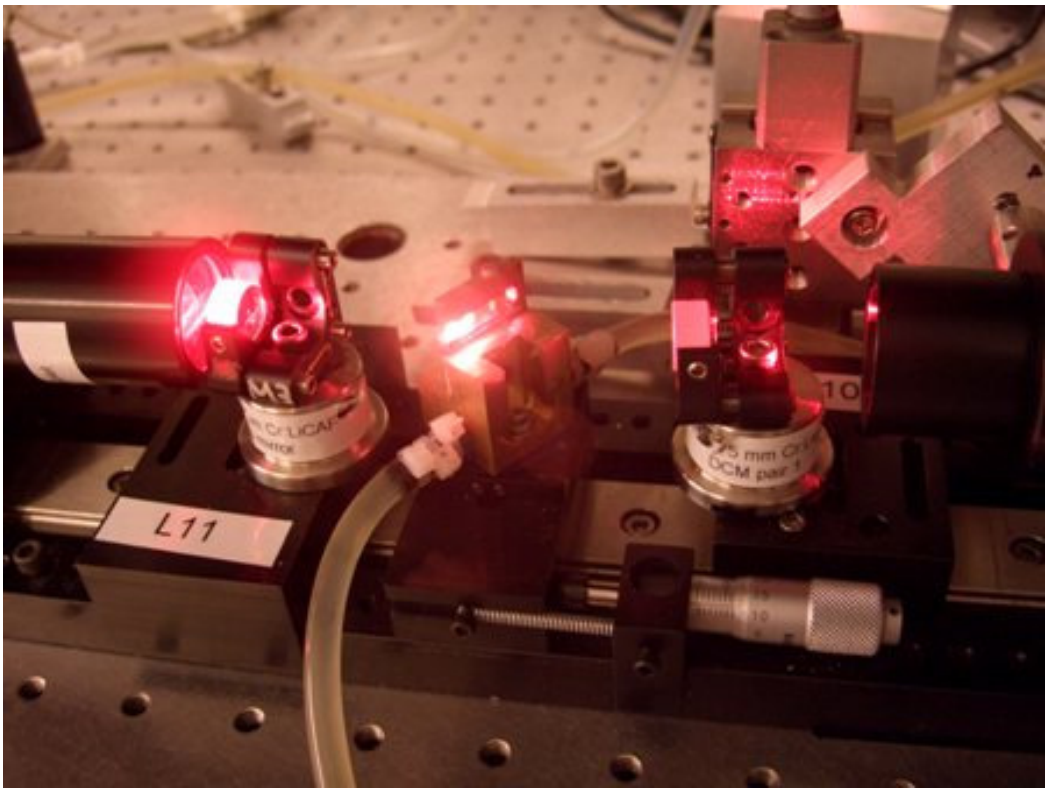

Figure 3.40: Picture showing the Cr:LiCAF crystal, pump mirrors and the focusing lenses. Note the large pump beam size on the focusing lens. This large beam size, which can be adjusted by the collimating lens, has been used to obtain a tighter focus inside the crystal.

3.6 Performance Comparison of Different 800 nm SESAMs/SBRs

All the mode-locking results described above were taken with the MIT 800 nm SESAM/SBR with a quantum well absorber and 2 layers of HR coating (MIT-800-QW-2HR). This SBR had a modulation depth of about 0.6%, which was quite suitable for the low gain Cr:LiCAF laser media. However, besides this SBR, we have also grown an 800 nm SESAM/SBR with a bulk absorber. Table 3.3 lists all the different 800 nm SESAMs/SBRs that we have at hand. Considering also the high reflective coated versions, we had 5 different 800 nm SESAMs/SBRs. More details on these SESAMs/SBRs can be found in Appendix E (relevant sections are indicated in Table 3.3).

SESAM/SBR Name	Short Name	Modulation depth (%)	Section
MIT 800 nm SESAM/SBR with bulk absorber	MIT-800-Bulk	2.2	E3
One pair HR layer coated MIT 800 nm SESAM/SBR with bulk absorber	MIT-800-Bulk-HR	0.8	E4
MIT 800 nm SESAM/SBR with quantum-well absorber	MIT-800-QW	4.2	E5
One pair HR layer coated MIT 800 nm SESAM/SBR with quantum-well absorber	MIT-800-QW-HR	1.6	E6
Two pairs HR layer coated MIT 800 nm SESAM/SBR with quantum-well absorber	MIT-800-QW-2HR	0.6	E7

Table 3.3: List of SESAMs/SBRs centered around 800 nm that was grown during the period of this PhD. Detailed information on these SESAMs/SBRs can be found in Appendix E.

During this PhD, we didn't have time to test all the 800 nm SESAMs/SBRs in detail, so we cant present a detailed comparative study here. However, here we will try to shortly described the expected performance from each SESAM/SBR. First of all, the 800 nm bulk SESAMs/SBRs without any high-reflective coating (MIT-800-Bulk), has too much modulation (~2.2%). Hence, when we tried to use it in the Cr:LiCAF laser, we generally observed frequent burnings on the SESAM/SBR. Same was true with the 800 nm quantum well SESAM/SBR (MIT-800-QW), which has even higher modulation depth (~4.2%). The modulation depth of one layer HR coated 800 nm quantum well SESAM/SBR (MIT-800-QW-HR) was 1.6%, which was also too high too be useful in Cr:LiCAF lasers.

We could obtain stable cw mode-locked operation with MIT-800-Bulk-HR and MIT-800-QW-2HR SESAMs/SBRs, which both have reasonable level of modulation depths. Both SESAMs/SBRs provided similar performance. However, the reflectivity bandwidth of MIT-800-QW-2HR is broader than MIT-800-Bulk-HR due to an additional high reflective coating layer. Moreover, MIT-800-QW-2HR has a quantum well absorber design with an estimated band edge at ~835 nm. It also has just one allowed transition; hence, we expect it to have a smooth and wavelength independent density of states profile. On the other hand, MIT-800-Bulk-HR SESAM/SBR has an estimated band edge around ~861 nm, which additional transitions at 832 and 790 nm. In short, we believe that MIT-800-QW-2HR SESAM/SBR should perform better compared to MIT-800-Bulk-HR SESAM/SBR, due to its broader bandwidth and

quantum well absorber design, which should enable lower saturation fluencies and wavelength independent nonlinear response. However, as we mentioned earlier, we didn't have time to investigate this experimentally.

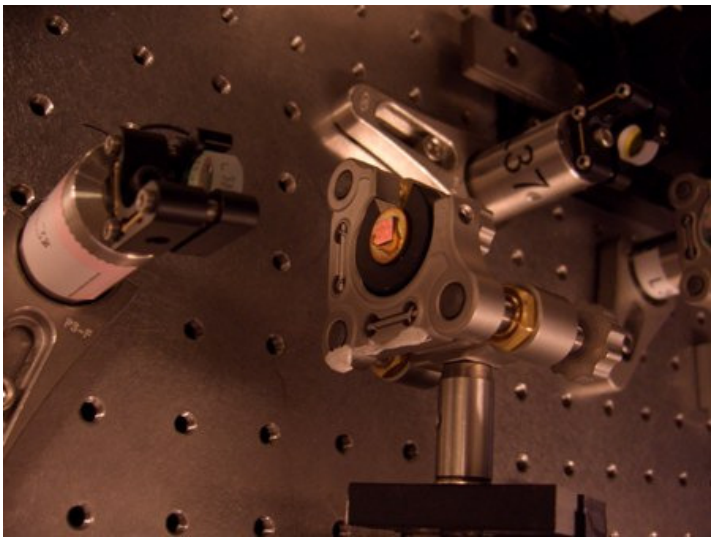

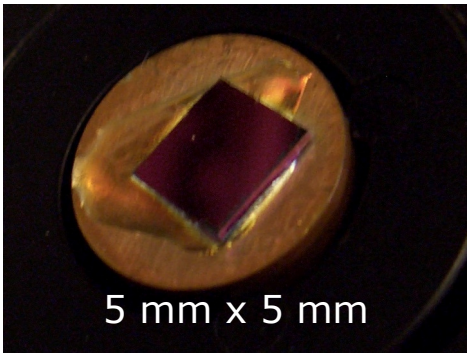

Figure 3.41: Picture of a sample from MIT-800-QW-2HR SESAMs/SBRs. We have generally used quite small SESAM/SBR pieces from the grown wafer.

3.7 Pure q-switched Operation of Cr:Colquiriite Lasers with SESAMs/SBRs

In section 2.9, we have described self q-switching behavior of Cr:Colquiriite lasers, which is attributed to a time-dependent nonlinear lensing effect inside the gain medium [240-245]. In this section, we will briefly described pure q-switched operation of Cr:LiCAF gain media by using a SESAM/SBR. Here, by pure q-switching we mean q-switching without mode-locking. We have also observed pure q-switched operation with Cr:LiSAF gain medium, but it was easier to observe in Cr:LiCAF probably due to its longer upper state lifetime.

Pure q-switched operation was generally observed when the effective spot size on the SESAM/SBR is relatively large (upon tight focusing one obtains q-switched mode-locked or cw mode-locked operation). As an example here, we will present pure q-switched operation of Cr:LiCAF laser. Figure 3.42 shows the obtained stable pulse train, which required fine adjustment of SESAM/SBR position for stability. The repetition rate of the pulse train is 35.18 kHz, and the pulses are quite broad (~μs FWHM). Figure 3.44 shows the optical spectra for cw, self q-switched and pure q-switched operation of Cr:LiCAF laser. Note that, the optical spectrum obtained in pure q-switched operation with SESAMs/SBRs is quite broad. These results were obtained by using MIT-800-QW-2HR SESAM/SBR, and a 2 % output coupler. The average output power was 150 mW, and the corresponding pulse energy was ~4.25 μJ.

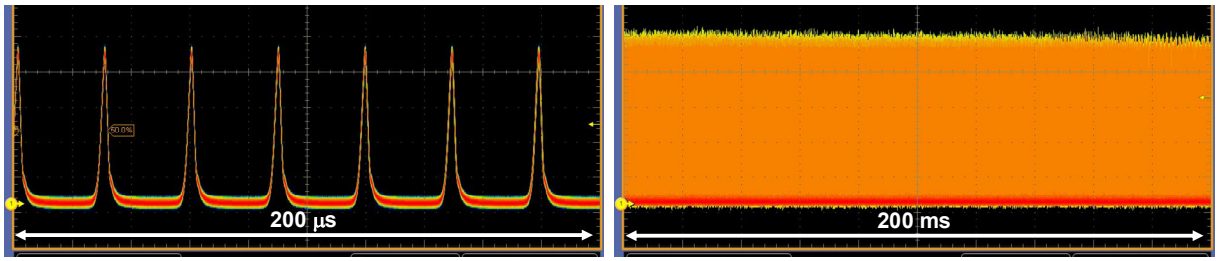

Figure 3.42: Recorded pulse train during pure q-switched operation of Cr:LiCAF laser.

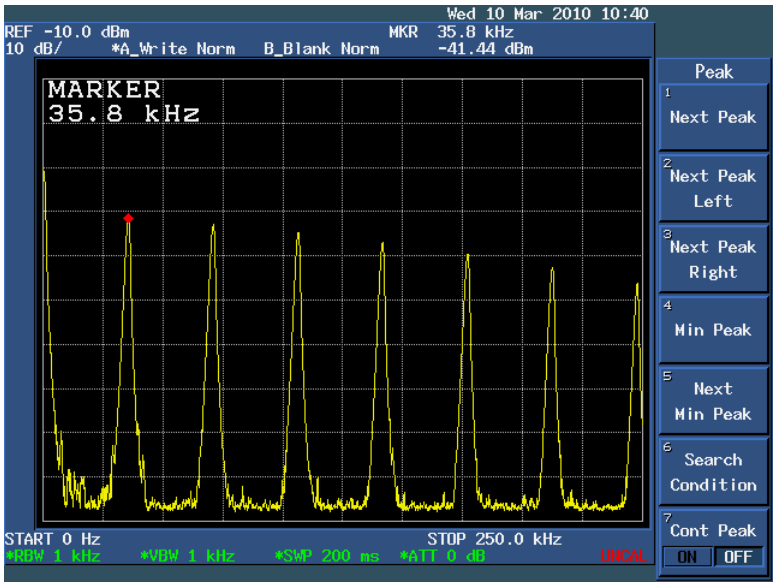

Figure 3.43: Recorded microwave spectrum during pure q-switched operation of Cr:LiCAF laser. The span is from 0 Hz to 250 kHz.

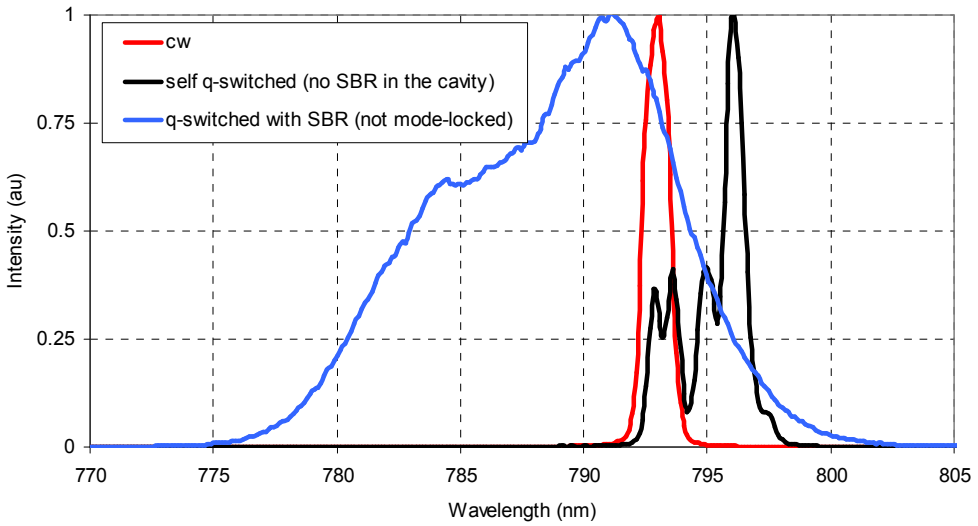

Figure 3.44: Recorded optical spectrum during pure q-switched operation of Cr:LiCAF laser. For comparison spectrums for pure cw operation and self q-switched operation are also shown.

3.8 Summary

We finish this Chapter with Table 3.4, which summarizes the cw mode-locked lasing results reported with Cr^{3+}:LiCAF media in literature to date using different pump sources. Table 3.4 includes the obtained average output power levels, pulse energies, and pulse widths. Representative results obtained during this PhD work were also included. Note that, we have performed fist single-mode diode pumping and fist SESAM/SBR mode-locking experiments with the Cr:LiCAF gain medium, which resulted in efficient and turn-key laser systems.

Pump source	Pulse width (fs)	Pulse energy (nJ)	Average power (mW)	Peak power (kW)	Rep rate (MHz)	Mode Locking	Year	Ref.
Krypton laser	170	~1.1	100	6.5	90	KLM	92	[176]
MMD	52	~0.8	75	15.4	95	KLM	98	[175]
	20	~0.14	13	7	95			
Ti:Sapphire	9	~2.2	220	244.4	97	KLM	02	[60]
MMD	10	~0.37	40	37	110	KLM	03	[174]
MMD	67	2.5	300	37.3	120	SESAM/SBR	08	[143],*
MMD	50	1.25	150	25	120	SESAM/SBR	08	[143],*
MMD	97	2.8	390	37.3	140	SESAM/SBR	08	[220],*
MMD	60	1.9	280	31.1	150	SESAM/SBR	08	[220],*
SMD	63	1.13	144	18	127	SESAM/SBR	08	[220],*
SMD	72	1.4	178	19.5	127	SESAM/SBR	08	[178],*
SMD	39	1.62	125	41.6	77	SESAM/SBR	10	*
SMD	98	9.92	95	101.2	9.58	SESAM/SBR	09	[191],*

Table 3.4: List of average output powers, pulse energies and pulse widths obtained with Cr:LiCAF gain media in cw mode-locked operation using different pump sources. Mode locking initiation mechanism and repetition rate of the lasers were also specified. MMD: Multimode diode, SMD: Single-mode diode. * Representative results that were obtained during this PhD.

CHAPTER 4

MODE-LOCKED CR:LISAF LASERS

In Chapter 3, we have presented mode-locking results with Cr:LiCAF gain medium. In this chapter, we will present our detailed mode-locking results with Cr:LiSAF gain medium. When we started working with Cr:Colquiriites in August 2006, we have initially started with Cr:LiCAF gain medium due to its better thermal properties and its ability to tune below 800 nm. However, as we saw in Chapter 2, among Cr:Colquiriites, Cr:LiSAF has the highest gain and broadest tuning range. It also has the highest emission cross section, which reduces the tendency of the laser towards q-switching and provides a wider working range with SESAM/SBR mode-locking. Especially, a wide cw mode-locking working range is quite important because it gives the flexibility to play with the laser parameters without running into q-switched mode-locking or multiple pulsing instabilities.

Before presenting the mode-locking results of Cr:LiSAF, first we want to talk more about the cw mode-locking working range in SESAM/SBR mode-locked lasers in more detail, since we think that this is quite important. Assume that we have identical Cr:LiCAF, Cr:LiSAF, Cr:LiSGAF and Ti:Sapphire lasers, with same lasing wavelength (~800 nm), same lasing thresholds, with the same cw lasing slope efficiency, same passive losses, same output coupling, same dispersion level inside the cavity, etc... Also, assume that we are trying to mode-lock these lasers with the same SESAM/SBR. This might sound like too much of an assumption, but actually these parameters are quite similar in these gain media (maybe except Ti:Sapphire) as the lasing results of Chapter 2 had shown. As a typical SESAM/SBR parameter set, assume that our SESAM/BR has 0.6% modulation depth, 300 μJ/cm^2 saturation fluence and two-photon absorption effect starts above ~20 mJ/cm^2 for 100-fs long pulses. Further assume the following effective beam sizes inside the gain media and on the SESAM/SBR: $A_{\text{eff,L}} \approx \pi(16)(20)$ μm^2, $A_{\text{eff,}A} \approx \pi(16)(16)$ μm^2. Then using Eq. 3.4, we can calculate the critical pulse energy required to obtain stable cw mod-locking for each gain media (we will neglect the effect of soliton pulse shaping, which will lower the critical pulse energy required for stable mode-locking below Eq. 3.4). Here, we assumed that, the only main difference is the emission cross section of the materials. Table 4.1 lists the calculated values for critical pulse energy for stable cw mode-locking.

Gain Medium	Ti:Sapphire	Cr:LiSAF	Cr:LiSGaF	Cr:LiCAF
Peak emission cross section (σ_{em}) [x10^{-20} cm^2]	41	4.8	3.3	1.3
Critical pulse energy (E_{pc}) [nJ]	6.7	19.4	23.4	37.2

Table 4.1: Calculated critical pulse energies for stable cw mode-locking for different gain media.

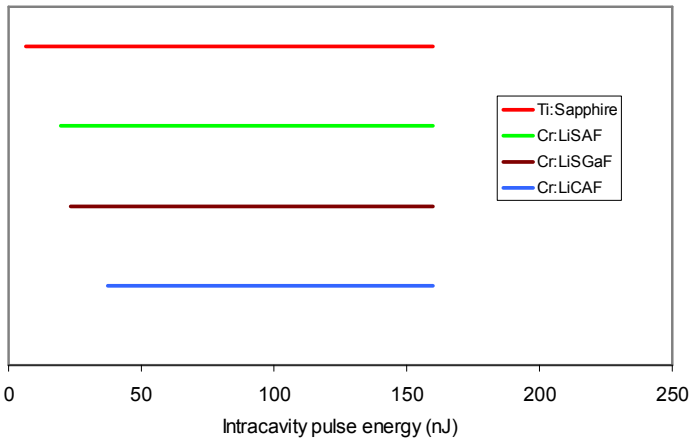

Figure 4.1: Calculated stable cw mode-locking working range for different gain media for 100-fs long pulses.

Note that, due to its orders of magnitude higher emission cross section, Ti:Sapphire has the lowest E_{pc} value. Among Cr:Colquiriites Cr:LiSAF is the best, where as Cr:LiCAF has the worst properties when it comes to obtaining stable cw mode-locking. The values in Table 4.1 are the required minimum intracavity pulse energies for obtaining stable cw mode-locking without q-switching instability. However, there is also the upper limit for the intracavity pulse energy levels, which is mainly determined by the multiple pulsing effects induced by two-photon absorption process in the SESAM/SBR (there is additional effects which might limit the intracavity pulse energies, but we will ignore them here). For our hypothetical SESAM/SBR, we assumed that two-photon absorption effect starts above ~20 mJ/cm^2 for 100-fs long pulses. Then for an effective absorber area of $A_{\text{eff},A} \approx \pi(16)(16)$ μm^2, this sets the upper limit for stable mode-locking to about ~160 nJ. Above this value, the laser will generate multiple pulsing instabilities. As we see in Fig. 4.1, which shows the cw working ranges of Cr:LiCAF, Cr:LiSAF, Cr:LiSGAF and Ti:Sapphire lasers, for ~100-fs level pulses the working range for cw mode-locking is comparable for each gain media, and even though Ti:Sapphire has advantages this is not significant. However, note that, two photon absorption process is stronger for shorter pulses; hence, this upper limit decreases to about ~80-nJ for 50-fs long pulses and to ~40-nJ for 25-fs long pulses. Fig 4.2 shows what happens for ~25-fs level pulses. Since the two photon absorption effect threshold is lower, now the working ranges are narrower, and having an higher emission cross section become quite advantageous. In short, because Cr:LiSAF has the highest emission cross section among Cr:Colquiriites, it is the easiest gain media to work with during mode-locked operation among Cr:Colquiriites. This also makes Cr:LiSAF the ideal

candidate for generating shortest pulses and demonstrating broadest femtosecond tuning range. We again stress that, our analysis here was simple and rough, and our aim was just to show the main effects.

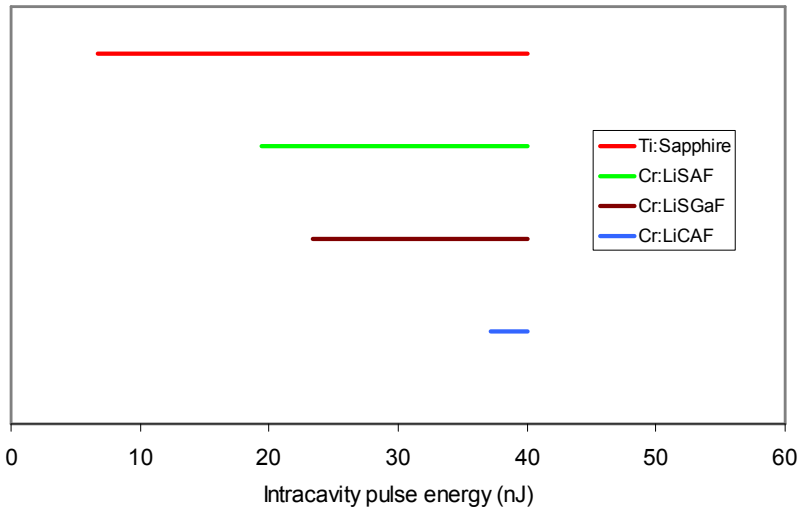

Figure 4.2: Calculated stable cw mode-locking working range for different gain media for 25-fs long pulses.

Case	Pulse width (fs)	Output power (mW)	Peak power (kW)	Pulse energy (nJ)	Rep rate (MHz)	Central wavelength (nm)	SESAM/SBR	Dispersion compensation method	Pump power (mW)	Section/ Refe.
1	75	156	18.2	1.36	114	850	MIT-850-bulk	DCMs	~600	[59]
2	46	149	38.1	1.76	85	870	MIT-850-bulk	FS Prism pair	~600	[59]
3	74	187	29.7	2.2	85	859	MIT-850-bulk	FS Prism pair	~600	[59]
4	36	110	29.4	1.06	104	850	MIT-850-bulk	FS Prism pair	~600	4.3
5	75	140	16	1.2	116	855	MIT-850-bulk	DCMs	~600	4.2
5	~136	~142	12.1	1.64	85	832-866	MIT-850-bulk	DCMs	~600	4.5
6	~75	~127	~20.9	~1.57	81	842-870	MIT-850-bulk	DCMs	~600	4.5
7	~3000	~150	-	~1.6	105	855	MIT-850-bulk	-	~600	4.1
8	26	85	38.5	1	85	850	MIT-850-bulk-HR	DCMs	~600	4.4
9	~188	~170	~9.95	~1.87	91	828-873	MIT-850-bulk-HR	DCMs	~800	4.6
10	~140	~180	~12.86	~1.8	110	835-870	MIT-850-bulk-HR	DCMs	~800	4.6
11	~55	110	~1.8	~0.11	1000	865	MIT-850-bulk-HR	DCMs	~1000	[161]
12	~85	147	~1.45	~0.147	1000	865	MIT-850-bulk-HR	DCMs	~1000	[161]
13	85	144	13.7	1.17	123	812	MIT-800-QW-2HR	GTI & DCMs	~600	4.7, [59]
14	41	121	34.9	1.43	84	814	MIT-800-QW-2HR	FS Prism pair	~600	4.8, [59]
15	~140	90	7.1	~1	83	803-831 (791-795)	MIT-800-QW-2HR	DCMs	~800	4.9
16	90	205	20.7	1.86	110	890	MIT-910-bulk	DCMs	~700	4.10
17	~150	~100	~10	~1	~100	890-923	MIT-910-bulk	DCMs	~700	4.11
18	38	167	47.3	1.8	93	880	MIT-860-QW-Oxidized	DCMs	~1000	4.13
19	~140	~140	~11.4	~1.6	85	800-905	MIT-860-QW-Oxidized	DCMs	~1000	4.12

Table 4.2: Summary of cw mode-locking results obtained with Cr:LiSAF gain media. All the results reported in this table have an uncertainty of about ±10%. DCMs: Double-chirped mirrors, GTIs: Gires–Tournois interferometer mirrors.

Table 4.2 lists some of the key mode-locking results obtained with Cr:LiSAF gain media during this PhD thesis. With Cr:LiSAF gain media, all the mode-locking results were performed by single-mode diode pumped systems. This is Cr:LiSAF gain medium's thermal properties is not as good as Cr:LiCAF,

and with multimode diode pumping with an asymmetric beam profile, we didn't expect significant power scaling; hence, we haven't applied multi-mode pumping to Cr:LiSAF. For dispersion compensation we have used custom-designed double-chirped mirror (DCMs) set which is described in detail in Appendix A. Commercially available DCM and/or Gires–Tournois interferometer mirrors (GTIs) from Layertec was also used. Moreover, we have used fused silica prism pair as an additional dispersion tuning element.

SESAM/SBR Name	Short Name	Modulation depth (%)	Section
MIT 850 nm SESAM/SBR with bulk absorber	MIT-850-Bulk	2.2	E1
One pair HR layer coated MIT 850 nm SESAM/SBR with bulk absorber	MIT-850-Bulk-HR	0.8	E2
MIT 910 nm SESAM/SBR with bulk absorber	MIT-910-Bulk	1.7	E8
Two pairs HR layer coated MIT 800 nm SESAM/SBR with quantum-well absorber	MIT-800-QW-2HR	0.6	E7
MIT 860 nm oxidized/broadband SESAM/SBR with quantum well absorber	MIT-860-QW-Oxidized	0.75	E10

Table 4.3: List of SESAMs/SBRs that is used in mode-locking of Cr:LiSAF. Detailed information on these SESAMs/SBRs can be found in Appendix E.

Also, since the gain bandwidth of Cr:LiSAF is broader than Cr:LiCAF, we have performed mode-locking experiments at a wider wavelength range covering the region from 800 nm to ~900 nm (with Cr:LiCAF it was only around 800 nm). To cover this wavelength range, we have used several regular SESAMs/SBRs with different central reflectivity wavelengths (~800 nm, ~850 nm and ~900 nm), since each regular SESAM/SBRs has a bandwidth of only ~50 nm around their central reflectivity. Table 4.3 lists the SESAMs/SBRs that were used in the experiments. For mode-locking around ~800 nm, we have used MIT 800 nm SESAM/SBR with quantum well absorber and 2 layers of HR coating (MIT-800-QW-2HR). For mode-locking around ~850 nm, we have used MIT 850 nm SESAM/SBR with a bulk absorber. Both bare (MIT-850-bulk) and 1 layer HR coated (MIT-850-bulk-HR) versions of this SESAM/SBR have been used. For mode-locking around 910 nm we have used MIT 910 nm SESAM/SBR with a bulk absorber (MIT-910-bulk). Lastly, we have also designed an oxidized/broadband SESAM/SBR for Cr:LiSAF gain media (MIT-860-QW-Oxidized), which enabled mode-locking from ~790 nm to ~920 nm. This SESAM/SBR was also used in the fs tuning experiments and actually gave the broadest fs tuning range ever obtained from a SESAM/SBR mode-locked laser. More details about these SESAMs/SBRs can be found in Appendix E.

In the following sections, we will give the details of some of the mode-locking results obtained with Cr:LiSAF gain media. In Section 4.1 we will present mode-locking of Cr:LiSAF laser with positive cavity dispersion, where the generated pulsewidths were in the ps range. In Section 4.2, we will present typical mode-locked operation results of the single-mode diode pumped Cr:LiSAF laser around 850 nm. Section

4.3 and 4.4 will discuss sub-50-fs pulse generation from Cr:LiSAF around 850 nm using MIT-850-bulk and MIT-850-bulk-HR SESAMs/SBRs, respectively. Similarly, Section 4.5 and Section 4.6 discusses femtosecond tuning experiments with Cr:LiSAF laser around 850 nm, using MIT-850-bulk and MIT-850-bulk-HR SESAMs/SBRs, respectively. In Sections 4.7-4.9, we will present typical mode-locked operation, sub-50-fs pulse generation and tuning results of the single-mode diode pumped Cr:LiSAF laser around ~800 nm. Typical mode-locked operation and mode-locked tuning results around 900 nm will be presented in Sections 4.10 and 4.11. In section 4.12 and 4.13 we will present tuning and sub-50-fs pulse generation experiments with MIT-860-QW-Oxidized SESAM/SBR. Finally, in Section 4.14, we will summarize mode-locking experimental results with Cr:LiSAF gain medium.

4.1 Mode-Locking with Positive Dispersion

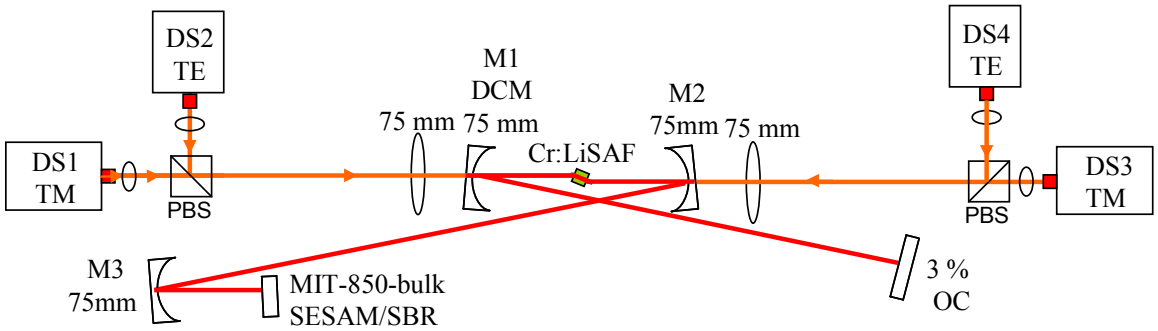

Figure 4.3: Schematic of the single-mode diode pumped Cr:LiSAF laser that was mode-locked with total positive cavity dispersion. The total incident pump power on the crystal is about 600 mW.

We would like to start presenting the mode-locking results with Cr:LiSAF gain medium with describing the mode-locked operation of a Cr:LiSAF laser cavity with positive dispersion. Hence, soliton pulse shaping mechanism is not present and pulses are solely stabilized and shaped by the SESAM/SBR. Figure 4.3 shows a schematic of the single-mode diode-pumped Cr^{3+}:LiCAF laser cavity that was used in cw mode-locking experiments. The cavity was similar to what was used in cw laser experiments (Chapter 2). Four HL6545MG (~660 nm) single-mode diodes provided about ~600 mW of pump power. The gain medium was a 5-mm-long, Brewster-cut, 1.5% Cr-doped Cr^{3+}:LiSAF crystal mounted with indium foil in a copper holder. The crystal absorbed 99% and 72% (0.9 x 80%) of the incident TM and TE polarized pump lights, respectively, and the total absorbed pump power was ~550 mW. Neither the crystal nor diodes required water cooling. For mode-locking experiments, we have used MIT 850 nm SESAM/SBR with a bulk absorber (MIT-850-bulk), which has 2.2% modulation depth. Mirrors M1 is from MIT Cr:LiSAF pump mirror set with ~ $-80fs^2$ group velocity dispersion per bounce, and M2-M3 is from

Layertec Cr:Colquiriite pump mirror set I, which has around ~0 fs^2 of dispersion. The Cr:LiSAF crystal has about 23 fs^2/mm dispersion around 850 nm. Considering also the dispersion of intracavity air and the SESAM/SBR, we have obtained the curve shown in Fig. 4.4 as the estimate for total cavity dispersion. Note that, the total cavity dispersion is positive, and is around 120 fs^2 around 850 nm. The slope in the estimated dispersion curve is mostly due to the third order dispersion of Cr:LiSAF crystal.

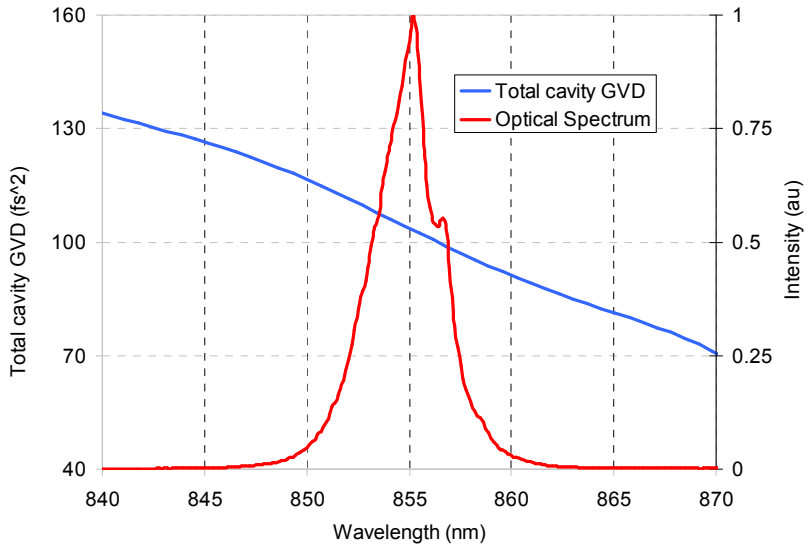

Figure 4.4: Estimated total cavity dispersion for the Cr:LiSAF laser that is mode-locked with positive cavity dispersion. Obtained optical spectrum in mode-locked regime is also shown.

When mode-locked the laser produced ~3ps long chirped pulses centered around ~855 nm. The SESAM /SBR mode-locked laser was self-starting, and immune to environmental fluctuations. Figure 4.4 also shows the optical spectrum which has a bandwidth of about ~3.5 nm around 855 nm. The spectrum is broad enough to support ~50 fs long pulses. However, since soliton pulse shaping was not present, the pulses were highly chirped with a measured width of about ~3 ps (Fig. 4.5). The average output power was about 150 mW, corresponding to a pulse energy of ~1.43 nJ, at the repetition rate of 105 MHz. Figure 4.6 shows the measured pulse train for the pulses. Note that compared to the Cr:Colquiriite lasers mode locked with negative dispersion, the measured RF spectrum has a larger background noise. We can attribute this to the absence of soliton-pulse shaping mechanism.

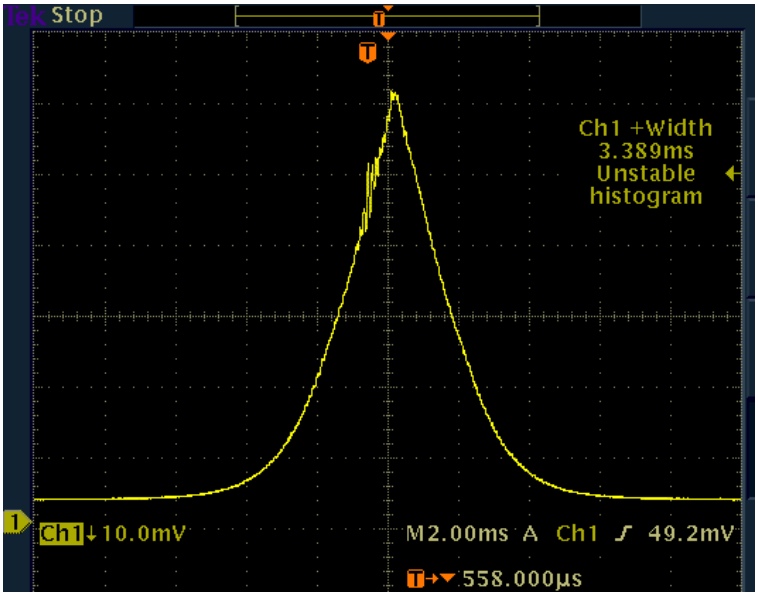

Figure 4.5: Measured background free autocorrelation trace for the ~3.2 ps, ~1.43 nJ pulses.

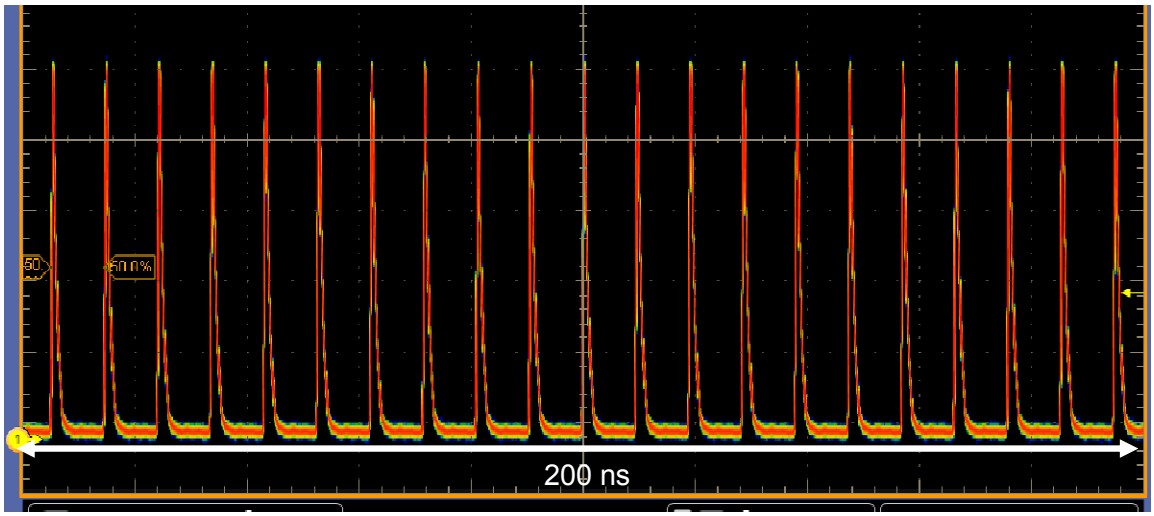

Figure 4.6: Measured pulse train for the ~3.2 ps, ~1.43 nJ pulses.

We note here that, due to the high amount of chirp, the peak powers of the pulses are quite low. Hence, the two photon absorption effects and multiple pulsing instabilities will start at much higher intracavity pulse energy levels compared to soliton pulse shaped lasers. Hence, this mode-locking regime will be advantageous for application where one wants to scale the pulse energies. Ideally, these chirped pulses can be compressed back close to their Fourier transform limited pulsewidth with proper dispersion compensation.

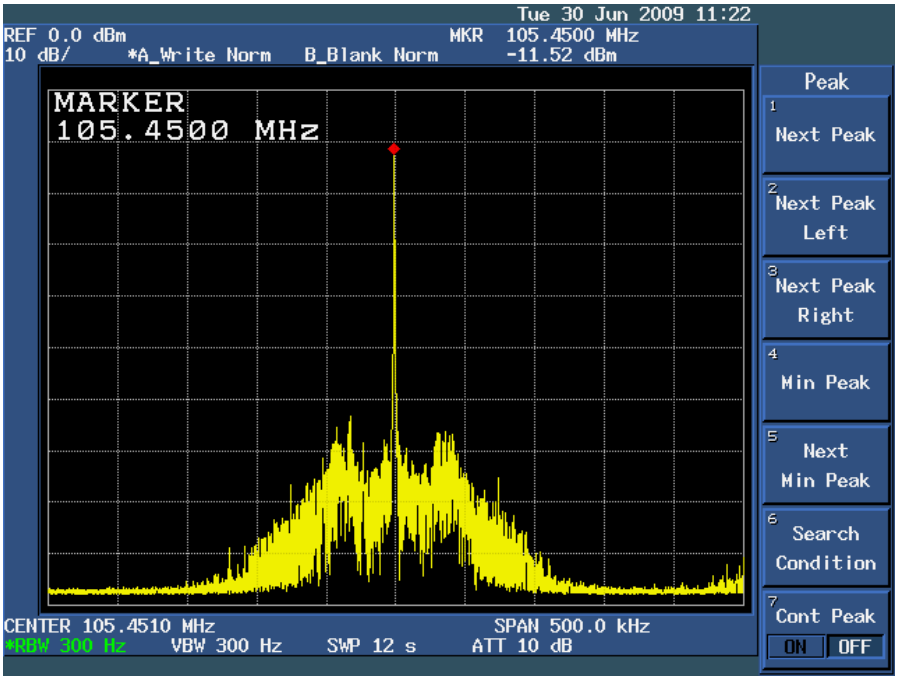

Figure 4.7: RF spectrum for the ~3.2 ps, ~1.43 nJ pulses. The RF spectrum is relatively noisy in comparison with Cr:Colquiriite lasers mode-locked with negative level of cavity dispersion.

4.2 Typical Mode-Locked Operation of Cr:LiSAF Laser around 850 nm

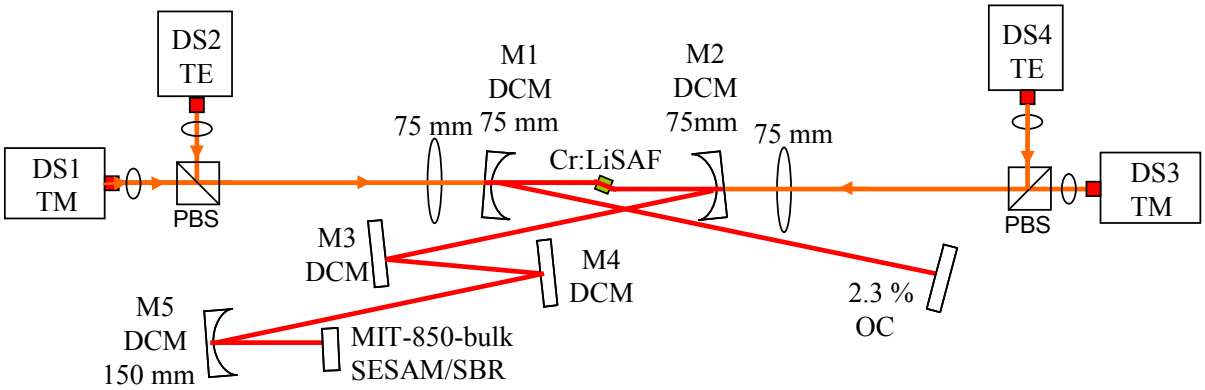

Figure 4.8: Schematic of the single-mode diode pumped Cr:LiSAF laser that was mode-locked with total negative cavity dispersion. The total incident pump power on the crystal is about 600 mW.

In this section, we will present some typical results from mode-locked Cr:LiSAF laser. Figure 4.8 shows the Cr:LiSAF laser, which is actually very similar to the laser above, except that we now have more DCM mirrors to provide negative dispersion. All the DCM mirrors used in the study were from MIT Cr:LiSAF pump mirror set which provided about ~ -80 fs^2 group velocity dispersion per bounce. Figure 4.9 shows the estimated total cavity dispersion level, where the dispersion estimate includes 10 bounces on DCM mirrors, 10 mm of Cr:LiSAF, the intracavity air and the SESAM/SBR dispersion. The estimated dispersion around 850 nm was about -530 fs^2. The dispersion curve is mainly shaped by the dispersion of

the MIT-850-bulk SESAM/SBR which has a quite narrow bandwidth around 850 nm. When mode-locked the laser produced ~75 long pulses with 140 mW average power at a repletion rate of 116 MHz (corresponding pulse energy ~1.2 nJ). The optical spectrum was centered around 855 nm and had a bandwidth of ~10.5 nm (also shown in Fig. 4.9). This bandwidth is broad enough to support ~73-fs transform limited pulses. The measured pulsewidth was ~75-fs, which shows that output pulses from the laser had negligible chirp. Fig. 4.10 shows the measured RF spectrum of the pulses, where we see a clean strong peak around ~116.2 MHz. The ~75 kHz side bands are due to the intensity noise of the laser, which is caused by the noise in pump laser diode drivers. Hence, when the pump diodes are driven with low noise sources, these side bands also disappear.

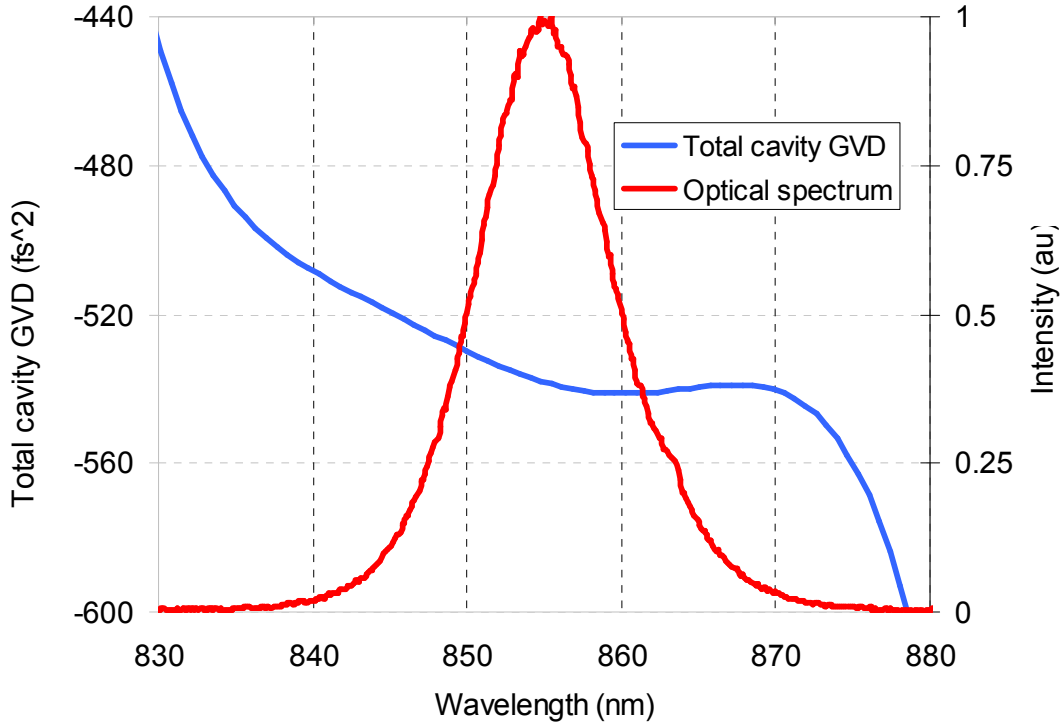

Figure 4.9: Estimated total cavity dispersion for the Cr:LiSAF laser that is mode-locked with negative cavity dispersion. Obtained optical spectrum in mode-locked regime is also shown. The laser produced ~75 fs pulses with ~1.2 nJ pulse energy.

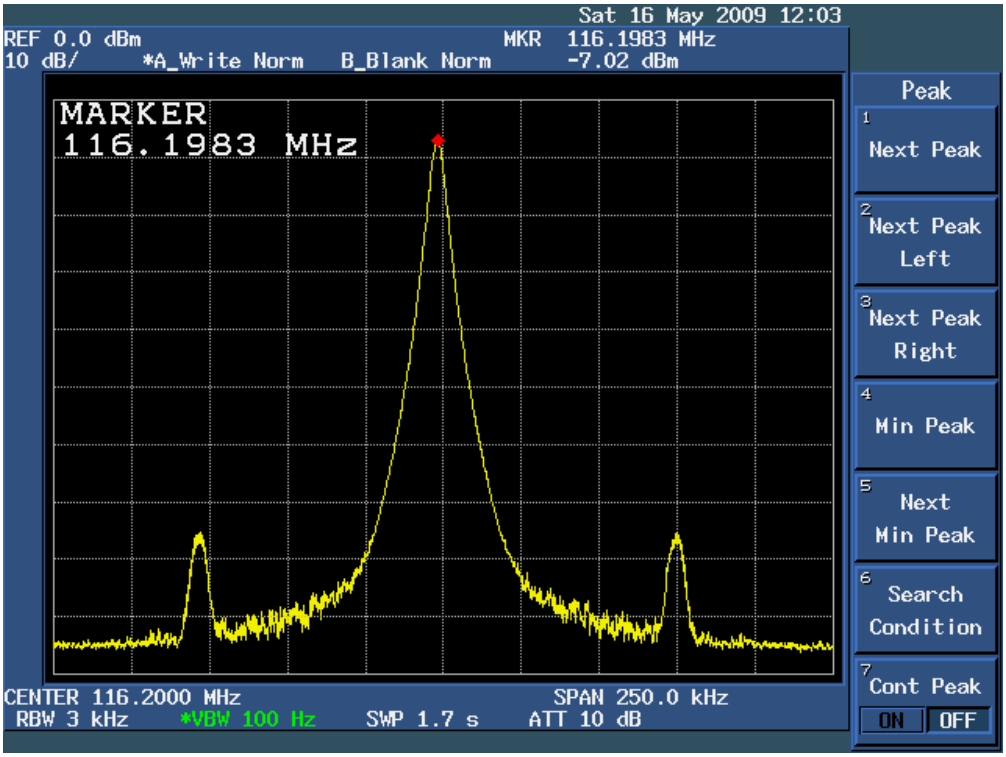

Figure 4.10: Measured RF spectrum for the ~75 fs, ~1.2 nJ pulses.

4.3 Sub-50-fs Pulses from Cr:LiSAF Laser using MIT-850-bulk SESAM/SBR

The pulsewidths reported above (~75 fs) was obtained at an estimated cavity dispersion level of -530 fs^2. To obtain shorter pulses one can be reduce the dispersion amount by using less bounces on DCM mirrors. However, this will not allow fine dispersion tuning, since this only allows discrete dispersion variation (~-160 fs^2 in round trip). With Cr:LiSAF laser we have used a fused silica prism pair for fine tuning of cavity the dispersion.

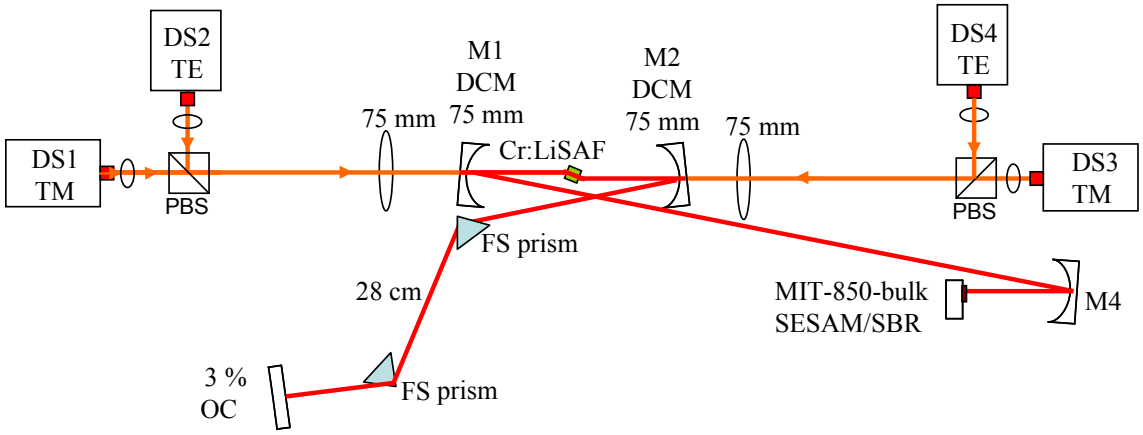

Figure 4.11: Schematic of the single-mode diode pumped Cr:LiSAF laser, where the dispersion compensation was performed by use of DCMs and a fused silica prism pair. The total incident pump power on the crystal is about 600 mW.

Figure 4.11 shows the Cr:LiSAF laser, which is again very similar to the lasers described above, except that it now contains a fused silica prism pair for fine dispersion tuning. Without the prism pair, the estimated total cavity dispersion was ~ -30 fs^2 (~ -320 fs^2 from DCMs, +230 fs^2 from Cr:LiSAF crystal, and +60 fs^2 from intracavity air). We have chosen a fused silica prism separation of 28 cm, which provided about ~ -300 fs^2 of GVD around 850 nm at minimal prism material insertion (Figs. 4.12-4.13). With adjusting the fused silica prism material insertion, it was possible to fine tune the total cavity dispersion (Fig. 4.14). Figure 4.15 shows the optical spectrum for the shortest pulses we could obtain from the laser. The average output power was 110 mW, which corresponds to a pulse energy of ~1.06 nJ, at the repetition rate of 104 MHz. The optical spectrum was centered around ~850 nm, with a FWHM of ~22 nm, which is enough to support transform limited ~34.5 fs pulses. The measured pulsewidth with using a background free autocorrelator was ~36-fs, as shown in Fig. 4.16. Fig. 4.17 shows the measured optical spectrum with the reflectivity of the MIT-850-bulk SESAM/SBR. Fig. 4.17 clearly shows that the reflectivity bandwidth of the SESAM/SBR limits the obtainable pulsewidth to ~35-fs level for the MIT-850-bulk SESAM/SBR.

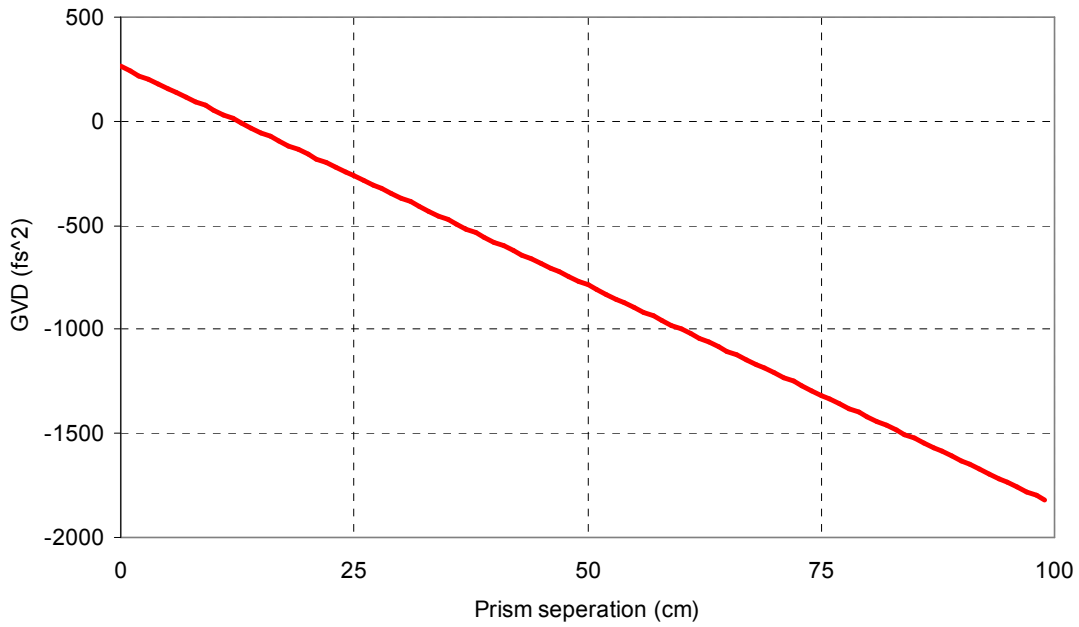

Figure 4.12: Calculated variation of dispersion from a fused silica prism pair with prism separation assuming minimal prism insertion.

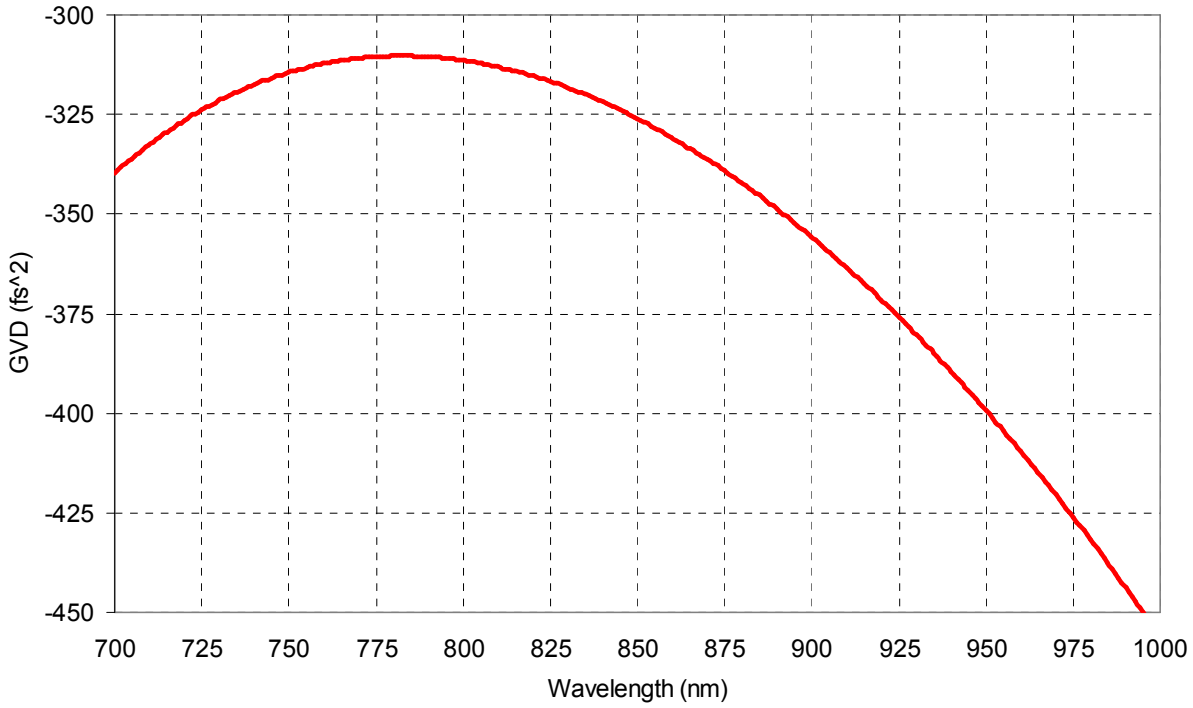

Figure 4.13: Calculated variation of dispersion from a fused silica prism pair with wavelength assuming minimal prism insertion at a prism separation of 28 cm.

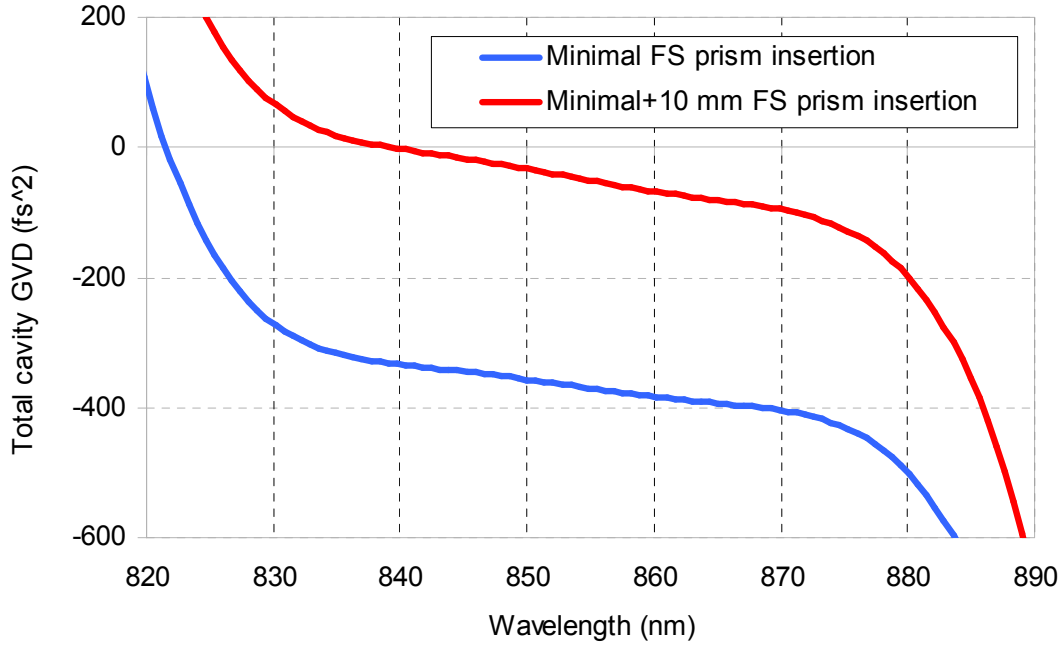

Figure 4.14: Estimated total cavity dispersion for the Cr:LiSAF laser with a prism pair. The estimation is done for the cases where (i) there is minimal FS prism material insertion (b) there is 10 mm of additional FS prism material insertion. Both of the estimates assume a FS prism pair separation of ~28 cm. The dispersion curve bandwidth is limited by the dispersion of MIT-850-bulk SESAM/SBR.

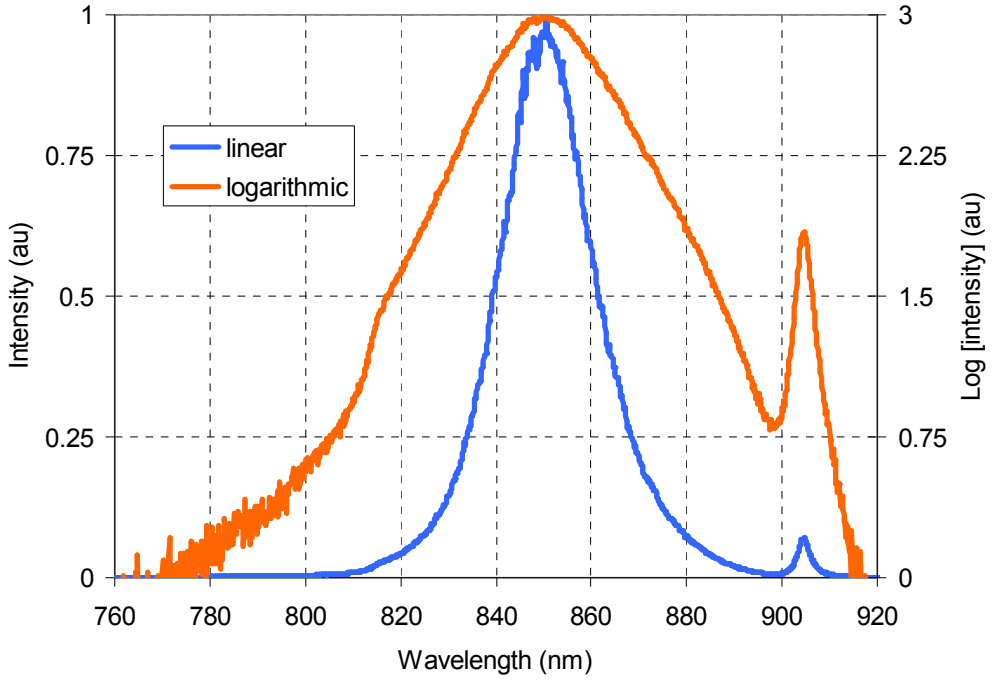

Figure 4.15: Optical spectrum for the ~36 fs 1.06 nJ pulses shown in linear and logarithmic scales.

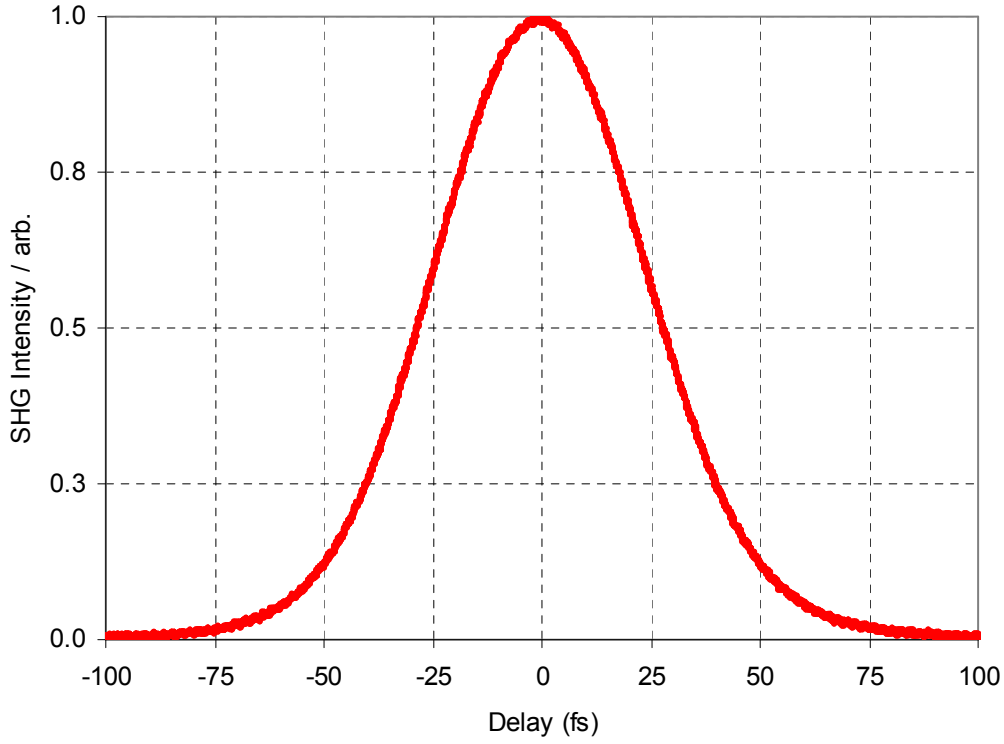

Figure 4.16: Measured background free autocorrelation trace for the ~36 fs 1.06 nJ pulses.

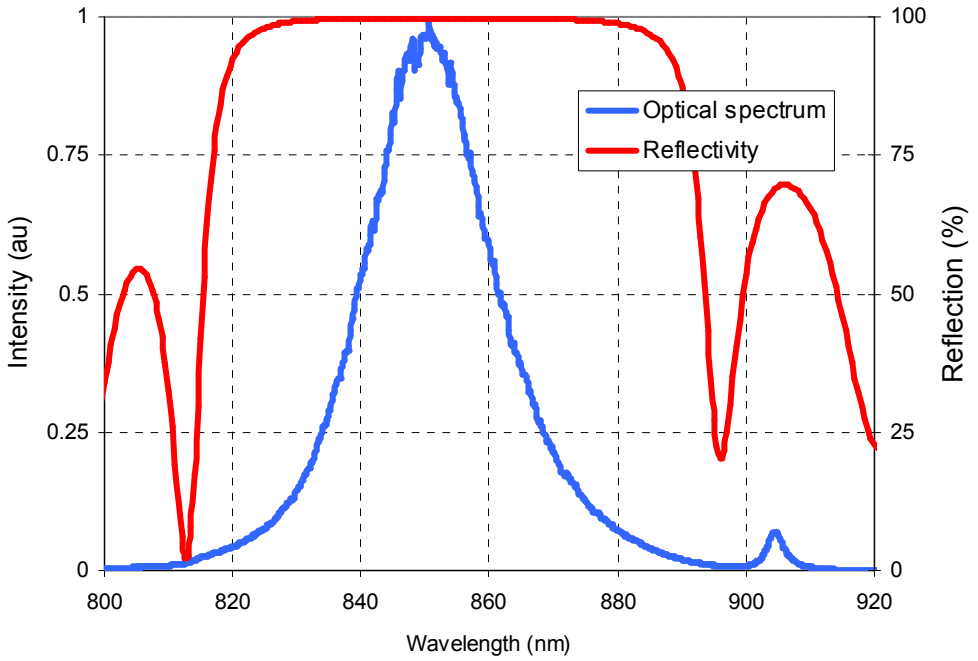

Figure 4.17: Measured optical spectrum the ~36 fs 1.06 nJ pulses is shown with the reflectivity curve for MIT-850-bulk SESAM/SBR.

4.4 Sub-50-fs Pulses from Cr:LiSAF Laser using MIT-850-bulk-HR SESAM/SBR

As we have seen in the previous section, the bandwidth of MIT-850-bulk SESAM/SBR limited the obtainable pulsewidths from the Cr:LiSAF laser to ~35 fs level. In the experiments we have also used one pair of SiO2/TiO2 high reflector layer coated version of this SESAM/SBR (MIT-850-bulk-HR). The HR coating reduced the modulation depth of the SESAM/SBR from 2.2% to 0.8% and improved the reflectivity bandwidth from 58 nm to 68 nm (specified for reflectivity> 99%). The HR coating also broadens the GVD bandwidth of the SESAM/SBR. We refer the reader to Appendix D for a more detailed description of these SESAMs/SBRs.

One can expect to obtain shorter pulses with the HR coated version of MIT-850-bulk SESAM/SBR due to the improved bandwidth (assuming reduced modulation depths won't cause any instability in the laser). To test this, we have build a Cr:LiSAF laser that was almost identical to the cavity in the earlier section, except that we have replaced the MIT-850-bulk SESAM/SBR with MIT-850-bulk-HR SESAM/SBR. With the HR coated 850 nm SESAM/SBR, we have obtained ~26-fs pulses with ~1-nJ pulse energy at a repetition rate of 85 MHz. Fig. 18 shows the optical spectrum of the pulses, which is centered around ~850 nm, with a FWHM of ~33 nm, which ideally could support sub-23-fs transform limited pulses. The measured pulsewidth ~26-fs was slightly longer than the transform limited value,

indicating a time bandwidth product of around ~0.36. This is the shortest pulses we have obtained from Cr:Colquiriites during this PhD work.

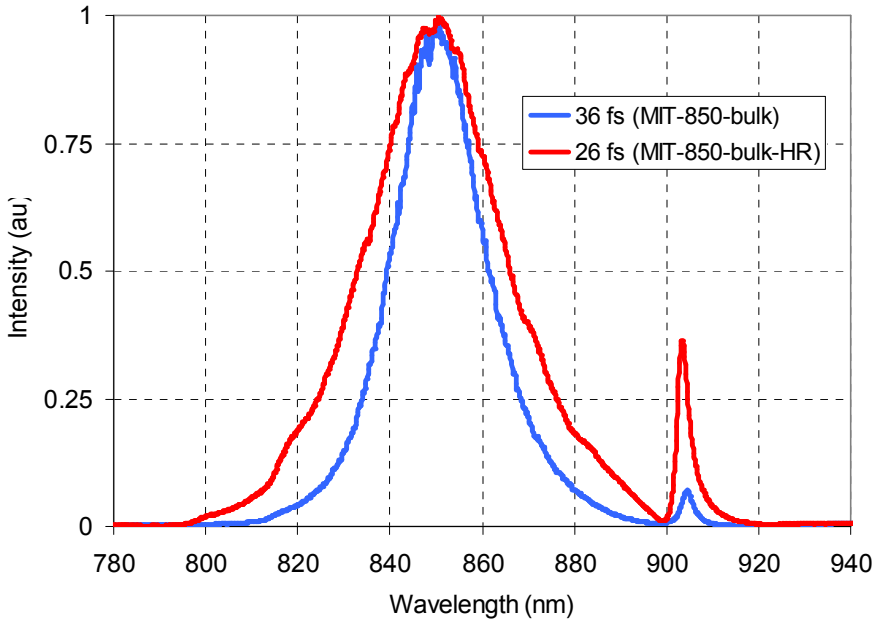

Figure 4.18: Measured optical spectrum the ~26 fs ~1 nJ pulse obtained with MIT-800-bulk-HR SESAM/SBR. For comparison ~36 fs 1.06 nJ pulses obtained with MIT-850-bulk SESAM/SBR is also shown.

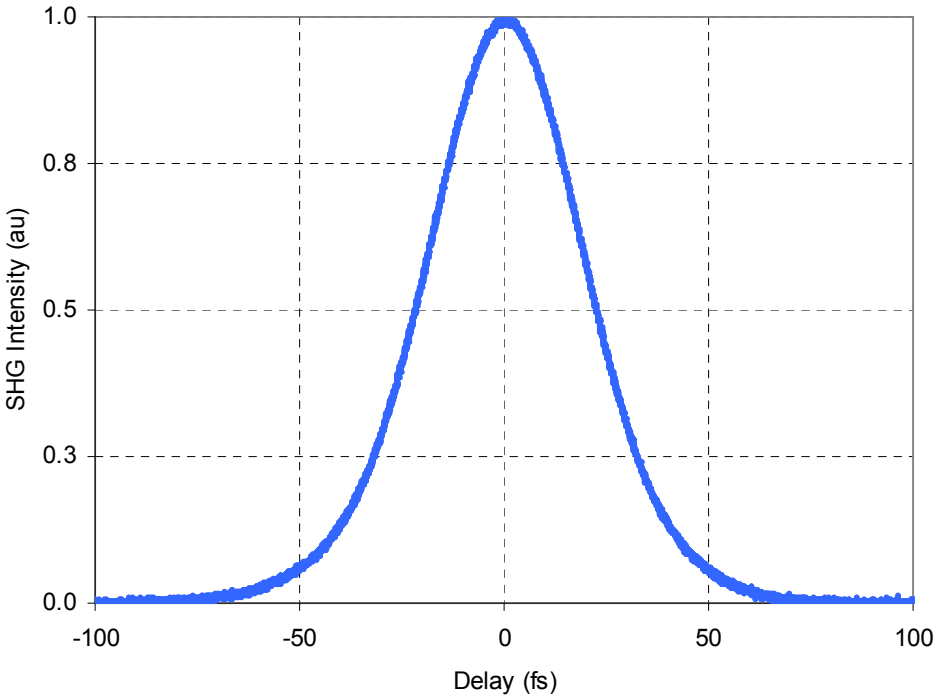

Figure 4.19: Measured background free autocorrelation trace for the ~26 fs 1 nJ pulses.

4.5 Mode-locked Tuning of Cr:LiSAF Laser with MIT-850-bulk SESAM/SBR

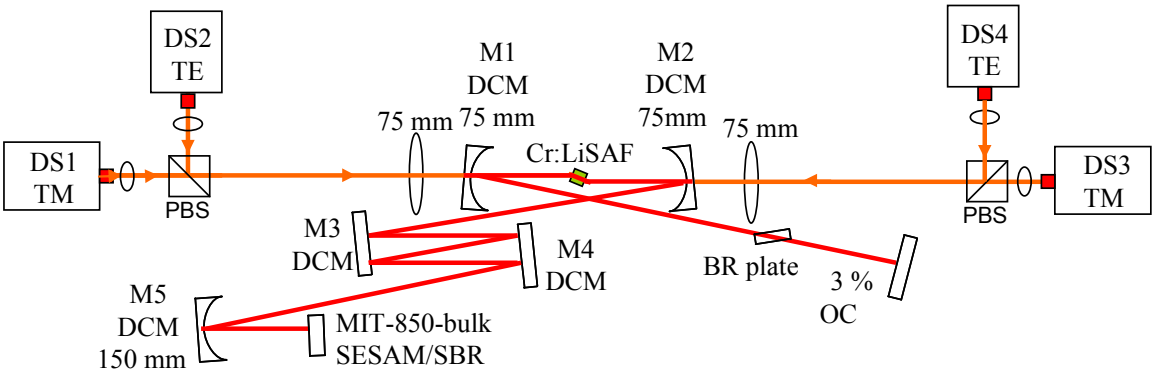

Figure 4.20: Schematic of the single-mode diode pumped Cr:LiSAF laser that was used in mode-locked tuning experiments. MIT-850-bulk SESAM/SBR is sued for mode-locking. Estimated total cavity dispersion is ~ -600 fs^2. The total incident pump power on the crystal is about 600 mW.

Figure 4.20 shows the schematic for the Cr:LiSAF laser that we have used in tuning experiments in mode-locked regime. In this section we will focus on tuning experiments with MIT 850 nm SESAM/SBR with bulk absorber (MIT-850-bulk). Again, the laser cavity is very similar to what was already described above. A specially designed, 3 mm thick crystal quartz birefringent filter, with a crystal axis pointing out of the crystal surface, was used to tune the central wavelength of the pulse spectrum. The estimated cavity dispersion was around ~ -600 fs^2, and it was quite flat in the MIT-850-bulk SESAM/SBR reflectivity range (Fig. 4.21).

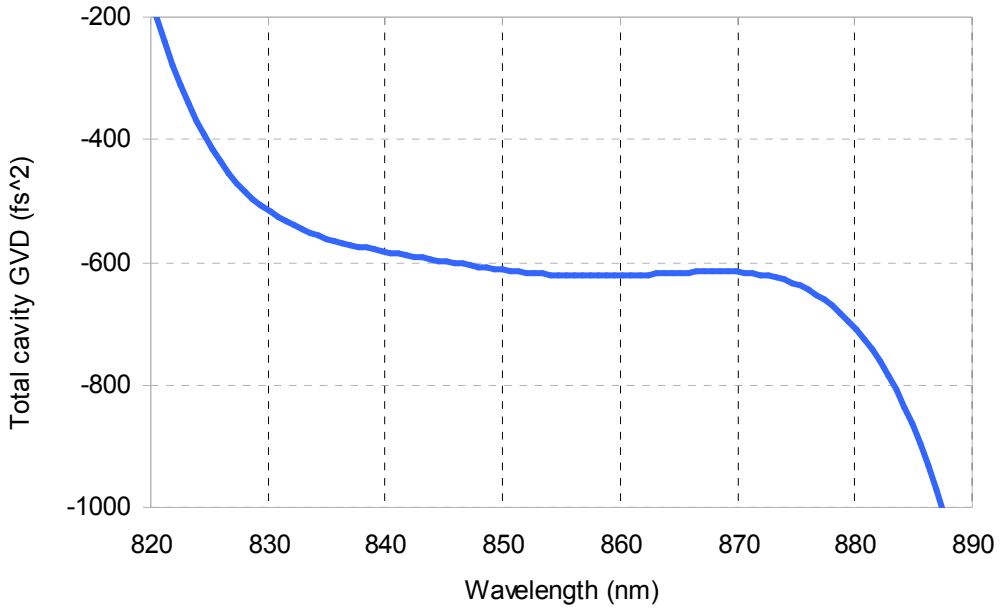

Figure 4.21: Estimated total cavity dispersion for the cavity that was shown in Fig. 4.20. The cavity dispersion estimate includes 14 bounces on DCMs, 10 mm of Cr:LiSAF, ~7.3 mm of fused silica from the BR plate, ~3.75 m of intracavity air, and one bounce on MIT-850-bulk SESAM/SBR.

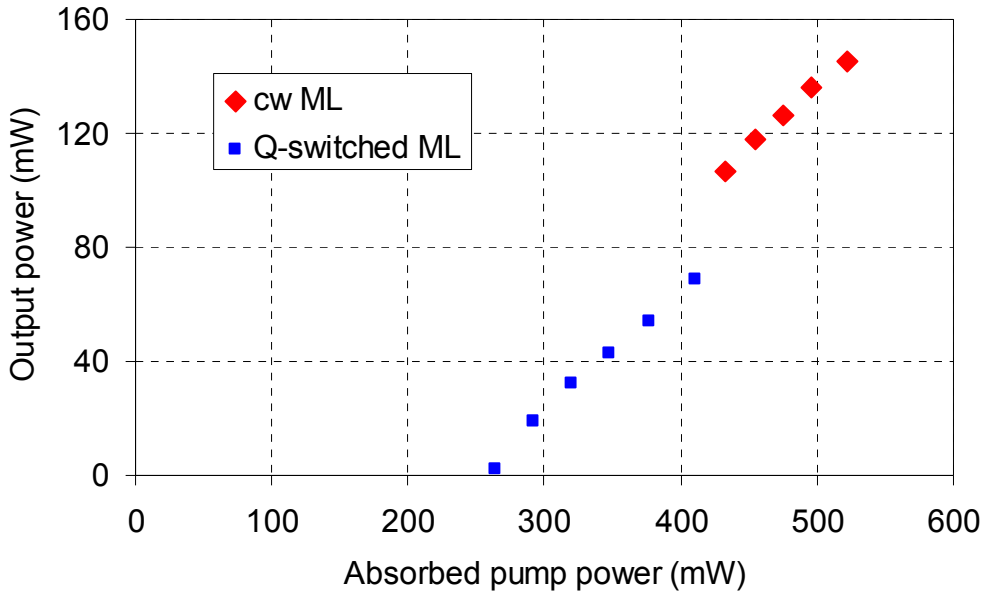

Figure 4.22: Efficiency curve for the single-mode diode pumped mode-locked Cr^{3+}:LiSAF laser that is used in tuning experiments. MIT-850-bulk SESAM/SBR is used for mode-locking.

Figure 4.22 shows the efficiency curve when the laser was mode-locked at a central wavelength of ~855 nm. At this central wavelength, the laser produced ~146-fs pulses with ~145 mW of average output power at a repletion rate of ~86 MHz. It was possible to tune the central wavelength of the laser by just rotating the BR tuning plate. The laser was continuously tunable from 832.5 nm to 865.7 nm (33.2 nm tuning range). Figure 4.23 shows the obtained variation of pulse energy and pulsewidth with changing central wavelength of the pulse optical spectrum, for ~sub-150-fs pulses. The laser pulsewidth and average output power was almost constant along the full tuning bandwidth. On average, the laser generated ~136 fs pulses with ~142 mW of average power at a repetition rate of 81.6 MHz (~1.64 nJ pulse energy). The data was taken with a 3% output coupler, at an absorbed pump power of ~530 mW. The output power of the laser stayed almost constant even at the tuning edges, showing that the decrease in power performance due to changing crystal gain or increasing loss due to SESAM/SBR or other cavity elements is not limiting the tuning yet.

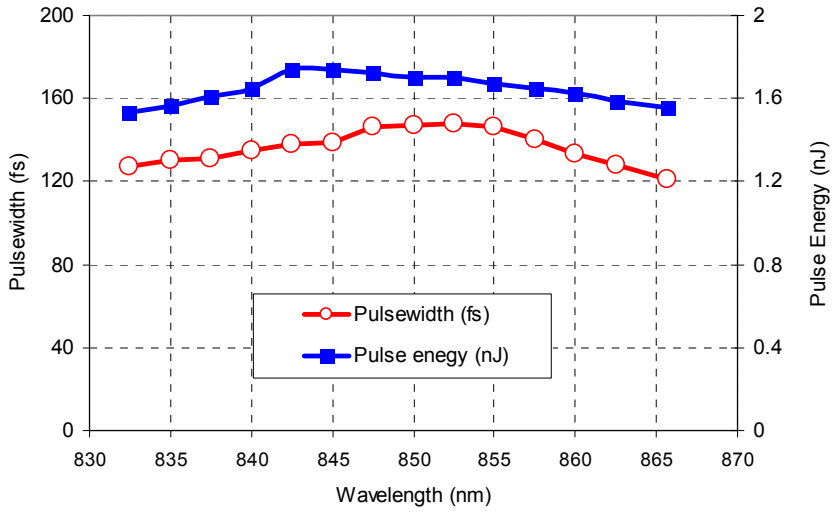

Figure 4.23: Summary of tuning for sub-150-fs pulses, which shows the variation of pulsewidth and pulse energy as the laser central wavelength is tuned by the rotation of the intracavity birefringent filter element. The laser produced about 140-fs pulses with ~1.64 nJ of pulse energy at a repetition rate of ~86.3 MHz. The average output power was ~142 mW, at an absorbed pump power of ~530 mW, with a 3% output coupler. MIT-850-bulk SESAM/SBR was used. The total tuning range is ~33.2 nm (832.5 nm to 867.5 nm).

Figure 4.24 shows example optical spectra taken at discrete steps in the demonstrated tuning range of the Cr:LiSAF laser with the MIT-850-bulk SESAM/SBR. Calculated small signal reflectivity of the SESAM/SBR is also shown. We believe that tuning of the laser below ~832.5 nm is limited by the reflectivity and dispersion bandwidth of the MIT-850-bulk SESAM/SBR (note the increase in dispersion, which is shown at Fig. 4.21). On the long wavelength side, when we tried to tune the laser above ~867.5 nm, a cw peak appeared around ~880 nm, which then disturbed the tuning. The appearance of this cw peak is due to a mistake in absorber design for this SBR. This SESAM/SBR used ~5 nm thick GaAs layer as the absorber where the estimated band edge is around 870 nm (Appendix E). Hence, when the laser central wavelength is tuned above ~870 nm, there is almost no saturable absorption at these wavelengths and the laser tend to work in pure cw regime, which limits the mode-locked tuning range.

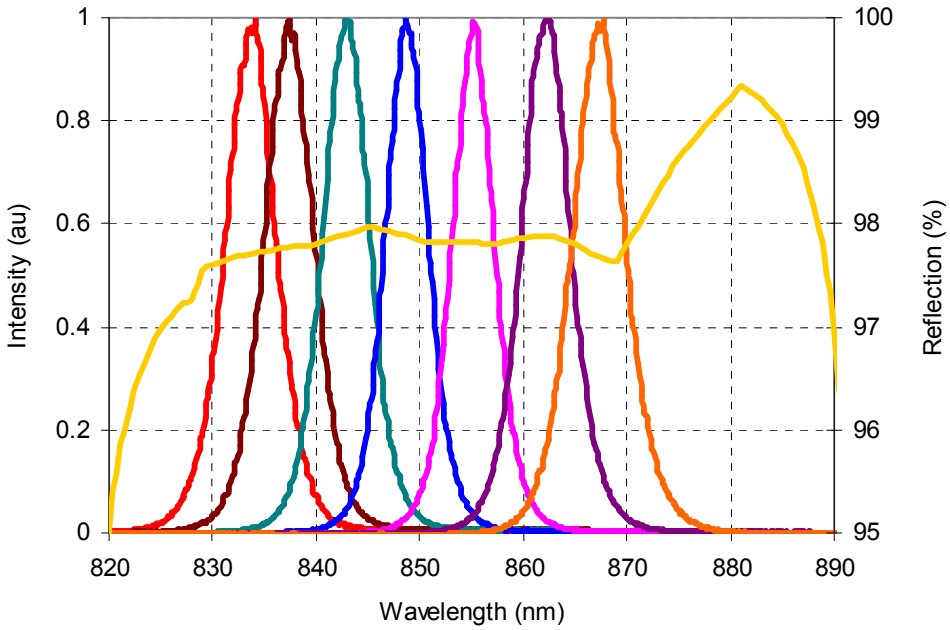

Figure 4.24: Example spectra from the Cr^{3+}:LiSAF laser, showing tunability of central wavelength of the laser from 832.5 nm to 867.5 nm, for the sub-150-fs pulses. The data is taken with the MIT-850-bulk SESAM/SBR. Calculated small signal reflectivity of the SESAM/SBR is also shown.

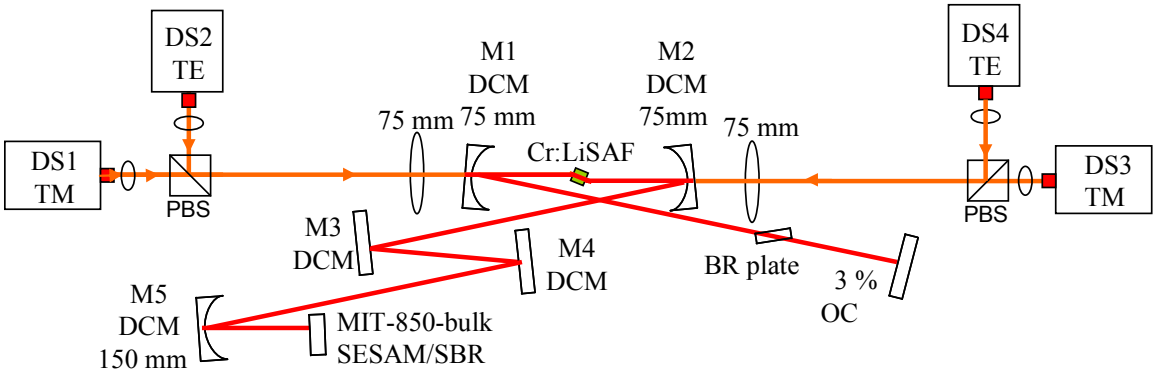

Figure 4.25: Schematic of the single-mode diode pumped Cr:LiSAF laser that was used in mode-locked tuning experiments. MIT-850-bulk SESAM/SBR is used for mode-locking. Estimated total cavity dispersion is ~ -300 fs^2. The total incident pump power on the crystal is about 600 mW.

To be able to obtain tuning with shorter pulses, we have decreased the number of bounces on DCM mirrors from 14 to 10 (Figure 4.25). This decreased the total estimated cavity dispersion from ~ -600 fs^2 to -300 fs^2. As expected from a soliton mode-locked laser, decreasing the intracavity dispersion level from ~ -600 fs^2 to ~ -300 fs^2 level roughly doubled the pulsewidths, which decreased from ~140 fs to ~75 fs. Figure 4.26 shows the obtained variation of pulse energy and pulsewidth with changing central wavelength of the pulse optical spectrum, for ~sub-80-fs pulses. The central wavelength of the laser could be tuned continuously from ~842 nm to ~870 nm (~28 nm tuning), by just rotating the birefringent filter element (the data in Fig. 4.21 was taken at discrete wavelengths with a separation of ~2.5 nm). The laser

pulsewidth and average output power was almost constant along the full tuning bandwidth. On average the Cr:LiSAF laser generated ~75 fs pulses with ~127 mW of average power at a repetition rate of 81.6 MHz (~1.56 nJ pulse energy). Note that, the obtained tuning range with ~75 fs pulses (~28 nm) is slightly narrower than what was obtained with ~140 fs level pulses (~33 nm).

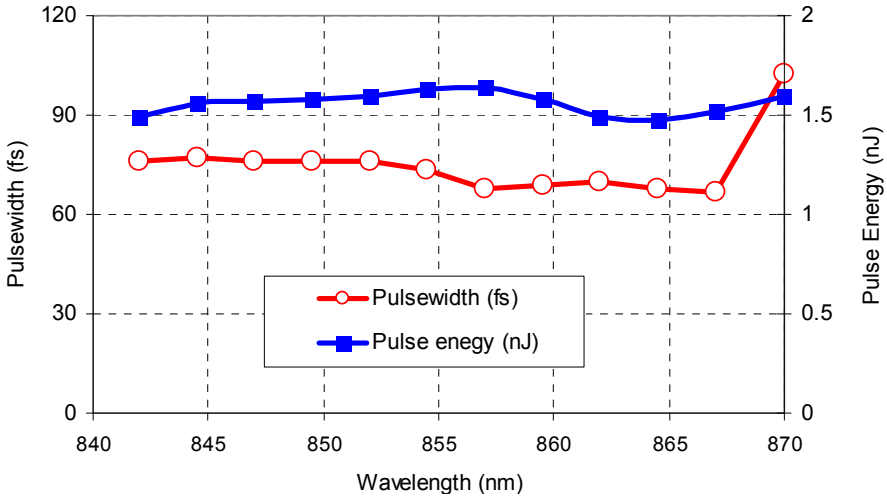

Figure 4.26: Summary of tuning for sub-80-fs pulses. The graph shows the variation of laser pulsewidth and pulse energy as the laser central wavelength is tuned by the rotation of the intracavity birefringent filter element. Note that the pulsewidth and the pulse energy stayed almost constant along the full tuning range. The laser produced about 75-fs pulses with ~1.56 nJ of pulse energy at a repetition rate of ~81.6 MHz. The average output power was ~127 mW, at an absorbed pump power of ~530 mW, with a 3% output coupler. MIT-850-bulk SESAM/SBR is used for mode-locking. The total tuning range is ~28 nm (842 nm to 870 nm).

Figure 4.27 shows example optical spectra for the sub-80-fs pulses, along with the variation of the estimated total cavity dispersion. The relatively large fluctuation in the GVD curve is mostly due to the MIT-850 bulk SESAM/SBR, which had a quite narrow GVD bandwidth with relatively large deviations from 0 fs^2, when one moves away from the central wavelength (850 nm). Similar to the case with ~140-fs pulses, tuning above ~870 nm was limited by the absorption edge of the GaAs absorber in the MIT-850-bulk SESAM/SBR where as tuning below ~842 nm is limited by the dispersion and reflectivity bandwidth of the SESAM/SBR.

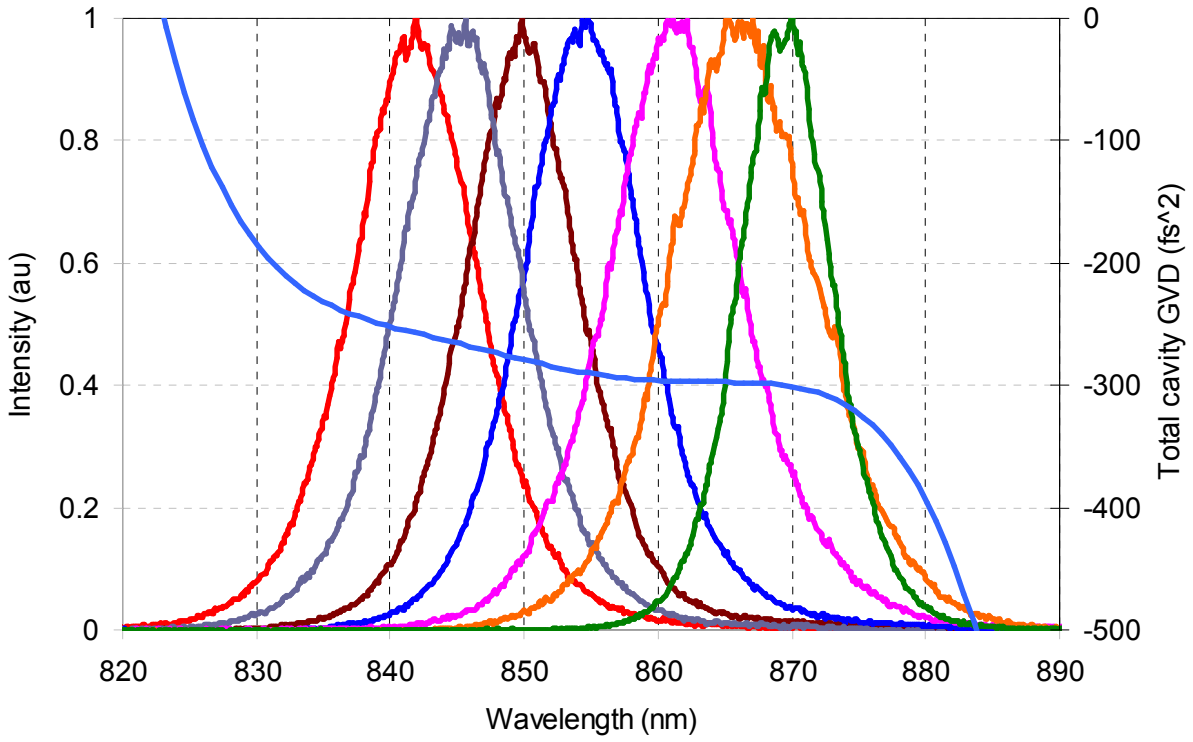

Fig. 4.27: Example spectra from the Cr^{3+}:LiSAF laser, showing tunability of central wavelength of the laser from 842 nm to 870 nm, for the sub-80-fs pulses. Estimated total cavity dispersion is also shown. The dispersion estimate includes 1 bounce on SESAM/SBR, 10 bounces on DCMs, ~3.6 m of intracavity air, 10 mm of Cr:LiSAF material and 7.3 mm of quartz substrate (from the birefringent tuning plate). The data is taken with the MIT-850-bulk SESAM/SBR.

4.6 Mode-locked Tuning of Cr:LiSAF Laser with MIT-850-bulk-HR SESAM/SBR

In section 4.4, we have seen that the HR coated version of MIT 850 nm bulk SBR enables slightly shorter pulsewidths due to the increased bandwidth. In this section, we will investigate the effect of this additional HR coating on the femtosecond tuning range. As we have mentioned, the HR coating reduced the modulation depth of the MIT-850-bulk SESAM/SBR from 2.2% to 0.8% and improved the reflectivity bandwidth from 58 nm to 68 nm (specified for reflectivity> 99%). We note here that besides the increased reflectivity, we also expect the decreased modulation depth to have a positive effect in tuning experiments. This is because we have experimentally shown that MIT-850-bulk-HR SESAM/SBR has a larger working range compared to MIT-850-bulk SESAM/SBR.

Figure 4.28 shows the schematic for the Cr:LiSAF laser that we have used in tuning experiments in mode-locked regime. MIT 850 nm SESAM/SBR with bulk absorber and one layer of HR coating was used in mode-locking experiments (MIT-850-bulk-HR). Again, the laser cavity is very similar to what was already described above. As a minor difference this time the laser is pumped by four 640 nm diodes (HL6385DG) rather than four 660 nm diodes (HL6545MG), and the total incident pump power on the crystal is about 800 mW (see Appendix B for more details). The estimated total cavity dispersion was

around ~ -900 fs^2. The central wavelength of the laser could be tuned continuously from ~828 nm to ~873 nm (~45 nm tuning), by just rotating the birefringent filter element (Figs. 4.29-4.31). On average the Cr:LiSAF laser generated ~188 fs pulses with ~170 mW of average power at a repetition rate of 91 MHz (~1.87 nJ pulse energy). Tuning range was limited by the SESAM/SBR bandwidth on the short wavelength side, and by the GaAs absorption edge on the long wavelength side.

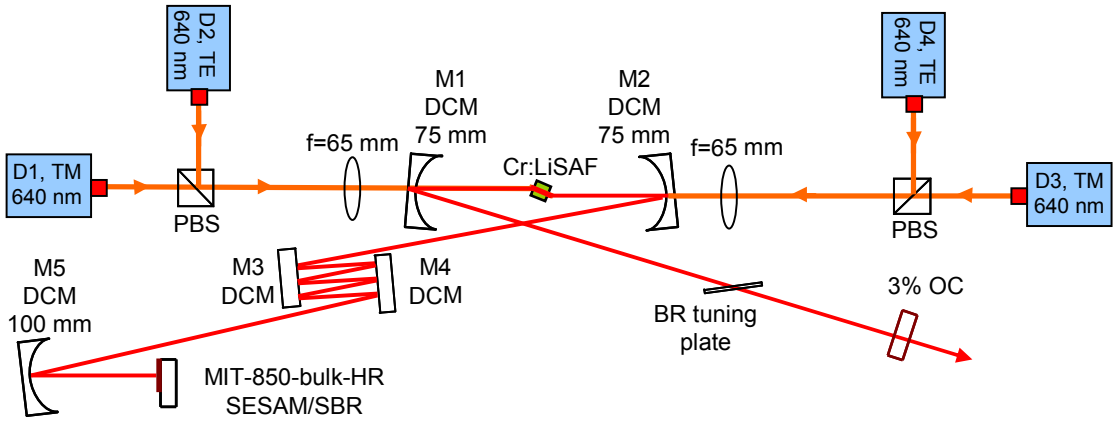

Figure 4.28: Schematic of the single-mode diode pumped Cr:LiSAF laser that was used in mode-locked tuning experiments. MIT-850-bulk-HR SESAM/SBR is used for mode-locking. Estimated total cavity dispersion is ~ -900 fs^2. The total incident pump power on the crystal is about 800 mW.

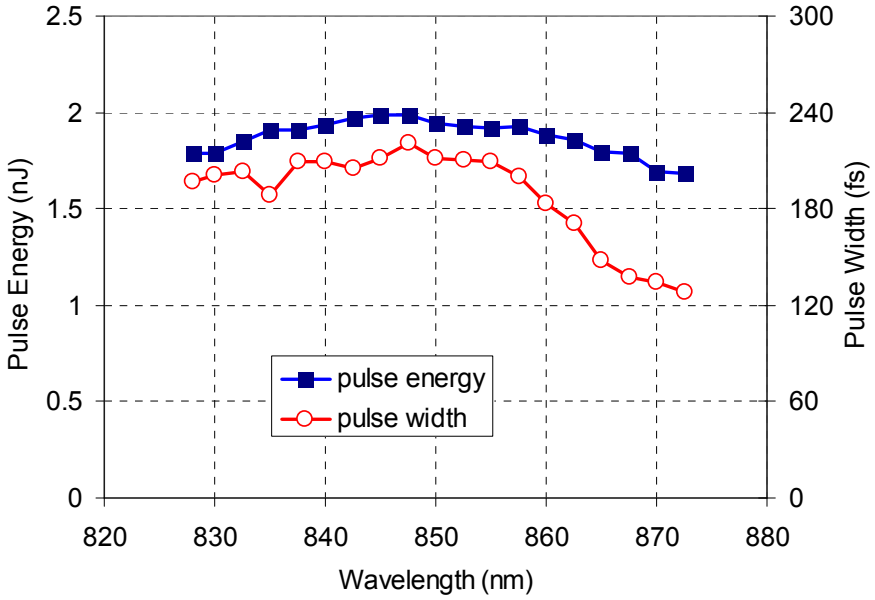

Figure 4.29: Summary of fs tuning with sub-200-fs pulses using MIT-850-bulk-HR SESAM/SBR. The graph shows the variation of laser pulsewidth and pulse energy as the laser central wavelength is tuned by the rotation of the intracavity birefringent filter element. The laser produced about ~190-fs pulses with ~1.87 nJ of pulse energy at a repetition rate of ~91 MHz. The average output power was ~170 mW, at an absorbed pump power of ~720 mW, with a 3% output coupler. The total tuning range is ~45 nm (828 nm to 873 nm).

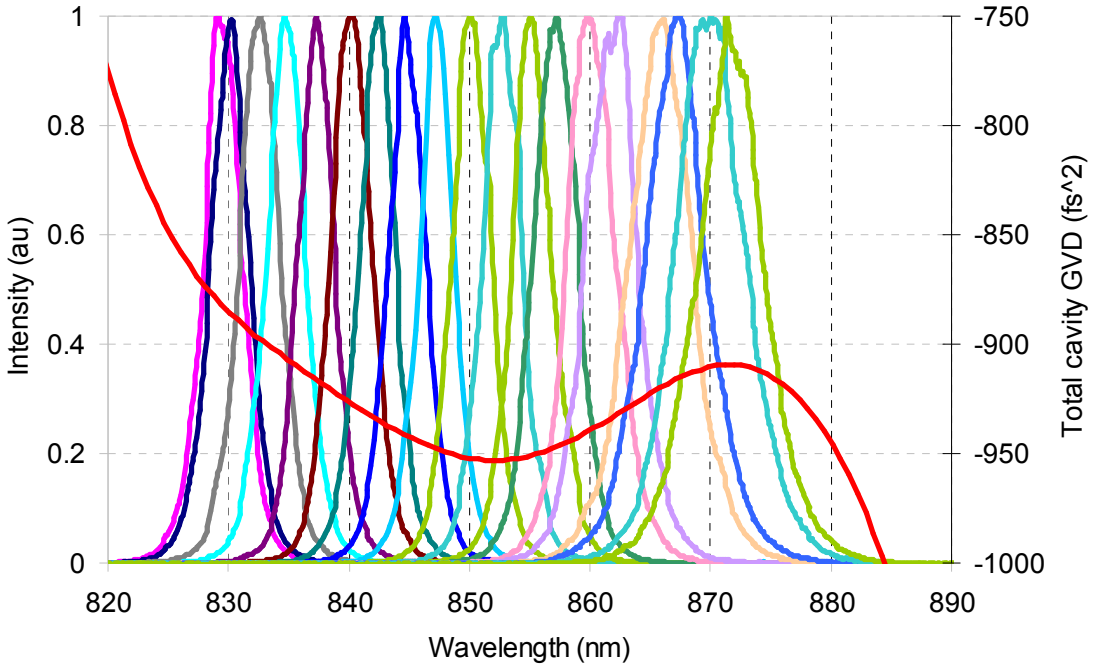

Fig. 4.30: Example spectra from the Cr^{3+}:LiSAF laser, showing tunability of central wavelength of the laser from 828 nm to 873 nm, for the ~sub-200-fs pulses. Estimated total cavity dispersion is also shown. The dispersion estimate includes 1 bounce on SESAM/SBR, 18 bounces on DCMs, ~3 m of intracavity air, 10 mm of Cr:LiSAF material and 7.3 mm of quartz substrate (from the birefringent tuning plate). The data is taken with the MIT-850-bulk-HR SESAM/SBR.

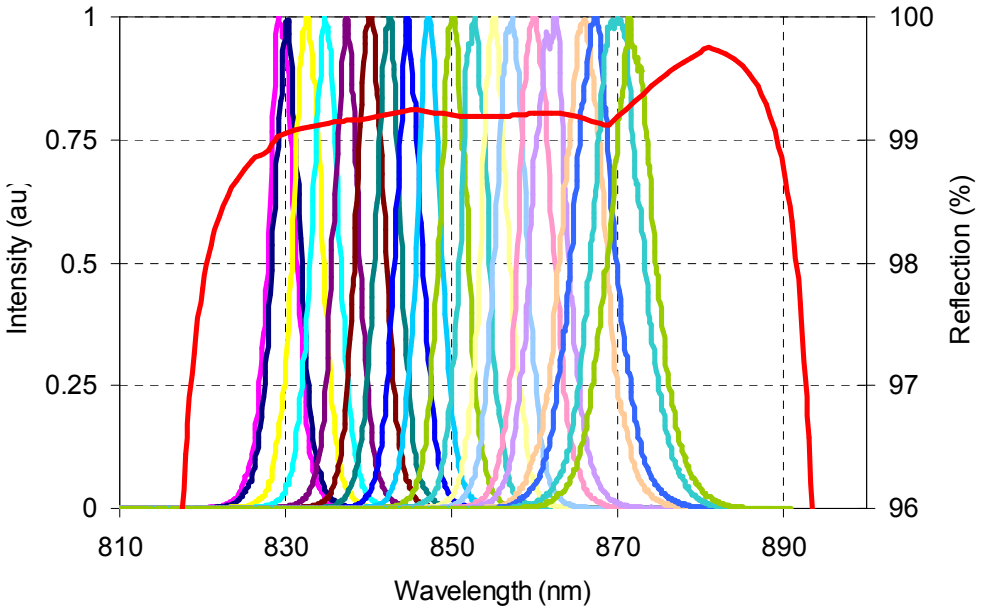

Figure 4.31: Example spectra from the Cr^{3+}:LiSAF laser, showing tunability of central wavelength of the laser from 828 nm to 873 nm, for the ~sub-200-fs pulses. The data is taken with the MIT-850-bulk-HR SESAM/SBR. Calculated small signal reflectivity of the SESAM/SBR is also shown.

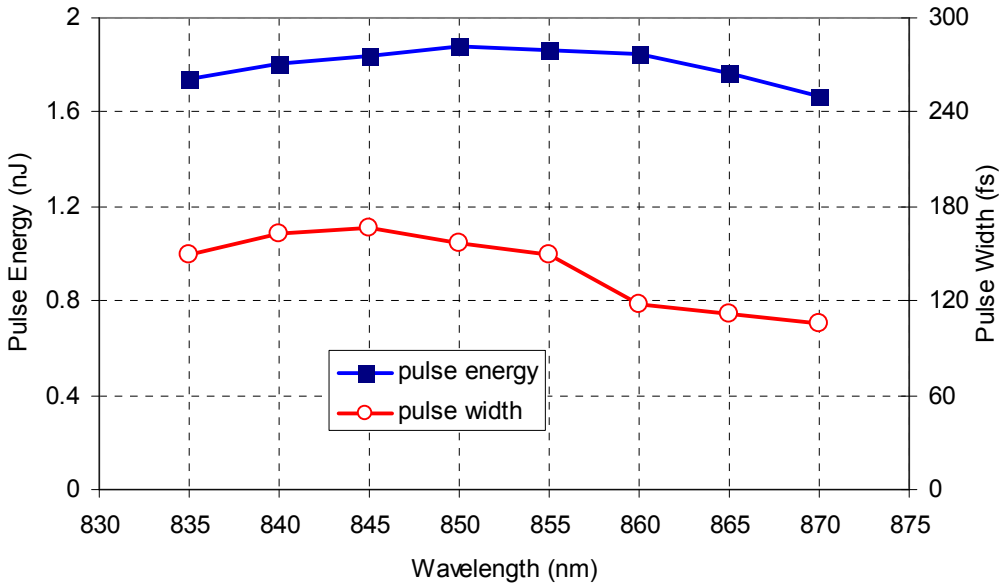

Figure 4.32: Summary of fs tuning with ~150-fs pulses using MIT-850-bulk-HR SESAM/SBR. The graph shows the variation of laser pulsewidth and pulse energy as the laser central wavelength is tuned by the rotation of the intracavity birefringent filter element. The laser produced about ~140-fs pulses with ~1.8 nJ of pulse energy at a repetition rate of ~110 MHz. The average output power was ~180 mW, at an absorbed pump power of ~720 mW, with a 3% output coupler. The total tuning range is ~35 nm (835 nm to 870 nm).

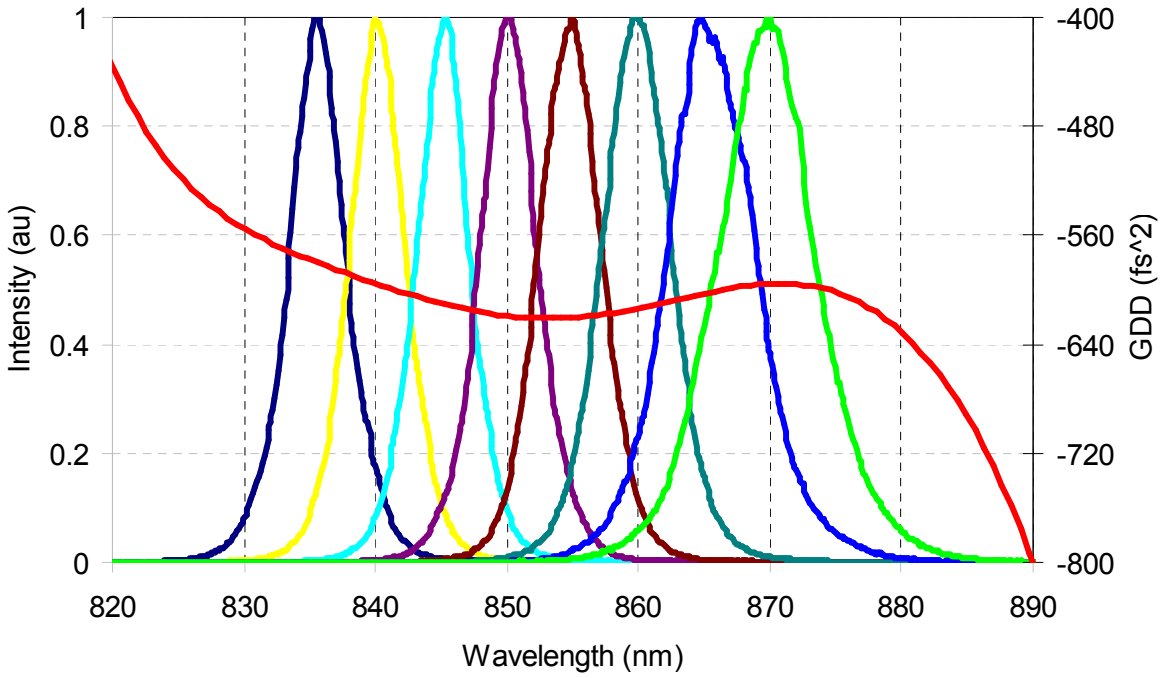

Fig. 4.33: Example spectra from the Cr^{3+}:LiSAF laser, showing tunability of central wavelength of the laser from 835 nm to 870 nm, for the ~150-fs pulses. Estimated total cavity dispersion is also shown. The dispersion estimate includes 1 bounce on SESAM/SBR, 14 bounces on DCMs, ~3 m of intracavity air, 10 mm of Cr:LiSAF material and 7.3 mm of quartz substrate (from the birefringent tuning plate). The data is taken with the MIT-850-bulk-HR SESAM/SBR.

To be able to obtain tuning with shorter pulses, we have decreased the number of bounces on DCM mirrors from 18 to 14. This decreased the total estimated cavity dispersion from ~ -900 fs^2 to -600 fs^2. At this dispersion level, we could obtain continuous tunability ~835 nm to ~870 nm (~35 nm tuning), by just rotating the birefringent filter element (Figs. 4.32-4.33). Compared to tuning with ~200-fs pulses, the tuning range get quite narrower especially on the short wavelength side, which is a result of narrower working range of the SESAM/SBR with shorter pulses. If we compare the fs tuning results obtained with the MIT-850-bulk and MIT-850-bulk-HR SESAMs/SBRs, we have seen that the additional HR coating enables a slightly broader tuning range.

4.7 Typical Mode-Locked Operation of Cr:LiSAF Laser around 800 nm

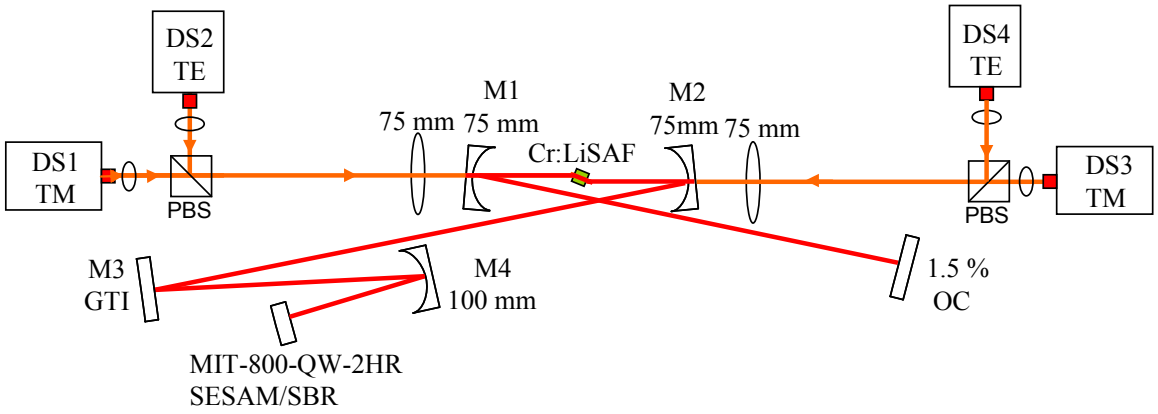

Figure 4.34: Schematic of the single-mode diode pumped Cr:LiSAF laser that was used in mode-locking experiments around 800 nm. MIT-800-QW-2HR SESAM/SBR is used for mode-locking. Estimated total cavity dispersion is ~ -900 fs^2. The total incident pump power on the crystal is about 600 mW.

In Chapter 2, we have seen that the cw tuning range of Cr:LiSAF extends from 775 nm to 1042 nm. So besides around 850 nm, Cr:LiSAF can generate pulses around 800 nm, 900 nm, and also potentially around 950 nm and 100 nm. In this section, we will start to present mode-locking results of Cr:LiSAF gain medium around 800 nm. Figure 4.34 shows schematic of a typical Cr:LiSAF laser mode-locked around 800 nm. To shift the central wavelength of the mode-locked spectrum around ~800 nm, we are using MIT 800 nm SESAM/SBR with quantum well absorber and two layers of HR coating. This SESAM/SBR has a modulation depth of around 0.6%, and also extensively used in mode-locking experiments with Cr:LiCAF (see Chapter 3 and Appendix E for more details). The laser used pump mirrors from Layertec Cr:Colquiriite pump mirror set I (M1, M2, and M4), which doesn't provide any dispersion compensation (GVD ~ 0 fs^2 around 800 nm, see Appendix A for more details). Dispersion compensation is provided by a GTI mirror from Layertec GTI mirror set I, which adds -550±50 fs^2 of

dispersion per bounce. We note here that, it is also possible to use MIT Cr:LiSAF pump mirrors in this experiment, here we are just giving a representative example.

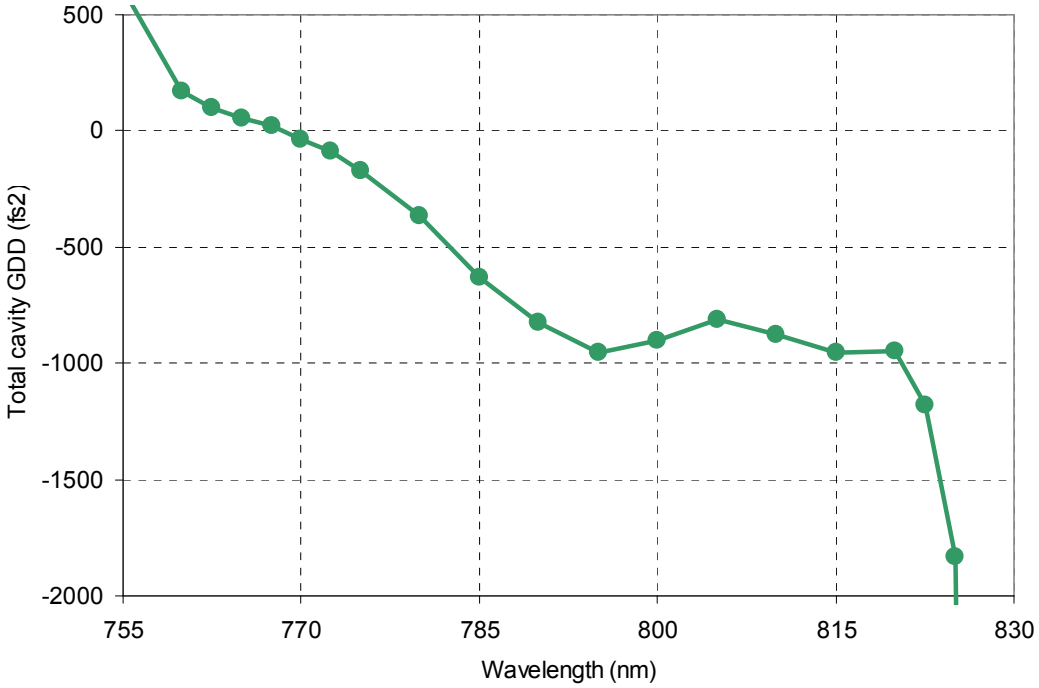

Figure 4.35: Estimated total cavity dispersion for the cavity that was shown in Fig. 4.34. The cavity dispersion estimate includes 2 bounces on GTI mirror, 10 mm of Cr:LiSAF, ~2.5 m of intracavity air, and one bounce on MIT-800-QW-2HR SESAM/SBR.

Figure 4.35 shows the estimated total cavity dispersion, which is around ~900 fs^2. Dispersion curve is not smooth due to the GVD oscillations of GTI mirror, and also due to the edge of reflectivity of the MIT-800-QW-2HR SESAM/SBR around ~825 nm. Figure 4.36 shows the measured efficiency curve of the laser. Note the relatively large mode-locking range of the laser, where we have obtained stable cw mode-locking for pump powers between ~250-550 mW. At the full pump power the laser generated ~85-fs pulses with 144 mW average power at a repetition rate of 123 MHz. The corresponding pulse energy and peak power were 1.17 nJ and 13.7 kW, respectively. Figure 4.37 shows the recorded optical spectrum for the ~85-fs pulses. The optical spectrum is centered around 812 nm, and had a FWHM of ~7.8 nm. The spike in the optical spectra around 845 nm is possibly generated by the GTI mirrors rapid GVD oscillations. In general, while we were using GTI mirrors in Cr:Colquiriite lasers, for pulsewidths below ~100-fs these kind of spikes in optical spectrum is quite common. Figure 4.38 shows the calculated Fourier transform limited pulse intensity for the optical spectrum, which has a FWHM of ~81.4-fs. The measured pulsewidth using the autocorrelator is ~85-fs (Fig. 4.39), which shows that the chirp in the

output pulses is quite low. Figure 4.40 shows the measured RF spectrum, where the main peak around 123.1377 MHz is >60-dB above the noise level.

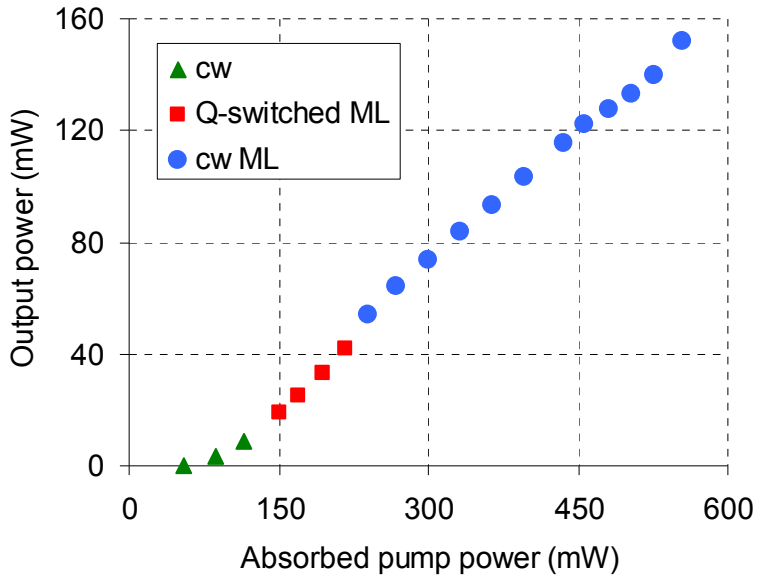

Figure 4.36: Efficiency curve for the single-mode diode pumped mode-locked Cr^{3+}:LiSAF laser taken while using MIT-800-QW-2HR SESAM/SBR for mode-locking.

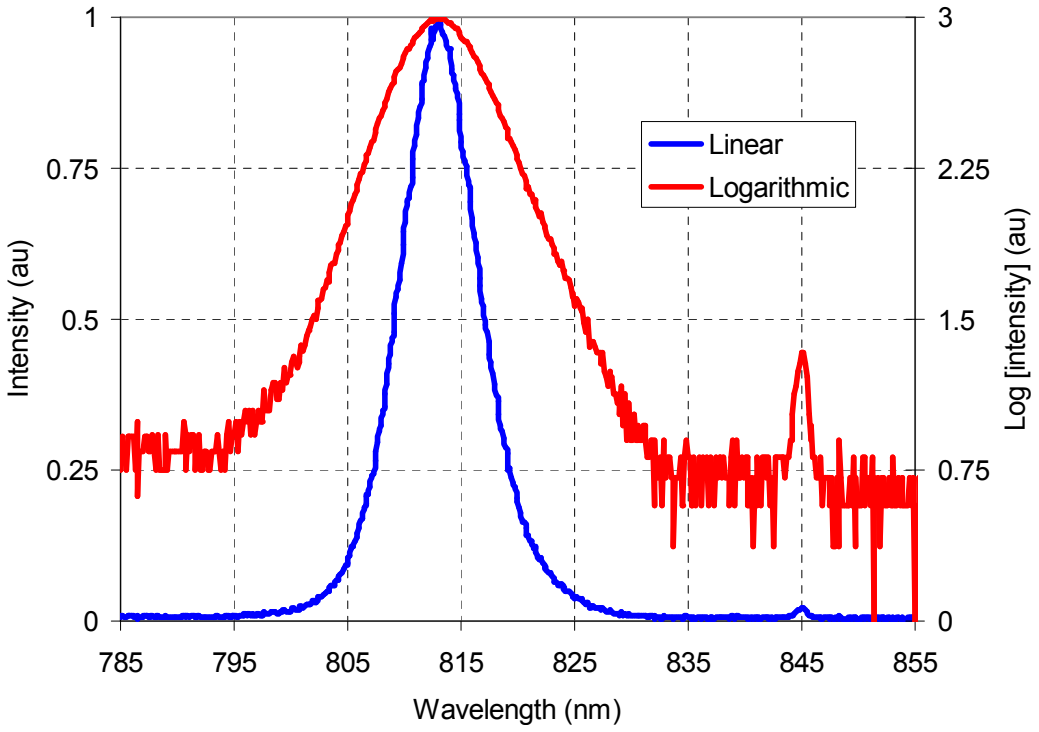

Figure 4.37: Optical spectrum for ~85-fs 1.17-nJ pulses in linear and logarithmic scales. MIT-800-QW-2HR SESAM/SBR was used for mode-locking. A GTI mirror is used for dispersion compensation.

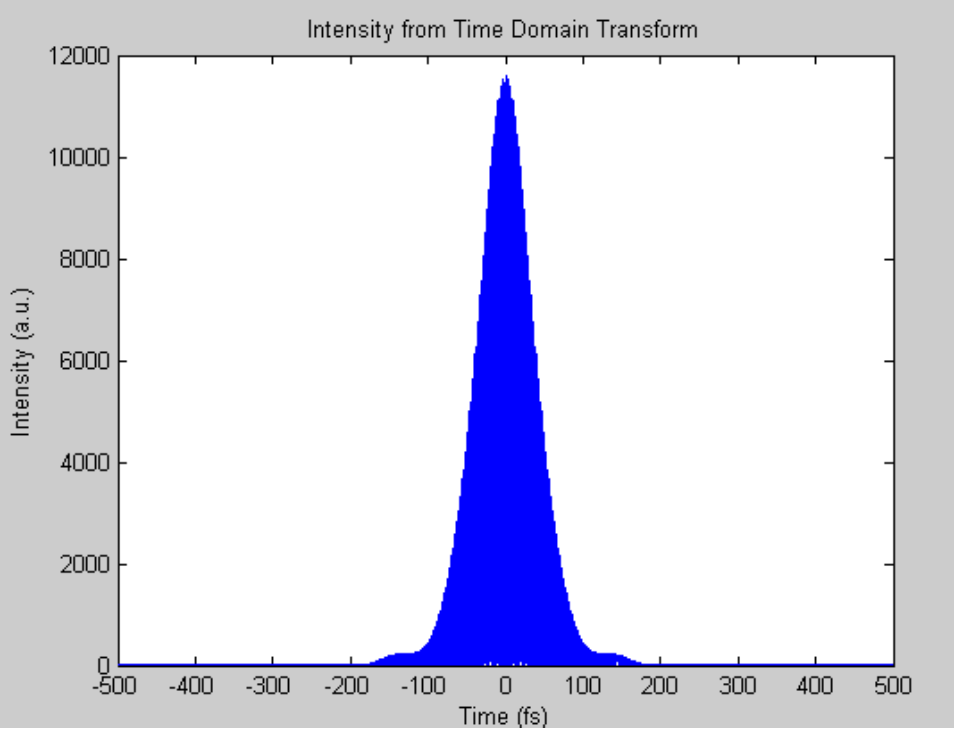

Figure 4.38: Fourier transform limited pulse intensity for the optical spectrum that is shown in Fig. 4.36. The FWHM of the pulse is 81.4 nm.

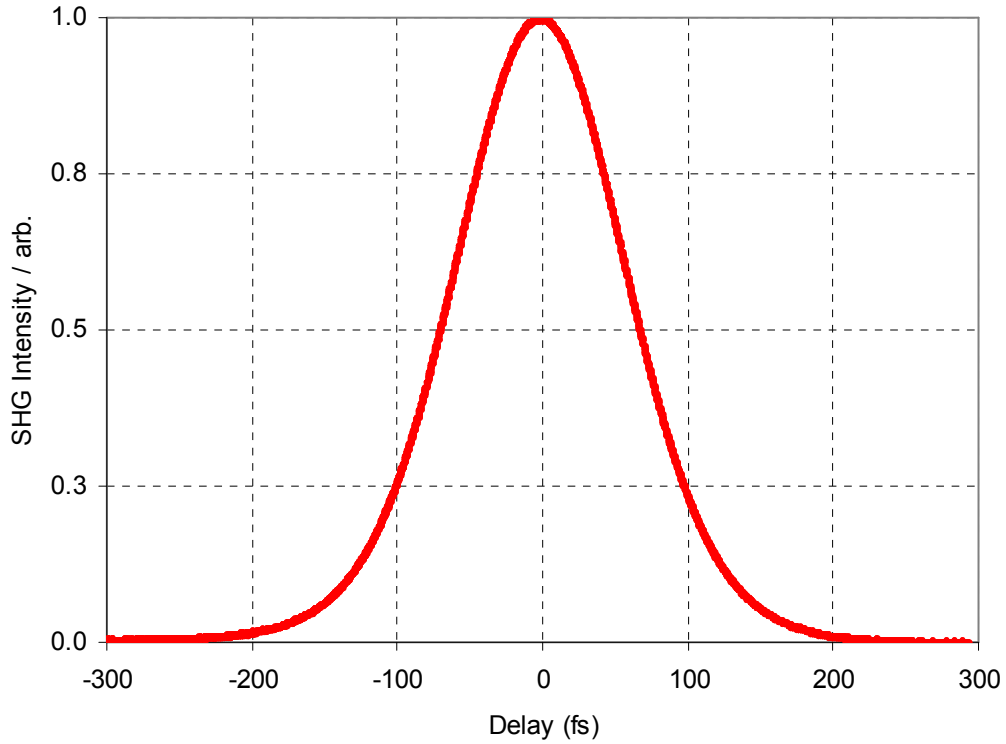

Figure 4.39: Measured autocorrelation trace for the ~85-fs 1.17-nJ pulses form the Cr:LiSAF laser. MIT-800-QW-2HR SESAM/SBR was used for mode-locking. A GTI mirror is used for dispersion compensation.

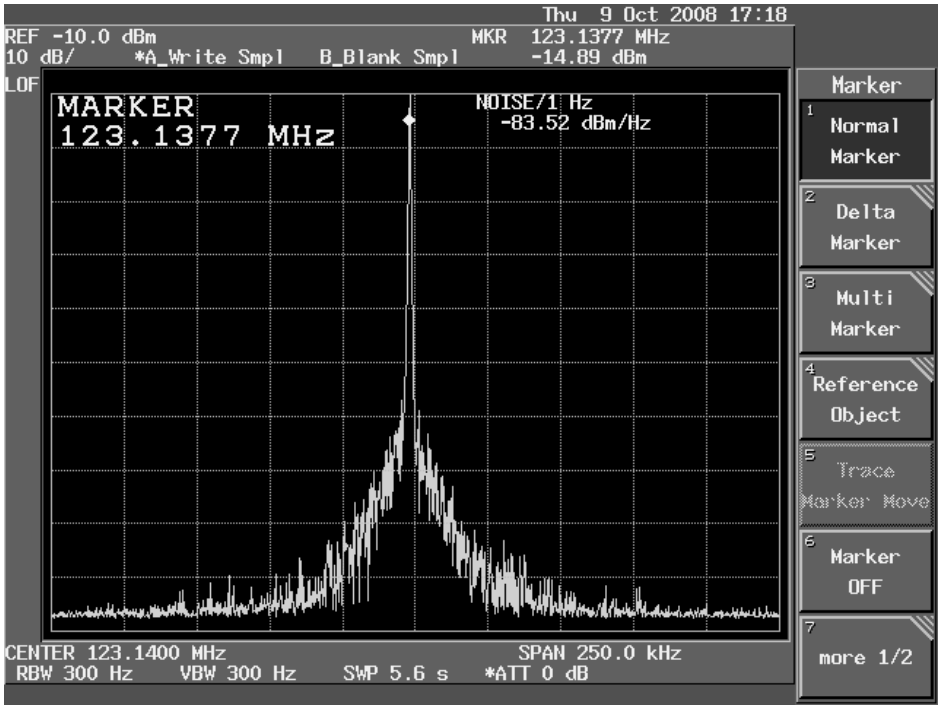

Figure 4.40: Measured microwave spectrum for the ~85-fs 1.17-nJ pulses form the Cr:LiSAF laser. MIT-800-QW-2HR SESAM/SBR was used for mode-locking. A GTI mirror is used for dispersion compensation. Repetition rate of the pulse train is 123.1377 MHz.

4.8 Sub-50-fs Pulses from Cr:LiSAF Laser around 800 nm

For demonstrating sub-50-fs pulse generation around ~800 nm with the Cr:LiSAF laser, we have used the laser cavity that was shown in Fig. 4.41. Dispersion compensation was performed by a fused silica prism pair, and M1-M3 is pump mirrors from Layertec Cr:Colquiriite pump mirror set I (Appendix A). By adjust the prism insertion, we could get pulses as short as ~41-fs form the Cr:LiSAF laser. Figure 4.42 shows optical spectrum and autocorrelation trace for the 41 fs, 1.43 nJ pulses. The data was taken with a 3% output coupler, at an absorbed pump power of ~530 mW. The separation between the FS prisms was ~40 cm, and a curved mirror with a 15 cm radius of curvature focused the beam on the SESAM/SBR. The 5-mm-long, 1.5% Cr-doped Cr:LiSAF crystal (GVD ~22.5 fs^2/mm) and intracavity air produced a total GVD of ~300 fs^2. The estimated total dispersion of the cavity with minimal prism insertion was ~ -250 fs^2. Tuning the dispersion by adjusting the prism material insertion, the laser produced pulses as short as 41-fs (assuming $sech^2$ pulses) with 121 mW average power and 18.6 nm bandwidth around a wavelength of 814 nm at 84 MHz (~1.43-nJ pulse energy). The estimated total cavity dispersion to produce the 41-fs pulse was ~ -50 fs^2. The time-bandwidth product was ~0.34, close to the transform limit of 0.315 for $sech^2$ pulses. Note that the spectrum has wings down to 780 nm, which is the cw tuning limit for Cr:LiSAF gain media.

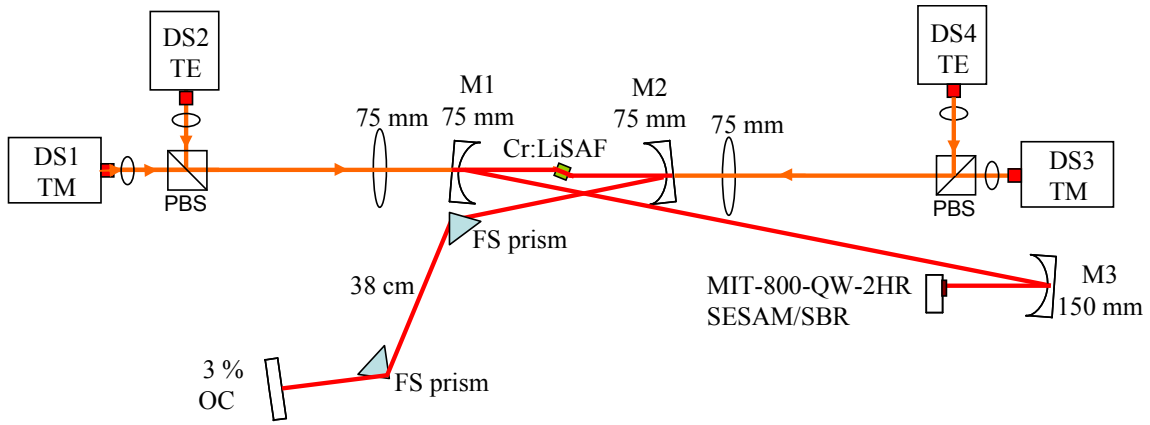

Figure 4.41: Schematic of the single-mode diode pumped Cr:LiSAF laser that was used in mode-locking experiments around 800 nm. MIT-800-QW-2HR SESAM/SBR is used for mode-locking. A fused silica prism pair is used for dispersion compensation. The total incident pump power on the crystal is about 600 mW.

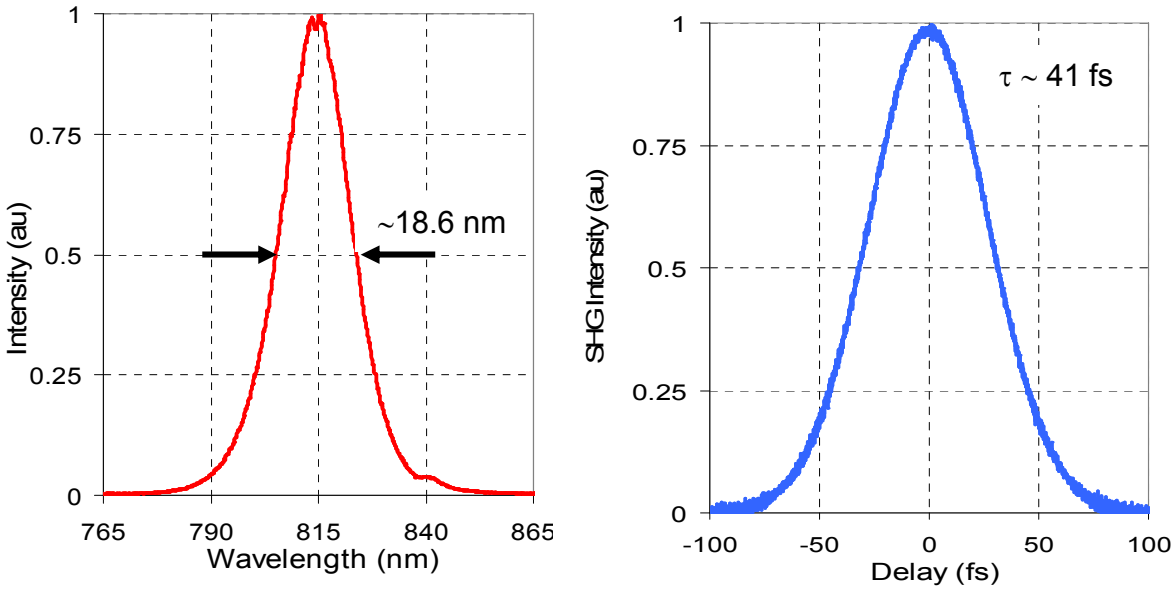

Figure 4.42: Spectrum and autocorrelation of the single-mode diode-pumped mode locked Cr^{3+}:LiSAF laser with a 3% output coupler at an absorbed pump of ~530 mW. A SBR/SESAM designed for 800 nm operation was used. The autocorrelation FWHM is 63 fs, corresponding to a 41-fs pulse duration (assuming $sech^2$ shape). The average output power is 121 mW, corresponding to a 1.43 nJ pulse energy at 84-MHz repetition rate. The spectrum bandwidth is 18.6 nm (FWHM) at ~814 nm. The measured time-bandwidth product is ~0.34.

4.9 Mode-locked Tuning of Cr:LiSAF Laser with MIT-800-QW-2HR SESAM/SBR

Figure 4.43 shows the schematic of the Cr:LiSAF laser that we have used in mode-locked tuning experiments around 800 nm. Four 640 nm diodes provided up to ~800 mW of pump power on the Cr:LiSAF crystal. Dispersion compensation is provided by use of DCM mirrors from the MIT Cr:LiSAF pump mirror ser, which provided ~ -80 fs^2 of dispersion per bounce (Appendix A). Similar to the tuning experiments described so far, a special BR filter is used to tune the central wavelength of the mode-locked

spectrum. Figure 4.4 shows the estimated cavity dispersion, where the total dispersion amount is about ~1000 fs^2. However, note that dispersion curve is not smooth. First of MIT Cr:LiSAF mirror set is designed in the wavelength range from ~795 nm to ~940 nm; hence, dispersion increase below ~795 nm is due to this mirror set. Also, above 825 nm, we have seen a sharp decrease in dispersion curve, which is dues to the reflectivity edge of MIT-800-QW-2HR SESAM/SBR. Of course this non-smooth GVD curve is not optimum for tuning experiments.

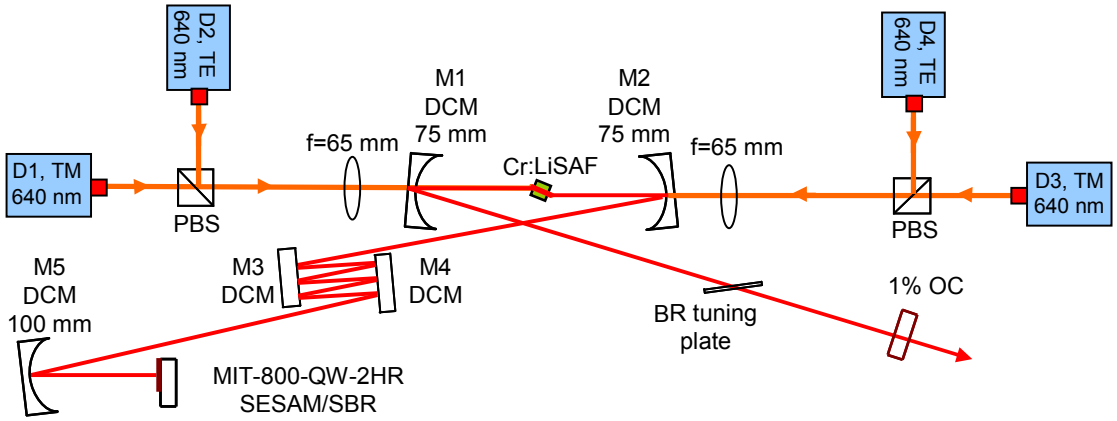

Figure 4.43: Schematic of the single-mode diode pumped Cr:LiSAF laser that was used in mode-locked tuning experiments around 800 nm. MIT-800-QW-2HR SESAM/SBR is used for mode-locking. Dispersion compensation is provided by use of DCM mirrors from MIT Cr:LiSAF pump mirror set. The total incident pump power on the crystal is about 800 mW.

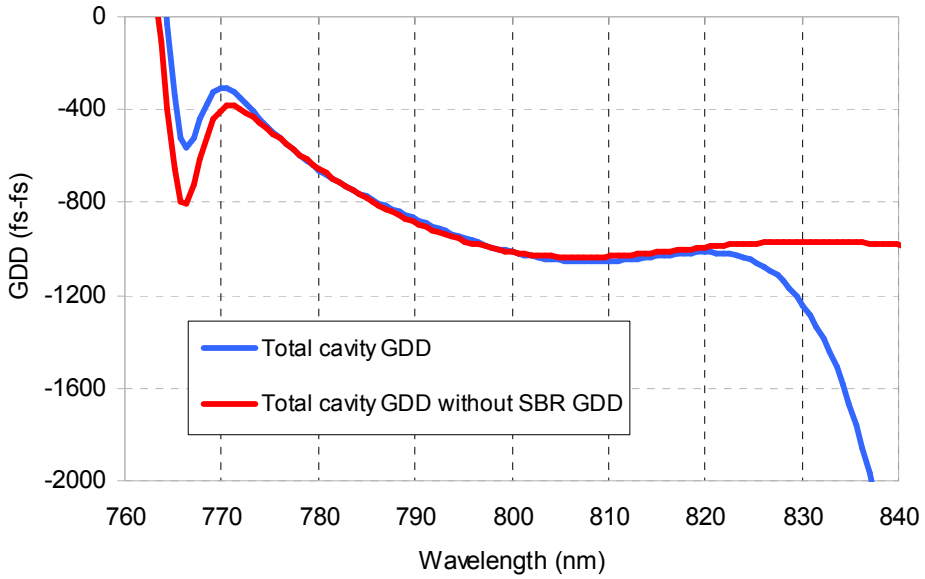

Figure 4.44: Estimated total cavity dispersion for the cavity that was shown in Fig. 4.43. The cavity dispersion estimate includes 18 bounces on DCMs, 10 mm of Cr:LiSAF, ~7.3 mm of fused silica from the BR plate, ~3.5 m of intracavity air, and one bounce on MIT-800-QW-2HR SESAM/SBR. We have also shown the total cavity dispersion without the bounce on MIT-800-QW-2HR SESAM/SBR.

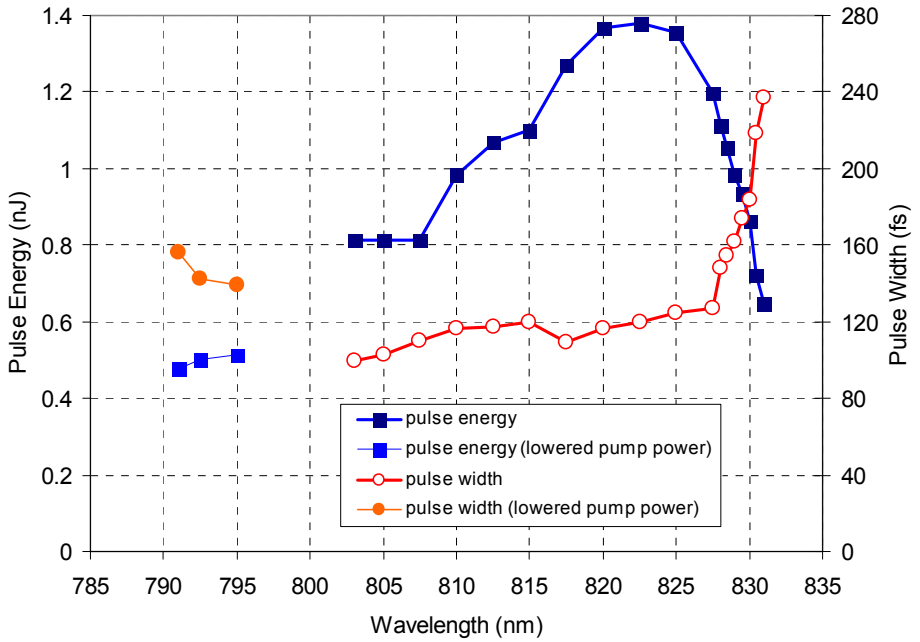

Figure 4.45: Summary of fs tuning experiments of Cr:LiSAF laser around 800 nm, with ~140-fs pulses using MIT-800-QW-2HR SESAM/SBR. The graph shows the variation of laser pulsewidth and pulse energy as the laser central wavelength is tuned by the rotation of the intracavity birefringent filter element. The laser produced about ~140-fs pulses with ~1 nJ of pulse energy at a repetition rate of ~83 MHz. The average output power was ~90 mW, at an absorbed pump power of ~720 mW, with a 1% output coupler. The total tuning range is ~28 nm (803 nm to 831 nm). At a reduced pump power level, the laser also tuned from 791 nm to 795 nm.

Figure 4.45 summarizes the obtained tuning results. By just rotation of the BR plate, it was possible to continuously tune the mode-locked laser central wavelength from 803 nm to 831 nm. On average the Cr:LiSAF laser generated ~140 fs pulses with ~90 mW of average power at a repetition rate of 83 MHz (~1 nJ pulse energy). Tuning range was limited by the SESAM/SBR reflectivity and dispersion bandwidth on the long wavelength side (Figs. 4.46 and 4.47). We can see this by the decrease in average output power as we tune the laser above 825 nm, which is due to the increased amount of loss from the SESAM/SBR. Above 825 nm, decreased output power and increased cavity dispersion level also caused an increase in the measured pulsewidths. We believe that below 803 nm tuning was limited by the increase in dispersion. Actually, by decreasing the pump powers a little, it was possible to obtain tuning in the 791 nm to 795 nm range. Also note that water absorption lines in this wavelength region was not strong enough to prevent our fs tuning experiments (Fig. 4.48). Cw tuning experiments of Cr:LiSAF that we described in Chapter 3 showed that, Cr:LiSAF can lase down to 775 nm in cw regime. Hence, with a proper DCM set, it might be possible to demonstrate a broader continuous mode-locked tuning range around 800 nm with Cr:LiSAF gain medium.

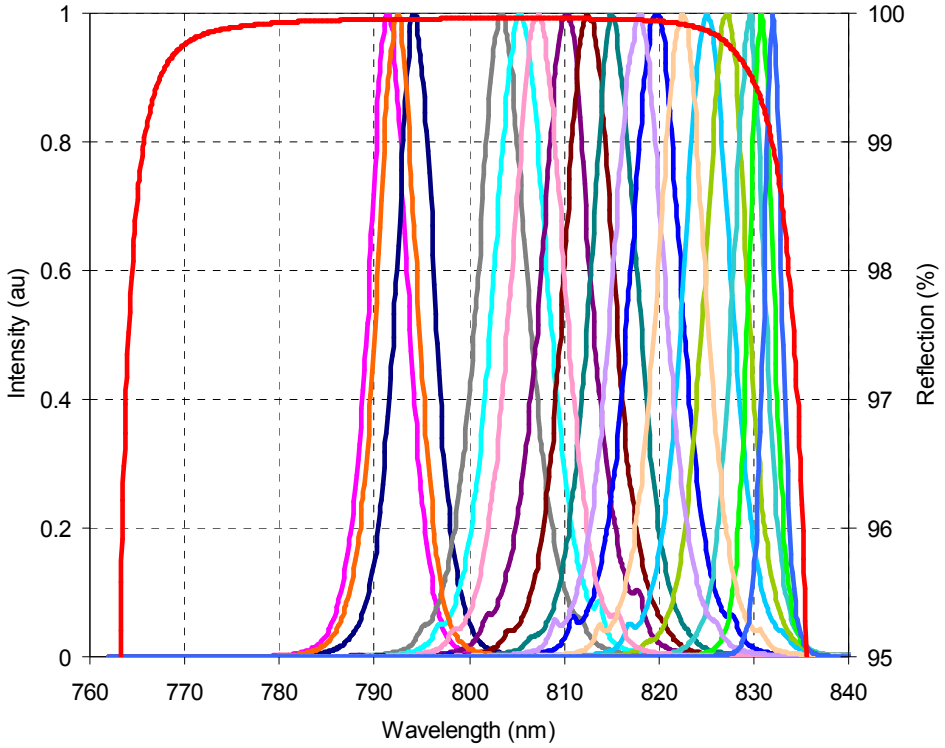

Figure 4.46: Example spectra from the Cr^{3+}:LiSAF laser, showing tunability of central wavelength of the laser from 803 nm to 831 nm, for the ~140-fs pulses (also tuned from 791 nm to 795 nm at a reduced pump power level). The data is taken with the MIT-800-QW-2HR SESAM/SBR. Calculated saturated reflectivity of the SESAM/SBR is also shown.

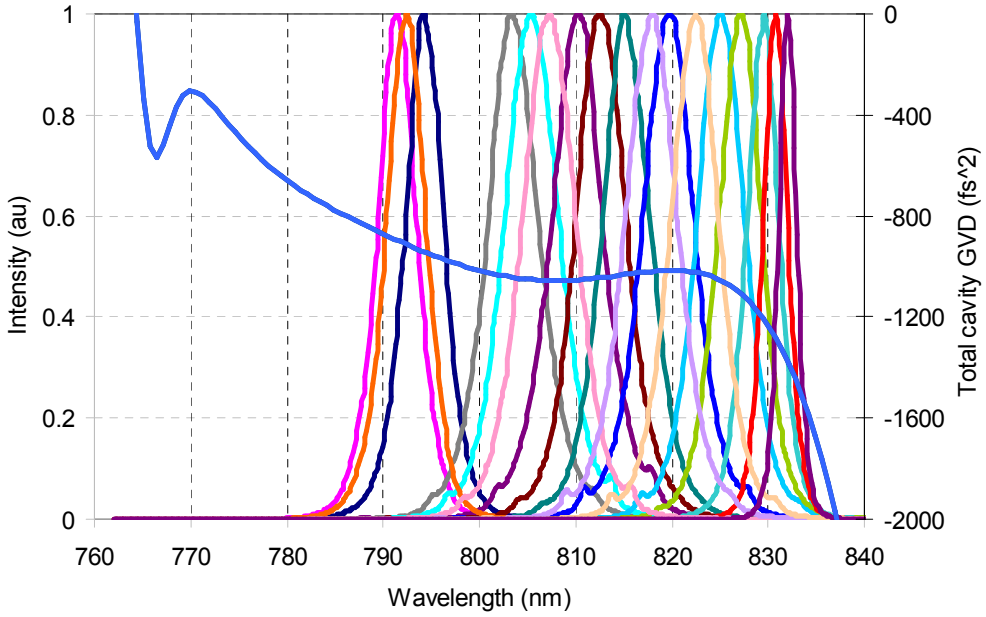

Figure 4.47: Example spectra from the Cr^{3+}:LiSAF laser in the demonstrated tuning rage is shown with the estimated total dispersion of the cavity. The central wavelength of the laser tuned continuously from 803 nm to 831 nm, for the ~140-fs pulses (also tuned from 791 nm to 795 nm at a reduced pump power level). The data is taken with the MIT-800-QW-2HR SESAM/SBR. Calculated saturated reflectivity of the SESAM/SBR is also shown.

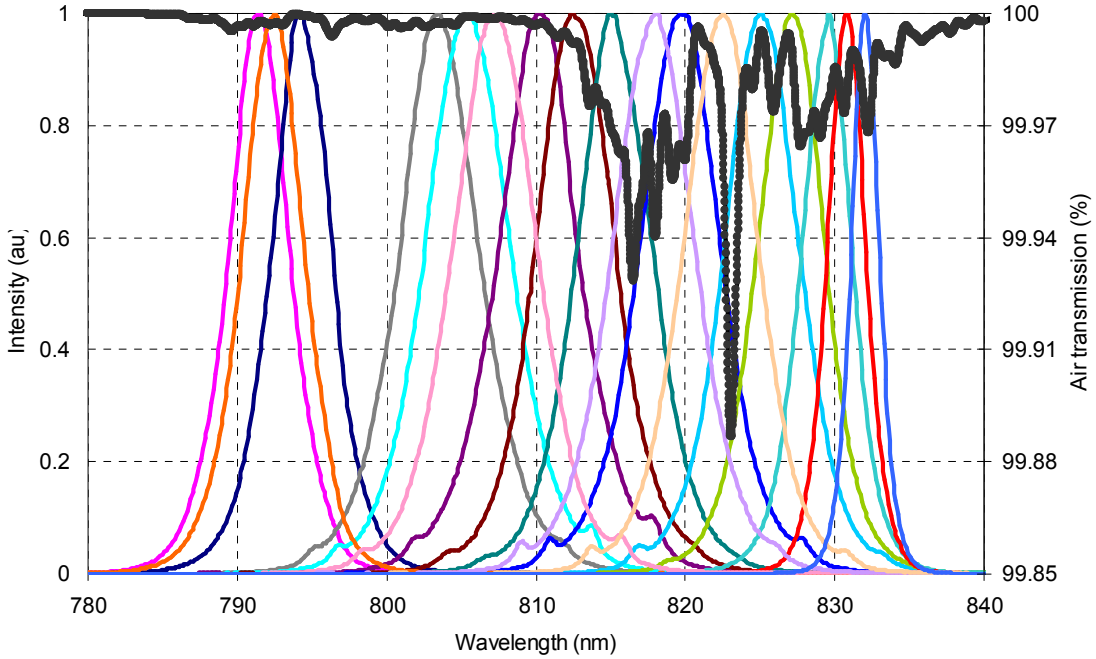

Figure 4.48: Calculated transmission of 3 m of air for a Gaussian pulse with a 0.5 nm FWHM is shown with the demonstrated tuning spectrum of the Cr:LiSAF laser around 800 nm. Water absorption lines did not prevent continuous tuning of the spectra in this region.

4.10 Typical Mode-Locked Operation of Cr:LiSAF Laser around 900 nm

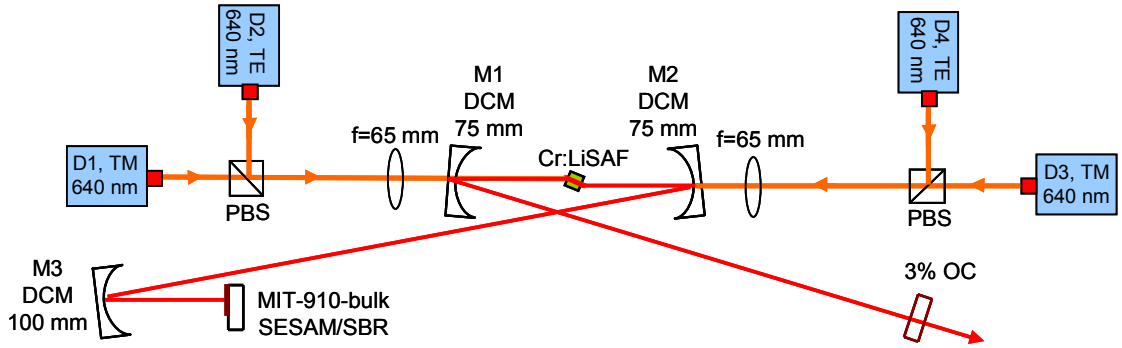

Figure 4.49: Schematic of the single-mode diode pumped Cr:LiSAF laser that was used in mode-locking experiments around 900 nm. MIT-910-bulk SESAM/SBR is used for mode-locking. Dispersion compensation is provided by use of DCM mirrors from MIT Cr:LiSAF pump mirror set. The total incident pump power on the crystal is about 700 mW.

Figure 4.49 shows schematic of a typical Cr:LiSAF laser mode-locked around 900 nm. To shift the central wavelength of the mode-locked spectrum around ~900 nm, we have used MIT 910 nm SESAM/SBR with bulk absorber. This SESAM/SBR has a modulation depth of around 1.5% (see Appendix E for more details). M1-M3 is DCM mirrors from Cr:LiSAF pump mirror set. Figure 4.50

shows the measured efficiency curve for the laser. Stable self-starting cw mode-locking could be obtained for pump absorbed powers above ~450 mW. At the full pump power the laser generated ~90-fs pulses with 205 mW of average power at a repetition rate of ~110 MHz (corresponding pulse energy ~1.86 nJ).

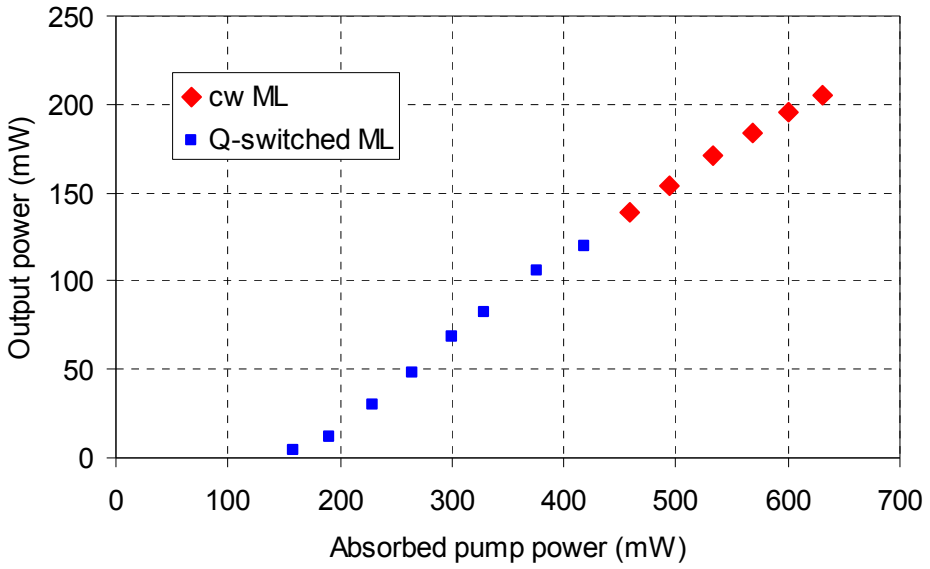

Figure 4.50: Measured efficiency curve for the single-mode diode pumped mode-locked Cr^{3+}:LiSAF laser taken while using MIT-910-bulk SESAM/SBR for mode-locking.

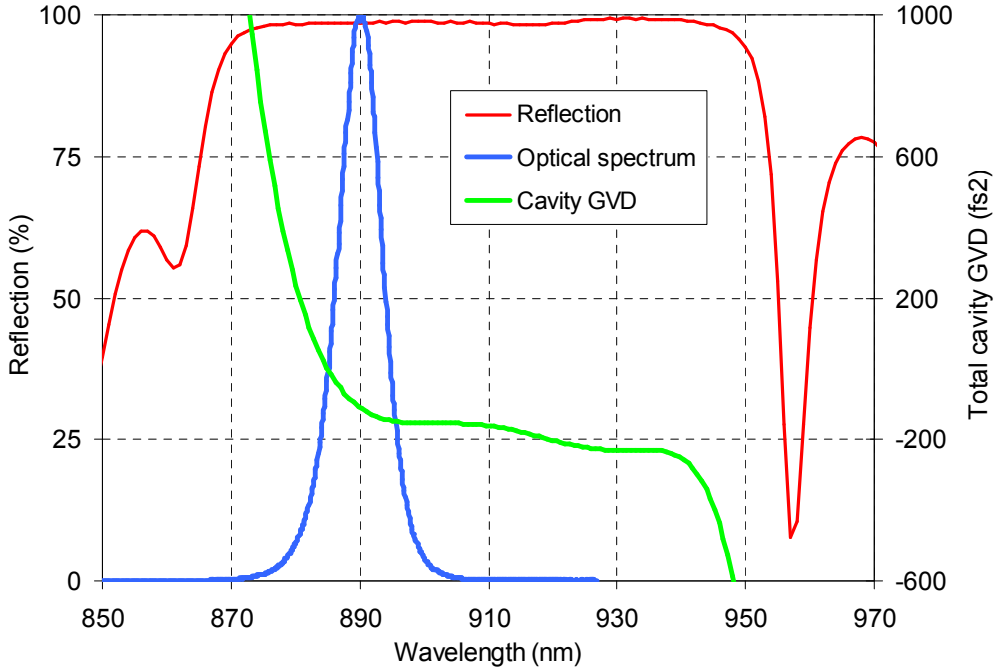

Figure 4.51: Measured optical spectra for the ~90-fs ~1.86 nJ pulses from the Cr:LiSAF laser mode-locked by MIT-910-bulk SESAM/SBR. Estimated total cavity dispersion and measured reflectivity of the SESAM/SBR is also shown.

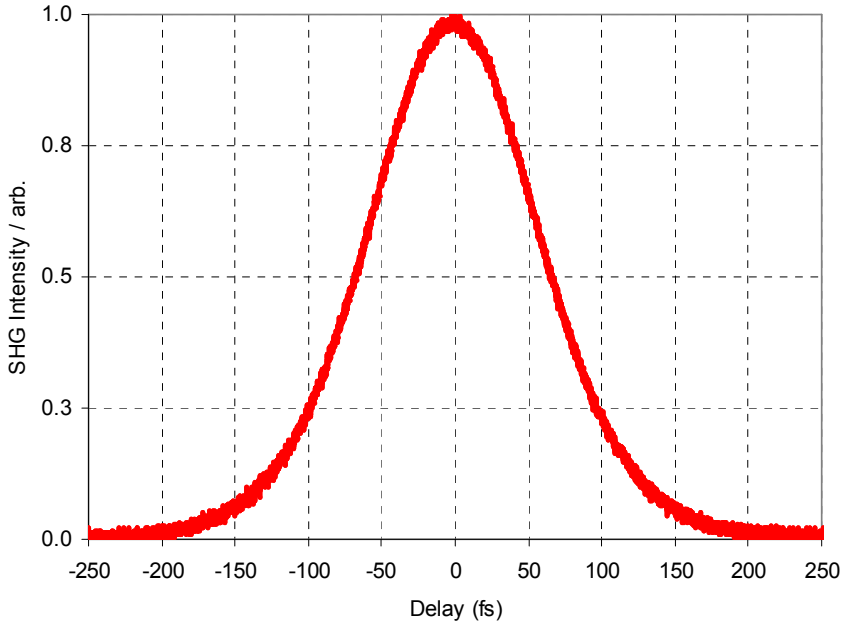

Figure 4.52: Measured background free autocorrelation trace for the ~90-fs ~1.86 nJ pulses from the Cr:LiSAF laser mode-locked by MIT-910-bulk SESAM/SBR.

4.11 Mode-locked Tuning of Cr:LiSAF Laser with MIT-910-bulk SESAM/SBR

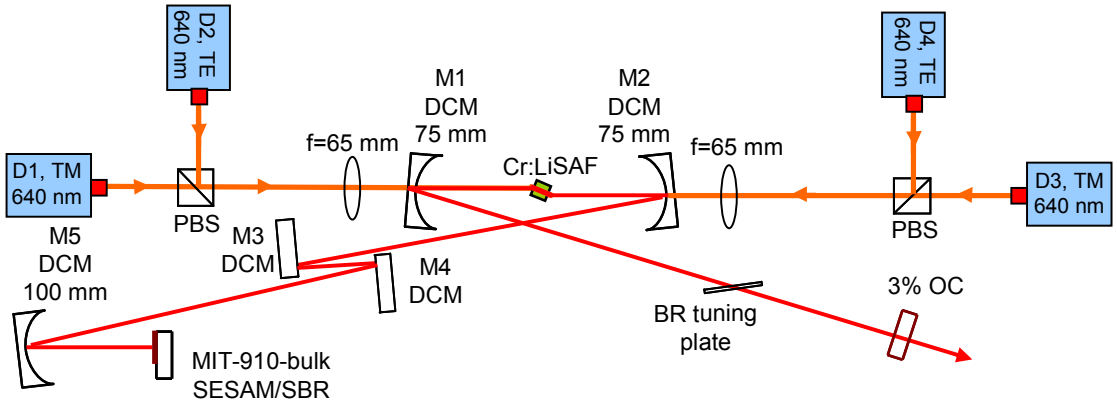

Figure 4.53: Schematic of the single-mode diode pumped Cr:LiSAF laser that was used in mode-locked tuning experiments around 900 nm. MIT-910-bulk SESAM/SBR is used for mode-locking. Dispersion compensation is provided by use of DCM mirrors from MIT Cr:LiSAF pump mirror set. The total incident pump power on the crystal is about 700 mW.

Figure 4.53 shows schematic of a typical mode-locked Cr:LiSAF laser that we have used to test tuning around 900 nm. Unfortunately, with the MIT-910-bulk SESAM/SBR we could not get broad continuous tuning ranges. When we just rotated the BR plate to tune the central wavelength of the mode-locked spectra in general tuning was obtained in just 5-10 nm range. Similarly, when we inserted a prism pair to fine tune the dispersion and obtain shorter pulses, the result was also unsuccessful. This we believe might

be caused by the dispersion from the water lines in air around these wavelengths. To prove that, one needs to purge the laser cavity and try tuning, however we didn't have time to investigate this.

Figure 4.54 shows all the spectra we get in tuning trials with MIT-910-bulk SESAM/SBR. We stress here that, we didn't get all the spectra in Fig. 4.54 from the same laser. To be able to cover all the range we have not only played with the BR plate, but we have also changed the SESAM/SBR position and/or cavity dispersion amount. The tuning range we get covers the region from 890 nm to 922 nm. The average output powers were above 100 mW (>1-nJ pulse energies), and the pulsewidths varied anywhere between 75fs to 300 fs. We believe that tuning below 890 nm is limited by the dispersion and reflectivity bandwidth of the SESAM/SBR, whereas tuning above 922 nm is limited by the absorption edge of the bulk absorber inside the SESAM/SBR. The measured signal reflectivity curve in Fig. 4.54 shows that, the absorption edge for this SSAM/SBR is around ~920 nm, which was a mistake we have made in designing the InGaAs bulk absorber for this SESAM/SBR. Also note that, the water absorption lines gets quite stronger above 930 nm, which might limit tuning by itself for un-purged laser cavities (Fig. 4.55).

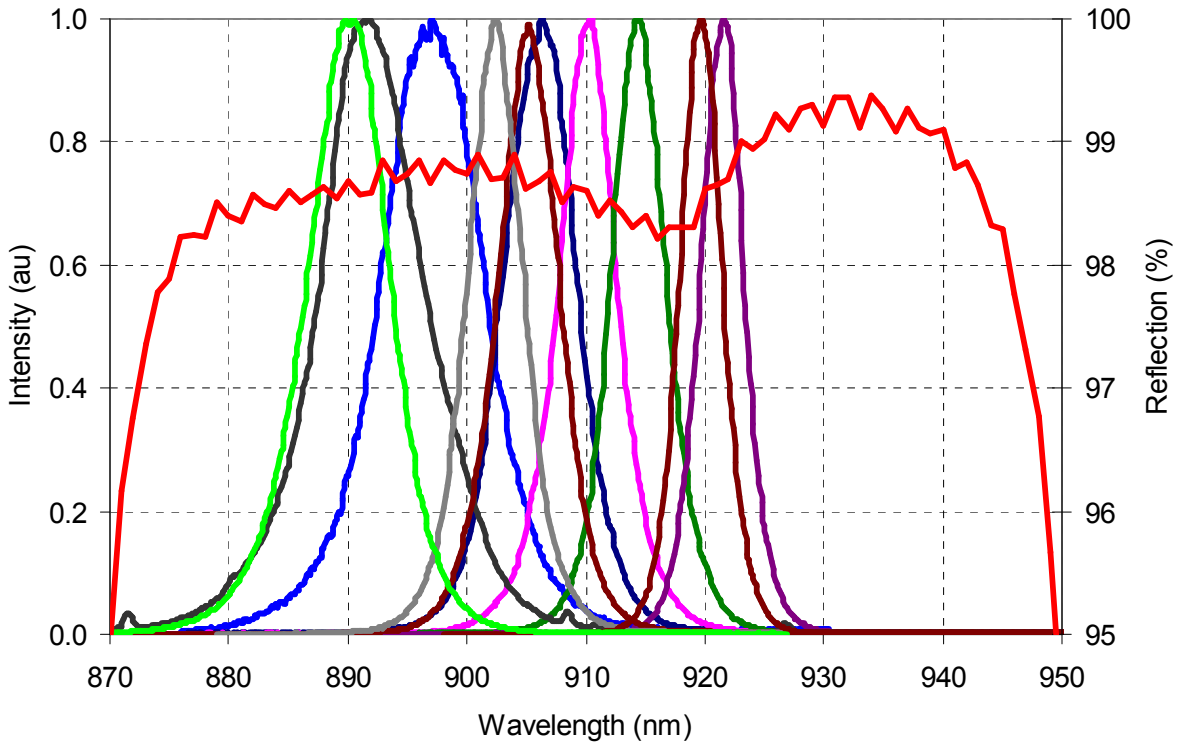

Figure 4.54: Example spectra from the Cr^{3+}:LiSAF laser, showing tunability of central wavelength of the laser from 890 nm to 922 nm. The data is taken with the MIT-910-bulk SESAM/SBR. Measured small signal reflectivity of the SESAM/SBR is also shown. The measured reflectivity data is kindly provided by Dr. Gale Petrich.

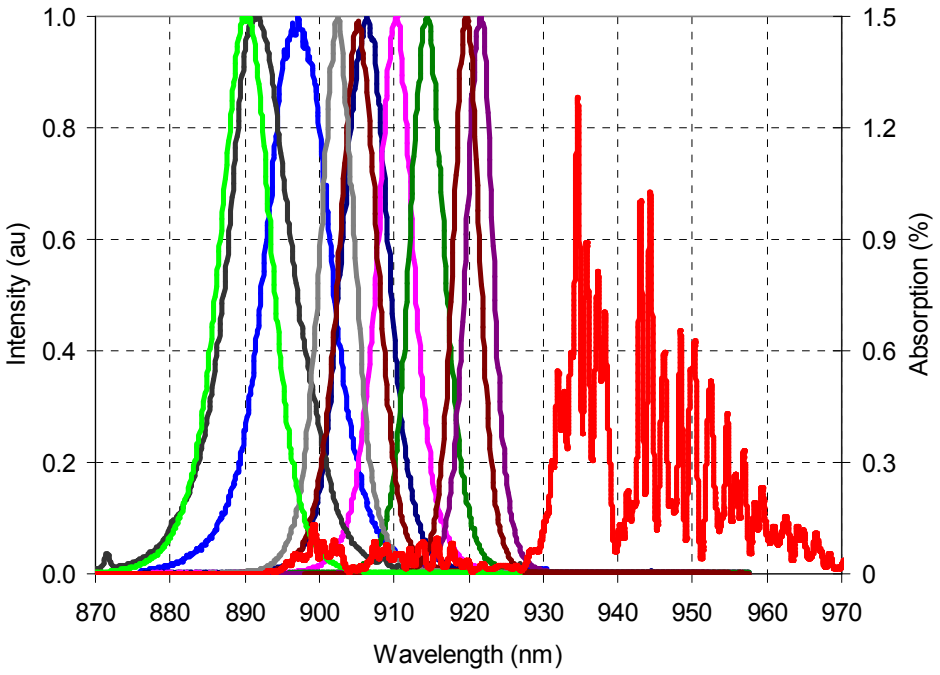

Figure 4.55: Obtained optical spectra in mode-locked tuning experiments with MIT-910-bulk SESAM/SBR is shown with the calculated nominal absorption of 3 m of air.

4.12 Mode-locked Tuning of Cr:LiSAF Laser with MIT-860-QW-Oxidized SESAM/SBR

Typically, in standard SESAMs/SBRs, absorbers are integrated onto AlGaAs/AlAs Bragg mirrors, and the low-index contrast (Δn~0.5-0.6) between the layers results in narrow bandwidth mirrors (~70 nm, R>%99.5). Due to this bandwidth limitation from the low-index contrast Bragg mirrors, tuning ranges from the SESAM/SBR mode-locked Cr:LiSAF lasers were restricted to about 50 nm as we have seen above. In this section, we will describe a low-cost, diode-pumped Cr:LiSAF laser with >100 nm of mode-locked tuning range. A broadband SESAM/SBR was used to initiate and sustain mode-locking (MIT-860-QW-Oxidized, see Appendix E for more details). Dispersion-compensating mirrors (DCM) optimized for the Cr:LiSAF gain media enable a relatively smooth group velocity dispersion (GVD) over the whole tuning range. A specially-designed birefringent (BR) plate was used for tuning. By just rotating the BR plate, the central wavelength of the mode-locked pulses is tuned continuously from 800 nm to 905 nm (a 105 nm tuning range). The pulses are nearly transform-limited over the entire tuning range, with an average pulsewidth and average pulse energy of ~140 fs and ~1.6 nJ, respectively. To the best of our knowledge, this is the broadest tuning range reported for any SESAM/SBR mode-locked femtosecond solid state laser.

A schematic of the single-mode diode-pumped Cr:LiSAF laser that was used in femtosecond tuning experiments is shown in Fig. 4.56. The gain medium was pumped by four 640 nm and two 660 nm linearly-polarized, single-mode diodes (D1-D6) with circular outputs. A maximum pump power of ~150

mW and ~200 mW was available from the 640 nm and 660 nm diodes, respectively. The output of the diodes was first collimated by aspheric lenses and then combined using polarizing beam splitting (PBS) cubes and dichroic filters. Two 65-mm focal length lenses focused the pump beams in the Cr:LiSAF crystal. The 6-mm long Cr:LiSAF crystal has a Cr concentration of 1.5% and absorbed >99% and >77% (0.9 x 85%) of the incident TM- and TE-polarized pump at 640 and 660 nm respectively. An astigmatically-compensated, x-folded laser cavity, with 75 mm radius of curvature (roc) pump mirrors (M1-M2) was used in the laser experiments. The cavity was first optimized for CW operation, generating 400 mW of output power with 1W of incident pump power, using a 3% output coupler. Then, for initiating and sustaining mode-locked operation, the broadband SESAM/SBR was inserted into the cavity, at a second focus that was generated by M35 (ROC = 150 mm). For soliton pulse-shaping, dispersion compensation was employed with custom-designed DCMs with a GVD of ~ -80 fs^2 per bounce. The total cavity dispersion was estimated to be -750 fs^2. A specially-designed quartz birefringent plate was used to tune the central wavelength of the pulse spectrum.

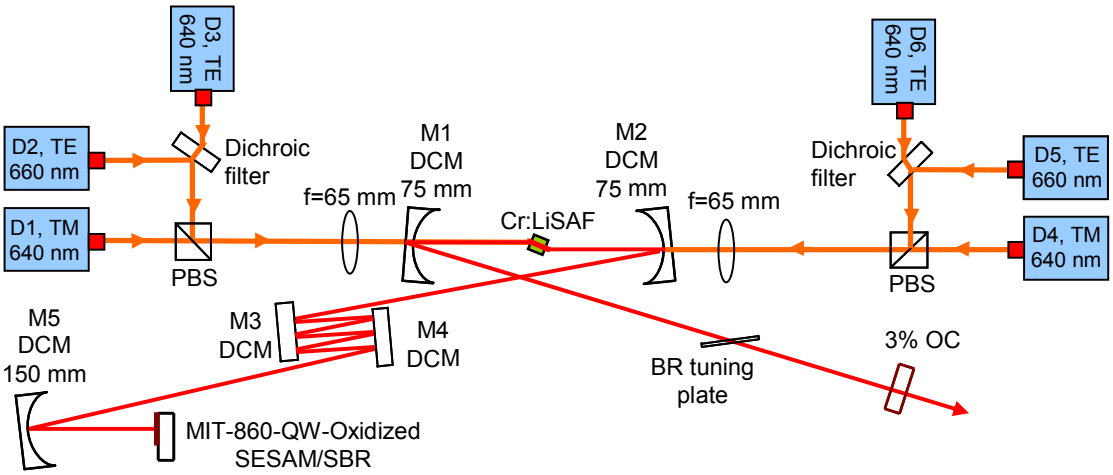

Figure 4.56: Schematic of the single-mode diode pumped Cr:LiSAF laser that was used in mode-locked tuning experiments with the broadband/oxidized SESAM/SBR (MIT-860-QW-Oxidized). Dispersion compensation is provided by use of DCM mirrors from MIT Cr:LiSAF pump mirror set. The total incident pump power on the crystal is about 1 W.

The broadband SESAM/SBR that was used in this study contained 7 pairs of $Al_{0.19}Ga_{0.81}As/Al_xO_y$ as the Bragg stack, and a 6 nm thick strained $In_{0.14}Ga_{0.86}As$ quantum well (sandwiched between $Al_{0.19}Ga_{0.81}As$ barriers) as the absorber section. The SESAM/SBR was originally grown by molecular beam epitaxy with AlAs layers and $Al_{0.19}Ga_{0.81}As$ layers as the Bragg mirror. Mesas having diameters of 500μm were etched and the AlAs was transformed into Al_xO_y by wet thermal oxidation [6]. Figure 4.57

shows a picture of the MIT-860-QW-Oxidized SESAM/SBR sample. The sample had about 500 mesas on it.

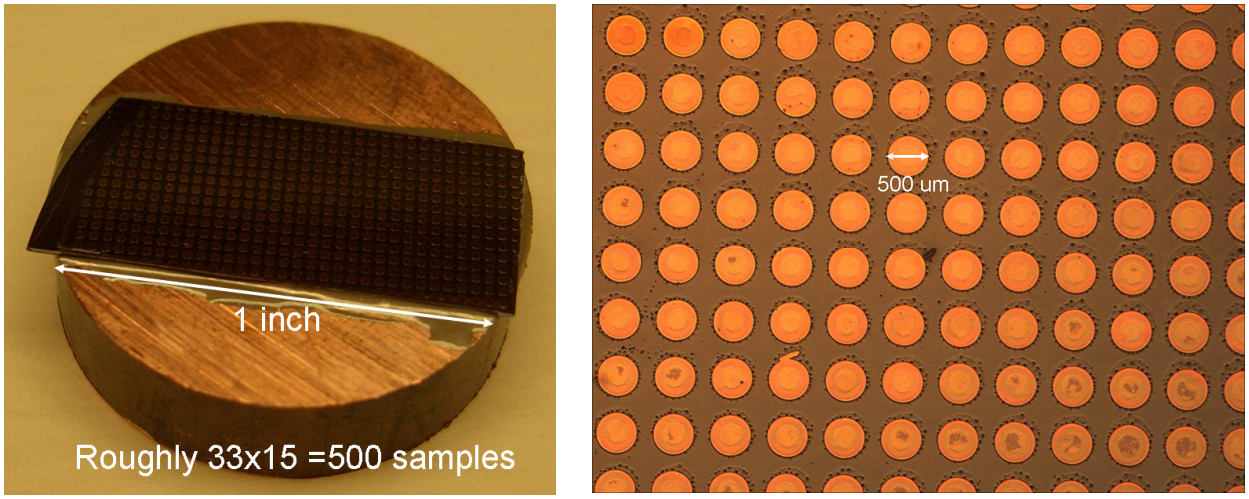

Figure 4.57: (Left) Picture of MIT-860-QW-Oxidized SESAM/SBR sample. (Right) Microscopy images of the sample, showing small 500 μm mesas. The sample had about ~500 mesas to use in mode-locking trials.

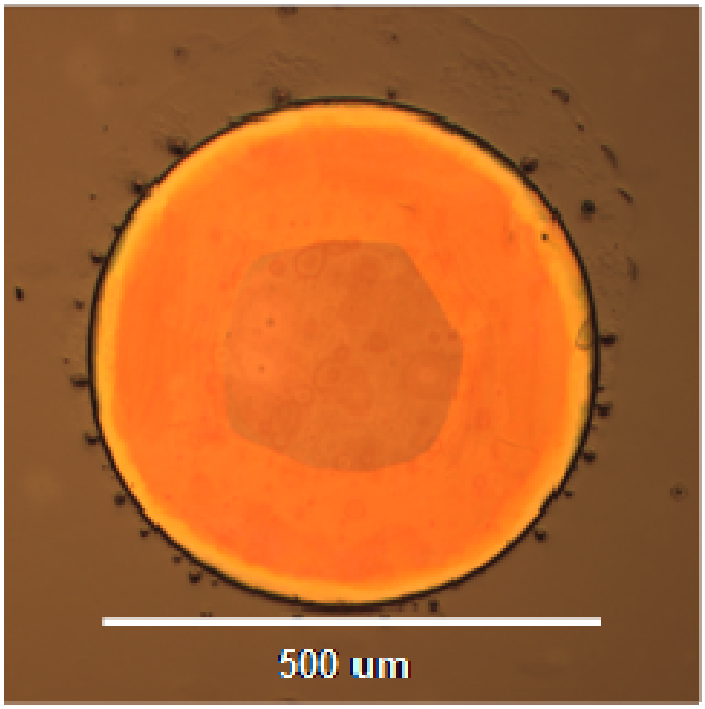

Figure 4.58: Picture of a typical mesa on MIT-860-QW-Oxidized sample. The center regions of the mesa were not fully oxidized.

Figure 4.57 also shows a microscopy image of the sample. Each mesa had a size of 500 μm; however, center regions of the mesas were not fully oxidized (Fig. 4.58). However, for a typical beam waist of ~30 μm on the SESAM/SBR, even the non-perfectly oxidized sample was usable in the laser. We are currently in the process of optimizing the oxidization process, where we hope to obtain fully oxidized

mesas. The use of low-index Al_xO_y material (n~1.6), in place of AlAs (n~3), in the Bragg mirror stack increased the index contrast from ~0.5 to ~1.9, and enabled a reflectivity bandwidth of ~300 nm centered at 850 nm [249]. Two considerations were included in the absorber design to enable broadband tuning. First, the position of the quantum well inside the standing wave electric field pattern was chosen to obtain a constant linear saturable absorption. Secondly, the quantum well thickness was chosen to remove any discontinuities in the density of states in the SESAMs/SBRs tuning range. Also, operating in the soliton regime relaxed the dependence on SESAM/SBR recovery time [250]. We refer the reader to Appendix E for more information in this oxidized SESAM/SBR (MIT-860-QW-Oxidized).

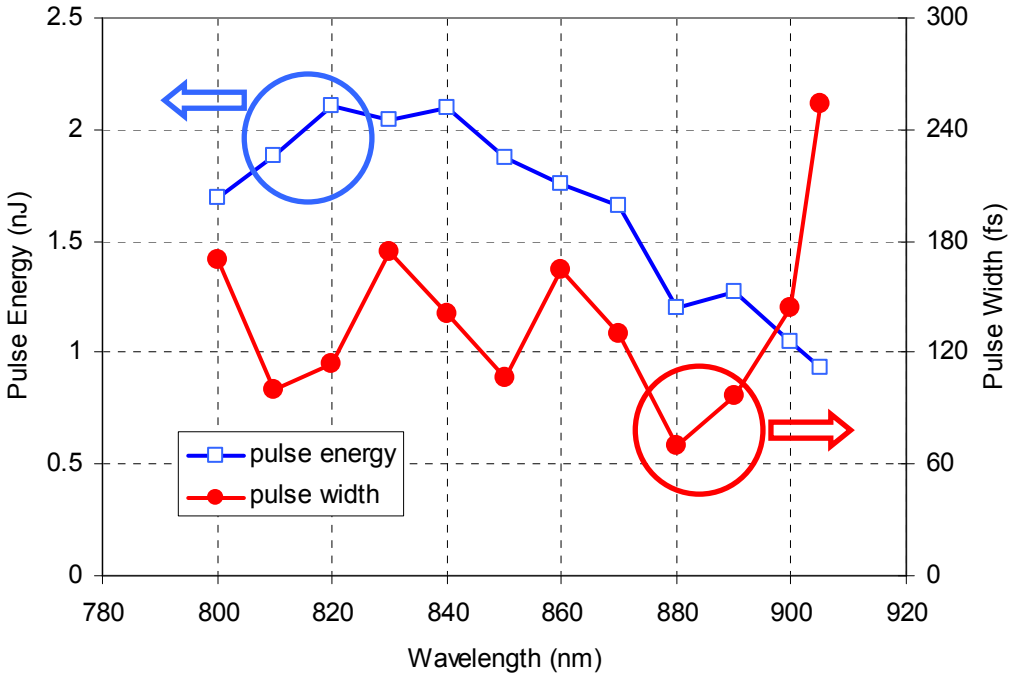

Figure 4.59: Summary of fs tuning experiments of Cr:LiSAF laser using MIT-860-QW-Oxidized SESAM/SBR. The graph shows the variation of laser pulsewidth and pulse energy as the laser central wavelength is tuned by the rotation of the intracavity birefringent filter element. The laser produced about ~140-fs pulses with ~1.6 nJ of pulse energy at a repetition rate of ~85 MHz. The average output power was ~140 mW, at an absorbed pump power of ~900 mW, with a 3% output coupler. The total tuning range is ~105 nm (800 nm to 905 nm).

Figure 4.59 summarizes the femtosecond tuning results. Mode-locking was self-starting and robust against environmental fluctuations. Continuous tuning from 800 nm to 905 nm was achieved by just adjusting the angle of the BR tuning plate. Figure 4.59 shows the measured pulsewidth and pulse energy within the tuning range. The average pulse duration and pulse energies were ~140 fs and ~1.6 nJ, respectively. The repetition rate of the laser was 85.5 MHz, and the measured RF signal peak was >70 dB above the background noise level. We note here that, the obtained average powers is lower compared to a regular SESAM/SBR mode-locked Cr:LiSAF laser [4]. At this pump power, using a regular SESAM/SBR with a reflectivity bandwidth centered around 850 nm, we could able to obtain ~250 mW average powers

from Cr:LiSAF laser (~100-fs, 2.5 nJ pulses at 100 MHz). The difference in performance is attributed to the higher passive losses of the broadband SESAM/SBR, which might be lowered by improving the oxidization process. Figure 4.60 shows a typical efficiency curve of the mode-locked Cr:LiSAF laser taken with the broadband SESAM/SBR. There is some noticeable increase in laser threshold and some noticeable decrease in laser slope efficiency. However, the cw modelocked working range of the Cr:LiSAF is still quite wide, which actually enables this broadband tuning. We also note that, thermal effects are more significant in the broadband SESAM/SBR compared to the regular SESAM/SBR. This is somehow expected due to the lower thermal conductivity of the Al_xO_y, and higher passive losses of the structure. However, the oxidized SESAM/SBR can still be used in the laser, without any active cooling.

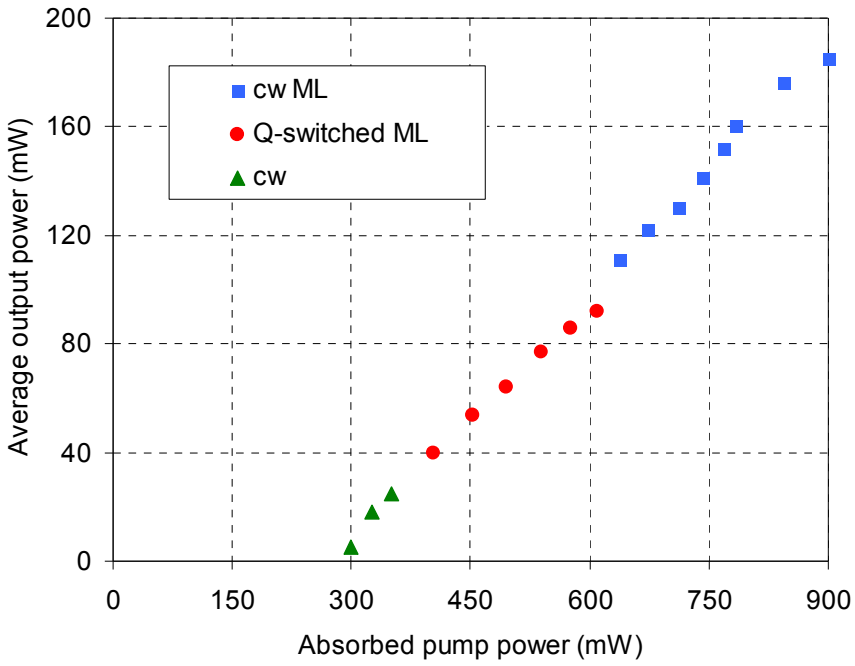

Figure 4.60: Typical laser efficiency curve of Cr:LiSAF laser with the oxidized broadband SESAM/SBR.

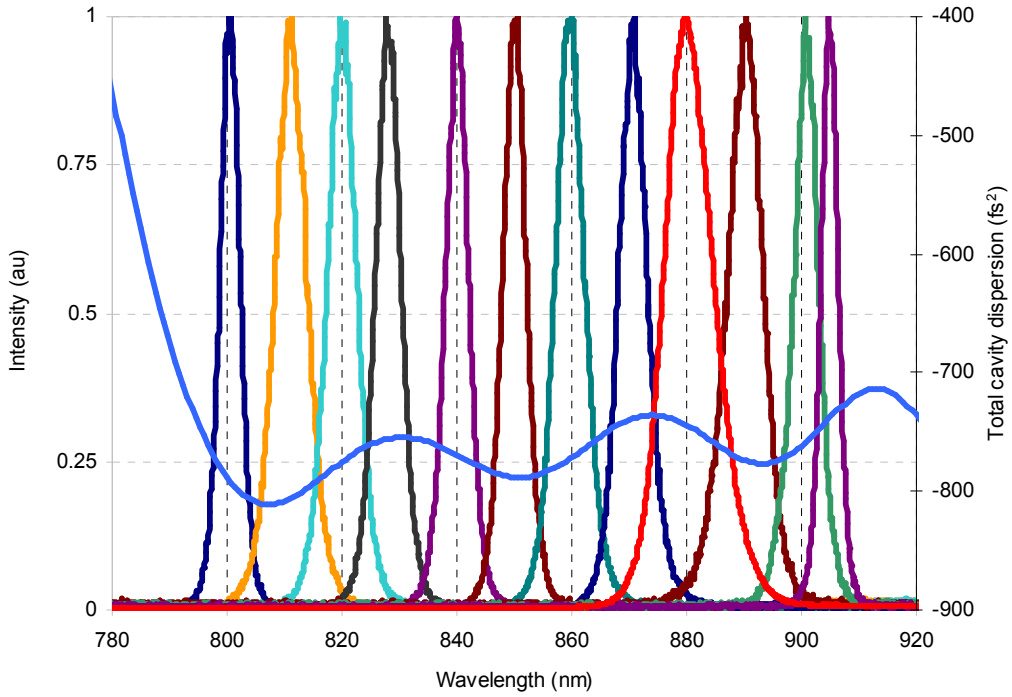

Figure 4.61: Estimated total cavity dispersion is shown with sample spectra from the demonstrated tuning range. The cavity dispersion estimate includes 18 bounces on DCMs, 10 mm of Cr:LiSAF, ~7.3 mm of fused silica from the BR plate, ~3.5 m of intracavity air, and one bounce on MIT-800-QW-Oxidized SESAM/SBR.

Figure 4.61 shows the estimated total cavity dispersion along with sample optical spectra along the demonstrated tuning range. The dispersion estimate included 12 mm of Cr:LiSAF material, ~7.3 mm of fused silica from the BR plate, ~3.5 m of intracavity air and 18 bounces on DCM mirrors. It was possible to obtain shorter pulses by decreasing the number of bounces on DCM mirrors (as short as ~30-fs); however, with shorter pulses we couldn't obtain continuous tuning. This is expected because for shorter pulses, two-photon absorption process starts earlier, which cause multiple pulsing instabilities. Hence, SESAM/SBR mode-locked lasers has narrower working range for shorter pulses, which makes tuning harder (small changes in output power, dispersion etc.. can push the laser into q-switching or multiple pulsing instabilities).

The laser tuning range was limited by the gain bandwidth of the Cr:LiSAF medium on the short wavelength side, and by the absorber band edge of the SEAM/SBR on the long wavelength side (~920 nm). One can potentially use an absorber with a band edge at longer wavelengths, which might enable tuning above ~900 nm region. However, gain of Cr:LiSAF is not flat and decreases above 900 nm, and there is strong water absorption lines in the 930-960 nm region. Also, putting the absorption edge at a longer wavelengths risks tunability at shorter wavelengths. Hence, in our initial SESAM/SBR design, we aimed to tune Cr:LiSAF in the 800-900 nm region and the results have shown that it is possible.

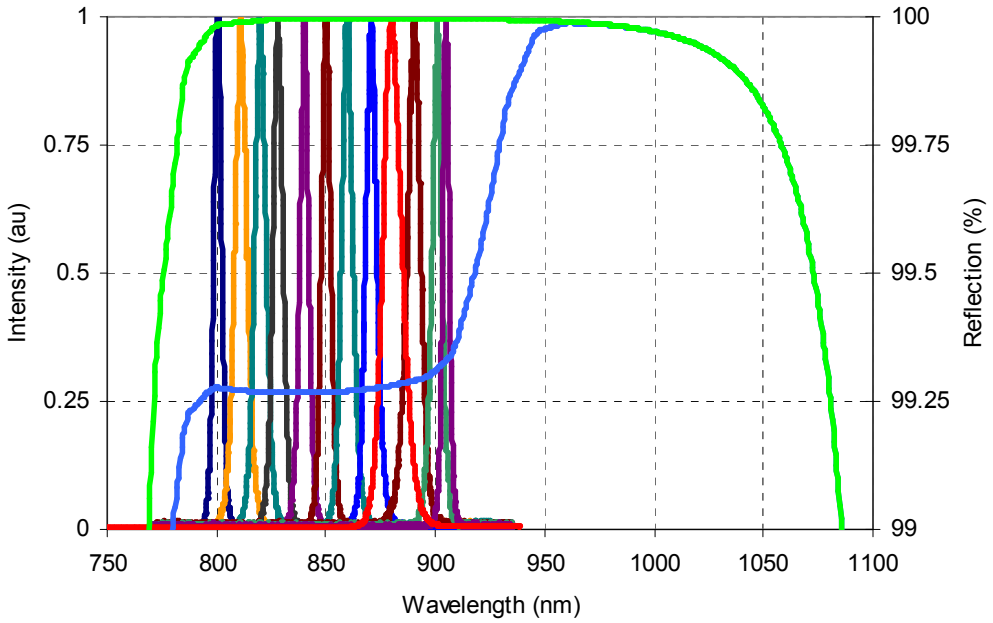

Figure 4.62: Example spectra from the Cr^{3+}:LiSAF laser, showing tunability of central wavelength of the laser from 800 nm to 905 nm, for the ~140-fs, ~1.6 nJ pulses. The data is taken with the MIT-860-QW-Oxidized SESAM/SBR. Calculated small signal and saturated reflectivity of the SESAM/SBR is also shown.

Figure 4.62 shows sample optical spectra that were taken in ~10 nm intervals within the continuous tuning range. The calculated small signal and saturated reflection of the oxidized SESAM/SBR are also shown. We can clearly see the band edge of the absorber around ~920 nm. Note that the SESAM/SBR mirror structure absorbs strongly below ~780 nm, due to the use of $Al_{0.19}Ga_{0.81}As$ in the Bragg stack. One can increase the Al content and shift the absorption edge to shorter wavelengths; however, this will increase the risk of oxidizing the $Al_{0.19}Ga_{0.81}As$ layer, which is not desired. Since Cr:LiSAF is not expected to tune below ~780 nm, we have chosen to use $Al_{0.19}Ga_{0.81}As$ in the grown structure.

Figure 4.63 shows the transmission of 3 m of air in our region of interest. Note that, even though there are some absorption lines in the demonstrated tuning range (~800 to 905 nm), these lines are relatively weak. Possibly, with an oxidized SESAM/SBR with a band edge around ~950 nm or ~1000 nm, it might be possible to tune the Cr:LiSAF laser in a broader range (~800 nm to ~950 nm or event ~1000 nm). However, Fig. 4.61 shows that tuning around 930 would require a purged cavity. Moreover, gain of Cr:LiSAF decreases beyond 900 nm, which will pose an additional difficulty for tuning above 900 nm. In summary, we believe the demonstrated tuning range in this study is the broadest tuning range ever reported for any SESAM/SBR mode-locked femtosecond solid-state laser to date. This work shows that it is possible to combine the advantages of self-starting mode-locked operation and broadband tuning using a SESAM/SBR.

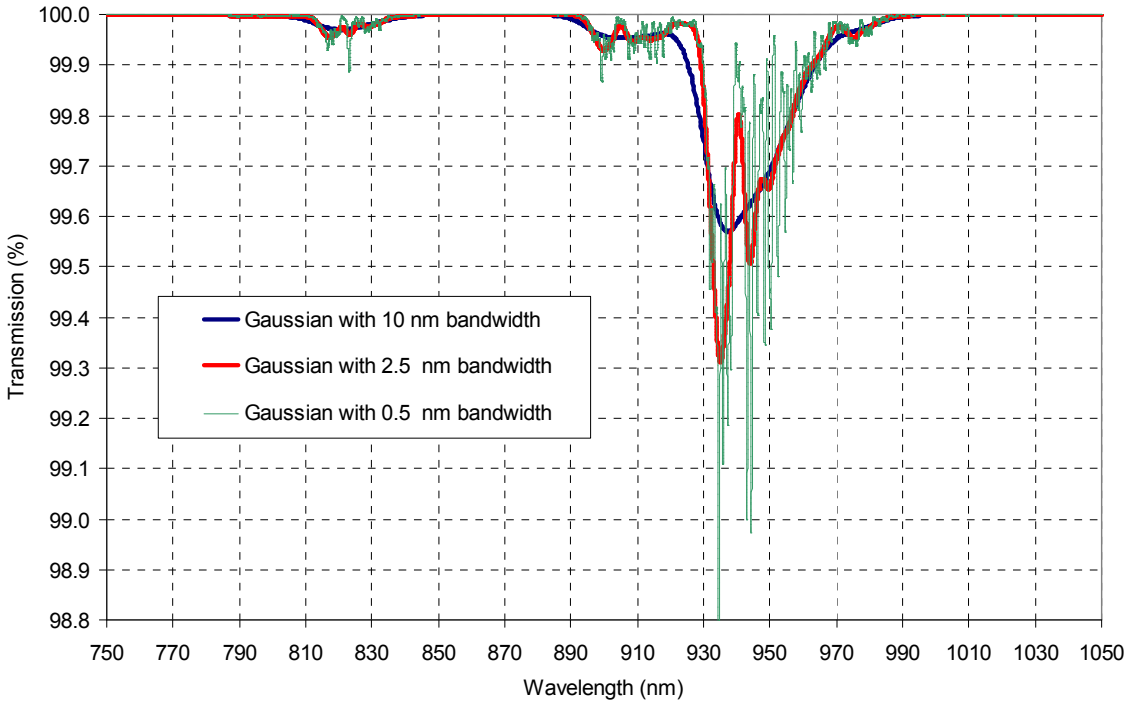

Figure 4.63: Calculated transmission of 3 m of air for a pulse with a Gaussian spectrum and a width of 0.5 nm, 2.5 nm and 10 nm (USA average).

4.13 Sub-50-fs Pulse Generation with MIT-860-QW-Oxidized SESAM/SBR

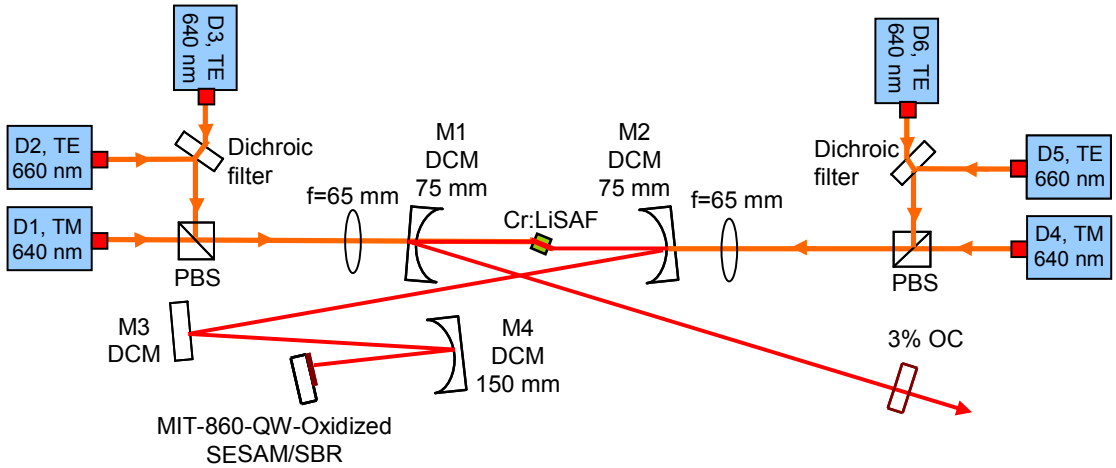

Figure 4.64: Schematic of the single-mode diode pumped Cr:LiSAF laser that was used in mode-locking experiments with the broadband/oxidized SESAM/SBR (MIT-860-QW-Oxidized). Dispersion compensation is provided by use of DCM mirrors from MIT Cr:LiSAF pump mirror set. The total incident pump power on the crystal is about 1 W.

We have also tried short pulse generation from the Cr:LiSAF laser using the MIT-860-QW-Oxidized SESAM/SBR. However, we could note get pulsewidths below ~30-fs due to multiple pulsing instabilities

or appearance of cw spike on the spectrum. The bandwidth of the SESAM/SBR was actually enough to support ~10-fs level pulses. Increasing the modulation depth of the oxidized SESAM/SBR might help to solve these instabilities. In this section, as a representative example, we will present the generation of ~38-fs 1.8 nJ pulses with the MIT-860-QW-Oxidized SESAM/SBR.

Figure 4.64 shows a schematic of the single-mode diode-pumped Cr:LiSAF laser, which was very similar to the setup just described except the number of bounces on DCM mirrors is decreased to produce shorter pulses. When mode-locked at full pump power, the laser produced ~38-fs pulses with 1.8-nJ pulse energy at a repetition rate of 93 MHz. The corresponding average power and peak power were 167 mw and 47.3 kW respectively. Figure 4.65 shows the obtained optical spectrum along with the estimate for cavity dispersion level. The optical spectrum is centered around ~880 nm, with a FWHM of ~26.5 nm, which is broad enough to support ~31-fs level transform limited pulses. This corresponds to a time bandwidth product of about ~0.40, which shows the slight chirp in the output pulses.

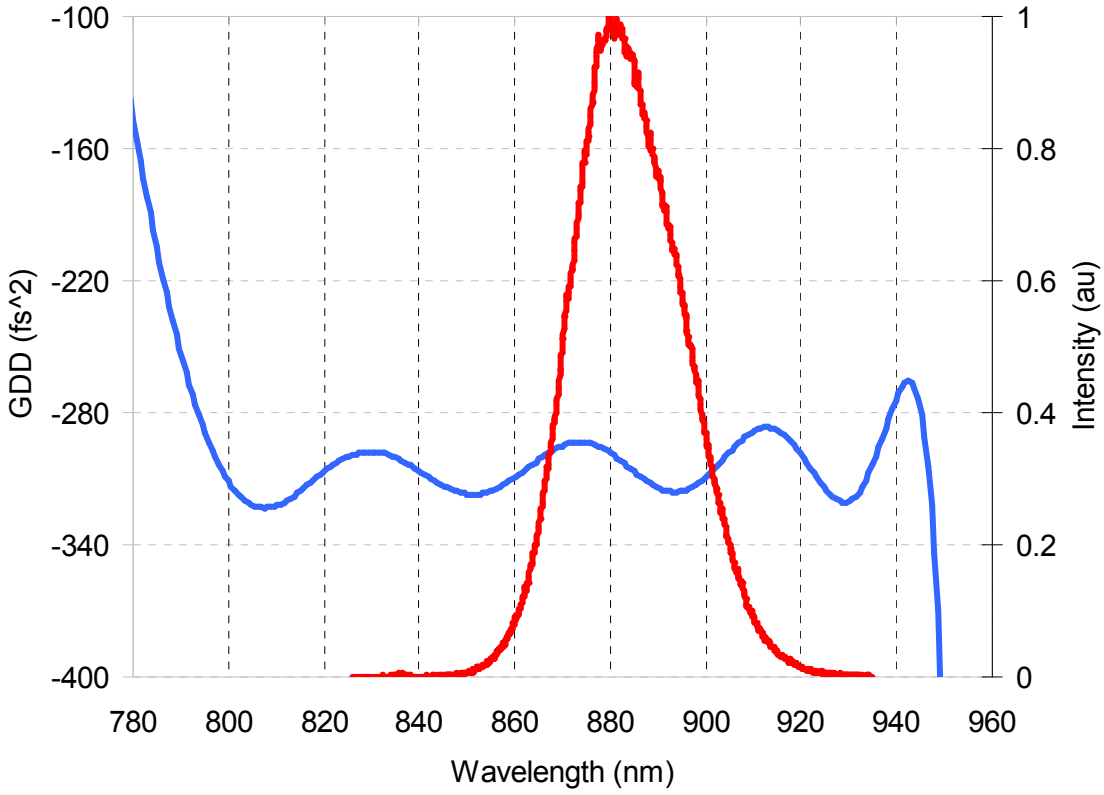

Figure 4.65: Estimated total dispersion for the cavity is shown along with the obtained optical spectrum. The cavity dispersion estimate includes 8 bounces on DCMs, 10 mm of Cr:LiSAF, and ~3 m of intracavity air.

4.14 Summary

We finish this Chapter with Table 4.4, which summarizes the cw mode-locked lasing results reported in literate with Cr^{3+}:LiSAF gain medium using different pump sources. Table 4.4 includes the obtained average output power levels, peak powers, pulse energies, and pulse widths. The mode-locking mechanisms that was used in each study was also listed. Representative results obtained during this PhD work were also included for comparison. Note that the obtained pulse energies from single-mode diode pumped 100 MHz Cr:LiSAF lasers is about an order of magnitude higher in our recent studies compared to the earlier work, which is mainly due to the improvements in laser diode technology (Fig. 4.65).

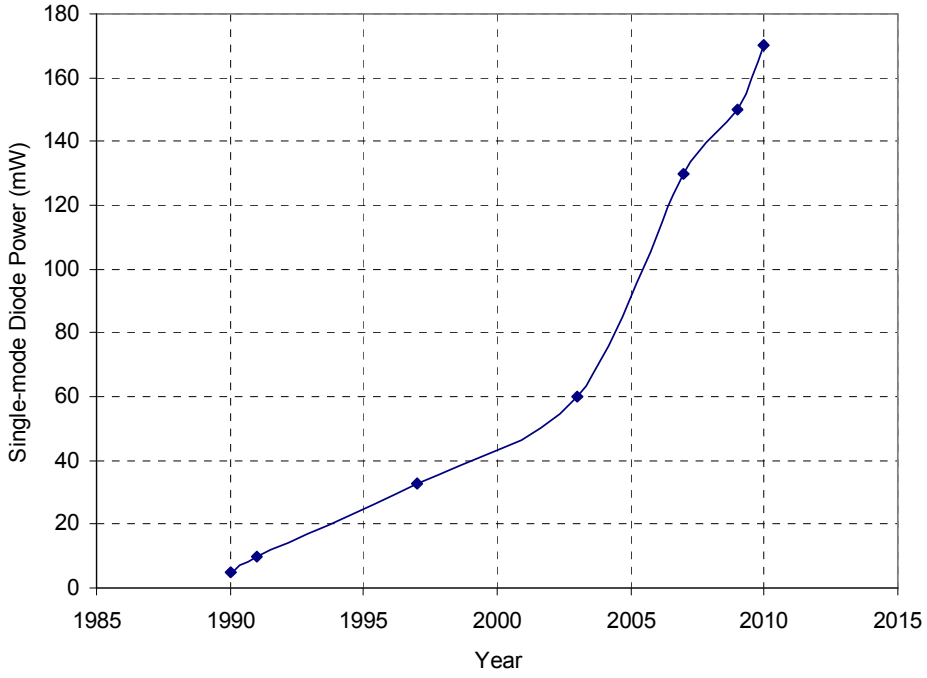

Figure 4.65: Variation of cw output powers available from commercial single-mode diodes with time.

Pump source	Pulse width (fs)	Pulse energy (nJ)	Peak power (kW)	Average power (mW)	Rep rate (MHz)	Mode Locking	Year	Ref.
Krypton	150	0.61	4.07	50	82	KLM/AOML	92	[150]
Argon	50	-	-	10-20	-	Dye cell	92	[251]
Argon	50	1.79	35.8	150	84	KLM	92	[151]
Argon	33	-	-	120	-	Dye cell	92	[252]
Argon	93	-	-	5	-	SESAM/SBR	93	[253]
MMD	$100x10^3$	0.14	0.0014	35	250	AOML	93	[154]
MMD	$70x10^3$	0.008	0.0001	2	250	Quant-well	93	[153]
MMD	98	0.63	6.38	50	80	SESAM/SBR	94	[254]
MMD	97	0.03	0.35	2.7	80	KLM	94	[255]
SH of Nd:YLF (659 nm)	$30 x10^3$	0.04	0.0015	3.5	80	AOML	94	[256]
SH of Nd:YLF (659 nm)	90	0.2	2.2	20	100	KLM	94	[257]
MMD	70	-	-	50	-	KLM	95	[258]
	45	-	-	30				
MMD	40	-	-	70	-	KLM	95	[194]
	27	-	-	10				
MMD	34	0.53	15.4	42	80	KLM	95	[259]
MMD	100	0.06	0.62	11	178	SESAM/SBR	95	[260]
SH of Nd:YAG (532 nm)	90	1.06	11.8	100	85	KLM	96	[261]
Krypton	15	1	66.7	70	70	KLM	97	[62, 169]
SMD	60	0.017	0.29	3.14	180	KLM	97	[155]
MMD	45	0.6	13.3	105	176	SESAM/SBR	97	[250]
MMD	50	2.27	45.4	340	150	SESAM/SBR	97	[142]
	110	3.34	30.4	500				
Krypton	37	-	-	10	-	KLM	97	[262]
MMD	26	-	-	6.2	-	KLM	97	[263]
MMD	80	1.25	15.6	110	88	KLM	98	[264]
SMD	57	0.04	0.7	6.5	150	SESAM/SBR	98	[159]
MMD	12	0.03	2.7	6.5	200	KLM	99	[162]
MMD	10	0.01	1.2	2.3	200	KLM	00	[64]
SMD	146	0.003	0.02	3	1000	SESAM/SBR	01	[163]
SMD	122	0.07	0.57	35	470	SESAM/SBR	02	[156]
SMD	151	0.38	2.5	20	~400	SESAM/SBR	02	[158]
	113	0.28	2.5	15	~400			
SMD	39	0.75	19.2	6.5	8.6	SESAM/SBR	03	[160]
SMD	46	1.76	38.1	149	85	SESAM/SBR	09	[59],*
SMD	55	0.11	1.8	110	1000	SESAM/SBR	10	[161],*
SMD	26	1	38.5	85	85	SESAM/SBR	10	*

Table 4.4: List of average output powers, pulse energies and pulse widths obtained with Cr:LiSAF gain media in cw mode-locked operation using different pump sources. Mode locking initiation mechanism and repetition rate of the lasers were also specified. MMD: Multimode diode, SMD: Single-mode diode. * Representative results that were obtained during this PhD.

CHAPTER 5

MODE-LOCKED CR:LISGAF LASERS

In Chapters 3 and 4, we have presented mode-locking results with Cr:LiCAF and Cr:LiSAF gain media, respectively. In this chapter, we will present our mode-locking results with Cr:LiSGaF gain medium. As we saw in Chapter 2, lasing region of Cr:LiSGaF overlap with Cr:LiSAF gain medium; hence, it doesn't offer a new spectral window of operation. Also, compared to Cr:LiSGaF, Cr:LiSAF has higher emission cross section, resulting in a higher gain, wider tuning range and wider stable cw mode-locked tuning range. Cr:LiSGaF has slightly higher thermal conductivity and slightly higher critical temperature for fluoresce quenching, which might help with thermal effects. However, for both of the crystals, current pump power levels from single mode diodes (~1W form six diode) is low enough to operate the laser with negligible thermal effects. Other advantages of Cr:LiSGaF include slightly higher intrinsic slope efficiency and slightly higher nonlinear refractive index. However, again these are not strong reasons to chose Cr:LiSGaF over Cr:LiSAF. Because of all these reasons we have mostly focused on Cr:LiSAF during this PhD work (also to Cr:LiCAF since it enables lasing below 800 nm and it has significant advantageous in terms of thermal effects). We will still provide some representative mode-locking experimental results with Cr:LiSGaF gain medium in this chapter. However, compared to Chapters 3 and 4, our discussion will be very brief.

Case	Pulse width (fs)	Output power (mW)	Peak power (kW)	Pulse energy (nJ)	Rep rate (MHz)	Central wavelength (nm)	SESAM/SBR	Dispersion compensation method	Pump power (mW)	Refe.
1	55	139		1.83	75	860	MIT-850-bulk	DCMs	~600	[59]
2	52	172		2.0	86	867	MIT-850-bulk	FS Prism pair	~600	[59]
3	82	186		2.31	81	815	MIT-800-QW-2HR	GTI & DCMs	~600	[59]
4	54	147		1.71	86	820	MIT-800-QW-2HR	FS Prism pair	~600	[59]

Table 5.1: Summary of cw mode-locking results obtained with Cr:LiSGaF gain media. All the results reported in this table have an uncertainty of about ±10%. DCMs: Double-chirped mirrors, GTIs: Gires–Tournois interferometer mirrors.

Table 5.1 lists some of the key mode-locking results obtained with Cr:LiSGaF gain media during this PhD thesis. Results from the Cr:LiSGaF laser were quite similar to those obtained from the Cr:LiSAF laser. The Cr:LiSGaF laser generated pulse energies as high as ~2.3 nJ, and pulsewidths as short as 52 fs. Using the two SBR/SESAMs (MIT-850-bulk and MIT-800-QW-2HR), pulses that were centered around

810 or 860 nm could be generated. Since the details of the experiments are similar to Cr:LiSAF laser, discussion will be brief for Cr:LiSGaF.

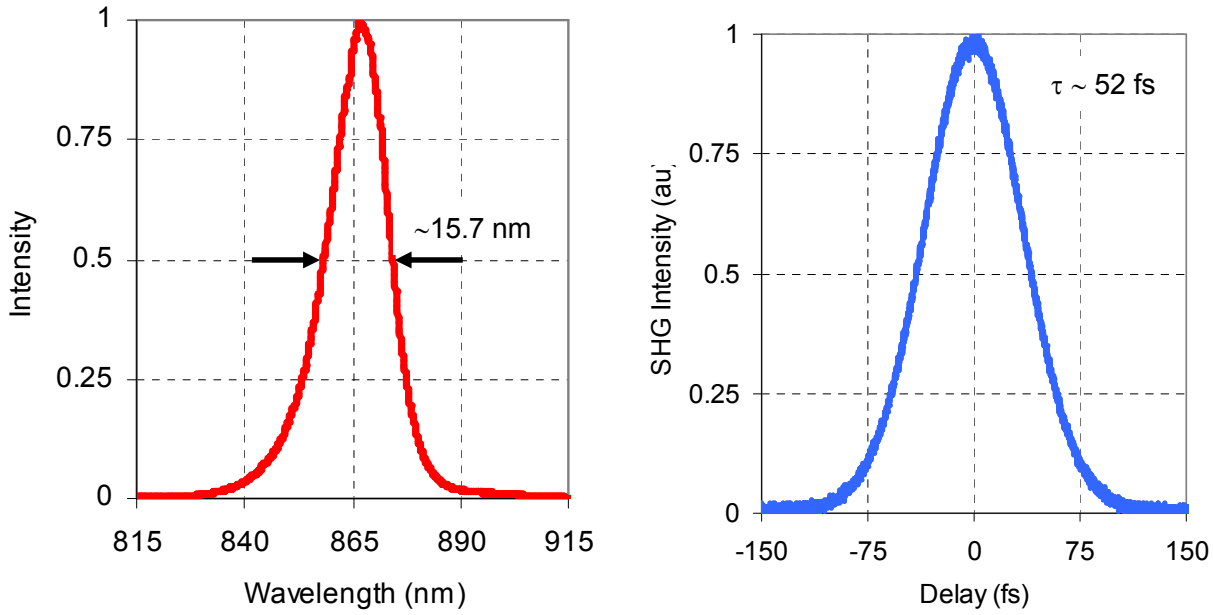

Figure 5.1: Spectrum and autocorrelation trace for the 52-fs, 2 nJ pulses generated with the single-mode diode-pumped Cr:LiSGaF laser, using FS prisms for dispersion compensation. The average output power was 172 mW, at an absorbed pump power of ~530 mW, with a 3% output coupler. The spectral bandwidth was 15.7 nm (FWHM) centered around ~867 nm and the time-bandwidth product is ~0.33. MIT-850-bulk SESAM/SBR was used in mode-locking experiments.

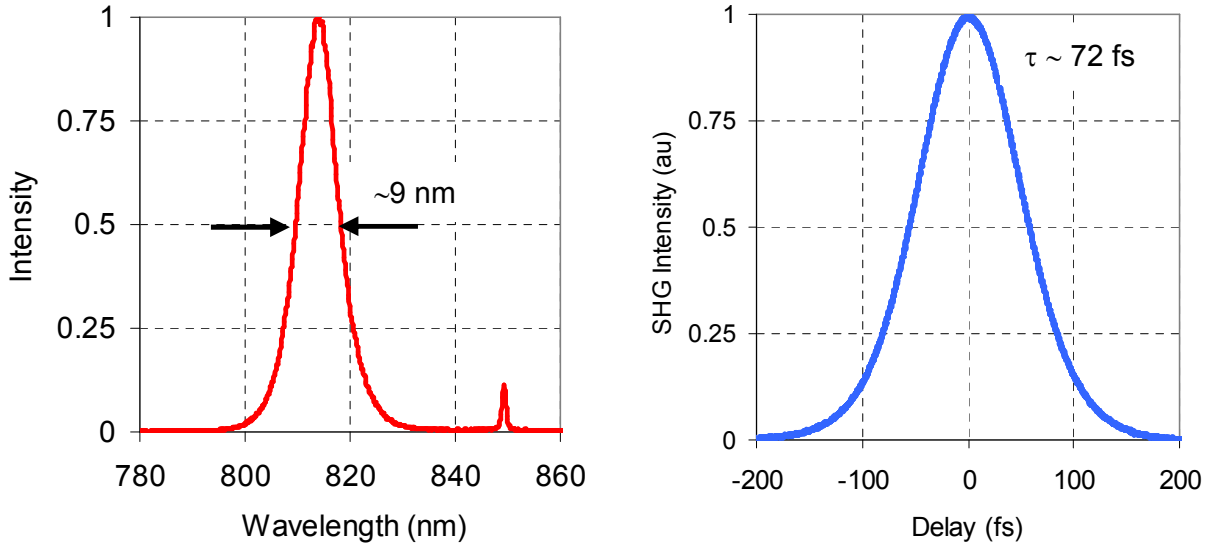

Figure 5.2: Spectrum and autocorrelation of 72-fs, 2.31 nJ pulses from the single-mode diode-pumped Cr:LiSGaF laser, using a GTI mirror for dispersion compensation. The average output power was 186 mW, at an absorbed pump power of ~560 mW, with a 3% output coupler. MIT-800-QW-2HR SESAM/SBR was used in the experiments.

Figure 5.1 shows examples of the spectra and autocorrelation using the 850 nm SBR/SESAM, with a 3% output coupler at an absorbed pump power of ~530 mW. Dispersion compensation was performed with a FS prism pair that is separated by 42 cm. The 5-mm-long, 3% Cr-doped Cr:LiSAF crystal (GVD ~28 fs^2/mm) and intracavity air produced a total GVD of ~320 fs^2. A curved mirror with a 15 cm radius of curvature focused the beam on the SBR/SESAM. Mode-locking was self-starting, and robust against environmental disturbances. The laser produced 52 fs pulses with 172 mW average power and exhibits a 15.7 nm spectral bandwidth near 867 nm at 86 MHz (~2-nJ pulse energy) and has a time bandwidth product of ~0.33. The estimated total cavity dispersion to generate 52-fs pulses was ~ -50 to -100 fs^2.

Figure 5.2 shows a spectrum and autocorrelation for the Cr:LiSGaF laser, obtained using the 800 nm SBR/SESAM (MIT-800-QW-2HR), and a GTI mirror for dispersion compensation (from Layertec GTI mirror set I, see appendix A for more details). The laser generated 72 fs pulses with 186 mW average power and 9 nm spectral bandwidth centered around 815 nm, at a repetition rate of 81 MHz (~2.31 nJ pulse energy). The spike in the spectrum around 850 nm is due to the GVD oscillations of the GTI mirror. GTI mirrors can provide large amounts of dispersion in one bounce, enabling one to build compact cavities. Moreover, since the number of bounces required for dispersion compensation is low, the total intracavity loss is minimized. However, their GVD curve has large oscillations which cause modulations in the spectra (especially for sub-100 fs pulses). Similar spectral modulation was also observed using GTI mirrors with Cr:LiSAF and Cr:LiCAF lasers [191].

CHAPTER 6

EXTENDED CAVITY CR:LICAF LASER

In this Chapter, we will describe efficient cw mode-locked operation of an extended multipass-cavity (MPC) $Cr^{3+:}$LiCAF laser, pumped by inexpensive single spatial mode laser diodes. A SESAM/SBR with a modulation depth of 0.6% was used to initiate and sustain stable mode-locked operation (MIT-800-QW-2HR SESAM/SBR). Addition of the MPC reduced the pulse repetition rate to ~10 MHz level. With only 540 mW of absorbed pump power, we obtained 98-fs, 9.9-nJ pulses with 95 mW of average power at a repetition rate of 9.58 MHz, with a corresponding peak power of ~101 kW. By further increasing the negative dispersion of the cavity, we also generated 310-fs, 15.2-nJ pulses with 160 mW of average power (10.51 MHz repletion rate) and ~49 kW peak power. The optical-to-optical conversion efficiency was 15.8 % and 26.7 %, for the 98-fs and 310-fs configurations, respectively. To the best of our knowledge, these are the highest peak powers and pulse energies obtained from any Cr^{3+}:Colquiriite laser to date. The peak power levels demonstrated in this work suggest that the MPC Cr:LiCAF laser has the potential to become a cost-effective alternative to standard Ti:Sapphire lasers in some applications requiring high energy/peak power femtosecond pulses near 800 nm.

As we discussed earlier in previous chapters, possible diode pump sources for Cr :Colquirrites include laser diode arrays [142], broad-stripe single-emitter diodes [143, 153, 174, 177, 220], as well as single transverse-mode laser diodes [160, 178, 220]. The peak powers obtainable from colquiriite media can be increased by scaling the output energy and/or reducing the pulsewidths. To date, the highest peak power obtained from a diode pumped Cr^{3+}:Colquiriite laser was ~45 kW (50 fs, 2.27 nJ pulses at 150 MHz), where a 15-W laser diode array was used to pump a Cr:LiSAF laser [142]. In recent experiments, we reported 67-fs pulse generation with energies as high as 2.5 nJ from a Cr^{3+}:LiCAF laser pumped by five 1-W broad-stripe emitters, corresponding to a peak power of ~37 kW [143]. With single-mode diode pumping, four single-mode pump diodes with a total absorbed power of 570 mW were used to generate 72-fs, 1.4-nJ pulses at a repetition rate of 127 MHz, resulting in peak powers of ~19.5 kW [178].

Although higher peak powers were obtained with multimode diode pumping [142, 143], single mode diode pumping offers numerous advantages including lower cost, better matching between pump and laser modes, significantly lower lasing thresholds, reduced thermal effects, and higher efficiency [178, 220]. For example, mode-locked optical-to-optical conversion efficiencies of ~28% have been demonstrated with single-mode diode pumping [178], whereas only 6 % and 7.5% efficiency could be

obtained with arrays [142], and broad-stripe single-emitter diodes, respectively [143]. Furthermore, for single mode diode pumping, no cooling is needed for the pump diodes or the laser crystal, enabling the development of compact, portable systems. However, since the pump powers available from single mode diodes are limited, the resulting pulse energies are lower. To overcome this problem, the output energy can be scaled up by extending the cavity length to lower the pulse repetition rate. If the average output power is nearly constant, lowering the repetition rate leads to higher output energies provided that additional dispersion is introduced to balance the nonlinearities. Multipass cavities (MPC) can be used to extend the cavity lengths with a relatively compact arrangement of mirrors [160, 265]. The MPC concept has already been applied to a Cr:LiSAF laser to obtain 39-fs, 0.75 nJ pulses at a repetition rate of 8.6 MHz [160]. The pulse energy obtained in [160] was limited by the fact that high-power single-mode diodes and low-loss resonator optics were not available at the time.

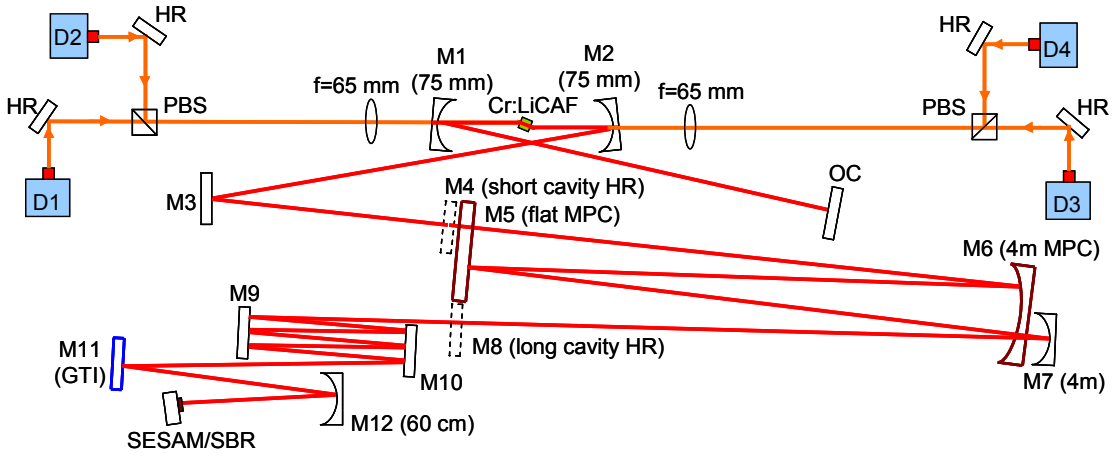

Figure 6.1: Schematic for the short and the extended-cavity (MPC) Cr^{3+}:LiCAF laser.

Figure 6.1 shows a schematic of the experimental setup for the short and the extended-cavity (MPC) Cr^{3+}:LiCAF laser. Four, linearly-polarized, ~660-nm single-mode diodes, costing only $150 each, (VPSL-0660-130-X-5-G, Blue Sky Research) were used as the pump source (D1-D4). The diode output beams were collimated using 4.5-mm focal length lenses, coupled via polarizing beam splitter cubes (PBSs), and then focused inside the crystal using 65-mm focal length lenses. The short cavity was a standard astigmatically compensated, x-fold laser resonator, which was similar to the cavity described in [178].

The continuous-wave (cw) resonator for the short cavity consisted of two curved pump mirrors (M1 and M2, R=75 mm), a flat end high reflector (M4), and a flat output coupler (OC). Pump mirrors (M1-M2) had transmission values >95% at the pump wavelength (~660-nm) and had a reflectivity > 99.9% from 740 to 860 nm (for more information see Layertec Cr:Colquiriite pump mirror set I, in Appendix A). Arm lengths of ~35 cm (OC arm) and ~50 cm were used to obtain an estimated laser mode size of ~20 μm x 28 μm (sagittal x tangential) inside the Cr:LiCAF crystal, which has a refractive index of n~1.4. The

gain medium was a 2.5-mm-long, 1.5-mm-tall, Brewster-cut, 11% Cr-doped Cr^{3+}:LiCAF crystal purchased from VLOC, Inc.. The crystal absorbed >98% of the incident pump for both polarizations, corresponding to a total of 540 mW of pump power. In cw laser experiments with the short cavity, the highest output power was 271 mW, obtained by using a 0.85% output coupler, with a slope efficiency of 54%. Measuring the lasing thresholds with 7 different output couplers, we estimated the round trip loss of the short cavity to be 0.43 ± 0.1% (Fig. 6.2).

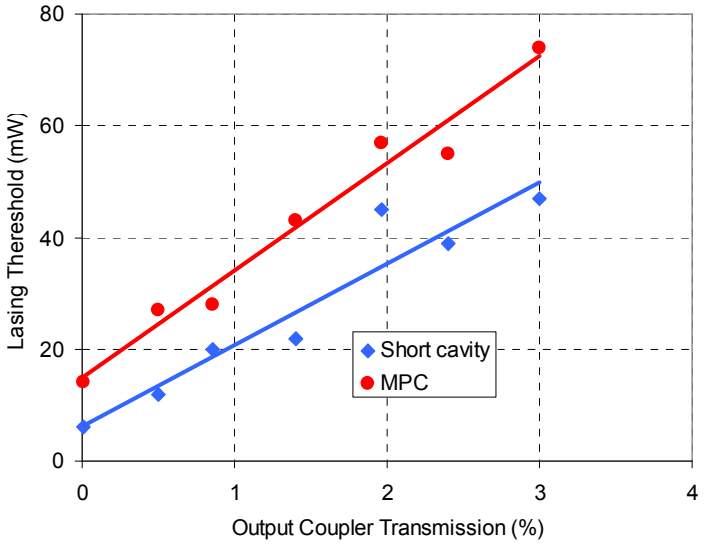

Figure 6.2: Measured lasing thresholds with different output couplers for the short and extended cavity (MPC) cw Cr:LiCAF laser. Using Findlay-Clay analysis, we have estimated the passive losses for the short and MPC cavity as 0.43 ± 0.1% and 0.77 ± 0.1%, respectively.

The cavity length was extended by removing the end high reflector M4 and adding a q-preserving MPC, consisting of a flat (M5) and a curved (M6, R=4 m) high reflector. The separation between the MPC mirrors was 1 m, resulting in an angular advance of 60° per round trip on each MPC mirror. Beam injection and extraction were achieved by using notches carved on the mirrors. Because of the notches, 6 full round trips were not completed and to make the MPC q-preserving, the beam was reflected by a second curved mirror with R=4 m (M7) and reftro-reflected by a flat end high reflector (M8) at a distance of 1 m from M7 [265]. From the cw lasing data, the insertion loss of the MPC was estimated to be 0.35% ± 0.1 (Fig. 6.2). With the addition of the MPC, the high reflector arm length increased from ~0.5 m to ~12.5 m (0.5 m + 2x6x1 m), which reduced the repetition rates to ~10-11 MHz. Finally, the optimum output coupling for the extended cavity increased to ~3%, where we obtained 213 mW of cw output power with a slope efficiency of 48% (Figure 6.3).

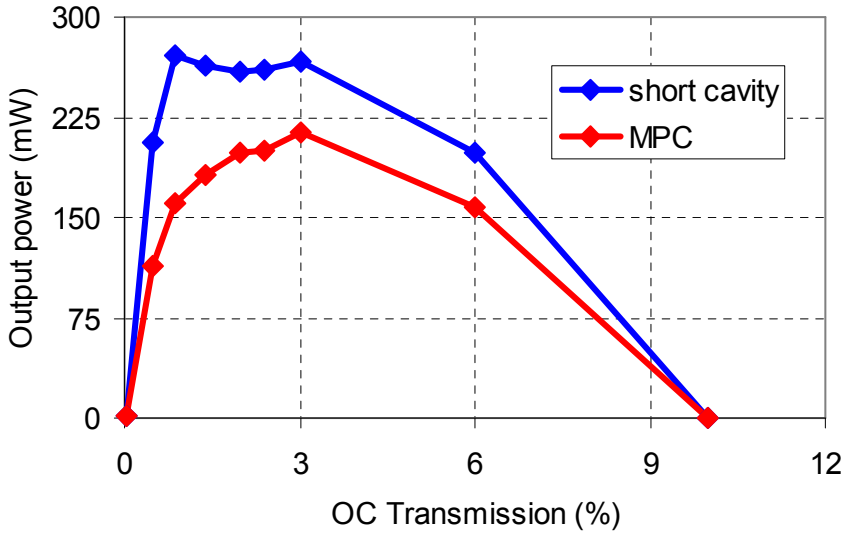

Figure 6.3: Measured variation of maximum obtainable cw laser output power for the short and extended cavities at an incident pump power of ~600 mW.

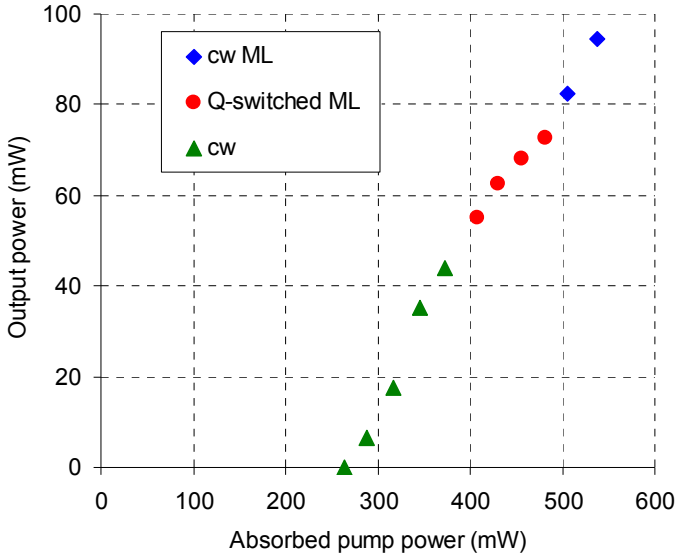

Figure 6.4: Measured variation of average output power with absorbed pump power for the MPC Cr:LiCAF laser producing 98-fs, 9.92 nJ pulses.

For mode-locking experiments, additional mirror bounces (6 bounces on M9 and M10 and 2 bounces on M11) were used to provide the necessary group velocity dispersion (GVD). Except for the pump mirrors, output coupler, the GTI mirror (M11) and M12, all the optics used in the cavity were chirped mirrors with a GVD of ~ -40 ±5 fs^2 per bounce from 730 to 870 nm (see Layertec DCM mirror set III, in Appendix A). The GTI mirror (M11) had a GVD of ~ -550 ±100 fs^2 per bounce from 775 to 815 nm (see Layertec GTI mirror set I, in Appendix A). Including the dispersion of the pump mirrors, crystal, air, SESAM/SBR, the estimated total round-trip cavity dispersion was ~ -2000 ±300 fs^2 (785-815 nm). MIT-

800-QW-2HR SESAM/SBR with a low nonsaturable loss (~0.25 %) was used to initiate and sustain mode locking. More details about this SESAM/SBR can be found in Appendix E. A curved mirror (M12) with R=60 cm was used to focus the intracavity laser beam onto the SESAM/SBR. Mode locking was not self starting and required slightly tapping the SESAM/SBR, but once initiated, the mode-locked laser was immune to environmental fluctuations. Figure 6.4 shows the measured slope efficiency of the MPC Cr:LiCAF laser (using a 2.4% output coupler). For absorbed pump powers below ~400 mW, the laser worked in cw regime. When the pump power is increased above ~400 mW, the laser started to work in q-switched mode-locked regime. Finally, above ~500 mW of absorbed pump power we could obtain stable cw mode-locked operation. When modelocked at the full pump power (~540 mW absorbed), the laser produced 9.92 nJ pulses with 95 mW average power at a 9.58 MHz repetition rate. Figure 6.5 shows the measured optical spectra and the autocorrelation trace. The main part of the spectra centered around 782.7 nm has a FWHM of ~6.75 nm, which supports ~95.5 fs Fourier limited pulses assuming a $sech^2$ pulse shape. The measured autocorrelation trace has a FWHM of ~151.3 fs, which corresponds to a pulsewidth of ~98 fs for $sech^2$ pulse shape. The time bandwidth product was ~0.323, close to the transform limit of 0.315 for $sech^2$ pulses. The corresponding peak power of the pulses was ~101.2 kW.

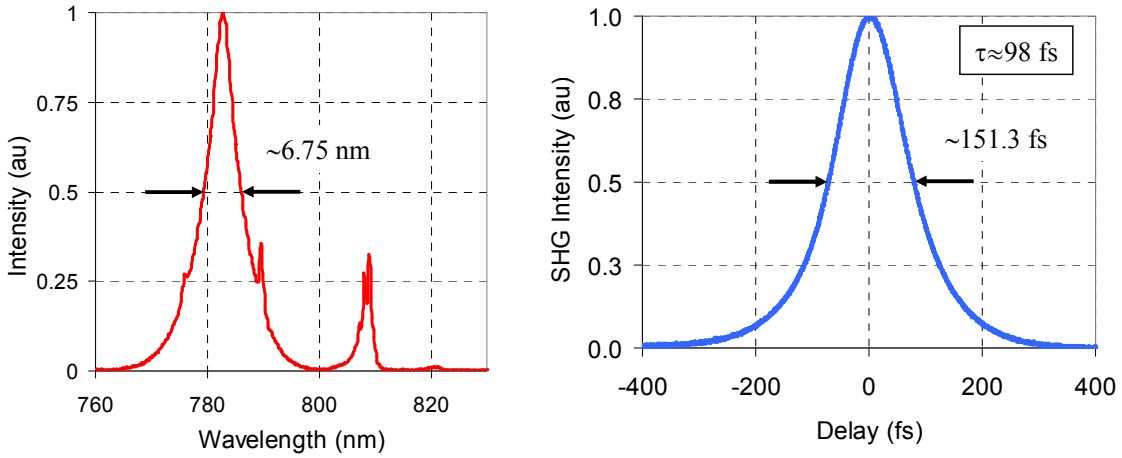

Figure 6.5: Measured optical spectra and background-free intensity autocorrelation trace for the 98-fs, 9.92 nJ pulses at 9.58-MHz, with 95 mW of average output power (~101 kW peak power), taken using the 2.4% OC.

The side lobe in the spectra around 809 nm was due to the GVD oscillations introduced by the GTI mirror (Fig. 6.6), and similar oscillations were also observed while using the GTI mirror with the short cavity. Despite this disadvantage, the GTI mirror provides large amounts of dispersion in one bounce. In comparison, to provide the same amount of dispersion (~ -550 fs^2), one would need 13-14 bounces from regular DCMs which will increase the loss of the cavity, and hence limit the pulse energies. This is especially a problem in a low-gain medium such as Cr:LiCAF. Pulse energies were limited by the onset of mode-locking instabilities which produced wings on the autocorrelation traces (due to multiple pulsing

instabilities). We believe that these instabilities are the result of two photon absorption in the SESAM/SBR. Increasing the spot size on the SESAM/SBR reduces the two photon absorption, but also trades off the effective saturable absorber cross section, making initiation of mode-locking more difficult. Operating the laser with longer pulses reduces the two photon absorption.

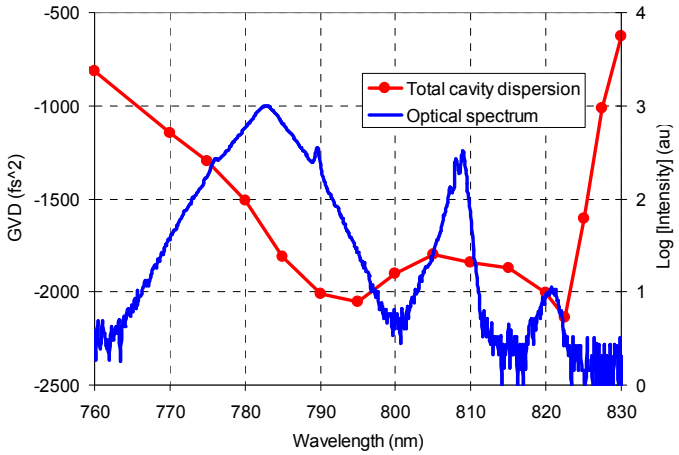

Figure 6.6: Measured optical spectrum in logarithmic scale is shown with the estimated total intracavity dispersion level for the 98-fs, 9.92 nJ pulses.

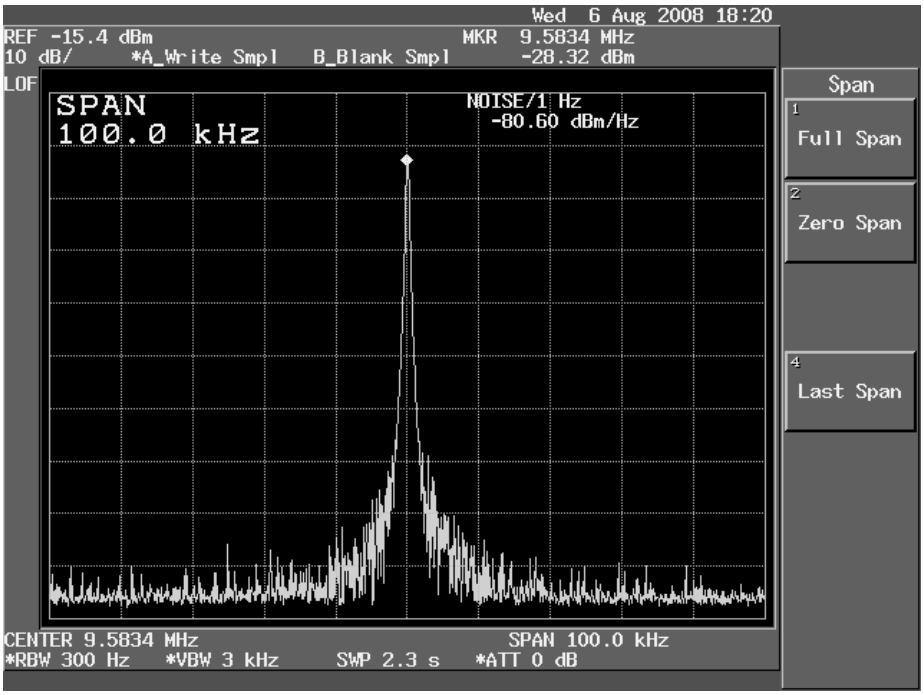

Figure 6.7: Measured RF spectrum of the mode-locked MPC Cr:LiCAF laser (for the 98-fs, 9.92 nJ pulses). The repetition rate of the laser is measured as 9.5834 MHz. The main peak is >70 db above the noise level.

Figures 6.7-6.8 show the mode-locked pulse train and the RF spectrum of the output, respectively. At full power, the pulse train was stable with no sign of Q-switching instabilities. The peak in the RF

spectrum corresponding to the cavity repetition rate near 10 MHz was above the noise level by 70-80 dB (Fig. 4 (b)).

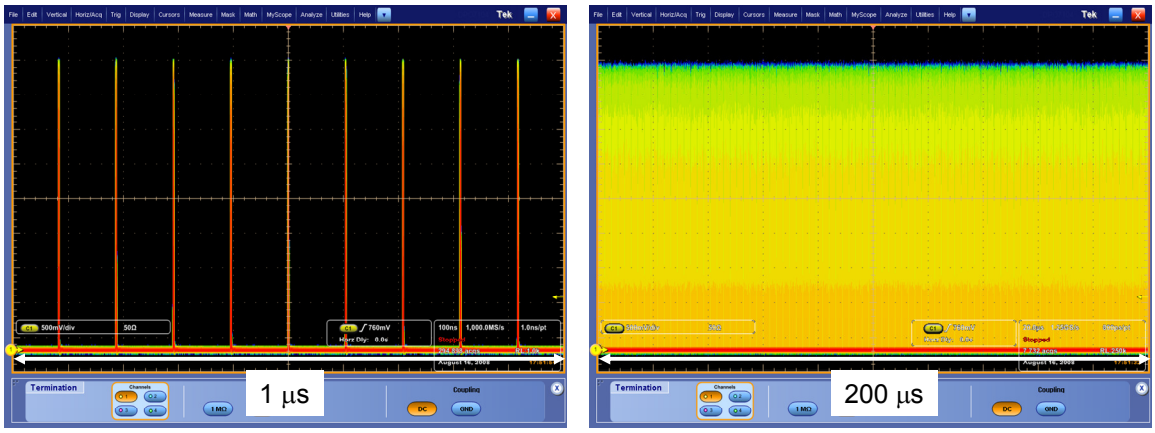

Figure 6.8: Measured pulse train from the cw mode-locked MPC Cr:LiCAF laser producing 98-fs, 9.92 nJ pulses.

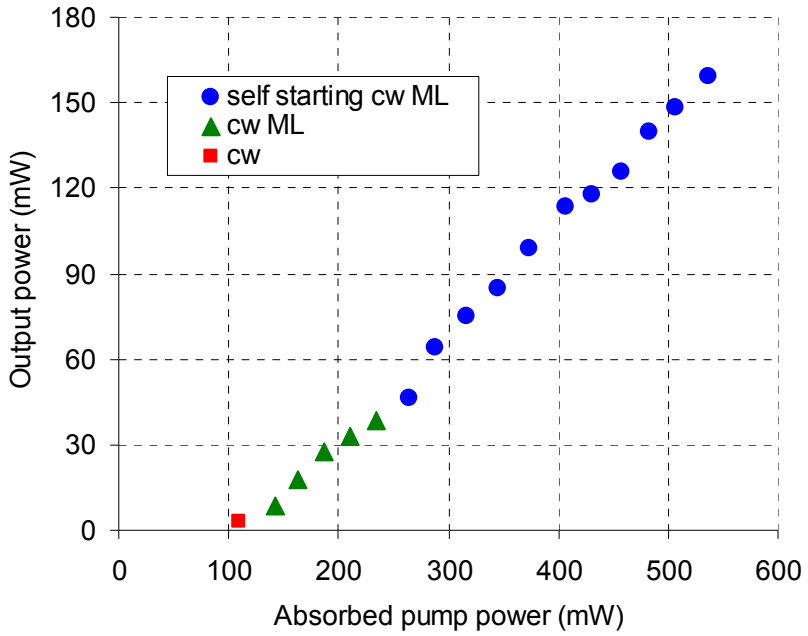

Figure 6.9: Measured variation of average output power with absorbed pump power for the MPC Cr:LiCAF laser producing 310-fs, 15.2-nJ pulses.

When the dispersion of the cavity was increased further to ~ -4000 ±500 fs^2 by using more GTI bounces, we obtained 310-fs, 15.2 nJ pulses with 160 mW average power at 10.51 MHz (corresponding peak power ~49.1 kW). For this case, a curved mirror with R = 15 cm was used to focus the beam on the SESAM/SBR, and mode locking was self-starting. Figure 6.9 shows the efficiency curve for this case, which shows a wider working range for cw mode-locking due to decreased pulse widths. Figure 6.10 shows the spectrum and the autocorrelation trace, taken with the 2.4% output coupler at full pump power

(~540 mW). This time the spectrum was narrow enough to fit in only one of the minima in the GVD curve, hence a smooth spectrum could be obtained (Fig. 6.11). The time bandwidth product was ~0.325, which is close to the transform limit of 0.315 for sech^2 pulses.

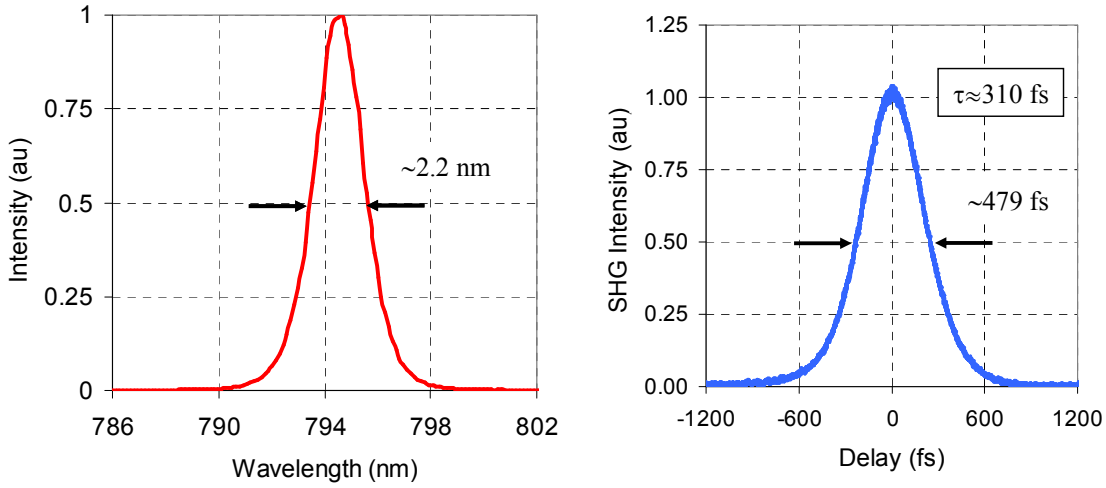

Figure 6.10: Measured optical spectra and autocorrelation trace for the 310-fs, 15.2-nJ pulses at 10.51-MHz, with 160 mW of average output power (~49 kW peak power), taken using the 2.4% OC.

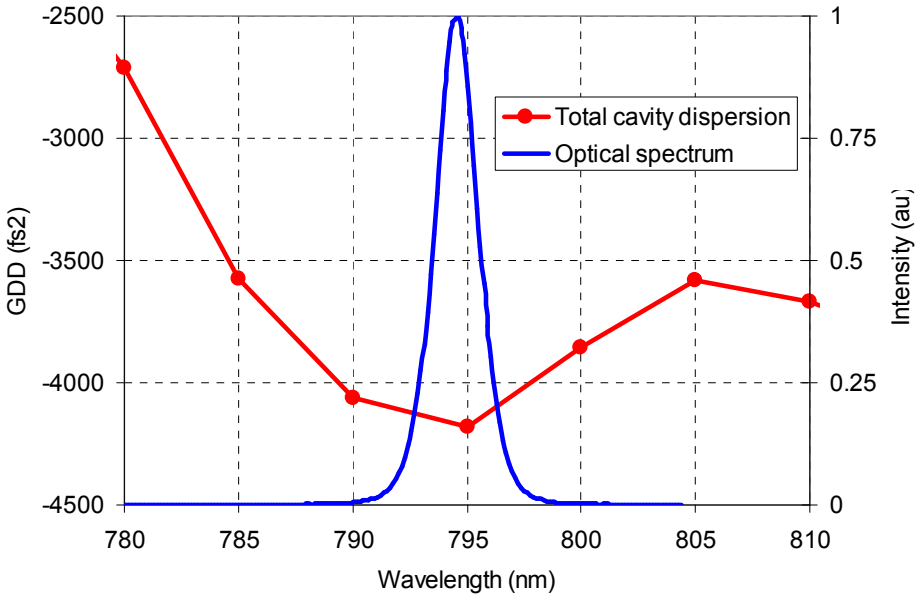

Figure 6.11: Measured optical spectrum is shown with the estimated total intracavity dispersion level for the 310-fs, 15.2-nJ pulses.

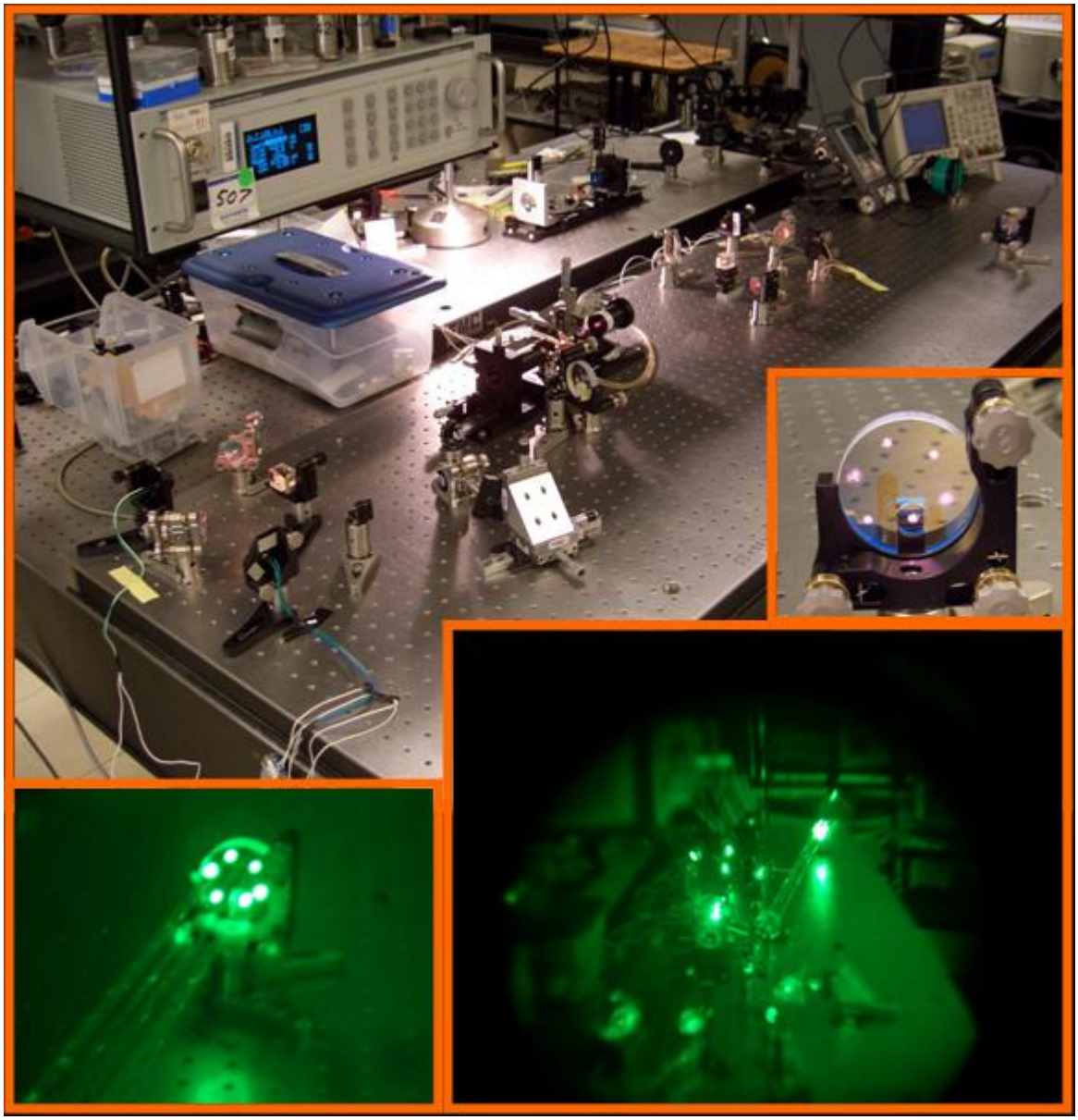

Figure 6.12: Pictures from the MPC Cr:LiCAF laser cavity.

In conclusion, we have demonstrated cw mode-locked operation of an extended cavity Cr^{3+}:LiCAF laser pumped by inexpensive single-mode laser diodes. Up to ~15.2 nJ pulse energies and peak powers as high as ~101 kW were demonstrated. SESAM/SBR initiated mode locking enabled stable and robust cw mode-locked operation. We believe the reported pulse energies and peak powers are the highest obtained to date from any Cr:Colquiriite laser oscillator. These results show that with the advent of high power single-mode diode technology and better-quality mirrors, cost-effective femtosecond Cr^{3+}:Colquirite laser systems generating peak powers >100 kW can be developed, which would enable the replacement of expensive Ti:Sapphire technology for selected femtosecond laser applications.

CHAPTER 7

CAVITY DUMPED CR:LISAF LASER

As the experimental results in the previous chapters have already demonstrated, Cr^{3+}-doped colquiriites are attractive materials for femtosecond pulse generation mainly because they can be directly pumped by inexpensive single-mode diodes [1, 4, 59, 178]. Direct-diode pumping of Cr^{3+}:Colquiriite lasers allows high electrical-to-optical efficiencies, compactness, and ease of use [59, 178]. Pumping Cr^{3+}:Colquiriites with single-mode diodes, ~50-100 fs pulses with ~1-2.5 nJ pulse energies and ~20 kW peak powers can be demonstrated from standard ~100 MHz cavities [178, 220]. The pulse energies and peak powers are limited by the available pump power (~600 mW to ~1W of pump power is available from four single-mode diodes). Slightly higher peak powers can be obtained with multimode diode pumping (~40 kW) [142, 143, 220], at the expense of reduced efficiency and increased complexity.

For Cr^{3+}: Colquiriite lasers to become a strong competitor to existing Ti:Sapphire technology, pulse energies and peak powers need to be scaled. One approach to scale the pulse energies from laser oscillators is to reduce the repetition rate of the cavity. As described in Chapter 6, using an extended cavity single-mode diode pumped Cr:LiCAF laser operating at 9.58 MHz, we have demonstrated 98-fs pulses with 9.9 nJ of pulse energy and ~101 kW of peak power [191]. Another approach to scaling the pulse energies is to use cavity dumping. Cavity dumping has been successfully applied to solid-state lasers such as Ti:Sapphire lasers [266-269], ytterbium-doped lasers [270, 271] and neodymium-doped lasers [271]. From a cavity-dumped Ti:Sapphire laser, 60-fs duration pulses with 450 nJ of pulse energy have been demonstrated [268]. A recent study achieved pulse energies above 1100 nJ level with chirped pulse durations of ~5 ps, but recompression of the chirped pulses was not demonstrated, although bandwidths were sufficient to support sub-100-fs pulse durations [269].

In this Chapter, we will report the first cavity-dumping experiments with a Cr^{3+}:Colquiriite laser, aimed at scaling the pulse energies and peak powers. Among the Cr^{3+}:Colquiriites, Cr^{3+}:LiSAF was used since it has a higher emission cross-section, larger gain and reduced susceptibility against Q-switching instabilities [59, 220]. The crystal was pumped by four ~150-mW single-mode laser diodes at 660 nm. Mode locking was initiated and sustained with a semiconductor saturable absorber mirror (MIT-800-QW-2HR) [272], also known as a saturable Bragg reflector (SBR) [273]. Cavity dumping at repetition rates of up to 50 kHz generated nearly transform limited ~120 fs pulses, with pulse energies > 100 nJ. Pulse

energies of 87 nJ, 77 nJ, 68 nJ and 62 nJ were obtained at repetition rates of 100 kHz, 200 kHz, 500 kHz and 1 MHz, respectively. This study demonstrates that low-cost Cr^{3+}:Colquiriite lasers can reach ~MW level peak powers.

Figure 7.1 shows a schematic of the cavity-dumped Cr^{3+}:LiSAF laser. The crystal was pumped by four linearly-polarized ~660-nm AlGaInP single-mode diodes (D1-D4) with circular output (HL6545MG, see Appendix B for more details). Operating at 220 mA current (above the rated driving current of 170-210 mA), a maximum pump power of ~150-160 mW per diode was obtained. The diode outputs were collimated by aspheric lenses (f = 4.5 mm) and combined using polarizing beam splitting cubes (PBS). Two f = 75-mm lenses focused the pump beams in the Cr:LiSAF crystal to a beam waist of w_0 = ~25 μm. Water cooling was not required for the diodes and crystal. The Cr-doped Cr^{3+}:LiSAF crystal (VLOC, Inc.) was Brewster-cut, 5-mm-long, 1.5-mm-tall and 1.5% doped which absorbed ~99% and ~72% (0.9 x 80%) of the incident TM and TE polarized pumps, respectively. The laser used an astigmatically compensated X-fold cavity formed by two 75-mm radius-of-curvature (roc) mirrors.

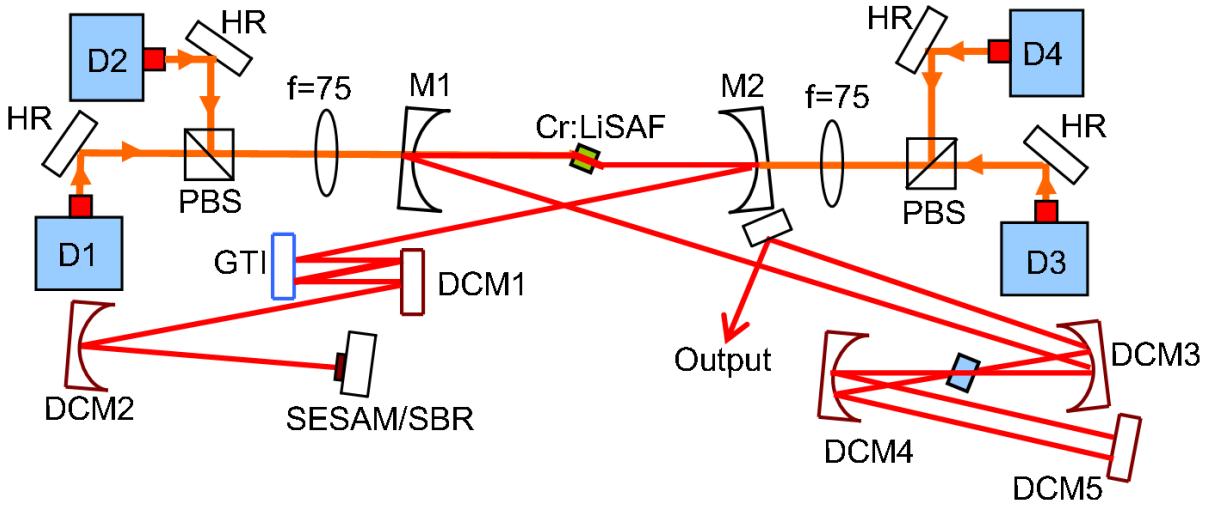

Figure 7.1: Schematic of the cavity dumped, single-mode diode-pumped Cr^{3+}:LiSAF laser system.

The ~3-mm thick, fused silica acousto-optic cavity dumper was placed at Brewster's angle into a second Z-fold focus ($w_0 \cong 30$ μm) with 100 mm radius mirrors. The cavity dumper was driven by a high-speed RF driver (64380-SYN-9.5-2, Neos Technologies, Inc.), with ~10-ns wide RF pulses at >10W of peak power (Fig. 7.2). The RF driver was synchronized to the intracavity circulating pulse using a portion of the output (detected with a fast photodetector) to trigger the RF driver. The cavity dumper had a single-pass diffraction efficiency of ~30% (Fig. 7.3), and was used in double-pass configuration to obtain 50-60% dumping efficiencies. The double pass configuration retroreflects the forward diffracted beam

(incident on DCM5) to interferometrically recombine with the beam in the cavity and generates an output in one direction (incident on DCM3). Efficiency is optimized by controlling the position of acousto-optic cell and the RF pulse phase and delay [16]. A metallic high reflector was used to pick off the dumped beam after its second pass through the dumper.

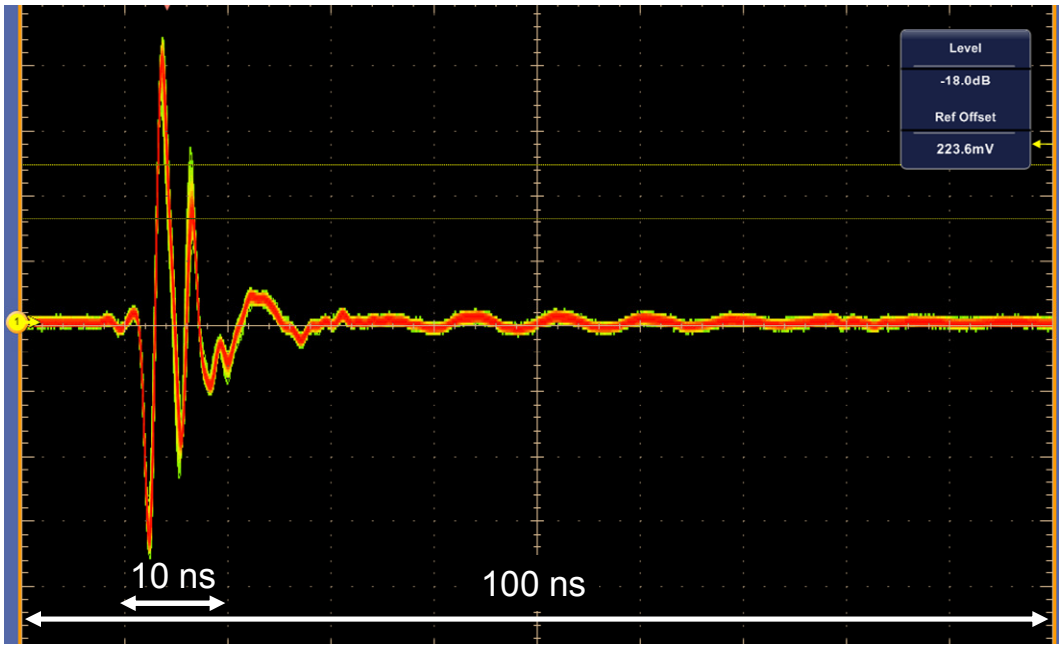

Figure 7.2: Oscilloscope trace of the RF pulses from the high-speed RF driver (64380-SYN-9.5-2).

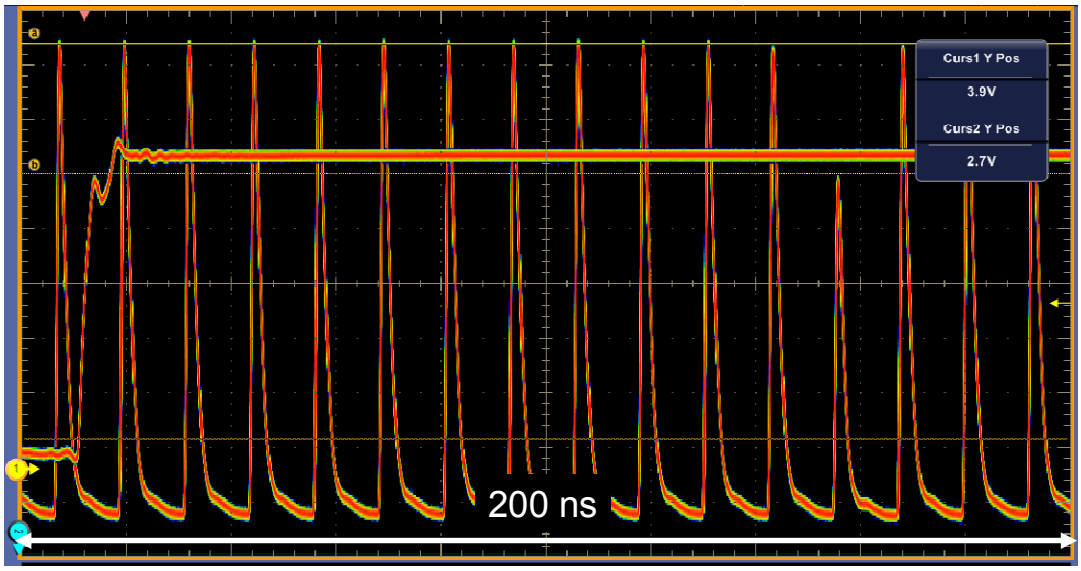

Figure 7.3: Oscilloscope trace showing the measured single pass diffraction efficiency of the cavity dumper. Trigger signal for the RF driver is also shown. There is an adjustable delay between the trigger signal and the diffraction event. Note that the diffracted pulse magnitude decreases from 3.9 to 2.7 (arbitrary units), which indicates a diffraction efficiency of 30.76%.

Dispersion compensation was mainly performed by a Gires–Tournois interferometer (GTI) mirror, with ~ -550±50 fs^2 group velocity dispersion (GVD) per bounce (Layertec GTI mirror set I, see Appendix A for more details). Double-chirped mirrors (DCMs), with a ~ -80±5 fs^2 GVD were also used for dispersion tuning, to optimize pulsewidths (MIT Cr:Colquiriite pump mirror set, see Appendix A for more details). The estimated total round-trip cavity dispersion was ~ -2250 fs^2. The 3 mm thick cavity dumper had a double pass dispersion of ~200 fs^2. However, the self-phase modulation in the cavity dumper acousto-optic cell (~$0.5x10^{-6}$rad/W) was comparable to the self-phase modulation in the laser crystal (~$0.3x10^{-6}$rad/W), and this required operating the laser at a larger negative dispersion. A saturable absorber mirror with a reflectivity bandwidth centered at 800 nm initiated and sustained mode-locking (MIT 800 nm SESAM/SBR with quantum well absorbers and two layer of HR coating, for more details see Appendix E). The SESAM/SBR had a modulation depth of ~0.6%, a saturation energy fluence of ~280 μJ/cm^2 and parasitic two-photon absorption (TPA) occurred for fluences above ~25 mJ/cm^2. A 250 mm radius curved mirror (DCM2) was used to focus onto the SESAM/SBR. Mode locking was self starting and the laser was immune to environmental fluctuations. An output coupler was not used in the cavity in order to increase the intracavity pulse energies. The laser dynamics were monitored using leakage from the GTI mirror, which had a ~0.03% transmission (~5 mW).

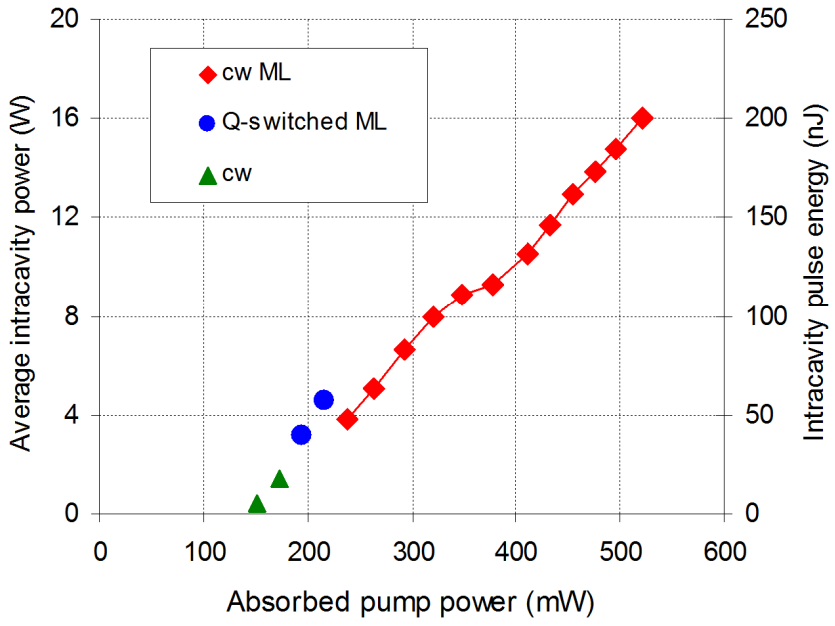

Figure 7.4: Variation of the intracavity laser power with absorbed pump power. The laser operates at different regimes as the pump power is increased. cw: continuous-wave operation, Q-switched ML: Q-switched mode-locked operation, cw ML: continuous-wave mode-locked operation. Corresponding pulse energies for cw ML are also shown.

Figure 7.4 shows the measured intracavity average power versus absorbed pump power. The laser threshold was ~150 mW and operated cw for pump powers up to ~200 mW. For pump powers between ~220 mW and ~250 mW, the laser operated in the Q-switched mode locked regime. For pump powers above ~250 mW, stable and self-starting cw mode-locking was obtained (cw ML). Figure 7.4 also shows the corresponding pulse energies for cw mode-locked operation. At an absorbed pump power of ~520 mW, the laser produced 118-fs pulses with an average intracavity power of ~16 W at 80 MHz repetition rate (~200 nJ intracavity pulse energy). The spectrum was centered at ~823 nm, with a 6.5-nm (FWHM) bandwidth, corresponding to a ~0.345 time-bandwidth product. The lasing wavelength was determined by the SESAM/SBR and GTI mirror. We believe that it should be possible to generate wavelengths from ~810 nm to ~1000 nm using different saturable absorber and GTI mirrors. The intracavity power levels and intracavity pulse energies were limited by the available pump power and the passive losses of the SESAM/SBR (~0.5%), Cr:LiSAF crystal (~0.2%), GTI mirror (~0.03 %) and DCM mirrors (~0.005%).

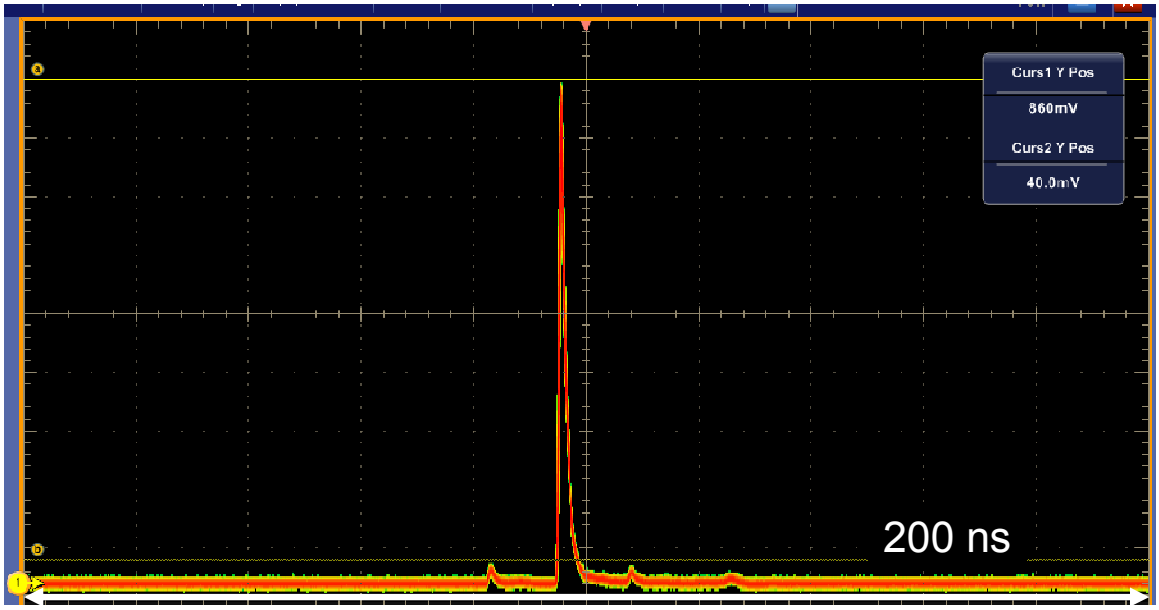

Figure 7.5: A representative dumped pulse from the laser, with a contrast ration of ~1:21.

Dumping frequency (kHz)	Pulse energy (nJ)	Pulse width (fs)	Average power (mW)	Peak power (kW)	Dumping efficiency (%)
10	112	120	1.12	930	56
20	105	120	2.09	870	52
50	98	121	4.9	810	49
100	87	122	8.73	720	44
200	77	124	15.3	620	38
500	68	130	34	520	34
1000	62	143	62	430	31

Table 7.1: Summary of the cavity dumping results with the single-mode diode pumped Cr:LiSAF laser.

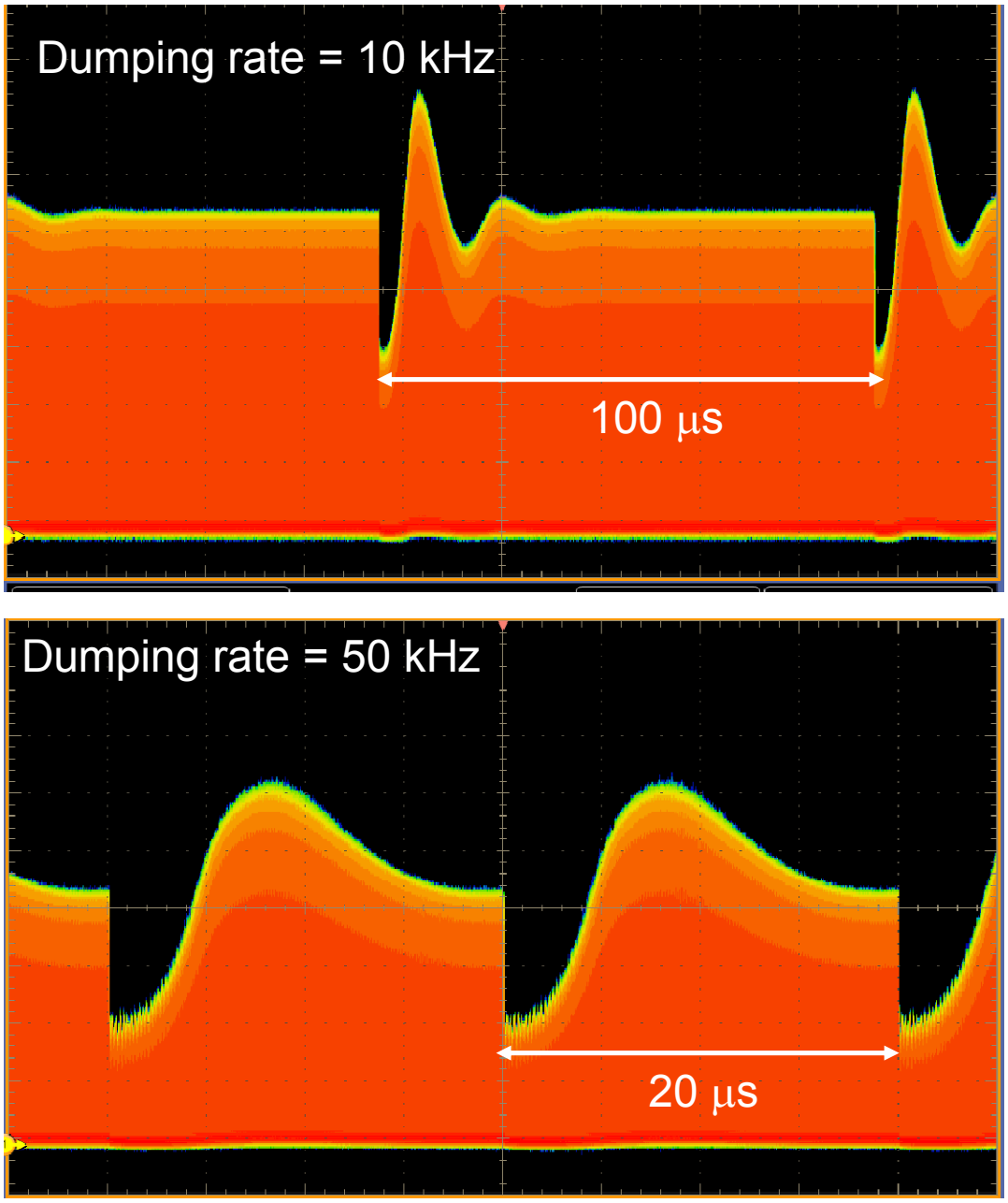

Figure 7.6: Measured dynamics of intracavity pulse train at dumping rates of 10 and 50 kHz.

Table 7.1 summarizes the cavity dumping performance of the Cr:LiSAF laser. For repetition rates up to 50 kHz, dumping efficiencies of ~50%, and pulse energies of ~100 nJ could be obtained repeatedly and the dumping had very little effect on laser dynamics. The contrast ratio between the dumped output pulses and the neighboring pulses was >20:1 (Fig. 7.5). The highest pulse energy was 112 nJ, obtained at a repetition rate of 10 kHz. For this case, the pulse duration was ~120 fs, corresponding to a peak power of 930 kW. Figure 7.6 shows examples of the measured intracavity pulse train dynamics for dumping rates

of 10 and 50 kHz. In both cases, the dumping event generates fluctuations in intracavity pulse energy; however, the laser remains stable in the cw mode-locked regime. Dumping at 10 kHz shows that the interplay between the population inversion and intracavity pulse energy first produces an overshoot of intracavity pulse energy which then relaxes back to steady state within ~30 μs. At 50 kHz dumping rate (and above), the next dumping event occurs before the transient has relaxed. This transient is related to the relaxation oscillation resonance and Q-switching instabilities and limits the pulse energy that can be extracted.

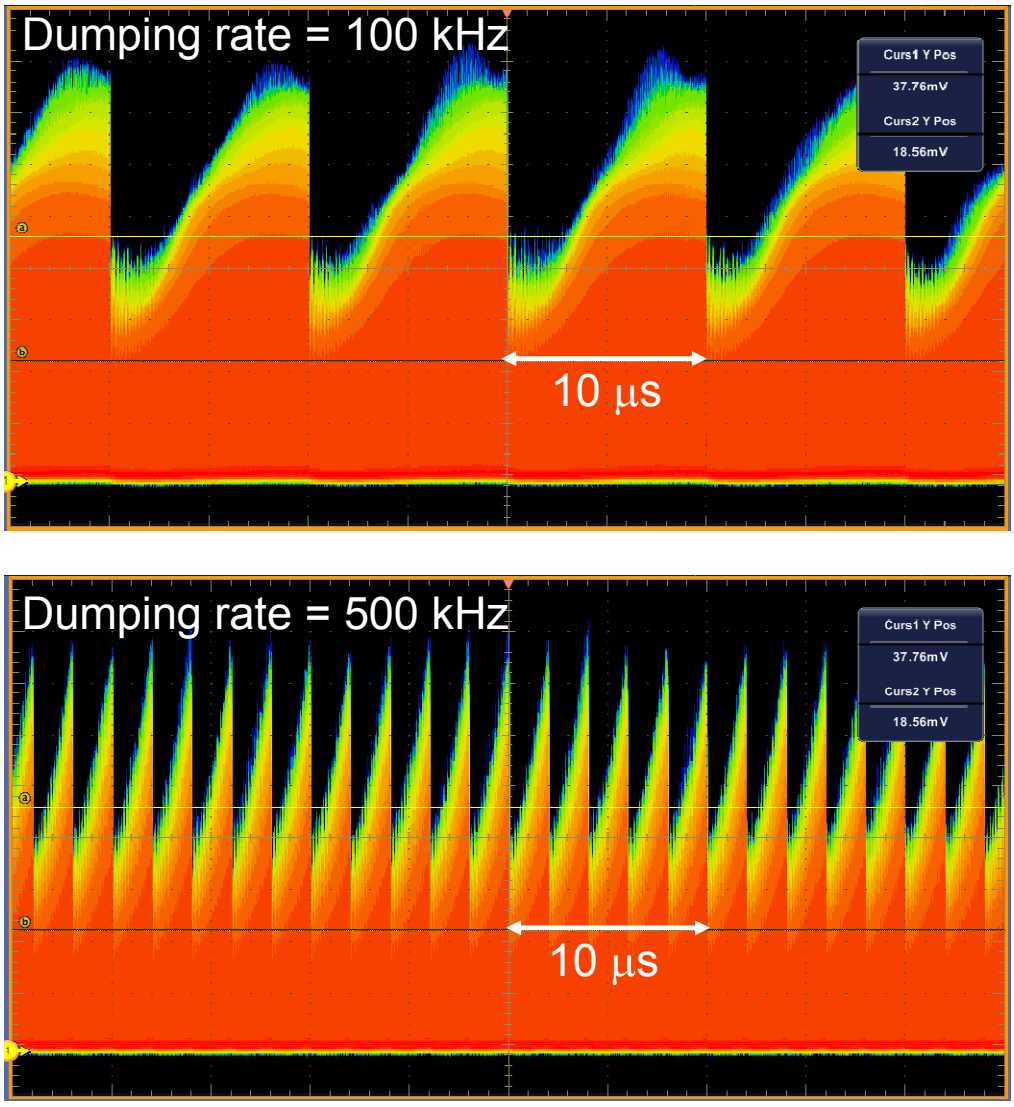

Figure 7.7: Instability in the pulse formation dynamics, which is caused by applying a high dumping ratio. The figure shows the measured dynamics of intracavity pulse train at dumping rates of 100 kHz and 500 kHz. By decreasing the applied RF power to the cavity dumper (dumping efficiency), it was possible to obtain stable intracavity pulse formation dynamics and also a stable dumped pulse train (Fig. 7.8).

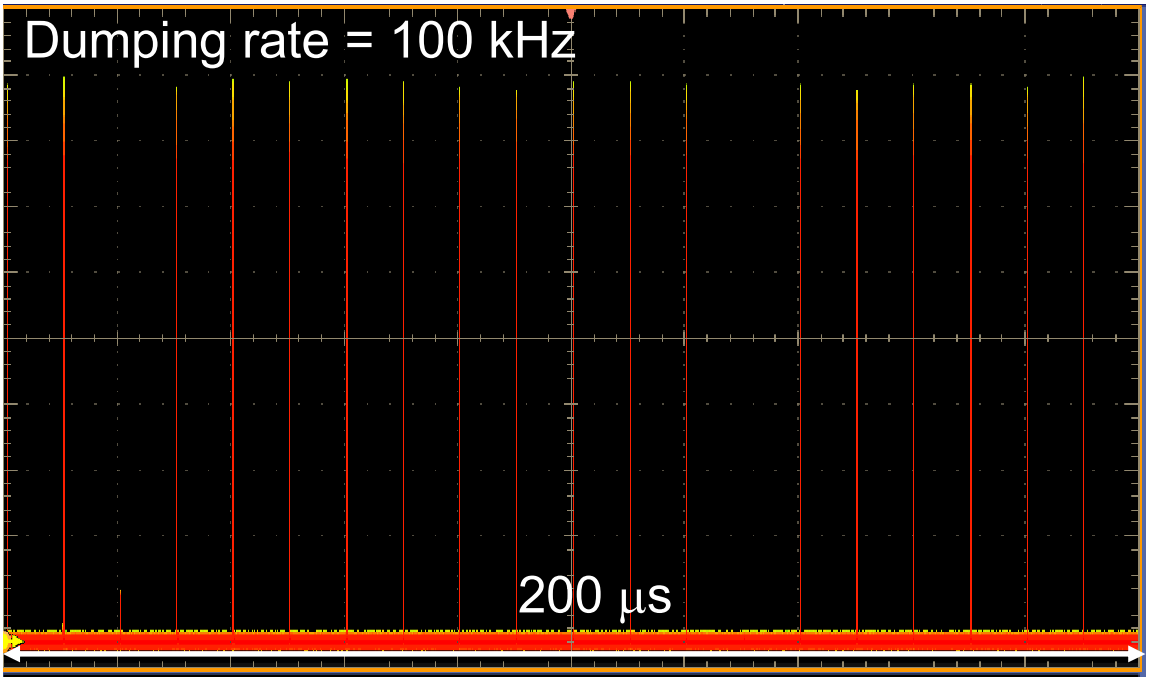

Figure 7.8: Stable dumped pulse train at a repetition rate of 100 kHz.

For dumping repetition rates above 50 kHz, extracting ~50% of the intracavity pulse energy caused shot-to-shot instability in pulse energy and duration of the dumped pulse train due to q-switching instabilities (Fig. 7.7). Hence, for dumping rates above 50 kHz, the dumping ratio is decreased in order to obtain a stable dumped pulse train (pulse energy fluctuation of about ±2-3%). For example, at 100 kHz dumping rate, pulse energies of 110 nJ could be obtained at a dumping efficiency of 55%; however, the dumped pulse train had pulse-to-pulse instability. Obtaining a stable pulse train required reducing the dumping efficiency to 44%, resulting in 87 nJ pulses (Fig. 7.8). Moreover, for dumping rates above 200 kHz, the pulse duration and spectrum also start to change considerably because the dumping event is frequent enough to significantly change the intracavity laser dynamics. For example, at 1 MHz, only 62 nJ pulses with an increased pulse duration of 144 fs and an average output power of 62 mW could be generated. Figure 7.9 and 7.10 shows the measured spectra and autocorrelation at several different dumping frequencies, where the trace labeled with “dumper off” shows the laser output without cavity dumping.

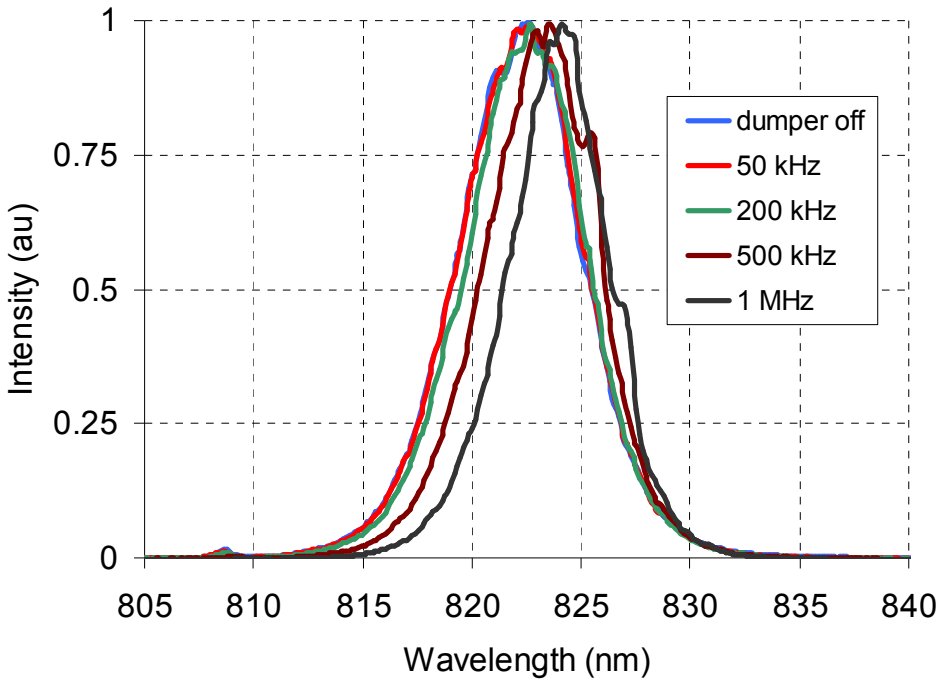

Figure 7.9: Measured optical spectra from the cavity dumped Cr^{3+}:LiSAF at several dumping rates. "Dumper off" shows output without cavity dumping.

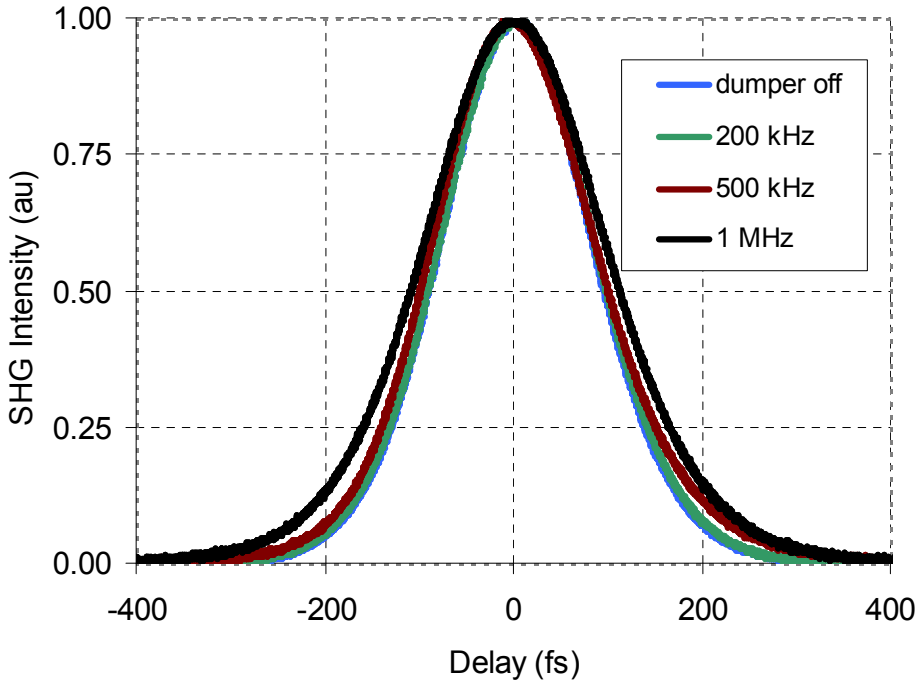

Figure 7.10: Measured second harmonic autocorrelation traces from the cavity dumped Cr^{3+}:LiSAF at several dumping rates. "Dumper off" shows output without cavity dumping.

The pulse durations (~120 fs) which could be generated were limited by the working range of the SESAM/SBR where the intensity is sufficient to produce absorption saturation, but not high enough to produce parasitic two-photon absorption. When we tried to shorten the pulses below ~120 fs, pulse breakup and multiple pulse instabilities occurred due to the high incident instantaneous intensities on the saturable absorber. In principle it is possible to reduce the pulse break up instabilities of the saturable absorber mirror by increasing the focused spot size. However, this increases the Q-switching tendency, which limits the usable dumping efficiencies (pulse energies) at high repetition rates [270]. It might be possible to improve pulse durations and energies by designing a saturable absorber mirror with a larger working range, or by operating in the positive dispersion regime to reduce peak intensities.

In summary, we have presented what is to our knowledge the first demonstration of cavity dumping of a Cr:Colquiriite laser. Pulse energies as high as ~112 nJ, and peak powers up to ~930 kW have been achieved. The peak powers are sufficient to enable a wide range of experiments such as white-light generation, micromachining, deep multiphoton microscopy imaging and others.

CHAPTER 8

MULTIPHOTON MICROSCOPY WITH A LOW COST CR:LICAF LASER

Multi-photon microscopy (MPM) is a powerful tool for biomedical imaging, enabling molecular contrast and integrated structural and functional imaging on the cellular and subcellular level. However, the cost and complexity of femtosecond laser sources that are required in MPM are significant hurdles to widespread adoption of this important imaging modality. In this chapter, we will describe femtosecond diode pumped Cr:LiCAF laser technology as a low cost alternative to femtosecond Ti:Sapphire lasers for MPM. Representative examples of MPM imaging in neuroscience, immunology, endocrinology and cancer research using Cr:LiCAF laser technology will be presented. This study demonstrates the potential of this laser source for use in a broad range of MPM applications.

8.1 Introduction

Multiphoton microscopy (MPM), also known as multiphoton excitation fluorescence microscopy, is a kind of optical sectioning fluorescence microscopy [274], and along with confocal microscopy, it is now one of the most powerful imaging modalities in biomedical microscopy. MPM enables 4-dimensional (x-y-z-t, [275]) high-resolution deep imaging of biological samples with minimal damage to the sample[141, 275-278], and hence facilitates imaging of both intact tissue and live animals. Nowadays, MPM is widely used in several diverse areas of biology such as neuroscience, immunology, embryology and cancer research [276]. MPM use nonlinear effects such as two/three photon excitation and second/third harmonic generation [276] to excite the sample, which enables 3-dimentional optical sectioning (3-D localized excitation [276]) by preventing out-of-focus excitation [274]. It is this nonlinear excitations scheme that provides an advantage to MPM compared to traditional (linear) microscopy techniques such as confocal microscopy. The main advantages of MPM compared to linear microscopy are: (i) less amount of photodamage to the sample (polymerization, temperature effects) [275, 278, 279], (ii) possibility of deep tissue imaging [278], and (iii) higher resolution in scattering tissue [276].

Choosing an optimum laser source is very critical for MPM, since parameters of the laser source, such as average power, pulsewidth, repetition rate, i.e., affect the quality of the obtained image directly. To understand this, we can look at MPM using two-photon excitation (TPE) as an example. TPE excitation is the most widely used nonlinearity in MPM, due to the availability of suitable laser sources. Unless otherwise stated, in this paper we will mostly focus on TPE microscopy. In addition to two-photon

fluorescence excitation [275, 276, 278, 280-284], which is the most commonly used in MPM, other nonlinear processes have been applied for imaging including: second harmonic generation (SHG) [285-291], coherent anti-Stokes Raman scattering [292], three-photon fluorescence excitation (3PE) [293-296] and third harmonic generation (THG) [297-301].

One of the factors determining the quality of the obtained MPM images is the strength of the fluorescence signal. Upon TPE, the time averaged fluorescence signal strength per molecule can be expressed as [302]:

$$\langle I \rangle \cong \delta_2 P_{ave} P_{peak} \left(\frac{NA^2}{hc\lambda_{exc}} \right)^2 \cong \delta_2 \eta \frac{P_{ave}{}^2}{\tau_p f} \left(\frac{NA^2}{hc\lambda_{exc}} \right)^2, \tag{8.1}$$

where h is Planck's constant, c is speed of light, λ_{exc} is the excitation wavelength, δ_2 is the TPE cross section of the fluorescent dye molecule (fluorophore) at λ_{exc}, η is the quantum yield of the fluorophore at the emission wavelength, NA is the numerical aperture of microscope objective, P_{ave} (P_{peak}) is the average (peak) laser power on the sample, and τ_p and f are the pulsewidth and the repetition rate of the laser, respectively.

The first restriction on the laser source is on its wavelength. To see any emission signal at all, as a prerequisite, the wavelength of the laser source (λ_{exc}) should lie within the TPE bandwidth of the fluorophore used. TPE bands of the common molecular fluorophores centered mostly in the near infrared region between 700-1000 nm, with typical bandwidths (FWHM) of ~100 nm [275, 303, 304]. We will talk about this issue in much more detail, later in the discussion section.

From the first part of Eq. 8.1, we also see that the obtainable fluorescence intensity is proportional to the product of peak power and average power applied to the sample. Since, the average power you can apply to a sample is limited by factors such as thermal effects, which might cause sample damage; the way to increase the fluorescence signal strength is to increase the peak power of the laser. Hence, a modelocked laser producing fs pulses is the best choice for MPM experiments ($P_{ave} \cong \tau_p P_{peak} f$). Even though Eq. 8.1 suggests the usage of pulses as short as possible, in general pulsewidths of 50-100 fs is the optimal choice for MPM [276, 277]. This is because: (i) for shorter pulses it gets very difficult to precompensate the group delay dispersion (GDD) of the microscope optics, hence a ~10 fs pulse might even produce weaker fluoresce signal than a 100 fs pulse without proper dispersion precompensation [305], (ii) as the pulsewidth gets very short, the spectrum of the pulse might become wider than the absorption band of the fluorophore, which would decrease the absorption level, and (iii) in general a ~10 fs laser is much more expensive and hard to operate than a ~100 fs laser.

The other important laser parameter for MPM is the repetition rate of the laser source. A high repetition rate laser is beneficial since it lowers the required scan time. However, most of the fluorophore dyes used in MPM has an upper state lifetime of about 5 ns, and for very high repetition rates (f>200 MHz), absorption saturation would limit the obtainable signal strengths [274]. In general a repetition rate of around 100 MHz is an optimum choice for MPM applications [274, 275, 302], and for historical reasons most of the systems use a repetition rate of 80 MHz. For a laser producing 50-100 fs pulses, at a repetition rate of around 100 MHz, an average power level of 200 mW would be enough for most of the applications areas of MPM [275, 302].

Main Source	Additional Elements	Wavelength coverage (nm)	Peak power (kW)	Average output power (W)	Pulse width (fs)	Repetition rate (MHz)	Reference
Ti:Sapphire		680-1080	~300	~3	~100	80	[306, 307]
		~800	~300	0.3	~12	75	[308]
	OPO & SHG	550-2250	~8-80	0.2-2	<~300	80	[309, 310]
Yb systems		~1050	~150	3	<250	76	[311]
Nd systems		~1050	~40	>0.4	150-200	70-150	[312]
	PCF & SHG	546-687	9.4	0.053	~100	120	[313, 314]
	OPO	1450-1630	2.4	0.13	450	120	[315]
Diode laser	amplifier	980		0.035	3500	10	[304]
		783	0.105	0.273	5200	500	[316]
	SHG & amplifier	770	1.1	0.005	5000	1	[317]
	SHG & PCF & amplifier	1030	1.1	0.1	7000	10	[318]
		920	0.25	0.25	1000	50	
Cr:LiSAF		860	~3.25	0.044	90	150	[201]
			~3.75	0.03	100-200	80	[319]
Cr:LiCAF		800	~25	0.18	70	100	*

Table 8.1: Representative list of laser sources that have been used for multiphoton microscopy. *Denotes the Cr:LiCAF laser that will be described in this work.

Table 8.1 is a representative list of laser sources that have been used for MPM. During its early stages of progress, MPM imaging had been done using colliding pulse dye lasers [274, 276, 320], which was the only source at these times that could generate sub-ps pulses with sufficient peak powers, at repetition rates of around 100 MHz [274]. However, due to the complexity and maintenance issues [141, 276], dye lasers are far away from being an ideal reliable source for MPM.

The first breakthrough of MPM had happened with the development of Ti:Sapphire lasers, which are more practical and user friendly compared to dye lasers [276, 321]. Ti:Sapphire lasers could generate pulses with hundred kW's of peak power, and they are broadly tunable (680 to 1080 nm) [306-310]. The tunability range could be further extended to the visible and mid-infrared regions with the help of optical nonlinear schemes such as optical parametric oscillators (OPOs), photonic crystal fibers (PCFs) and second harmonic generation (SHG) [309, 310]. Today's commercial MPM systems use fully automated

Ti:Sapphire lasers as the excitation source, where the user adjusts the central wavelength and average power of the laser using a computer easily [306, 307]. The user-friendly Ti:Sapphire laser technology has enabled the current (relatively) wide-spread use of MPM. However, Ti:Sapphire lasers has also some drawbacks. The main disadvantage of femtosecond technology based on Ti:Sapphire is its high cost. Ti:Sapphire gain media requires pumping at the green region of the spectrum. Unfortunately, at this region of the spectrum, direct diode pumping is not available and currently available pump sources use the second harmonic generated by the diode pumped Nd doped systems. These Nd based systems are bulky and a standard pump laser cost in the $50-100k range, making the overall cost of the Ti:Sapphire lasers and the MPM systems quite high. This high cost of the MPM systems sets a barrier to new researchers who wants to enter this field, and limits the wide-spread use of MPM technology [276].

Besides the popular (but expensive) Ti:Sapphire laser, several other laser sources have been demonstrated to be useful for multiphoton microscopy. One alternative is using Neodymium or Ytterbium based systems that could provide ~200 fs pulses with ~100 kW of peak power around 1050 nm [274]. The main disadvantage of these rare earth element lasers is their quite narrow emission bandwidth, which prevents tunability. Also ~1050 nm is suitable for excitation of several of the dyes, but most of the frequently used fluorophores had a TPE band around ~800 nm [275], where these sources cant reach directly. However, as with Ti:Sapphire, nonlinear effects could be used to provide tunability to these sources, at the expense of increased complexity and cost [313-315].

One other interesting source for MPM, which could be promising in the long run, is based on diode lasers, which are compact, easy to use and low cost sources. In gain-switched operation, diode lasers could provide ~ps pulses and using external amplifiers peak powers above ~1kW level could be obtained [304, 316-318]. Their repetition rate is easily adjustable by simply changing the driving frequency of the current source, which might be advantageous in some MPM experiments. However, low peak power levels, issues related to amplified-spontaneous-emission and tunability are major drawbacks preventing their effective use in MPM.

In this chapter, we will describe the Cr:LiCAF laser as a promising light source for MPM. Cr:LiCAF belongs to the family of Cr^{3+}-doped colquiriites solid-sate laser gain media, where the most well-known members are: Cr:LiSAF [4, 155, 156, 158, 159, 322], Cr:LiSGaF [323], and Cr:LiCAF [60, 324-326]. Similar to Ti:Sapphire, Cr:Colquiriites have broad emission bandwidths around 800 nm, enabling the generation of pulses as short as ~10-fs [60]. The possibility of developing a low cost and efficient femtosecond technology based on diode pumped Cr:Colquiriites was suggested more than five years ago with the demonstration of battery powered femtosecond operated Cr:LiSAF laser [155, 156, 158, 159]. The main advantage of Cr:Colquirites over Ti:Sapphire is that they can be directly diode-pumped by inexpensive diodes in the red region of the spectrum; hence, the total material costs of an

entire laser system could be below ~$10k [141]. We believe that, with the recent advances, Cr:Colquiriites lasers have the potential to become efficient and low-cost excitation light sources for MPM and could enable wide-spread use of MPM technology, by reducing cost.

Cr:Colquiriite lasers have previously been demonstrated for MPM imaging (Table 8.1) [201, 319]. Using an 500-mW master oscillator power amplifier (SDL, Inc.) with a diffraction limited beam as the pump source, Svoboda et al. developed a Cr:LiSAF laser producing 90-fs pulses with 0.3 nJ pulse energy at ~860 nm and a repetition rate of 150-MHz for MPM [201]. However, this pump source is very expensive and the available peak power from the laser was below 5 kW, limiting deep tissue imagining in scattering media. A multimode diode pumped Cr:LiSAF laser with similar specifications of 100-200 fs pulse duration, 0.375 nJ pulse energy at 80 MHz repetition rate was also used to demonstrate MPM imaging; however, peak powers were limited [319].

8.2 Cr:LiCAF Laser Source

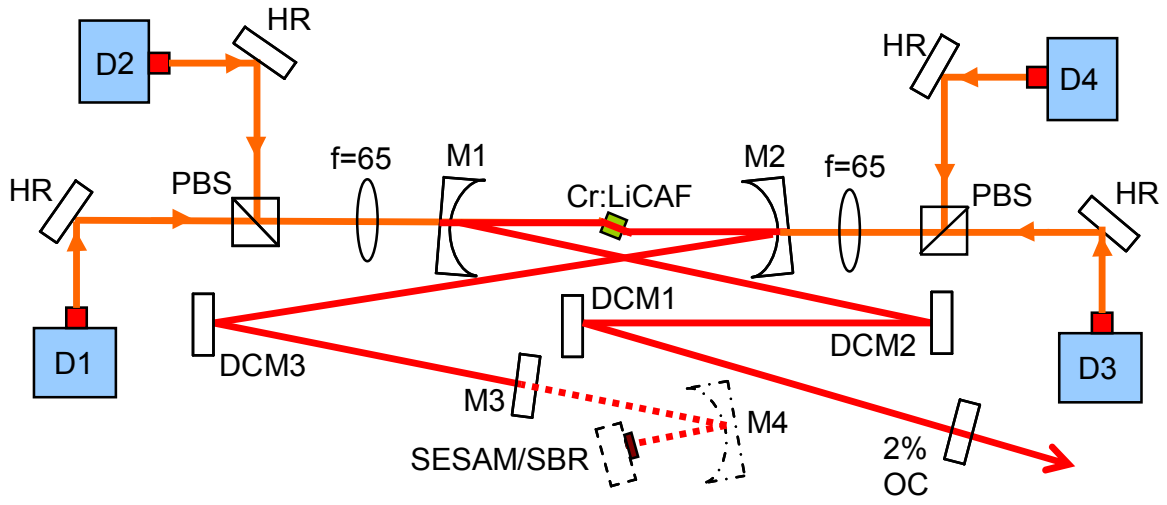

Figure 8.1: Schematic of the single-mode diode-pumped Cr^{3+}:LiCAF laser used in multi-photon microscopy experiments. D1-D4: Single-mode pump diodes at 660 nm, HR: 45° high reflectors at 660 nm, f: visible achromatic doublets with a focal length of 65 mm, PBS: polarizing beam splitter cube, M1-M2: pump mirrors with R= 75 mm, M3: flat high reflector, M4: curved high reflector with R=150 mm, OC: 2% output coupler, DCM1-DCM3: flat double-chirped mirrors with ~-50 fs^2 dispersion per bounce, SESAM/SBR: semiconductor saturable absorber mirror / saturable Bragg reflector. Dashed lines indicate the mode-locked laser cavity.

Figure 8.1 shows a schematic of the single-mode diode-pumped Cr^{3+}:LiCAF laser used in these multi-photon microscopy experiments. The laser is similar to the mode-locked Cr:LiCAF lasers that we have described in Chapter 3. The total round trip cavity GVD was about ~-100 fs^2. The MIT 800 nm SESAM/SBR with quantum well absorber and layers of HR coating (MIT-800-QW-2HR) initiated and sustained mode locking, but the pulse shaping occurred mainly by a soliton pulse-shaping mechanism. When mode locked, the laser produced 70-fs pulses (assuming $sech^2$ pulses) with 180 mW average power

and 10.2 nm spectral bandwidth near 800 nm at 100 MHz (~1.8-nJ pulse energy) (Fig. 8.3). The corresponding peak powers were as high as 25 kW. The time bandwidth product was ~0.335, close to the transform limit of 0.315 for $sech^2$ pulses. The demonstrated electrical-to-optical conversion efficiency of the laser was close to ~8%.

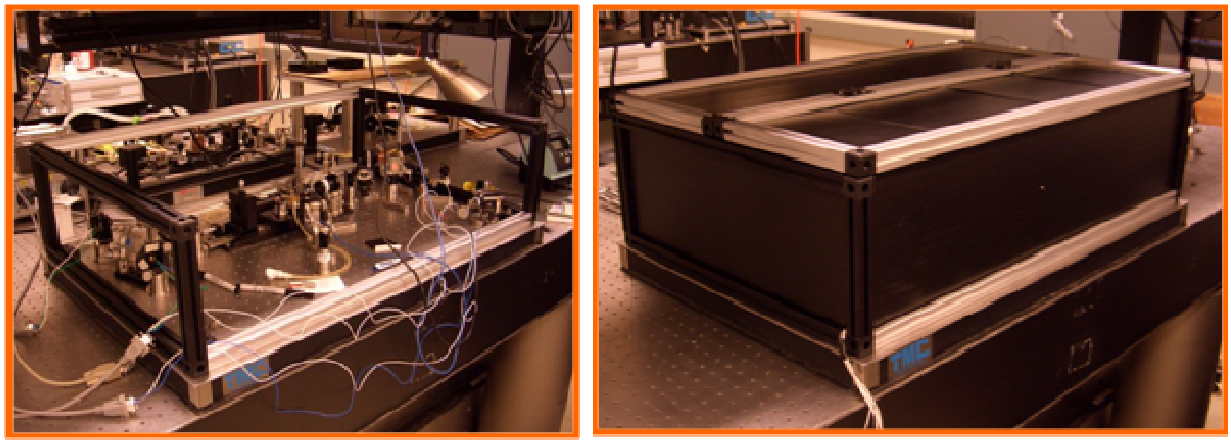

Figure 8.2: Picture of the Cr:LiCAF laser that is used in MPM experiments.

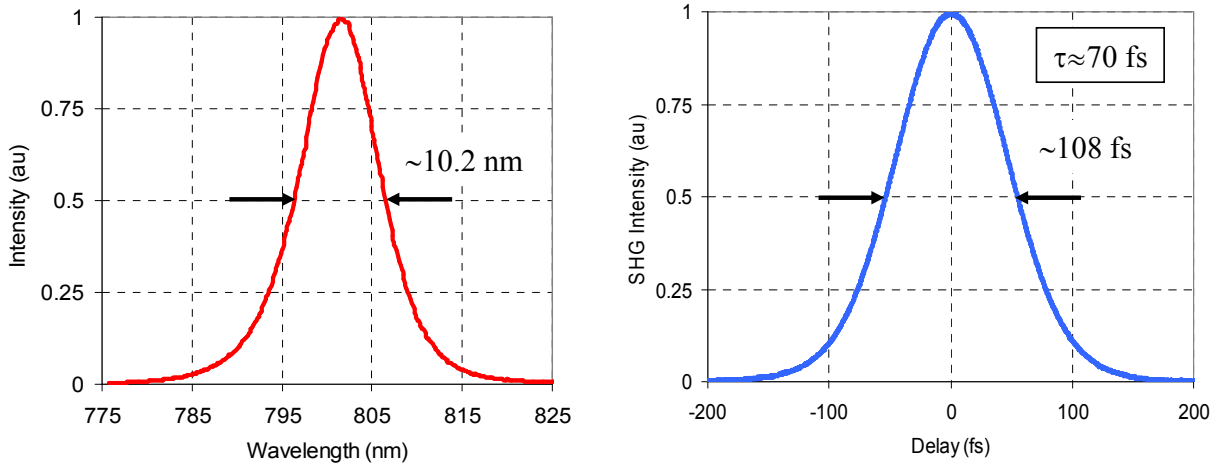

Figure 8.3: Measured spectrum and second harmonic autocorrelation taken with the single-mode diode-pumped mode locked Cr^{3+}:LiCAF laser using the 2% output coupler at an absorbed pump power of ~600 mW. The FWHM of the autocorrelation is 108 fs, corresponding to a 70-fs pulse duration (assuming $sech^2$ pulse shape). The average output power is 180 mW, corresponding to a pulse energy of 1.8 nJ for the 100-MHz repetition rate cavity. The spectrum has a bandwidth of 10.2 nm (FWHM) centered around ~800 nm. The corresponding time bandwidth product is ~0.335.

The Cr:LiCAF laser has a simple layout, uses commercial optomechanics (except the SESAM/SBR), and the total material cost of the entire laser system could be reduced below ~$10k. The laser has also a low maintenance cost compared with traditional frequency doubled pump lasers [274] and very low

electrical consumption. Moreover, the laser does not require water cooling and the diodes can be powered by batteries [156, 158]; hence, the laser can be made compact and portable. Lastly, due to SBR/SESAM-initiated mode locking the laser is quite stable, thus enabling long-term use in a laboratory environment.

8.3 Multi-photon microscopy setup

Multiphoton imaging experiments were performed using a commercial two-photon microscope, where we have replaced the regular Ti:Sapphire laser with the Cr:LiCAF laser (Ultima, Prairie Technologies, Inc.). Epi-illumination configuration was used for excitation, and the excitation beam was scanned in the xy plane, perpendicular to the optical axis z, by a pair of conventional galvanometer-based scanners. A motorized stage was used to fine position the microscope objective along the optical axis. The emission signal from the sample was reflected by a high-pass dichroic mirror positioned close to the back aperture of the objective and detected by a four-channel detector. At the entrance of the four-channel detector the emission signal was split into two arms, and each arm contained a filter cube and a pair of photomultiplier tubes (PMTs). The output signal current from the PMTs was amplified and the signal digitized by a 12-bit analog-to-digital converter (ADC) at 2.5×10^6 samples/sec. While generating the multiphoton microscopy image, the intensity for each pixel of the image frame was calculated by summing all of the ADC samples obtained during the pixel dwell time. For image processing, a 3x3x3 median filter and histogram equalization was used.

The total transmission of the system through the microscope together with the Olympus LUMPlanFI/IR 40X WI objective (NA = 0.8; working distance = 3.3; water immersion) was around 20% for 800-nm laser light. This relatively low efficiency of the system was mostly due to a pair of additional dichroic mirrors in our Ultima microscope setup, and additional losses because of sub-optimal beam diameter. To adjust the optical power on the imaged sample, a continuously variable optical neutral density filter was used, which was placed after the laser output coupler. Pulses from the laser were dispersion pre-compensated by using four SF10 prisms, to cancel the pulse broadening effects by the microscope optics. By introduction a group velocity dispersion (GVD) of about -8000 fs^2, we could keep the pulsewidths on the sample around ~100 fs.

8.4. Representative MPM images taken with Cr:LiCAF Laser

8.4.1 Imaging of the cortical vasculature and blood flow

One of the important application areas of MPM is imaging of highly scattering brain tissue [283, 327-329]. The fluorescence signal intensity that can be generated within the focal volume decays exponentially with imaging depth z and is approximately proportional to $\exp(-2z/l_s)$, where l_s is the optical scattering mean free path [278, 329-331]. The maximum imaging depth one can get in an optically turbid

media is a complex function of the optical properties of the sample, the excitation light, and the detection system, and is ultimately limited by fluorescence generated near the sample surface [331]. It is possible to penetrate up to 1 mm of depth into the neocortex, by reducing the pulse repetition rate fo the laser while keeping the average laser power constant [332, 333]. However, at depths beyond 600 μm background fluorescence signal becomes significant and resolution may be severely degraded due to spherical aberrations, unless adaptive optics compensation methods are used [334-337]. Hence, technical difficulties related to the availability of optical excitation sources, increased background fluorescence and loss of resolution, limits most brain imaging applications of MPM to a depth of ~600 μm [283, 338, 339]. To achieve these imaging depths, typically 180-250 mW of the optical power was presented on the sample surface [329, 330, 340, 341].

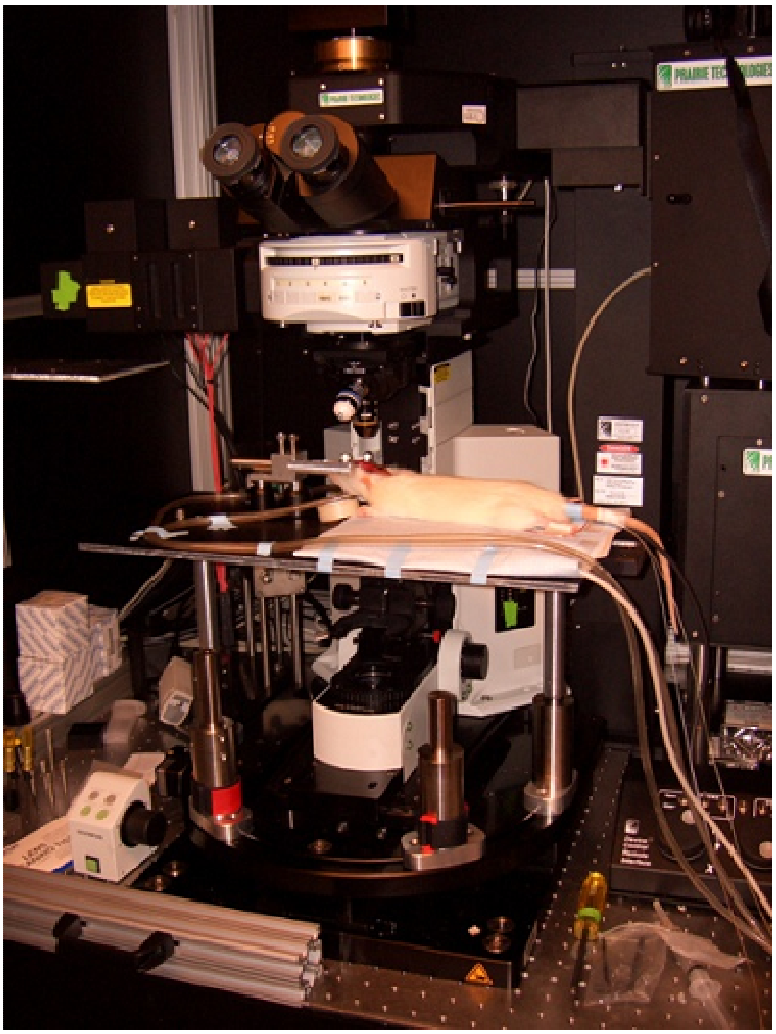

Figure 8.3: Rat animal prepared for brain imaging that is placed under the commercial two-photon microscope.

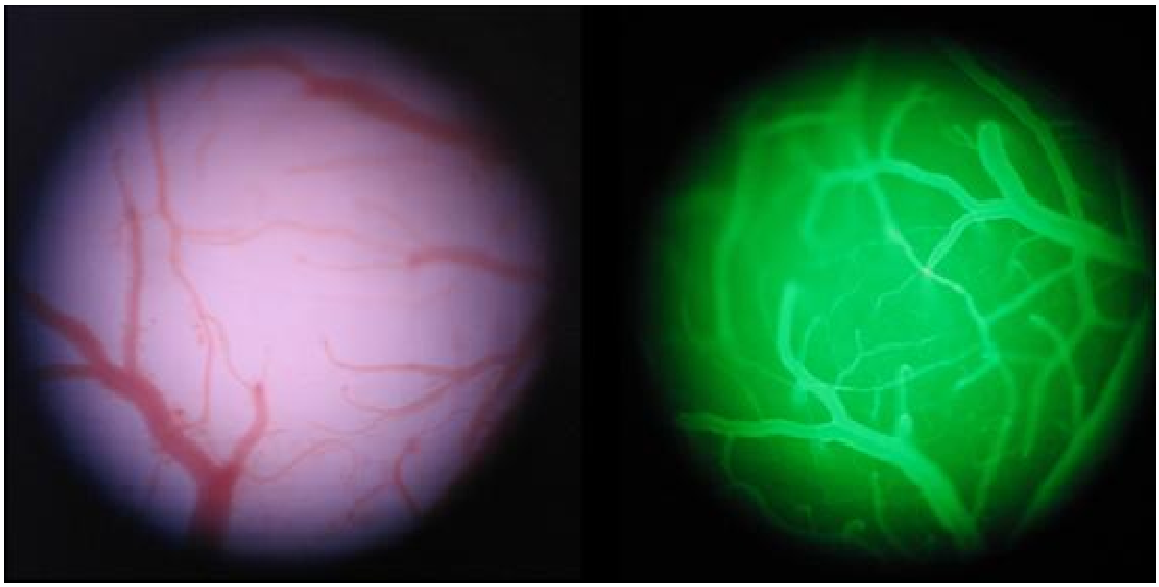

Figure 8.4: (Left) regular microscopy image of the rat brain. (b) Single photon excitation image of the rat brain.

Figure 8.5 (a) shows a maximum intensity projection (MIP) along the z axis of a 250-µm-thick 3D stack of the cortical vasculature labeled with Dextran-conjugated fluorescein (FITC). The imaging was performed using an Olympus UPlanFL 10X objective (NA = 0.3). The 3D stack contains 26 frames acquired with a Δz = 10 µm step over a large, 932 x 932-μm^2 field of view (FOV). Figure 8.5(b) represents the MIP along the z axis of a 400-µm-thick stack of the FITC-labeled cortical vasculature. The position of the stack was marked with the window in Fig. 8.5(a) and contains 400 frames acquired with a Δz = 1 µm step. Imaging was performed using an Olympus LUMPlanFI/IR 40X WI objective. Each frame was averaged four times to improve signal-to-noise ratio (SNR) and to smooth the appearance of gaps due to non-labeled red blood cells. In order to compensate for the loss of SNR with the imaging depth, the excitation light power incident on the sample and the dwell time per pixel were manually adjusted every Δz = 50 µm. For imaging depths below 300 µm, the dwell time per pixel was as high as 4 µs. For depths of 300-350 µm and 350-400 µm, the dwell time was increased to 10-µs and 20-µs per pixel, respectively. The optical power of the excitation light incident on the sample was increased from only several milliwatts when imaging the sample surface, to the maximally available power of 35 mW at the larger sample depths. The relatively small power levels required for imaging at the larger depths, compared to previously reported values [329, 330, 340, 341], could be attributed to the 2-3 times shorter pulse widths used here as well as increased averaging, and possible differences in the design of the detection system. In addition, imaging depth might be reduced by increased absorption from the close proximity of the large vessels, the increase in the scattering coefficient of the brain tissue in older animals, or blood and dye leakage from the vasculature.

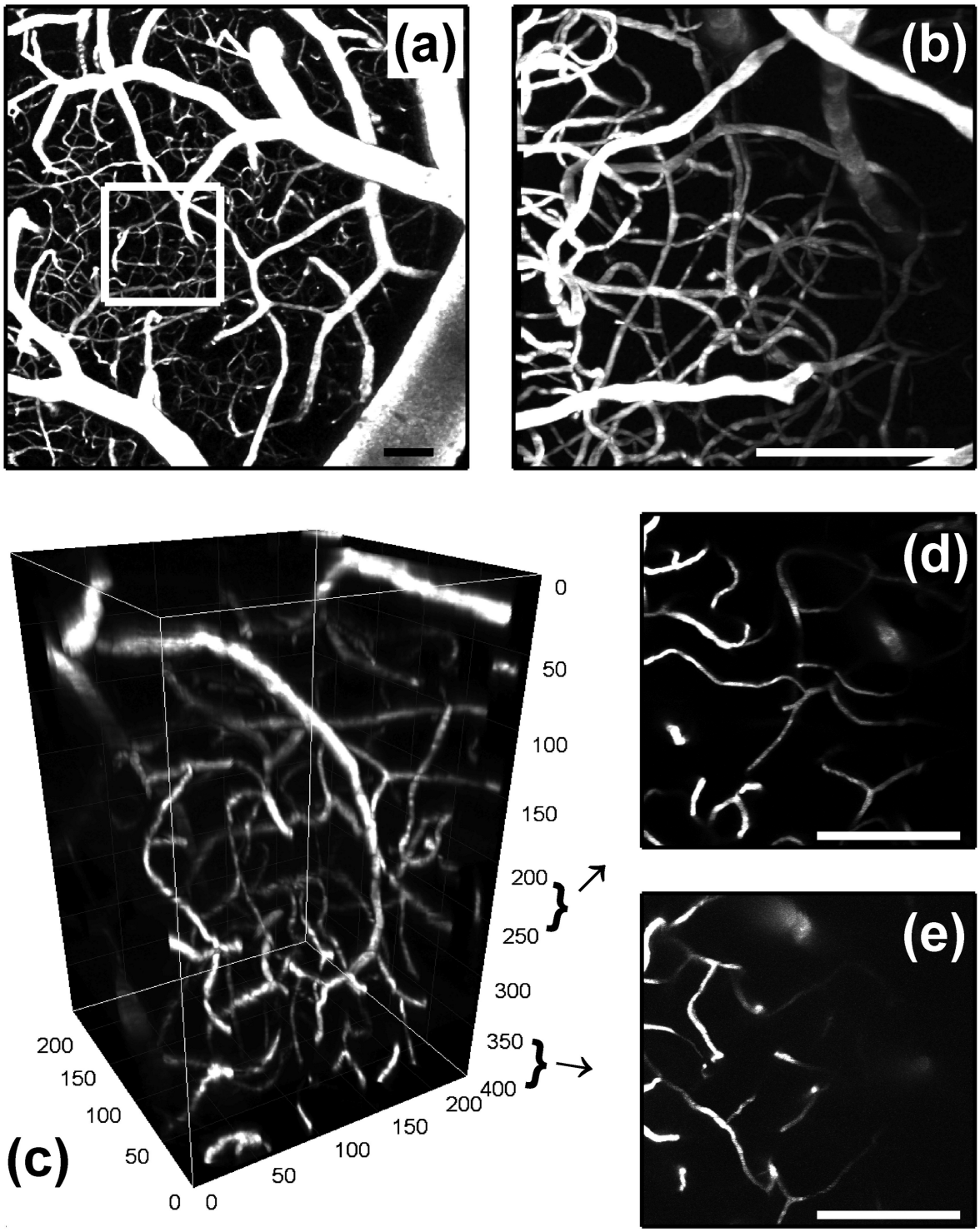

Figure 8.5: Images of cortical vasculature stained with FITC. (a) MIP along the z direction of a 250-µm-thick 3D stack with a 932 x 932 µm^2 FOV. The data set consists of 26 frames acquired at 10-µm increments. (b) MIP along the z direction of a 400-µm-thick 3D stack with a 233 x 233 µm^2 FOV. The lateral (x, y) position of the image is marked with the window in (a). The data set consists of 400 frames acquired at 1-µm increments. The same data set is presented as a volumetric image in (c) and two MIPs along the z direction of 50-µm-thick regions are presented at depths of 200 µm and 350 µm in (d) and (e), respectively (Media 1). Scale bar is 100 µm.

The volumetric image of the whole 3D stack, spanning 233 x 233 x 400 μm^3, was created using a software package, Imaris (Bitplane AG), and is shown in Fig. 8.5(c). Figures 8.5(d) and 8.5(e) show the MIPs of 50-μm-thick regions at depths of 200 μm and 350 μm, respectively.

One important application of 2PM in brain imaging is the measurement of red blood cell (RBC) velocity [329]. The arrow in Fig. 8.6(a) shows the location of the velocity measurement 120 μm below the sample surface. We performed 1000 line scans along the vessel axis [Fig. 8.6(b)] with a line scan speed of 16.08 μm/ms and a line scan period of 1.49 ms. Imaging was performed using the Olympus LUMPlanFI/IR 40X WI objective. The dark bands in Fig. 8.6(b) were produced by the moving red blood cells. Blood cells appear as the dark spots in the two-photon microscopy images because they are not labeled with the dye. From the slope of the dark bands in Fig. 8.6(b), the RBC velocity is estimated as 0.6 mm/s.

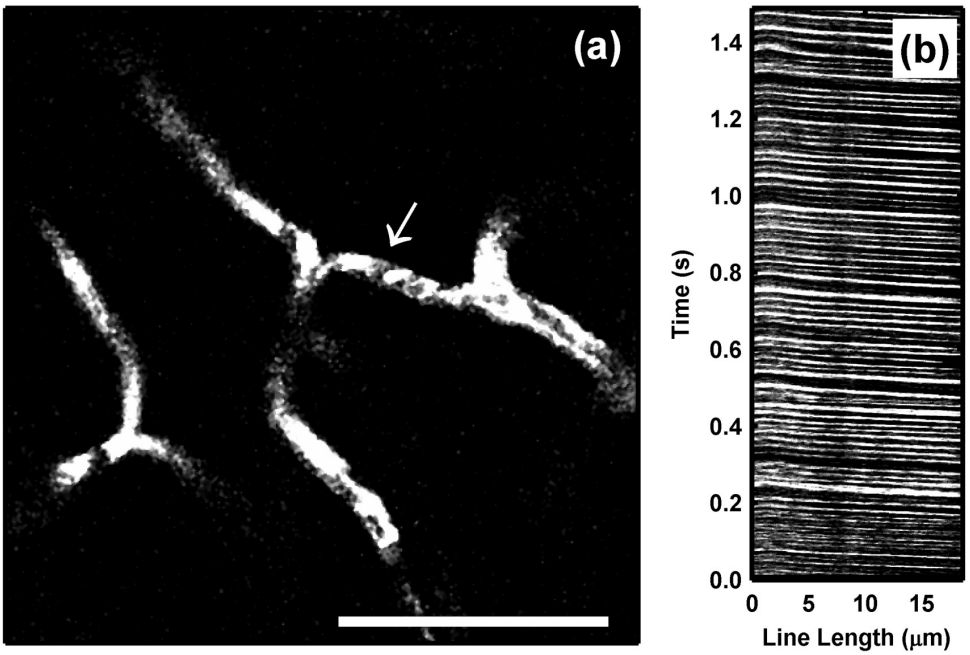

Fig. 8.6: Measurement of the RBC flow. (a) Two-dimensional image of the cortical vasculature labeled with FITC, with the white arrow marking the position of the line scan. The scale bar is 50 μm. (b) The intensity plot of 1000 line scans taken along the axis of the blood vessel during 1.49 s. The length of the individual line scan is 18.69 μm. The estimated RBC velocity is 0.6 mm/s.

A very exciting characteristic of the Cr:LiCAF laser, with respect to MPM, is the possibility of changing the laser operating regime from mode-locking to Q-switched mode-locking by simply playing with the SESAM/SBR position (see Chapter 3 for a more detailed discussion). It is well known that significant improvements in SNR and imaging depth in MPM can be achieved by reducing the pulse repetition rate while keeping the average power constant [332, 333]. By using the regenerative amplifier an imaging depth of 1 mm into the highly scattering brain tissue was obtained with the average power of

only 45 mW at a repetition rate of 200 kHz [332]. In the Q-switching regime our Cr:LiCAF laser provides 150 mW of average power at a 50-kHz repetition rate. During the 20-μs period the laser produces a 3-μs (full-width half-maximum) burst of the intense pulses. The repetition rate of the pulses within the burst is 100 MHz and the maximum energy is ~25.5 nJ, or ~15 times higher than in a mode-locking regime. Ideally, this would correspond to a 225-fold higher 2P excitation efficiency for the maximum energy pulses in the Q-switching regime than for those in the mode-locking regime, assuming equal pulse widths. However, when the Cr:LiCAF laser works in Q-switched mode-locked regime, the pulses are only shaped by SESAM/SBR (without significant contribution from soliton pulse shaping mechanism), and the mode-locked pulses are ~3-5 ps long.. When using a 20-μs pixel dwell time, we observed in the Q-switching regime a two-fold decrease in the signal strength, with respect to the mode-locking regime. This also suggests a several-picoseconds-wide pulse width in the Q-switching regime.

To demonstrate the application of the Q-switching laser regime to MPM we performed another imaging experiment with the cortical vasculature. Figure 8.7(a) shows the MIP along the z axis of a 610-μm-thick 3D stack of the FITC-labeled blood plasma. The imaging was performed with the Olympus LUMPlanFI/IR 40X WI objective in the Q-switching regime of the Cr:LiCAF laser. The distance between consecutive frames was $\Delta z = 1$ μm. To obtain equal excitation optical power for each pixel we used the pixel dwell time of 20 μs, which was equal to the period of bursts in the Q-switching regime. Each frame was averaged two times. The excitation light power presented on the sample was manually adjusted from 8 mW, when imaging the sample surface, to the maximally available 30 mW, at sample depths beyond 350 μm. Images lasting the final 60 μm (below the depth of 550 μm) were obtained with an increased number of 16 averages per frame. Figure 8.7(b) shows the MIP of a 60-μm-thick cortical region at a depth of 550 μm; Fig. 8.7(c) is the volumetric image of the whole 3D stack, spanning 233 x 233 x 610 μm^3.

The penetration depth and image quality are better in Fig. 8.7 than in Fig. 8.5, although the fluorescence signal strength at a 20-μs pixel dwell time was lower in the Q-switching regime than in the mode-locking regime. This could be due partially to the different optical properties of the brain tissue of the two animals used in these experiments (scattering and absorption coefficients, vessel density at the particular location). However, the most significant difference was likely the more successful surgical preparation of the animal used to obtain Fig. 8.7.

Another major application area of MPM is imaging of neuronal activity and organization [283]. Figure 8.8 shows examples of structural images of astrocytes and cortical vasculature. Astrocytes are the most abundant macroglial cells in the brain with numerous projections that anchor neurons to their blood supply. Their active role in the brain function is currently the subject of intensive research [342]. Figure 8.8 shows the MIP along the z axis of a 20-μm-thick volumetric image of the neocortex. The blood plasma was labeled with FITC and the astrocytes were labeled with Sulforhodamine 101 (SR101).

Imaging was performed with the Olympus LUMPlanFI/IR 40X WI objective. The distance between consecutive frames was $\Delta z = 1$ μm and the imaging depth was 200 μm. The average excitation optical power on the sample was 20 mW and the pixel dwell time was 4 μs. Each frame was averaged eight times. Numerous processes of astrocytes and their connections with the microvasculature endothelium are clearly visible.

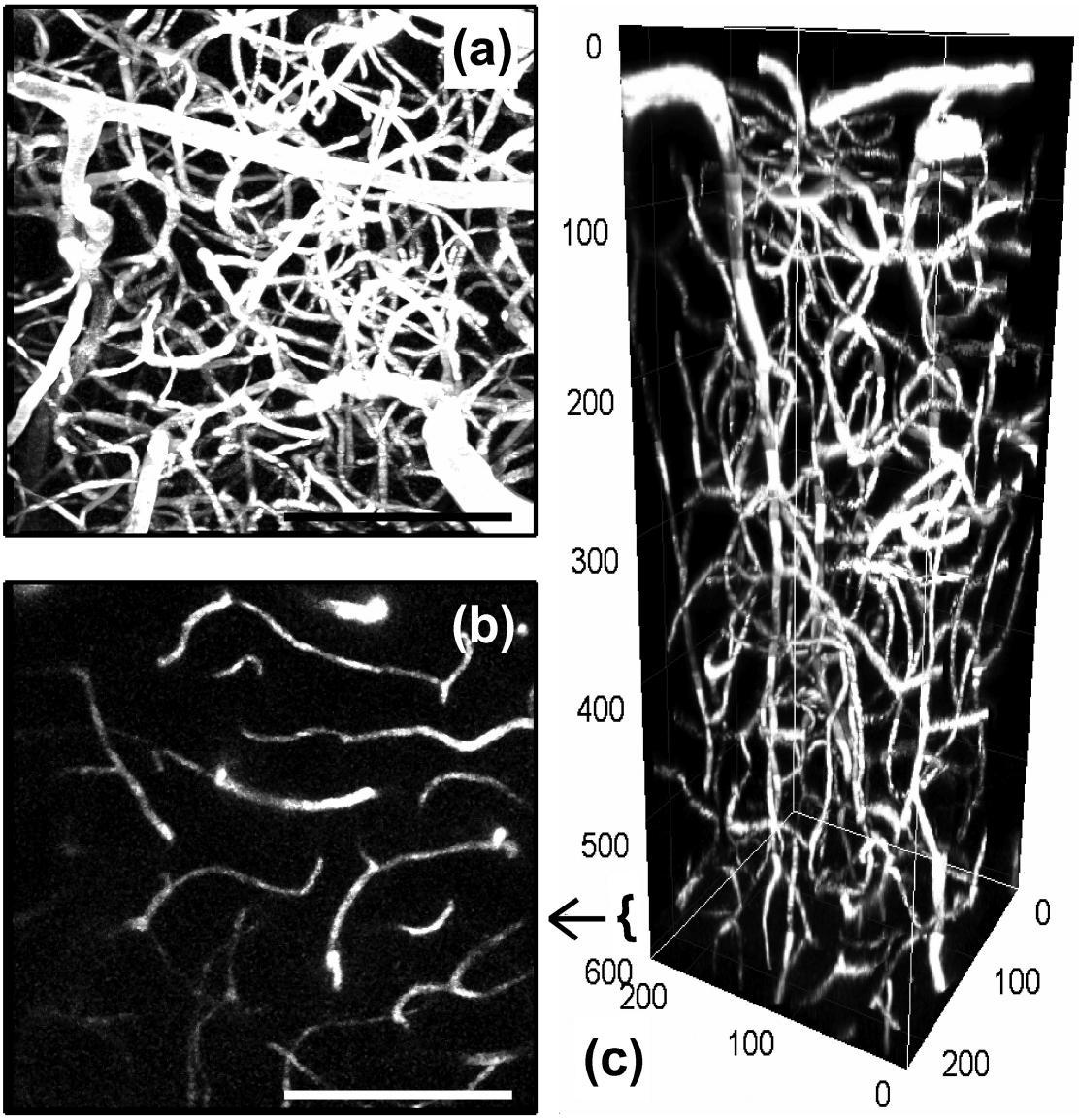

Figure 8.7: Images of cortical vasculature stained with FITC obtained in the Q-switching regime of the Cr:LiCAF laser. (a) MIP along the z direction of a 610-μm-thick 3D stack with a 233 x 233 μm^2 FOV. The data set consists of 610 frames acquired at 1-μm increments. (b) MIP along the z direction of a 60-μm-thick region at a depth of 550 μm. (c) Volumetric image of the whole data set. Scale bar is 100 μm.

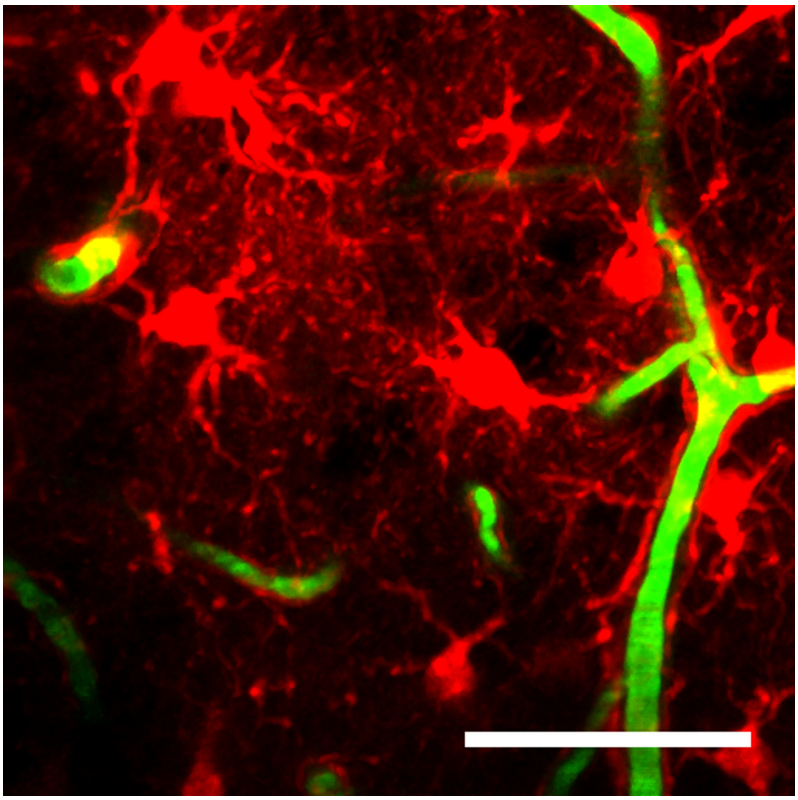

Figure 8.8: MIP of a 20-µm-thick 3D stack image of the neocortex with astrocytes labeled with SR101 (red) and cortical vasculature stained with FITC (green). The data set has a FOV of 233 x 233 μm^2 and it consists of 20 frames acquired at 1-µm increments (Media 2). The imaging depth is 200 µm below the cortical surface. Scale bar is 100 µm.

8.4.2 Imaging of Lymph Nodes

In situ and intravital imaging has become a burgeoning field of immunology and the dynamic behavior of immune cells in lymph nodes has been a primary focus of initial studies[343]. The utility of the Cr:LiCAF laser for MPM intravital microscopy was demonstrated using a representative example. Popliteal lymph nodes were exposed microsurgically and static and time-lapse high-resolution recordings were obtained using an Olympus LUMPFL60X/W IR objective with NA=1.1 (Fig. 8.9). An incident power of 20 mW at the sample surface was sufficient to obtain an excellent signal-to-noise ratio for cells and structural tissue elements at depths of more than 100 µm in the tissue. No signs of photobleaching or phototoxicity were evident during the acquisition of time-lapse recordings.

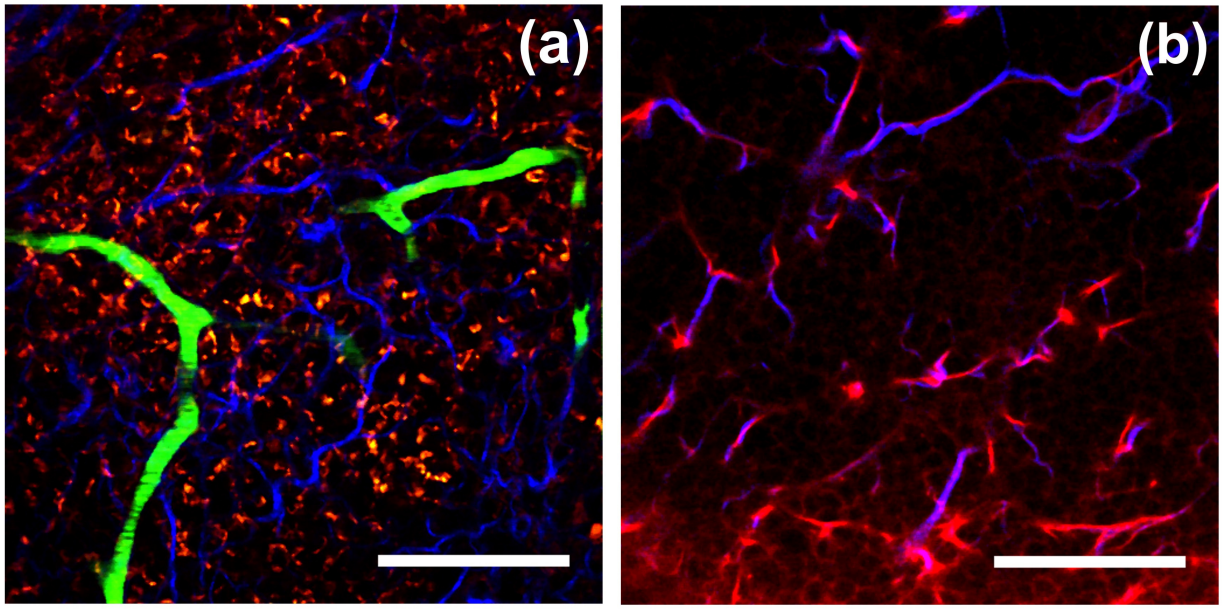

Fig. 8.9: Intravital micrographs of a mouse popliteal lymph node. The image (a) was obtained after intravital staining of mitochondria in lymph node cells though i.v.-injection of Rhodamine 6G (red) and labeling of the blood plasma with FITC (green). SHG signals from reticular collagen fibers are shown in blue. The image (b) shows the lymph node conduit system filled through subcutaneous injection of the low-molecular-weight protein lysozyme tagged with Alexa Fluor 633 (red) into the footpad drained by this lymph node. The conduits accompany the collagen network (blue). Scale bars are 50 µm. The imaging depths are 100-150 µm (a) and 30-75 µm (b).

8.4.3 Imaging of Histological Specimens

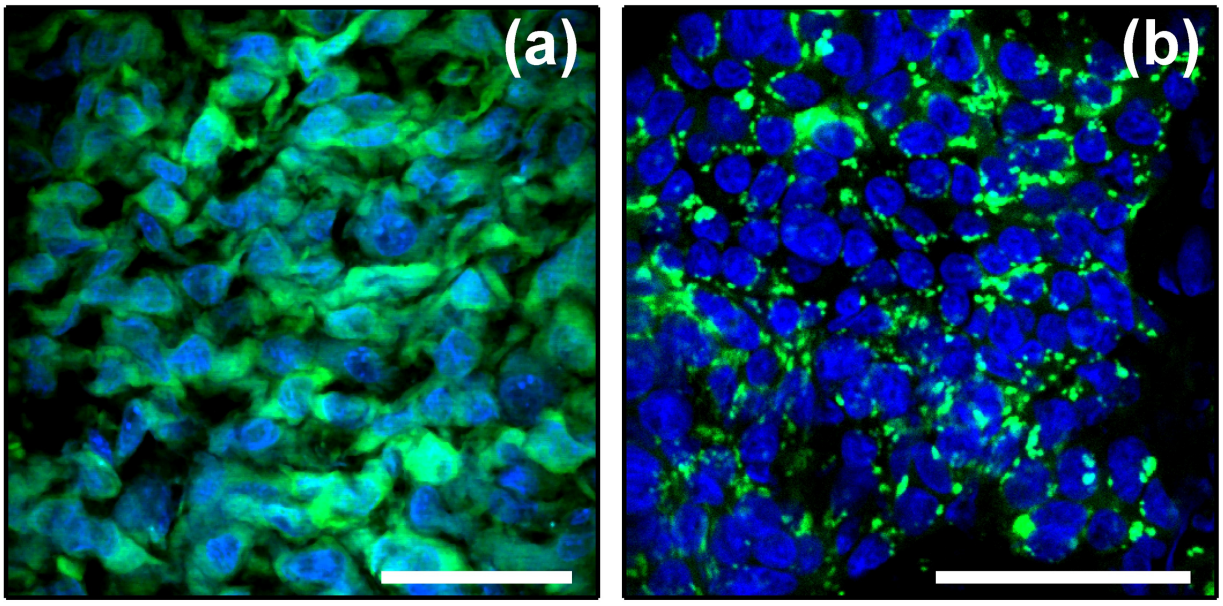

Fig. 8.10: Imaging of the histological specimen. (a) GFP-expressing 9L fliosarcoma tumor. Green color depicts cell cytoplasm stained with GFP. (b) Pancreatic islets with insulin-producing beta cells. Green color represents FITC staining of insulin granules. In both images cell nuclei were stained with DAPI (blue color). Scale bars are 50 µm.

Figure 8.10 presents representative MPM images of histological specimens. Figure 8.10(a) shows GFP-expressing 9L fliosarcoma tumor with readily detectable green cytoplasmic staining depicting green fluorescent protein (GFP). Insulin-producing beta cells in pancreatic islets are clearly recognizable by characteristic punctuate FITC staining of insulin granules [green color, Fig. 8.10(b)]. In both images, blue DAPI staining depicts cell nuclei. Figs. 8.10(a) and 8.10(b) were obtained using Olympus LUMPFL60X/W IR and LUMPlanFI/IR 40X WI objectives, respectively, with 4-μs pixel dwell times.

8.5. Summary and Discussion

These results demonstrate that a femtosecond Cr:LiCAF laser can be successfully used as a light source for multi-photon microscopy. Examples of two-photon and second harmonic generation imaging from several research areas such as neurology, immunology, cancer and diabetes research are presented. The images obtained are of equal quality to previously published MPM data [276, 280, 283, 342]. The average laser power was 180 mW, which should be appropriate for the majority of MPM applications. In our setup, as much as 35 mW average power was available on the sample. This is sufficient for MPM imaging up to several hundreds of micrometers deep into highly scattering brain tissue. However, with additional effort, transmission through the microscope optics could be improved more than twofold. For applications requiring even higher average power levels, it is possible to use Cr:Colquiriite lasers pumped by multimode diodes. A femtosecond Cr:LiCAF laser pumped by broad-stripe single-emitter diodes [143, 344], has the potential to generate average mode locked powers approaching 1 W level (See chapter 3). The drawback of a multimode diode pumped system would be increased complexity and price compared to single-mode diode pumping.

In our imaging experiments the central wavelength of the Cr:LiCAF laser was fixed at ~800 nm. However, the emission bandwidth of the Cr:LiCAF medium is broad enough to provide wavelength tuning from ~750 nm to ~850 nm. In the current setup, tunability was limited because a standard SESAM/SBR with only ~50 nm bandwidth was used for mode locking [325, 326]. However, broadband oxidized saturable absorber mirrors [345, 346], with ~300 nm bandwidth have been developed which would enable the Cr:LiCAF laser to operate across its entire tuning range (See Chapter 4). Oxidized SESAM/SBR technology can be also applied to generate ~10-20 fs pulse durations from Cr:LiCAF laser, which, with proper dispersion compensation, would be beneficial in some MPM experiments.

Although the more expensive Ti:Sapphire femtosecond oscillator, or frequency doubling from optical parametric oscillators (OPO), offers a broader range of wavelengths, the tuning range of the Cr:LiCAF could be sufficient for excitation of most available dyes. Based on the examples provided in this work, and from the available TPE cross sections in the literature [275, 296, 303, 347-354], the major classes of

fluorescent dyes should be efficiently excitable with the Cr:LiCAF laser, including the following: fluorescein-, rhodamine-, and coumarine-based fluorophores; calcium indicators; quantum dots; cyanines (Cy2, Cy5); some fluorescent proteins (wild type GFP, eCFP, eGFP); intrinsic tissue fluorophores (folic acid, riboflavin, retinol); and others. Depending on the dye concentration and the tissue environment, it is also possible to have efficient excitation of the fluorophore even at wavelengths that are further from its TPE cross-section maximum (see, for example, DAPI fluorescence in Fig. 8.10). To reach wavelengths above 850 nm, it is possible to use Cr:LiSAF, another Cr:Colquiriite crystal, which has a tuning range between ~800 nm and ~950 nm (see Chapter 4 for more details). Since the cost of these lasers is low and they can be made compact, it may be possible to build two such lasers in parallel that would cover the entire spectral range from ~750 nm to ~950 nm.

In summary, this study demonstrates that the performance of diode pumped femtosecond Cr:LiCAF lasers are sufficient to enable a wide range of MPM imaging applications which do not require broad excitation wavelength tunability. The use of low cost, single mode pump diodes for Cr:LiCAF lasers enables a significant reduction in cost and complexity compared to femtosecond Ti:Sapphire technology. Multi-photon microscopy is one of the most powerful optical imaging modalities in biomedical research. The development of lower cost femtosecond laser technology promises to be an important step in enabling wider spread use of multi-photon microscopy, accelerating fundamental research in biology and medicine.

CHAPTER 9

TIMING JITTER NOISE CHRACTERIZATION OF CR:LISAF LASER

Accurate measurement of timing jitter noise of optical pulse trains from mode-locked lasers is a challenging task, due to their inherent ultralow noise characteristics. For typical solid-sate mode-locked lasers, theoretical analysis estimates a timing jitter in the attosecond regime at high frequencies (≥ ~10 kHz) [355, 356]; whereas, it is quite challenging to achieve sub-10-fs resolution in a timing jitter measurement. The most common measurement method uses a high-speed photodetector to generate a microwave signal, which is then bandpass filtered at higher harmonics, and a microwave mixer measures the phase noise of the selected harmonic [357]. Although this method is often employed, excess phase noise may be generated in the photodetection process and the measurement accuracy is inherently limited by the resolution of the microwave mixer [358]. Another method for measuring timing jitter noise is interferometric cross correlation [359], which allows higher sensitivity measurements. However, this method has a limited measurement range (less than an optical cycle), making it hard to use for free running mode-locked lasers. Moreover, this method measures optical phase noise rather than the timing jitter noise. Balanced nonlinear optical intensity cross correlation is an all optical domain technique which can precisely measure the timing jitter noise of mode-locked lasers in a simple and direct way [358, 360]. Balanced nonlinear cross correlation has high sensitivity, sufficient detection range, and does not suffer from excess photodetection noise. Furthermore, balanced photodetection of the cross-correlation signal greatly reduces coupling of laser intensity noise to the measured timing jitter.

In this Chapter, we present attosecond resolution timing jitter characterization of femtosecond diode pumped Cr:LiSAF lasers by using a single crystal balanced optical intensity cross correlator. Cr:LiSAF lasers are low-cost, compact, efficient, enable turn-key operation and are expected to show ultra-low timing jitter [59]. Two home-built, diode-pumped, saturable absorber mirror mode-locked, 100 MHz repetition rate Cr:LiSAF lasers, were synchronized using a nonlinear optical cross correlator in a low-bandwidth (~1 kHz) phase-locked loop (PLL) configuration. The resulting timing jitter noise spectral density between the two lasers was observed. Since the two lasers where identically constructed, the timing jitter measured outside the locking bandwidth reflects $\sqrt{2}$ times the timing jitter of an individual laser. The balanced nonlinear optical cross correlator provides a measurement resolution of ~2×10^{-10} fs^2/Hz at 100 kHz (-195 dBc at 1 GHz carrier). The upper limit for the integrated timing jitter of the

Cr:LiSAF lasers was measured to be 137 as in [10 kHz-10 MHz]. To the best of our knowledge, this is the lowest reported value of timing jitter for any mode-locked solid-state laser, and demonstrates the inherently low noise character of mode-locked lasers at high frequencies. This study shows the potential of low-cost fs Cr:LiSAF laser systems as ultra-low timing jitter sources [59], and the advantage of the balanced optical cross correlation for timing jitter measurements [358, 360].

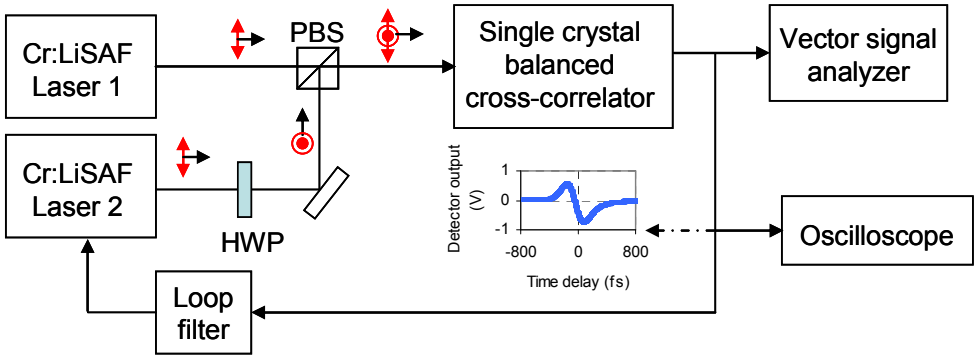

Figure 9.1: Schematic of the timing detector method.

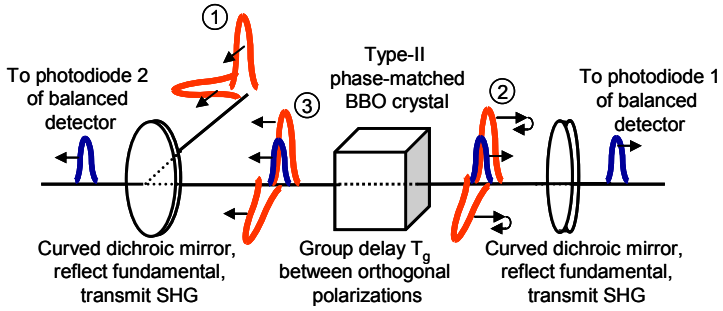

Figure 9.2: Implementation of single crystal balanced optical cross correlator.

Figures 9.1 and 9.2 show the schematic of the timing jitter noise measurement using balanced optical cross correlation. Two home-built, diode pumped, saturable absorber mode-locked, 100 MHz Cr:LiSAF lasers provided about ~100-fs long ~1-nJ pulses around 850 nm. The output beams are combined using a half-wave plate (HWP) and a polarizing beam splitter cube (PBS). The combined laser output is sent to the first dichroic mirror of the cross correlator, which focuses the beams inside a 400 μm thick type-II phase matching optimized BBO crystal for 850nm. The second harmonic (SH) generated in the forward pass is transmitted through the second dichroic mirror and then directed to the first photodiode of the balanced detector (New Focus 2107-FS). The nonlinear crystal also provides group delay (T_g~100 fs) between the orthogonal polarizations. The returning beams (at the fundamental) are focused back in to the nonlinear crystal, where the SH is generated and detected by the second photodiode of the balanced

detector. The signal from the balanced detector is proportional to the timing delay between the two pulses. The cross correlator signal at low frequencies is also used as the error signal for the PLL, which synchronizes the lasers by actuating a small PZT in one of the lasers. Once the lasers are synchronized with the low-bandwidth PLL, the signal in the high frequency range is directly proportional to the relative timing jitter of the free running lasers, which is uncorrelated [358, 360].

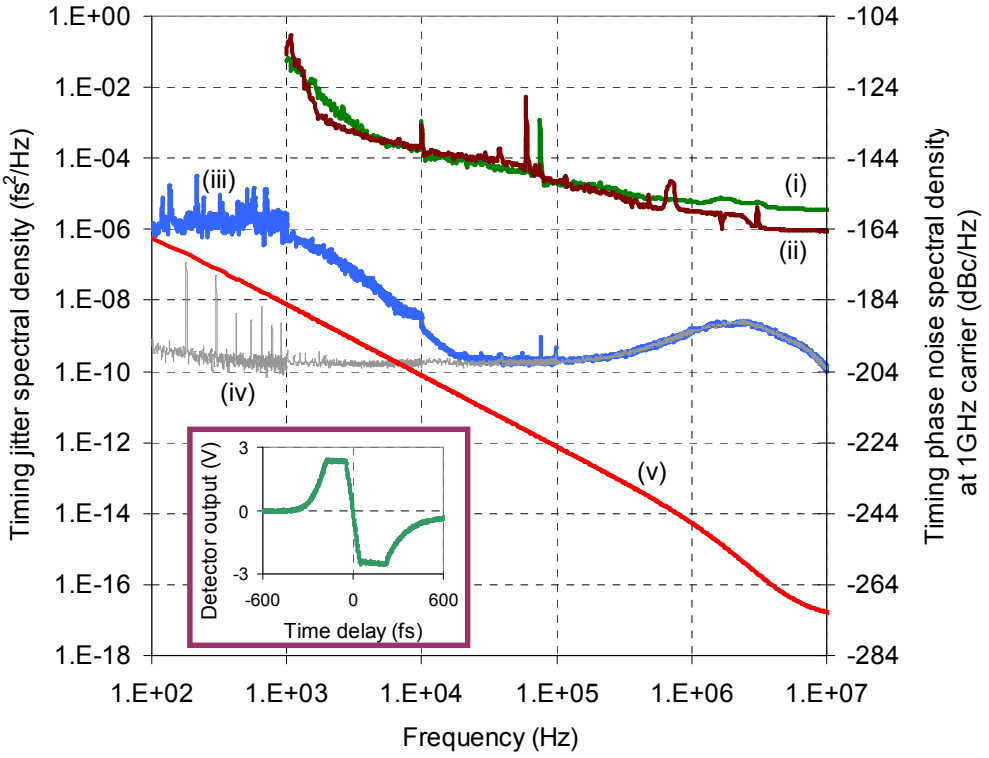

Fig. 9.3: Timing jitter spectral density measurement between two Cr:LiSAF lasers. Secondary axis shows the corresponding phase noise referenced to a 1 GHz carrier. (i)-(ii): Measured jitter density of laser 1 and 2 using the signal source analyzer. (iii): Measured jitter density between laser 1 and 2 using the balanced cross correlator setup. (iv): Background noise level of the balanced cross correlator measurement. (v): Theoretically estimated timing jitter spectral density (for one laser). Inset: Measured cross correlation curve when the lasers are not synchronized.

Fig. 9.3 summarizes the timing jitter measurement results. Curves (i) and (ii) show the jitter density measurement of laser 1 and 2 using a commercial signal source analyzer (Agilent E5052B) and using the 10th harmonic at 1GHz. The result indicates an integrated timing jitter of ~10 fs from 10 kHz to 10 MHz, which is limited by the signal source analyzer. The measured noise level is orders of magnitude higher then the theoretically estimated noise level (curve (v)). Curve (iii) shows the measured timing jitter spectral density between both lasers using the balanced nonlinear optical cross correlator. Curve (iv) shows the background level for this measurement, which is dominated by the resonance around ~2.5 MHz that is due to the non-ideal frequency response of the balanced detector. The estimated theoretical jitter density level due to quantum noise for the Cr:LiSAF lasers is also plotted in Fig. 2 (curve (v)), where the

integrated timing jitter from 10 kHz to 10 MHz is about 1.3 as. The measured integrated timing jitter from 10 kHz to 10 MHz is 137 as. From the background measurement (iv), we can conclude, that only a few tens of attoseconds maybe due to the actual timing jitter of the laser in the range from 1-10 kHz. The rest of the measurement is due to the detector background. This measurement clearly demonstrates, that the quantum limited timing jitter of short pulse solid-state lasers beyond 10 kHz is in the sub-100 as and potentially even below 10 as. Further studies will focus on improving the sensitivity by optimizing the SH generation efficiency and by using an improved balanced detector to truly detect quantum limited performance.

CHAPTER 10

CONCLUSIONS

The main aim of this PhD work has been to develop robust, ultra low-cost (5-10 k$), highly-efficient and tunable femtosecond laser technology based on diode-pumped Cr^{3+}:Colquiriite gain media (Cr^{3+}:LiCAF, Cr3+:LiSAF and Cr3+:LiSGaF). The absorption band of Cr^{3+}:Colquiriites around 650 nm facilitates direct diode pumping, and enables the usage of low-cost diodes, which as a result decreases the cost of the laser system. In most of the experiments described in this thesis, we have used 660 nm 130 mW AlGaInP single-mode diodes (HL6545MG, Hitachi) as the pump source, which cost only ~$150.

By pumping Cr^{3+}:Colquiriites with these inexpensive single-mode diodes, we have demonstrated continuous-wave output powers >250mW with slope efficiencies >50%, and electrical to optical conversion efficiency of 12.%. Record continuous-wave tuning ranges were also demonstrated for Cr^{3+}:LiSAF (775-1042 nm), Cr^{3+}:LiSGaF (777-977 nm), and Cr^{3+}:LiCAF (754-871 nm). Neither the crystals, nor the 660 nm 130 mW AlGaInP single-mode diodes (HL6545MG, Hitachi) required water cooling. Hence, this allows the construction of compact, efficient and battery powered laser systems.

SESAMs/SBRs were used to initiate and sustain cw mode-locked operation which enabled the construction of turn-key, self-starting laser systems. Typical performance was ~50-100-fs pulses, with 1-2 nJ of pulse energies, from ~100 MHz repetition rate cavities. Record electrical-to-optical conversion efficiencies of about 10% were demonstrated in cw mode-locked regime. The central wavelength of the spectra were around ~800 nm for Cr:LiCAF, and for ~815 nm, ~850 nm or ~900 nm for Cr:LiSAF and Cr:LiSGAF, where the wavelength of operation is determined the central reflectivity wavelength of the SESAM/SBR used. By proper dispersion compensation pulsewidths as short as ~25-fs with Cr:LiSAF and ~40-fs with Cr:LiCAF could be obtained. With Cr:LiSAF the obtained pulsewidths were limited by the SESAM/SBR bandwidth, where as for Cr:LiCAF SESAM/SBR working range limited the obtainable pulsewidths.

We have shown that the obtained average output powers can be scaled up by using recently available higher power single-mode diodes (642 nm 150 mW single mode diodes, HL6385DG). Using the HL6385DG laser diodes as pump sources, which requires cooling, we have demonstrated cw powers >400 mW, and average powers of 300 mW in cw mode-locked regime (~3-nJ, ~100-fs pulses at 100 MHz). The superior thermal properties of Cr:LiCAF gain media also enabled pumping with ~1.5 W

single-emitter multimode diodes (cost ~1k$). From the multimode diode pumped Cr:LiCAF laser, we have obtained cw powers above 2W, and mode-locked average powers of ~390 mW.

We have also performed detailed femtosecond tuning experiments with Cr:Colquiriite gain media. Mode-locked tuning experiments of Cr:LiCAF gain media, with a regular 800 nm SESAM/SBR resulted in a mode-locked tuning range from 767 nm to 817 nm with ~130-fs long pulses. With Cr:LiSAF gain medium, using regular SESAMs/SBRs centered around 800 nm, 850 nm, and 910 nm, mode-locked tuning ranges of 803-831 nm, 828-873 nm and 890-923 nm were demonstrated, respectively. From a Cr:LiSAF laser mode-locked with a broadband oxidized SESAM/SBR, a record tuning range from 800 nm to 905 nm was demonstrated with ~150-fs long pulses.

We have also performed experiments aiming to scale the pulse energies available from Cr:Colquiriite lasers. Using an extended cavity Cr:LiCAF laser, pulse energies >15-nJ with peak powers exceeding 100 kW were obtained. We have also performed the first cavity-dumping experiments with a Cr:Colquiriite laser and demonstrated pulse energies >100-nJ, and peak powers approaching MW level, at repetition rates up to 50 kHz from a single-mode diode pumped Cr:LiSAF system. We note here that, of course the cost and complexity of these higher energy systems is not same as the simple ~100 MHz level Cr:Colquiriite lasers.

As an example application area for this low cost technology, we have performed multiphoton microcopy with a single-mode diode pumped Cr:LiCAF laser. We have also performed attosecond resolution timing jitter characterization experiments of the femtosecond Cr:LiSAF laser, and measured a record low upper limit for the integrated timing jitter of the Cr:LiSAF laser (137 as in 10 kHz-10 MHz range). This showed that low-cost, efficient and compact fs Cr:Colquiriite lasers can also be a useful source for microwave electronics.

APPENDIX A

SPECIFICATIONS OF THE OPTICS USED IN CR:COLQUIRRITE LASERS

In this Appendix, we will provide the specifications of the frequently used optics in Cr:Colquiriites laser experiments. Most of the mirrors we have used are commercial stock item mirrors from Layertec [361]. As an exception, we have (i) a custom made pump mirror set (MIT Cr:LiSAF mirror set) which is optimized for broadly tunable ultrashort pulse generation in Cr:LiSAF (ii) a custom made mirror set which was used in extended cavity Cr:LiCAF laser experiments (Layertec MPC Cr:LiCAF mirror set).

A.1 MIT Cr:LiSAF Pump Mirror Set

The design of MIT Cr:LiSAF mirror set was kindly performed by Dr. Jonathan Birge [362], who was a PhD student in Prof. Kärtner's group at that time (March 2009). This mirror set was designed to produce approximately -80±10 fs^2 GDD per bounce over 150 nm of bandwidth (800-950 nm), which was essential for several studies we have performed, such as the ultrabroad tuning study in femtosecond regime or for the GHz Cr:LiSAF study. This is because commercial broadband dispersion compensating mirrors with a flat GDD curve generally provide only ~ -40 fs^2 of GDD per bounce. Hence, for example for GHz cavities with only a few mirror bounces, the GDD per bounce from commercial mirrors is insufficient to provide the required negative dispersion.

While determining the specs for the design we have consider the following: (i) We looked at the gain curve of Cr:LiSAF, and matched the reflectivity bandwidth of the mirror set to the gain curve of Cr:LiSAF gain medium. The mirror set should ideally cover the range from 780 nm to 1050 nm (ii) Due to the low gain nature of Cr:Colquiriites, we desired to have very high reflectivity value to obtain the best performance (>99.99%). (iii) We desired a pump window around 650 nm with less than 5% reflectivity, that could allow the use of different diode pump lasers from 640 nm to 670 nm. (iv) Finally, we desired the mirror to provide flat -200 fs^2 dispersion for the Cr:LiSAF laser cavity shown in Fig. A1. This dispersion level is somehow optimum for obtaining stable ~50-100-fs ~2 nJ pulses from a ~100 MHz Cr:LiSAF laser with a 2-3% output coupler (assuming a spot size of ~20 μm inside the crystal). The -200 fs^2 total cavity dispersion value chosen here is a round number (Fig. A2). In the actual experiments, we have noticed that the required dispersion level for a fixed pulsewidth (i.e. ~100-fs), varies from laser to laser. This we believe is because of the varying level of self phase modulation: it is hard to build lasers with exactly same pump and laser beam focusing even one uses the same set of optics. Figure A2 (right) shows the design goal for dispersion to obtain the required -200 fs^2 dispersion. Note that, the desired

dispersion has some slope to cancel the third order dispersion of the Cr:LiSAF crystal and the intracavity air. Also note that the design goal for dispersion also enables development of GHZ level Cr:LiSAF lasers as shown in Figure A3.

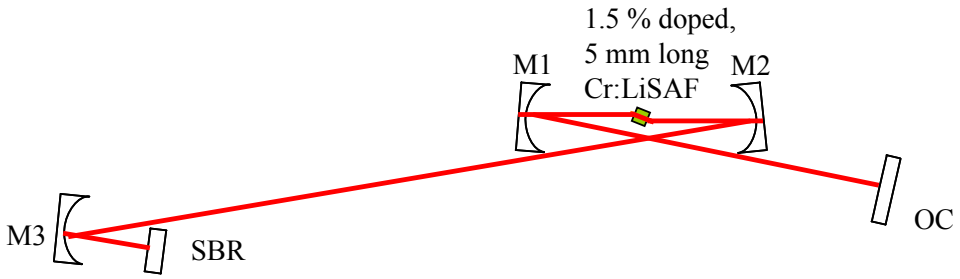

Figure A1: A simple ~100 MHz repetition rate Cr:LiSAF laser cavity. The cavity contains a 5mm long, 1.5% chromium doped Cr:LiSAF crustal, an SBR to initiate and sustain mode-locking, and 3 dispersion compensating mirrors (M1-M3), which are also pump mirrors.

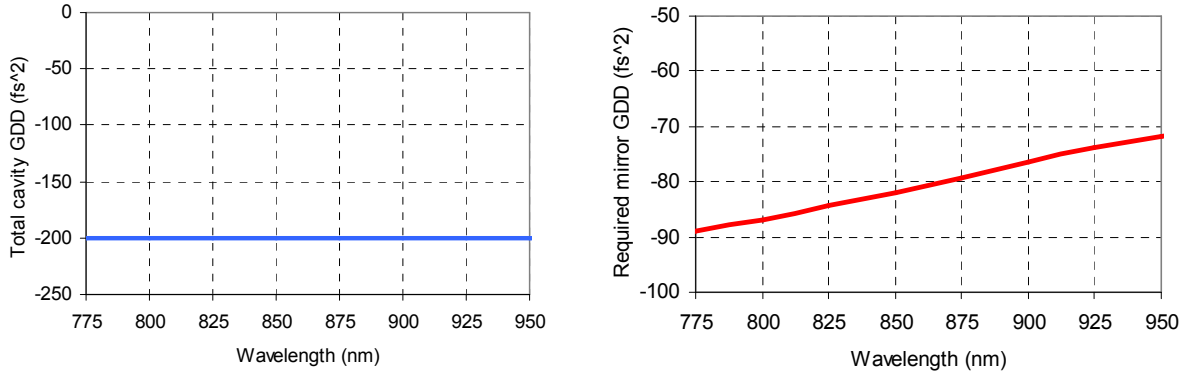

Figure A2: (Left) Desired total cavity dispersion for the cavity shown in Fig. A1. The cavity dispersion estimate includes Cr:LiSAF crystal, intracavity air (3 m) and 6 bounces on the DCM mirror set. We assumed that SESAM/SBR and the output coupler have zero dispersion. (Right) Required amount of dispersion on single bounce from the mirror set (design goal for dispersion). The design goal for dispersion can be fitted by a simple equation y=0.095x-162.53, where y (GDD) is in fs^2 units and x (wavelength) is in nm units.

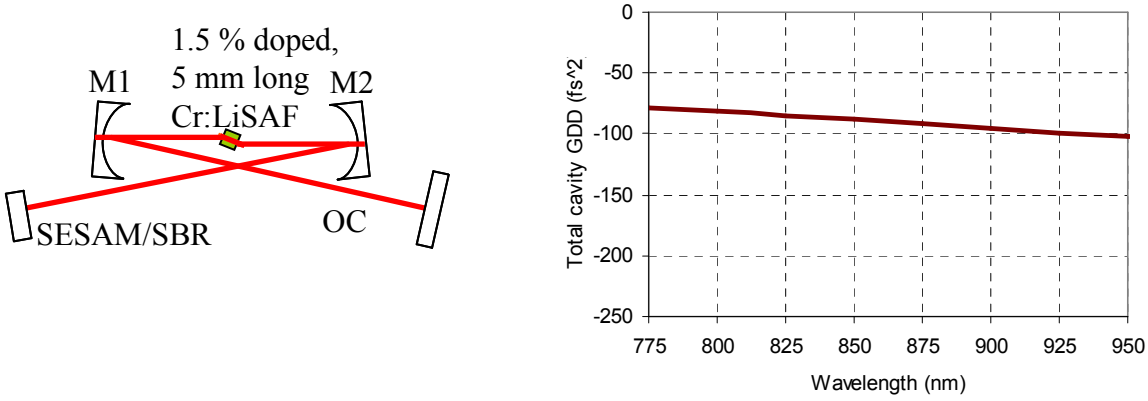

Figure A3: (Left) A 1-GHz repetition rate Cr:LiSAF laser (Left) Calculated total cavity dispersion for the GHz Cr:LiSAF laser. Note than, since the specs of the DCM mirrors were optimized for the 100 MHz cavity shown in Fig. A1, for the 1 GHz laser estimated total cavity dispersion is not flat.

During the mirror design, we have tried several approaches aiming to match all the required four parameters that were mentioned above simultaneously, which was enabled by an efficient analytical computation method that calculates and optimizes dispersion (to any order) of multilayer coating with high accuracy [363]. Figure A4-A7 shows the reflectivity curve of the final design which was grown. Fig. A4-A7 also include the measured reflectivity of the mirror set, which shows that the actual growth was quite close to the design. Figure A8 shows the design goals for group delay and group delay dispersions and the actual design.

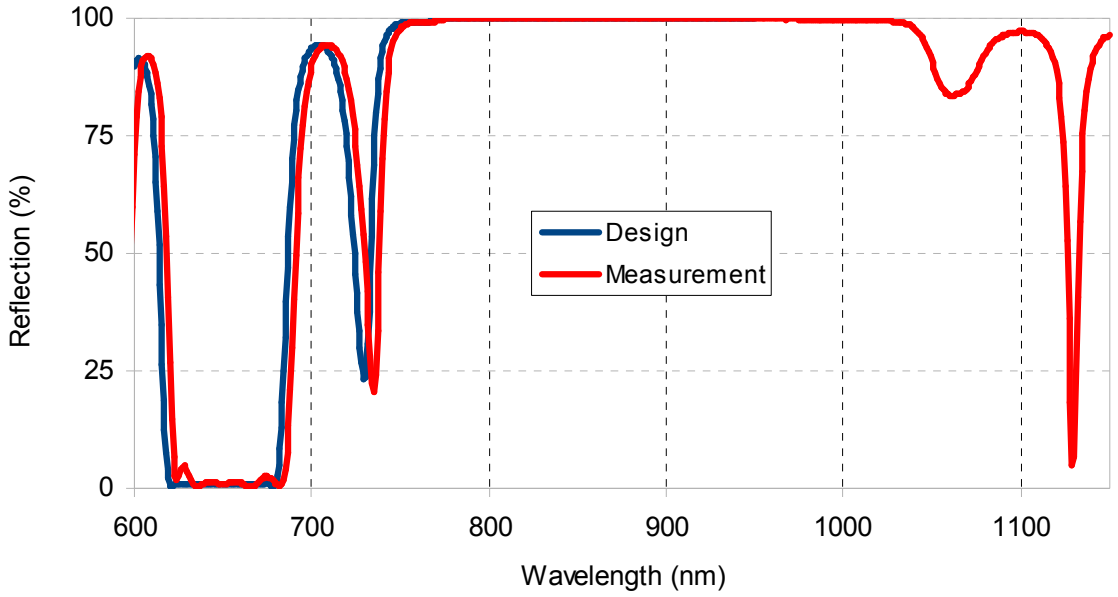

Figure A4: Designed and measured reflectivity of the MIT Cr:LiSAF mirror set.

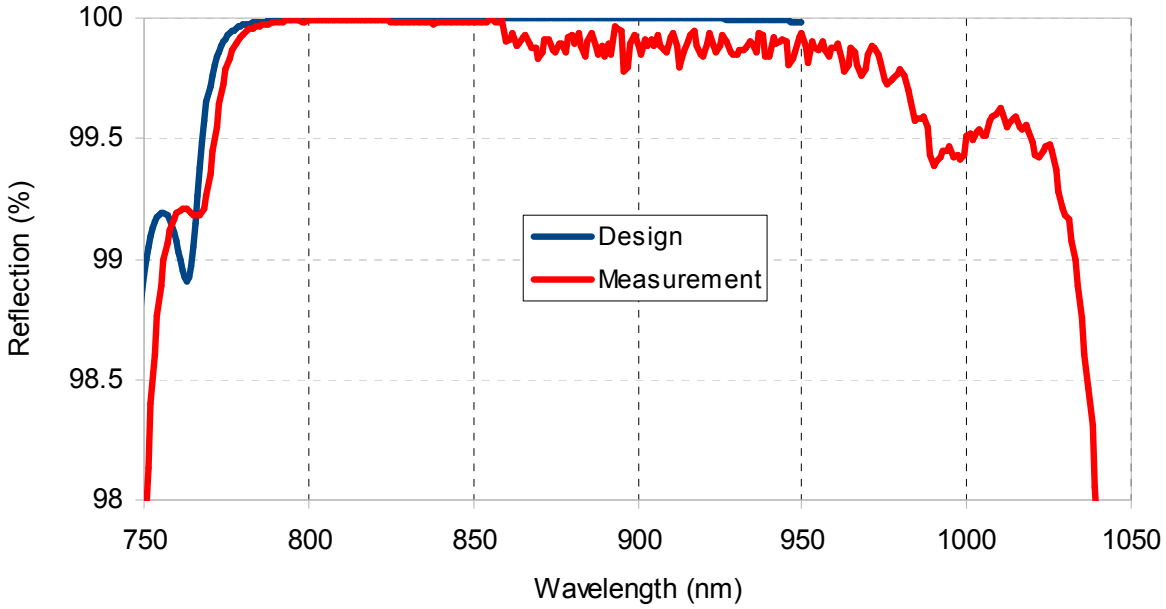

Figure A5: Designed and measured reflectivity of the MIT Cr:LiSAF mirror set. Zoomed into the reflectivity band.

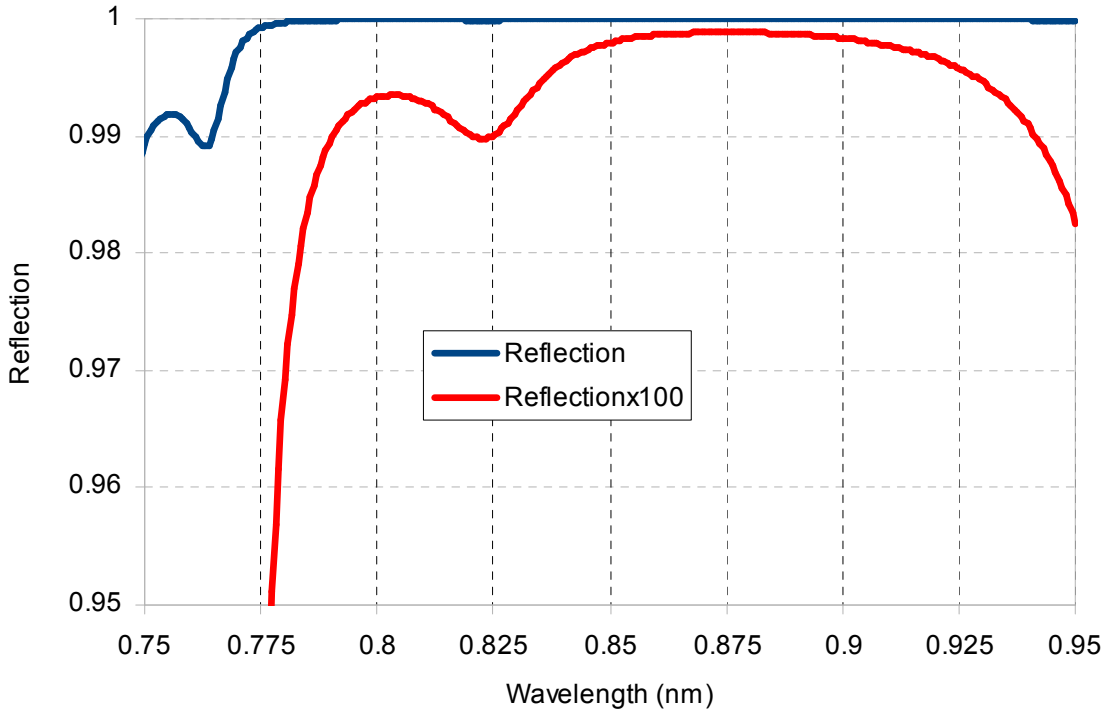

Figure A6: Designed reflectivity of the MIT Cr:LiSAF mirror set. Zoomed into the reflectivity band. Reflection x 100 is also shown.

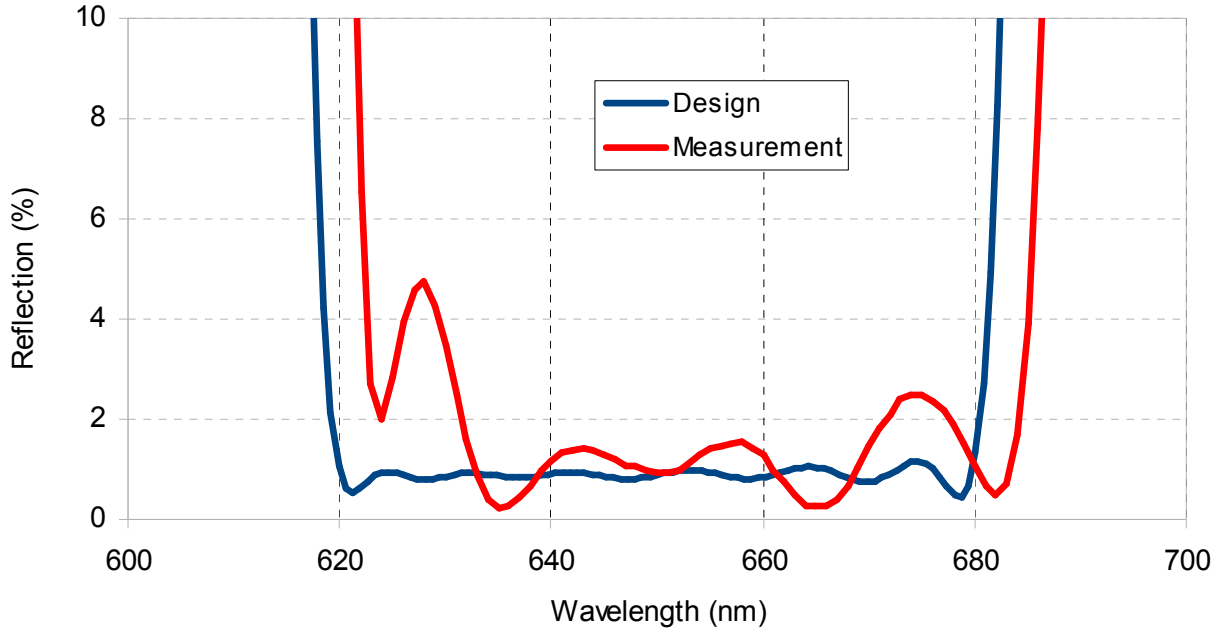

Figure A7: Designed and measured reflectivity of the MIT Cr:LiSAF mirror set. Zoomed into the pump band.

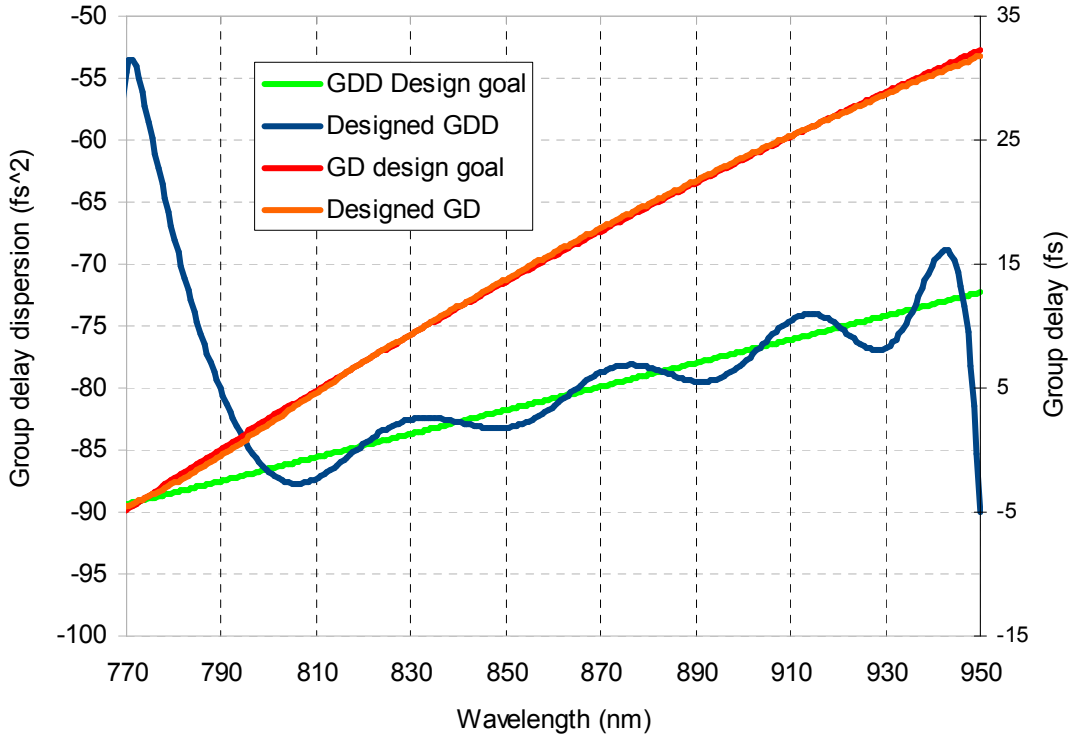

Figure A8: Designed and desired group delay and group delay dispersion for the MIT Cr:LiSAF mirror set.

We have also investigated the loss level of the MIT Cr:LiSAF mirror set carefully. To do this, we measured the cw laser performance of Cr:LiSAF laser using both MIT Cr:LiSAF mirror set and regular Layertec mirror sets at different output coupling levels (Figure A9). Based on these data, we estimated the loss level at 840 nm at single pass as 0.015 to 0.02 % level. We have measured that about 0.005% of this loss is leakage loss, which is consistent with the design (Fig. A6). The remaining 0.01 to 0.015% should be attributed to other type of losses including scattering loss. We note that this loss value is estimated for 840 nm, and since the free-running Cr:LiSAF laser mostly works at 860 nm in mode-locked regime, the leakage loss is expected to be lower (Fig. A6). In conclusion, compared to the Layertec Cr:Colquiriite set I, parasitic losses seem to be high. However, to be fair Layertec Cr:Colquiriite set I, is a regular mirror without any dispersion compensation, etc; hence, it is not a quite fair comparison. Also, we note that with a 3% output coupler (close to optimum output coupling), obtained performance is almost same with both mirror sets. As a final note, for a possible MPC study with high number of bounces, or for the GHz study with lower output coupling values, or for the cavity dumping study with high number of bounces and with almost zero output coupling, the parasitic losses of the MIT Cr:LiSAF set might limit the performance.

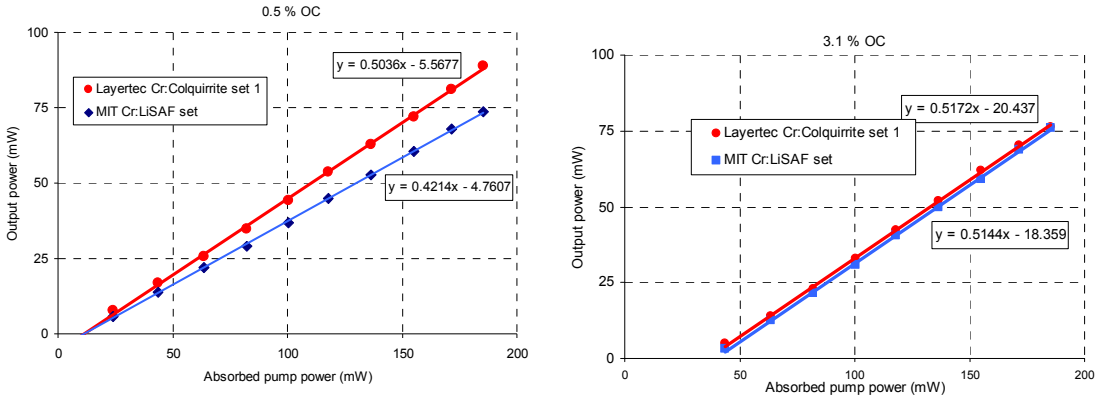

Figure A9: Measured cw performance of a cw Cr:LiSAF laser using MIT Cr:LiSAF set and Layertec Cr:Colquiriite set 1 with 0.5 % (left) and 3.1 % (right) output couplers.

In the mirror design fused silica was used as the substrate and SiO_2 and Nb_2O_5 were used in the Bragg stack. Figure A10-A11 gives more information on the designed mirror structure.

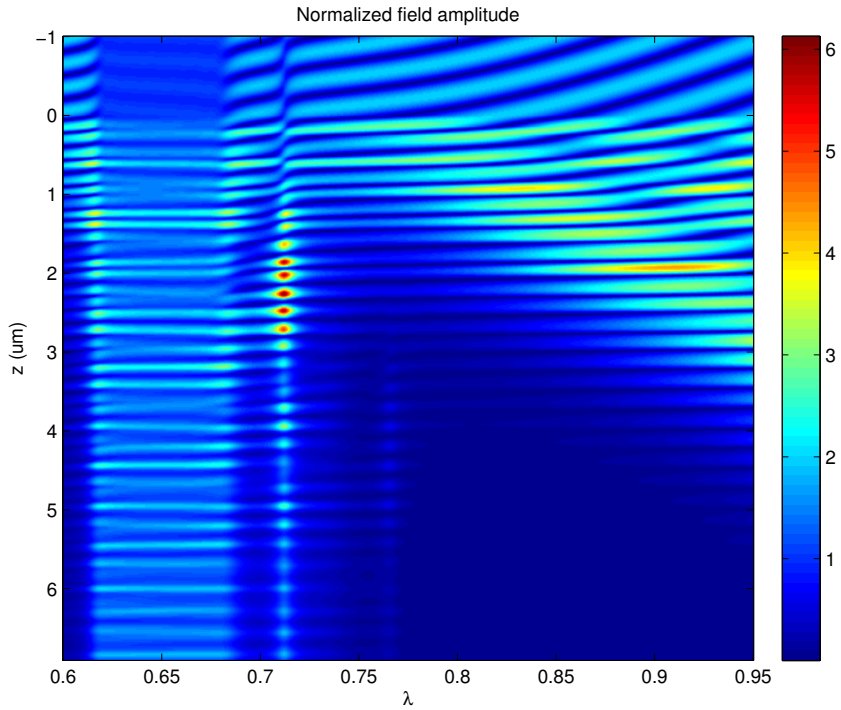

Figure A10: Internal field amplitude as a function of wavelength, showing the deeper penetration (and thus group delay) for longer wavelengths. This information is kindly provided by Dr. Jonathan Birge.

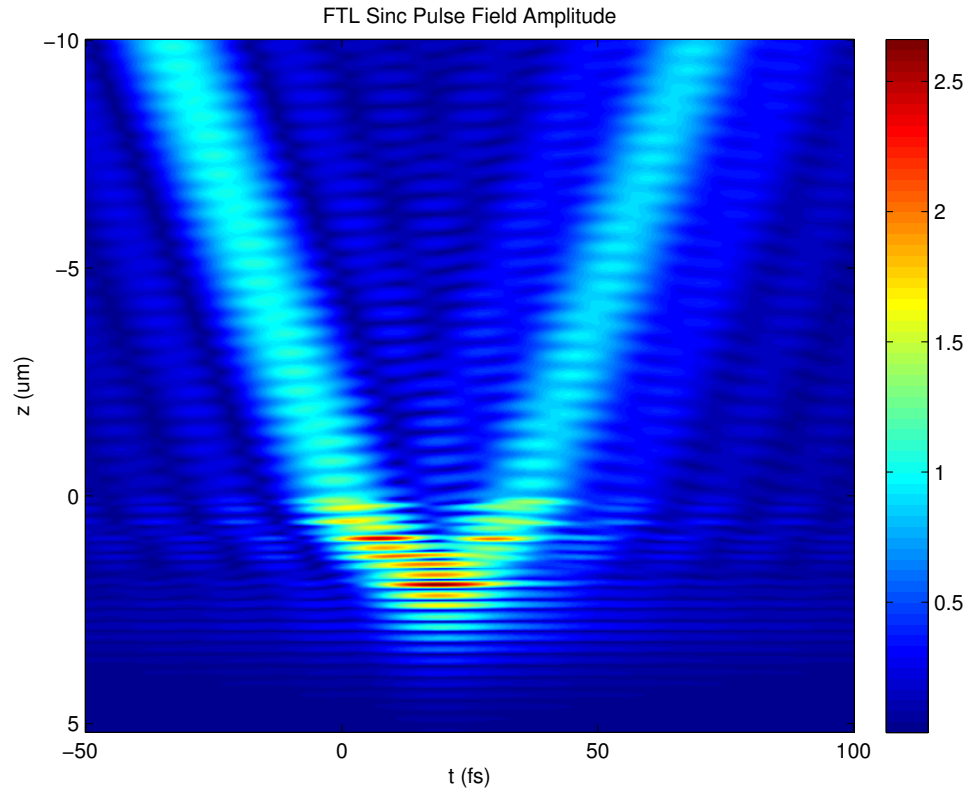

Figure A11: This information is kindly provided by Dr. Jonathan Birge.

Number	Mirror diameter (inch)	Mirror radius of curvature (mm)	Thickness (mm)	Quantity	Application	Substrate firm	Lab Code 1	Lab Code 2
1	2	plane	9.5	3	MPC	Lambda Research	S1-S3	LAMDA-FLAT-SAF
2	2	4000	6.35	2	MPC	Lambda Research	S4-S5	-
3	2	2000	6.35	2	MPC	Lambda Research	S6-S7	-
4	1	plane	9.5	4	multiple bounce	CVI	S8-S11	CVI-SAF
5	1	plane	6.35	25	multiple bounce	Lambda Research	S12-S36	LAMDA-SAF
6	1	100	9.525	2	cavity Dumping	VLOC	S37-S38	VLOC-100-SAF
7	1	150	6.35	2	cavity Dumping	Lambda Research	S39-S40	LAMDA-150-SAF
8	1	250	6.4	2	cavity Dumping	CVI	S41-S42	CVI-250-SAF
9	1	300	9.5	2	cavity Dumping	CVI	S43-S44	CVI-300-SAF
10	0.5	plane	6.4	20	folding cavity	CVI	S45-S64	CVI-SAF
11	0.5	plane	6.35	30	folding cavity	Lambda Research	S65-S94	LAMDA-SAF
12	0.5	plane	3	3	PZT mirror	VLOC	S95-S97	VLOC-SAF
13	0.5	4000	9.5	2	MPC pick off	CVI	S98-S99	CVI-4-SAF
14	0.5	2000	6.35	2	MPC pick off	VLOC	S100-S101	VL-2m-SAF
15	0.5	1500	6.35	2	MPC related	VLOC	S102-S103	VL-1.5m-SAF
16	0.5	1000	6.35	2	MPC related	Lambda Research	S104-S105	LAMDA-1M-SAF
17	0.5	750	9.5	2	MPC related	CVI	S106-S107	CVI-750-SAF
18	0.5	500	6.35	2	SBR focus	VLOC	S108-S109	VL-500-SAF
19	0.5	400	6.35	2	SBR focus	VLOC	S110-S111	VL-400-SAF
20	0.5	300	6.35	2	SBR focus	VLOC	S112-S113	VL-300-SAF
21	0.5	200	6.35	4	SBR focus	VLOC	S114-S117	VL-200-SAF
22	0.5	150	6.35	8	SBR focus	VLOC	S118-S125	VL-150-SAF
23	0.5	100	6.35	16	alternate pump mirror	VLOC	S126-S141	VL-100-SAF
24	0.5	75	9.525	6	pump mirror	VLOC	S142-S147	VL-75-SAF
25	0.5	75	6.35	4	pump mirror	Lambda Research	S148-S151	LAMDA-75-SAF
26	0.5	75	9.5	10	pump mirror	CVI	S152-S161	CVI-75-SAF
27	0.5	50	9.5	14	high rep rate	CVI	S162-S175	CVI-50-SAF
28	0.5	25	9.5	9	high rep rate	CVI	S176-S184	CVI-25-SAF
29	0.5	25		1	high rep rate	VLOC	S185	VLOC-25-SAF
30	0.5	10	9.5	4	high rep rate	CVI	S186-S189	CVI-10-SAF
31	0.5	-400	6.35	2	high rep rate	VLOC	S190-S191	VLOC- -400- SAF
32	0.5	-600	6.35	2	high rep rate	VLOC	S192-S193	VLOC- -600- SAF
33	0.5	-1000	6.35	4	high rep rate	VLOC	S194-S197	VLOC- -1000- SAF

Table A1: Specification of the mirrors in MIT Cr:LiSAF mirror set.

A.2 MIT Cr:LiCAF Pump Mirror Design (not grown)

Dr. Jonathan Birge has also designed a mirror set for Cr:LiCAF; however, this design have not been grown yet. We will present it here for the purpose of completeness. We note that the specs for the design can be improved. For example the earlier specs did not consider the third order dispersion of the Cr:LiCAF crystal, hence the designed mirror set has a flat dispersion. In short, it is quite important to re-optimize this design in the future, if one have the motivation to grow a separate Cr:LiCAF mirror set.

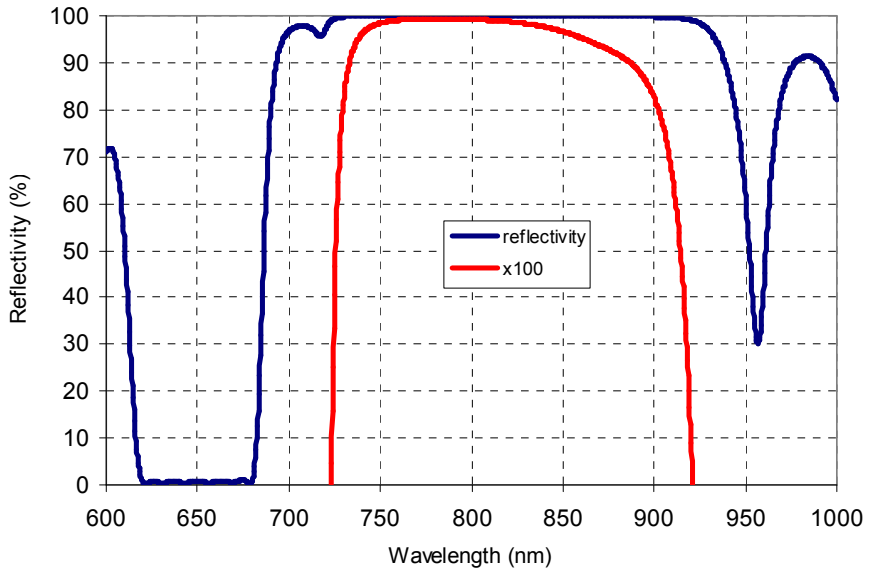

Figure A12: MIT Cr:LiCAF mirror set design reflectivity curve.

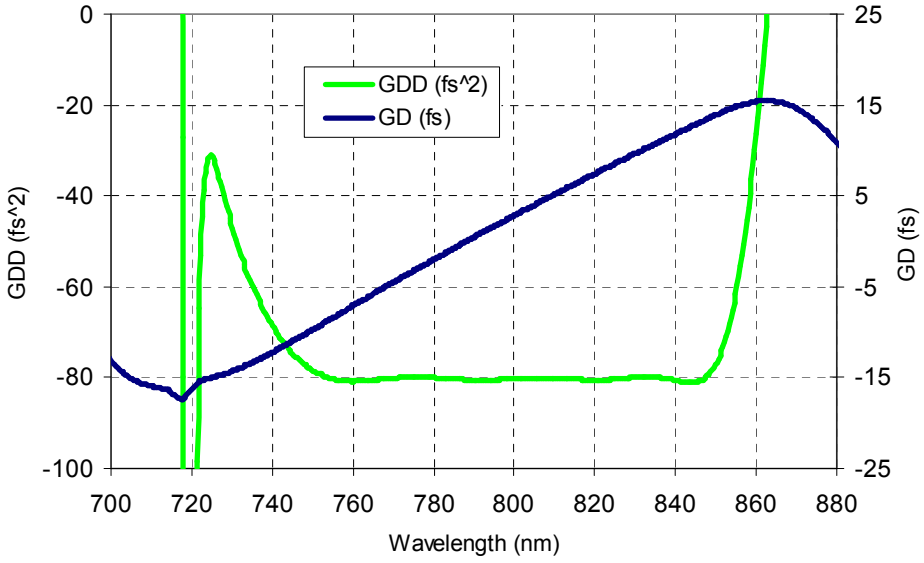

Figure A13: MIT Cr:LiCAF mirror set design GD and GDD curves.

A.3 Layertec Cr:Colquiriite Pump Mirror Set I

We have extensively used the following mirror set from Layertec stock items in our experiments [364-367]. This mirror is highly reflective from 750 to 850 nm with a reflectivity greater than 99.9%, and it also has a suitable pump window around 650 nm. The main drawback of this mirror set is it does not provide negative dispersion which is required for femtosecond pulse generation. However, for cw experiments, it has very low loss, approaching 99.99% limit. In our inventory we have several flat and several curved (roc: 50 mm, 75 mm and 150 mm) mirrors from this set.

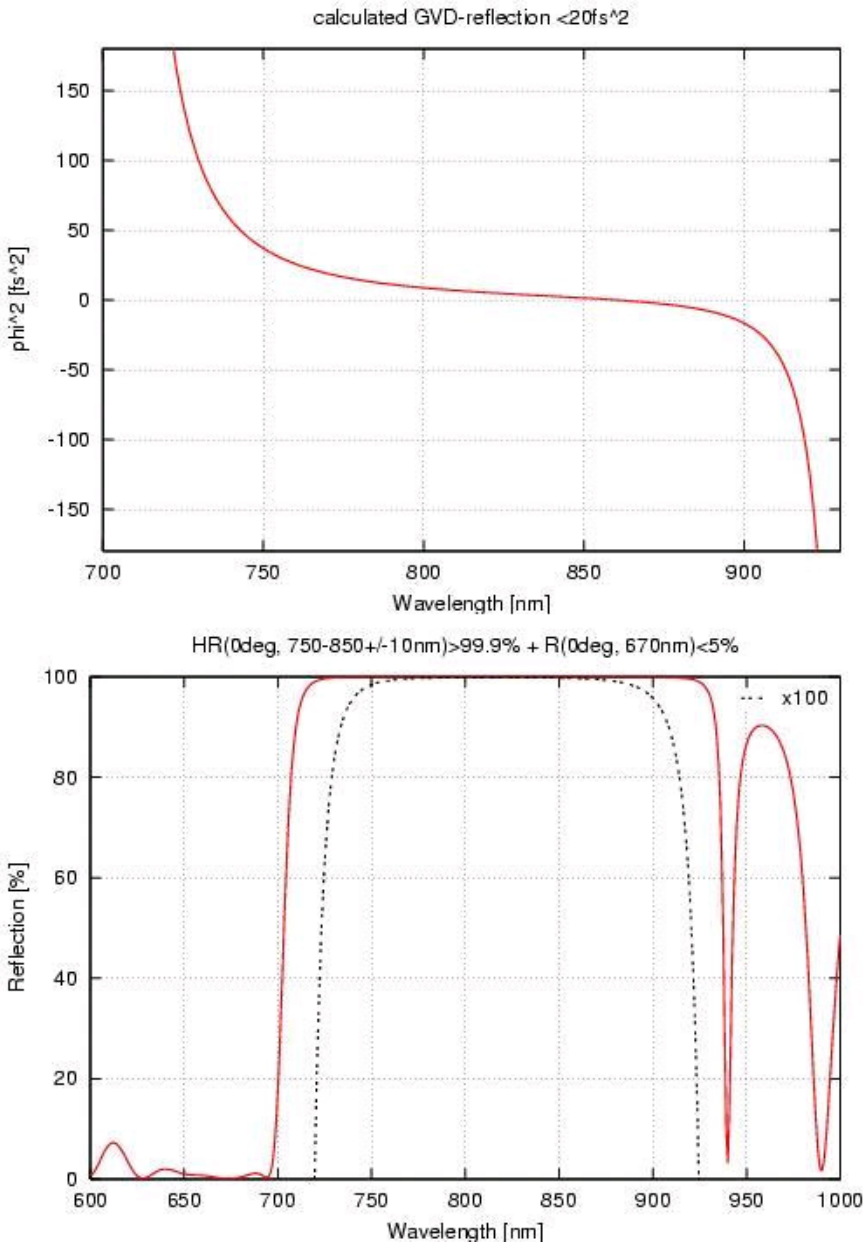

Figure A14: Calculated reflectivity and dispersion curves for Layertec Cr:Colquiriite pump mirror set I [364]. Courtesy of Layertec.

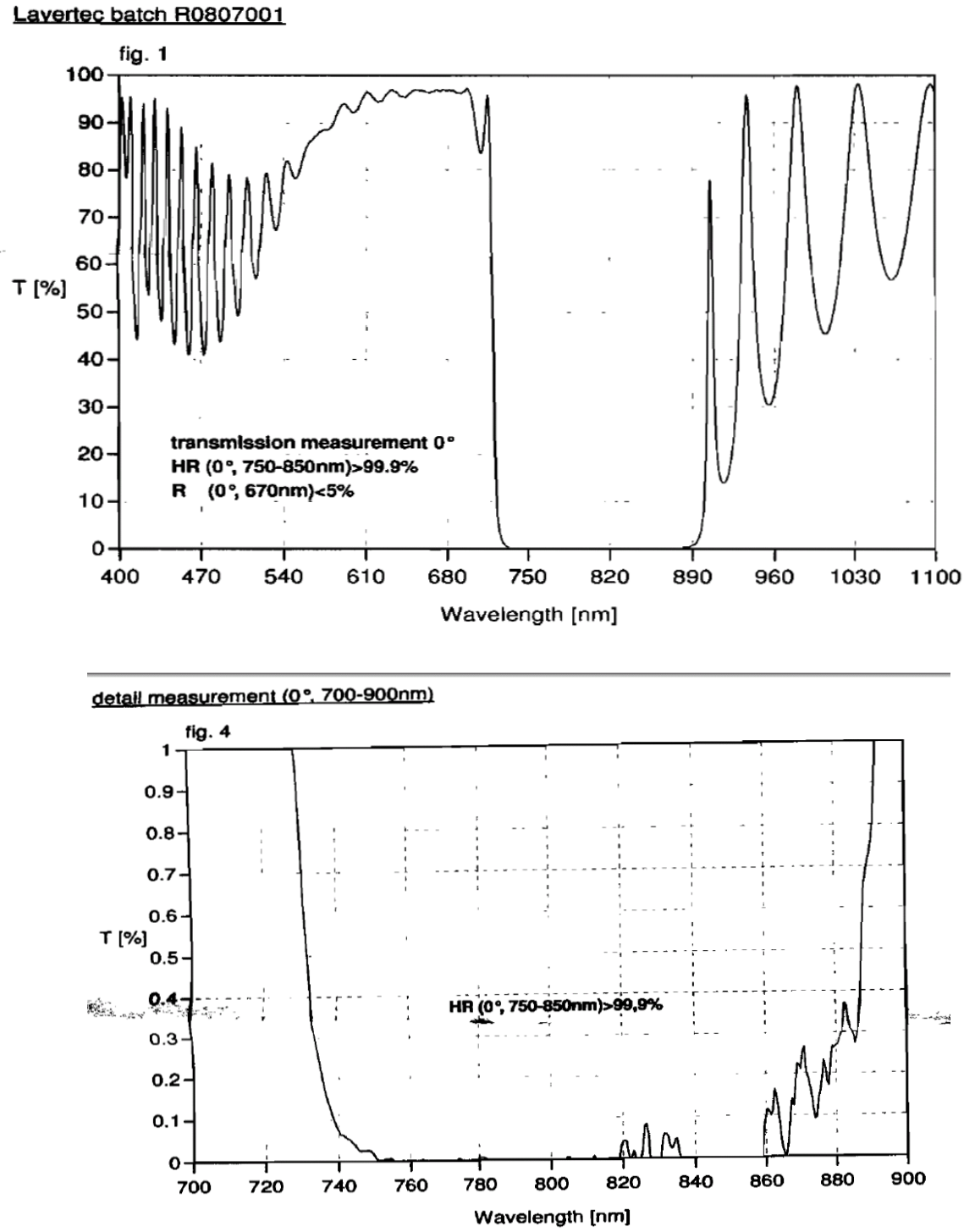

Figure A15: Measured reflectivity curves for Layertec Cr:Colquiriite pump mirror set I [364]. Courtesy of Layertec.

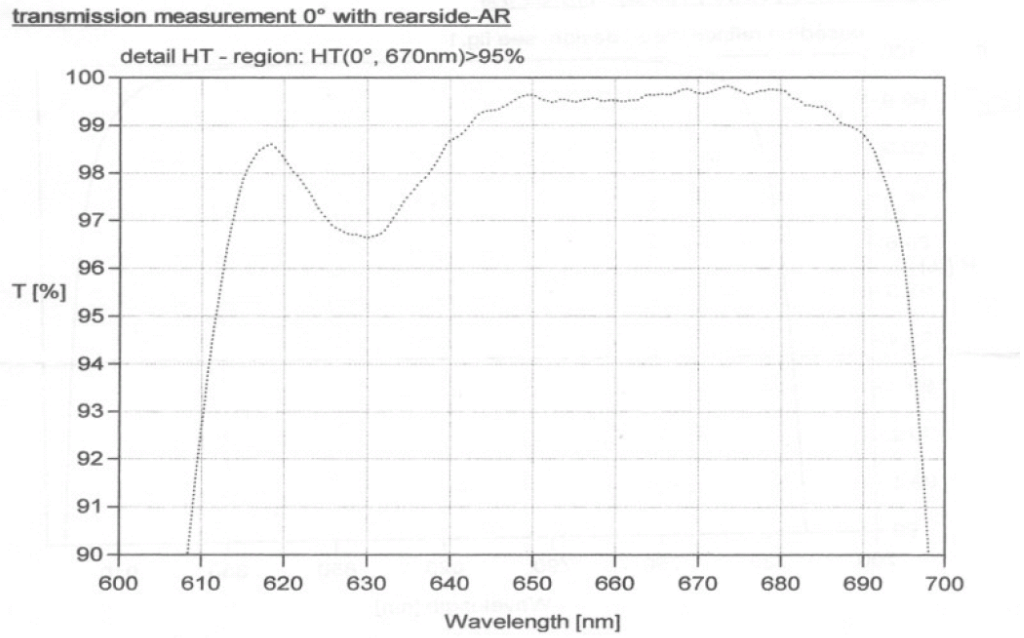

Figure A16: Measured transmission curve for Layertec Cr:Colquiriite pump mirror set I [364]. Courtesy of Layertec.

A.4 Layertec Cr:Colquiriite Pump Mirror Set II

Coating: HR(0°, 730-1030±5nm)>99.8% + R(0°, 650-690nm)<5%, GVD~-50±40fs²(750-920nm)

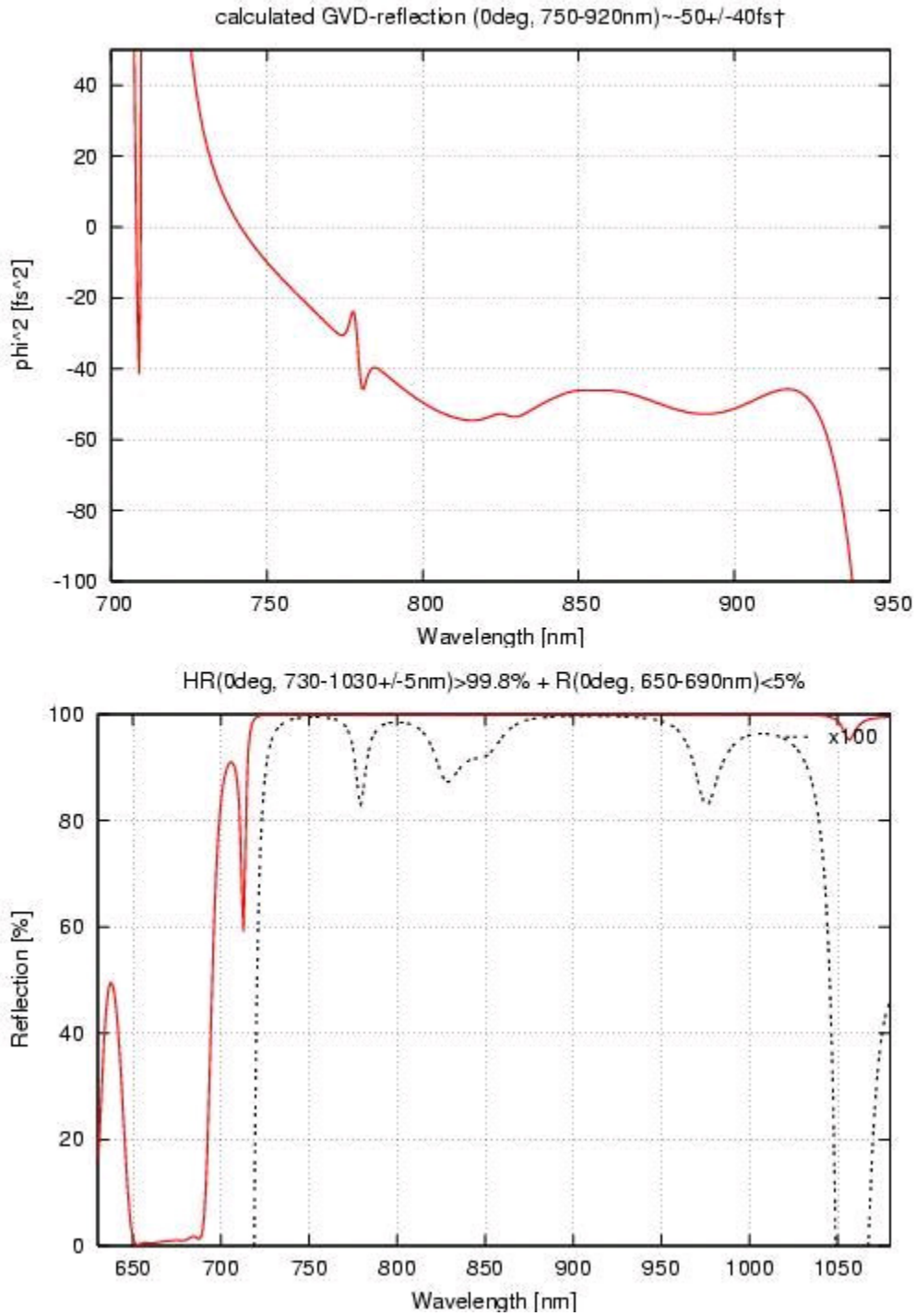

Figure A17: Calculated reflectivity and dispersion curves for Layertec Cr:Colquiriite pump mirror set II [368]. Courtesy of Layertec.

A.5 Layertec DCM Mirror Set I

Coating: HR(0°, 700-870±8nm)>99.9%, GVD=-40±15fs²(725-880nm)

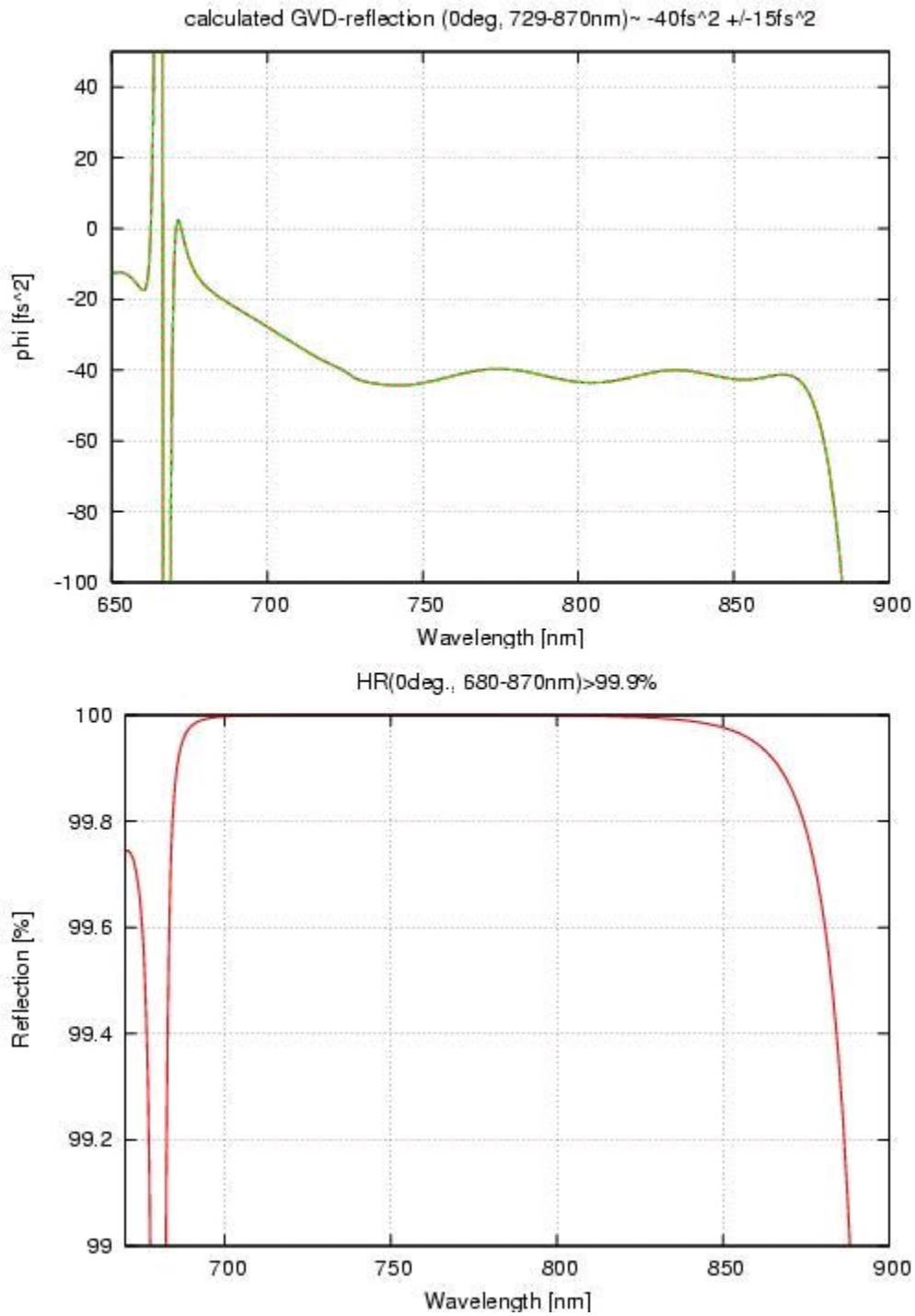

Figure A18: Calculated reflectivity and dispersion curves for Layertec DCM set I [369]. Courtesy of Layertec.

A.6 Layertec DCM Mirror Set II

Coating: HR(0°, 750-920nm)>99.8%, GVD~ -45±10fs²

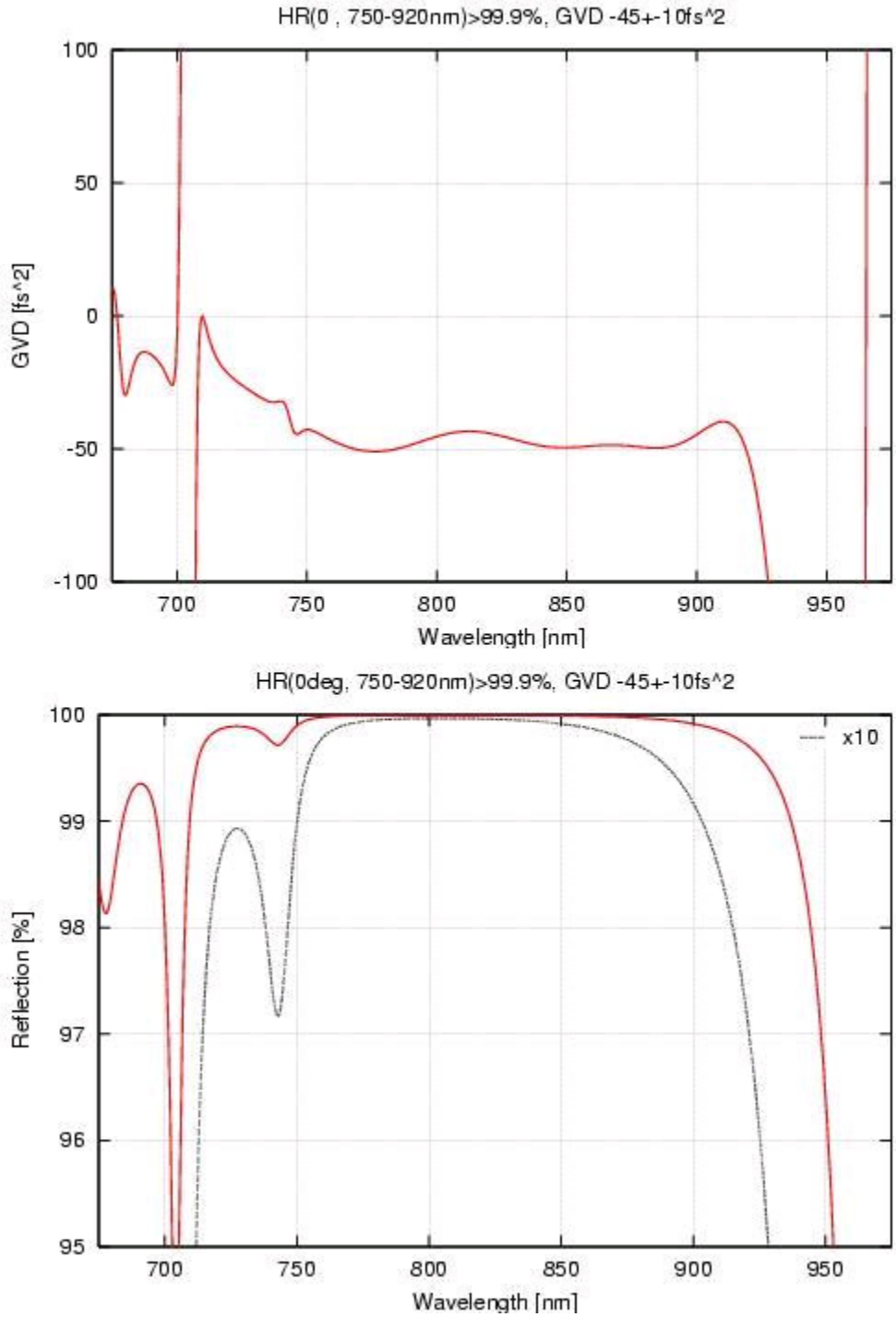

Figure A19: Calculated reflectivity and dispersion curves for Layertec DCM set II [370]. Courtesy of Layertec.

A.7 Layertec DCM Mirror Set III (custom designed for MPC Cr:LiCAF project)

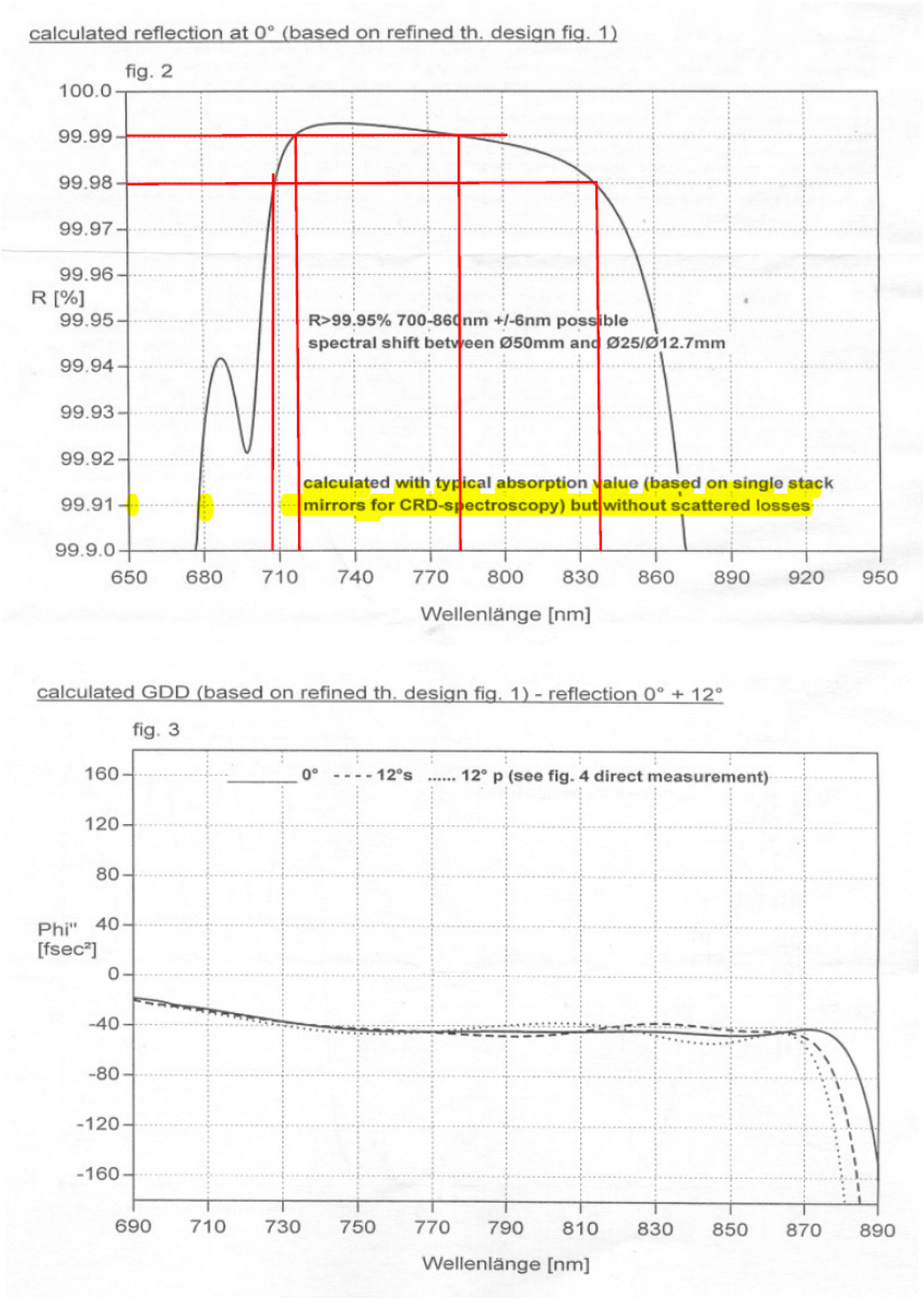

Figure A20: Calculated reflectivity and dispersion curves for Layertec DCM set III. Courtesy of Layertec.

A.8 Layertec GTI Mirror Set I

Coating: HR(0°, 720-920nm)>99.9%, GVD(790-815nm)~ -550±50fs²

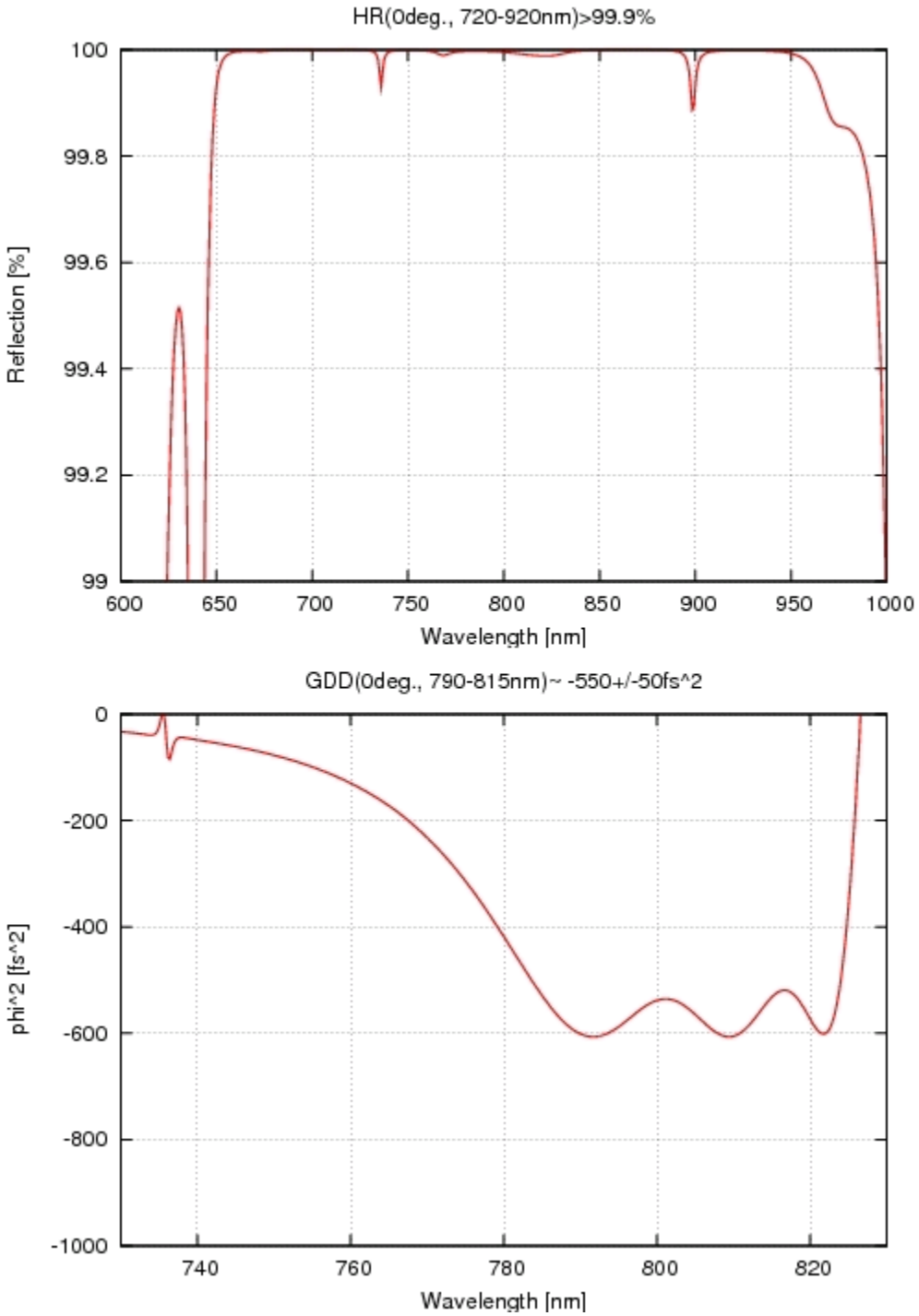

Figure A21: Calculated reflectivity and curves for Layertec GTI mirror set I [371]. Courtesy of Layertec.

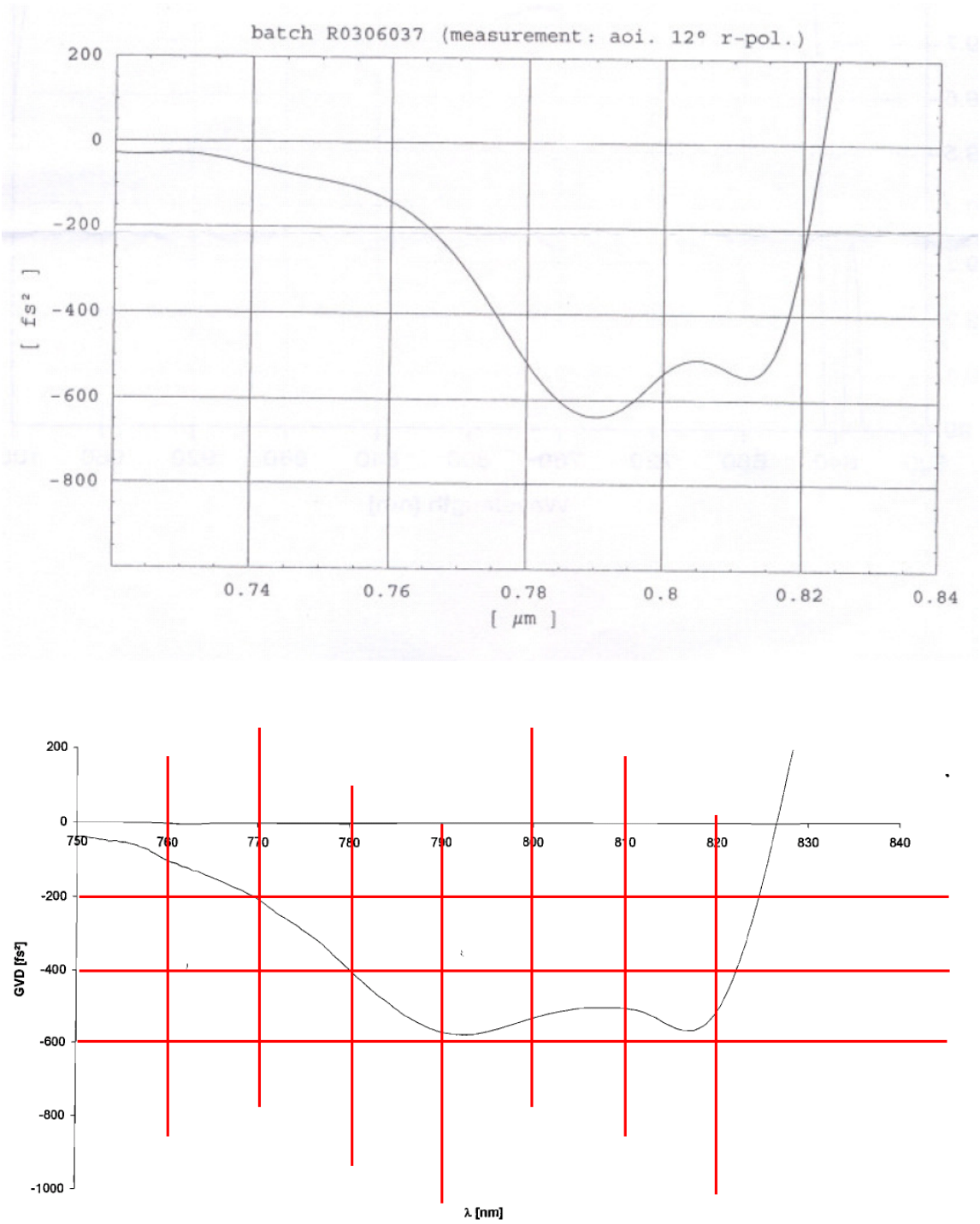

Figure A22: Measured dispersion curves for Layertec GTI mirror set I (mirrors were from two different coating runs). Courtesy of Layertec.

A.9 Layertec GTI Mirror Set II

Coating: HR(0°, 720-920nm)>99.9%, GVD(790-815nm)~ -550±50fs²

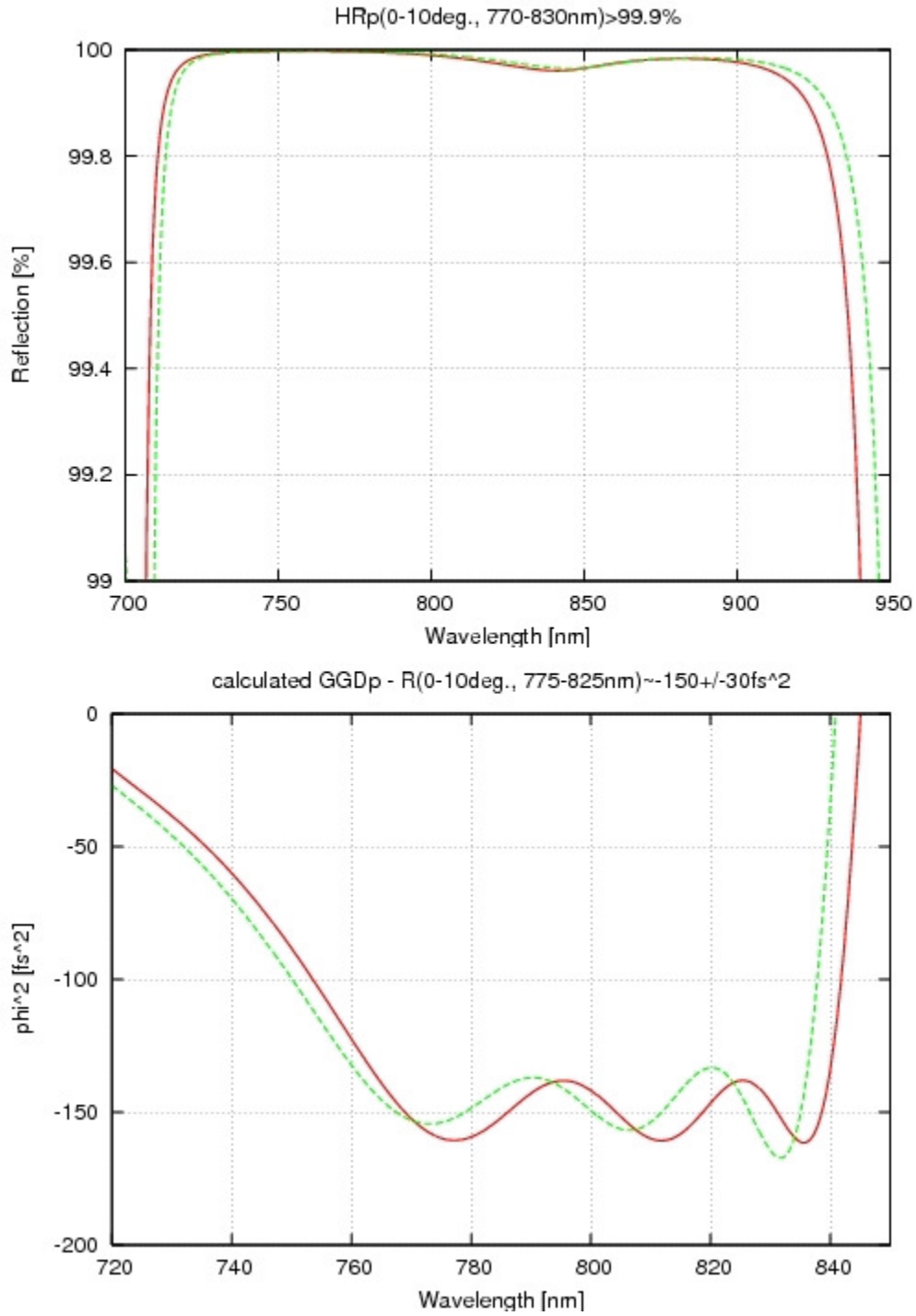

Figure A 23: Calculated reflectivity and dispersion curves for Layertec GTI mirror set II [372]. Courtesy of Layertec.

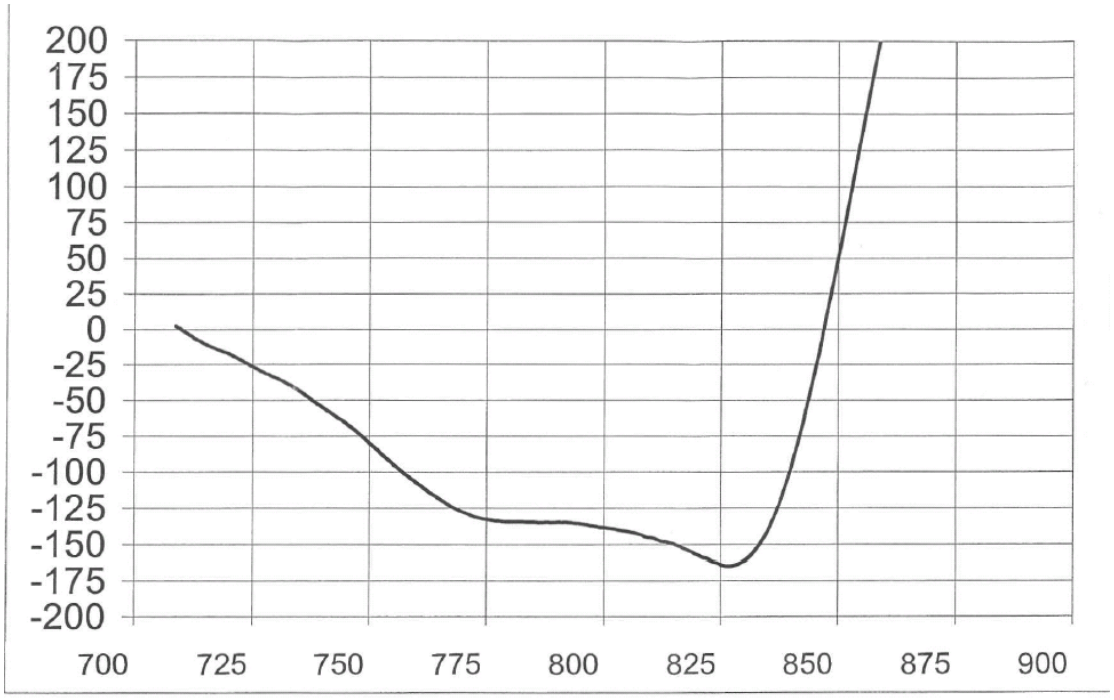

Figure A 24: Measured dispersion curves for Layertec GTI mirror set II. Courtesy of Layertec.

APPENDIX B

SPECIFICATIONS OF THE PUMP LASER DIODES

In this Appendix, we will provide the specifications of the laser diodes we have used for pumping the Cr:Colquiriite lasers. In Section B1, we will provide the specs of the 660 nm 130 mW single mode diodes (HL6545MG) [373]. In Section B2, we will present the properties of the 642 nm 150 mW single mode diodes (HL6385DG), which become available in 2009 (we have started using it in July 2009) [374]. Finally, In Section B.3, we will describe the properties of the high-power (~1.5 W) single-emitter multimode pump diodes around 650 nm that was used to pump the Cr:LiCAF gain medium.

We note here that red-diode laser technology keeps improving. For example, Optnext just released a 637 nm 170 mW diode in Jan 2010 (HL63133DG) [238]. Also, recently, a 1-W, nearly transform-limited (M^2~1.3) 650 nm diode laser source was demonstrated [239]. It is clear that these advances will have a direct positive impact on the specifications of Cr:Colquiriite lasers in the future.

B.1 Properties of 660 nm 130 mW Single-Mode Diodes (HL6545MG)

In this section, we will summarize the properties of the 660 nm 130 mW AlGaInP single-mode diodes (HL6545MG, Hitachi) that we have used as the pump source in most of the experiments (this was the highest power single-mode red-diode available at that time) [373]. Figure B.1 shows a picture of the bare diode, and the diode in its holder. The single mode diode had an asymmetric beam profile with an aspect ratio of ~2 ($\theta_{\perp}\approx17°$, $\theta_{//}\approx10°$); hence, cylindrical microlenses were required to obtain a circular beam profile. Besides providing a circular beam, the cylindrical microlens also corrects for the inherent astigmatism of the beam [375]. Figure B.2 shows the diode output beam profile with and without the cylindrical microlens. The diodes were purchased with a built-in microlens (Figure B.3) from Blue Sky Research (VPSL-0660-130-X-5-G) [376]. The cost of the diodes including the built-in microlens is only ~$150 (price without the microlens is ~$50) [377]. The diode was held by using the commercial collimating tube package from Thorlabs, LT230P-B (costs ~$110) [378], which uses a 4.5 mm focal length aspheric lens with an NA of 0.55 (A230TM-B) [379]. We have mainly used expensive low-noise high-current diode drivers from ILX or Newport to drive this diode; which have more specs than required for this job (if one doesn't need low noise performance). This diode only requires ~200 mA to operate; hence, actually it can be driven by very low cost drivers such as FL593FL 0.5A from Wavelength

Electronics (cost ~$230) [380]. Moreover, the FL593FL driver can be powered by batteries, which might become important for some specific applications.

A maximum output power of ~160mW could be obtained by driving the diodes at a current of 220 mA (Figure B5). However, this is above the rated output power of 130 mW, where the rated driving current is 170-210 mA. Due to overdriving, we have observed diode burning time to time, but this was quite rare. In the laser experiments, no active cooling was applied to the lens tube, since the improvement on diode output power upon cooling was less than 10%. The diode output wavelength was dependent on driving current (~660±2 nm, Figure B6), but this is not a problem for Cr:Colquiriite gain media with broad absorption bands. Note that this diode could also be operated in pulsed mode (Fig. B8).

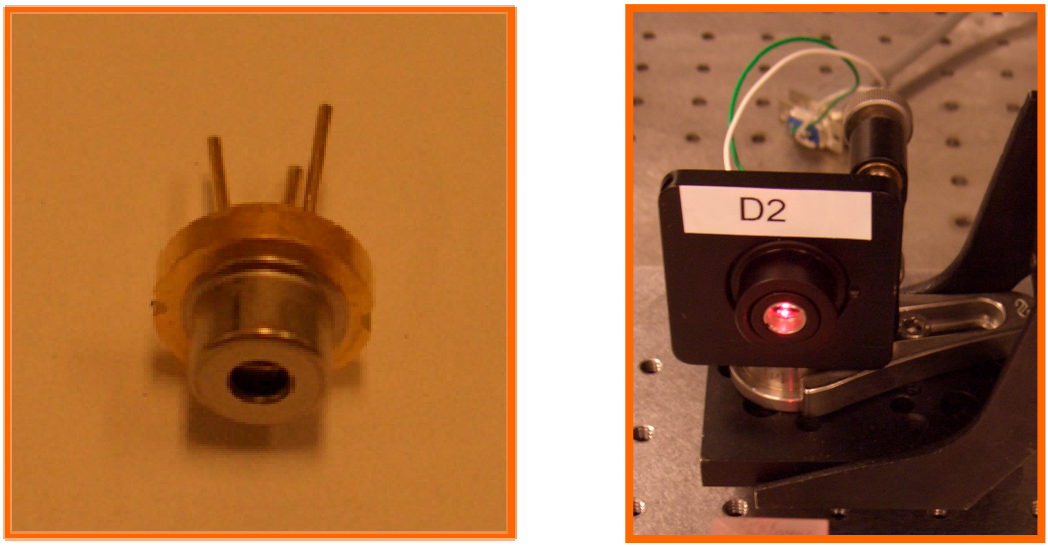

Figure B.1: (Left) Picture of the single mode-diode (HL6545MG). The diode includes a built-in cylindrical microlens, which is not visible in this picture. (Right) Single-mode diode in operation, a regular 1" mirror holder is used for alignment.

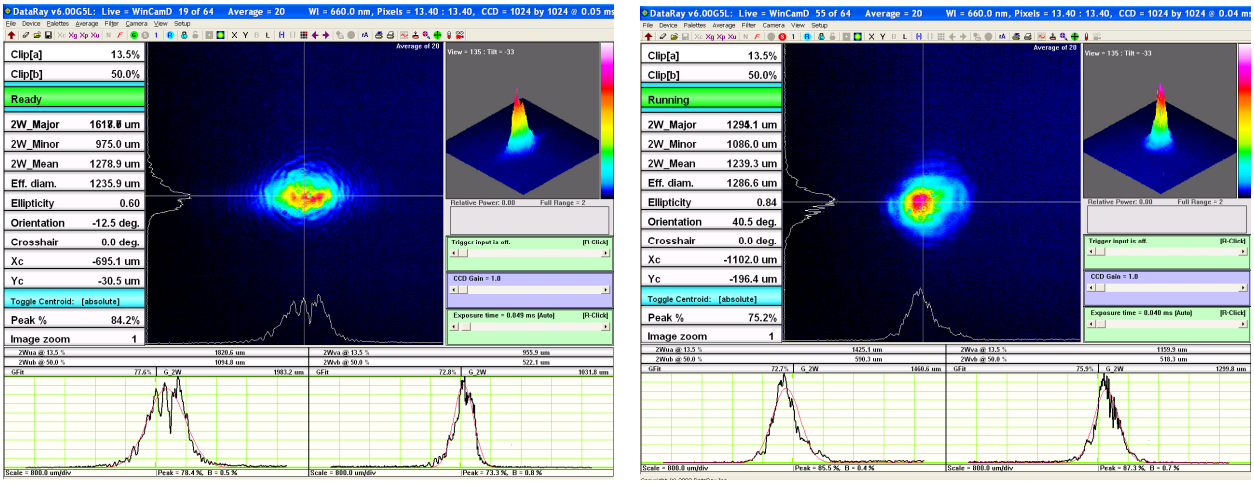

Figure B2: Single-mode diode output beam profile measured (left) without and (right) with the cylindrical microlens. The aspect ratio of the beam was measured as (left) ~2 and (right) ~1.05, showing the improvement in beam circularity.

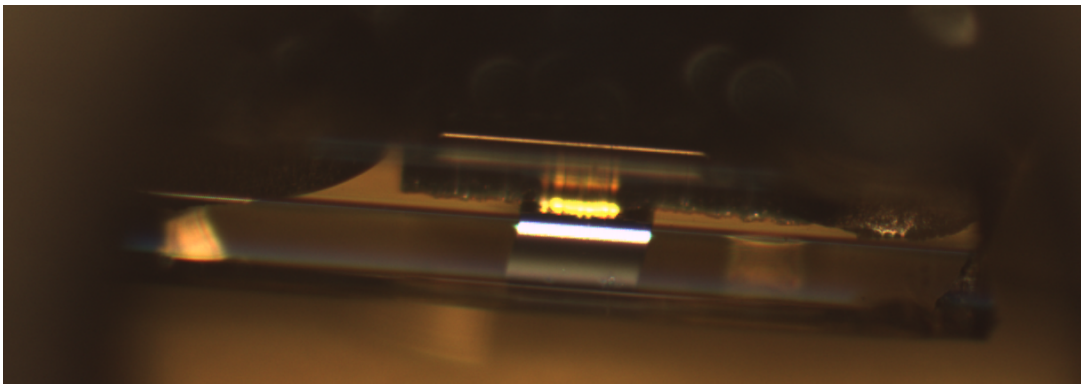

Figure B3: Microscopy image of the built-in cylindrical microlens on the single mode diode.

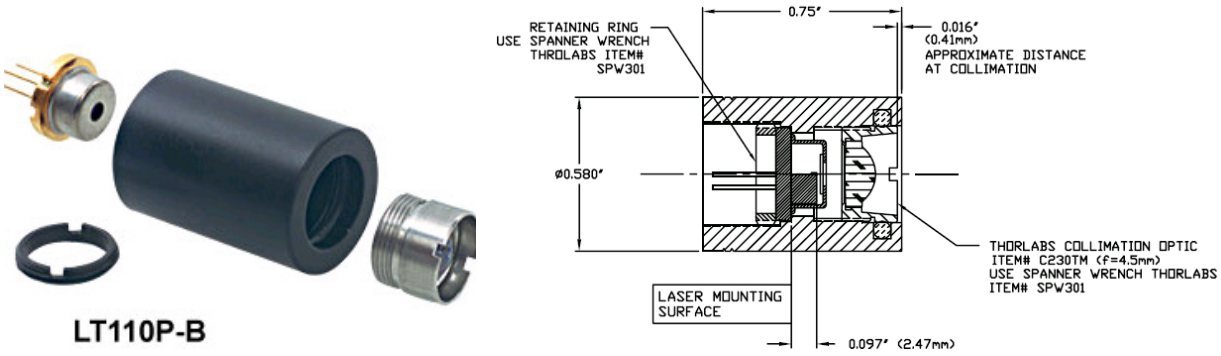

Figure B4: LT230P-B collimating tube package that was used in collimating the single mode diodes [378, 381]. Courtesy of Thorlabs. This information is provided here under the fair use doctrine of United States copyright law [11].

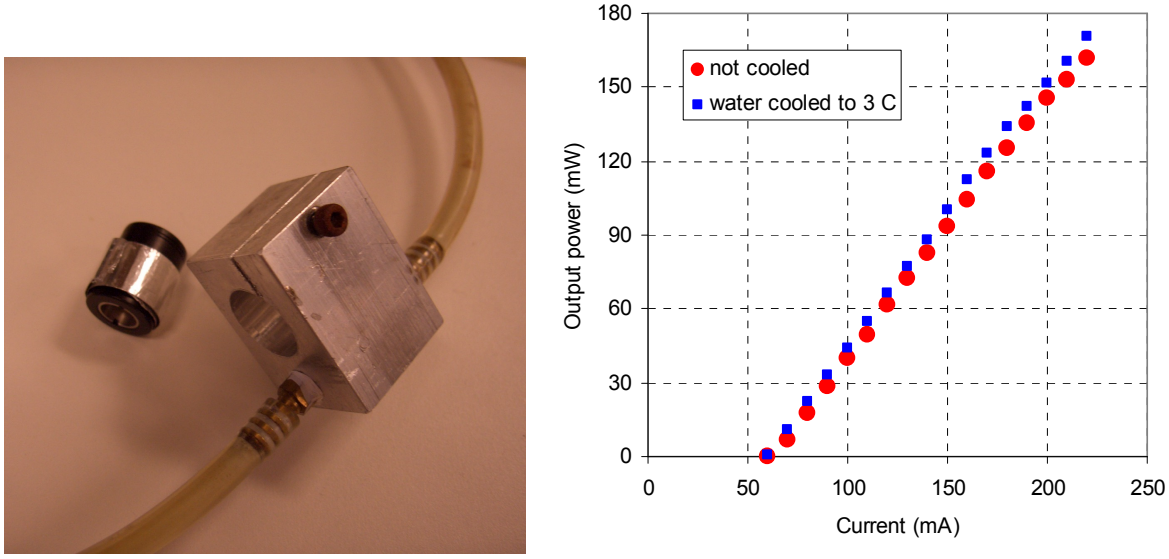

Figure B5: (Left) LT230P-B collimating tube package and an aluminum holder with water cooling. (Right) Measured laser output power with and without cooling of the aluminum holder. Cooling improved the obtainable laser powers from ~160 mW to only ~170 mW at a 220 mA drive current. Hence, in the experiments we have not applied water cooling to the HL6545MG diodes.

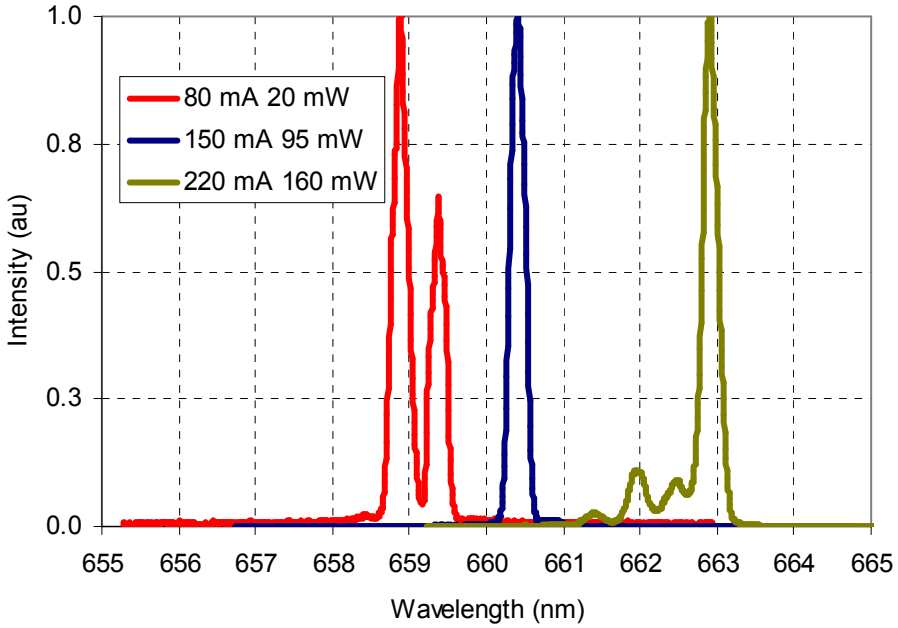

Figure B6: Variation of HL6545MG diode laser wavelength with diode current, due to increased thermal load on the diode.

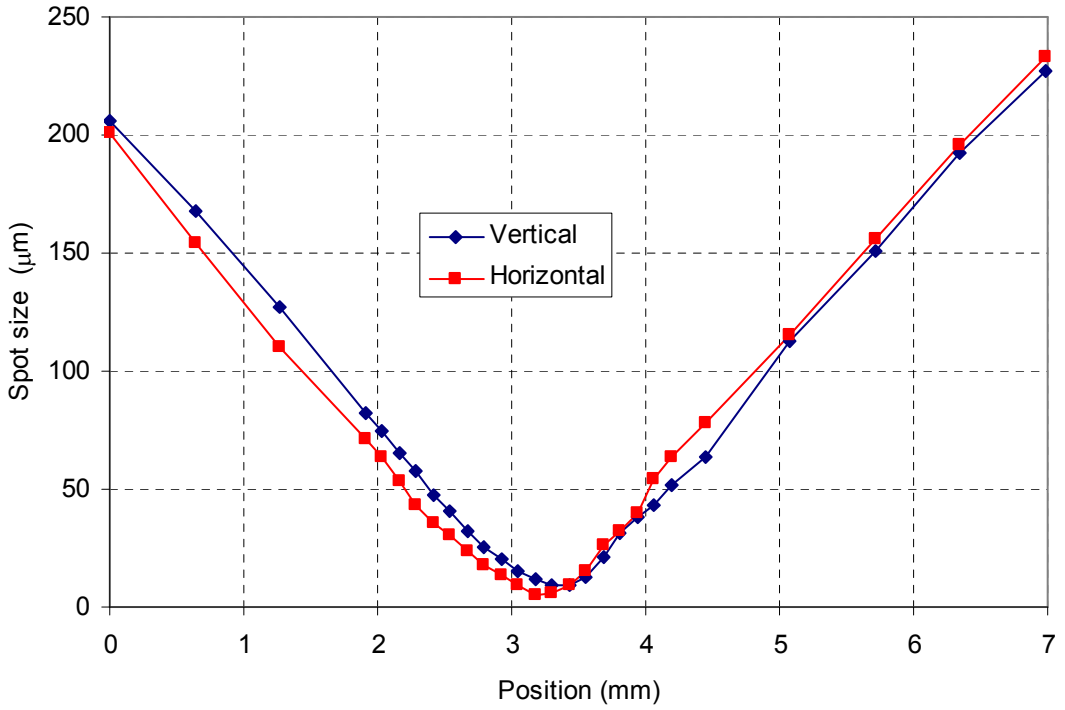

Figure B7: Measured variation of spot size with distance for the HL6545MG diode around the focus of a 35 mm lens . We measured an M^2 value of 1.01 for the horizontal axis and 1.05 for the vertical axis.

opnext
Powered by HITACHI

HL6545MG

Visible High Power Laser Diode for Recordable-DVD

ODE-208-038C (Z)
Rev.3
Feb. 24, 2006

Description

The HL6545MG is a 0.65 µm band AlGaInP laser diode (LD) with a multi-quantum well (MQW) structure. It is suitable as a light source for large capacity optical disc memories, such as H/H type Recordable-DVD, and various other types of optical equipment.

Features

- Operating temperature: 75°C Max
  (300 mW(pulse), pw = 30 ns, duty = 35 %)
- Visible light output : λp = 660 nm Typ
- Low operating current :
  Iop(1) = 170 mA Typ (Po = 120 mW)
  Iop(2) = 345 mA Typ
  (Po = 300 mW(pulse), pw = 30 ns, duty = 35 %)

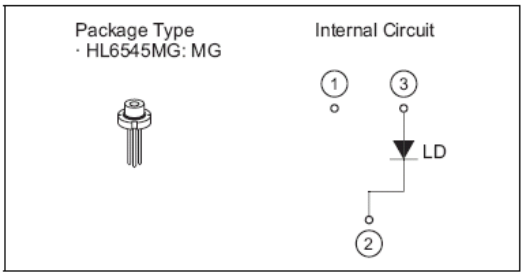

Note: This type is under development. Therefore, this data sheet may be changed without notice.

Absolute Maximum Ratings

(T_C = 25°C)

Item	Symbol	Ratings	Unit
Optical output power	P_O	130	mW
Pulse optical output power	$P_{O(pulse)}$	300 *	mW
LD reverse voltage	$V_{R(LD)}$	2	V
CW Operating temperature	$Topr_{(CW)}$	–10 to +75	°C
Pulse Operating temperature	$Topr_{(pulse)}$	–10 to +75	°C
Storage temperature	Tstg	–40 to +85	°C

Note: Pulse condition : Pulse width = 30 ns , duty = 35 %

Electrical Characteristics

(T_C = 25°C)

Item	Symbol	Min	Typ	Max	Unit	Test Conditions
Threshold current	Ith	—	55	75	mA	—
Operating current(1)	$I_{OP}(1)$	—	170	210	mA	P_O = 120 mW
Operating current(2)	$I_{OP}(2)$	—	345	—	mA	P_O = 300 mW(pulse) pw = 30 ns, duty = 35 %
Operating voltage	V_{OP}	—	2.45	3.0	V	P_O = 120 mW
Lasing wavelength	λp	652	660	664	nm	P_O = 120 mW
Beam divergence parallel to the junction(1)	θ//(1)	7.5	10.0	12.0	deg.	P_O = 120 mW
Beam divergence perpendicular to the junction	θ⊥	15	17	19	deg.	P_O = 120 mW
Beam divergence parallel to the junction(2)	θ//(2)	7.5	—	—	deg.	P_O = 5 mW
Astigmatism	A_S	—	1	—	µm	P_O = 5 mW, NA = 0.55

Figure B8: Specifications for the HL6545MG diode[373]. Courtesy of Opnext. This information is provided here under the fair use doctrine of United States copyright law [11].

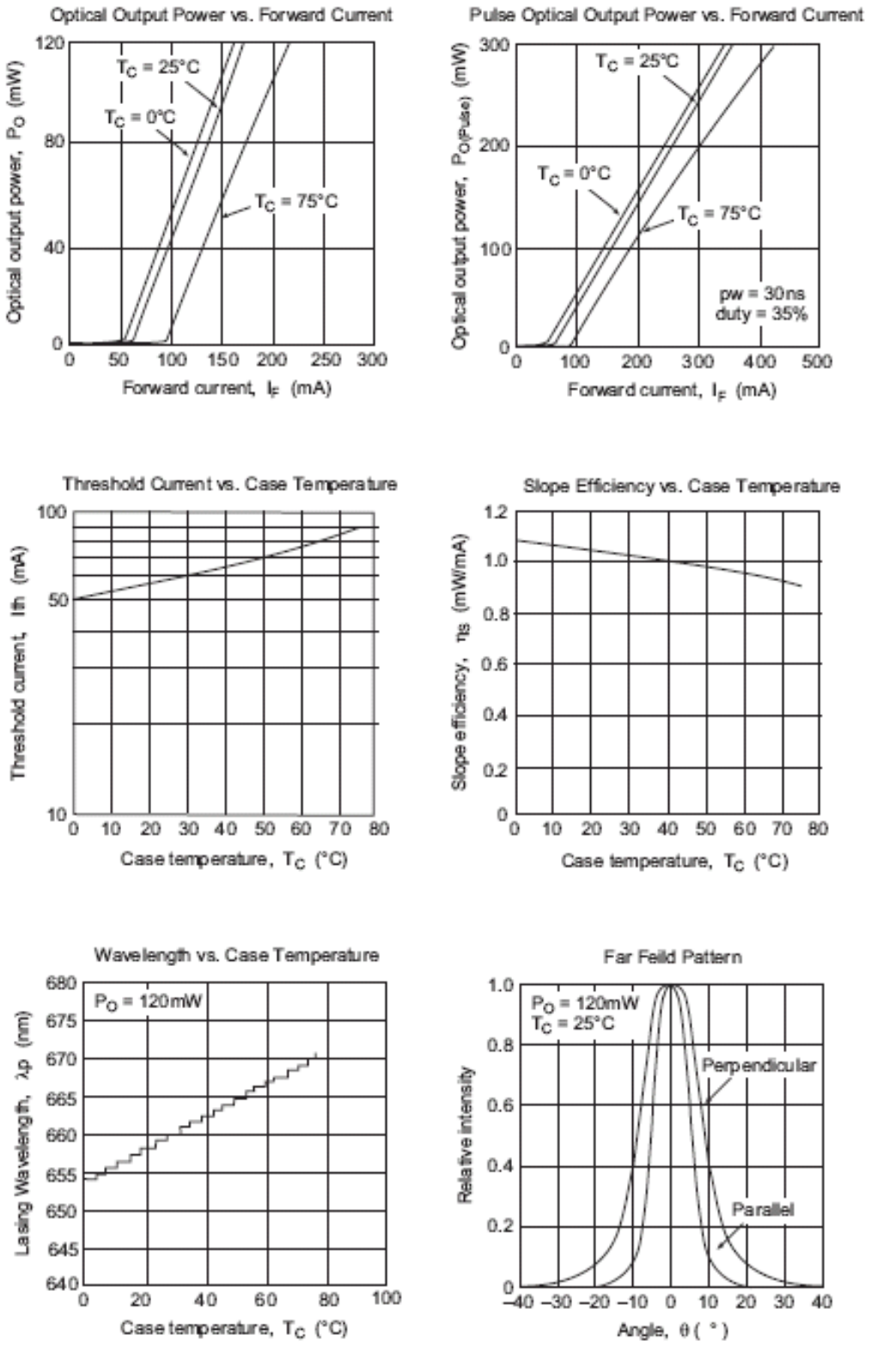

Figure B9: Typical characteristics curves for the HL6545MG diode[373]. Courtesy of Opnext. This information is provided here under the fair use doctrine of United States copyright law [11].

B.2 Properties of 642 nm 150 mW Single-Mode Diodes (HL6385DG)

In this section, we will provide the specifications of the 642 nm 150 mW AlGaInP single-mode diodes (HL6385DG, Hitachi), which we started to use in July 2009 [374]. Earlier versions (working samples) of this diode become available around February 2009 at a price of $310. Later, with the help of Dr. Peter Fendel from Thorlabs, we have purchased custom microlensed version of these diodes from Blue Sky Research at a price of $350 (bare diode price ~$250).

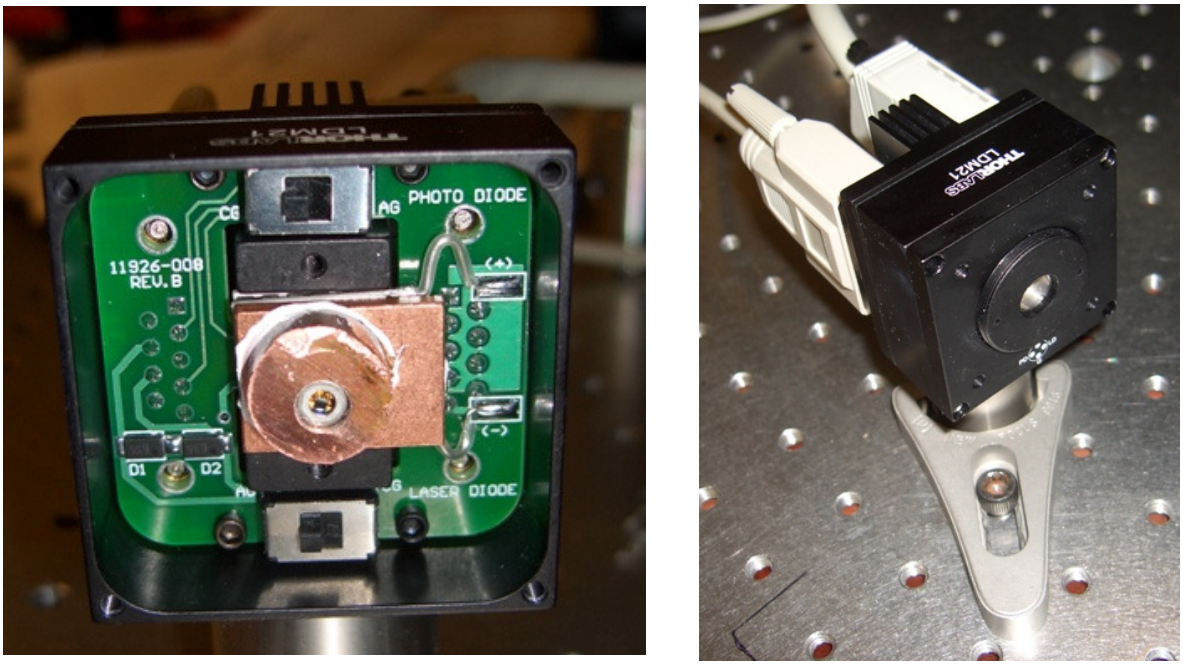

Figure B10: Pictures of the HL6385DG diode [374]. This diode required cooling, and a TEC cooled, temperature controlled mount from Thorlabs was used for holding the diode (LDM21) [382]. The diode is mounted using a home-made cupper holder, which is pressed to the TEC cooler. Thermal grease is used in between. A 4.5 mm focal length aspheric lens with an NA of 0.55 (A230TM-B) was used to collimate the diode output beam.

Unlike the 660 nm diodes that we have described in part B1, these HL6385DG required active cooling for efficient operation (Figure B10). To cool the diodes we have used LDM21 temperature controlled mounts from Thorlabs (cost ~$305) [382]. As the TEC and diode driver, we have used ITC8052 drivers (cost ~$1850) [383] with PRO8000 platform (cost ~$2500) [384]. A maximum output power of about ~200-210 mW around 640 nm could be obtained by driving the diodes at a current of 350 mA at a TEC set temperature of 15 °C (Figure B11). However, this is above the rated output power of 150 mW (25 °C), where the rated driving current is 280-350 mA. We have been using this diode at these setting for about a year now, and so far we haven't observed any diode damage. Also note that the ITC8052 driver is actually not strong enough to keep the TEC temperature at 15 °C, and for driving currents above ~250 mA equilibrium temperature of the TEC holder is above at 15 °C (ITC8052 driver

has a TEC current limit of 2 A). Currently, we are investigating water cooling option of this diode using a similar holder that was shown in Fig B5, and the initial test results look motivating (Fig. B12). We hope that optimizing the diode holder design will improve the performance. Usage of water cooling can help to reduce the cost of the pumping system greatly by eliminating the need to use the relatively expensive TEC drivers and holders.

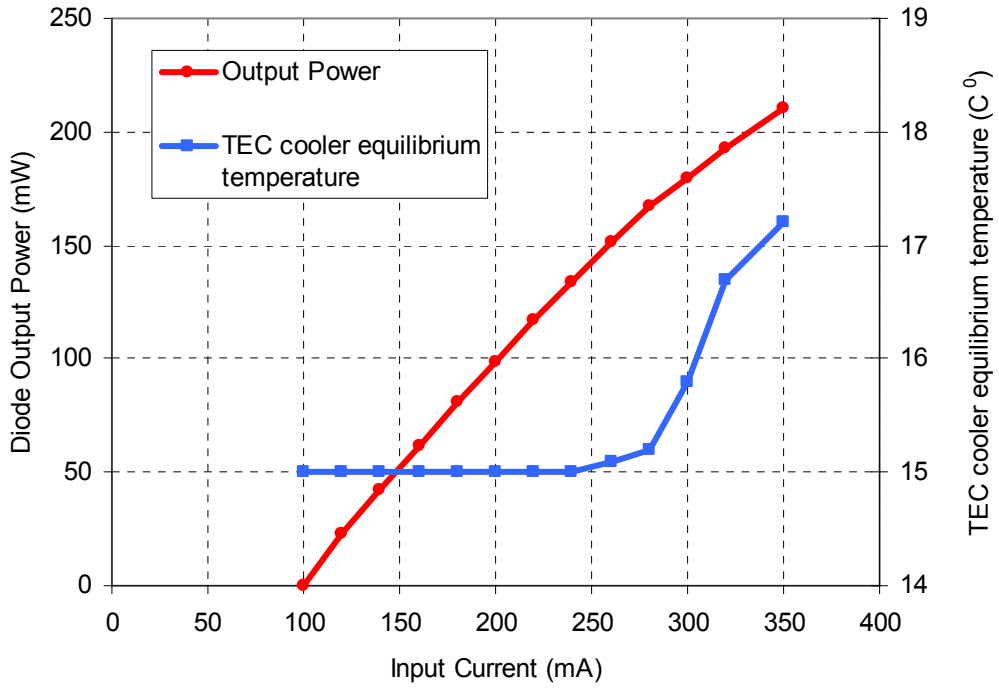

Figure B11: Measured variation of output power of the HL6385DG diode with driving current when the diode is TEC cooled using the LDM21 mount. The TEC cooler temperature is set to 15 C°; however at higher currents the equilibrium temperature was higher (TEC driver ITC8052 has a current limit of 2 A).

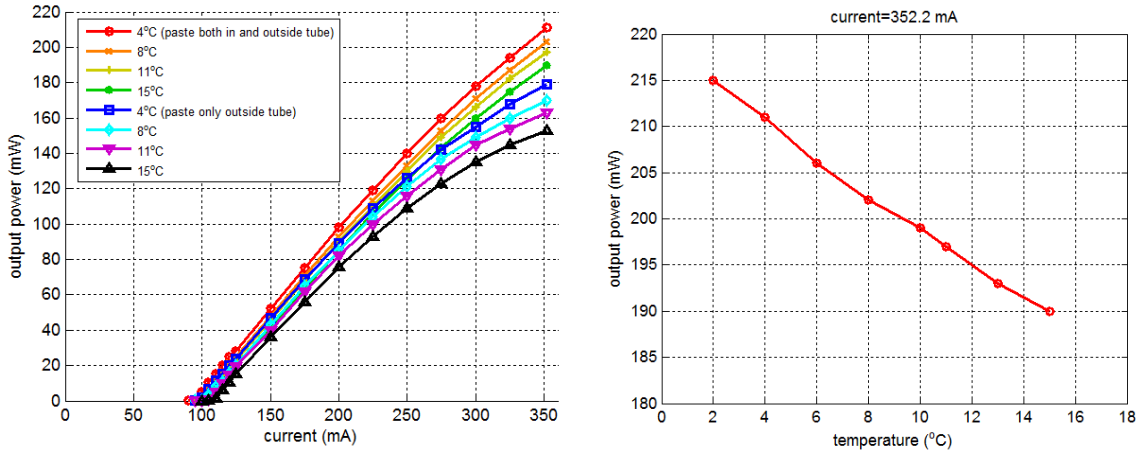

Figure B12: (Left) Measured variation of output power of the HL6385DG diode with driving current at several different water cooling temperatures when the diode is cooled using an holder that was shown in Fig B5. Usage of a thermal paste proved itself to be quite useful. (Right) Variation of diode output power with water temperature for the circulating water chiller. This data is kindly provided by our new PhD student, Jing Wang.

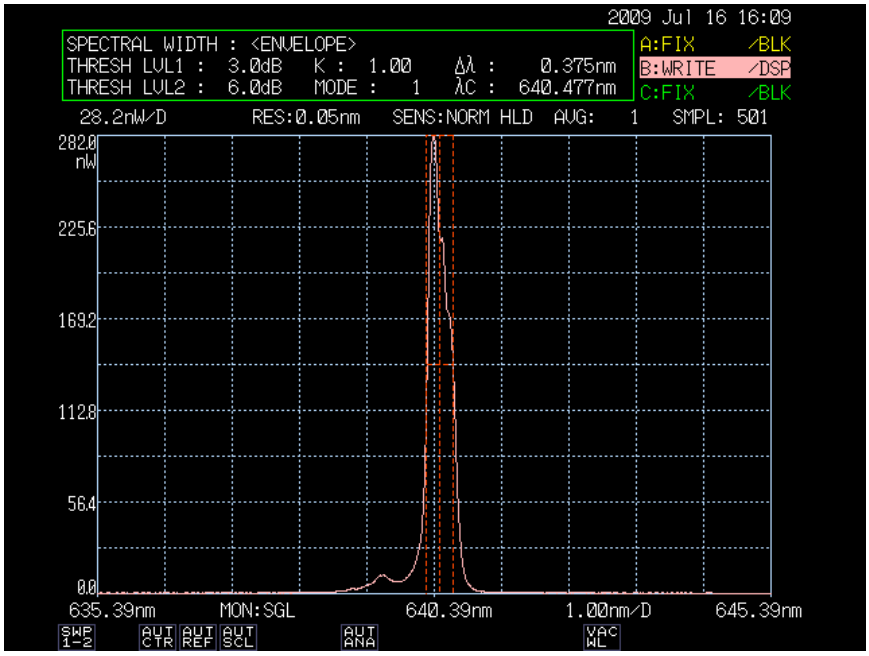

Figure B13: Measured diode wavelength at a current of 350 mA. The diode emits light at ~640.5 nm, with a FWHM of ~0.4 nm.

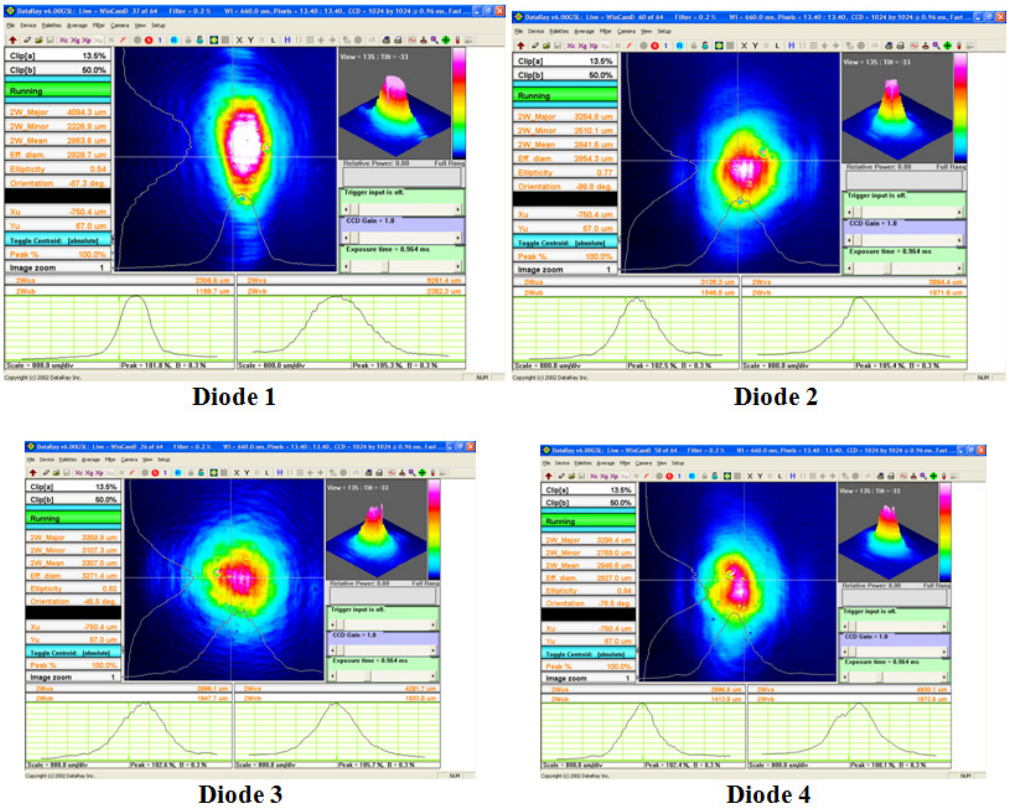

Figure B14: Measured beam profile from four different microlensed HL6385DG diode, only the first diode seem to have some remaining elipticity problem.

opnext

HL6385DG

Visible High Power Laser Diode

ODE2001-00 (M)
Rev.0
Apr. 03, 2008

Description

The HL6385DG is 0.64 μm band AlGaInP laser diodes with a multi-quantum well (MQW) structure. It is suitable as light sources for laser display and various other types of optical equipment.

Features

- Visible light output: 642 nm Typ
- Single longitudinal mode
- Optical output power: 150 mW CW
- Operating temperature: +40°C
- TE mode oscillation
- Small package: ϕ5.6mm

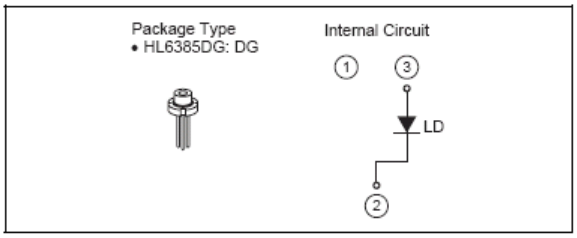

Absolute Maximum Ratings

(T_C = 25°C)

Item	Symbol	Ratings	Unit
Optical output power	P_O	150	mW
LD reverse voltage	$V_{R(LD)}$	2	V
Operating temperature	Topr	–10 to +40	°C
Storage temperature	Tstg	–40 to +85	°C

Note: Operating Temperature is defined by Case Temperature "Tc". High increase in temperature of LD chip itself is expected during operation due to high current density.
Thus, without proper heat dissipation, it is observed that no specific output power is achieved or it results to LD degradation. It is advised that sufficient measure of heat dissipation should be taken so that LD's maximum operating temperature is not exceeded during actual operation.

Optical and Electrical Characteristics

(T_C = 25°C)

Item	Symbol	Min	Typ	Max	Unit	Test Condition
Threshold current	Ith	—	110	140	mA	—
Operating current	I_{OP}	—	280	350	mA	P_O = 150 mW
Operating voltage	V_{OP}	—	2.6	3.0	V	P_O = 150 mW
Beam divergence parallel to the junction	θ//	6	9	13	°	P_O = 150 mW
Beam divergence perpendicular to the junction	θ⊥	13	17	22	°	P_O = 150 mW
Lasing wavelength	λp	635	642	647	nm	P_O = 150 mW

Figure B15: Specifications for the HL6385DG diode [374]. Courtesy of Opnext. This information is provided here under the fair use doctrine of United States copyright law [11].

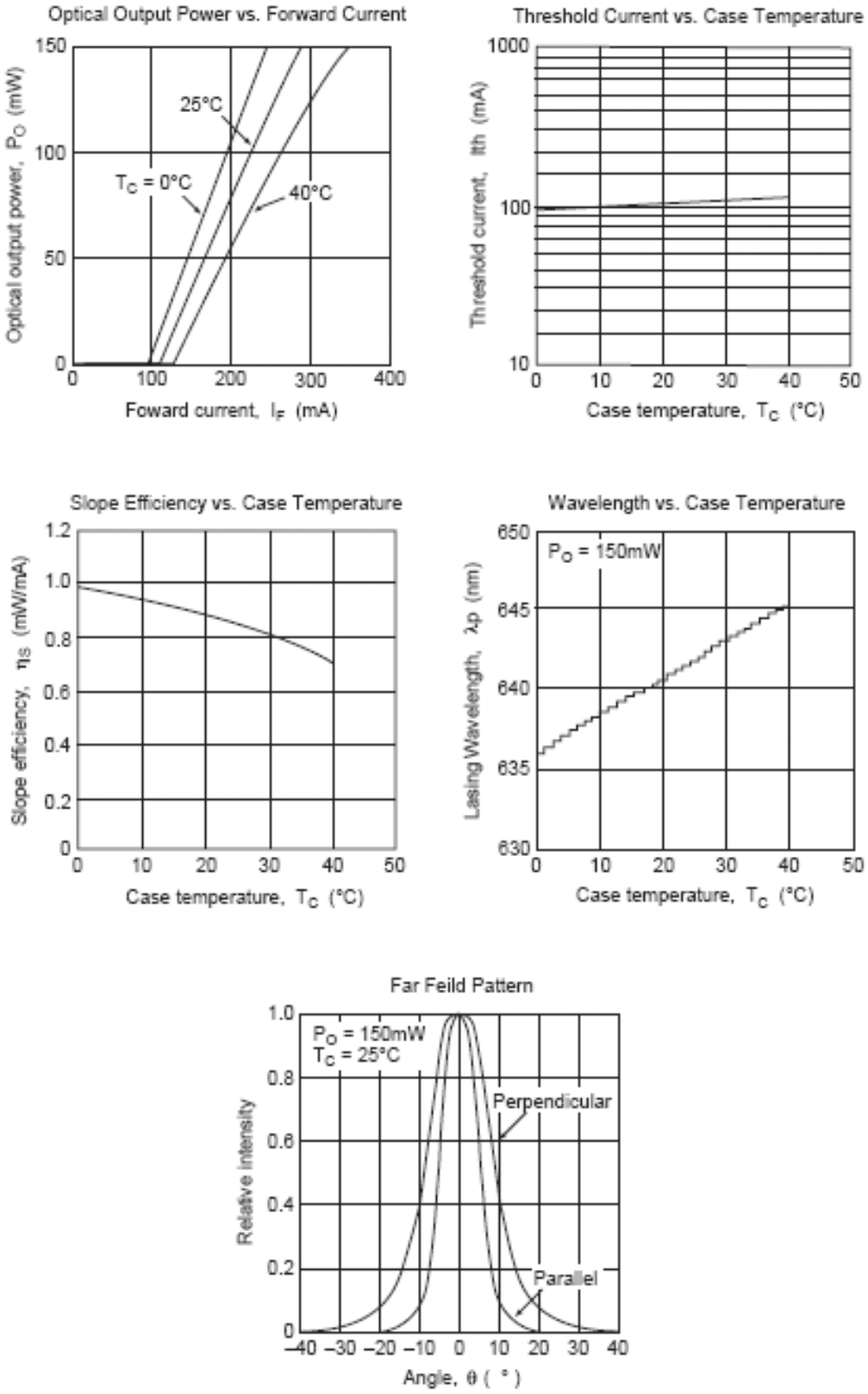

Figure B15: Specifications for the HL6385DG diode [374]. Courtesy of Opnext. This information is provided here under the fair use doctrine of United States copyright law [11].

B.3 Properties of Multimode Diodes

In this section, we will summarize the properties of the single-emitter multimode diodes, which were used as pump sources for Cr:LiCAF gain media. Single-emitter, multimode output diodes emitting around ~650 nm, was commercially available, and purchased from n-Light Photonics [385]. When the project was first initiated in July, 2006, the maximum output power from single-emitter multimode diodes was 1 W. Later, in August 2007, 1.5 W multimode diodes become available. During the experiments, we have realized that, besides providing higher pump power, the 1.5 W diodes has also provided slightly better laser operation, which we believe is due to the improvements in beam quality. In Chapter 4, we will mostly present the results obtained with the 1.5-W diodes; since this is the newest technology, and gave the best results. Results obtained with 1-W pumped Cr:LiCAF laser can be found in [143]. As of today (May 2009), 1.5 W is still the highest output power that could be provided by single-emitter multimode diodes around ~650 nm.

The single-emitter multimode diodes are available at the wavelengths of 665 nm, 680 nm and 690 nm with 1.5 W output and at 639 nm with 0.75 W of output. In this study, we have used the 665 nm diode (C-1.5-0665, n-Light); since, among the available wavelengths, with 1.5-W of output, this wavelength is closest to the absorption peak of Cr: Colquiriite gain media.

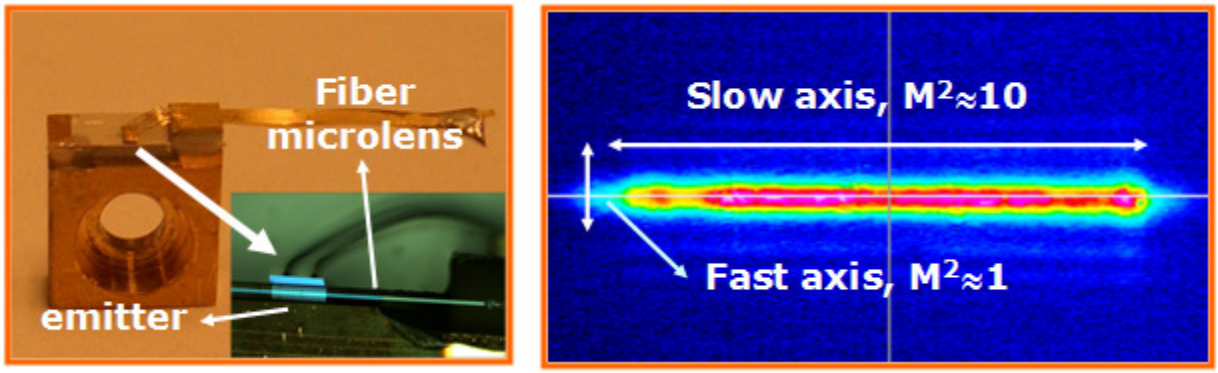

(a) (b)

Figure B16: (a) Picture showing the multimode diode with a c-mount package. The diode has a built-in cylindrical fiber microlens to collimate the diode output in the fast axis. (b) Laser diode output measured by a CCD camera. Note that this is not the image of diode facet. The diode emitter has a size of 1μm x 150 μm.

Figure B.16 (a) shows a picture of the 665 nm single-emitter multimode diode, from n-Light Photonics (C-1.5-0665, n-Light) [385]. The multimode diode, which cost only $900, provides about 1.5-W of output power at a central wavelength of ~665±5 nm. The diodes had a typical spectral width of ~1.5 nm (FWHM), and a temperature tuning coefficient of 0.15 nm/C°. In the experiments, due to its lower price we preferred to use c-mount packaged diodes [386]. However, the drawback of this package type is, the laser is in open air, with a simple heat-sink, and there is no protection for the delicate laser chip. We have

damaged several diodes during this project, either due to back reflection or due to water condensation on diode facet (Fig. B18 (b)). High-heat load (HHL) packaging provides safer operation, but the diode cost increases to $1550 (Fig. B17).

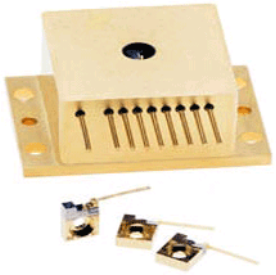

Figure B17: C-mount and high-heat load (HHL) type packaging for the multimode diodes [385]. Courtesy of n-Light.

The emitter size of the diode is 1μm x 150 μm, making the diode output beam quite asymmetric. The fast and slow axis of the diodes had a divergence of 43° and 10°, respectively. The length of the diode laser cavity is 1.5 mm (Fig. B18 (a)), which is also equal to the gain medium length (the length is 1 mm for the 1-W diodes). The diode laser cavity has very high output coupling, where the reflectivity of the front facet of the diode is only 4-5%. A cylindrical fiber micro-lens with a focal length of about ~100 μm is used to collimate the light along the fast axis (perpendicular to the plane of the junction). The distance between the diode output facet and the microlens is 20-30 μm. After the microlens, the fast axis divergence decreased from 43° to about 1.25°. The additional cost of microlensing the diode was $250, and was also provided by n-Light.

Diode output was diffraction limited along the fast axis, with an M^2 of 1-1.2, due to the small dimension in this axis (1 μm). In the slow axis (parallel to plane of the junction), the dimension is large (150 μm), and there is no factor that could suppress the higher order modes. Hence, in this axis, the diode output is multimode with a typical M^2 of ~8-10 (Fig. B16-(b)). Since, these are relatively high power diodes, and the thermal mass of the c-mount is quite small, the diode mount required active cooling. To provide the necessary cooling, we used a home-made mount, where we mounted the c-mount diode to a large aluminum holder, and then the holder was water cooled by circulating water from a chiller (Fig. B18-(c)). We note here that, diode mounting fixtures for c-mount diodes are also available commercially [387] (Fig. B18-(d)).

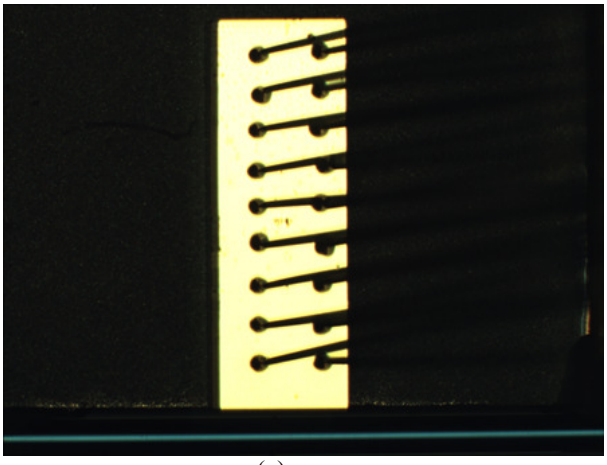

(a)

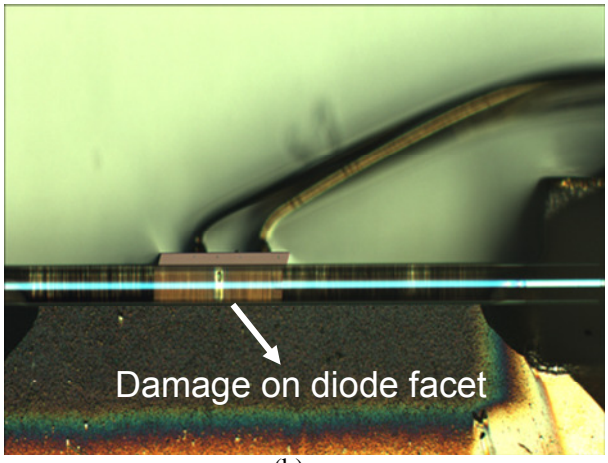

(b)

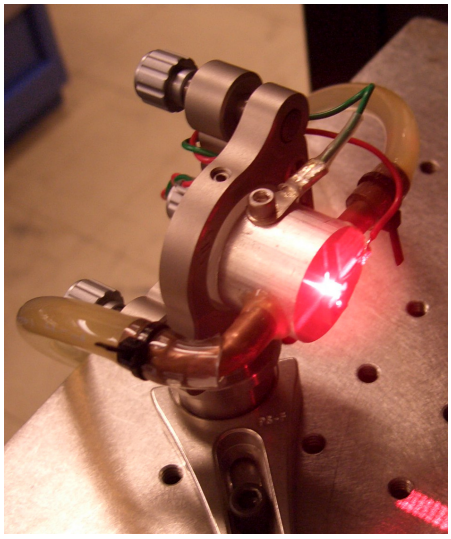

(c)

(d)

Figure B18: (a) Picture of the diode gain chip from top. Electrical connections are clearly visible, and equally distributed along the gain chip. It is also possible to see the cylindrical microlense, which appears as a flat blue line in front. (b) Picture of the diode gain chip from front, where we can see the damage on the front diode facet. We believe, the damage was caused by condensed water, while operating the diode at 15 °C, in a humid day. (c) Picture of the 1.5 W, ~665 nm, single-emitter multimode diodes. A home-made mount was used to hold the diode and to provide the required cooling. The c-mount diode was connected to an aluminum holder, which was water cooled by circulating chiller water. (d) A commercial temperature controlled c-mount fixture (ILX, LM-4409), where the cooling is provided by TEC coolers [388]. We haven't observed any problems related to out home-made mount, but commercial mounts might be a more reliable alternative to use. Courtesy of ILX Lightwave.

Figure B19 below shows the input current, output power curve for the 1.5-W, 665-nm, single emitter multimode diode. We have used ILX multi-channel laser diode controller (LDC-3916), with 3A current sources modules (LDC-3916338), to drive the diodes. The diodes have a lasing threshold of about ~550 mA, and provided up to 1.6-W of output power at a current of ~2.2 A (voltage ~2.22 V). The slope efficiency of the diodes is about 1.16 W/A, and the total electrical-to-optical efficiency of the diode is

around 34 % (~1.5/ (2x2.2)). This also shows that the remaining electrical input to the diodes, which is dissipated as heat, is relatively large (~3W), and the diodes should be cooled.

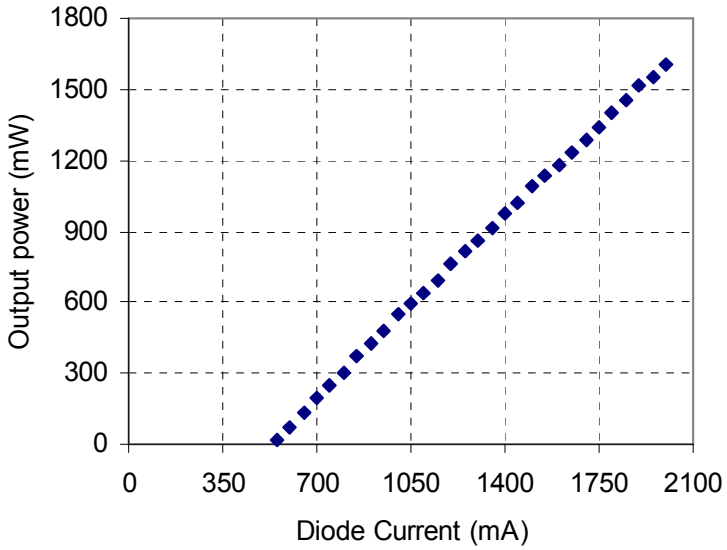

Figure B19: Efficiency curve for the 1.5-W, multimode n-Light diodes. The curve was taken while cooling the diode holder to a temperature of 20 °C.

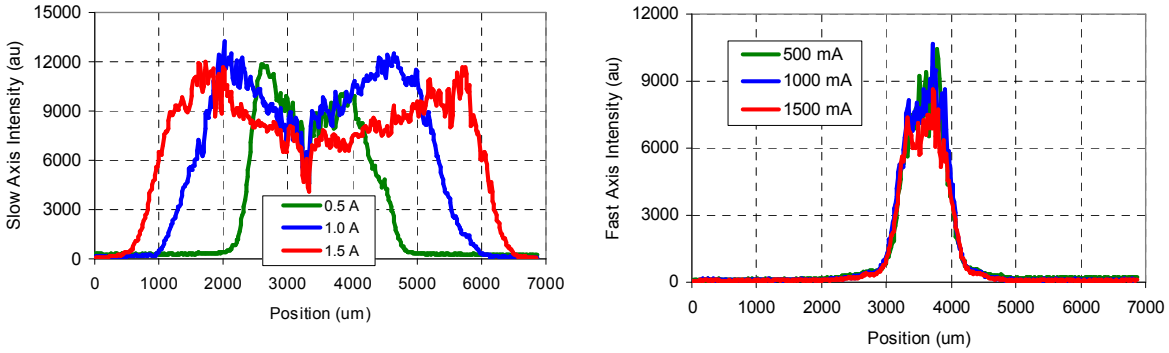

Figure B20: Variation of the diode beam shape with changing input current, for the slow and fast axis.

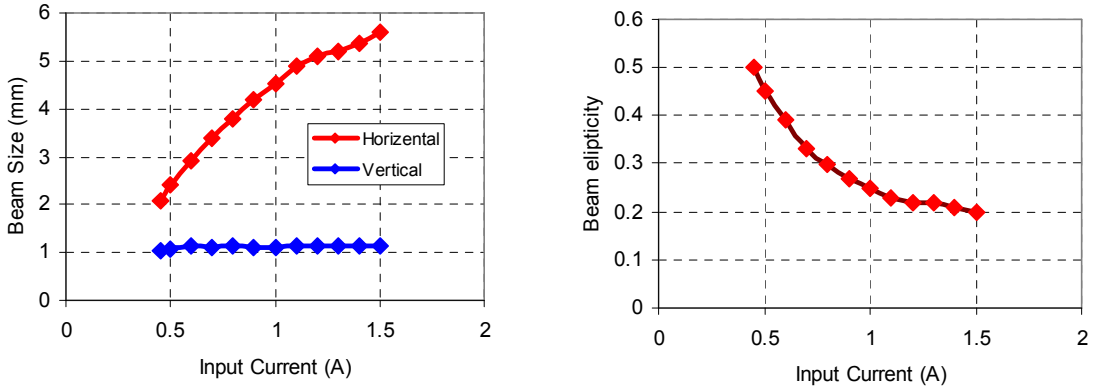

(a) (b)

Figure B21: (a) Variation of the diode beam size with changing input current, for the slow and fast axis. (b) Variation of the diode output beam elipticity with input current.

The diode lasers output beam properties heavily depended on the diode driving current, and the values we have specified above are for the maximum rated output power (1.5-W). Here, we will quickly present the specs of the diode laser beam at other driving currents. This might be of interest, because while using these diodes as pump sources for Cr:LiCAF lasers, we not only use them at their maximum rating, but at lower power settings as well (for example while taking the efficiency curves of the Cr:LiCAF laser). Figure B20 shows the variation of the beam shape (at far filed) with changing input current. Similarly, Fig. B21 (a) and (b) shows the variation of beam size and beam elipticity with input current. Figures show that, for the slow axis, as the input current increases, the beam size gets larger. This is because larger portion of the diode gain medium become active and starts to lase. Note that, beam shape in the fast axis is relatively insensitive to diode driving current, due to the small size in this axis. Due to the change in beam shape with power level, Findlay-Clay & Caird analysis with multimode diode pumped Cr:LiCAF laser did not give meaningful results. This problem might be solved by operating the diodes at a fixed power level, and by using a half-wave plate and a polarizing beam splitter cube to adjust the incident pump power.

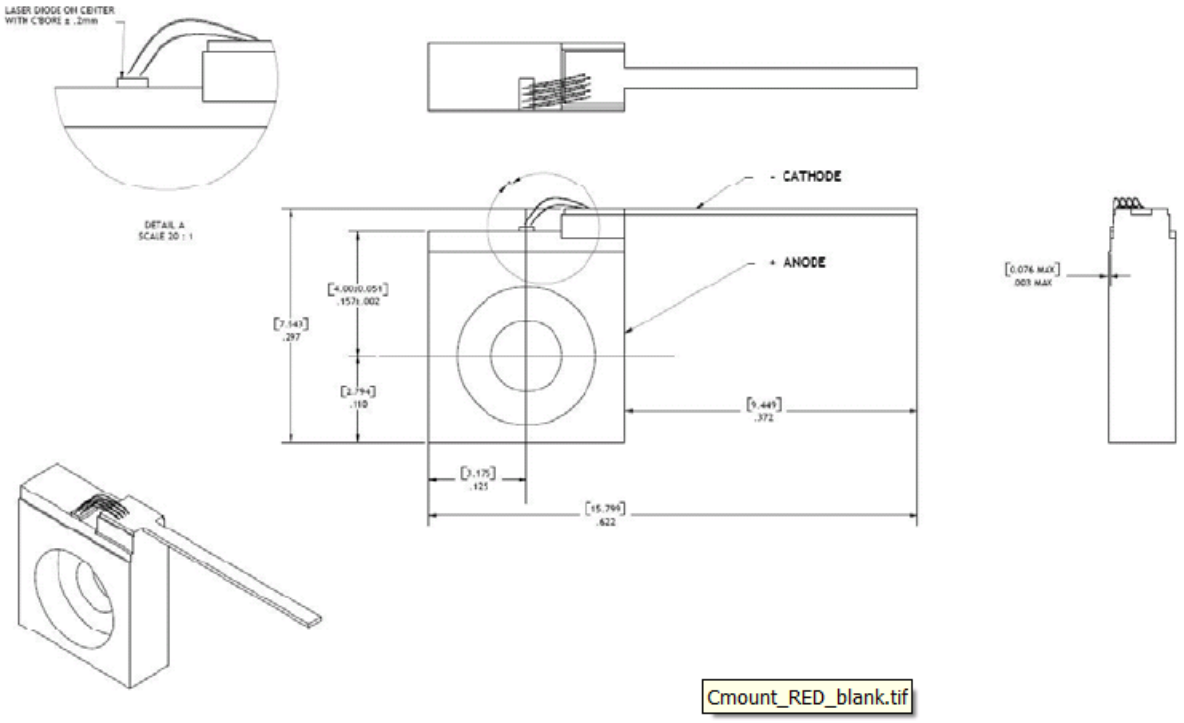

Figure B22: Package dimensions for the n-Light C-1.5-0665 diode [389]. Courtesy of n-Light. This information is provided here under the fair use doctrine of United States copyright law [11].

Typical device specification

		C-0.75-0639	C-1.5-0665	C-1.5-0680	C-1.5-0690
Optical					
Center wavelength	nm	639	665	680	690
CW output power	W	0.75	1.5	1.5	1.5
Center wavelength tolerance	nm	± 4	± 5	± 5	± 5
Emitter size	µm	150	150	150	150
Spectral width (FWHM)	nm	< 3	< 3	< 3	< 3
Slope efficiency	W / A	> 1	> 1	> 1	> 1
Polarization	TM or TE	TM	TE	TE	TE
Fast-axis divergence	Degrees	42°	43°	43°	43°
Slow-axis divergence	Degrees	10°	10°	10°	10°
Wavelength temperature coefficient[1]	nm / °C	0.15	0.15	0.15	0.15
Electrical					
Total conversion efficiency	%	20	25	25	25
Threshold current (I_{TH})	mA	700	660	668	680
Operating current (I_{OP})	mA	1500	1900	1900	1900
Operating voltage (V_{OP})	V	2.2	2.08	2.08	2.08
Series resistance (R_S)	Ω	0.15	0.1	0.1	0.1
Mechanical					
Lead soldering temperature (C-mount)	°C	150 (< 5 sec)	150 (< 5 sec)	150 (< 5 sec)	150 (< 5 sec)
Lead soldering temperature (HHL)	°C	250 (< 5 sec)	250 (< 5 sec)	250 (< 5 sec)	250 (< 5 sec)
Thermal					
Thermal resistance[2]	°C / W	10	10	10	10
Operating temperature range (C-mount)[3]	°C	-20 to +30	-20 to +30	-20 to +30	-20 to +30
Operating temperature range (HHL)[3]	°C	-20 to +50	-20 to +50	-20 to +50	-20 to +50
Storage temperature range[3]	°C	-20 to +80	-20 to +80	-20 to +80	-20 to +80
Thermoelectric cooler (HHL only)					
Drive current (Typical)	A	1.7	1.7	1.7	1.7
Drive voltage (Typical)	V	3.5	3.5	3.5	3.5
Thermistor resistance (25°C)	kΩ	10	10	10	10
Monitor photodiode (HHL only)					
Sensivity	µA/mW	1 to 10	1 to 10	1 to 10	1 to 10
Capacitance	pF	6	6	6	6
Breakdown voltage	V	25	25	25	25
Operating voltage	V	10	10	10	10

[1] The wavelength temperature coefficient is the wavelength shift per °C change at the diode junction.
[2] Thermal resistance is the diode junction temperature shift per incremental Watt of heat load.
[3] A non-condensing environment is required for storage and operation below ambient dew point.

Figure B23: Typical device specifications for the n-Light C-1.5-0665 diode [389]. Courtesy of n-Light. This information is provided here under the fair use doctrine of United States copyright law [11].

APPENDIX C

LIST of CR: COLQUIRIITE CRYTALS

In this appendix, we will provide a list of Cr:Colquiriite crystals that is in our inventory. Some of the crystals have been purchased/obtained and used during this PhD work, and some of them were from earlier Cr:Colquiriite projects of the MIT Optics and Quantum Electronics Group.

Quantity	Chromium Concentration (%)	Length (mm)	Thickness (mm)	Width (mm)	Cut	Coating	Source	Notes
1	10	2	3	4	Brewster-Brewster	-	VLOC	Broken (not usable), used in [59, 143, 178, 220], probably also used in [174]
1	8.4	2	2	3	Brewster-Brewster	-	VLOC	Broken in one of the earlier projects (still usable), ordered by Dr. Vikas Sharma, July, 2003, $985
1	11	1.5	2	3	Brewster-Brewster	-	VLOC	Ordered by UD, Jan 2007, $645
1	11	1.5	1	3	Brewster-Brewster	-	VLOC	Ordered by UD, Jan 2007, $645
1	11	2.5	1	3	Brewster-Brewster	-	VLOC	Ordered by UD, Jan 2007, $695, used in [191, 202]
1	11	2	1	3	Brewster-Brewster	-	VLOC	Ordered by UD, Jan 2007, $695
1	5	4	2	2.6	Brewster-Brewster	-	IKZ	Gave more than 2W cw power with multimode pumping
1	5	3	2	4.3	Brewster-Brewster	-	IKZ	
1	5	3.5	2	3.4	Brewster-Brewster	-	IKZ	
1	5	4	1	2.6	Brewster-Brewster	-	IKZ	
1	5	3	1	4.3	Brewster-Brewster	-	IKZ	
1	5	3.5	1	3.4	Brewster-Brewster	-	IKZ	
4	7	2	4	5	Plane-plane	S1 AR 780 & 852, S2 36%R @ 780 nm	VLOC	used in narrow linewidth laser project, in Prof. Kärtner's lab
6	7	2	4	5	Plane-plane	filter @ 782 nm	VLOC	used in narrow linewidth laser project, in Prof. Kärtner's lab

Table C1: List of the Cr:LiCAF crystals in our inventory.

Notes: IKZ: Leibniz Institute for Crystal Growth [390]. Dr. Detlef Klimm and Dr. Reinhard Uecker from IKZ kindly provided the 5% chromium doped boule that was used in preparing the 5% doped Cr:LiCAF crystals above (VLOC provided cutting and polishing of the samples at a price of $2000). We also thank Ms. Sue Busk from VLOC with her help with our inquiries [391]. The first crystal in the list is damaged by UD, in the

multimode diode pumping experiments, while the crystal was in its holder. We suspect that the crystal is cracked due to thermal expansion under heavy heat load.

Quantity	Chromium Concentration (%)	Length (mm)	Thickness (mm)	Width (mm)	Cut	Coating	Source	Notes
1	1.5	5	3	3	Brewster-Brewster	-	VLOC	Probably used in [160], currently quite lossy, with a few nice spots on the crystal
1	1.5	5	3	3	Plane-plane	AR 840-880 nm, HT 660-700 nm	VLOC	From earlier projects
1	1.5	5	3	3	Plane-plane	AR 840-880 nm, HT 660-700 nm	VLOC	From earlier projects, broken (not usable)
1	1.5	5	1.5	5	Brewster-Brewster	-	VLOC	Ordered by UD, Oct 2008, $500, used in [59, 165]
1	2.2	4	1.5	4	Brewster-Brewster	-	VLOC	Ordered by UD, Oct 2008, $500, has high thermal load
1	1.5	6	1.5	4	Brewster-Brewster	-	VLOC	Ordered by UD, Nov 2008, $500, used in timing jitter and GHZ [161]studies
1	1.5	7	1.5	5	Brewster-Brewster	-	VLOC	Ordered by UD, Sept 2009, $700, used in timing jitter
1	1.5	5.5	1.5	4	Brewster-Brewster	-	VLOC	Ordered by UD, Dec 2009, $650 used in timing jitter study

Table C2: List of the Cr:LiSAF crystals in our inventory.

Quantity	Chromium Concentration (%)	Length (mm)	Thickness (mm)	Width (mm)	Cut	Coating	Source	Notes
1	See note 1	1.8	3	5	Plano Brewster	HR 800-900, HT 660-680 nm	VLOC	PO 4500044110, from Sept 1997, ordered by B. Golubovic (?),$3200
1	See note 2	2.5	3	5	Plano/10 deg wedge	HR 800-900, HT 660-680 nm	VLOC	PO 4500044110, from Sept 1997, ordered by B. Golubovic (?),$3200
1	?	1	3	6	Plane-plane (?)	HR 800-900, HT 660-680 nm (?)	?	-
1	3	5	1.5	3	Brewster-Brewster	-	VLOC	Ordered by UD, Oct 2008, $925 used in [59]

Table C3: List of the Cr:LiSGaF crystals in our inventory.

Note-1: Absorption coefficient for E//c at 670 nm is > 9 cm^{-1}.

Note-2: Absorption coefficient for E//c at 670 nm is > 6 cm^{-1} but < 7 cm^{-1}.

APPENDIX D

HOW TO DESIGN SESAMs/SBRs?

Pioneered by Islam, Knox and Keller semiconductor saturable absorbers is a key element of today's photonics technology, especially for ultrafast passive mode-locked laser sources [37, 272, 273, 392-397]. One advantage of semiconductor saturable absorbers is their physical properties could be engineered for optimum operation for specific applications. When they are used for mode-locking ultrashort pulse lasers, semiconductor saturable absorbers are generally incorporated into mirrors, which are then named as semiconductor saturable absorber mirrors (SESAMs) [272], or as semiconductor saturable Bragg reflectors (SBRs) [273]. In this appendix, our aim is to describe how to design SESAMs/SBRs around 800-900 nm, which can be used in mode-locking of Cr:Colquiriite or Ti:Sapphire lasers. Here, we won't claim to be the expert of this, but we will just try to transfer our limited expertise. During the designs and for the simulations, we have used Optilayer thin film software version 4.48.

In this Appendix, we will separate SESAMs/SBRs into two categories: (i) Standard/regular or narrowband SESAMs/SBRs, and (ii) Broadband or oxidized SESAMs/SBRs. By standard SESAMs/SBRs we mean saturable absorber mirrors where the absorber is integrated onto regular AlGaAs/AlAs Bragg mirrors. Due to the low index contrast between AlGaAs/AlAs layers in the Bragg stack (Δn~0.5-0.6), standard SESAMs/SBRs has narrow bandwidth mirrors (~70 nm, R>%99.5). On the other hand, oxidized or broadband SESAMs/SBRs use AlGaAs/ Al_xO_y pairs in the Bragg mirror design (Al_xO_y is oxidized version of AlAs). The use of low-index Al_xO_y material (n~1.6), in place of AlAs (n~3), in the Bragg mirror stack increases the index contrast from ~0.5-0.6 to ~1.9, and enables a reflectivity bandwidth of ~300 nm [249].

In section D1 and D2, we will describe how to design the Bragg mirror for regular and oxidized SESAMs/SBRs, respectively. Then in section D3, we will describe how the design the absorber section of the SESAM/SBR, where the discussion will be applicable to both types of SESAMs/SBRs. In Appendix E, we will present a list of all the grown SESAMs/SBRs during this PhD thesis. Finally, Appendix F will present some interesting SESAM/SBR designs that might be useful for some future projects.

D.1 How to design Bragg Mirrors for Regular SESAMs/SBRs?

In this section, we will describe how to design the Bragg structure for regular SESAMs/SBRs. In regular SESAMs/SBRs, the Bragg structure will consist of layers of $Al_xGa_{1-x}As$/AlAs pairs. The reason to use $Al_xGa_{1-x}As$/AlAs pairs can be understood by looking at Fig. D1, which shows the band gap and lattice parameters for III-V semiconductor compounds. Notice that AlAs and GaAs has almost identical lattice constants, which allow the growth of large size and multiple layer structures like Bragg mirrors (otherwise strain induced stress will either limit the size of the structure or cause cracks, etc.).

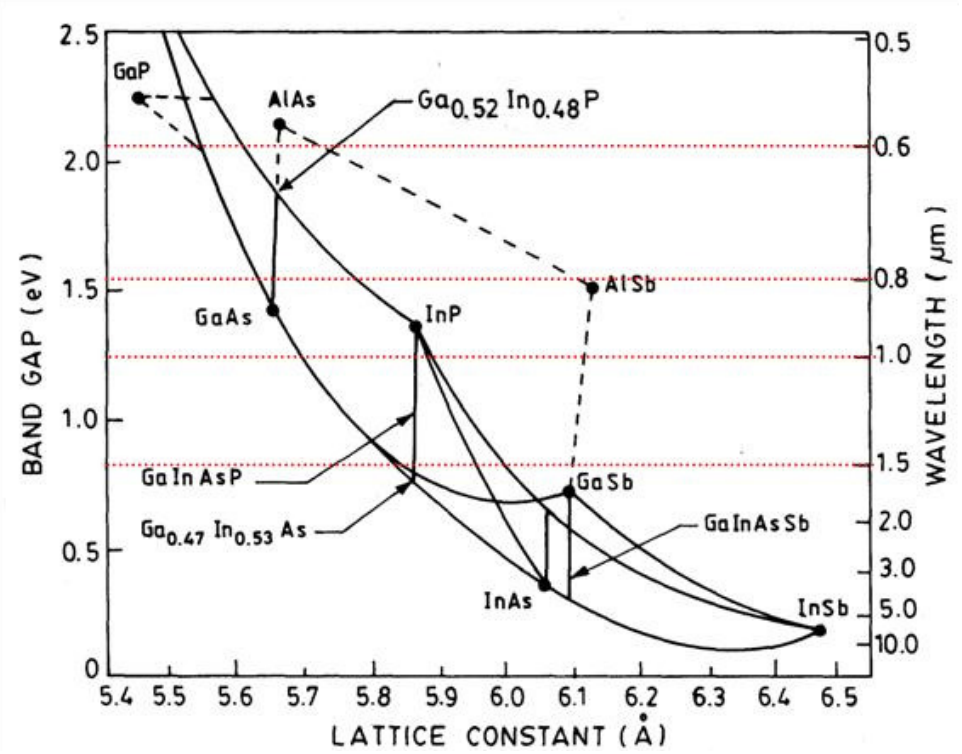

Figure D1: Band-gap versus lattice parameter for III-V compounds (this picture is taken from [398], and slightly modified afterwards). This picture is used here under the fair use doctrine of United States copyright law [11].

The main questions to answer in our Bragg mirror design are which composition of $Al_xGa_{1-x}As$ to use and how many pairs of layers to grow. To answer that, assume that, we want to design a regular SESAM/SBR with a reflectivity bandwidth centered around 850 nm (we have arbitrarily chosen this wavelength, the idea can be extended to others). Around 850 nm AlAs semiconductor has a refractive index of ~2.995, and GaAs has a refractive index of ~3.67. The compositional material $Al_xGa_{1-x}As$ will have a refractive index in between GaAs and AlAs. In a Bragg design, in general to obtain a broad reflectivity bandwidth one wants to use layer materials with largest refractive index difference. Hence, usage of GaAs and AlAs, which has the largest refractive index difference might look like a good idea. However, we should remember that these materials are semiconductors and below their band edge, they

will absorb light strongly (Figs. D2 & D3), and hence create unwanted losses in an optical elements (these losses are not saturable).

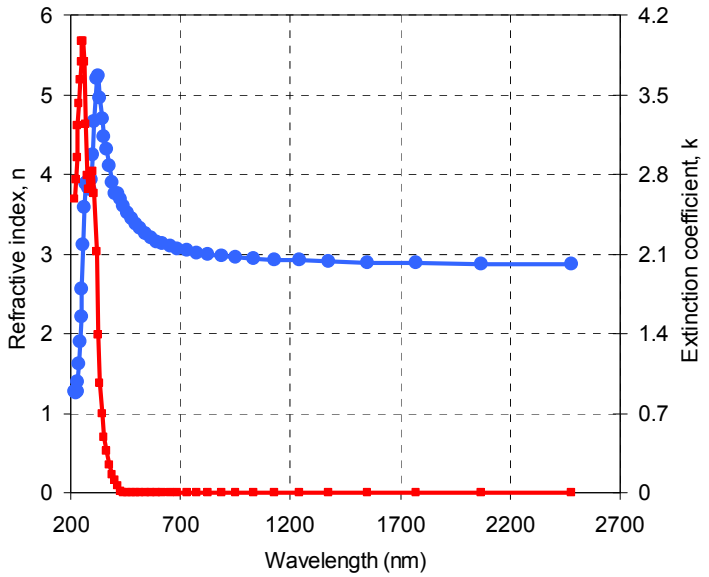

Figure D.2: Variation of refractive index and extinction coefficient with wavelength for AlAs at room temperature. Data is taken from [399], and the experimental data is from [400, 401]

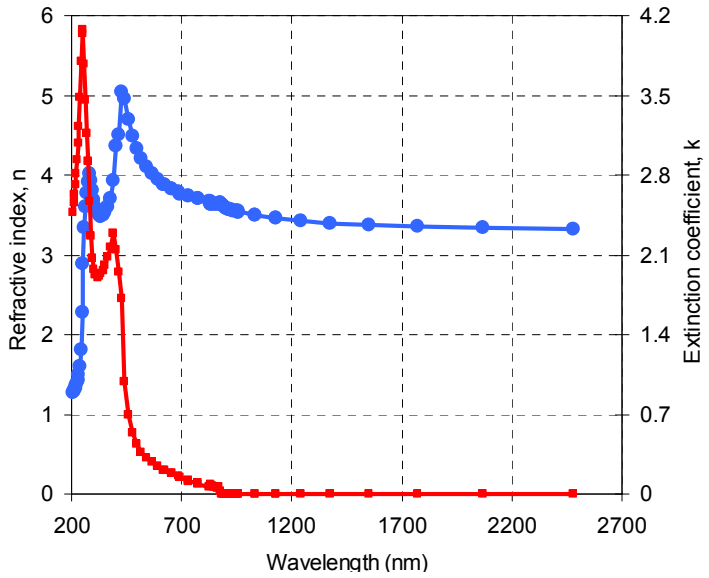

Figure D.3: Variation of refractive index and extinction coefficient with wavelength for GaAs at room temperature. Data is taken from [399] and [402], and the experimental data is from [403-406].

Band edge of AlAs is around ~575 nm [407]; hence, it is transparent above this wavelength (till IR transitions). This allows the usage of AlAs as the low index Bragg layer for an SESAM/SBR around ~850 nm. However, devices containing pure AlAs might be oxidized for the long run. Hence, in general it is a better idea to add just about 5% of Ga into AlAs, and use $Al_{0.95}Ga_{0.05}As$ as the low index layer. Addition

of 5% Ga will decrease the oxidization rate significantly, and this will increase the lifetime of the devices. Note that the refractive index of $Al_{0.95}Ga_{0.05}As$ around 850 nm is ~3.02, which is slightly higher than the refractive index of AlAs (~2.995). So by putting the 5% Ga, we lose a little from the reflectivity bandwidths we could get form the Bragg stack.

On the other hand, GaAs has a band edge of around ~872 nm at room temperature (Fig. D4, also see Fig. D5 which shows the temperature dependence of the band edge). Hence, it can't be used as the high index layer material of the Bragg stack, or otherwise in the mirror it will create loss for wavelengths below ~875 nm.

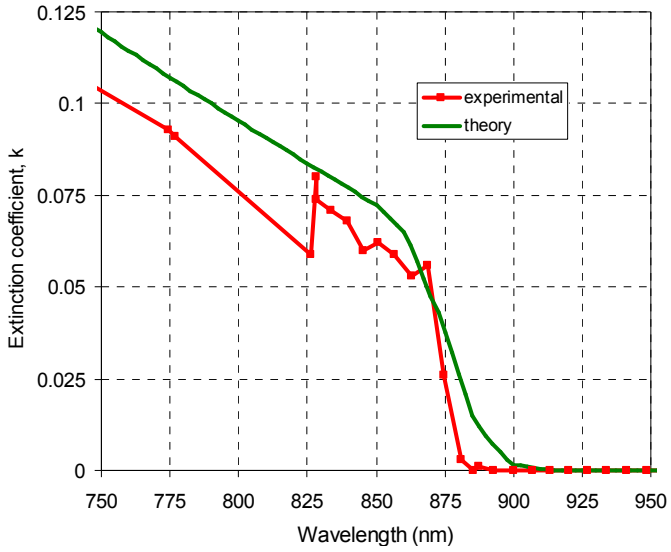

Figure D.4: Zoomed in version of Fig. D3., for the absorptive part of GaAs's refractive index [399, 402-406]. Experimental values reported by different groups show variations, which causes the jump in the experimental curve.

To prevent this unwanted absorptive loss, one can add Al into GaAs to shift the band edge to lower wavelengths. At room temperature (300 K) the direct band gap edge of $Al_xGa_{1-x}As$ can be calculated by using [408-410]:

$$E_g(x) = 1.424eV + (1.247eV)x \qquad \text{(D1)}$$

where x is the aluminum content (this equation is valid for $x < x_c = 0.45$, for $x > x_c$ gap is indirect). Figure D6 shows the calculated variation of $Al_xGa_{1-x}As$ band edge as a function of x using Eq. D1.

Again for our 850 nm SBR design, the Bragg stack is expected to be highly reflective from about ~810 nm to ~890 nm. Hence, we need to put the band edge of the high index layer well below 810 nm. Let us chose to use $Al_{0.14}Ga_{0.86}As$ as the high index layer, which has a band edge around ~778 nm. Figure D.8 shows the estimated refractive index data of $Al_{0.14}Ga_{0.86}As$. For this estimation we have started with the reported values for refractive index for $Al_{0.1}Ga_{0.9}As$ in [399] and then we shifted the refractive index

data by the band edge difference (~25.1 nm, band edge of $Al_{0.1}Ga_{0.9}As$ is at ~803.2 nm). This is a relatively crude method, but we need to use this method since experimental values of refractive index are available only for some specific concentrations, like 10%, 20%, etc. Also, our experience showed that it works quite well since the Al concentration differences we are using is small. Of course one can also use theoretically calculated refractive index curves, but here we will prefer to use the experimentally measured values in general.

So for our 850 nm SBR, in the Bragg mirror we will use $Al_{0.95}Ga_{0.05}As$ (n~3.017) as the low index material and $Al_{0.14}Ga_{0.86}As$ (n~3.545) as the high index material (Δn~0.528). The Bragg stack will consist of pairs of quarter wave layers. The required physical thickness to obtain a quarter wave layer is ~70.44 nm for $Al_{0.95}Ga_{0.05}As$ and ~59.44 nm for $Al_{0.14}Ga_{0.86}As$. For both layers the optical thickness is 212.5 nm (850/4).

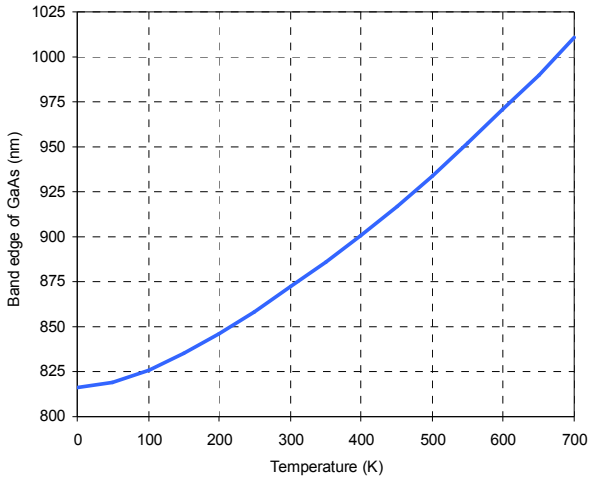

Figure D.5: Calculated variation of GaAs band edge with temperature [411, 412].

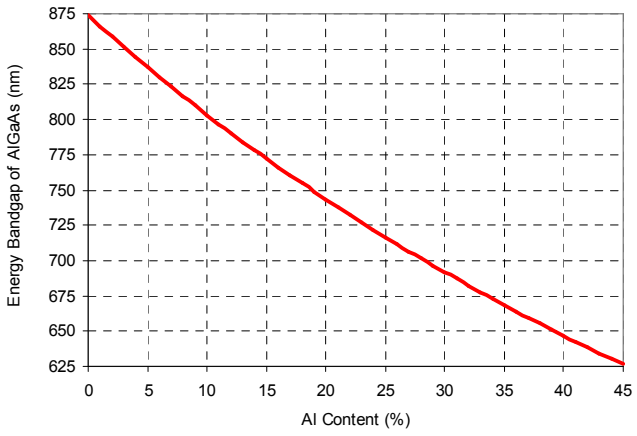

Figure D.6: Band edge (λ_g) of $Al_xGa_{1-x}As$ bulk absorber as a function of Al concentration (x).

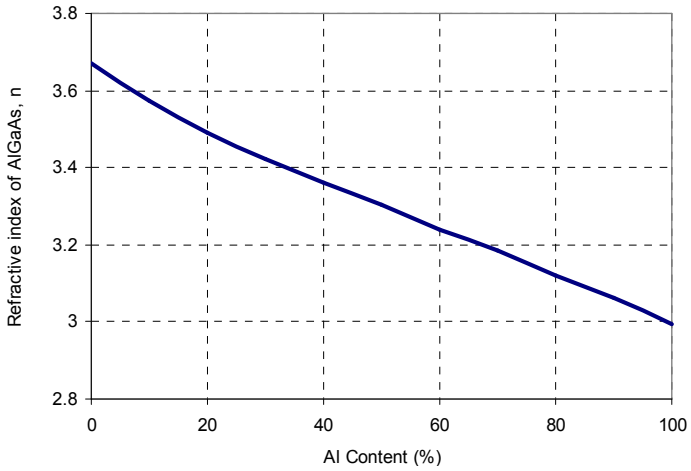

Figure D.7: Refractive index of $Al_xGa_{1-x}As$ as a function of Al concentration (x).

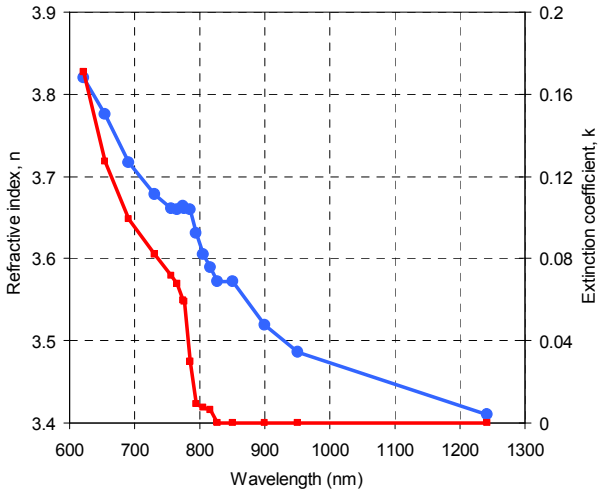

Figure D.8: Variation of refractive index and extinction coefficient with wavelength for $Al_{0.14}Ga_{0.86}As$ at room temperature. Solid lines are included as a guide to the eye.

Once we decide which layer material to use, the next question to answer is how may pairs of layers should we use. For our specific case here, Fig. D9 shows the calculated reflectivity of the Bragg stack for different number of Bragg layer pairs. Fig. D10, shows the variation of reflectivity at the central wavelength (850 nm), with increasing number of Bragg layer pairs. Since Cr:Colquiriite gain media is low gain in general, in the Bragg design we want reach a reflectivity level of at least 99.9%, which generally requires usage of 25 pairs or more number of Bragg layer pairs. Also note that, for number of pairs above ~25, the reflectivity does not really increase a lot. For example when the number of pairs is increased from 25 to 30, the central reflectivity increases from 99.965% to 99.993%, which is only a ~0.03% improvement in passive losses. So, in our designs we have usually chosen Bragg mirrors with 25 pairs, which is somehow an optimum point (increasing the number of Bragg mirror increases the difficulty of growing the structure and also increases the cost of the SESAM/SBR). Figure D.11 shows

the refractive index profile for this design. Figure D12, shows the standing wave electric field pattern inside the Bragg mirror simulated at the central wavelength (~850 nm). Note that, the electric filed enters quite deep into the mirror structure due to the low index difference, which explains why we need a relatively high number of Bragg layers to obtain 99.9% level reflectivity.

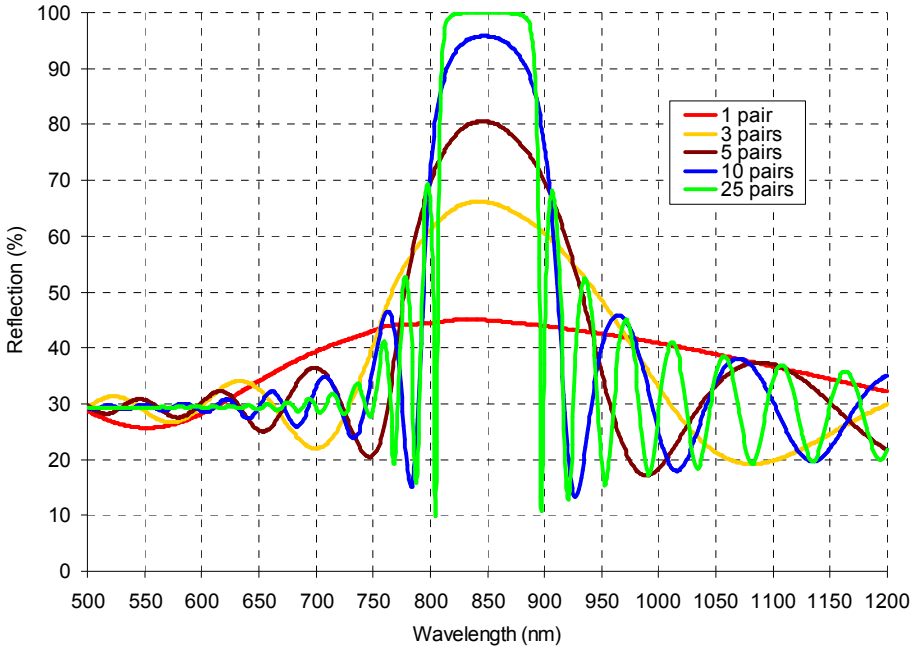

Figure D.9: Calculated reflection curves for Bragg mirrors with different numbers of pairs. The Bragg mirror is based on $Al_{0.95}Ga_{0.05}As$ and $Al_{0.14}Ga_{0.86}As$ materials.

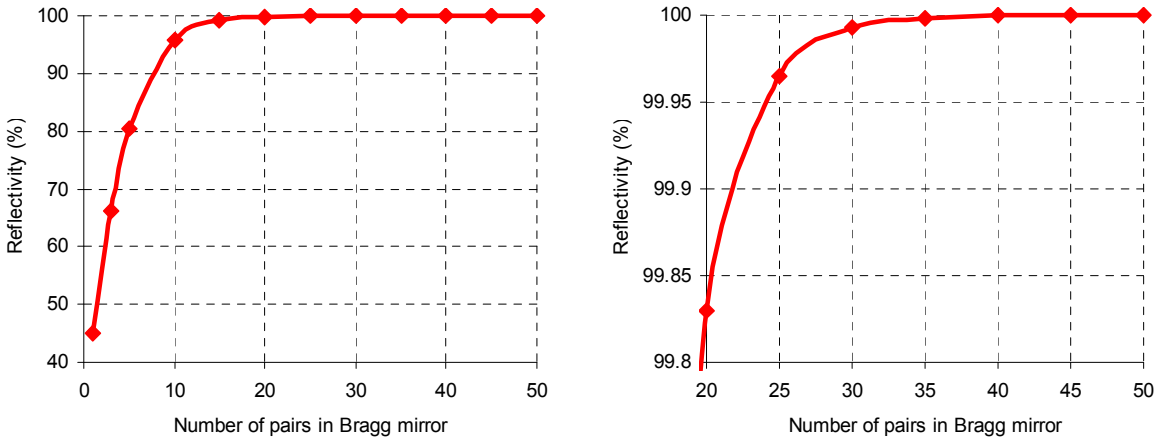

Figure D.10: Calculated variation of the value of reflection at the central wavelength (850 nm) with number of pairs in the Bragg mirror. The Bragg mirror is based on $Al_{0.95}Ga_{0.05}As$ and $Al_{0.14}Ga_{0.86}As$ materials, which has a index contrast of ~0.528. This graph is inspired from the graph in [413].

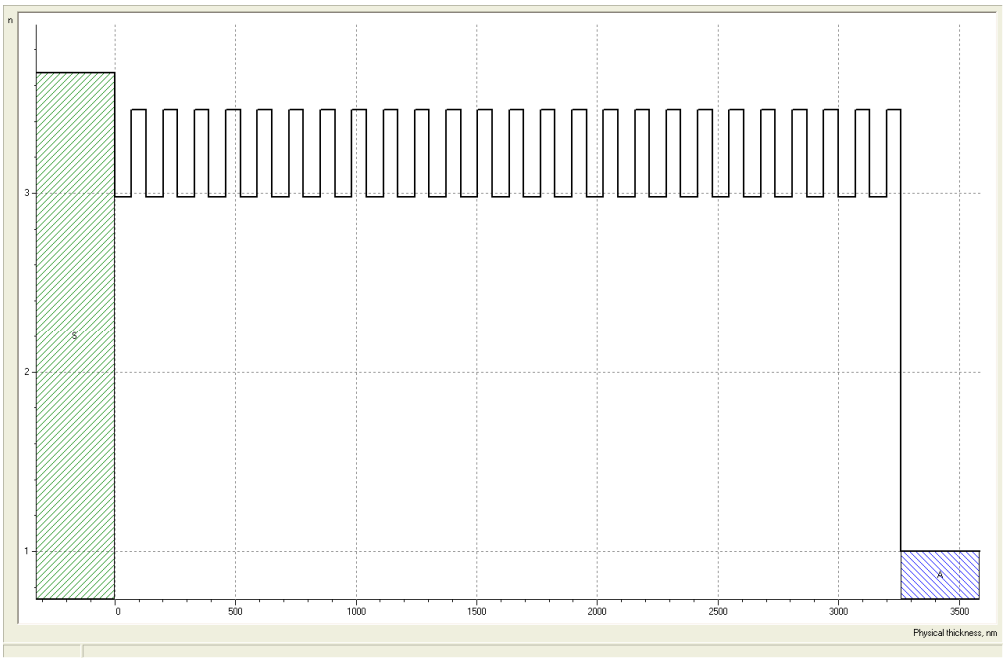

Figure D.11: Refractive index profile and the physical thickness of each layer for the 25 pair regular Bragg mirror, that is centered around ~850 nm. The Bragg mirror is based on $Al_{0.95}Ga_{0.05}As$ and $Al_{0.14}Ga_{0.86}As$ materials, which has a index contrast of ~0.528. The vertical axis is the refractive index and the horizontal axis is the material thickness.

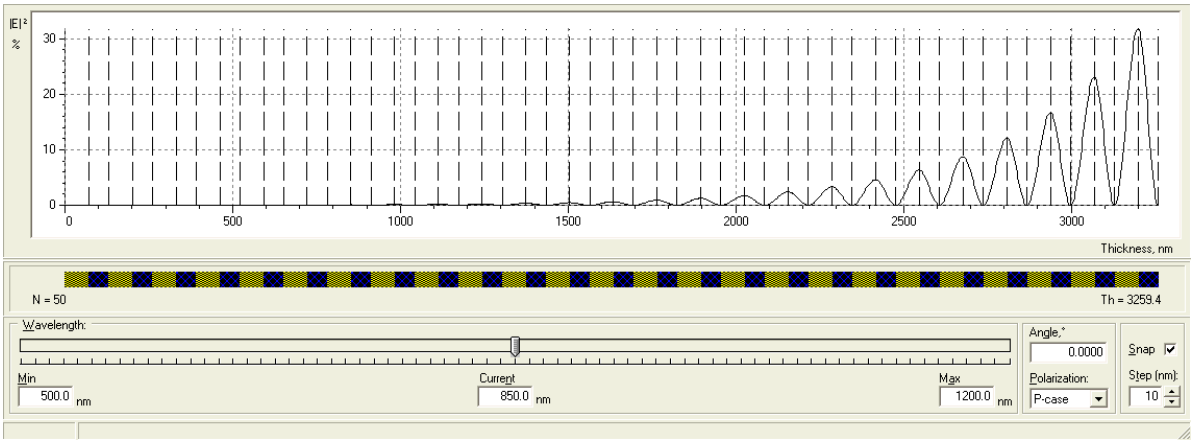

Figure D.12: The standing wave electric filed pattern for the 850 nm regular Bragg mirror at a wavelength of 850 nm.

D.2 How to design Bragg Mirrors for Oxidized/Broadband SESAMs/SBRs?

While designing a Bragg mirror for a 850 nm SESAM/SBR, we have seen that, we end up using $Al_{0.95}Ga_{0.05}As$ (n~3.017) and $Al_{0.14}Ga_{0.86}As$ (n~3.545) in the design, which has a refractive index difference of only ~0.528. This low index difference limits the bandwidths one could get from the Bragg structure, which then limits the pulsewidth and tunability range of the SESAM/SBR in mode-locked operation.

In an oxidized/broadband SESAMs/SBRs, one can use Al_xO_y material (n~1.6), as the low index layer, which increases the refractive index contrast from about ~0.5 to ~1.9. To describe the design process over an example, now assume that we want to design an oxidized SESAM/SBR for broadly tunable laser operation in Cr:LiSAF (~a tuning range from ~800 nm to ~920 nm). As the central wavelength of reflectivity we will chose ~860 nm, which is the center of the expected tuning range and also this is in general the free running central wavelength of mode-locked Cr:LiSAF lasers. Actually, we will see that, since the oxidized Bragg mirror is quite broadband, choosing the central wavelength is not as critical as regular SESAMs/SBRs.

In the oxidized SESAM/SBR design, the original Bragg structure consists of AlAs and $Al_xGa_{1-x}As$ pairs. Then after the growth, mesas having diameters of around ~500μm are etched and then the AlAs layers are transformed into Al_xO_y by wet thermal oxidation [6]. During oxidization, the AlAs layers shrinks in size about 12%, hence, the initial thickness of the AlAs layers should be adjusted to account for this effect. For a detailed discussion of this process, we refer the reader to Dr. Sheila Tandon's PhD thesis [414].

Similar to the Bragg mirror design, as the first step in designing the Bragg mirror structure, we should decide on which material to use as the high index layer (x in $Al_xGa_{1-x}As$). The expected femtosecond tuning range of Cr:LiSAF gain media is limited to about 800 nm in the low wavelength range. Hence, we should chose the Al content of $Al_xGa_{1-x}As$ such that, it won't create any unwanted losses above 800 nm. As a safe number here we will chose to use $Al_{0.17}Ga_{0.83}As$, which has a band edge of around 760 nm. Again the refractive index data for $Al_{0.17}Ga_{0.83}As$ can be obtained by shifting the closest available experimental data (~$Al_{0.2}Ga_{0.8}As$ is available at [399]), or by calculating the theoretical curve. Figure D13 shows the refractive index data for $Al_{0.17}Ga_{0.83}As$ material. The refractive index of $Al_{0.17}Ga_{0.83}As$ around 860 nm is ~3.5, creating an index contrast of ~1.9.

Once we decide the layer materials of the Bragg stack, again the next question to answer is how many pairs of layers we should use. For the oxidized Bragg mirrors, due to the large index contrast even a single pair of $Al_{0.17}Ga_{0.83}As/Al_xO_y$ layers has a reflectivity of about ~80%. Hence, the required number of pairs to reach a reflectivity of 99.99 is just 6 (Figure D.14 and D.15). Figure D.16 shows the refractive index profile for this design. Table D1 summarizes the oxidized Bragg mirror design. Figure D17, shows the standing wave electric field pattern inside the oxidized Bragg mirror simulated for 650 nm light. Fig. 17 shows that, compared to the regular Bragg mirror, high index contrast in the oxidized mirror enables reflection of light in the first few pairs of layers, decreasing the required number of layers in the Bragg stack. For comparison, Fig. D18 shows the reflectivity of regular and oxidized Bragg mirror design together. Fig. D18 shows that, the high refractive index contrast of the oxidized mirror enables a much

broader bandwidth compared to the regular Bragg mirror. If we compare the FWHM values, oxidized Bragg mirror has a bandwidth of ~466 nm, where the regular Bragg mirror has only has a FWHM of ~88 nm.

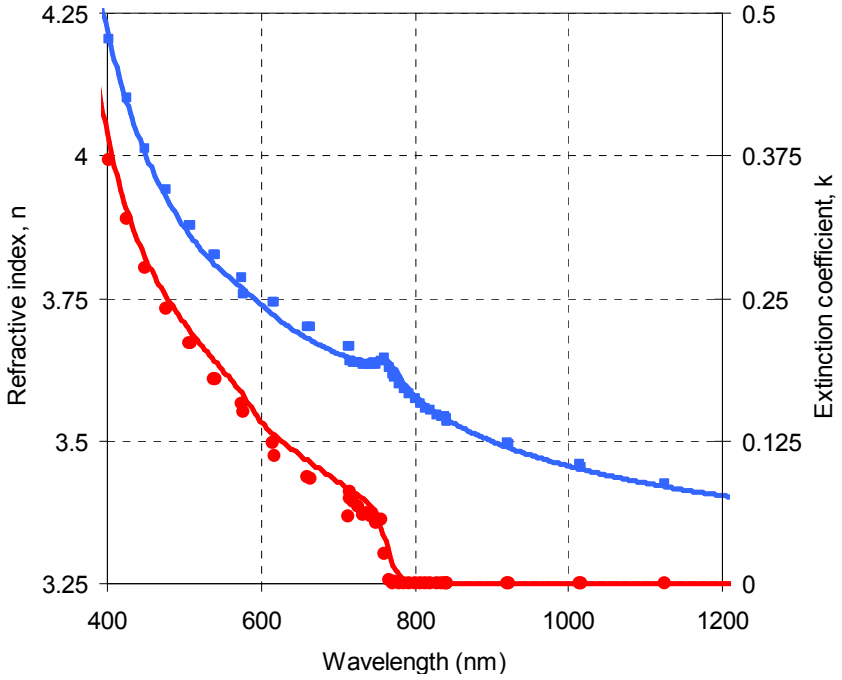

Figure D.13: Variation of refractive index and extinction coefficient with wavelength for $Al_{0.17}Ga_{0.83}As$ at room temperature. Solid lines are theoretical calculations, which show a little variation form the experimentally measured values.

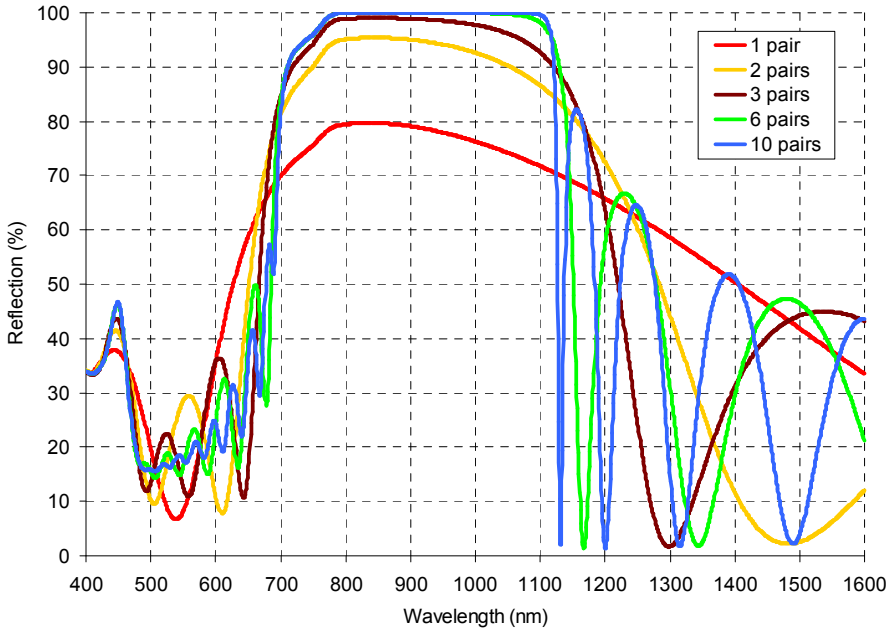

Figure D.14: Calculated reflection curves for oxidized Bragg mirrors with different numbers of pairs. Bragg mirror is based on $Al_{0.17}Ga_{0.83}As$ and Al_xO_y materials, which has a index contrast of ~1.9.

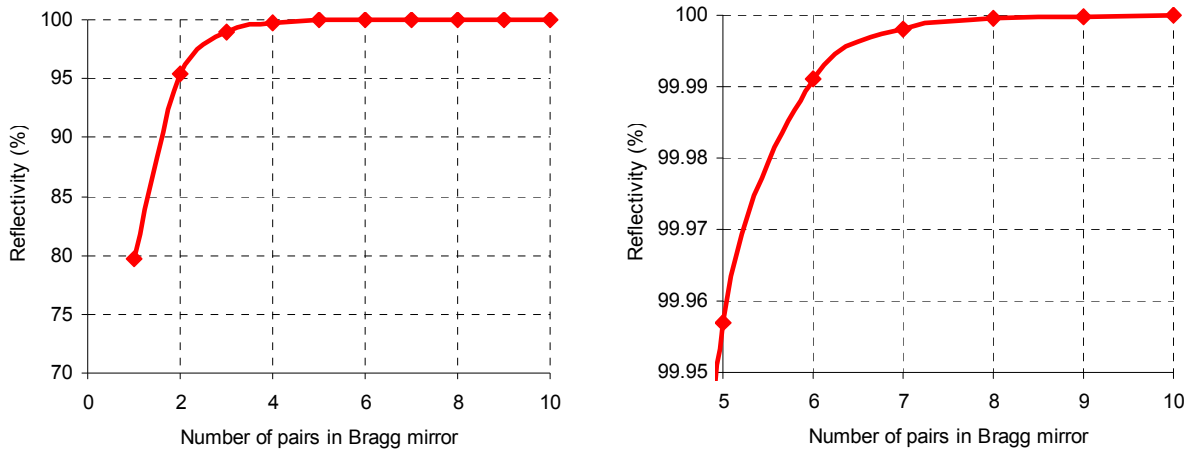

Figure D.15: Calculated variation of the value of reflection at the central wavelength (860 nm) with number of pairs in the oxidized Bragg mirror. The Bragg mirror is based on $Al_{0.17}Ga_{0.83}As$ and Al_xO_y materials, which has a index contrast of ~1.9.

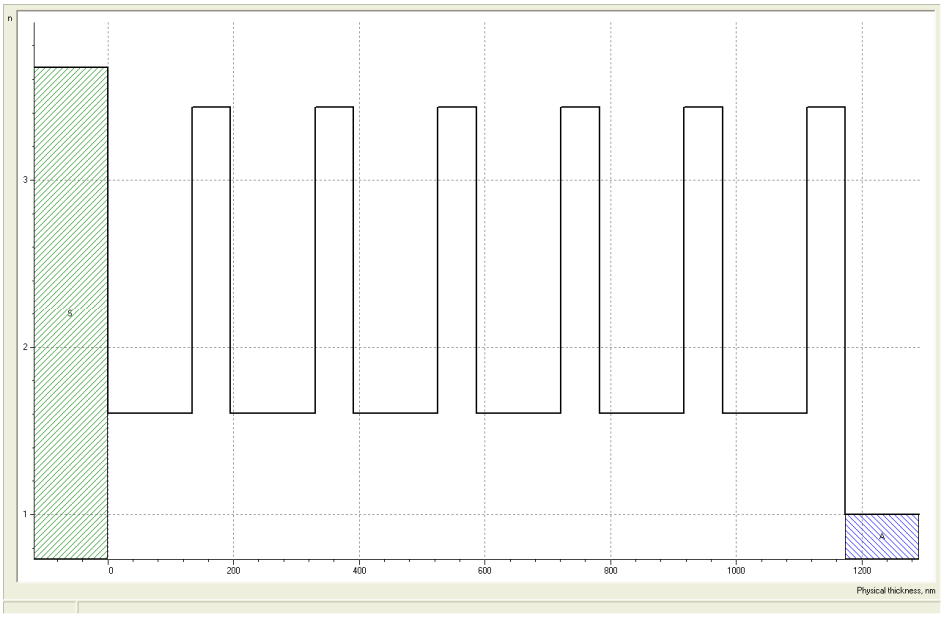

Figure D.16: Refractive index profile and the physical thickness of each layer for the 6 pair oxidized Bragg mirror. The oxidized Bragg mirror is based on $Al_{0.17}Ga_{0.83}As$ and Al_xO_y materials, which has an index contrast of ~1.9. The vertical axis is the refractive index and the horizontal axis is the material thickness.

Layer	Material	Physical thickness before oxidization (nm)	Physical thickness after oxidization (nm)	Optical Thickness (nm)	n	Purpose
0	GaAs	-	-	-	-	Substrate
1	AlAs→Al_xO_y	150.4	134.27	215	1.60	Bragg layer
2	$Al_{0.17}Ga_{0.83}As$	61.36	61.36	215	3.50	Bragg layer
…	…	…	…	…	…	Bragg layers
11	AlAs→Al_xO_y	150.4	134.27	215	1.60	Bragg layer
12	$Al_{0.17}Ga_{0.83}As$	61.36	61.36	215	3.50	Bragg layer

Table D1: 850 nm regular SESAM/SBR design with an quantum well absorber.

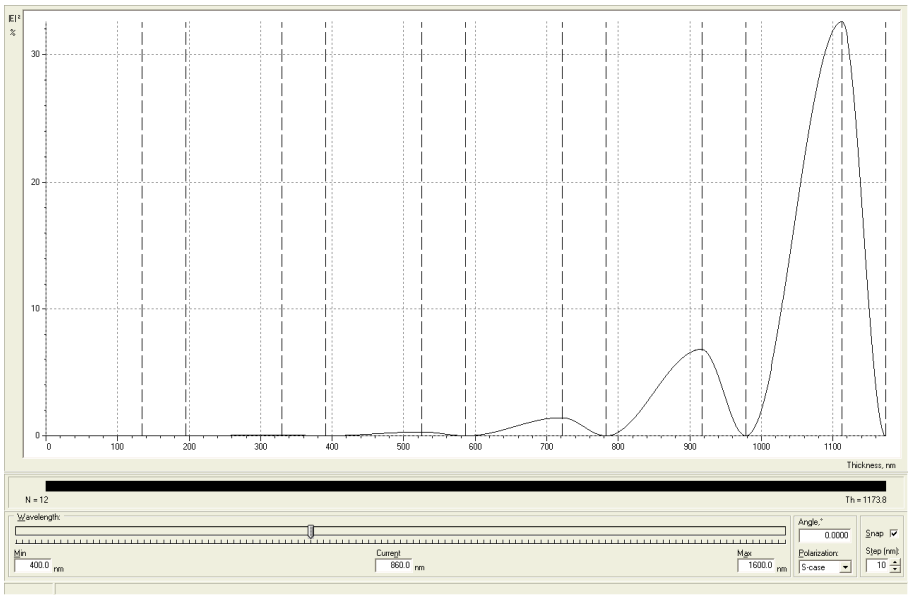

Figure D.17: The standing wave electric filed pattern for the oxidized broadband Bragg mirror at a wavelength of 860 nm.

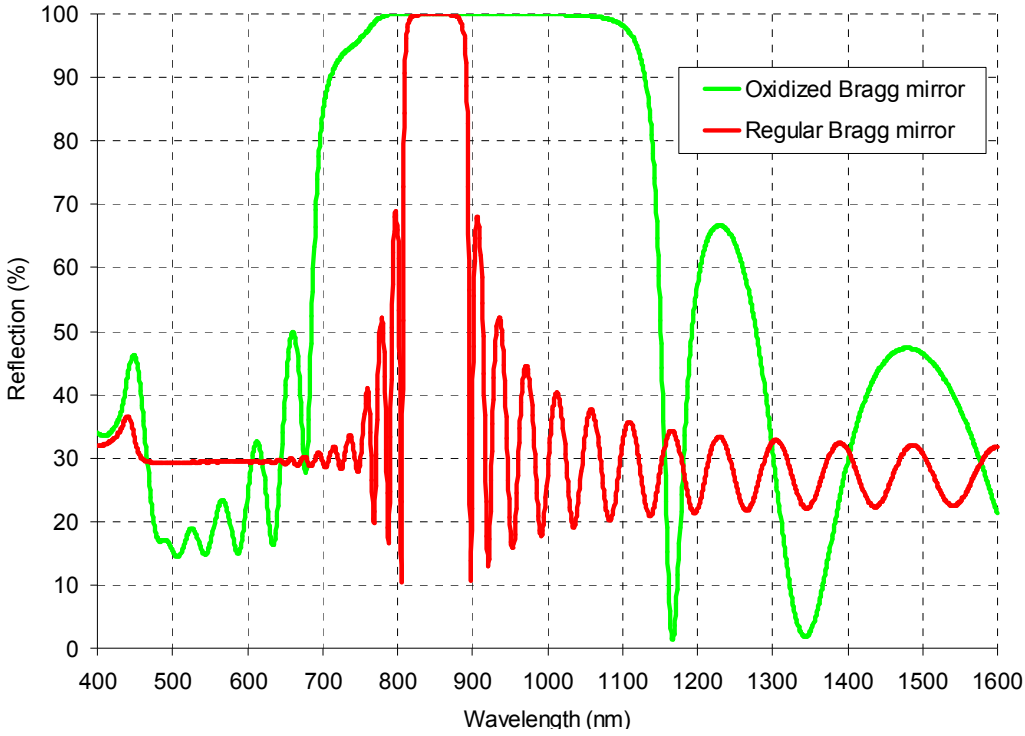

Figure D.18: Reflectivity of the regular and the oxidized Bragg mirror in the 400-1600 nm range.

Note that since we have used $Al_{0.17}Ga_{0.83}As$ material in the design, the Bragg mirror absorbs below ~790 nm (Fig. D.14). This is because for $Al_{0.17}Ga_{0.83}As$ material the absorption edge is at ~760 nm (Fig. D13). To prevent this absorption, one can chose to use $Al_{0.3}Ga_{0.7}As$ with an absorption edge at ~692 nm.

This will decrease the index contrast from ~1.9 to ~1.85, which is only a minor effect. However, the drawback of using $Al_{0.3}Ga_{0.7}As$ is it has higher oxidization rate compared to $Al_{0.17}Ga_{0.83}As$. Hence, in the process of oxidizing AlAs, the high index layer might oxidize as well, which might decrease the index contrast. Since we don't care about the reflectivity below ~800 nm for this specific SESAM/SBR design for Cr:LiSAF laser, and since the oxidization process is expected to be easier with $Al_{0.17}Ga_{0.83}As$, we have chosen to use $Al_{0.17}Ga_{0.83}As$ here. However, for a gain media like Ti:Sapphire using $Al_{0.3}Ga_{0.7}As$ is a better choice.

D.3 How to design the absorber layers for SESAMs/SBRs?

In this section, we would like to describe how we design the absorbers for the SESAMs/SBRs. The role of the absorber section is to create the desired saturable absorber action for stable cw mode-locking. The important parameters of design include the modulation depth of the absorber, the position of the absorber band edge with respect to the Bragg mirror reflectivity range, the wavelength dependence of density of states, the saturation fluence of the absorber, and the decay dynamics of the absorber.

In this section, we will work on the design of the absorber for the regular 850 nm SESAM/SBR; however, a similar approach can be used for designing absorbers for oxidized SESAM/SBRs also. Looking at the reflectivity curve of the regular 850 nm SESAM/SBR in Fig. D9 (for 25 pair Bragg stack), the reflectivity range extends from ~820 nm to ~880 nm (for R>99.5). In order to be able to create the same linear absorption at all wavelengths, the absorber should have a band edge above ~880 nm. However, if we put the absorber band edge too far away (for example to ~1000 nm), then the saturation fluence around 850 nm will be high, which is known to be not optimum for mode-locking. Here, we will try to choose an absorber with a band edge around ~900 nm. We won't put the band edge very close to the reflectivity edge around ~880 nm, to have some error margins, because there might be problems during the growth, which can easily shift things ±10 nm or more.

We know that band edge of GaAs is around ~873 nm, so it's not a good idea to just use GaAs as the absorber. Also ~873 nm is the absorption edge for bulk GaAs, where here by bulk we mean thick GaAs layers without significant quantum effects (thickness > ~30 nm). If we use a relatively thin GaAs absorber, the band edge will be further shifted to shorter wavelengths due to quantum effects.

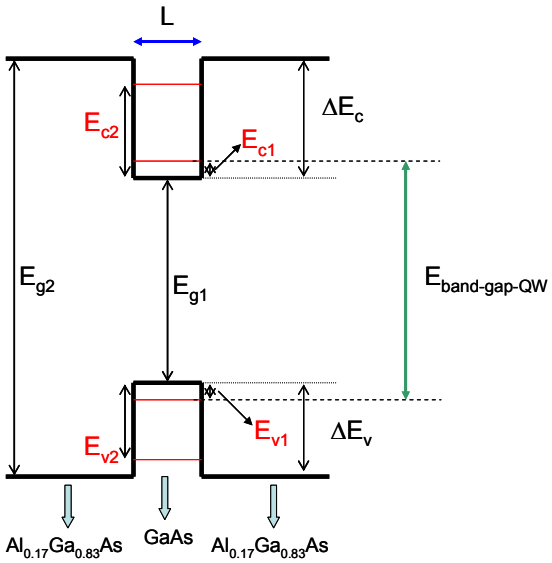

Figure D19: GaAs quantum well with a thickness of L sandwiched between $Al_{0.17}Ga_{0.83}As$ barrier layers.

To demonstrate the tuning effects, assume that we are using a GaAs absorber with a thickness of L, sandwiched between $Al_{0.17}Ga_{0.83}As$ barrier layers. To be able to calculate how the quantum effects shift the band edge, we will use a simple quantum well model as shown in Fig. D19, where $E_{band\text{-}gap\text{-}QW}$ is the band edge of the GaAs quantum well, E_{g1} is the band edge of bulk GaAs, E_{g2} is the band edge of bulk $Al_{0.17}Ga_{0.83}As$, ΔE_v and ΔE_c are the depth of the quantum wells for the valance band phonons and conduction band electrons, respectively. Also, E_{v1}, E_{v2}, … are the discrete energy levels of the valance band holes, and E_{c1}, $E_{c2,...}$ are the discrete energy level of the conduction band electrons.

In the quantum well absorber, the first allowed transition is from the E_{v1} level to the E_{c1} level, which is also the band edge for the quantum well structure. The second allowed transition is from E_{v2} to E_{c2} state. If there are more than one energy levels in the conduction band this will create jumps in the density of states at the corresponding transition energies. To calculate the band edge energy of the GaAs quantum well, we need E_{v1} and E_{c1}:

$$E_{band-gap-QW} = E_{g1} + E_{c1} + E_{v1} \tag{D.2}$$

The band edge for bulk GaAs is at ~872.5 nm, which then corresponds to energy of 1.424 eV (E_{g1}), where as the band edge of bulk $Al_{0.17}Ga_{0.83}As$ absorber is at ~759.4 nm, which corresponds to an energy of 1.636 eV (E_{g2}). Let $\Delta E_g = E_{g2} - E_{g1}$, which is the energy difference between GaAs and $Al_{0.17}Ga_{0.83}As$ layers ($\Delta E_g = 1636meV - 1424meV = 212meV$). This energy difference will be divided into ΔE_c and

ΔE_v. For AlGaAs/GaAs/AlGaAs quantum well structures the experimentally measured values for ΔE_c and ΔE_v are [48]:

$$\begin{aligned} \Delta E_c &= 0.67\Delta E_g \\ \Delta E_v &= 0.33\Delta E_g \end{aligned} \quad . \tag{D.3}$$

Here we note that different values are reported in the literature ($\Delta E_c = 0.62\Delta E_g$ [415], $\Delta E_c = 0.6\Delta E_g$ [408]), and the physics behind determining the band offset is quite complicated. Here we will used the experimentally measured values of band offset[48], which results in $\Delta E_c \approx 142meV$, and $\Delta E_v \approx 70meV$. For a finite quantum well, we can find the energy states for the symmetric and asymmetric solutions using:

$$Tan\left(\frac{\pi}{2}\sqrt{\frac{E}{E_L}}\right) = \sqrt{\frac{V_o - E}{E}} \tag{D.4}$$

$$Cot\left(\frac{\pi}{2}\sqrt{\frac{E}{E_L}}\right) = -\sqrt{\frac{V_o - E}{E}} \tag{D.5}$$

where V_o is the height of the potential well and E_L is the ground state energy of a well of width L with infinite potential walls ($E_L = \frac{\hbar^2\pi^2}{2mL^2}$, m is the mass, $\hbar$ is Planck's constant). For GaAs [48], while calculating E_L, for the conduction band we need use the mass of the electron (m = m_c = 0.067 m_0), and for the valance band we need to use the mass of the heavy holes (m = m_{HH} =0.46 m_0).

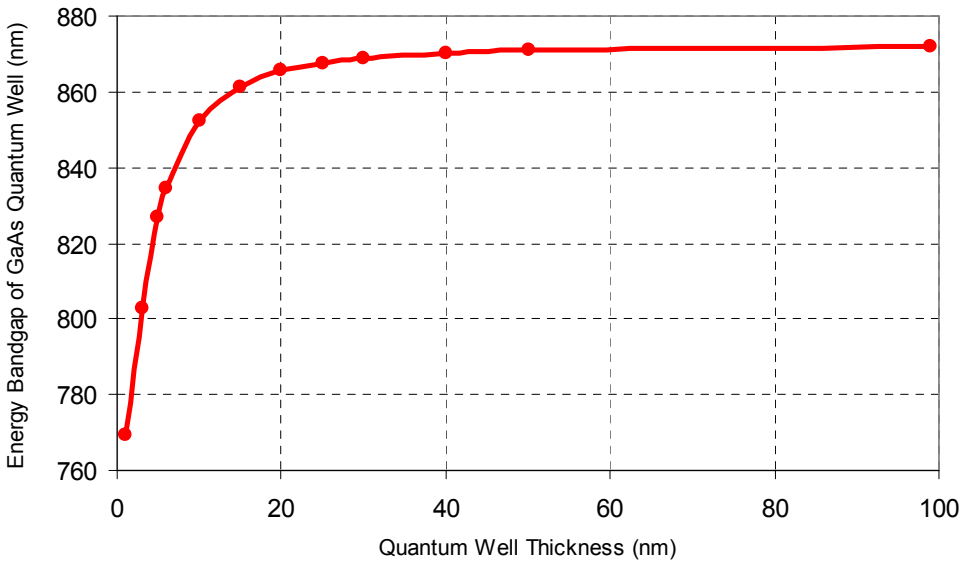

Figure D20: Calculated variation of GaAs quantum well band edge with quantum well thickness.

Figure D20 shows the calculated variation of band edge wavelength for the GaAs quantum well with varying quantum well thickness. Figure D20 shows that, for thicknesses below ~30 nm, the band edge start to shift considerably to the shorter wavelengths. Here we note that, experimentally, it is hard to build very thin layers, hence the thickness of quantum wells should be kept above ~5 nm in the design.

If we return to the absorber design problem, as we have mentioned pure GaAs is not suitable to use in the regular 850 nm SESAM/SBR design, since we want to design an absorber with a band edge around ~900 nm. Earlier we have seen that adding Al into GaAs shifts the band edge to shorter wavelengths. To shift the band edge to longer wavelengths one can add In into GaAs. In the literature, we have found two different formulas to estimate the band edge of bulk $In_xGa_{1-x}As$: one from Nahory [416]:

$$E_g(x) = 1.425eV - (1.501eV)x + (0.436eV)x^2 \tag{D.6}$$

and one from Corzine [408]:

$$E_g(x) = 1.424eV - (1.619eV)x + (0.555eV)x^2 \tag{D.7}$$

Unfortunately, they are giving slightly different results, which show the relatively large error-bars in our band-edge estimates (Fig. D22). Moreover, compared to AlGaAs, InGaAs has one additional challenge. Since InAs is not lattice matched to GaAs, addition of In into GaAs will induce strain in the structure, and this will split the energy levels and change the band edge position. The strained $In_xGa_{1-x}As$ energy band gaps and splitting between the heavy hole and light hole bands were calculated theoretically by Corzine [408], using standard relations for strained III-V compounds, known elastic stiffness coefficients, and the measured unstrained InGaAs band gap (see Appendix C in [408]) . When InGaAs is grown between GaAs, one can calculate the band edge of strained $In_xGa_{1-x}As$ using [408]:

$$E_{g-HH}(x) = 1.424eV - (1.061eV)x + (0.07eV)x^2 + (0.03eV)x^3 \tag{D.8}$$

$$E_{g-LH}(x) = E_{g-HH}(x) + (0.48eV)x - (0.43eV)x^2 + (0.152eV)x^3 \tag{D.9}$$

where HH and LH represents heavy and light holes band gap energies, respectively. Since density of states of LH is much lower than HH, we will here ignore the effect of LH.

Figure D22 shows the calculated band edge position variation of $In_xGa_{1-x}As$ for strained and unstrained cases. We note here that, Fig. D22 is for bulk materials and for the absorber design we should also consider quantum effects, which occurs strongly for thicknesses below 30 nm. In the absorber design, there are several advantages to use a quantum well absorber rather than a bulk absorber. First of all, in general the required modulation depths are quite low, and this forces us to use relatively thin absorbers anyway. Also, in a quantum well absorber the saturation fluence is lower than a bulk absorber in general.

Secondly, in a quantum well absorber, it is possible to engineer the quantum well parameters to obtain a relatively wavelength insensitive nonlinear absorption (density of sates / saturation fluence).

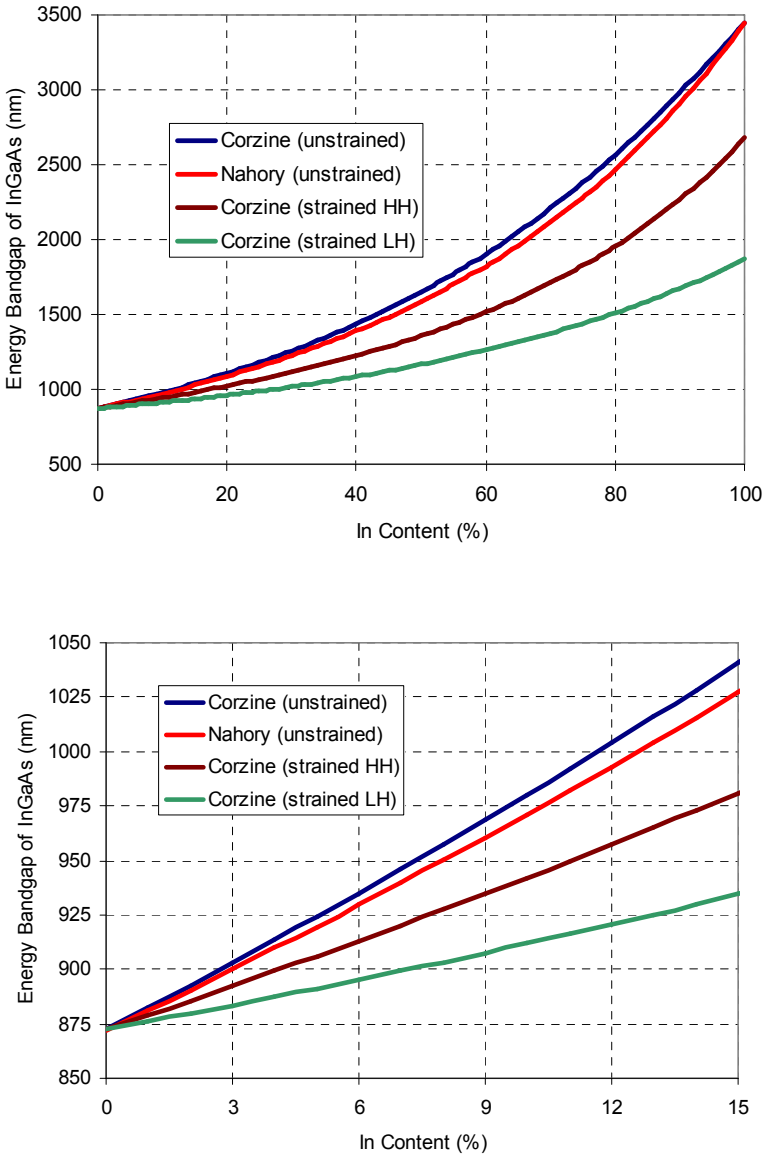

Figure D22: Calculated band edge position for unstrained and strained bulk $In_xGa_{1-x}As$ compound.

In concentration of the absorber	Possible transitions for L=6 nm (nm)	Possible transitions for L=7 nm (nm)
9	886	894 (1^{st}), 811 (2^{nd})
10	891	900 (1^{st}), 814 (2^{nd})
11	897	906 (1st), 816 (2nd)
12	903	912 (1st), 819 (2nd)

Table D2: Calculated transition wavelengths for 6-7 nm thick $Al_{0.14}Ga_{0.86}As$ /$In_xGa_{1-x}As$/ $Al_{0.14}Ga_{0.86}As$ quantum wells with 9-11% In concentration.

Table D2 shows calculated transition wavelengths for $Al_{0.14}Ga_{0.86}As$ /$In_xGa_{1-x}As$/ $Al_{0.14}Ga_{0.86}As$ quantum wells, with different In concentrations (x) and with different thickness (L). The calculations was similar to what we have described above for GaAs quantum wells. However, before looking at the results in detail, we want to briefly mention some additional error-bars in the calculation of quantum effects for InGaAs. First of all, for the strained AlGaAs/InGaAs/AlGaAs quantum well structures, there is an uncertainty in the conduction band offset, and people report values from 0.4 to 0.8 [415] (we have used: $\Delta E_c = 0.6\Delta E_g$ in out calculations). Also for stained $In_xGa_{1-x}As$ absorbers the effective mass depends on both In concentration (x) [408] and strain[48]. According to Corzine [408], the mass of conduction band varies with In concentration as:

$$m_c = 0.067 - 0.04x \tag{D.10}$$

where x is the In concentration. In the calculations above, we have neglected the variation of m_c with strain, since this is rather complex and we couldn't find a good reference describing the effect. For the heavy hole mass (m_{HH}) values of 0.38 m_0 for GaAs, 0.37 m_0 for $In_{0.2}Ga_{0.8}As$ and 0.34 m_0 for InAs has been reported in the literature, which seems to be relatively insensitive to the In concentration compared to m_c (we have used interpolated values in the calculations).

Looking at Table D2, a suitable absorber for the regular 850 nm SESAM/SBR is a 6 nm thick $Al_{0.14}Ga_{0.86}As$ /$In_{0.11}Ga_{0.89}As$/ $Al_{0.14}Ga_{0.86}As$ quantum well which has an estimated band edge around ~897 nm. Figure D23 shows the estimated refractive index data for this absorber, which we obtained by shifting the refractive index data for GaAs. Again this is because it is hard to find experimental data, and this approach works quite well in determining the refractive index when the In or Al concentration is low. We also note that, for the 6 nm thick $Al_{0.14}Ga_{0.86}As$ /$In_{0.11}Ga_{0.89}As$/ $Al_{0.14}Ga_{0.86}As$ absorber there is only one energy level in the conduction band (and only one allowed transition), hence the density of states and the saturation fluence is expected to be relatively smooth in the reflectivity range of the SESAM/SBR, which is a desired property for broad tuning applications. Note that, if one increases the width of the absorber from 6 nm to 7 nm, then there are two states in the conduction band, one at 906 and one at 806 nm, which means the density of states will have a jump around 806 nm.

Since now we also know the absorber structure we want to use, we can now combine the Bragg mirror design and the absorber design together to finalize the regular 850 nm SESAM/SBR design. Table D3 summarized the final design and Fig. D24 shows the corresponding refractive index structure with thicknesses. Note that a 5 nm thick GaAs cap layer is included to increase the lifetime of the device by preventing oxidization (GaAs oxidizes much slower compared to $Al_{0.14}Ga_{0.86}As$). The 6 nm thick

$In_{0.11}Ga_{0.89}As$ is sandwiched between 10 and 45 nm thick $Al_{0.14}Ga_{0.86}As$ layers. Note that, the total optical thickness of layers 52 through 55 is about a quarter wavelength. While determining the specific thicknesses of these layers, we have varied the thickness of 52nd and 54th layers to obtain a relatively flat (wavelength independent) linear absorption. This basically changes the position of the quantum well inside the standing electric field wave pattern, and enables the creation of similar linear absorption for different wavelengths. As an example, Fig. D25 shows the standing wave electric filed patters at the wavelengths of 830 and 870 nm. Note than the peak of the electric filed is closer to the absorber at 870 nm compared to 830 nm, balancing the stronger absorption coefficient of the absorber at shorter wavelengths, and enabling the creation of similar linear absorption levels at both wavelengths. Finally, Fig D26 shows the calculated reflectivity of the regular 850 nm SESAM/SBR. Small signal refers to low incident intensity level on the absorber, where the intensity is too low to even partially saturate the absorber; hence, the structure sees all the loss from the absorber. Saturated curve refers to full saturation of the absorber, which can be obtained high incident intensities, and while calculating this case, we just set the imaginary part of the refractive index for the absorber to zero. Note that, the obtained modulation depth is about 0.75%, which is ideal for mode-locking of Cr:LiSAF with tunable ~100-fs level pulses. If we were to design a SESAM/SBR to generate shorter pulses, it is in general a better idea to have a larger modulation depth, which can be obtained by using more than one absorber in the SESAM/SBR design.

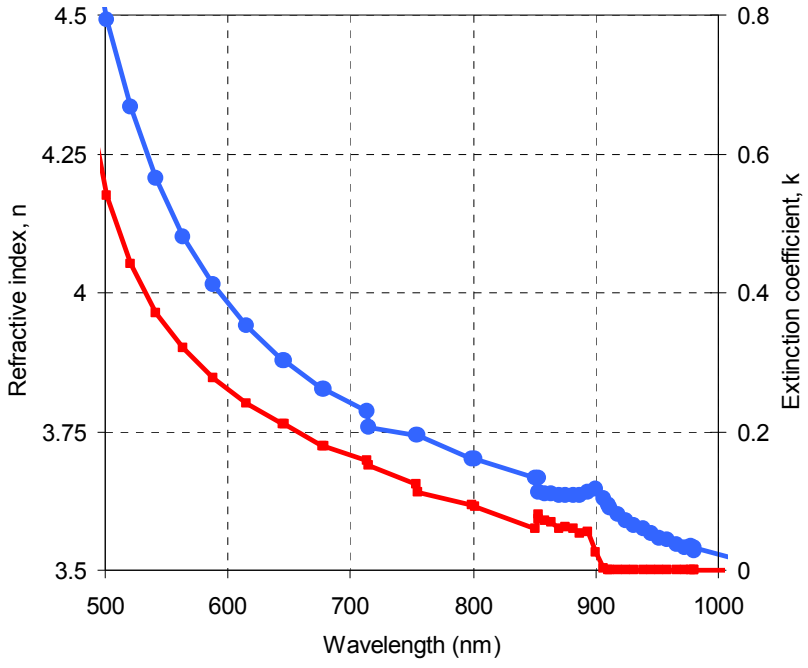

Figure D23: Variation of refractive index and extinction coefficient with wavelength for the 6 nm thick $Al_{0.14}Ga_{0.86}As$ /$In_{0.11}Ga_{0.89}As$/ $Al_{0.14}Ga_{0.86}As$ quantum well. Solid lines are included as a guide to the eye.

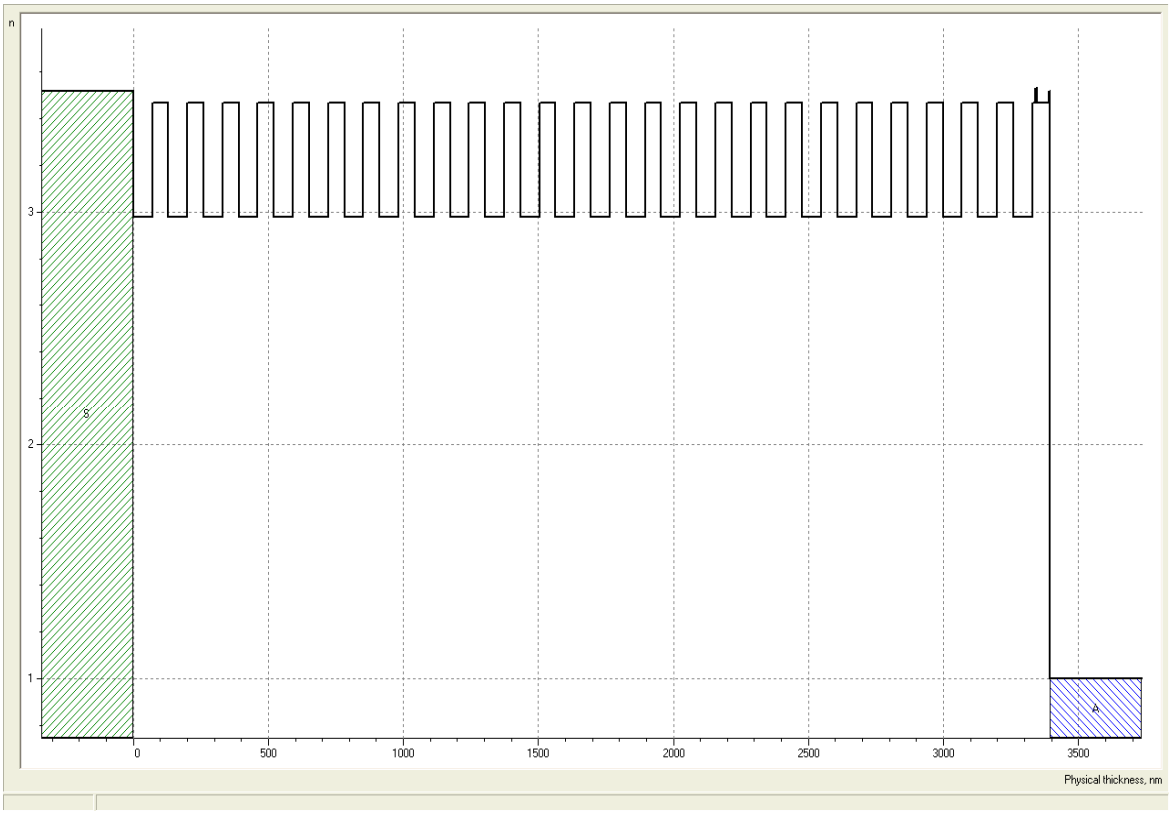

Figure D24: 850 nm regular SBR design. Refractive index profile and the physical thickness of each layer is shown. The vertical axis is the refractive index and the horizontal axis is the material thickness.

Layer	Material	Physical Thickness (nm)	Optical Thickness (nm)	n	Purpose
0	GaAs	-	-	-	Substrate
1	$Al_{0.95}Ga_{0.05}As$	70.44	212.50	3.02	Bragg layer
2	$Al_{0.14}Ga_{0.86}As$	59.54	212.50	3.55	Bragg layer
…	…	…	…	…	Bragg layers
49	$Al_{0.95}Ga_{0.05}As$	70.44	212.50	3.02	Bragg layer
50	$Al_{0.14}Ga_{0.86}As$	59.54	212.50	3.55	Bragg layer
51	$Al_{0.95}Ga_{0.05}As$	70.44	212.50	3.02	Bragg layer
52	$Al_{0.14}Ga_{0.86}As$	10	35.45	3.55	Barrier
53	$In_{0.11}Ga_{0.89}As$	6	22.00	3.67	Absorber
54	$Al_{0.14}Ga_{0.86}As$	45	159.54	3.55	Barrier
55	GaAs	5	18.17	3.63	Cap

Table D3: 850 nm regular SESAM/SBR design with an quantum well absorber.

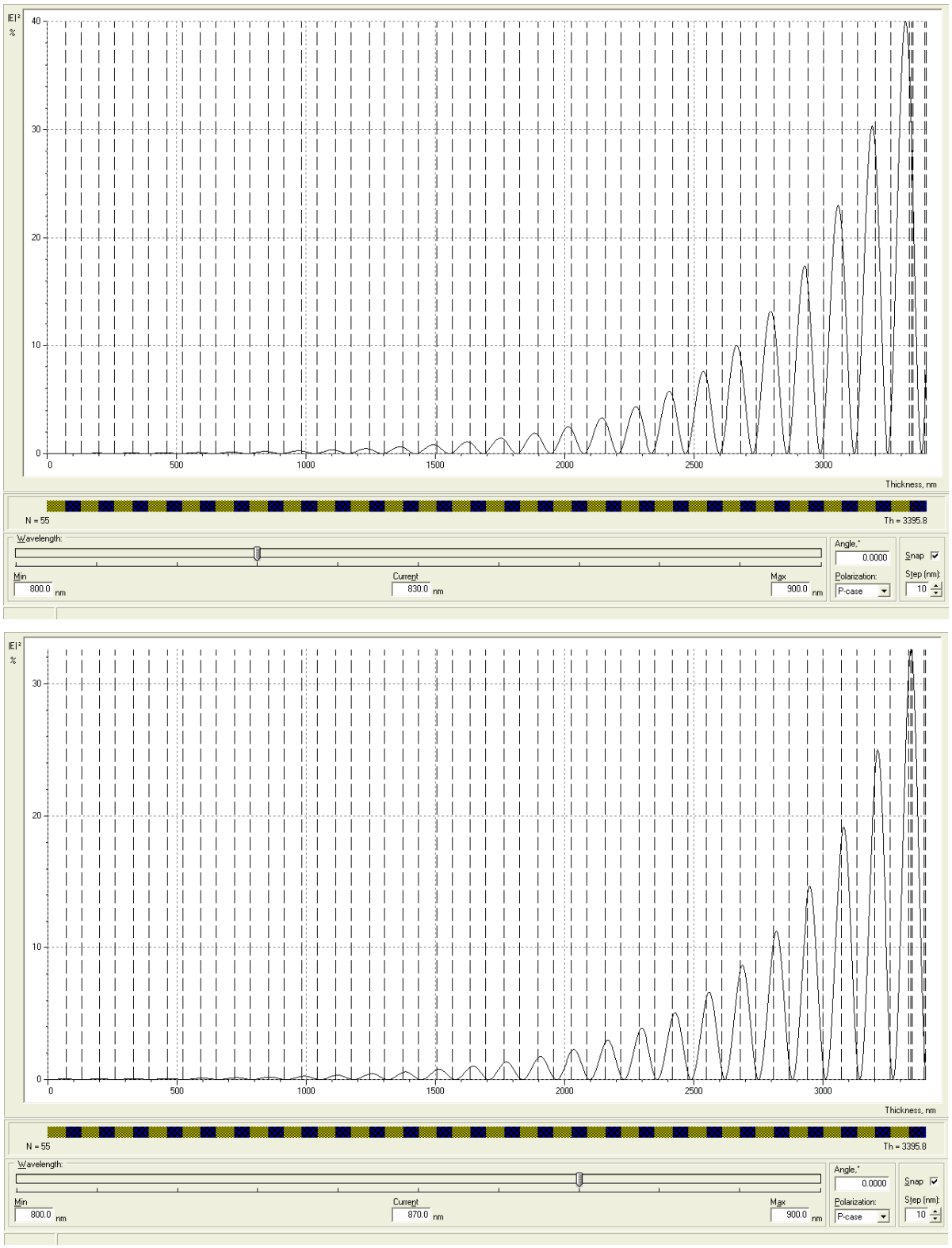

Figure D25: Standing wave electric filed pattern inside the regular 850 nm SESAM/SBR design at the wavelengths of 830 and 870 nm.

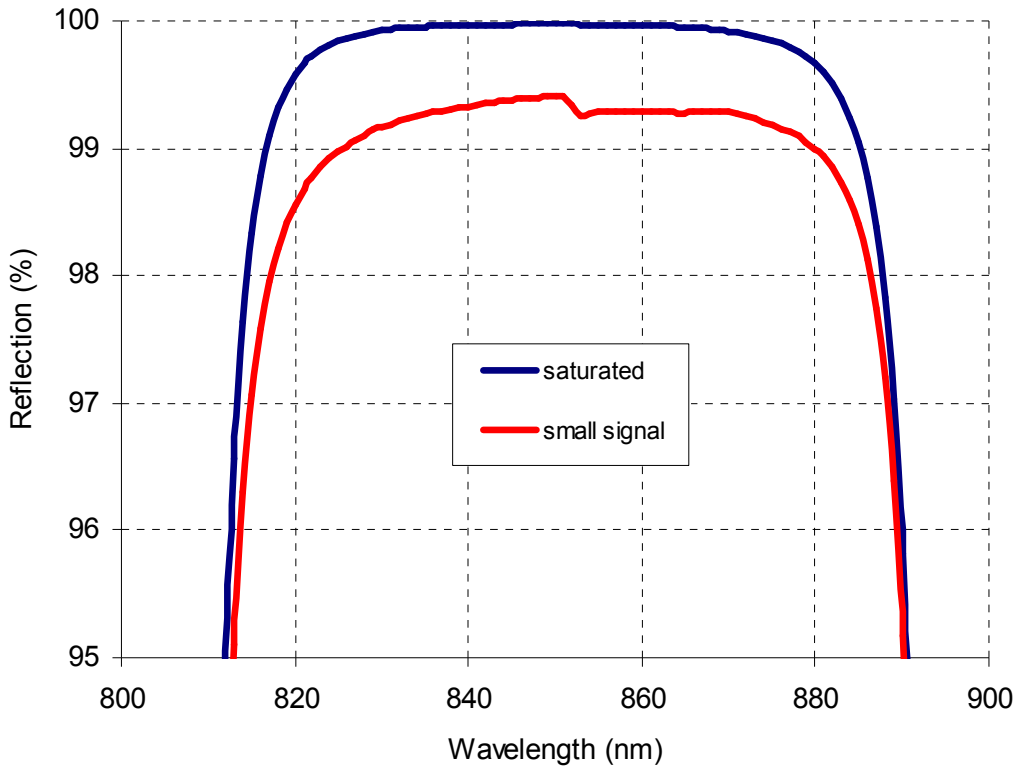

Figure D26: Calculated small signal and saturated reflection profiles of the regular 850 nm SESAM/SBR.

APPENDIX E

SESAM/SBR DESIGNS THAT WERE GROWN DURING THIS PHD

In this Appendix, we will provide information on SESAMs/SBRs that were grown during this PhD work. Table E1 lists the 6 SESAMs/SBRs that were designed by me, and then grown by our collaborator, Prof. Leslie Kolodziejski's Integrated Photonics Devices and Materials Research Group at MIT. For some of the SESAMs/SBRs, we have coated an additional SiO_2/ TiO_2 high reflector coating on top; hence, Table E1 contains 10 structures in total. Dr. Gale Petrich from Prof. Kolodziejski's group have performed all the growth, and also characterized the grown structures in detail (x-ray, spectrophotometer and ellipsometer measurements). We thank him by providing some of the information that we will present in this Appendix. Note here that, for each SESAM/SBR we will provide (i) simulation results based on design (ii) information on the actual grown structure, which is kindly provided by Dr. Gale. Table E1 also lists the appropriate section, for each SESAM/SBR.

SESAM/SBR Name	Short Name	Growth number	Section
MIT 850 nm SESAM/SBR with bulk absorber	MIT-850-Bulk	VA97	E1
One pair HR layer coated MIT 850 nm SESAM/SBR with bulk absorber	MIT-850-Bulk-HR		E2
MIT 800 nm SESAM/SBR with bulk absorber	MIT-800-Bulk	VA98	E3
One pair HR layer coated MIT 800 nm SESAM/SBR with bulk absorber	MIT-800-Bulk-HR		E4
MIT 800 nm SESAM/SBR with quantum-well absorber	MIT-800-QW	VA101	E5
One pair HR layer coated MIT 800 nm SESAM/SBR with quantum-well absorber	MIT-800-QW-HR		E6
Two pairs HR layer coated MIT 800 nm SESAM/SBR with quantum-well absorber	MIT-800-QW-2HR		E7
MIT 910 nm SESAM/SBR with bulk absorber	MIT-910-Bulk	VA119	E8
MIT 910 nm SESAM/SBR with quantum well absorber	MIT-910-QW	VA120	E9
MIT 860 nm oxidized/broadband SESAM/SBR with quantum well absorber	MIT-860-QW-Oxidized	VA130	E10

Table E1: List of SESAMs/SBRs that were grown during the period of this PhD (sorted in terms of growth order).

Table E2 provides information on SESAM/SBR specs such as modulation depth and absorber band edge position. We note here that, some of the SESAM/SBR designs we have grown can actually be improved considerably. The reason is that, they were grown before we learned the issues with SESAM/SBR design that we tried to describe in Appendix D. In Table E3, we will try to mention the problems and possible improvements for each SESAM/SBR.

SESAM/SBR Name	Modulation Depth (%)	Absorber band edge position (nm)	2nd transition position (nm)	3rd transition position (nm)
MIT-850-Bulk	2.2	~868	~854	~833
MIT-850-Bulk-HR	0.8			
MIT-800-Bulk	2.2	~862	~832	~790
MIT-800-Bulk-HR	0.8			
MIT-800-QW	4.2	~835	-	-
MIT-800-QW-HR	1.6			
MIT-800-QW-2HR	0.6			
MIT-910-Bulk	1.7	~929	~892	~846
MIT-910-QW	1.7	~907	-	-
MIT-860-QW-Oxidized	0.75	~920	~803	-

Table E2: Calculated modulation depth and absorber band edge positions for each SESAM/SBR. For some of the SESAM/SBR absorbers 2nd and 3rd transitions are also possible, and for those corresponding transition wavelengths are also provided.

SESAM/SBR Name	Notes
MIT-850-Bulk	Worked fine with Cr:Colquiriite lasers in general. The modulation depth (2.2 %) is a little bit high for Cr:Colquiriite gain media. Absorber is a bulk absorber, a QW absorber should perform better. Absorber band edge is around ~868 nm, which prevents tuning above this wavelength. Also, if the focus on the SESAM/SBR is not tight, the laser works at 870 nm in cw mode.
MIT-850-Bulk-HR	Modulation depth decreased to 0.8%, which is more appropriate for Cr:Colquiriite lasers. HR coated version enabled the generation of shorter pulses and broader tuning in Cr:LiSAF laser. Absorber design can be improved in general as described above.
MIT-800-Bulk	2.2 % modulation is too high for Cr:Colquiriites. Barely works with Cr:LiCAF.
MIT-800-Bulk-HR	0.8 % modulation depth is around optimum. Works nicely in Cr:LiSAF, and works OK in Cr:LiCAF.
MIT-800-QW	4.2 % modulation is too high for Cr:Colquiriites. Keeps burning in the laser
MIT-800-QW-HR	1.6 % modulation is too high for Cr:Colquiriites. Barely works with Cr:LiCAF.
MIT-800-QW-2HR	0.6 % modulation depth is around optimum. Works nicely in Cr:LiSAF, and almost all of the Cr:LiCAF data is obtained with this SESAM/SBR.
MIT-910-Bulk	Absorber edge is at the center of reflectivity. Still works from 890 nm to 920 nm in Cr:LiSAF. However, tuning is demonstrated discretely only (by changing SESAM/SBR focusing or cavity dispersion level). Continuous fs tuning range is just 5-10 nm's. Purging of the cavity might help.
MIT-910-QW	Absorber edge is at the center of reflectivity. Also, in the growth, reflectivity bandwidth range (or central wavelength for the Bragg stack) is shifted to longer wavelengths.
MIT-860-QW-Oxidized	Works OK; however, there are issues with oxidization, which should be solved. Since the mesas are not fully oxidized it is hard to find a working point on the sample. Passive losses are relatively high compared to regular SESAMs/SBRs. We have also observed SESAM/SBR damage due to accumulated heat with time.

Table E3: Short notes on each SESAM/SBR.

E.1 MIT 850 nm SESAM/SBR with bulk absorber (MIT-850-Bulk)

Layer	Material	Physical thickness (nm)	Optical thickness (nm)	n	Purpose
0	GaAs	-	-	-	Substrate
1	$Al_{0.95}Ga_{0.05}As$	69.32	212.50	3.06	Bragg layer
2	$Al_{0.17}Ga_{0.83}As$	61.42	212.50	3.46	Bragg layer
…					Bragg layers
49	$Al_{0.95}Ga_{0.05}As$	69.32	212.50	3.06	Bragg layer
50	$Al_{0.17}Ga_{0.83}As$	61.42	212.50	3.46	Bragg layer
51	$Al_{0.95}Ga_{0.05}As$	69.32	212.50	3.06	Bragg layer
52	$Al_{0.14}Ga_{0.86}As$	10	34.60	3.46	Barrier
53	GaAs	25	109.21	3.63	Absorber
54	$Al_{0.14}Ga_{0.86}As$	30	86.50	3.46	Barrier
55	GaAs	5	18.17	3.63	Cap

Table E4: MIT 850 nm regular SESAM/SBR design with bulk absorber.

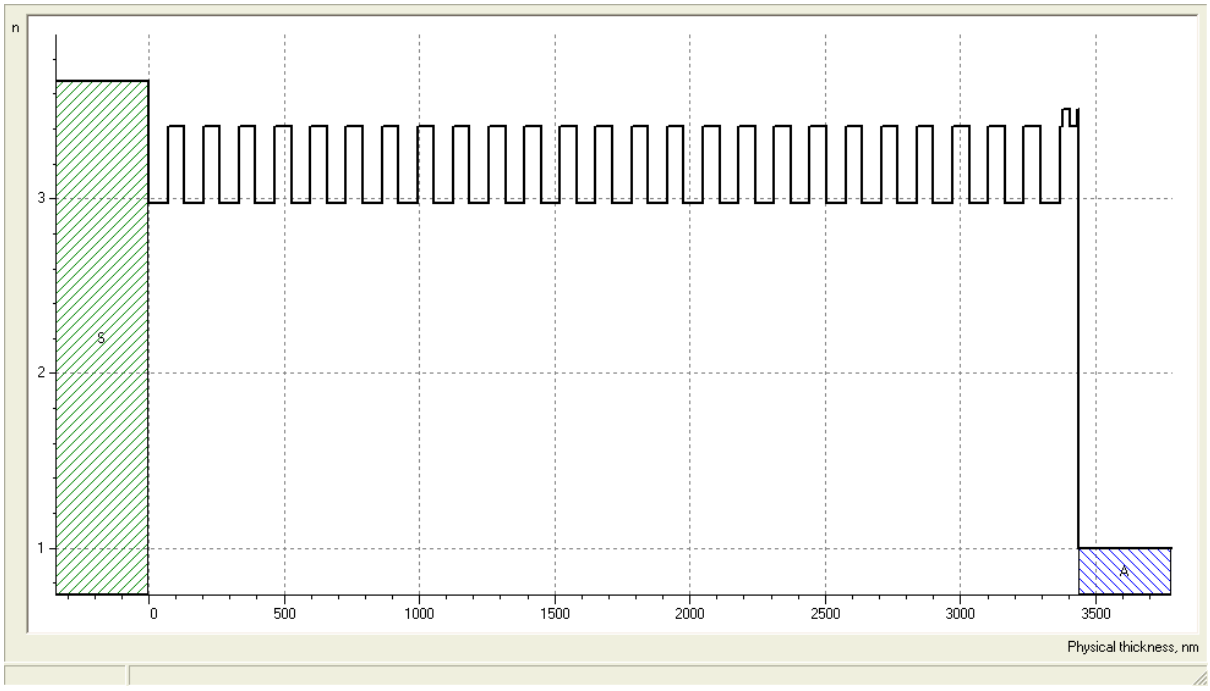

Figure E1: Index profile for MIT-850-Bulk SESAM/SBR design.

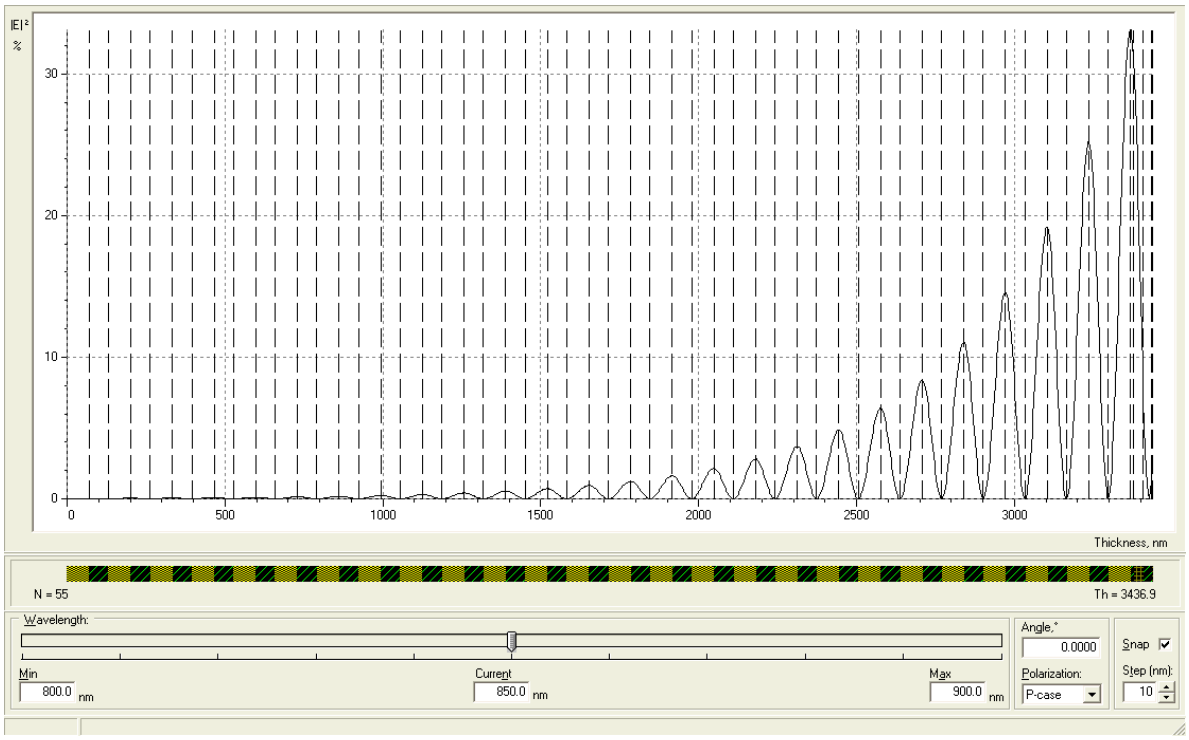

Figure E2: Electric field pattern for MIT-850-Bulk SESAM/SBR design.

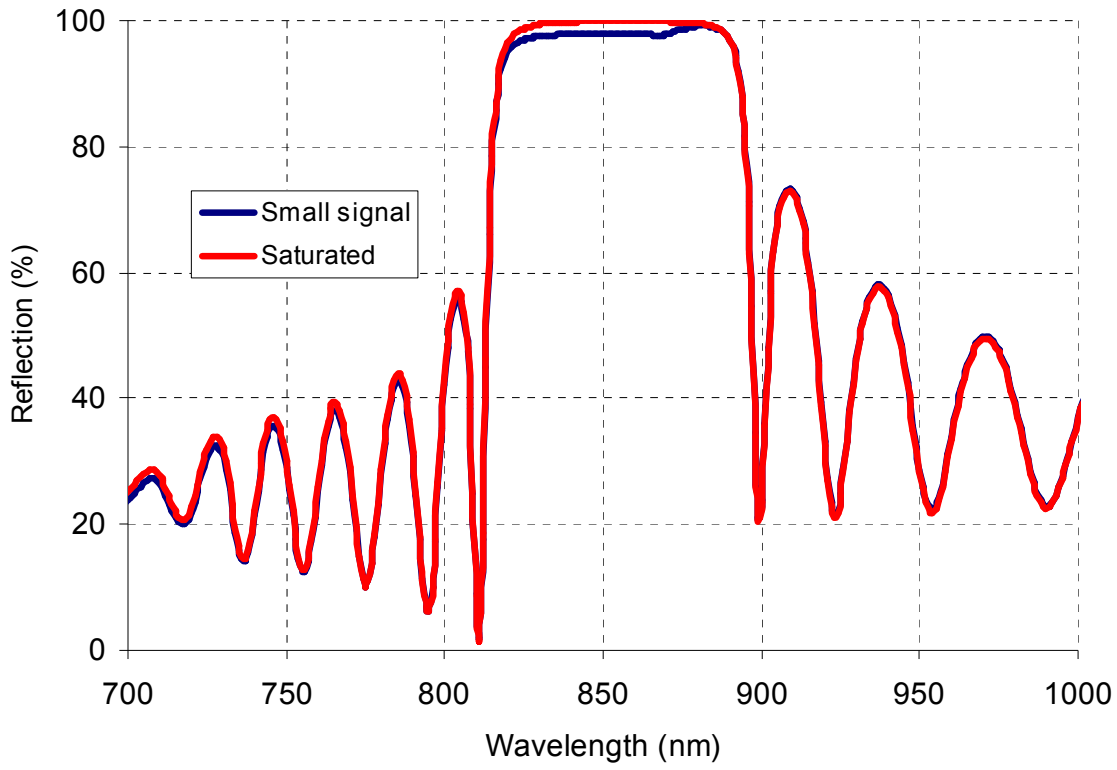

Figure E3: Calculated reflectivity for MIT-850-Bulk SESAM/SBR design.

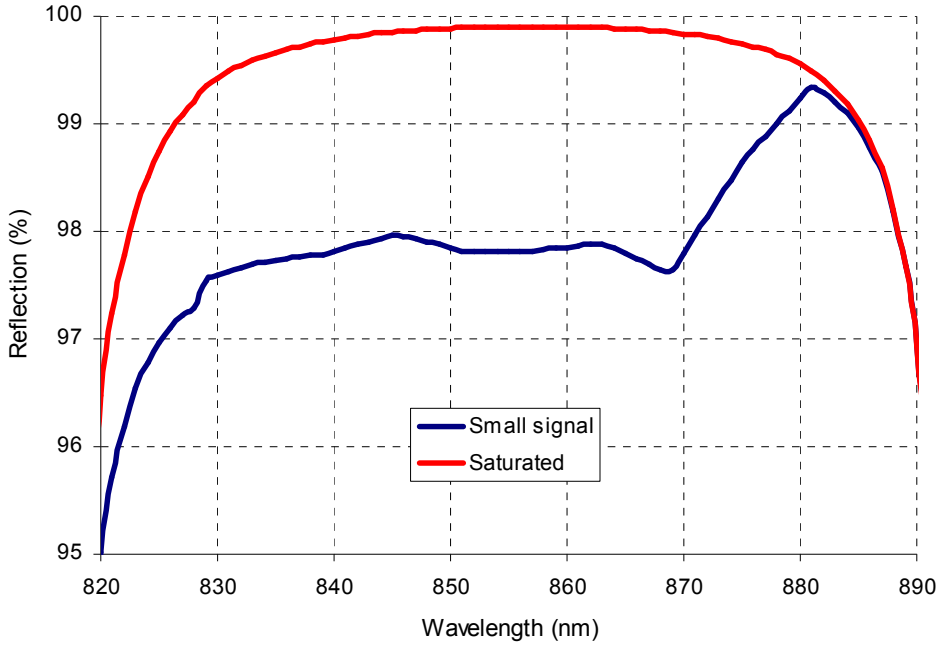

Figure E4: Calculated reflectivity for MIT-850-Bulk SESAM/SBR design (zoomed in).

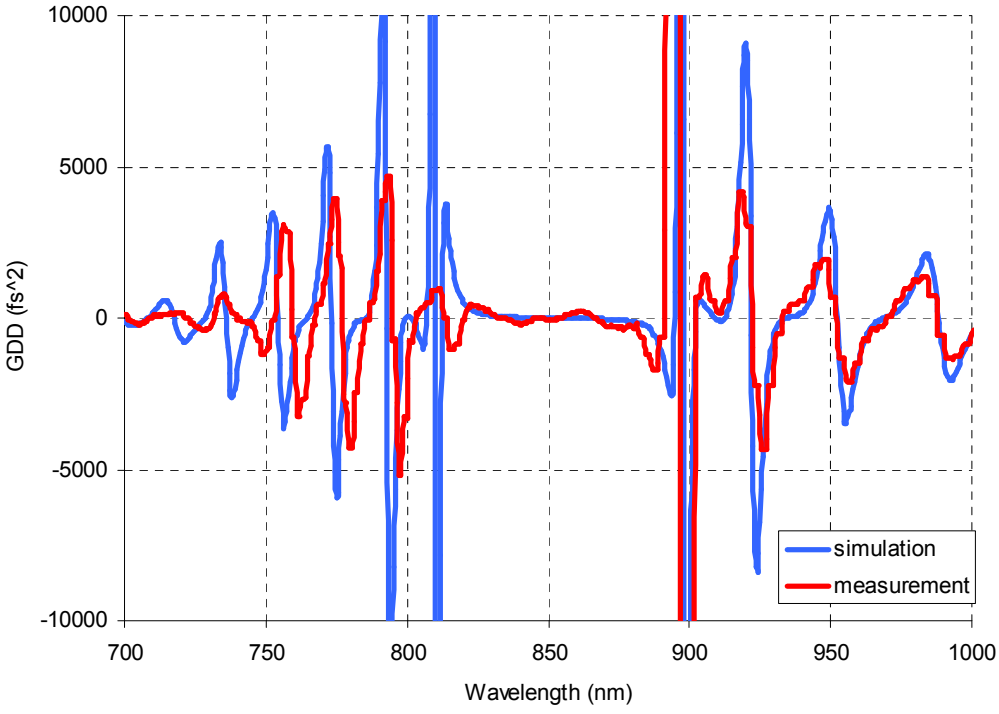

Figure E5: Calculated and measured GDD for MIT-850-Bulk SESAM/SBR design.

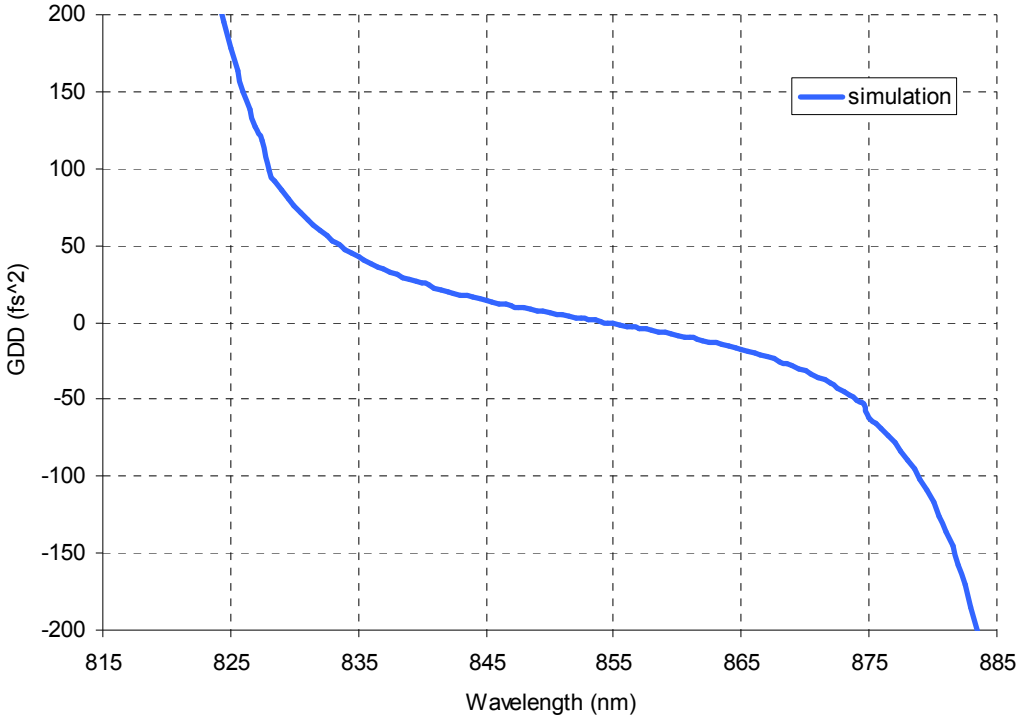

Figure E6: Calculated GDD for MIT-850-Bulk SESAM/SBR design (zoomed in).

	Desired Structure			Reflectivity Fit		Composite Xray Fit		WVASE: Max coupling		WVASE: Uncoupled	
		Thickness	Al content	Thickness	Al content	Thickness	Al Content	Thickness	Al Content	Thickness	Al Content
	GaAs	5		4.982		5.572		5.9026 ±1.15		4.967 ±0.343	
	AlGaAs	30	0.17	30.046	0.1709	30.688	0.160	25.871 ±3.55	0.11262 ±0.0023	29.981 ±1.17	0.17716 ±0.00502
	GaAs	25		24.979		25.2713		29.832 ±4.36		29.721 ±1.74	
	AlGaAs	10	0.17	10.015	0.1709	9.724	0.136	7.5133 ±2.26	0.11262 ±0.0023	4.3914 ±1.35	0.19603 ±0.0354
X 25	AlGaAs	69.3	0.95	70.403	0.9593	68.380	0.924	65.128± 0.217	0.92955 ±0.00851	64.127 ±0.498	0.8829 ±0.00566
	AlGaAs	61.4	0.17	61.427	0.1709	63.396	0.167	61.283 ±0.0208	0.11262 ±0.0023	61.265 ±0.349	0.1192 ±0.00119
	AlGaAs	69.3	0.95	70.403	0.9593	69.004	0.937	65.128 ±0.217	0.92955 ±0.00851	87.222 ±4.61	1 ±0.0771
	GaAs Substrate										

Figure E7: Summary of the desired structure and measured results for MIT-850-Bulk SESAM/SBR. Note: All the thicknesses are in nm's. This information is kindly provided by Dr. Gale Petrich.

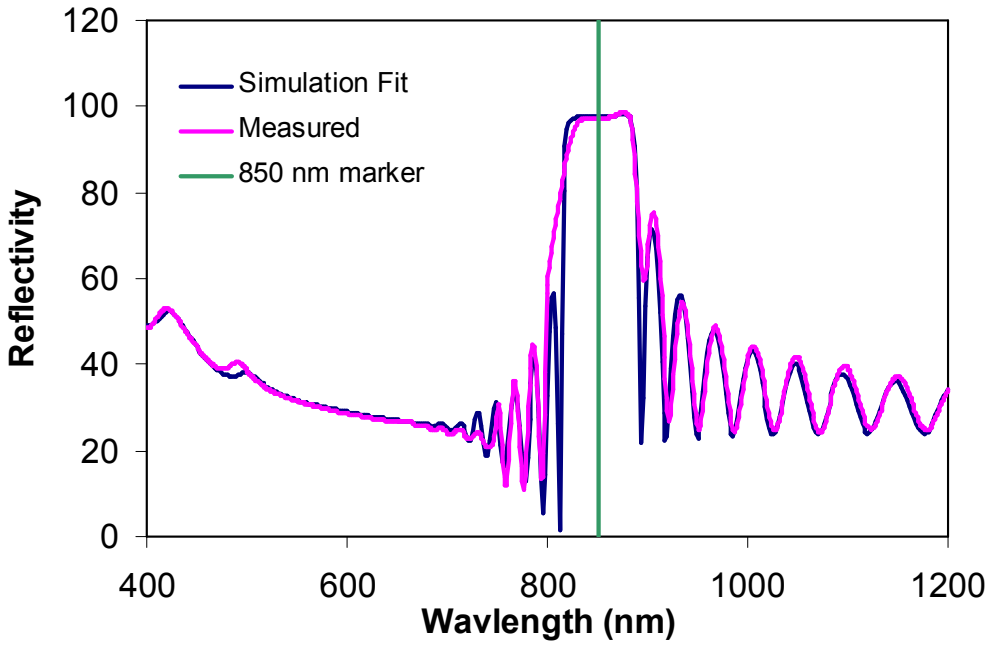

Figure E8: MIT-850-Bulk SESAM/SBR reflectivity data. Notes: (i) Data is taken using Cary 5i, (ii) There is a detector switch at 800 nm, (iii) Fit assumed constant growth rates. This information is kindly provided by Dr. Gale Petrich.

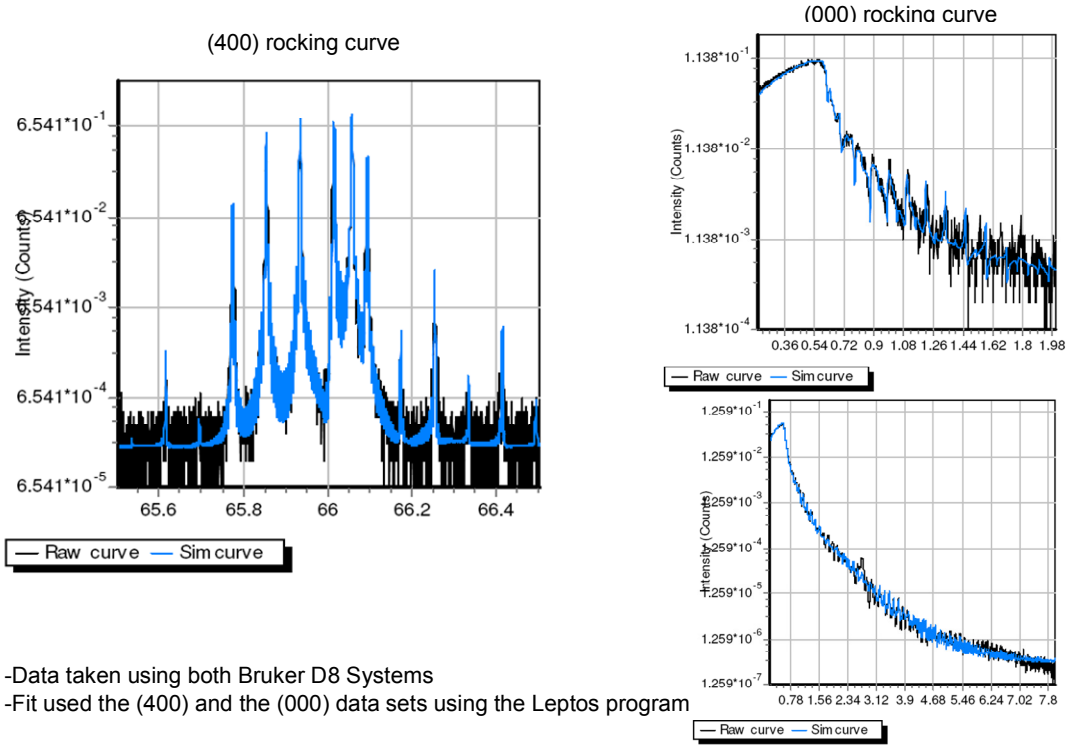

Figure E9: MIT-850-Bulk SESAM/SBR x-ray diffraction data. Notes: (i) Data is taken using both Bruker D8 systems, (ii) Fit used the (400) and the (000) data sets using the Leptos program. This information is kindly provided by Dr. Gale Petrich.

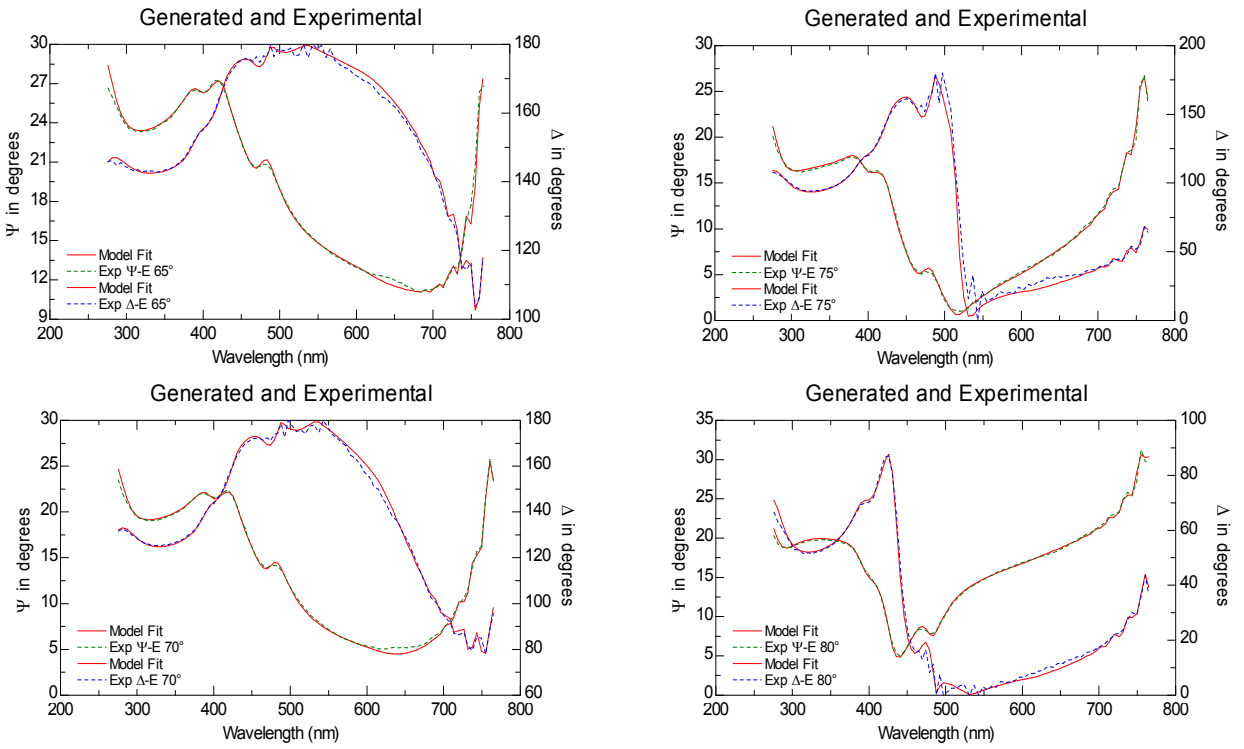

Figure E10: MIT-850-Bulk SESAM/SBR WVASE (Woollam Variable Angle Spectroscopic Ellipsometer) graphs. Notes: (i) Data is taken using J.A. Woollam M-88 ellipsometer, (ii) Fit calculated using all the data sets assuming that the layers are uncoupled. This information is kindly provided by Dr. Gale Petrich.

E.2 One Pair HR Coated MIT 850 nm SESAM/SBR with bulk absorber (MIT-850-Bulk-HR)

Layer	Material	Physical Thickness (nm)	Optical Thickness (nm)	n	Purpose
0	GaAs	-	-	-	Substrate
1	$Al_{0.95}Ga_{0.05}As$	69.32	212.50	3.06	Bragg layer
2	$Al_{0.17}Ga_{0.83}As$	61.42	212.50	3.46	Bragg layer
…	…	…	…	…	Bragg layers
49	$Al_{0.95}Ga_{0.05}As$	69.32	212.50	3.06	Bragg layer
50	$Al_{0.17}Ga_{0.83}As$	61.42	212.50	3.46	Bragg layer
51	$Al_{0.95}Ga_{0.05}As$	69.32	212.50	3.06	Bragg layer
52	$Al_{0.14}Ga_{0.86}As$	10	34.60	3.46	Barrier
53	GaAs	25	109.21	3.63	Absorber
54	$Al_{0.14}Ga_{0.86}As$	30	86.50	3.46	Barrier
55	GaAs	5	18.17	3.63	Cap
56	SiO_2	147.67	212.50	1.44	HR coating
57	TiO_2	89.29	212.50	2.38	HR coating

Table E5: One pair HR coated MIT 850 nm regular SESAM/SBR design with bulk absorber (MIT-850-Bulk-HR).

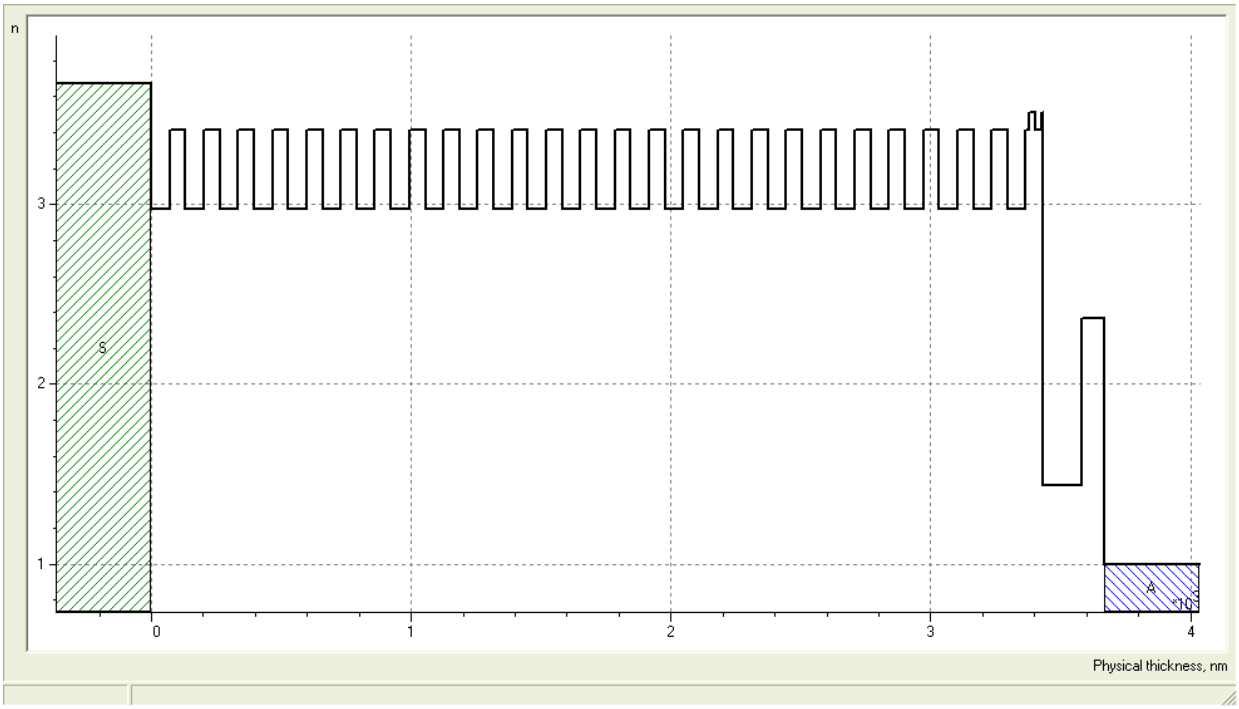

Figure E11: Index profile for MIT-850-Bulk-HR SESAM/SBR design.

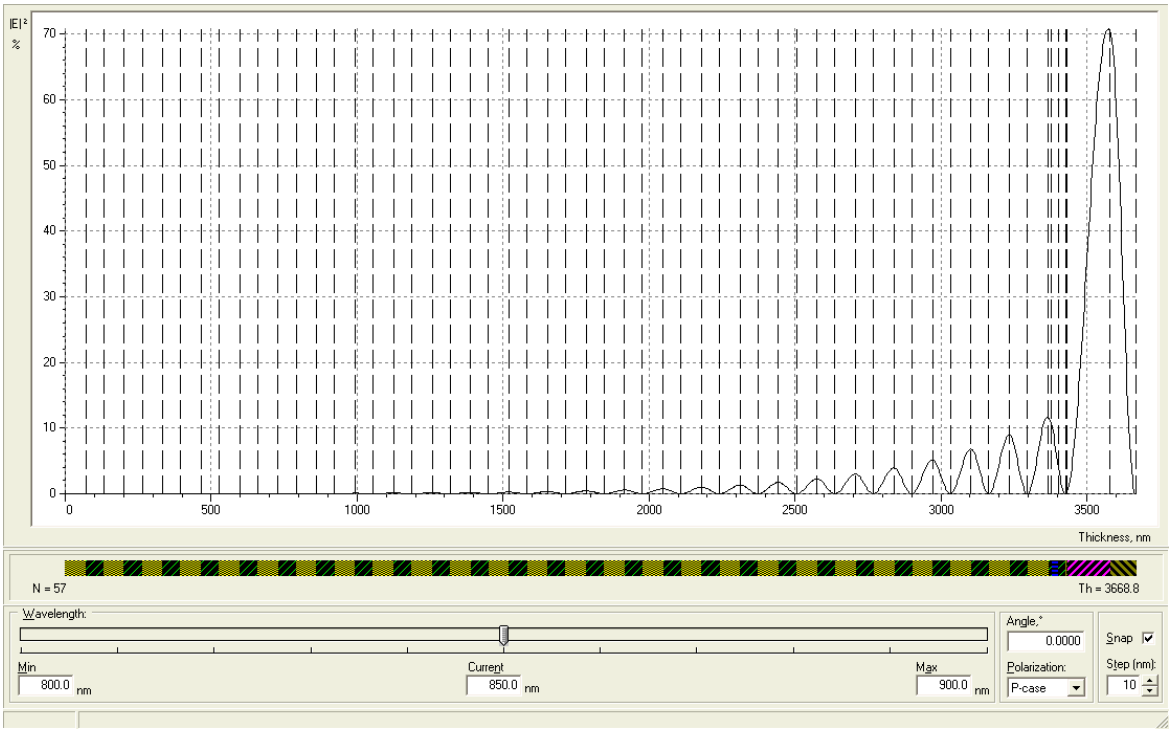

Figure E12: Electric filed pattern for MIT-850-Bulk-HR SESAM/SBR design.

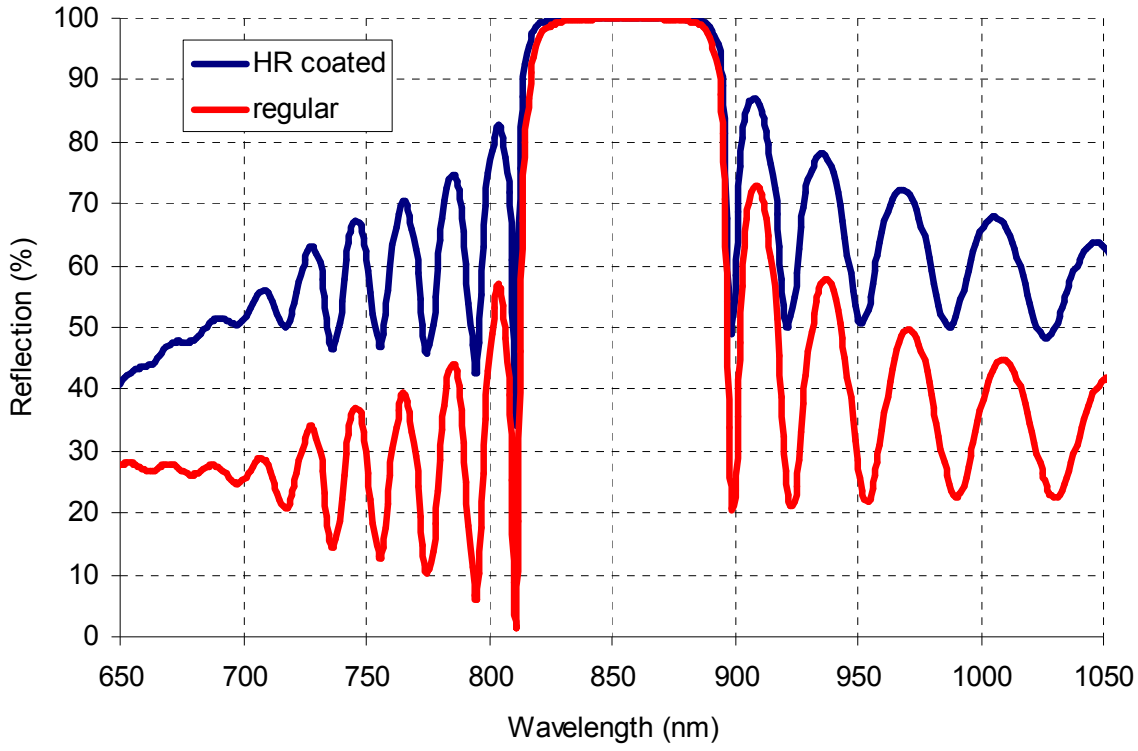

Figure E13: Calculated reflectivity for MIT-850-Bulk-HR SESAM/SBR design.

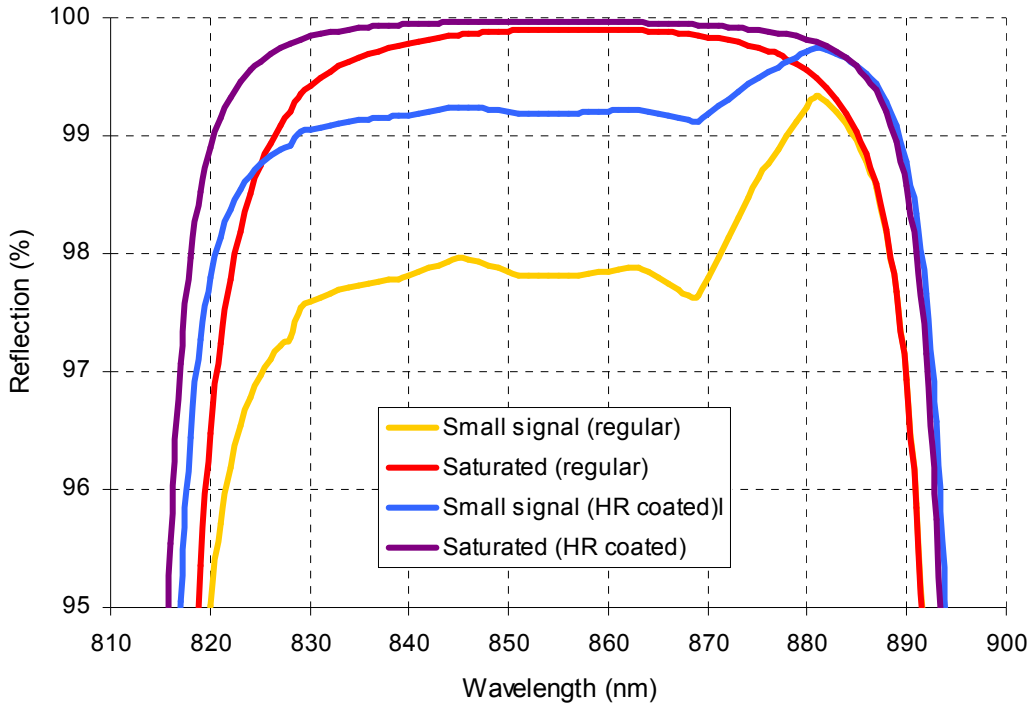

Figure E14: Calculated reflectivity for MIT-850-Bulk-HR SESAM/SBR design (zoomed in). Calculated reflectivity for MIT-850-Bulk SESAM/SBR is also shown for comparison.

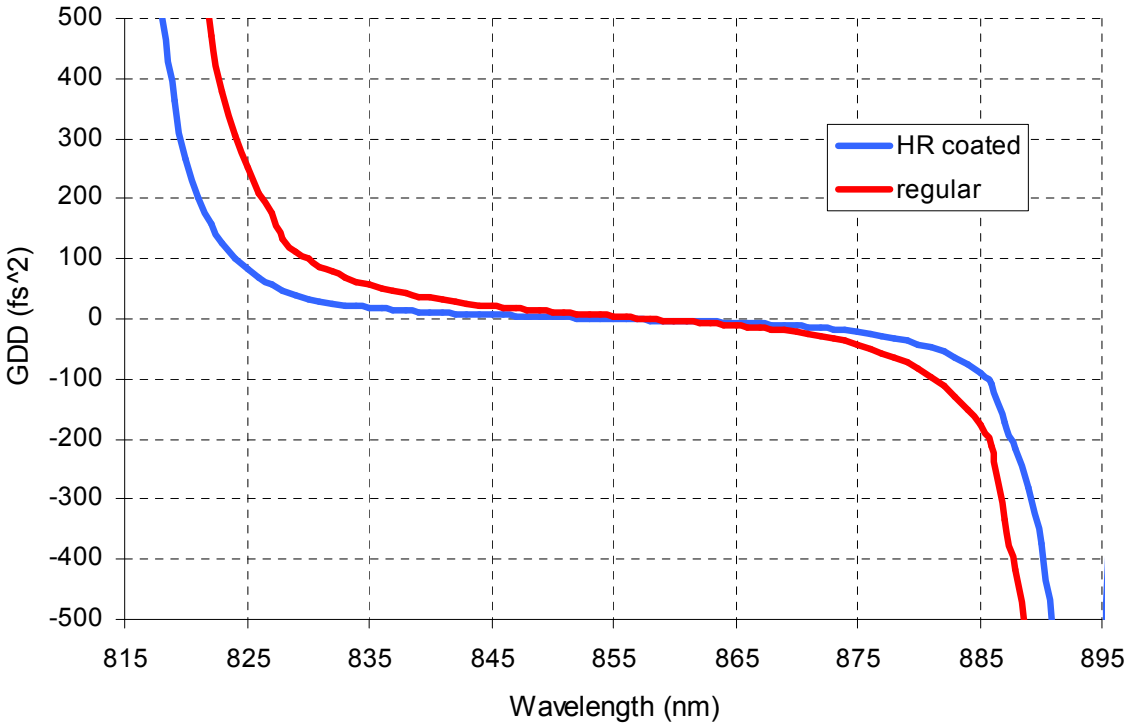

Figure E15: Calculated GDD for MIT-850-Bulk-HR SESAM/SBR design (zoomed in). Calculated GDD for MIT-850-Bulk SESAM/SBR is also shown for comparison.

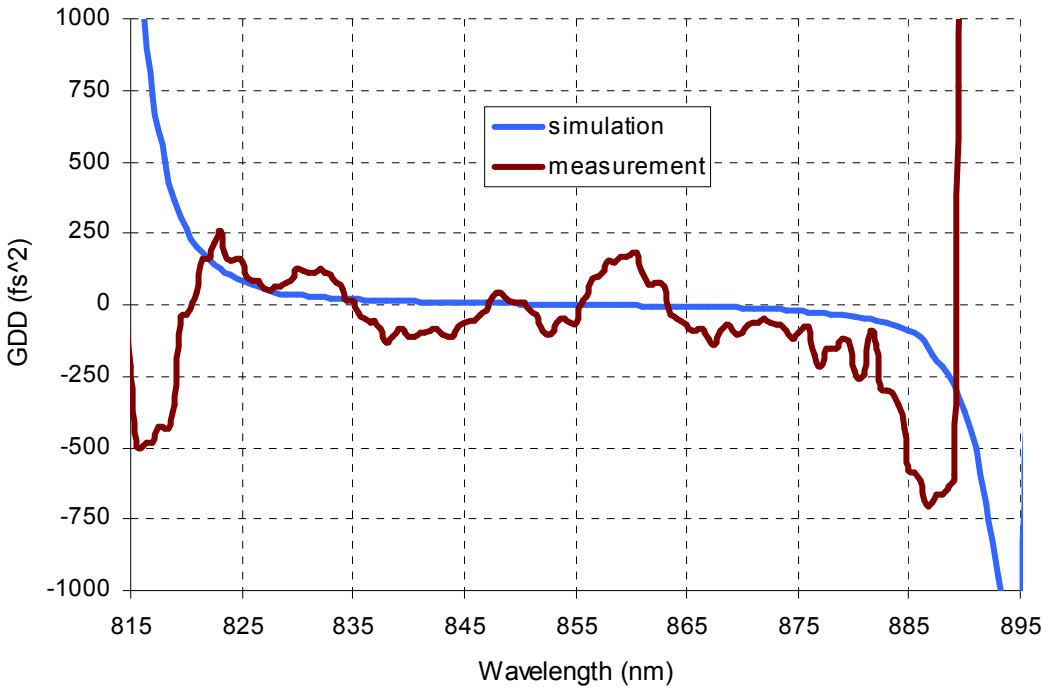

Figure E16: Calculated and measured GDD for MIT-850-Bulk-HR SESAM/SBR design (zoomed in).

E.3 MIT 800 nm SESAM/SBR with bulk absorber (MIT-800-bulk)

Layer	Material	Physical thickness (nm)	Optical thickness (nm)	n	Purpose
0	GaAs	-	-	-	Substrate
1	$Al_{0.95}Ga_{0.05}As$	65.84	200	3.04	Bragg layer
2	$Al_{0.17}Ga_{0.83}As$	57.15	200	3.50	Bragg layer
…					Bragg layers
49	$Al_{0.95}Ga_{0.05}As$	65.84	200	3.04	Bragg layer
50	$Al_{0.17}Ga_{0.83}As$	57.15	200	3.50	Bragg layer
51	$Al_{0.95}Ga_{0.05}As$	65.84	200	3.04	Bragg layer
52	$Al_{0.17}Ga_{0.83}As$	10	35	3.50	Barrier
53	GaAs	15	55.27	3.68	Absorber
54	$Al_{0.17}Ga_{0.83}As$	35	122.48	3.50	Barrier
55	GaAs	5	18.42	3.68	Cap

Table E6: MIT 800 nm regular SESAM/SBR design with bulk absorber (MIT-800-bulk).

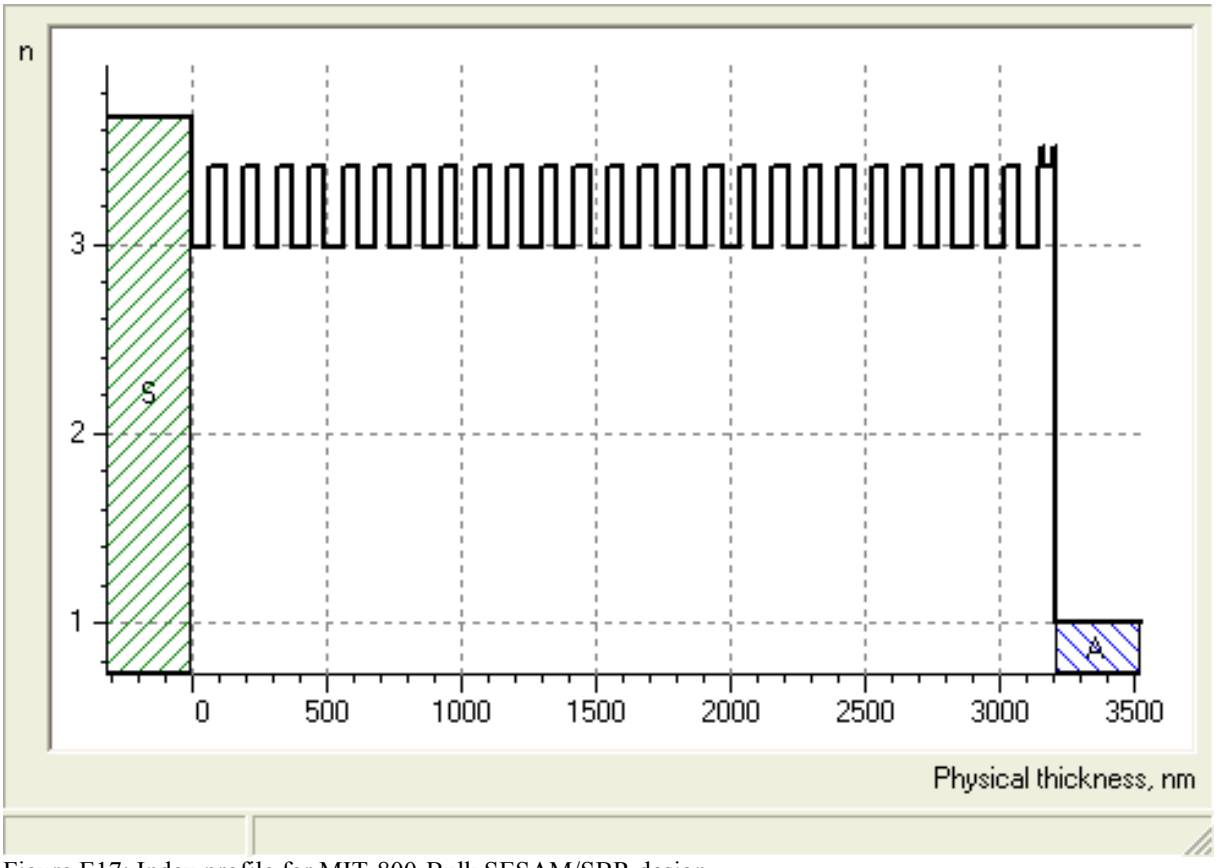

Figure E17: Index profile for MIT-800-Bulk SESAM/SBR design.

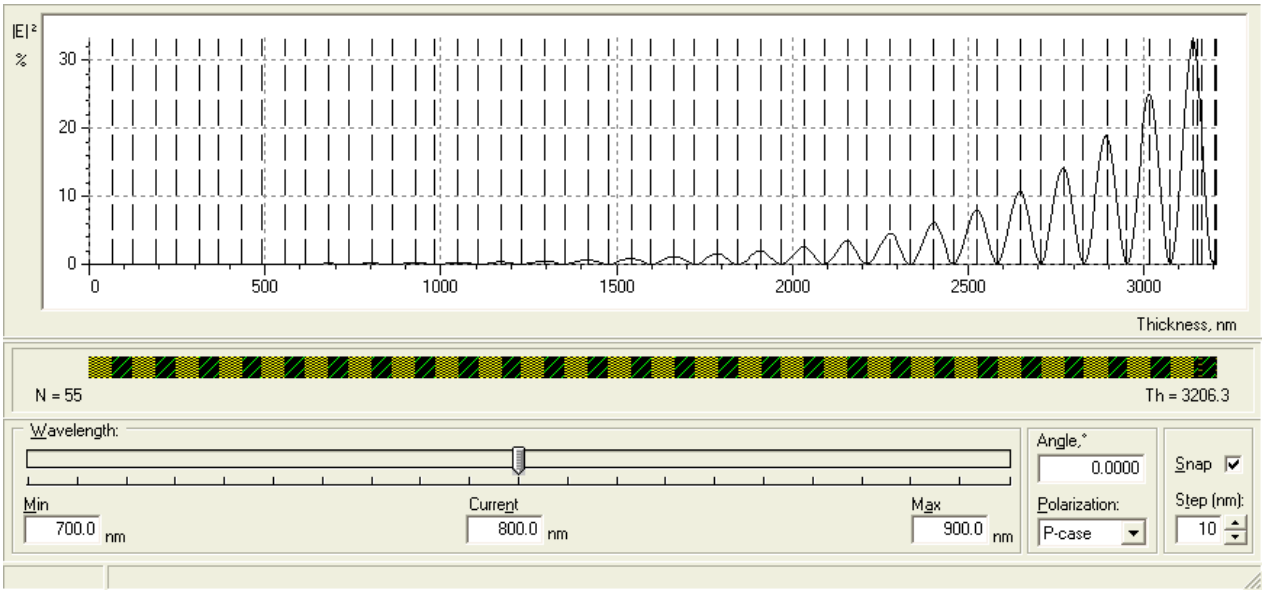

Figure E18: Electric field pattern for MIT-800-Bulk SESAM/SBR design.

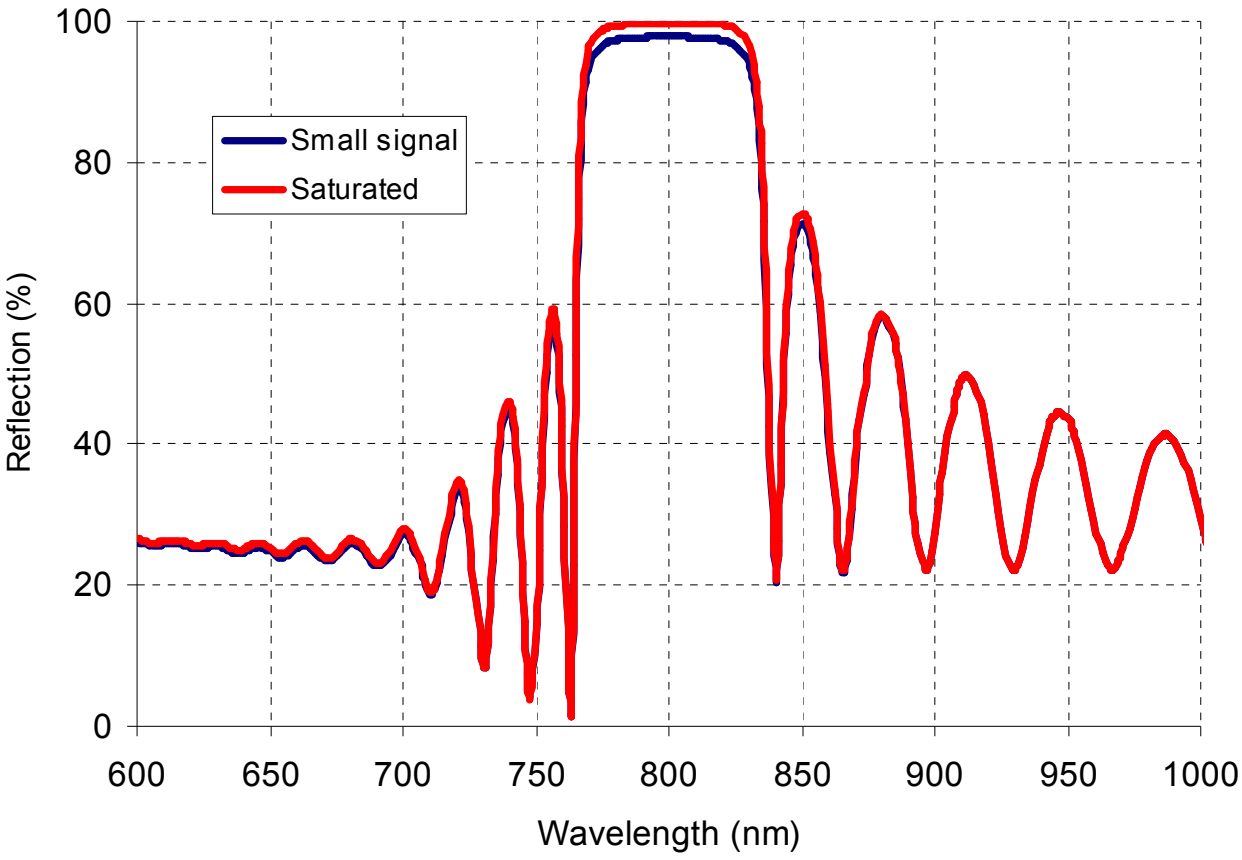

Figure E19: Calculated reflectivity for MIT-800-Bulk SESAM/SBR design.

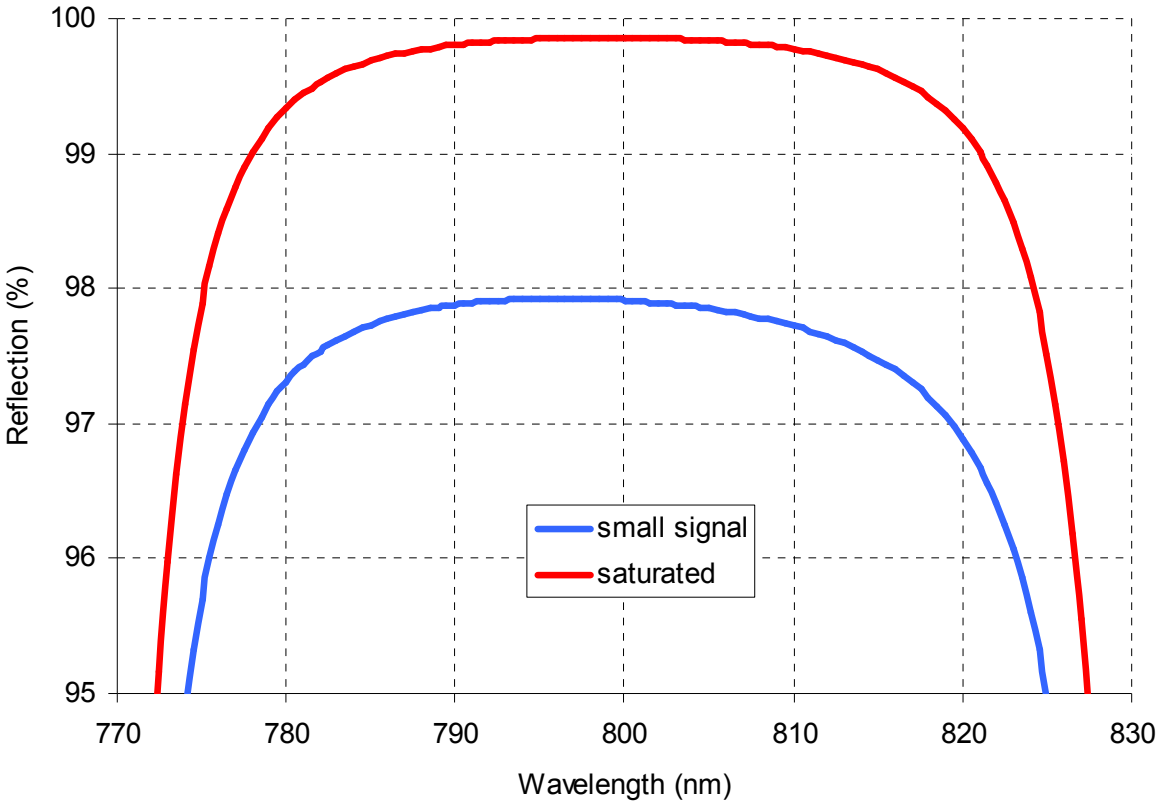

Figure E20: Calculated reflectivity for MIT-800-Bulk SESAM/SBR design (zoomed in).

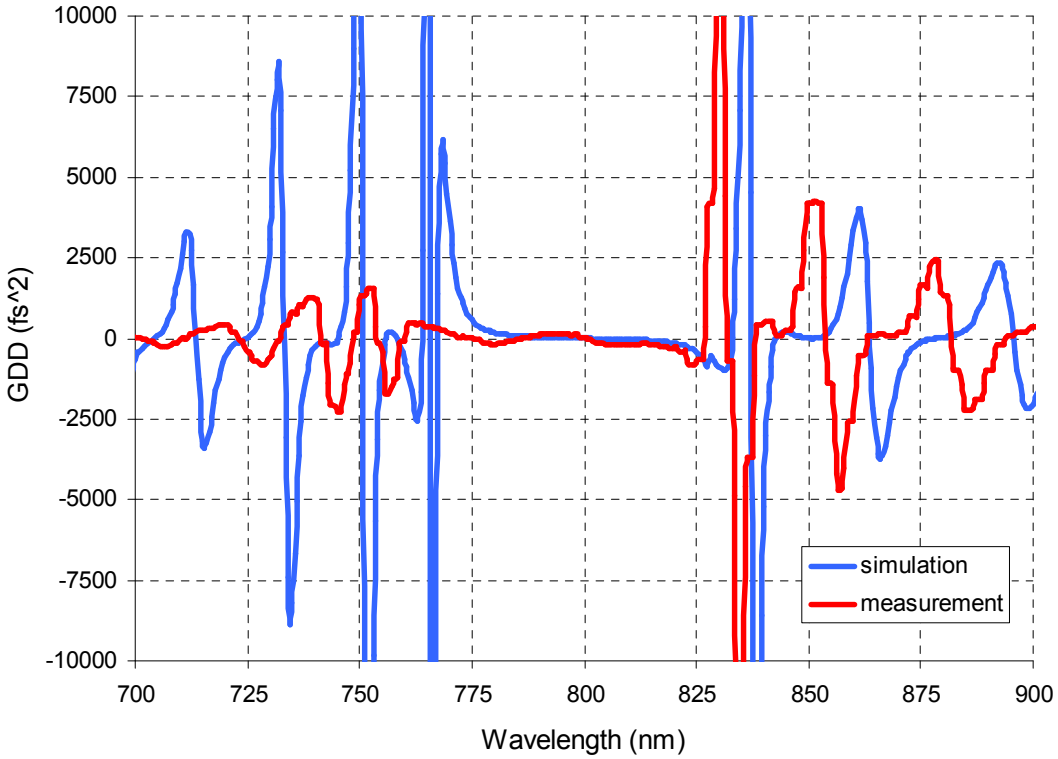

Figure E21: Calculated and measured GDD for MIT-800-Bulk SESAM/SBR design.

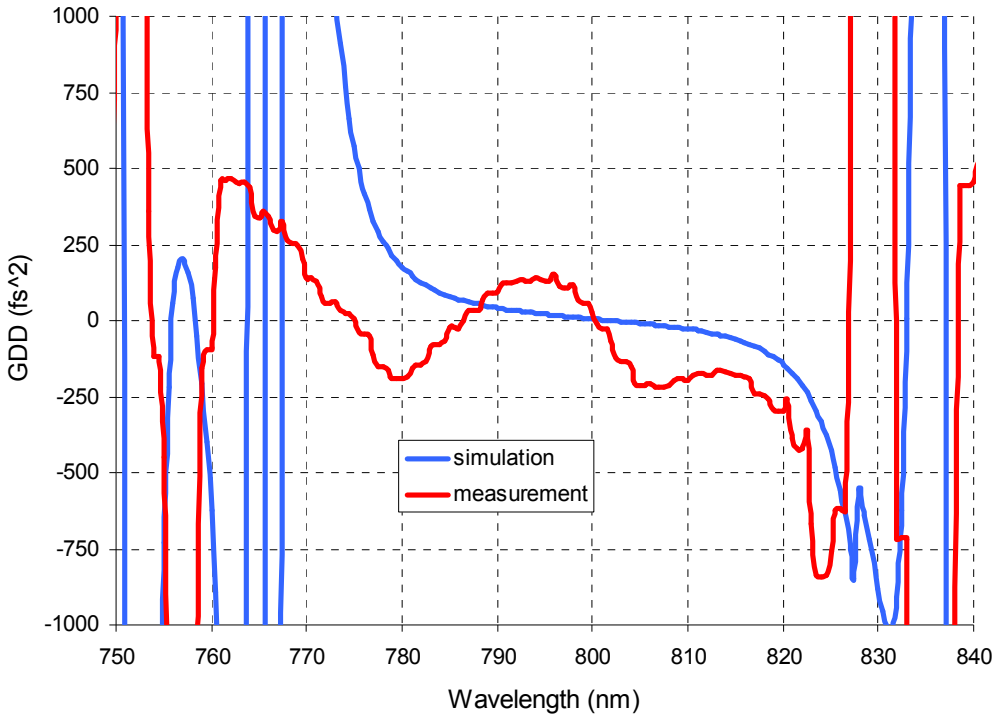

Figure E22: Calculated and measured GDD for MIT-800-Bulk SESAM/SBR design (zoomed in).

	Desired Structure			Reflectivity Fit		Composite Xray Fit		WVASE: Max coupling		WVASE: Uncoupled	
		Thickness	Al content	Thickness	Al content	Thickness	Al Content	Thickness	Al Content	Thickness	Al Content
	GaAs	5		4.950		5.713		2.7126 ±0.749		3.956 ±0.972	
	AlGaAs	35	0.17	33.274	0.1381	32.965	0.1996	31.699 ±2.34	0.15032 ±0.0026	31.235 ±2.9	0.1638 ±0.0166
	GaAs	15		14.822		15.045		19.967 ±4.4		15.398 ±4.8	
	AlGaAs	10	0.17	9.502	0.1381	8.808	0.1559	9.4363 ±2.91	0.15032 ±0.0026	12.853 ±3.12	0.15671 ±0.0351
X 25	AlGaAs	64.95	0.95	66.355	0.9463	64.941	0.9494	60.019 ±0.503	0.92793 ±0.0195	61.787 ±1.12	0.97156 ±0.011
	AlGaAs	57.5	0.17	54.310	0.1381	55.870	0.1686	58.397 ±0.0364	0.15032 ±0.0026	57.958 ±0.822	0.14906 ±0.0054
	AlGaAs	64.95	0.95	66.355	0.9463	73.512	0.9176	60.019 ±0.503	0.92793 ±0.0195	85.032 ±18.9	1 ±0.277
	GaAs Substrate										

Note: All thicknesses are in nanometers.

Figure E23: Summary of the desired structure and measured results for MIT-800-Bulk SESAM/SBR. Note: All the thicknesses are in nm's. This information is kindly provided by Dr. Gale Petrich.

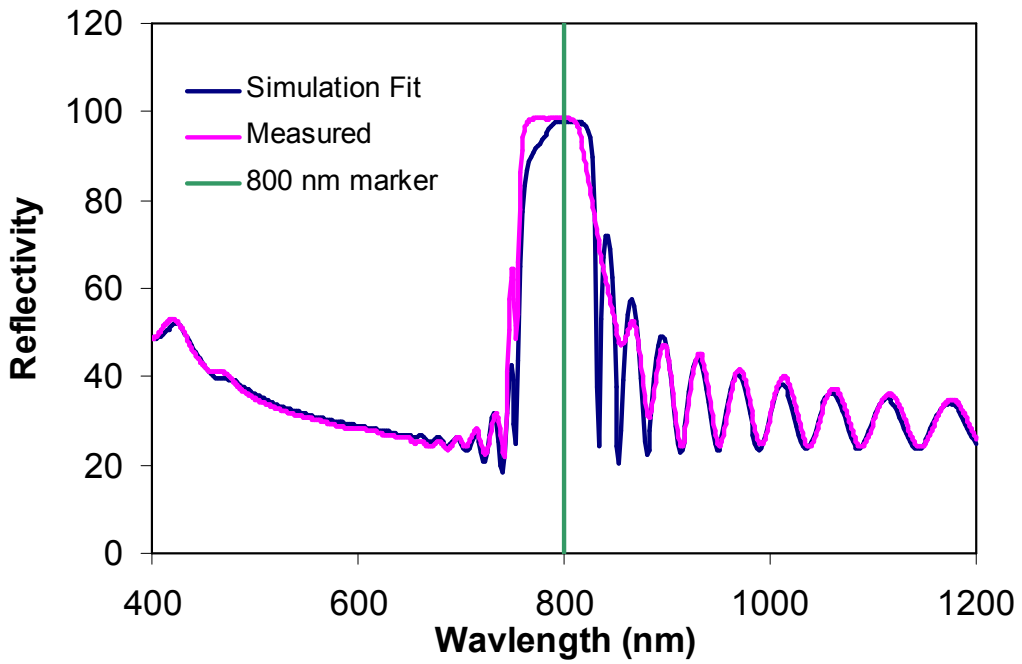

Figure E24: MIT-800-Bulk SESAM/SBR reflectivity data. Notes: (i) Data is taken using Cary 5i, (ii) There is a detector switch at 800 nm, (iii) Fit assumed constant growth rates. This information is kindly provided by Dr. Gale Petrich.

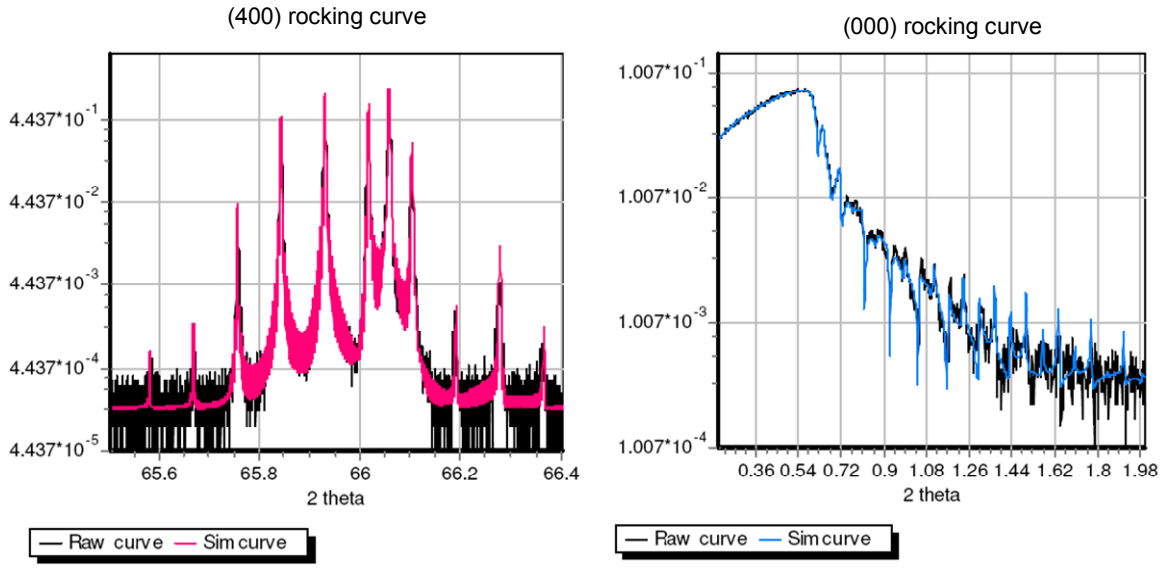

Figure E25: MIT-800-Bulk SESAM/SBR x-ray diffraction data. Notes: (i) Data is taken using both Bruker D8 systems, (ii) Fit used the (400) and the (000) data sets using the Leptos program. This information is kindly provided by Dr. Gale Petrich.

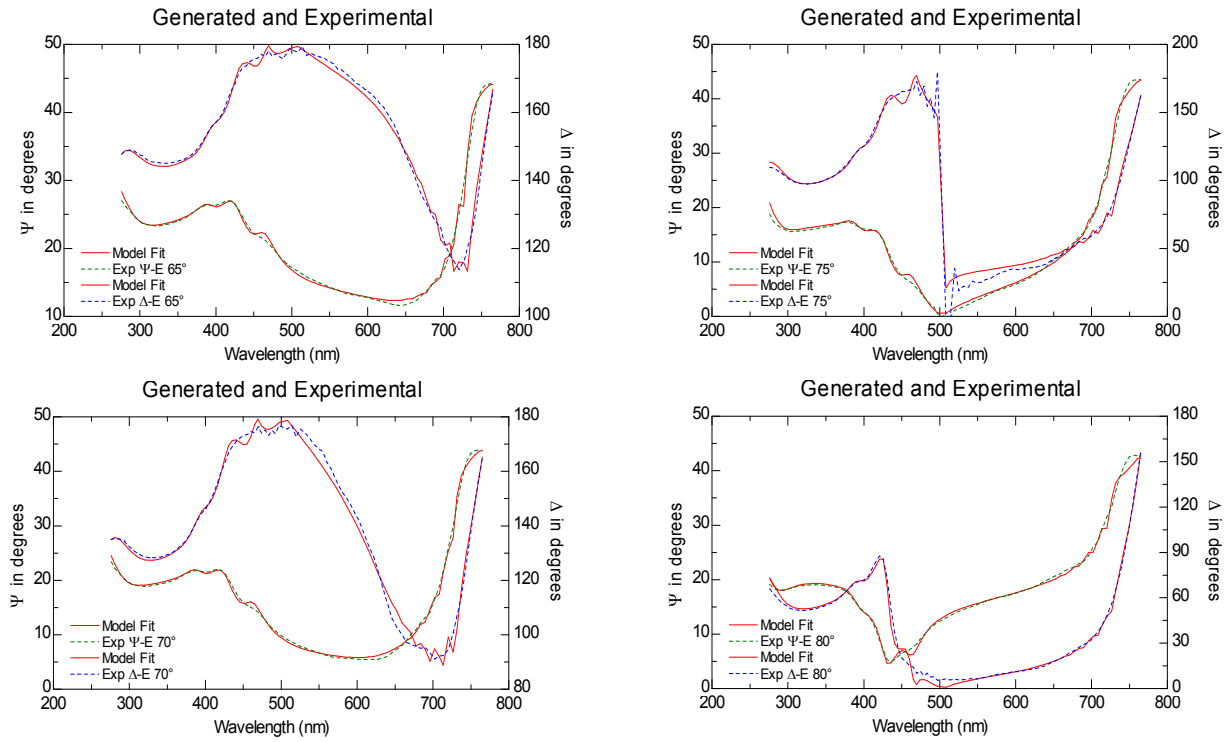

Figure E26: MIT-850-Bulk SESAM/SBR WVASE (Woollam Variable Angle Spectroscopic Ellipsometer) graphs. Notes: (i) Data is taken using J.A. Woollam M-88 ellipsometer, (ii) Fit calculated using all the data sets assuming that the layers are uncoupled. This information is kindly provided by Dr. Gale Petrich.

E.4 One Pair HR Coated MIT 800 nm SESAM/SBR with bulk absorber (MIT-800-bulk-HR)

Layer	Material	Physical thickness (nm)	Optical thickness (nm)	n	Purpose
0	GaAs	-	-	-	Substrate
1	$Al_{0.95}Ga_{0.05}As$	65.84	200	3.04	Bragg layer
2	$Al_{0.17}Ga_{0.83}As$	57.15	200	3.50	Bragg layer
…					Bragg layers
49	$Al_{0.95}Ga_{0.05}As$	65.84	200	3.04	Bragg layer
50	$Al_{0.17}Ga_{0.83}As$	57.15	200	3.50	Bragg layer
51	$Al_{0.95}Ga_{0.05}As$	65.84	200	3.04	Bragg layer
52	$Al_{0.17}Ga_{0.83}As$	10	35	3.50	Barrier
53	GaAs	15	55.27	3.68	Absorber
54	$Al_{0.17}Ga_{0.83}As$	35	122.48	3.50	Barrier
55	GaAs	5	18.42	3.68	Cap
56	SiO_2	138.89	200	1.44	HR coating
57	TiO_2	83.79	200	2.39	HR coating

Table E7: One pair HR coated MIT 800 nm regular SESAM/SBR design with bulk absorber.

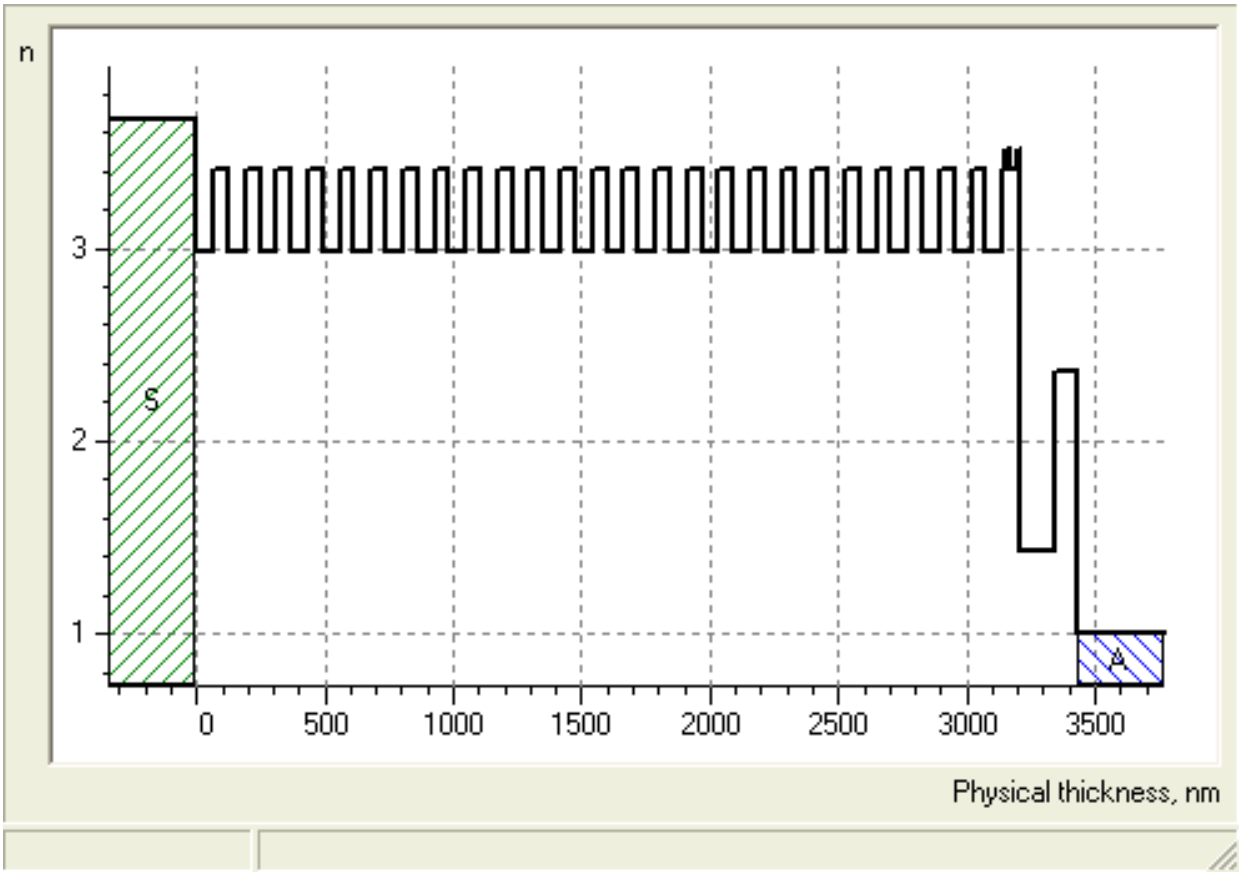

Figure E27: Index profile for MIT-800-Bulk-HR SESAM/SBR design.

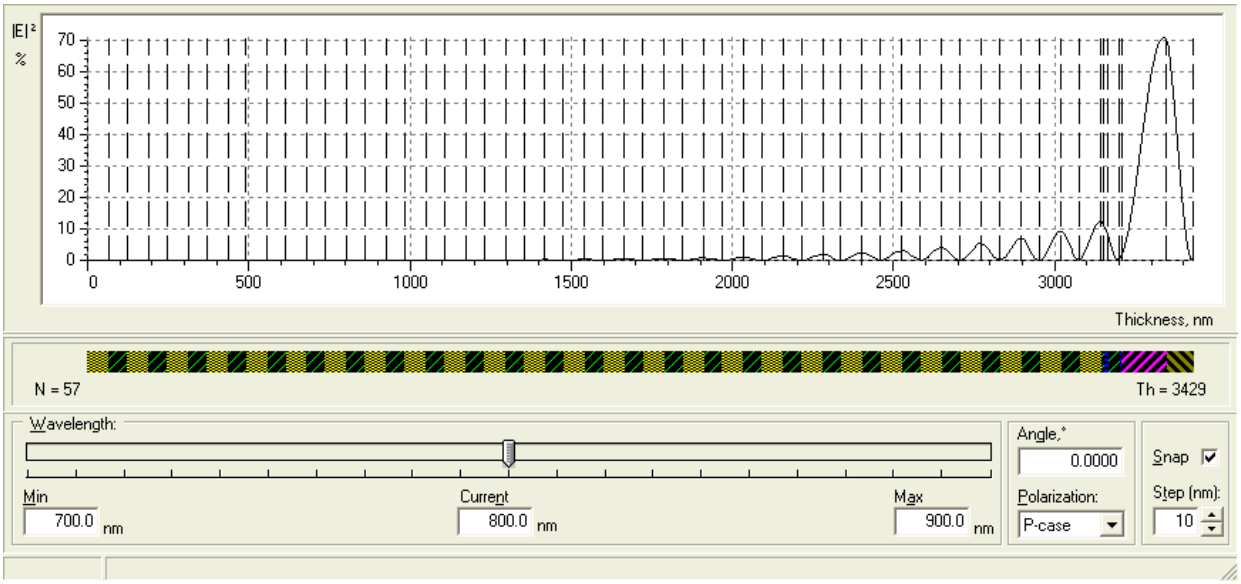

Figure E28: Electric field pattern for MIT-800-Bulk-HR SESAM/SBR design.

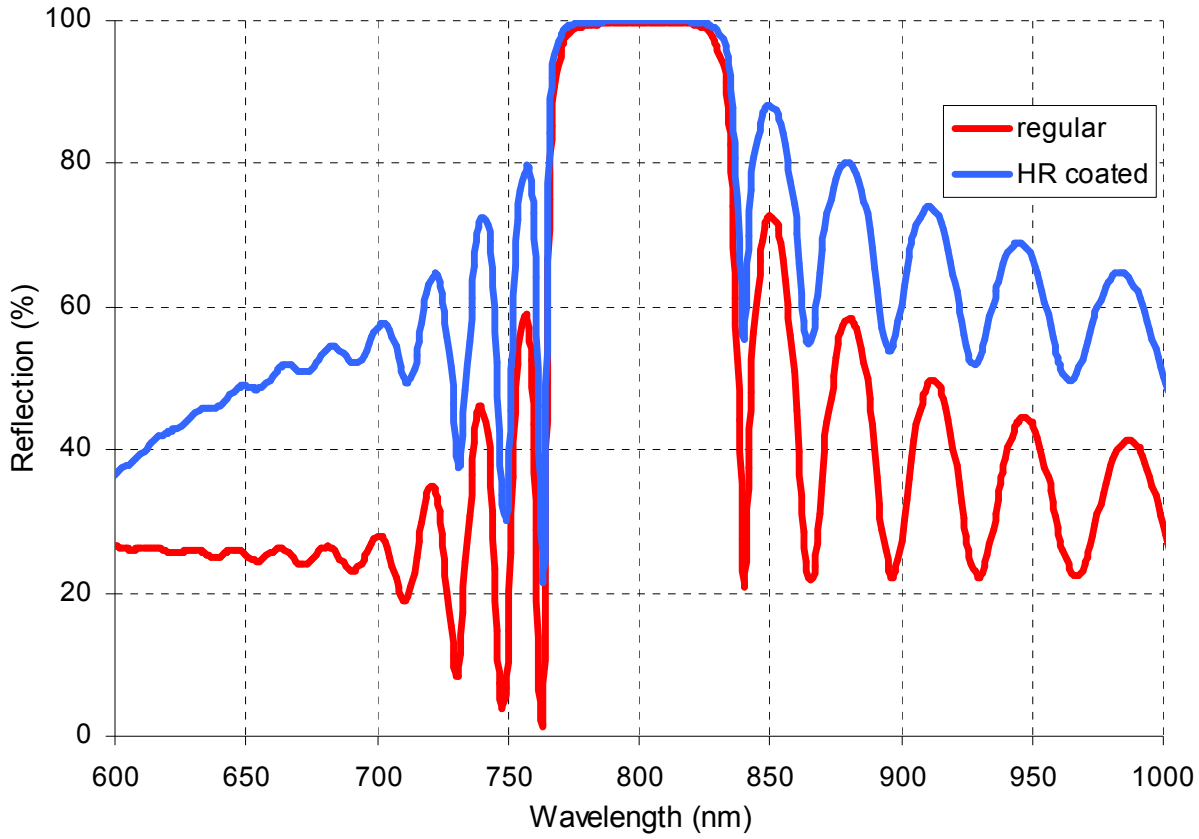

Figure E29: Calculated reflectivity for MIT-800-Bulk-HR SESAM/SBR design.

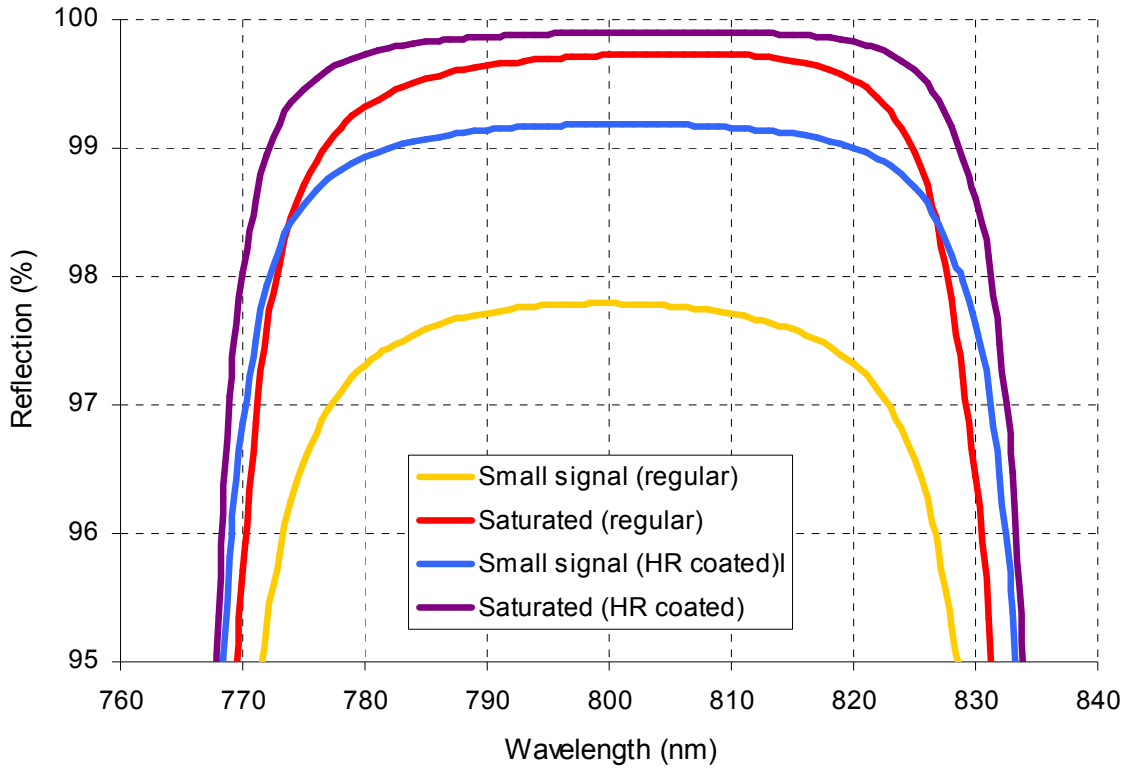

Figure E30: Calculated reflectivity for MIT-800-Bulk-HR SESAM/SBR design (zoomed in). Reflectivity for MIT-800-Bulk SESAM/SBR is also shown.

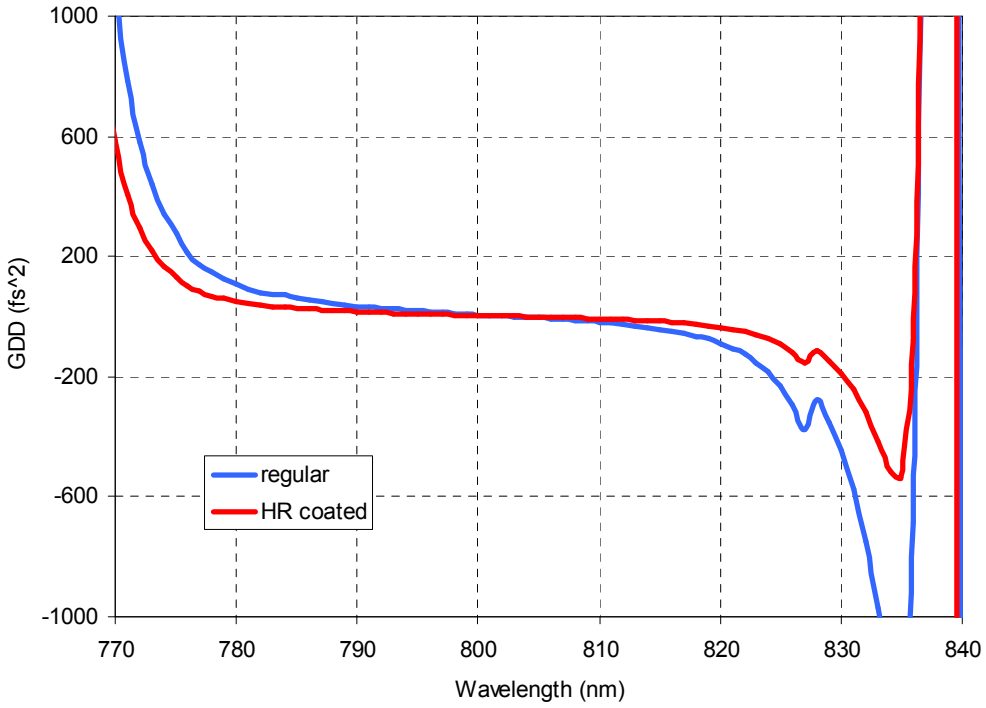

Figure E31: Calculated and measured GDD for MIT-800-Bulk SESAM/SBR design.

E.5 MIT 800 nm SESAM/SBR with quantum-well absorber (MIT-800-QW)

Layer	Material	Physical thickness (nm)	Optical thickness (nm)	n	Purpose
0	GaAs	-	-	-	Substrate
1	AlAs	66.55	200	3.01	Bragg layer
2	$Al_{0.17}Ga_{0.83}As$	57.15	200	3.50	Bragg layer
…					Bragg layers
49	AlAs	66.55	200	3.01	Bragg layer
50	$Al_{0.17}Ga_{0.83}As$	57.15	200	3.50	Bragg layer
51	AlAs	66.55	200	3.01	Bragg layer
52	$Al_{0.17}Ga_{0.83}As$	10	35	3.50	Barrier
53	GaAs	6	22.11	3.68	Absorber
54	$Al_{0.17}Ga_{0.83}As$	70	244.97	3.50	Barrier
55	GaAs	6	22.11	3.68	Absorber
56	$Al_{0.17}Ga_{0.83}As$	8	28	3.50	Barrier
57	GaAs	6	22.11	3.68	Absorber
58	$Al_{0.17}Ga_{0.83}As$	8	28	3.50	Barrier
59	GaAs	6	22.11	3.68	Absorber
60	$Al_{0.17}Ga_{0.83}As$	8	28	3.50	Barrier
61	GaAs	6	22.11	3.68	Absorber
62	$Al_{0.17}Ga_{0.83}As$	27	94.49	3.50	Barrier
63	GaAs	5	18.42	3.68	Cap

Table E8: MIT 800 nm regular SESAM/SBR design with quantum well absorber (MIT-800-QW).

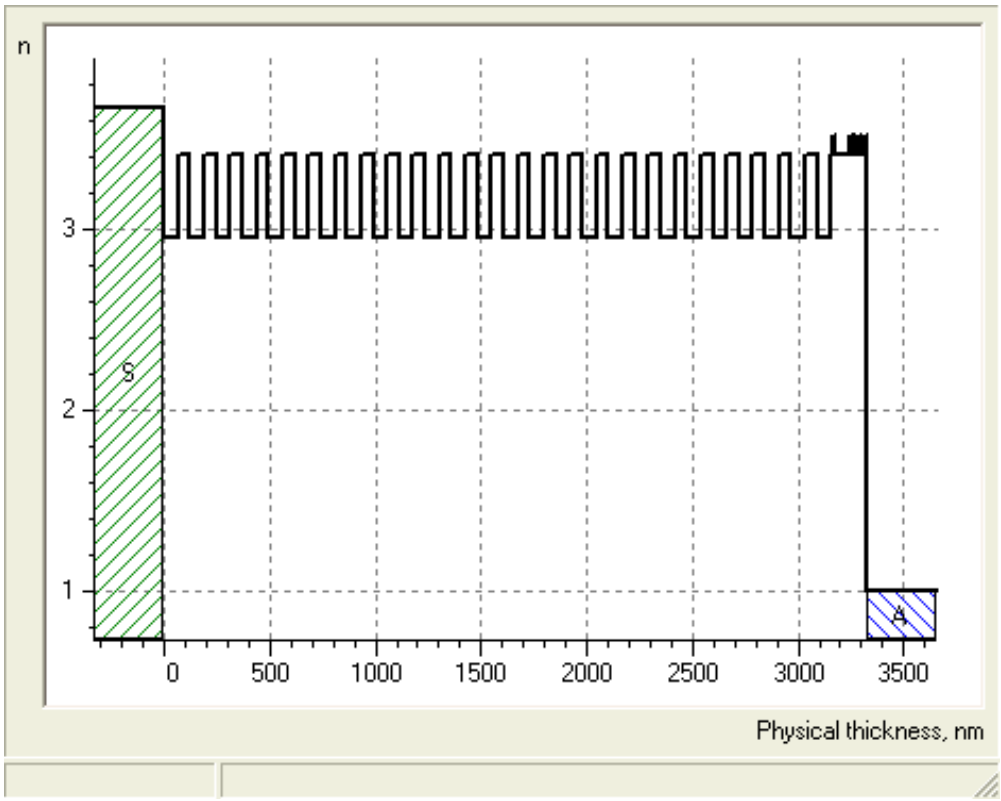

Figure E32: Index profile for MIT-800-QW SESAM/SBR design.

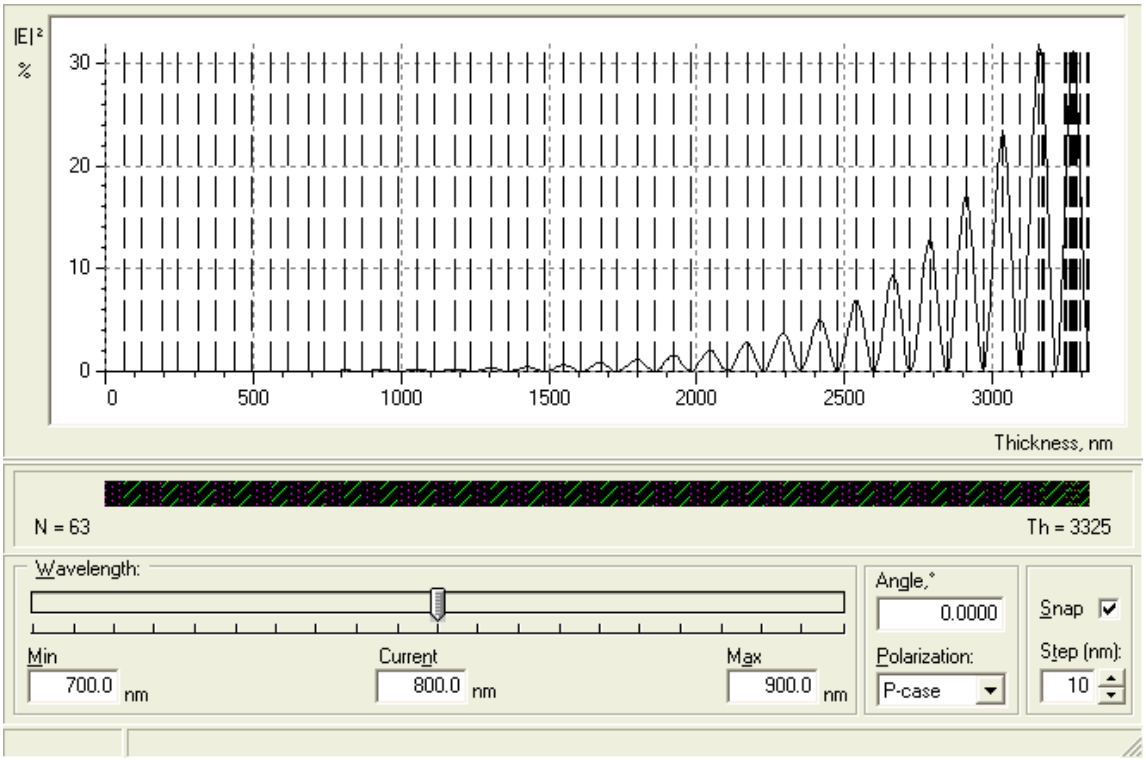

Figure E33: Electric field pattern for MIT-800-QW SESAM/SBR design.

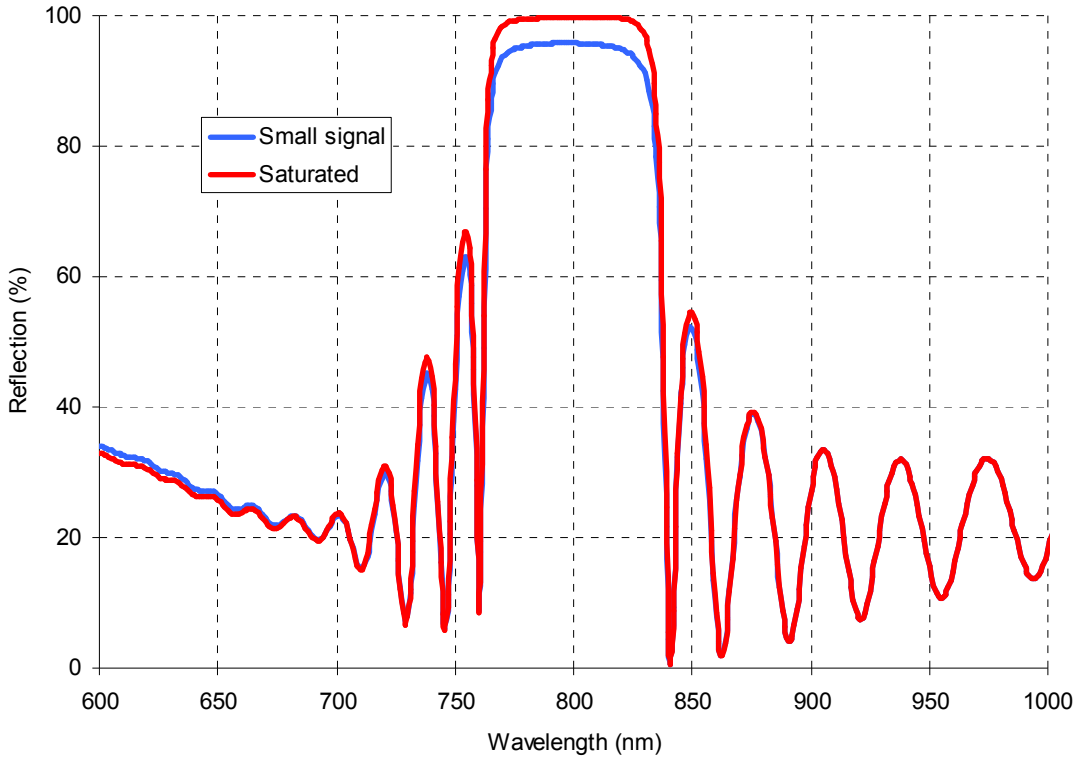

Figure E34: Calculated reflectivity for MIT-800-QW SESAM/SBR design.

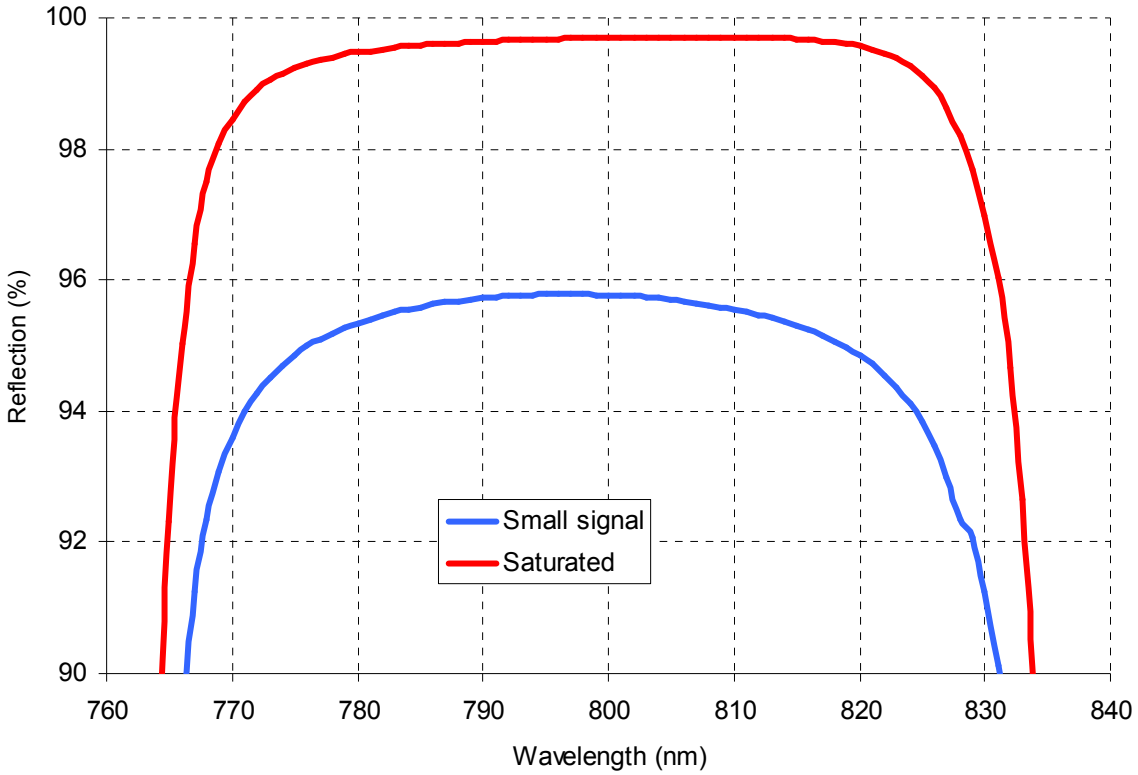

Figure E35: Calculated reflectivity for MIT-800-QW SESAM/SBR design (zoomed in).

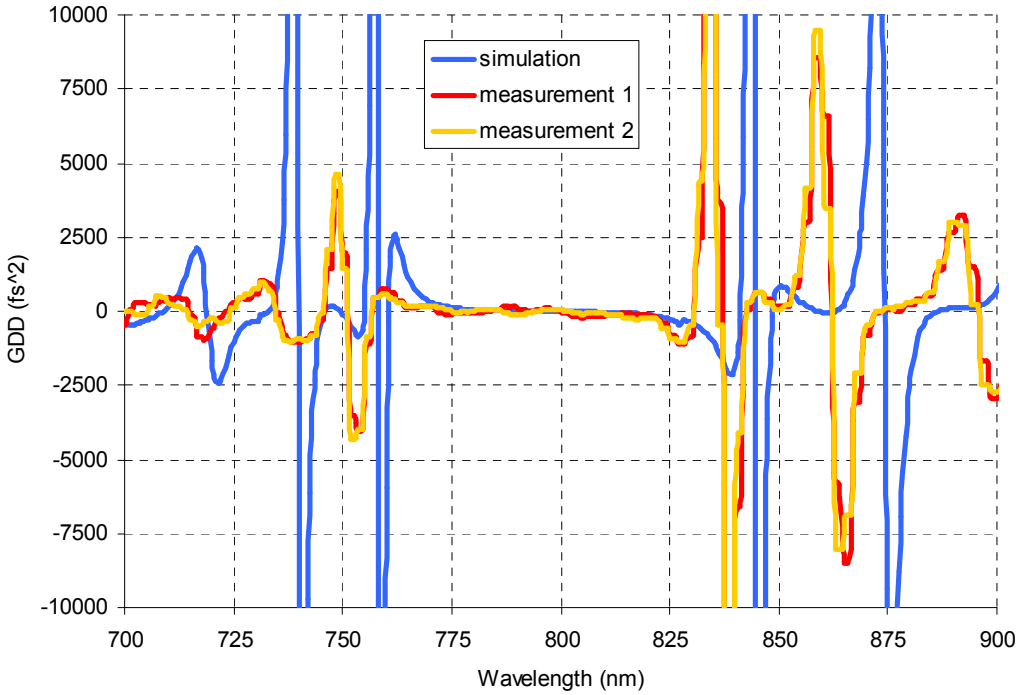

Figure E36: Calculated and measured GDD for MIT-800-QW SESAM/SBR design.

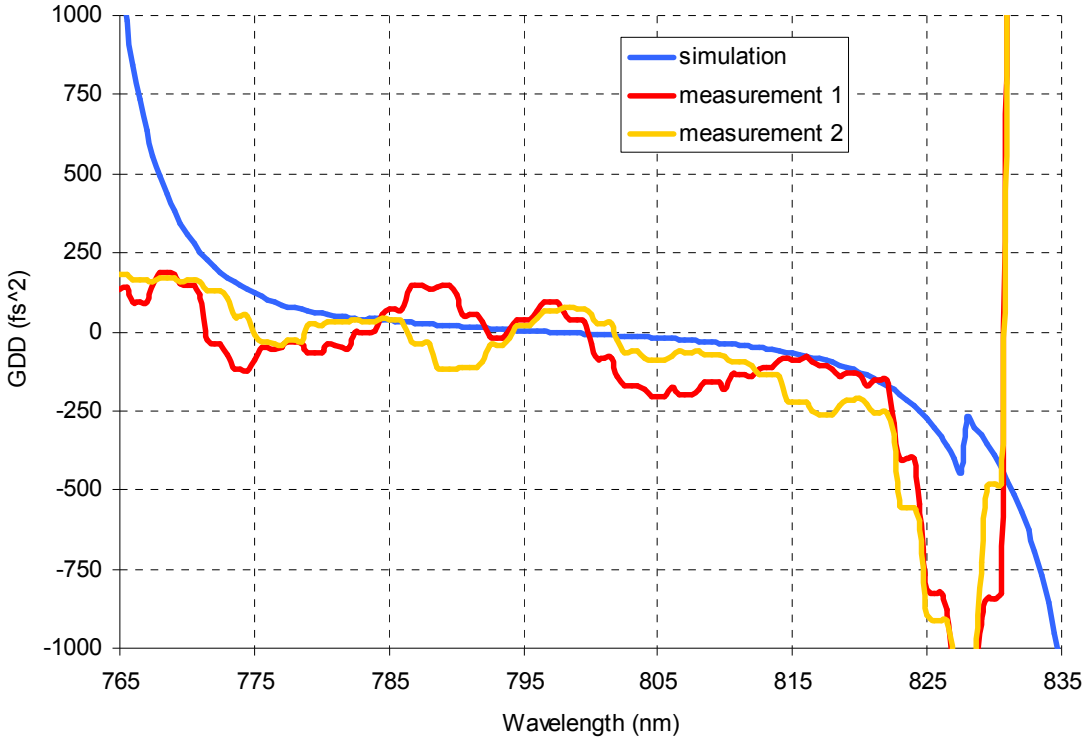

Figure E37: Calculated and measured GDD for MIT-800-QW SESAM/SBR design (zoomed in).

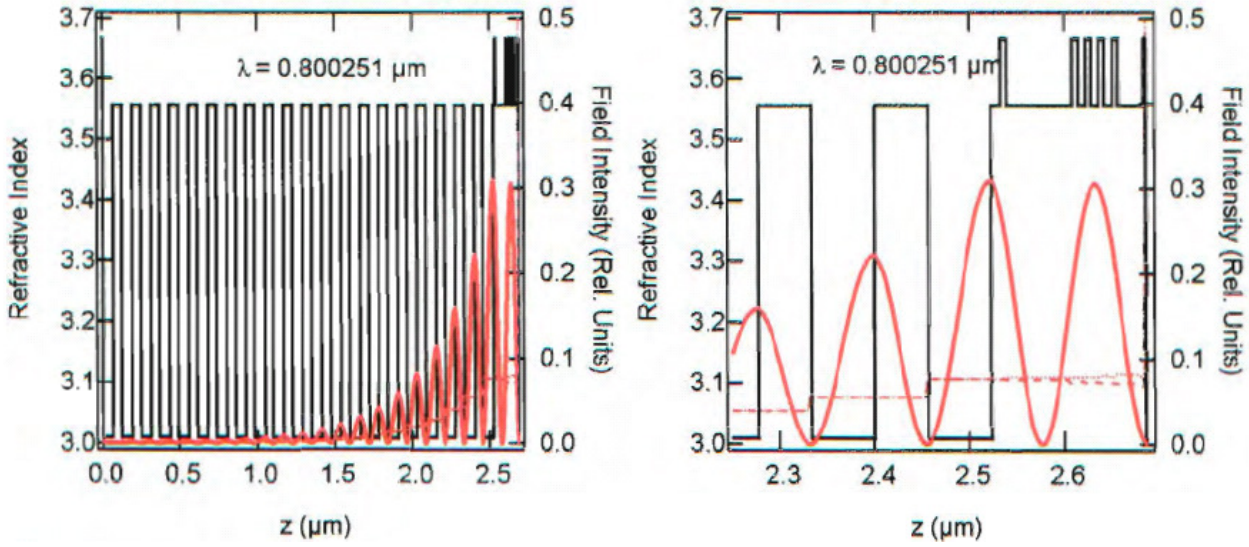

Figure E38: Electric field pattern for MIT-800-QW SESAM/SBR design. This information is kindly provided by Prof. Franz Kärtner.

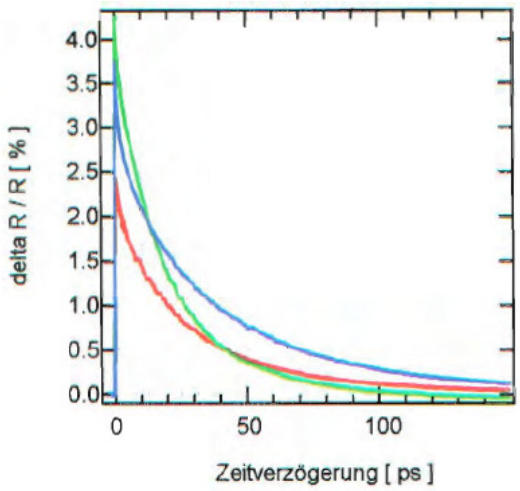

Abbildung 10: *Anregung 0.3 $\frac{mJ}{cm^2}$ 'grün': 780 nm / 'rot': 800 nm / 'blau': 820 nm (Messung 14/12/00)*

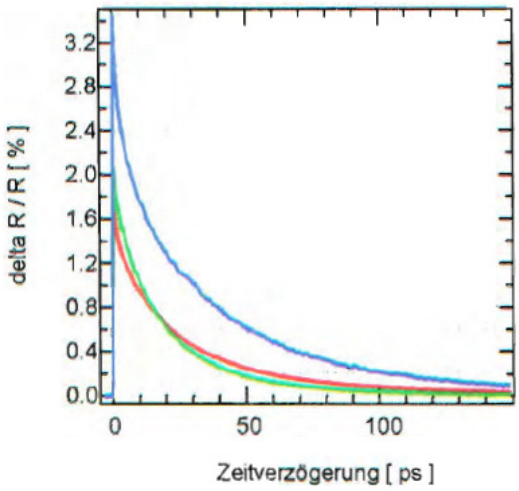

Abbildung 11: *Anregung 0.07 $\frac{mJ}{cm^2}$ 'grün': 780 nm / 'rot': 800 nm / 'blau': 820 nm (Messung 14/12/00)*

Figure E39: Measured lifetime of the absorber in MIT-800-QW SESAM/SBR. This information is kindly provided by Prof. Franz Kärtner.

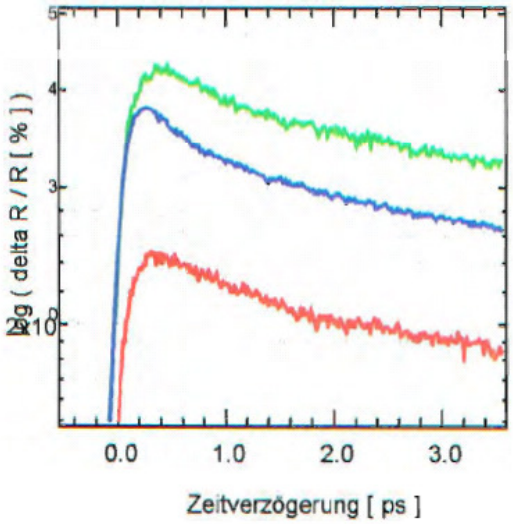

Abbildung 12: *Ausschnitt um Zeit-verzögerungsnullpunkt Anregung 0.3 $\frac{mJ}{cm^2}$ 'grün': 780 nm / 'rot': 800 nm / 'blau': 820 nm (Messung 14/12/00)*

Figure E40: Measured lifetime of the absorber in MIT-800-QW SESAM/SBR. This information is kindly provided by Prof. Franz Kärtner.

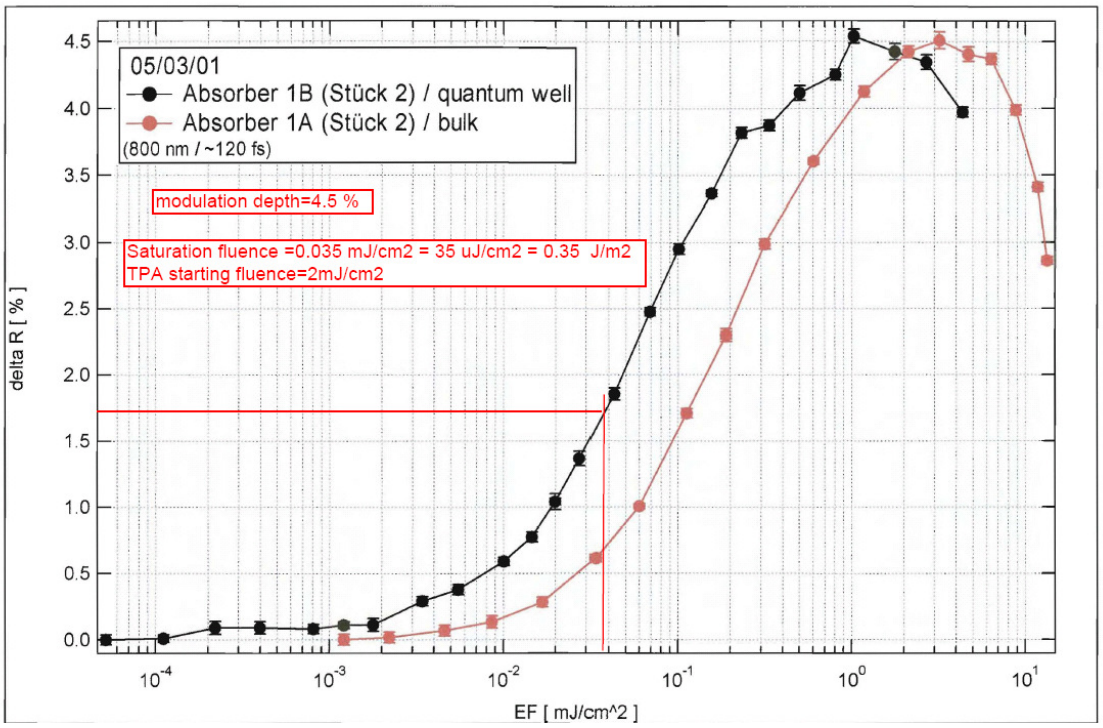

Figure E41: Measured variation of reflection with incident pulse energy fluence for MIT-800-QW SESAM/SBR. This information is kindly provided by Prof. Franz Kärtner.

Structure

	Structure	Desired		Reflectivity Fit Wafer 23		Coupled Composite Xray Fit Wafer 23	
		Thickness	Al content	Thickness	Al content	Thickness	Al Content
	GaAs	5		5.076		5.0639	
	AlGaAs	27	0.17	27.233	0.164	27.999	0.157
	GaAs	6		6.094		4.800	
	AlGaAs	8	0.17	8.052	0.164	8.942	0.157
X 3	GaAs	6		6.094		4.805	
	AlGaAs	70	0.17	70.418	0.164	69.871	0.157
	GaAs	6		6.094		4.801	
	AlGaAs	10	0.17	10.065	0.164	10.988	0.157
	AlAs	66.5		63.13		65.728	
X 25	AlGaAs	56.2	0.17	58.02	0.164	56.419	0.157
	AlAs	66.5		63.13		62.807	
	GaAs Substrate					5.0639	

HR-XRD

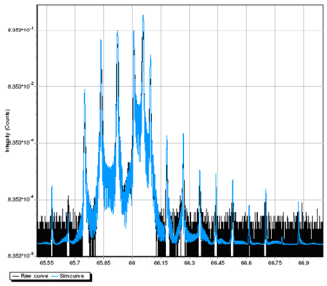

Reflectivity

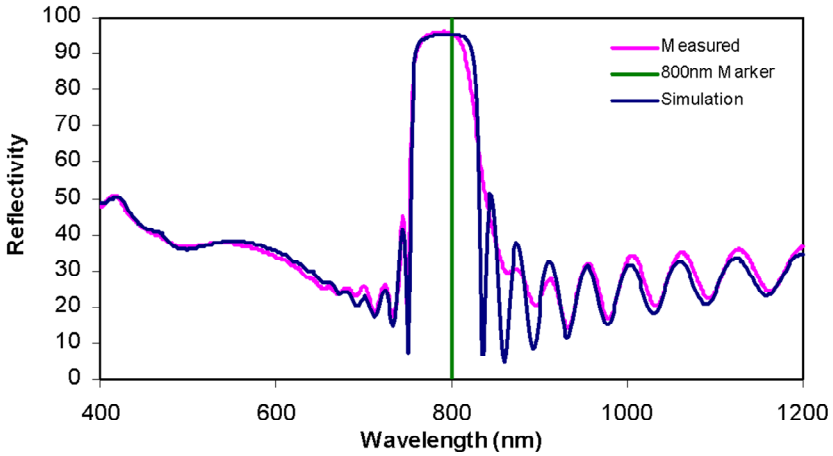

Figure E42: Summary of the desired structure and measured results for MIT-800-QW SESAM/SBR. Note: All the thicknesses are in nm's. This information is kindly provided by Dr. Gale Petrich.

E.6 One Pair HR Layer Coated MIT 800 nm SESAM/SBR with quantum-well absorber (MIT-800-QW-HR)

Layer	Material	Physical thickness (nm)	Optical thickness (nm)	n	Purpose
0	GaAs	-	-	-	Substrate
1	AlAs	66.55	200	3.01	Bragg layer
2	$Al_{0.17}Ga_{0.83}As$	57.15	200	3.50	Bragg layer
…					Bragg layers
49	AlAs	66.55	200	3.01	Bragg layer
50	$Al_{0.17}Ga_{0.83}As$	57.15	200	3.50	Bragg layer
51	AlAs	66.55	200	3.01	Bragg layer
52	$Al_{0.17}Ga_{0.83}As$	10	35	3.50	Barrier
53	GaAs	6	22.11	3.68	Absorber
54	$Al_{0.17}Ga_{0.83}As$	70	244.97	3.50	Barrier
55	GaAs	6	22.11	3.68	Absorber
56	$Al_{0.17}Ga_{0.83}As$	8	28	3.50	Barrier
57	GaAs	6	22.11	3.68	Absorber
58	$Al_{0.17}Ga_{0.83}As$	8	28	3.50	Barrier
59	GaAs	6	22.11	3.68	Absorber
60	$Al_{0.17}Ga_{0.83}As$	8	28	3.50	Barrier
61	GaAs	6	22.11	3.68	Absorber
62	$Al_{0.17}Ga_{0.83}As$	27	94.49	3.50	Barrier
63	GaAs	5	18.42	3.68	Cap
64	SiO_2	138.89	200	1.44	HR coating
65	TiO_2	83.79	200	2.39	HR coating

Table E9: One pair HR layer coated MIT 800 nm regular SESAM/SBR design with quantum well absorber (MIT-800-QW-HR).

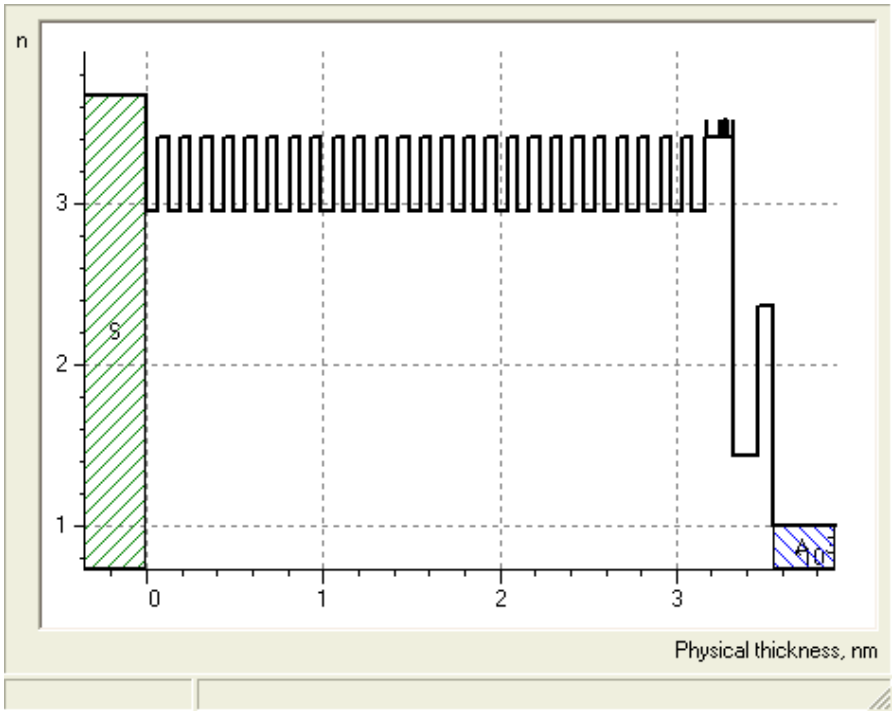

Figure E43: Index profile for MIT-800-QW-HR SESAM/SBR design.

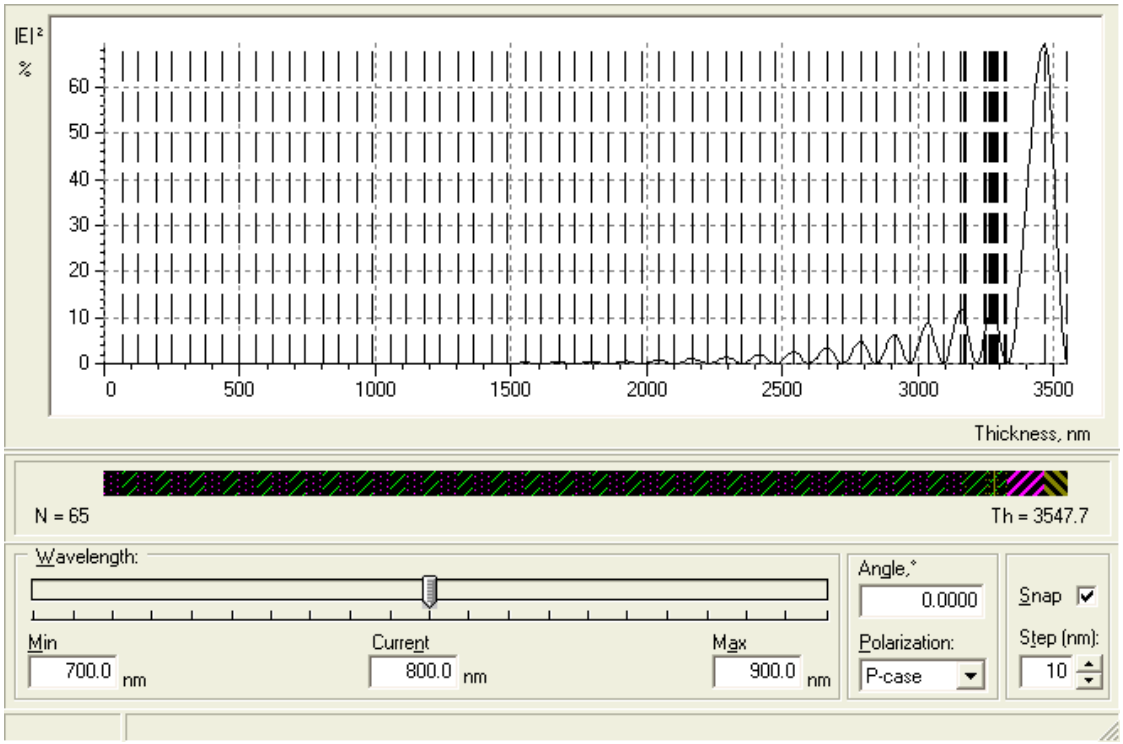

Figure E44: Electric field pattern for MIT-800-QW-HR SESAM/SBR design.

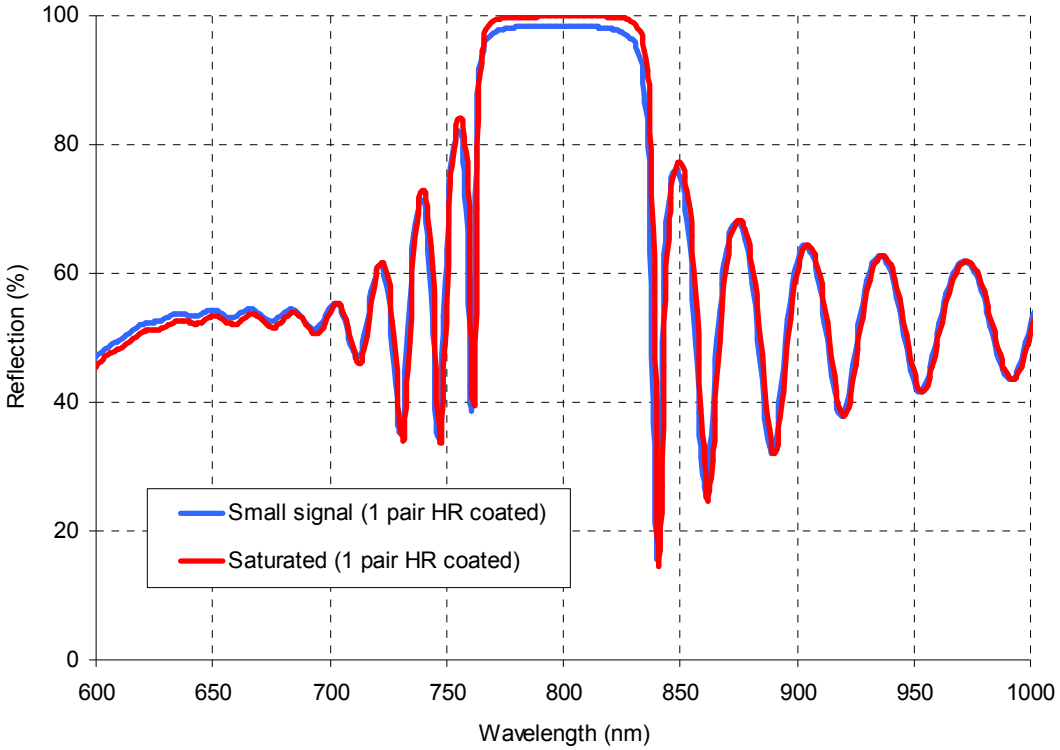

Figure E45: Calculated reflectivity for MIT-800-QW-HR SESAM/SBR design.

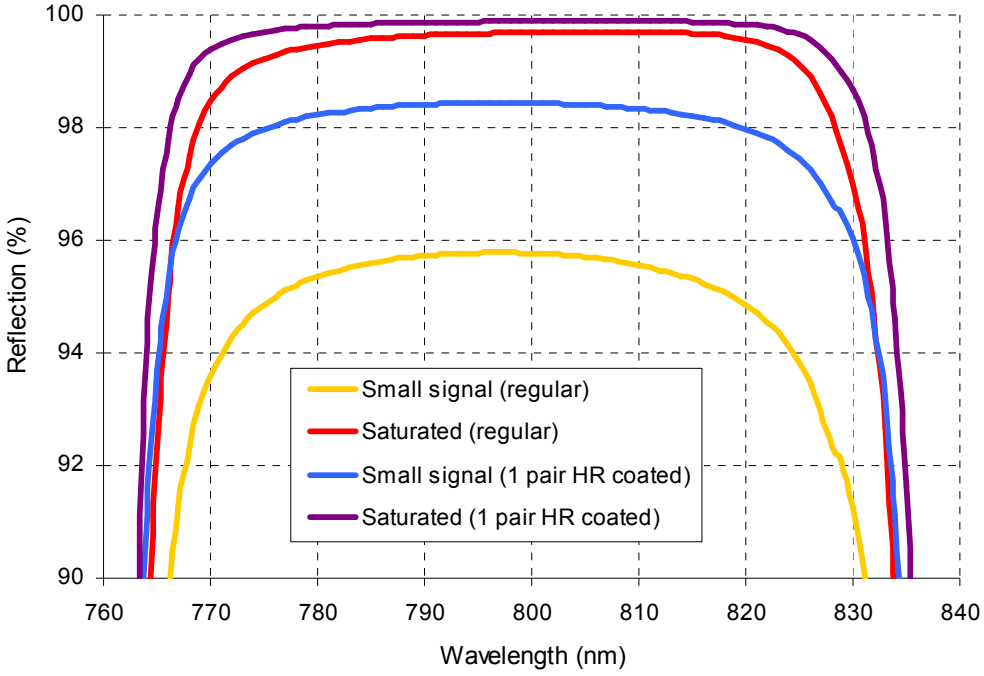

Figure E46: Calculated reflectivity for MIT-800-QW-HR SESAM/SBR design (zoomed in). Reflectivity of MIT-800-QW SESAM/SBR is also shown.

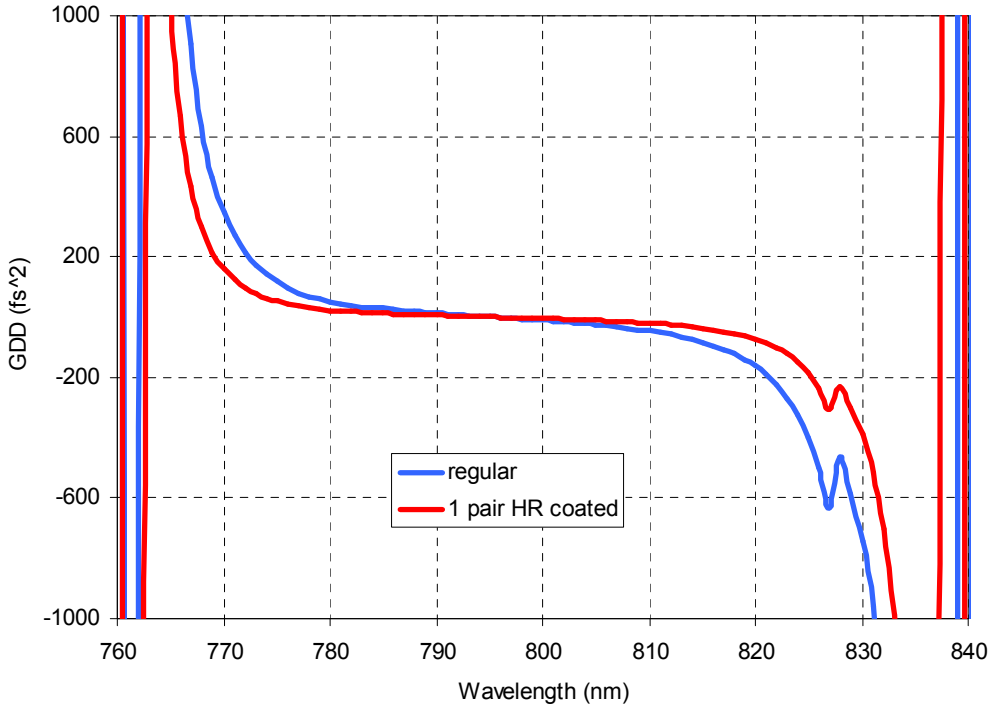

Figure E47: Calculated GVD for MIT-800-QW-HR SESAM/SBR design (zoomed in). GVD of MIT-800-QW SESAM/SBR is also shown.

E.7 Two Pairs HR Layer Coated MIT 800 nm SESAM/SBR with quantum-well absorber (MIT-800-QW-2HR)

Layer	Material	Physical thickness (nm)	Optical thickness (nm)	n	Purpose
0	GaAs	-	-	-	Substrate
1	AlAs	66.55	200	3.01	Bragg layer
2	$Al_{0.17}Ga_{0.83}As$	57.15	200	3.50	Bragg layer
…					Bragg layers
49	AlAs	66.55	200	3.01	Bragg layer
50	$Al_{0.17}Ga_{0.83}As$	57.15	200	3.50	Bragg layer
51	AlAs	66.55	200	3.01	Bragg layer
52	$Al_{0.17}Ga_{0.83}As$	10	35	3.50	Barrier
53	GaAs	6	22.11	3.68	Absorber
54	$Al_{0.17}Ga_{0.83}As$	70	244.97	3.50	Barrier
55	GaAs	6	22.11	3.68	Absorber
56	$Al_{0.17}Ga_{0.83}As$	8	28	3.50	Barrier
57	GaAs	6	22.11	3.68	Absorber
58	$Al_{0.17}Ga_{0.83}As$	8	28	3.50	Barrier
59	GaAs	6	22.11	3.68	Absorber
60	$Al_{0.17}Ga_{0.83}As$	8	28	3.50	Barrier
61	GaAs	6	22.11	3.68	Absorber
62	$Al_{0.17}Ga_{0.83}As$	27	94.49	3.50	Barrier
63	GaAs	5	18.42	3.68	Cap
64	SiO_2	138.89	200	1.44	HR coating
65	TiO_2	83.79	200	2.39	HR coating
66	SiO_2	138.89	200	1.44	HR coating
67	TiO_2	83.79	200	2.39	HR coating

Table E10: Two pairs of HR layer coated MIT 800 nm regular SESAM/SBR design with quantum well absorber (MIT-800-QW-2HR).

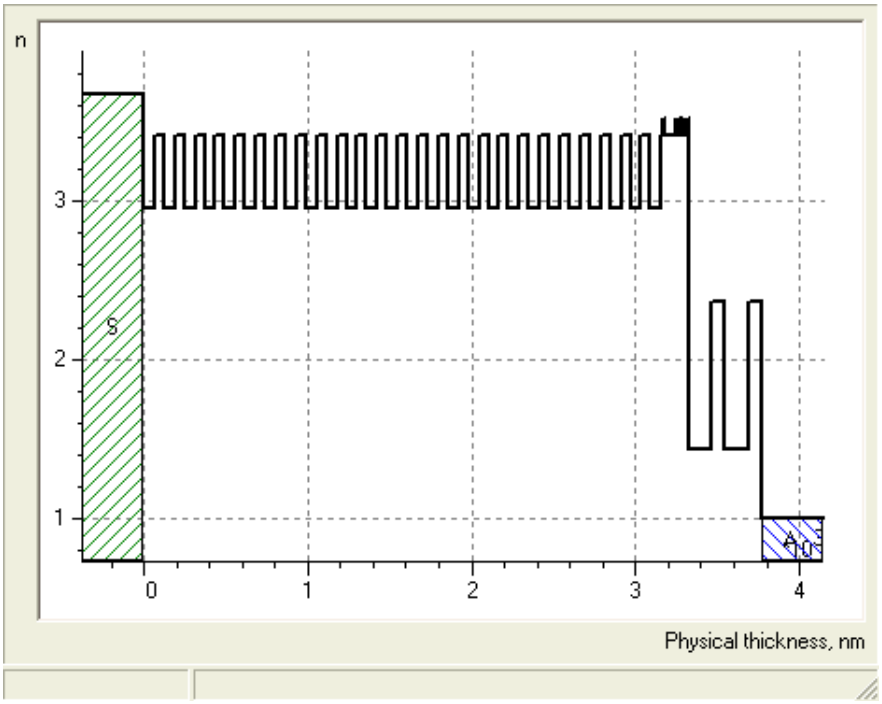

Figure E48: Index profile for MIT-800-QW-2HR SESAM/SBR design.

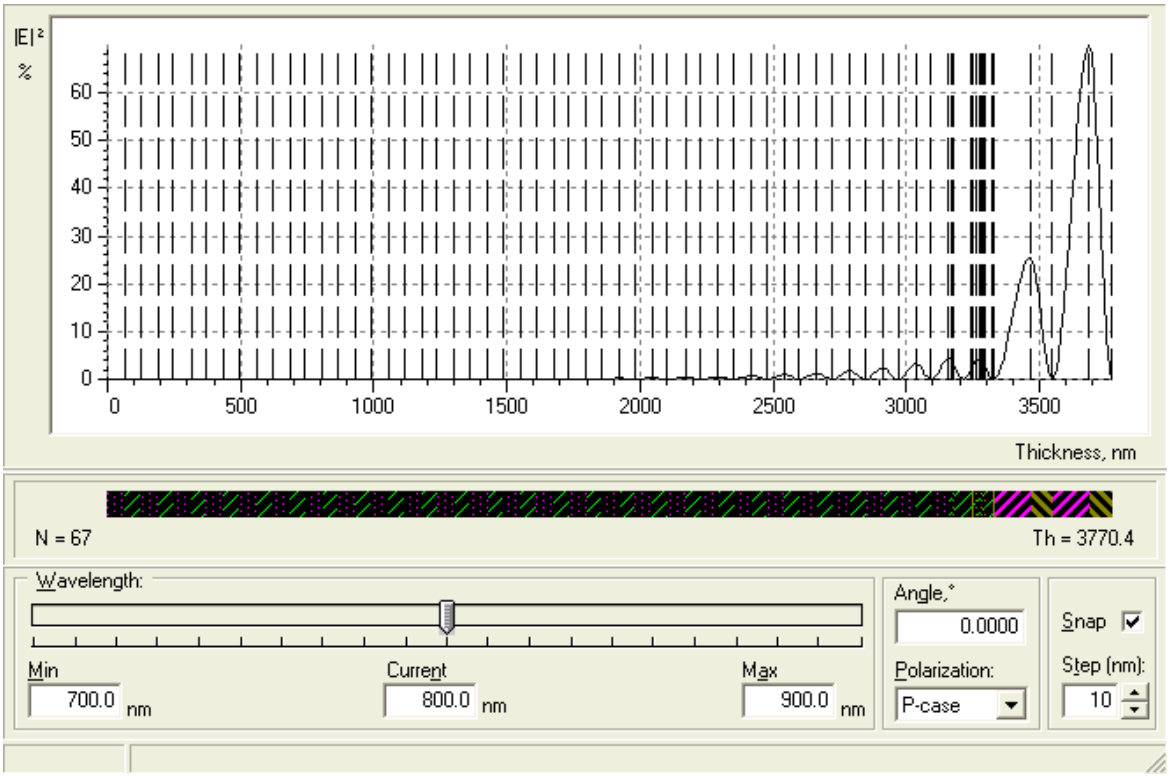

Figure E49: Electric field pattern for MIT-800-QW-2HR SESAM/SBR design.

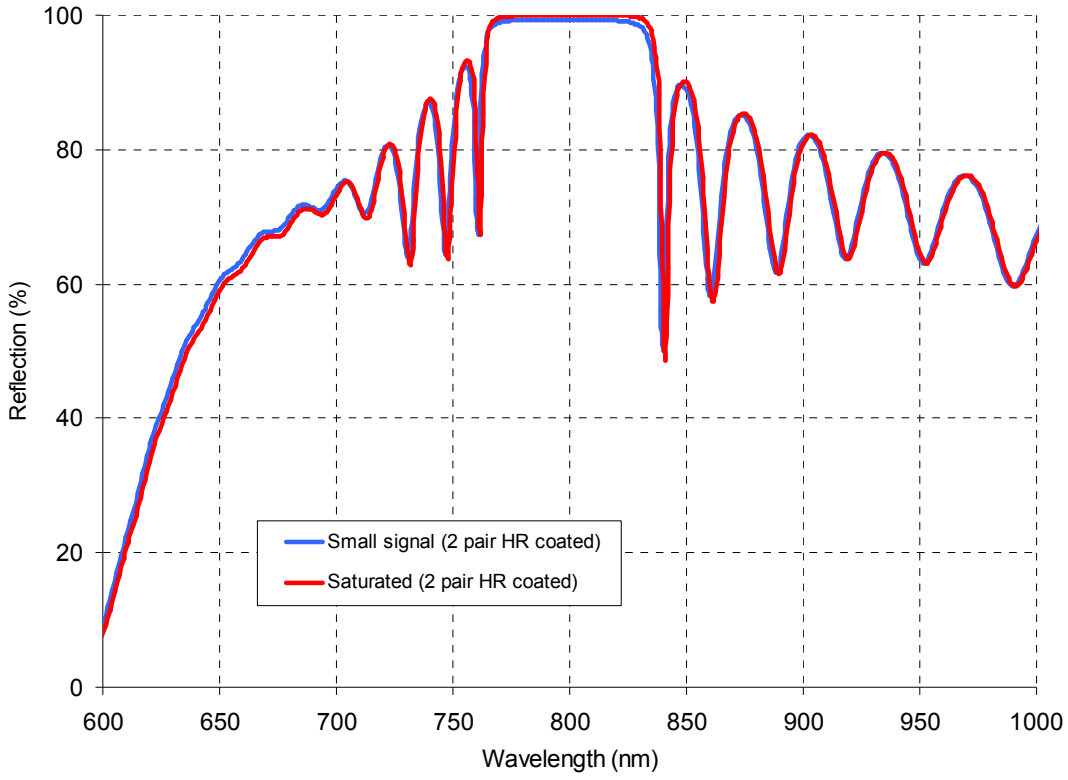

Figure E50: Calculated reflectivity for MIT-800-QW-2HR SESAM/SBR design.

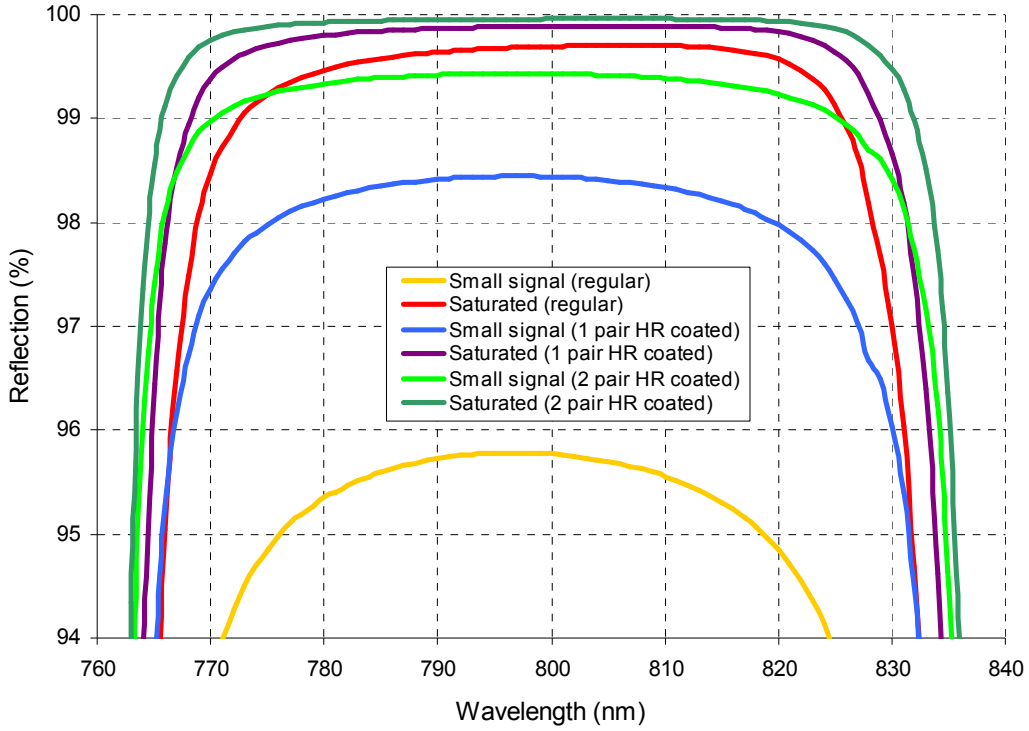

Figure E51: Calculated reflectivity for MIT-800-QW-2HR SESAM/SBR design (zoomed in). Reflectivity curves for MIT-800-QW-HR and MIT-800-QW are also shown.

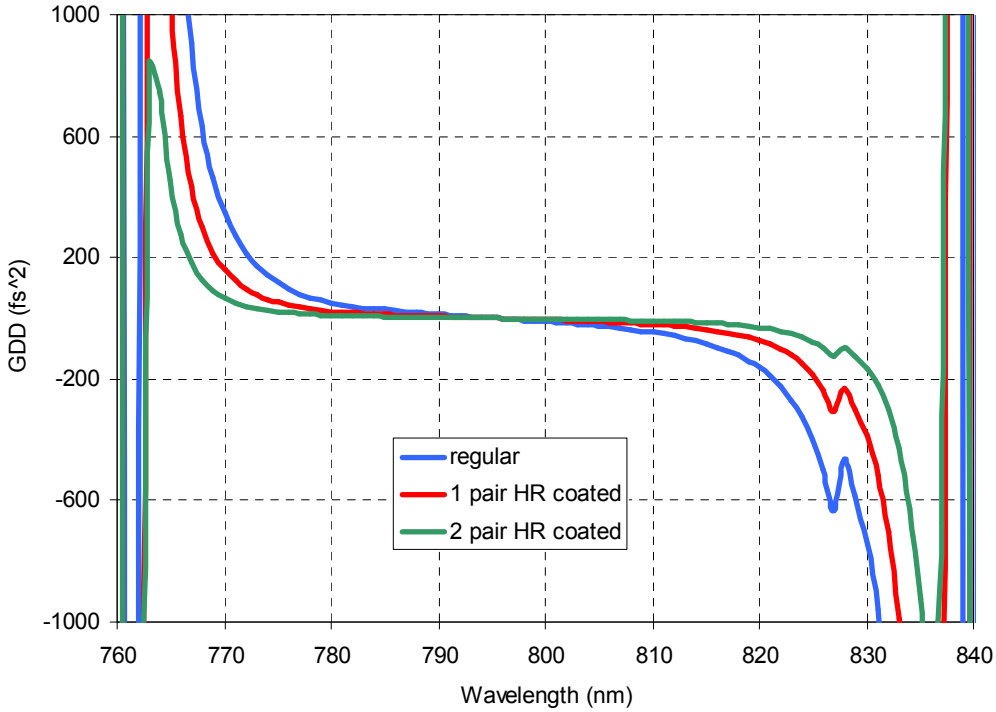

Figure E52: Calculated GDD for MIT-800-QW-2HR SESAM/SBR design (2 pair HR coated). GDD curves for MIT-800-QW-HR and MIT-800-QW are also shown.

E.8 MIT 910 nm SESAM/SBR with bulk absorber (MIT-910-bulk)

Layer	Material	Physical thickness (nm)	Optical thickness (nm)	n	Purpose
0	GaAs	-	-	-	Substrate
1	$Al_{0.95}Ga_{0.05}As$	75.87	227.5	3.00	Bragg layer
2	$Al_{0.05}Ga_{0.95}As$	64.1	227.5	3.55	Bragg layer
…	…	…	…	…	Bragg layers
49	$Al_{0.95}Ga_{0.05}As$	75.87	227.5	3.00	Bragg layer
50	$Al_{0.05}Ga_{0.95}As$	64.1	227.5	3.55	Bragg layer
51	$Al_{0.95}Ga_{0.05}As$	75.87	227.5	3.00	Bragg layer
52	$Al_{0.05}Ga_{0.95}As$	10	35.49	3.55	Barrier
53	$In_{0.1}Ga_{0.9}As$	15	55.99	3.73	Absorber
54	$Al_{0.05}Ga_{0.95}As$	40	141.97	3.55	Barrier
55	GaAs	5	17.89	3.58	Cap

Table E11: MIT 910 nm regular SESAM/SBR design with bulk absorber (MIT-910-bulk).

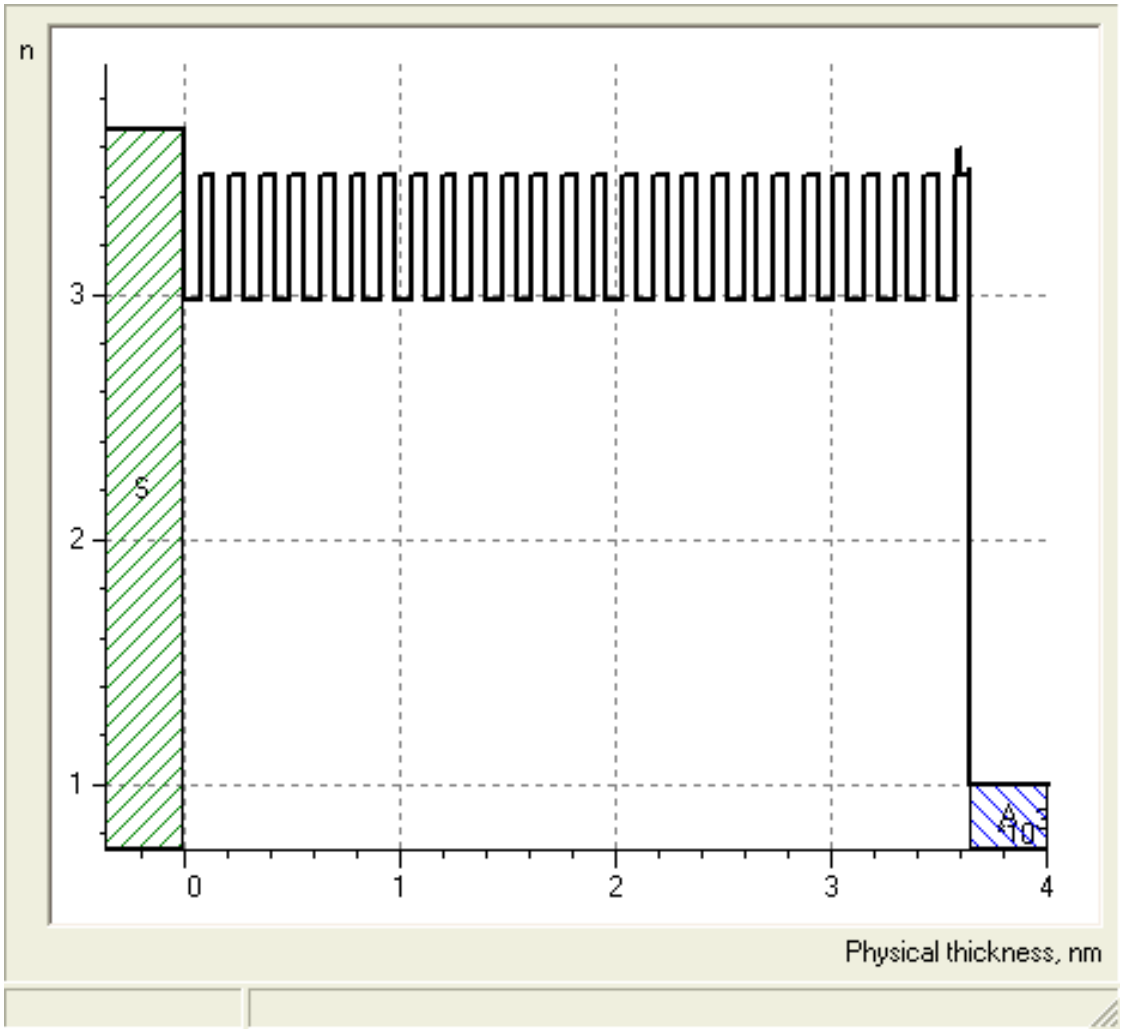

Figure E53: Index profile for MIT-910-bulk SESAM/SBR design.

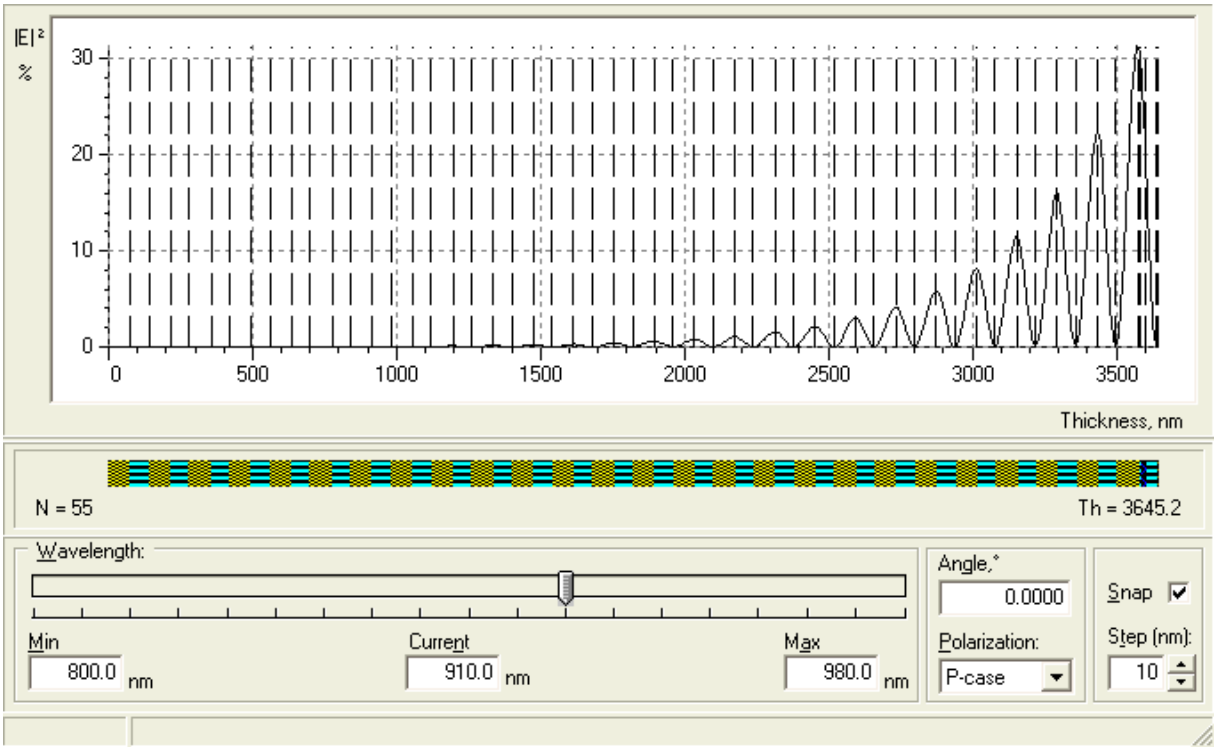

Figure E54: Electric field pattern for MIT-910-bulk SESAM/SBR design.

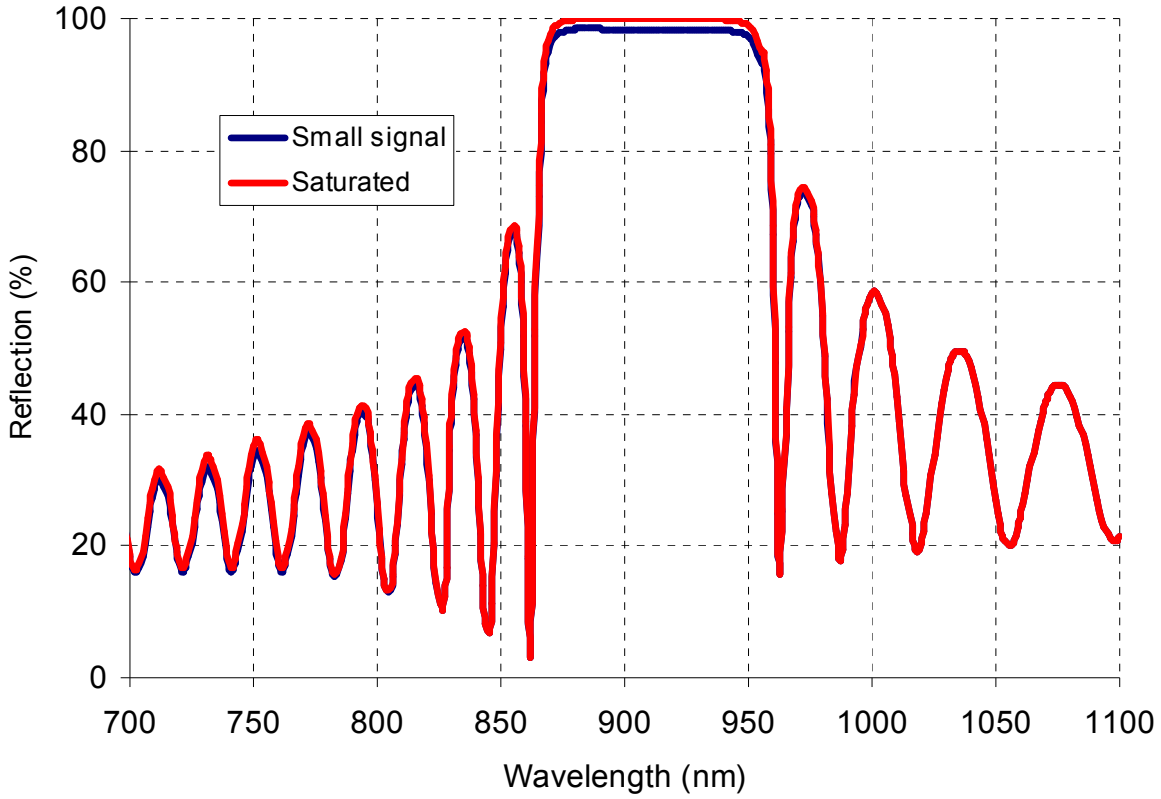

Figure E55: Calculated reflectivity for MIT-910-bulk SESAM/SBR design.

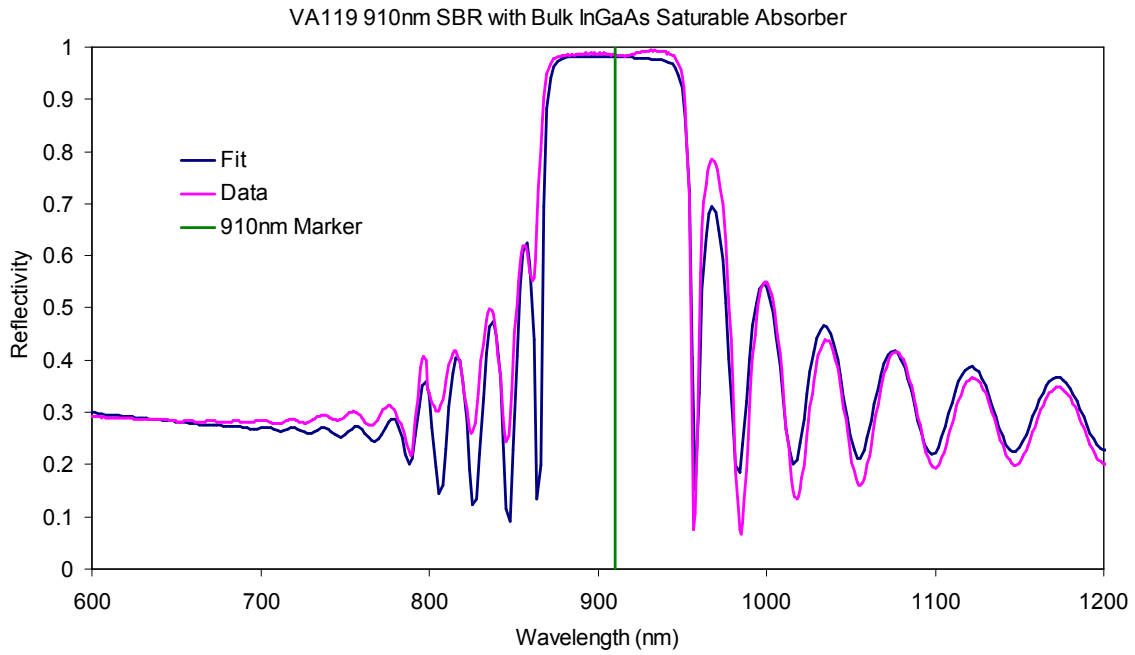

Figure E56: Measured reflectivity for MIT-910-bulk SESAM/SBR design. Note: In fitting the measured reflectivity, the indices of refraction for the GaAs and the AlGaAs layers were determined from the material tables that were provided with the J.A. Woollam ellipsometer. The indices of refraction for InGaAs were from a material table that was calculated using a parameterized InGaAs mode from J.A. Woollam Inc. Also, the growth rates from individual column III were assumed to be constant (Fig. 59). Hence, all the layers were coupled in terms of composition thickness. This information is kindly provided by Dr. Gale Petrich.

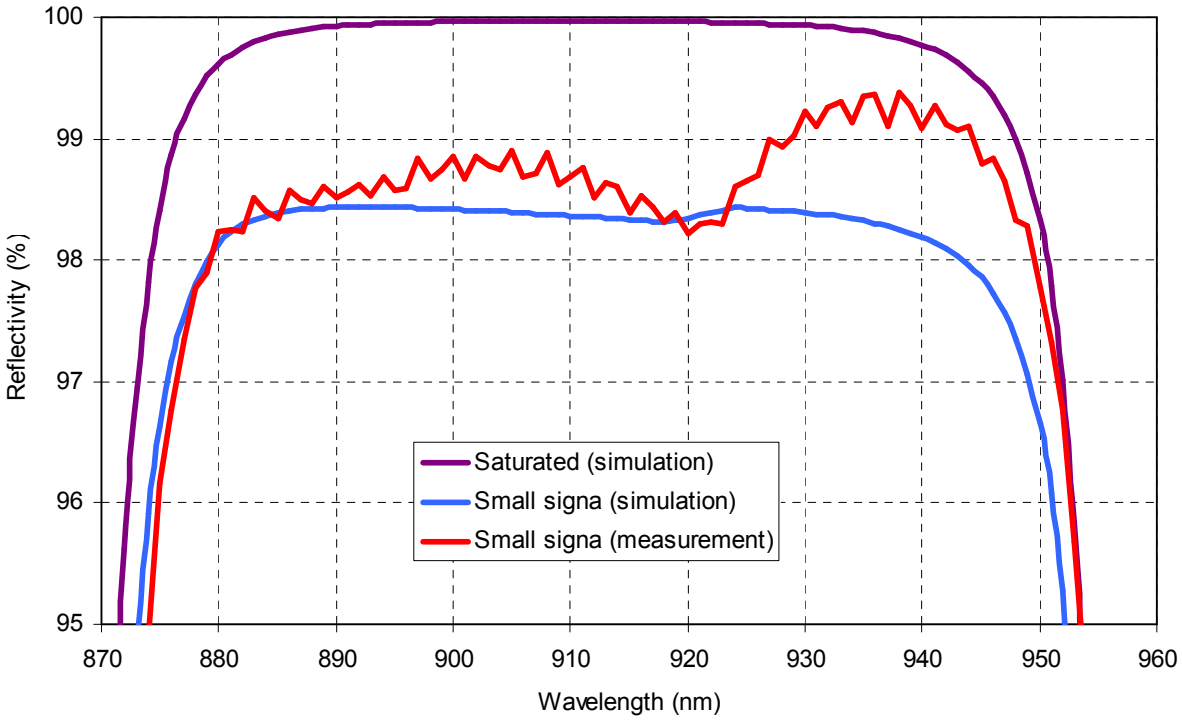

Figure E57: Calculated and measured reflectivity for MIT-910-bulk SESAM/SBR design (zoomed in). Reflectivity measurement is kindly provided by Dr. Gale Petrich.

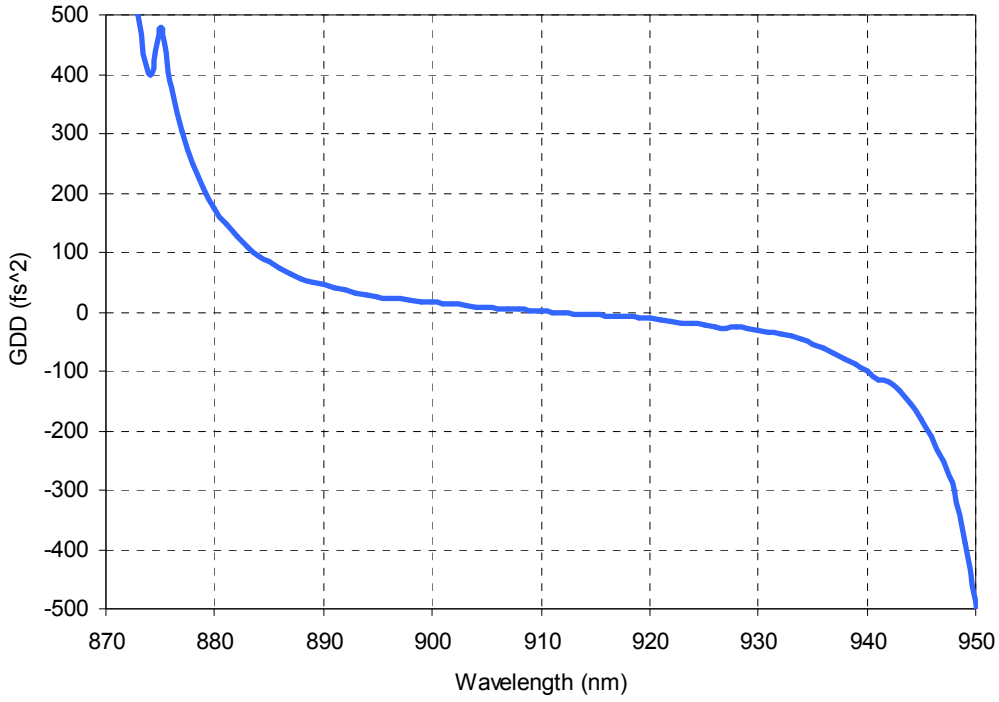

Figure E58: Calculated GDD for MIT-910-bulk SESAM/SBR design (zoomed in).

VA119: 910nm SBR with Bulk InGaAs Saturable Absorber

Sample VA119, a saturable Bragg reflector that is designed to be centered at 910nm with a bulk InGaAs saturable absorber was grown using molecular beam epitaxy. The sample was characterized using the Bruker D8 x-ray diffraction systems within CMSE, the Varian Cary 5i spectrophotometer system within CMSE and the J.A. Woollam M-88 variable angle spectroscopic ellipsometry system. The results are summarized in the following table.

Summary of the Desired Structure and Measured Results

	Structure	Desired		Reflectivity Fit		Composite Xray Fit Coupled		Composite Xray Fit Uncoupled		WVASE Fit: Coupled		WVASE Fit: Uncoupled	
		Thickness	Al or In content	Thickness	Al or In content	Thickness	Al or In Content	Thickness	Al or In Content	Thickness	Al or In Content	Thickness	Al or In Content
	AlGaAs	45.9	0.10	47.686	0.101	45.535	0.0916	45.987	0.110	44.068	0.0677± 0.00807	42.961 ±0.776	0.0891± 0.00562
	InGaAs	15	0.10	14.969	0.103	7.8069	0.123	6.114	0.156	8.609 ±0.143	0.0971± 0.0121	8.9334 ±3.2	0.145 ±0.0258
	AlGaAs	10.2	0.10	10.164	0.101	10.112	0.0916	11.461	0.074	9.903	0.0677± 0.00807	9.5508 ±2.89	0.0265± 0.0237
X 25	AlGaAs	75.87	0.95	75.650	0.948	77.022	0.937	77.353	0.936	79.235 ±0.717	1±0.02	80.151 ±0.697	1± 0.0215
	AlGaAs	65.4	0.10	65.233	0.101	64.953	0.0916	64.586	0.088	63.48 ±0.0977	0.0677± 0.00807	62.27 ±0.429	0.00131 ±0.0272
	AlGaAs	75.87	0.95	75.650	0.948	77.022	0.937	77.353	0.936	79.235 ±0.717	1±0.02	74.094 ±24.8	1±0.391
	GaAs Substrate												

Figure E59: Summary of the desired structure and measured results for MIT-910-bulk SESAM/SBR. Note: All the thicknesses are in nm's. This information is kindly provided by Dr. Gale Petrich.

Final Coupled Fit Results

N	R	Material	Cell input	Thickness	Roughness	Conc X Top, %
1	1	Al(x)Ga(1-x)As	Cx(Cy) + R	45.5350	0.3239	9.1616
2	1	Ga(1-x)In(x)As	Cx(Cy) + R	7.8069	2.4778	12.2730
3	1	Al(x)Ga(1-x)As	Cx(Cy) + R	10.1117	0.7508	9.1616
4	25	Al(x)Ga(1-x)As	Cx(Cy) + R	77.0226	1.3847	93.7340
5	25	Al(x)Ga(1-x)As	Cx(Cy) + R	64.9526	3.8704	9.1292
6	1	Al(x)Ga(1-x)As	Cx(Cy) + R	76.9914	0.0257	93.7340
SUB	1	GaAs	density	0.0000	0.0000	0.0000

(400) Rocking Curve
Using the Bruker high resolution system with the analyzer crystal

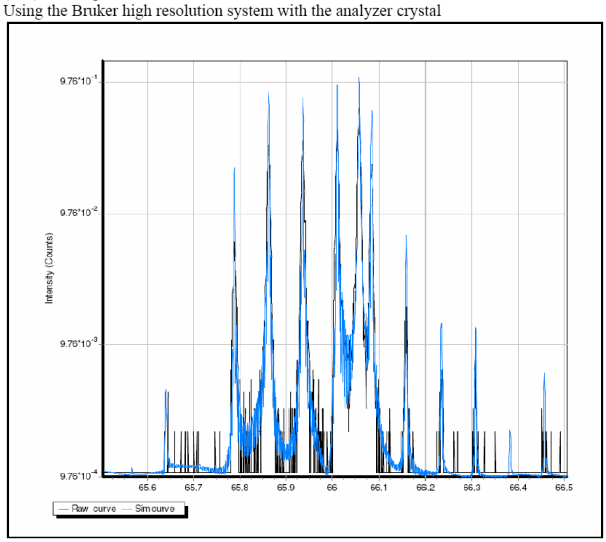

(000) Rocking Curve
Using the Bruker D8 high resolution system

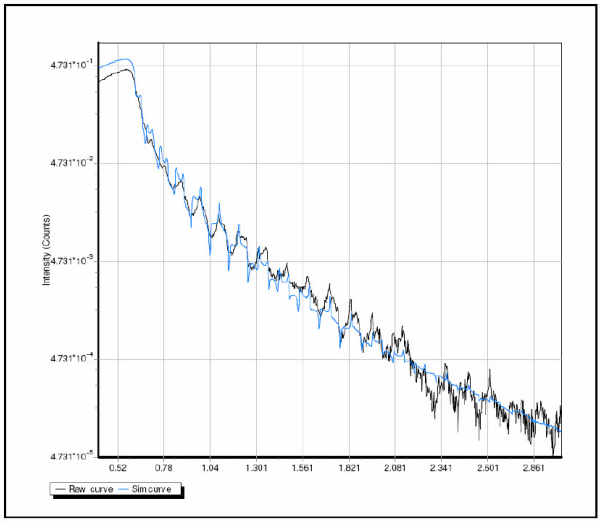

Figure E60: MIT-910-bulk SESAM/SBR x-ray diffraction data Note: The high resolution Bruker D8 X-ray system was used to measure the (400) and (000) rocking curves. However, all of the rocking curves were fit to a common model using the Leptos simulation package from Bruker. This information is kindly provided by Dr. Gale Petrich.

Final Uncoupled Fit Results

N	R	Material	Cell input	Thickness	Roughness	Conc X Top, %
1	1	Al(x)Ga(1-x)As	Cx(Cy) + R	45.9874	0.3252	10.9900
2	1	Ga(1-x)In(x)As	Cx(Cy) + R	6.1141	3.7395	15.5740
3	1	Al(x)Ga(1-x)As	Cx(Cy) + R	11.4610	2.2426	7.3922
4	25	Al(x)Ga(1-x)As	Cx(Cy) + R	77.3527	1.3769	93.6210
5	25	Al(x)Ga(1-x)As	Cx(Cy) + R	64.5863	3.7251	8.7849
6	1	Al(x)Ga(1-x)As	Cx(Cy) + R	77.3527	0.0001	93.6210
SUB	1	GaAs	density	0.0000	0.0000	0.0000

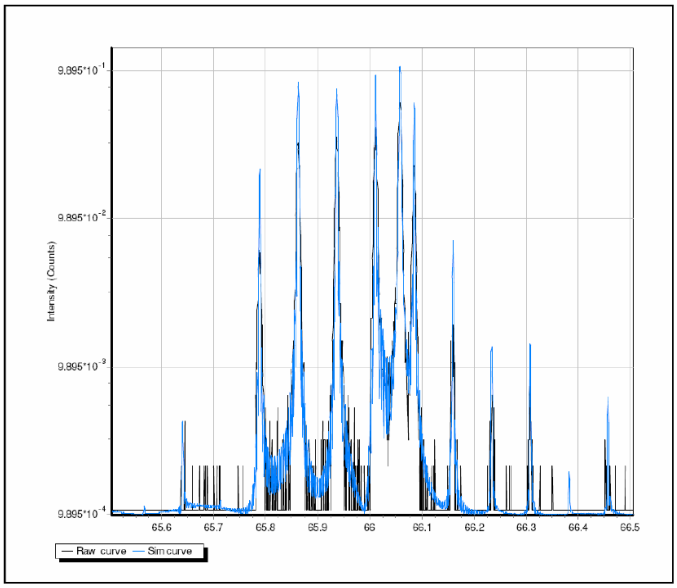

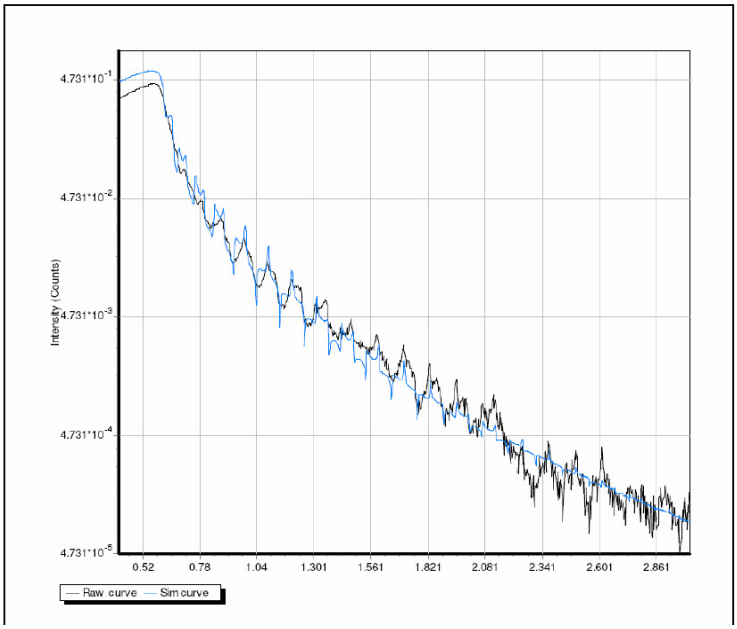

Figure E61: MIT-910-bulk SESAM/SBR x-ray diffraction data This information is kindly provided by Dr. Gale Petrich.

Fit 1) Similar layer's compositions and thicknesses are coupled

7	gaas-ox	1.0135 nm
6	algaas x=0.068	44.068 nm
5	ingaas x=0.097	8.6089 nm
4	algaas x=0.068	9.9029 nm
3	algaas x=1.000	79.235 nm
2	algaas x=0.068	63.48 nm
1	algaas x=1.000	79.235 nm
0	gaas	0.3 mm

25

MSE=5.545

Thick.1	79.235±0.717
Alloy.1	1±0.02
Thick.2	63.48±0.0977
Alloy.2	0.06767±0.00807
Thick.5	8.6089±0.143
Alloy.5	0.097077±0.0121
Thick.7	1.0135±0.0411
Angle0	65.386±0.0592
Angle1	70.423±0.0398
Angle2	75.382±0.0272
Angle3	80.413±0.0154

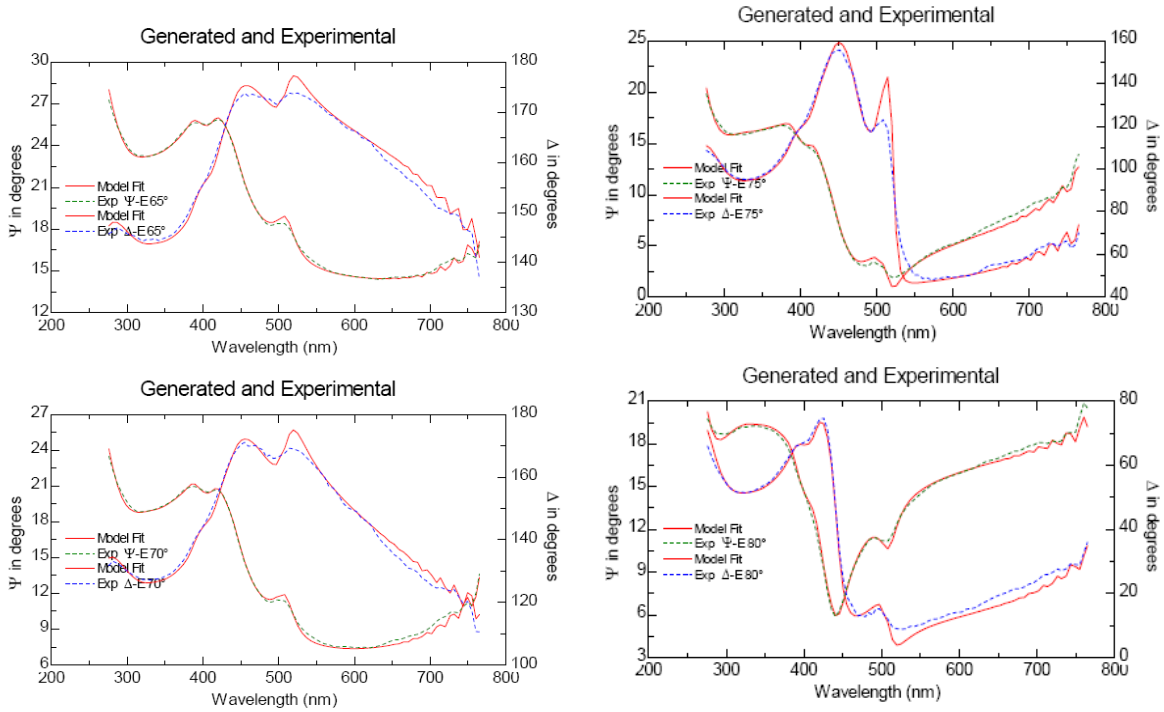

Figure E62: MIT-910-BULK SESAM/SBR WVASE (Woollam Variable Angle Spectroscopic Ellipsometer) graphs. Note: A.J.A Woollam M-88 WVASE system along with the WVASE software package was used to measure and fit the ellipsometric data. Data sets were taken at 65, 70, 75 and 80 degrees. All of the data sets were fit to a common model; however, with the model some of the layers were coupled. There are three fits within this summary. This information is kindly provided by Dr. Gale Petrich.

Fit 2) The Al compositions are coupled.

7	gaas-ox	0.93484 nm
6	algaas x=0.047	42.222 nm
5	ingaas x=0.109	9.7645 nm
4	algaas x=0.047	10.157 nm
3	algaas x=1.000	79.615 nm
2	algaas x=0.047	62.951 nm
1	algaas x=1.000	80.197 nm
0	gaas	0.3 mm

25

MSE=6.156

Thick.1	80.197±5.49
Alloy.1	1±0.00716
Thick.2	62.951±0.229
Alloy.2	0.046997±0.00938
Thick.3	79.615±0.255
Thick.4	10.157±2.9
Thick.5	9.7645±2.98
Alloy.5	0.10865±0.0374
Thick.6	42.222±0.79
Thick.7	0.93484±0.0463
Angle0	65.465±0.0662
Angle1	70.462±0.0446
Angle2	75.406±0.0308
Angle3	80.429±0.0177

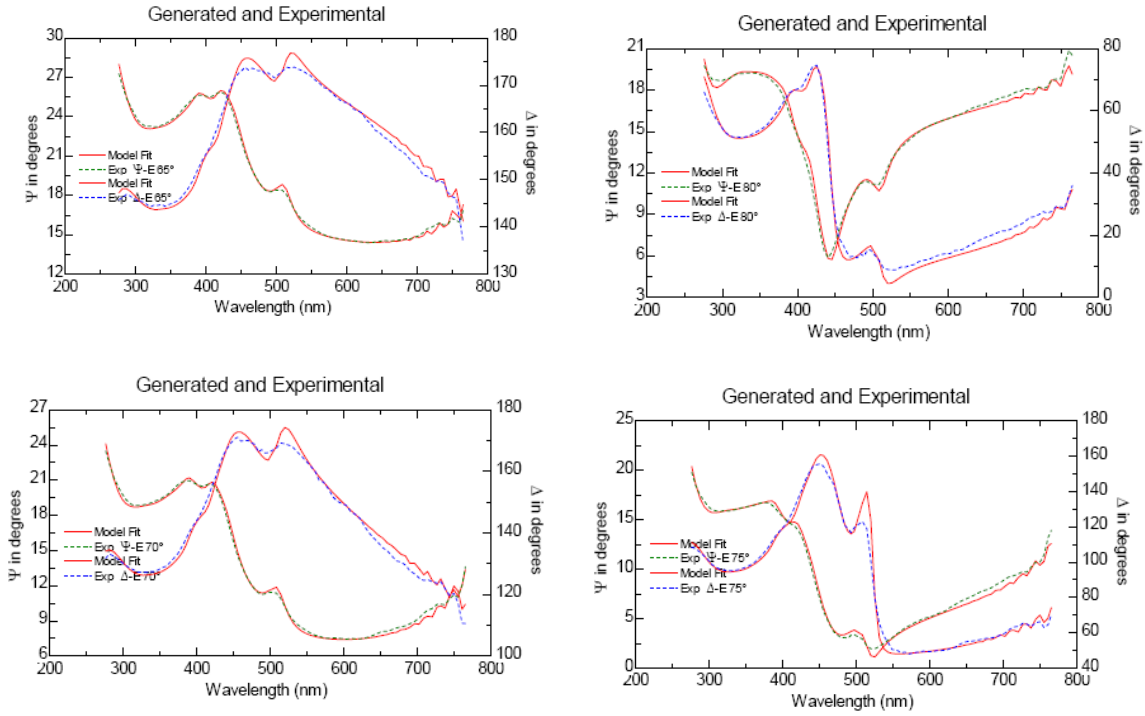

Figure E63: MIT-910-BULK SESAM/SBR WVASE (Woollam Variable Angle Spectroscopic Ellipsometer) graphs. This information is kindly provided by Dr. Gale Petrich.

Fit 3) All layer thicknesses and compositions are uncoupled

7	gaas-ox	1.1403 nm
6	algaas x=0.089	42.961 nm
5	ingaas x=0.145	8.9334 nm
4	algaas x=0.026	9.5508 nm
3	algaas x=1.000	80.151 nm
2	algaas x=0.001	62.27 nm
1	algaas x=1.000	74.094 nm
0	gaas	0.3 mm

25

MSE=4.853

Thick.1	74.094±24.8
Alloy.1	1±0.391
Thick.2	62.27±0.429
Alloy.2	0.0013137±0.0272
Thick.3	80.151±0.697
Alloy.3	1±0.0215
Thick.4	9.5508±2.89
Alloy.4	0.026459±0.0237
Thick.5	8.9334±3.2
Alloy.5	0.14487±0.0258
Thick.6	42.961±0.776
Alloy.6	0.089069±0.00562
Thick.7	1.1403±0.0574
Angle0	65.256±0.0446
Angle1	70.314±0.0409
Angle2	75.326±0.0288
Angle3	80.345±0.0185

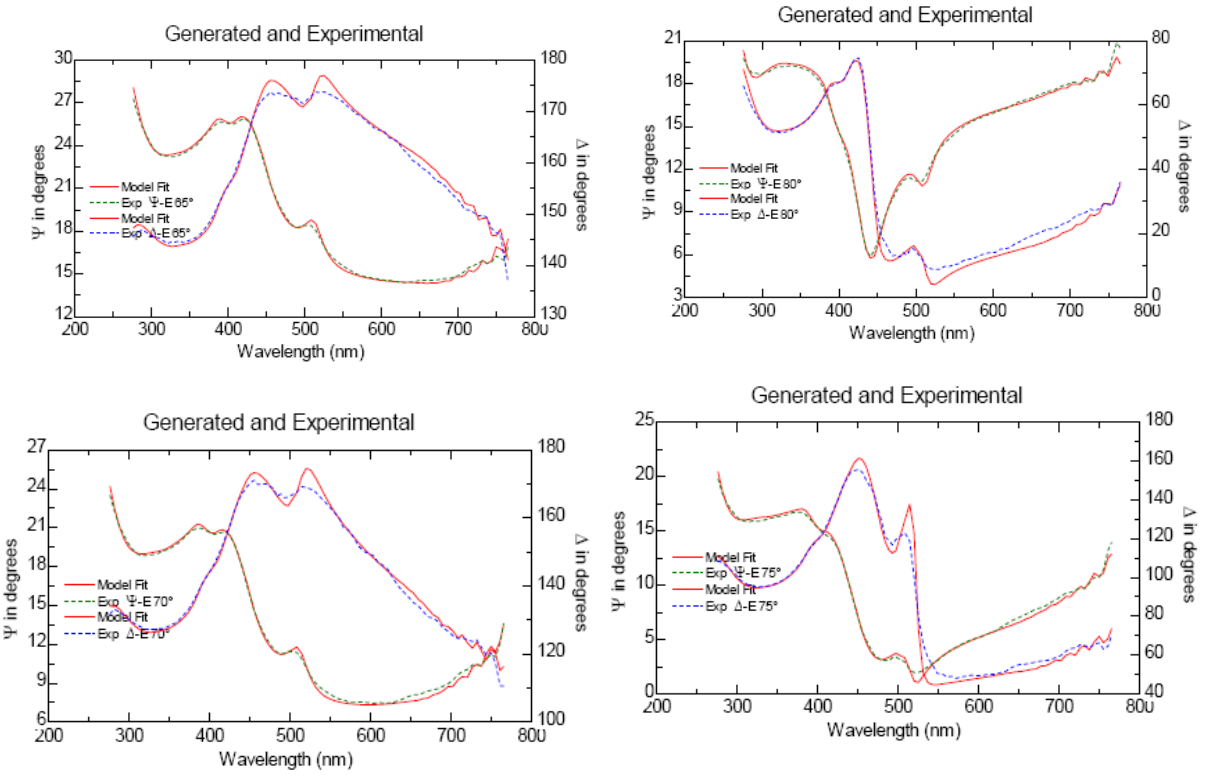

Figure E64: MIT-910-BULK SESAM/SBR WVASE (Woollam Variable Angle Spectroscopic Ellipsometer) graphs. This information is kindly provided by Dr. Gale Petrich.

E.9 MIT 910 nm SESAM/SBR with quantum well absorber (MIT-910-QW)

Layer	Material	Physical thickness (nm)	Optical thickness (nm)	n	Purpose
0	GaAs	-	-	-	Substrate
1	$Al_{0.95}Ga_{0.05}As$	75.87	227.5	3.00	Bragg layer
2	$Al_{0.05}Ga_{0.95}As$	64.1	227.5	3.55	Bragg layer
…	…	…	…	…	Bragg layers
49	$Al_{0.95}Ga_{0.05}As$	75.87	227.5	3.00	Bragg layer
50	$Al_{0.05}Ga_{0.95}As$	64.1	227.5	3.55	Bragg layer
51	$Al_{0.95}Ga_{0.05}As$	75.87	227.5	3.00	Bragg layer
52	$Al_{0.05}Ga_{0.95}As$	10	35.49	3.55	Barrier
53	$In_{0.12}Ga_{0.88}As$	6	22.29	3.73	Absorber
54	$Al_{0.05}Ga_{0.95}As$	8	28.39	3.55	Barrier
55	$In_{0.12}Ga_{0.88}As$	6	22.39	3.73	Absorber
56	$Al_{0.05}Ga_{0.95}As$	8	28.39	3.55	Barrier
57	$In_{0.12}Ga_{0.88}As$	6	22.39	3.73	Absorber
58	$Al_{0.05}Ga_{0.95}As$	30	106.48	3.55	Barrier
59	GaAs	5	17.89	3.58	Cap

Table E12: MIT 910 nm regular SESAM/SBR design with quantum absorber (MIT-910-QW).

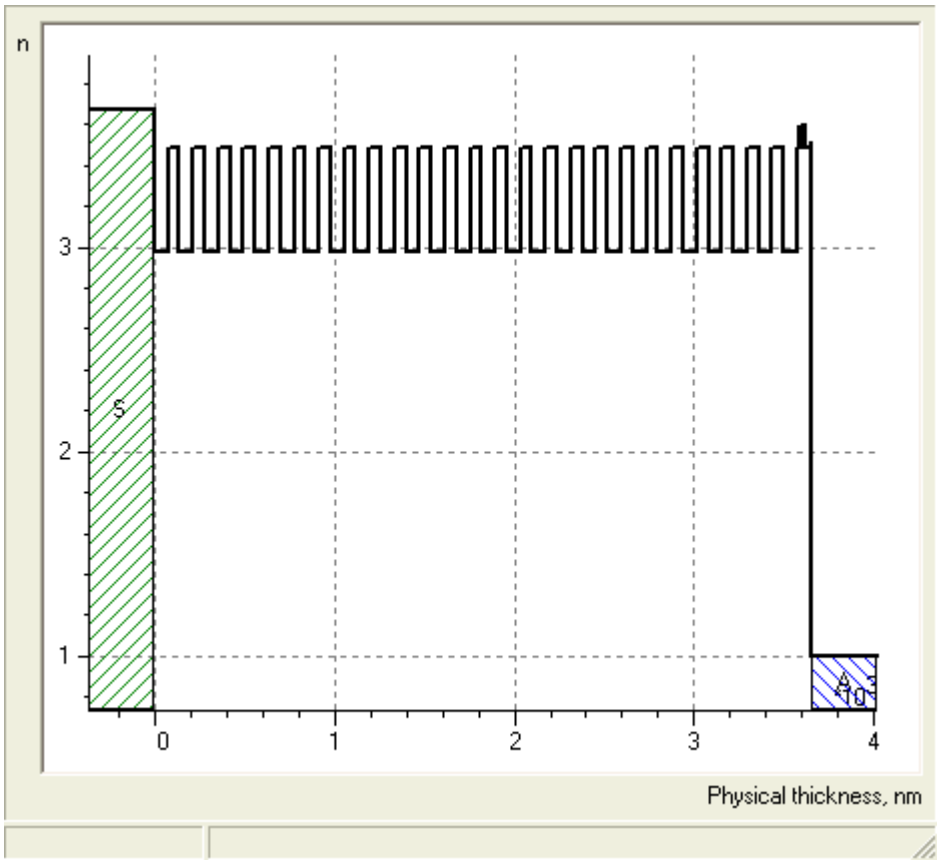

Figure E65: Index profile for MIT-910-QW SESAM/SBR design.

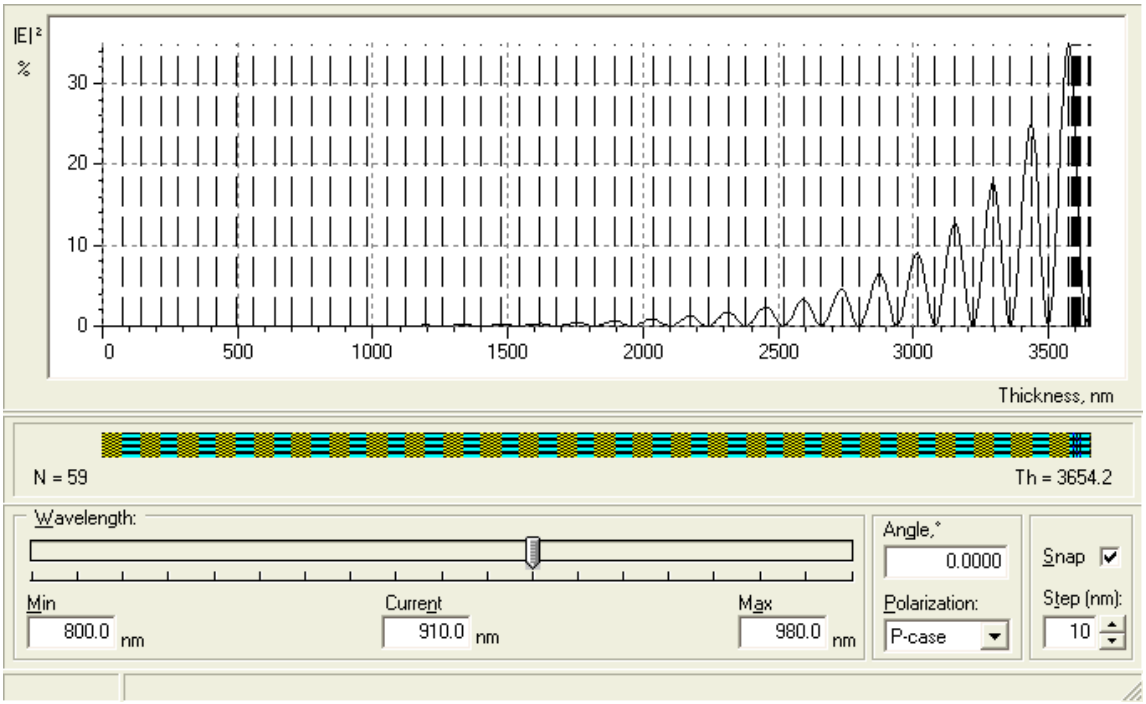

Figure E66: Electric field pattern for MIT-910-QW SESAM/SBR design.

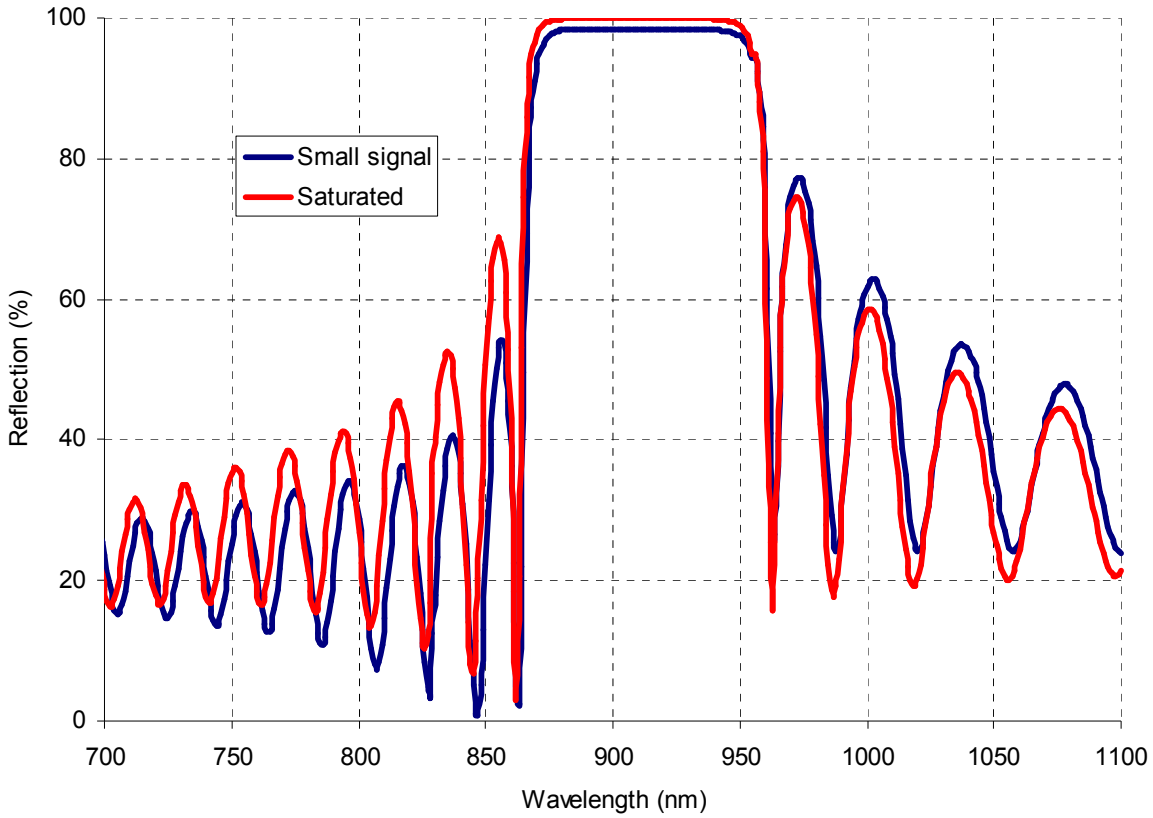

Figure E67: Calculated reflectivity for MIT-910-QW SESAM/SBR design.

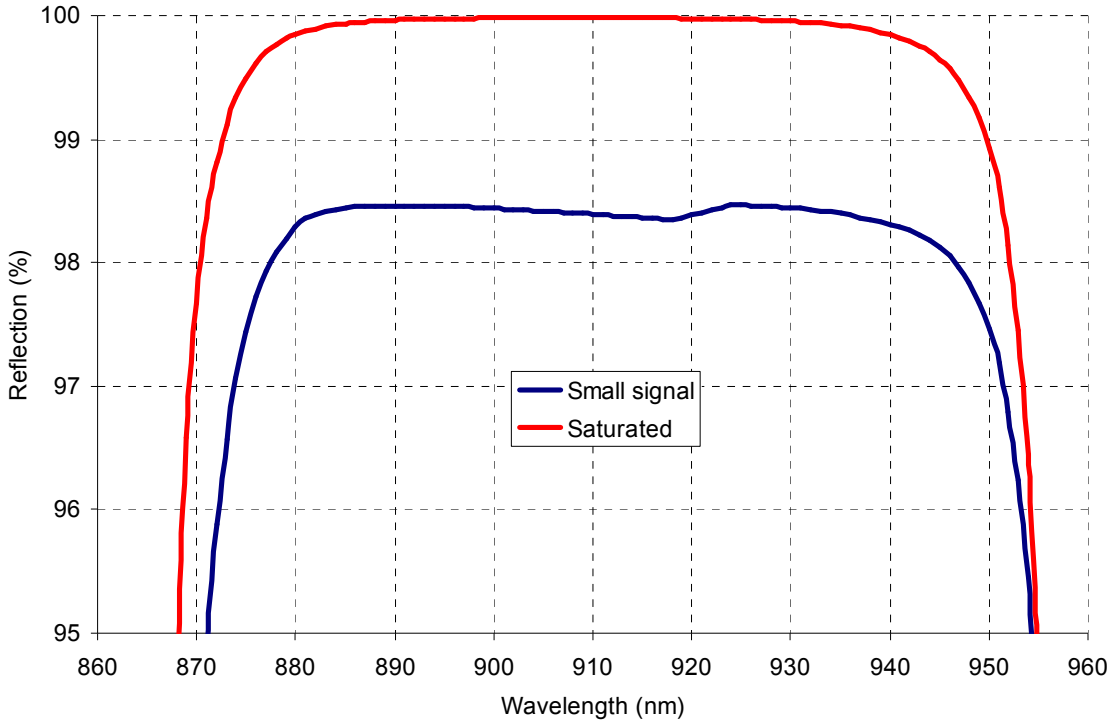

Figure E68: Calculated reflectivity for MIT-910-QW SESAM/SBR design (zoomed in).

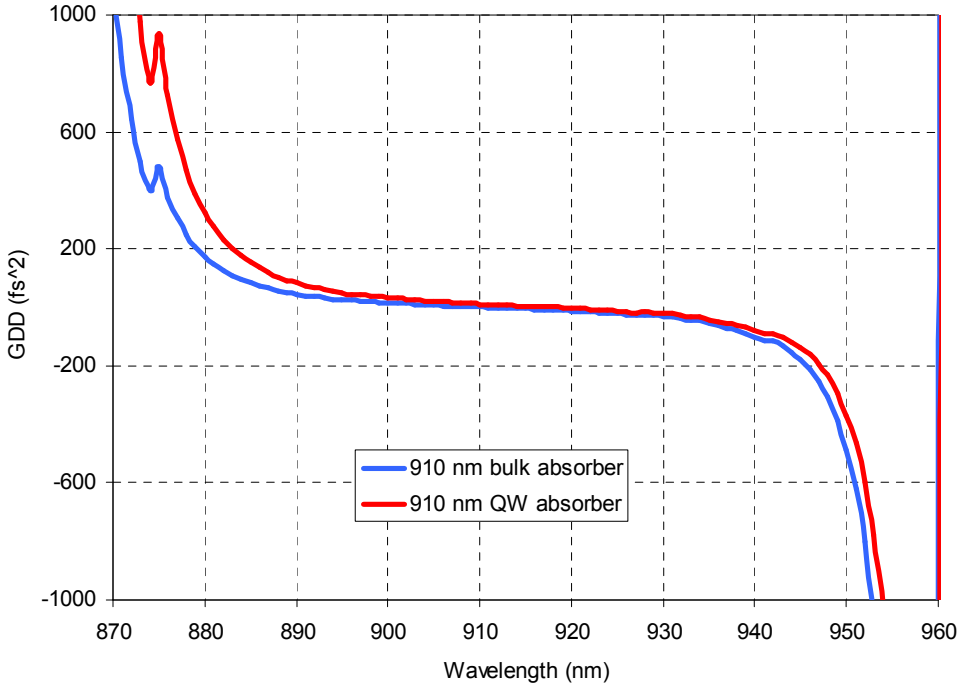

Figure E69: Calculated GDD for MIT-910-QW SESAM/SBR design. GDD of MIT-910-bulk SESAM/SBR is also shown.

VA120: 910nm SBR with InGaAs Qunatum Well Saturable Absorber

Sample VA120, a saturable Bragg reflector that is designed to be centered at 910nm with three InGaAs quantum wells in the saturable absorber section was grown using molecular beam epitaxy. The sample was characterized using the Bruker D8 x-ray diffraction systems within CMSE, the Varian Cary 5i spectrophotometer system within CMSE and the J.A. Woollam M-88 variable angle spectroscopic ellipsometry system. The results are summarized in the following table.

Summary of the Desired Structure and Measured Results

	Structure	Desired		Reflectivity Fit		Composite Xray Fit Coupled		Composite Xray Fit Uncoupled		WVASE Fit: Coupled		WVASE Fit: Uncoupled	
		Thickness	Al or In content	Thickness	Al or In content	Thickness	Al or In Content	Thickness	Al or In Content	Thickness	Al or In Content	Thickness	Al or In Content
	AlGaAs	27.54	0.10	27.762	0.104	28.33	0.108	28.69	0.086	26.707	0.0289 ±0.012	10.722 ±3.62	0.0534 ±0.0126
X3	AlGaAs	8.16	0.10	8.220	0.104	8.39	0.108	8.08	0.106	7.866	0.0289 ±0.012	11.005 ±3.62	0.0199 ±0.0294
	InGaAs	6.0	0.12	5.893	0.112	6.15	0.119	6.38	0.114	4.720 ±0.122	0±0.031	4.030 ±0.969	0.172 ±0.0567
	AlGaAs	10.2	0.10	10.216	0.104	10.49	0.108	10.37	0.125	9.880	0.0289 ±0.012	16.927 ±10.1	0 ±0.0299
X 25	AlGaAs	75.87	0.95	78.353	0.951	76.71	0.927	76.82	0.926	73.603 ±1.19	0.874 ±0.0369	72.044 ±0.942	0.8 ±0.0318
	AlGaAs	65.4	0.10	65.892	0.104	67.25	0.108	67.05	0.108	63.333 ±0.191	0.0289 ±0.012	60.543 ±0.193	0 ±0.0168
	AlGaAs	75.87	0.95	78.353	0.951	76.71	0.927	72.65	0.890	73.603 ±1.19	0.874 ±0.0369	72.044 ±0.942	0.8 ±0.0318
	GaAs Substrate												

Note: All thicknesses are in nanometers.

The individual measurements and simulation results are provided on the following pages.

Figure E70: Summary of the desired structure and measured results for MIT-910-QW SESAM/SBR. Note: All the thicknesses are in nm's. This information is kindly provided by Dr. Gale Petrich.

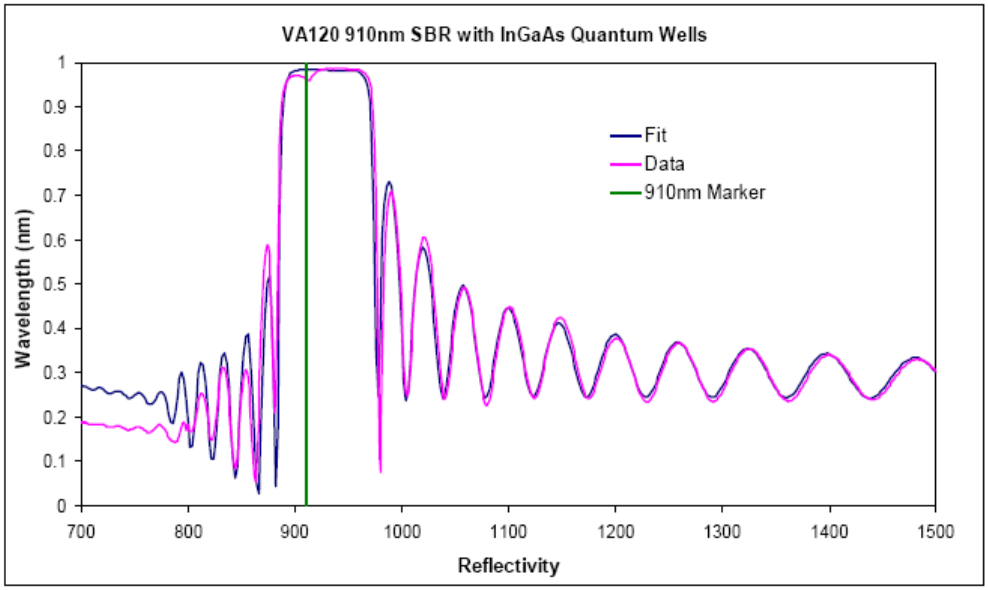

Figure E71: Measured reflectivity for MIT-910-QW SESAM/SBR design. The central wavelength of the Bragg stack at a longer wavelength than the desired value (~910 nm). Note: In fitting the measured reflectivity, the indices of refraction for the GaAs and the AlGaAs layers were determined from the material tables that were provided with the J.A. Woollam ellipsometer. The indices of refraction for InGaAs were from a material table that was calculated using a parameterized InGaAs mode from J.A. Woollam Inc. Also, the growth rates from individual column III were assumed to be constant (Fig. 59). Hence, all the layers were coupled in terms of composition thickness. This information is kindly provided by Dr. Gale Petrich.

Final Coupled Fit Results

N	R	Material	Cell input	Thickness	Roughness	Conc X Top, %
1	1	Al(x)Ga(1-x)As	Cx(Cy) + R	36.7226	0.6979	10.7850
2	1	Ga(1-x)In(x)As	Cx(Cy) + R	6.1468	0.0000	11.8640
3	2	Al(x)Ga(1-x)As	Cx(Cy) + R	8.3893	0.0000	10.7850
4	2	Ga(1-x)In(x)As	Cx(Cy) + R	6.1468	0.0000	11.8640
5	1	Al(x)Ga(1-x)As	Cx(Cy) + R	10.4922	0.0000	10.7850
6	25	Al(x)Ga(1-x)As	Cx(Cy) + R	76.7088	0.0000	92.6520
7	25	Al(x)Ga(1-x)As	Cx(Cy) + R	67.2473	0.0000	10.7850
8	1	Al(x)Ga(1-x)As	Cx(Cy) + R	76.7088	0.0000	92.6520
SUB	1	GaAs	density	0.0000	0.0000	0.0000

(400) Rocking Curve
Using the Bruker high resolution system

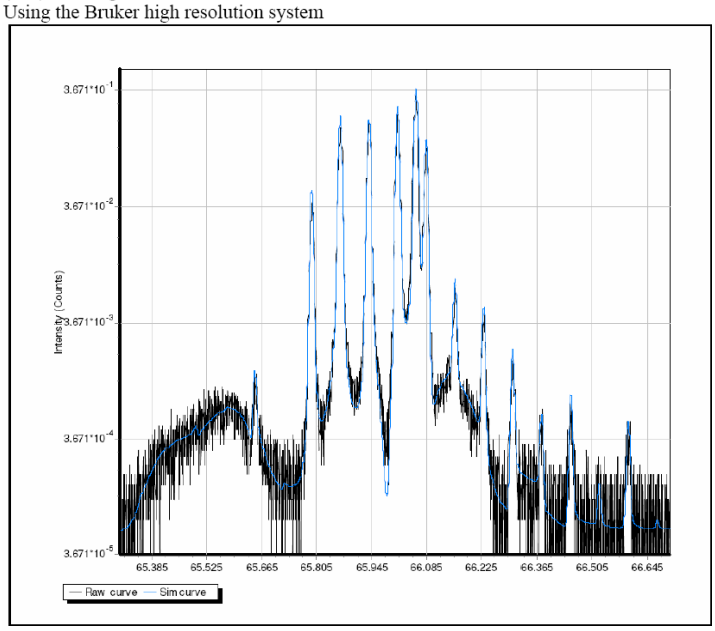

(000) Rocking Curve
Using the Bruker D8 high resolution system

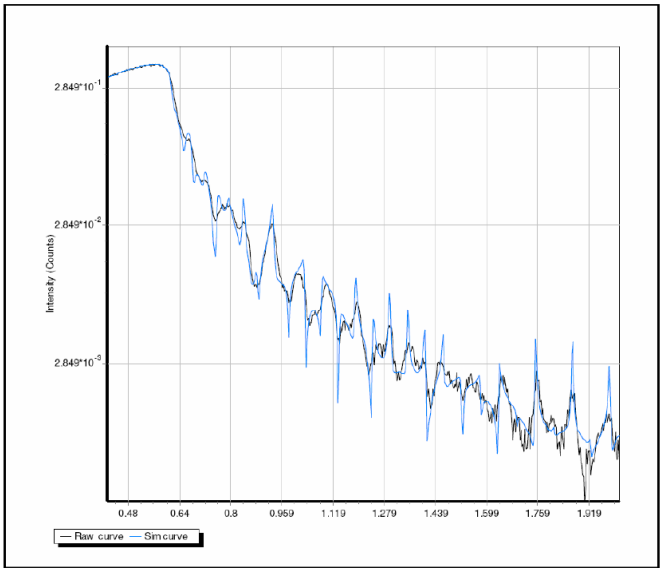

Figure E72: MIT-910-bulk SESAM/SBR x-ray diffraction data Note: The high resolution Bruker D8 X-ray system was used to measure the (400) and (000) rocking curves. However, all of the rocking curves were fit to a common model using the Leptos simulation package from Bruker. This information is kindly provided by Dr. Gale Petrich.

Final Uncoupled Fit Results

N	R	Material	Cell input	Thickness	Roughness	Conc X Top, %
1	1	Al(x)Ga(1-x)As	Cx(Cy) + R	28.6906	0.4545	8.6278
2	3	Al(x)Ga(1-x)As	Cx(Cy) + R	8.0762	1.3109	10.5850
3	3	Ga(1-x)In(x)As	Cx(Cy) + R	6.3820	0.0026	11.3770
4	1	Al(x)Ga(1-x)As	Cx(Cy) + R	10.3721	0.0001	12.5060
5	25	Al(x)Ga(1-x)As	Cx(Cy) + R	76.8198	1.3030	92.5870
6	25	Al(x)Ga(1-x)As	Cx(Cy) + R	67.0548	1.7280	10.7850
7	1	Al(x)Ga(1-x)As	Cx(Cy) + R	72.6528	0.0000	88.9820
SUB	1	GaAs	density	0.0000	0.0000	0.0000

(400) Rocking Curve
Using the Bruker D8 high resolution system

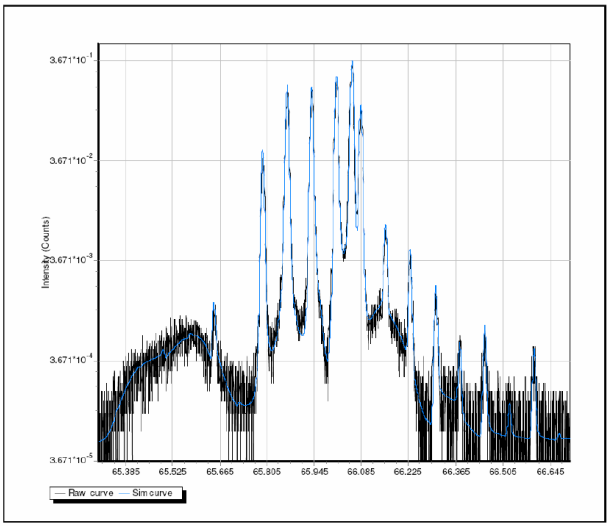

(000) Rocking Curve
Using the Bruker D8 high resolution system

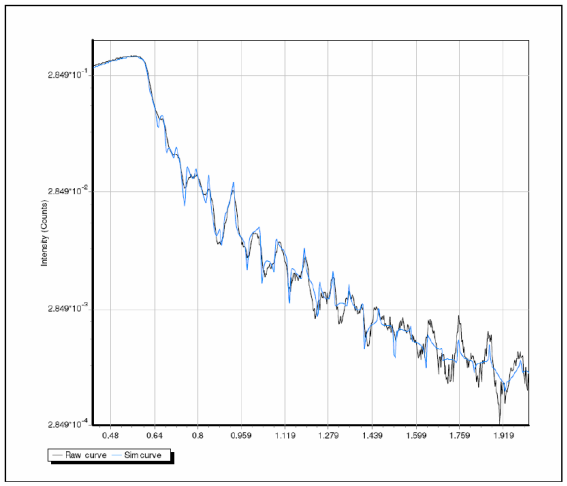

Figure E73: MIT-910-bulk SESAM/SBR x-ray diffraction data This information is kindly provided by Dr. Gale Petrich.

Fit 1) Similar layer's compositions and thicknesses are coupled

8	gaas-ox	0.89224 nm	
7	algaas x=0.029	26.707 nm	
6	algaas x=0.029	7.8659 nm	] 3
5	ingaas x=0.000	4.7195 nm	
4	algaas x=0.029	9.8799 nm	
3	algaas x=0.874	73.603 nm	] 25
2	algaas x=0.029	63.333 nm	
1	algaas x=0.874	73.603 nm	
0	gaas	0.3 mm	

MSE=6.975

Thick.1	73.603±1.19
Alloy.1	0.87408±0.0369
Thick.2	63.333±0.191
Alloy.2	0.028921±0.012
Thick.5	4.7195±0.122
Alloy.5	0±0.031
Thick.8	0.89224±0.0623
Angle0	65.409±0.103
Angle1	70.442±0.0588
Angle2	75.437±0.0514
Angle3	80.476±0.0286

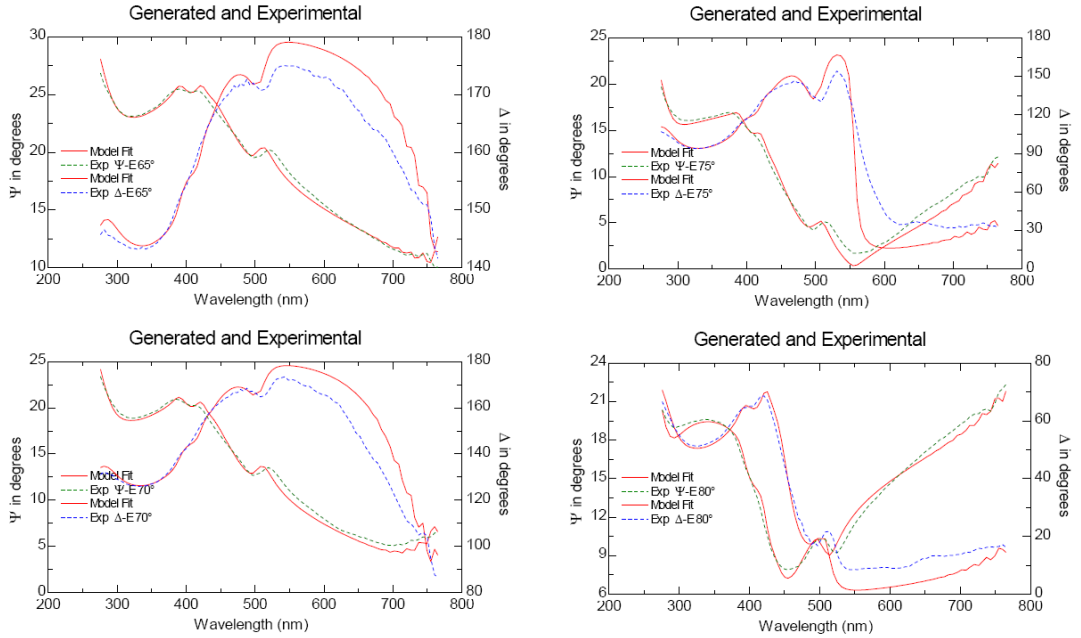

Figure E74: MIT-910-QW SESAM/SBR WVASE (Woollam Variable Angle Spectroscopic Ellipsometer) graphs. Note: A.J.A Woollam M-88 WVASE system along with the WVASE software package was used to measure and fit the ellipsometric data. Data sets were taken at 65, 70, 75 and 80 degrees. All of the data sets were fit to a common model; however, with the model some of the layers were coupled. There are three fits within this summary. This information is kindly provided by Dr. Gale Petrich.

Fit 2) The Al compositions and the thicknesses for the high Al content layers are coupled.

8	gaas-ox	0.68383 nm	
7	algaas x=0.000	6.9689 nm	
6	algaas x=0.000	9.9213 nm	] 3
5	ingaas x=0.200	6.7757 nm	
4	algaas x=0.000	15.838 nm	
3	algaas x=0.800	71.08 nm	] 25
2	algaas x=0.000	60.871 nm	
1	algaas x=0.800	71.08 nm	
0	gaas	0.3 mm	

MSE=6.235

Thick.1	71.08±1.24
Alloy.1	0.8±0.0407
Thick.2	60.871±0.215
Alloy.2	0±0.0106
Thick.4	15.838±3.04
Thick.5	6.7757±1.33
Alloy.5	0.2±0.0408
Thick.6	9.9213±2.1
Thick.8	0.68383±0.067
Thick.7	6.9689±1.88
Angle0	65.292±0.0979
Angle1	70.244±0.0722
Angle2	75.293±0.0525
Angle3	80.391±0.027

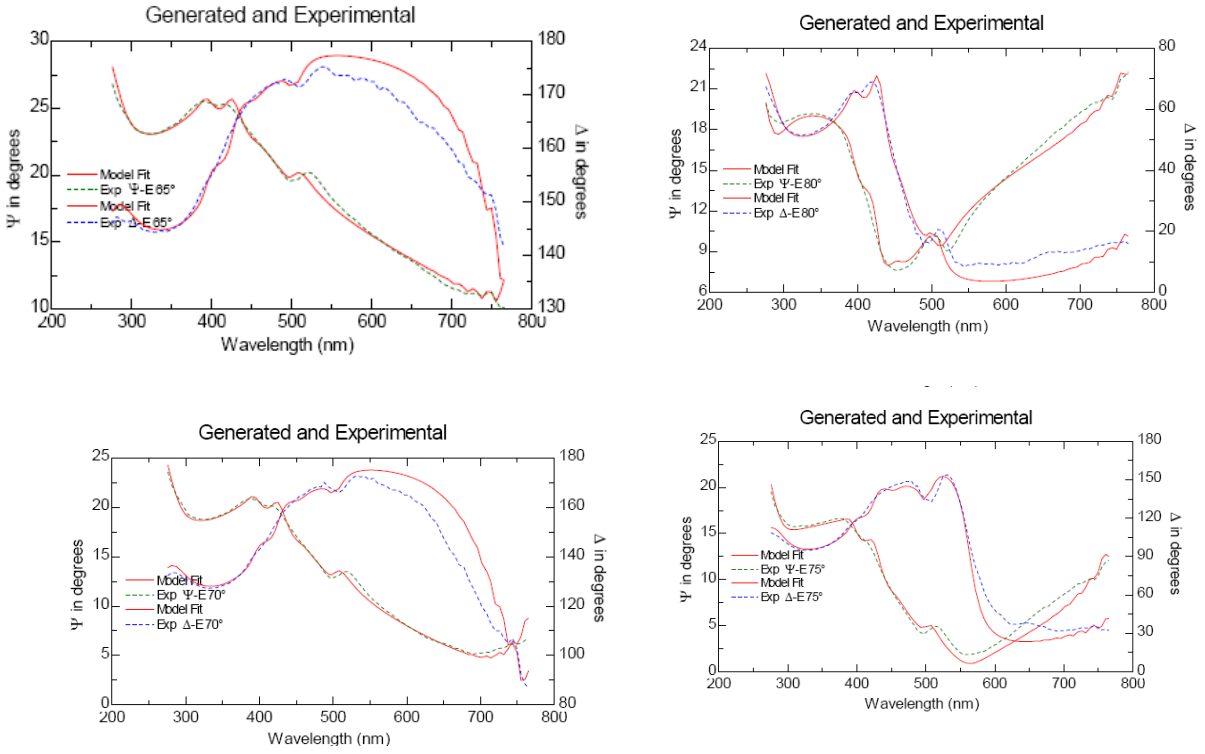

Figure E75: MIT-910-QW SESAM/SBR WVASE (Woollam Variable Angle Spectroscopic Ellipsometer) graphs. This information is kindly provided by Dr. Gale Petrich.

Fit 3) All layer thicknesses and compositions are uncoupled except for the DBR.

8	gaas-ox	1.2477 nm	
7	algaas x=0.053	10.722 nm	
6	algaas x=0.020	11.005 nm	] 3
5	ingaas x=0.172	4.0304 nm	
4	algaas x=0.000	16.927 nm	
3	algaas x=0.800	72.044 nm	] 25
2	algaas x=0.000	60.543 nm	
1	algaas x=0.800	72.044 nm	
0	gaas	0.3 mm	

MSE=5.436

Thick.1	72.044±0.942
Alloy.1	0.8±0.0318
Thick.2	60.543±0.193
Alloy.2	0±0.0168
Thick.4	16.927±10.1
Alloy.4	0±0.0299
Thick.5	4.0304±0.969
Alloy.5	0.17151±0.0567
Thick.6	11.005±3.62
Alloy.6	0.019856±0.0294
Thick.8	1.2477±0.0789
Thick.7	10.722±3.62
Alloy.7	0.053424±0.0126
Angle0	65.166±0.0785
Angle1	70.141±0.062
Angle2	75.266±0.0499
Angle3	80.349±0.0327

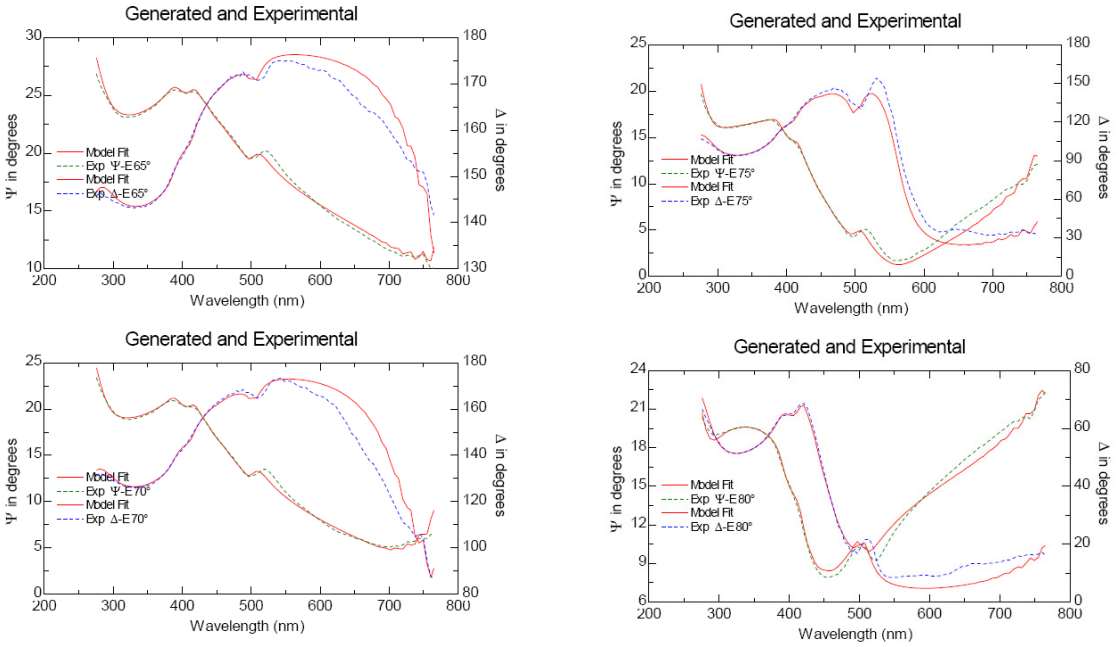

Figure E76: MIT-910-QW SESAM/SBR WVASE (Woollam Variable Angle Spectroscopic Ellipsometer) graphs. This information is kindly provided by Dr. Gale Petrich.

E.10 MIT 860 nm Oxidized/Broadband SESAM/SBR with Quantum-Well Absorber (MIT-860-QW-Oxidized)

Layer	Material	Physical thickness before oxidization (nm)	Physical thickness after oxidization (nm)	Optical thickness (nm)	n	Purpose
0	GaAs	-	-	-	-	Substrate
1	AlAs→Al_xO_y	150.4	134.27	215	1.60	Bragg layer
2	$Al_{0.17}Ga_{0.83}As$	61.36	61.36	215	3.50	Bragg layer
…	…	…	…	…	…	Bragg layers
11	AlAs→Al_xO_y	150.4	134.27	215	1.60	Bragg layer
12	$Al_{0.17}Ga_{0.83}As$	61.36	61.36	215	3.50	Bragg layer
13	AlAs→Al_xO_y	150.4	134.27	215	1.60	Bragg layer
14	$Al_{0.17}Ga_{0.83}As$	20	20	70.08	3.50	Barrier
15	$In_{0.15}Ga_{0.85}As$	6	6	22.04	3.67	Absorber
16	$Al_{0.17}Ga_{0.83}As$	15	15	52.56	3.50	Barrier
17	$Al_{0.1}Ga_{0.9}As$	5	5	17.81	3.56	Cap

Table E13: MIT 860 nm oxidized/broadband SESAM/SBR design with quantum well absorber (MIT-860-QW-Oxidized).

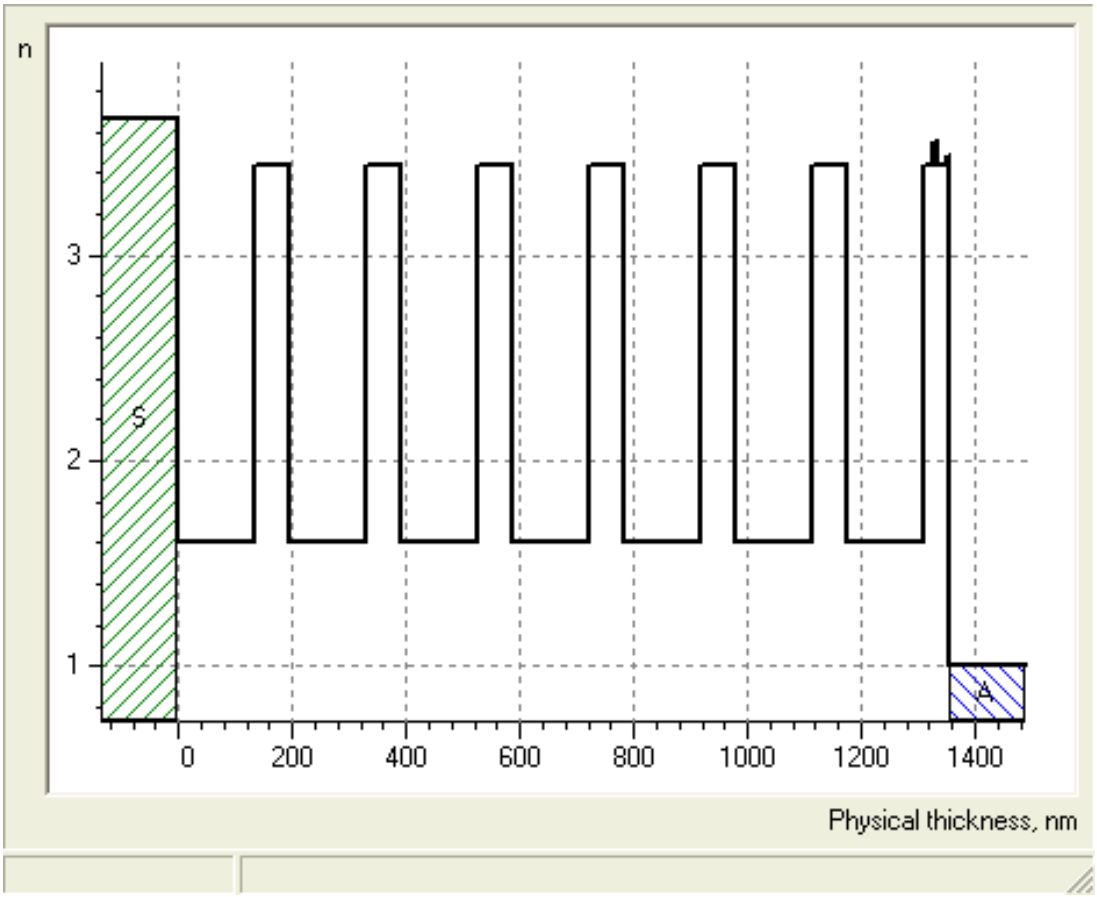

Figure E77: Index profile for MIT-860-QW-Oxidized SESAM/SBR design.

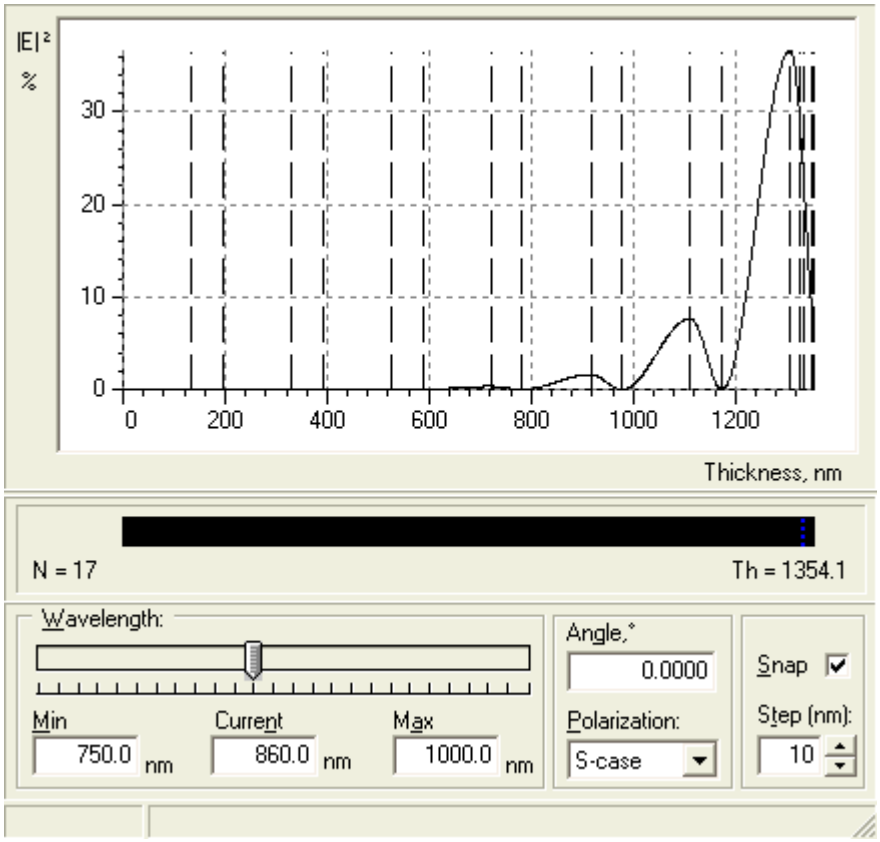

Figure E78: Electric field pattern for MIT-860-QW-Oxidized SESAM/SBR design.

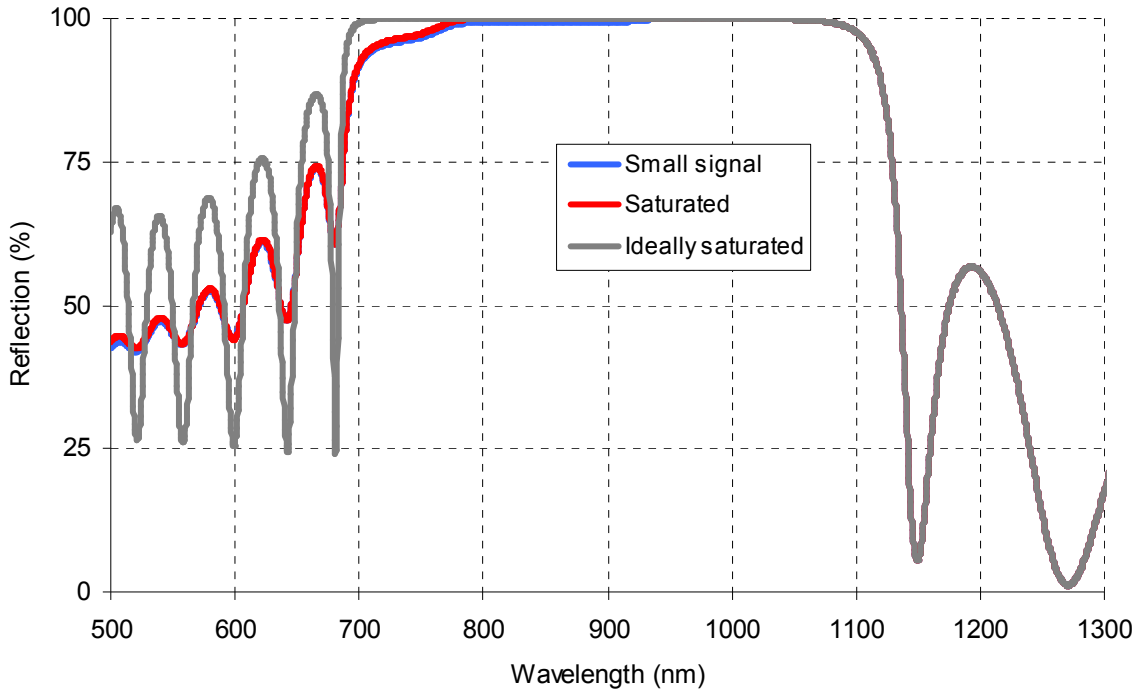

Figure E79: Calculated reflectivity for MIT-860-QW-Oxidized SESAM/SBR design.

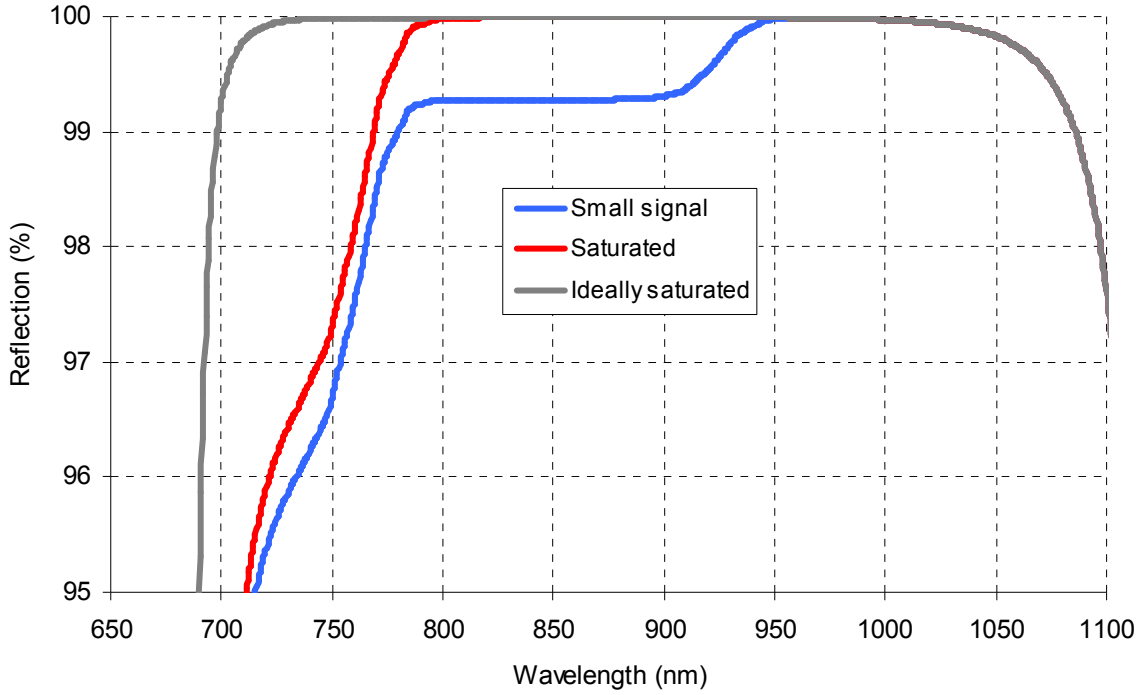

Figure E80: Calculated reflectivity for MIT-860-QW-Oxidized SESAM/SBR design (zoomed in).

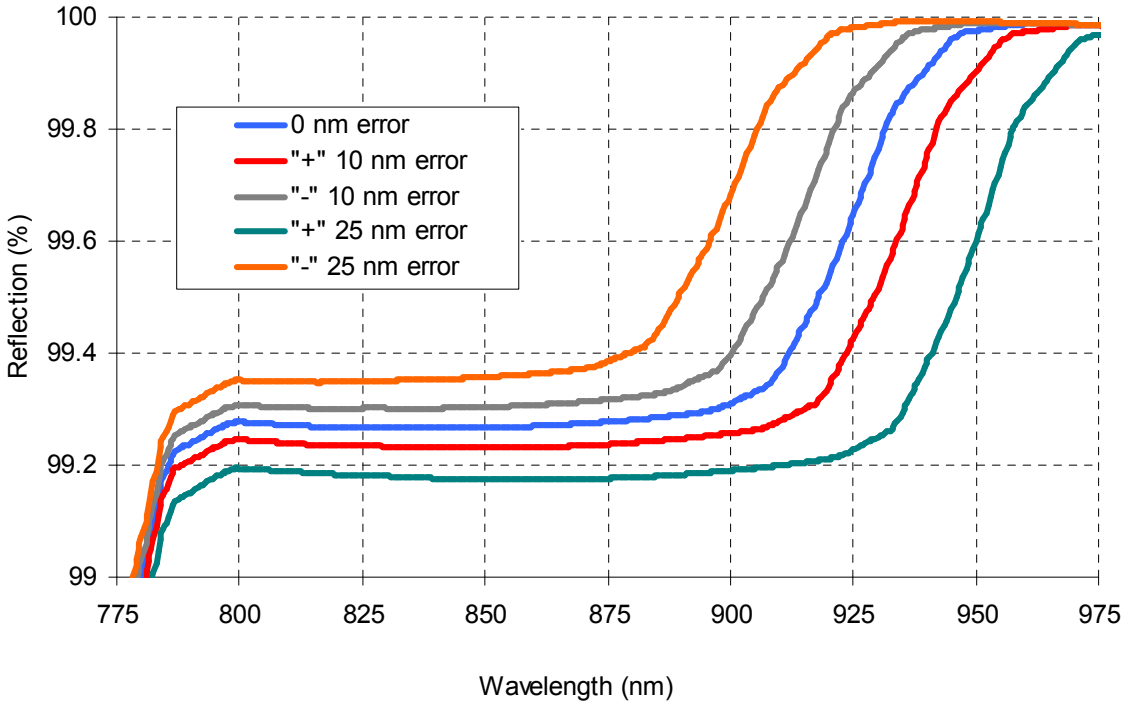

Figure E81: Calculated reflectivity for MIT-860-QW-Oxidized SESAM/SBR design (zoomed in). This graph shows how a shift in absorber band edge effects the reflectivity.

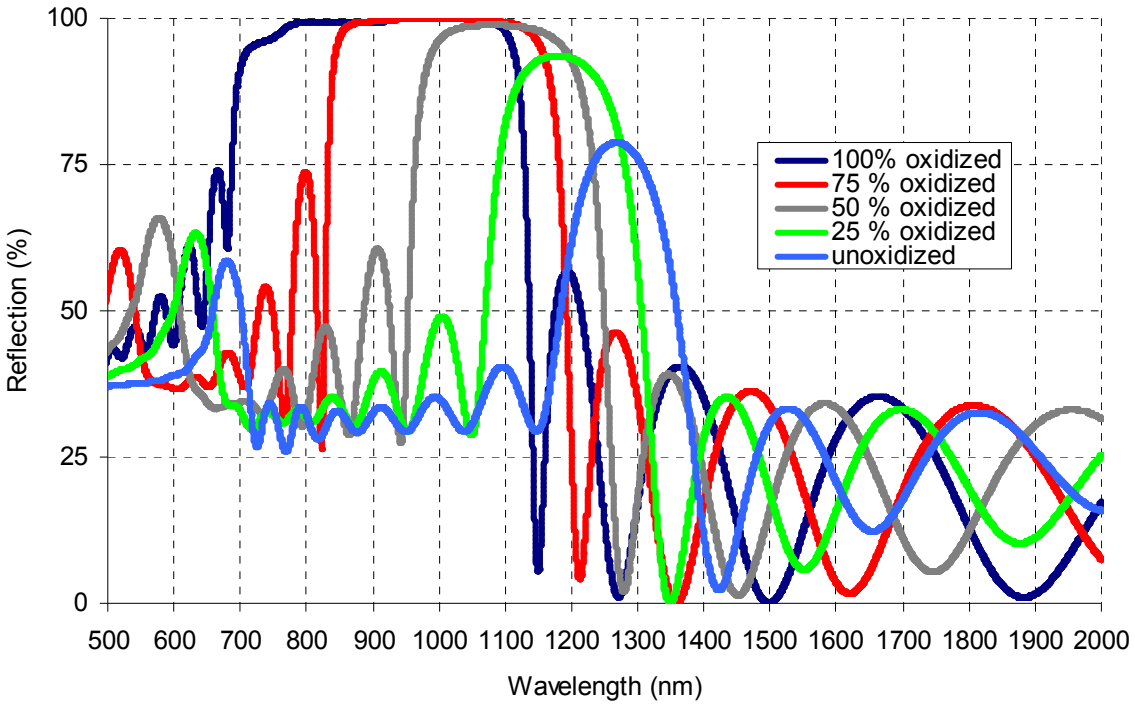

Figure E82: Calculated reflectivity for MIT-860-QW-Oxidized SESAM/SBR design. This graph shows how oxidization percentage effects the reflection. All of the layers were assume to have the same oxidization percentage.

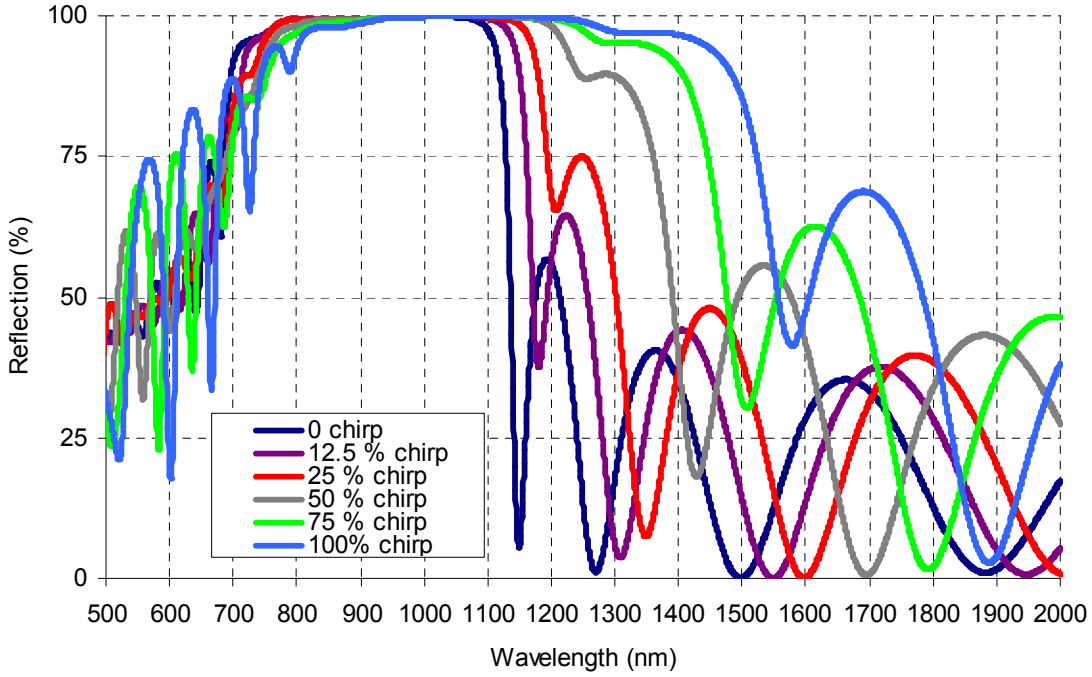

Figure E83: Calculated reflectivity for MIT-860-QW-Oxidized SESAM/SBR design. This graph shows how a chirp in the mirror caused by imperfect oxidization effects the reflection. “0 chirp” refers to all the layers being fully oxidized. “100 % chirp” refers to a situation where the fist layer is fully oxidized and the last layer is fully un-oxidized.

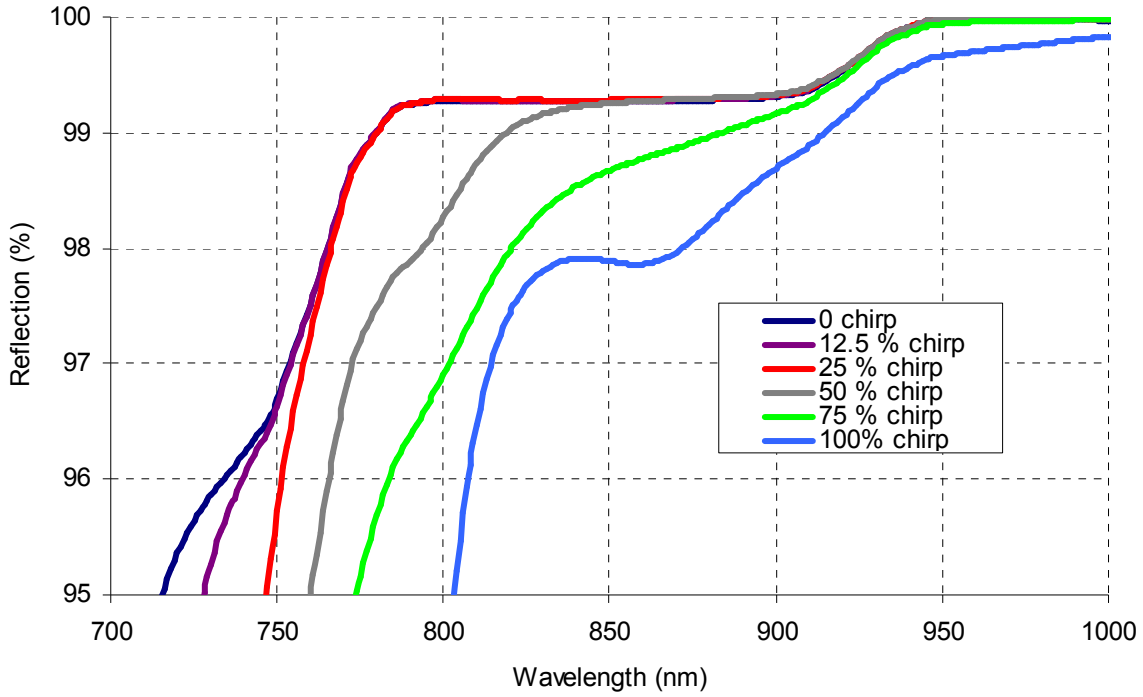

Figure E84: Zoomed in version of Figure E83.

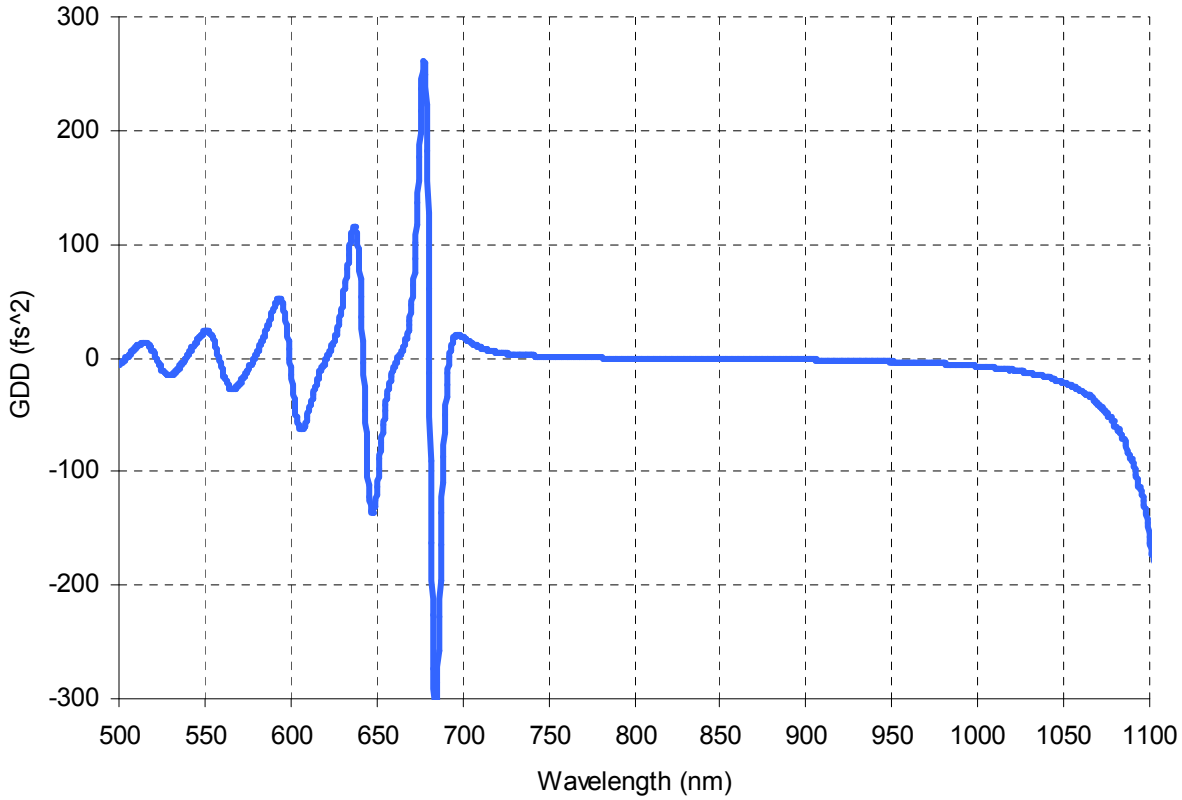

Figure E85: Calculated GDD for MIT-860-QW-Oxidized SESAM/SBR design.

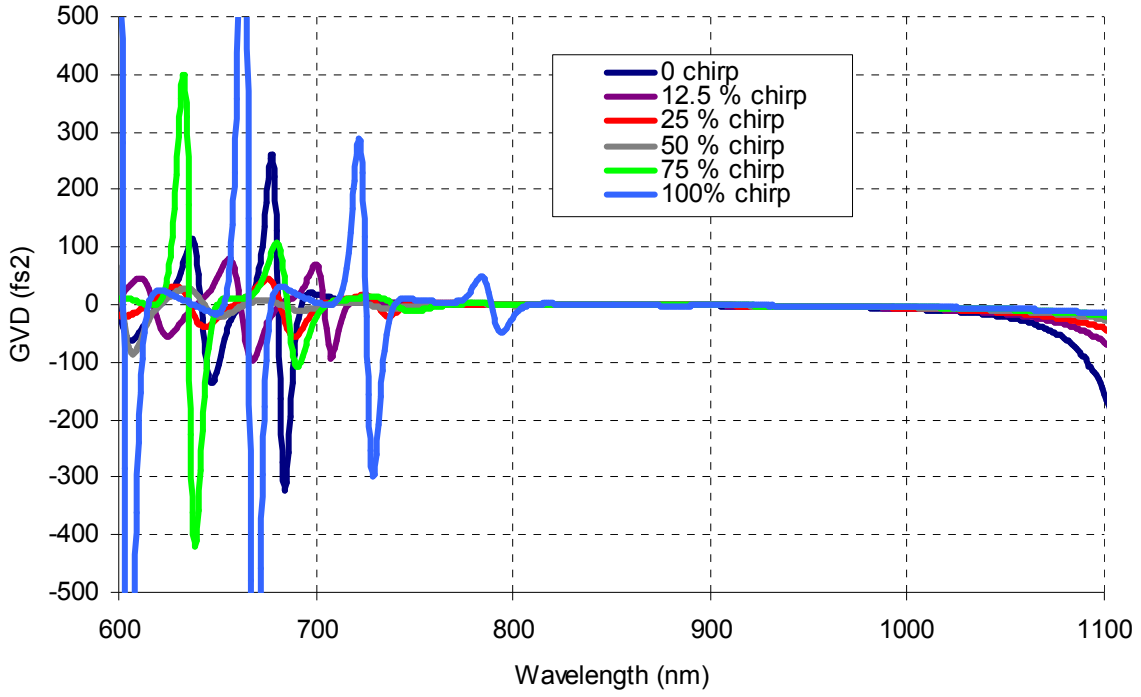

Figure E86: Calculated GDD for MIT-860-QW-Oxidized SESAM/SBR design. This graph shows how a chirp in the mirror caused by imperfect oxidization effects the dispersion. "0 chirp" refers to all the layers being fully oxidized. "100 % chirp" refers to a situation where the fist layer is fully oxidized and the last layer is fully un-oxidized.

VA130 9100nm SBR: Summary of the Desired Structure and Measured Results

	Desired Structure			Reflectivity Fit		Composite Xray Fit		WVASE: Max coupling		WVASE: Uncoupled	
		Thickness	Al, In content	Thickness	Al, In content	Thickness	Al, In Content	Thickness	Al Content	Thickness	Al Content
	AlGaAs	20	0.17	19.9	0.160	19.76	0.189	19.832 ±0.374	0.10391 ±0.0107	16.792 ±0.891	0.14317 ±0.0097
	InGaAs	6	0.15	6.69	0.237	6.12	0.141	4.5633 ±0.446	0.22241 ±0.0395	5.8355 ±0.923	0.35595 ±0.06
	AlGaAs	20	0.17	19.9	0.160	19.76	0.189	19.832 ±0.374	0.10391 ±0.0107	23.364 ±1.52	0.22795 ±0.0188
X 7	AlAs	150.4		143.6		148.9		146.46 ±0.382		144.9 ±0.365	
	AlGaAs	61.4	0.17	61.1	0.160	60.65	0.189	58.52 ±0.323	0.10391 ±0.0107	59.442 ±0.371	0.09257 ±0.0103
	GaAs Substrate										

Note: All thicknesses are in nanometers.
All fits to optical measurements used a relaxed parametric model for InGaAs

Figure E87: Summary of the desired structure and measured results for MIT-860-QW-Oxidized SESAM/SBR. Note: All the thicknesses are in nm's. This information is kindly provided by Dr. Gale Petrich.

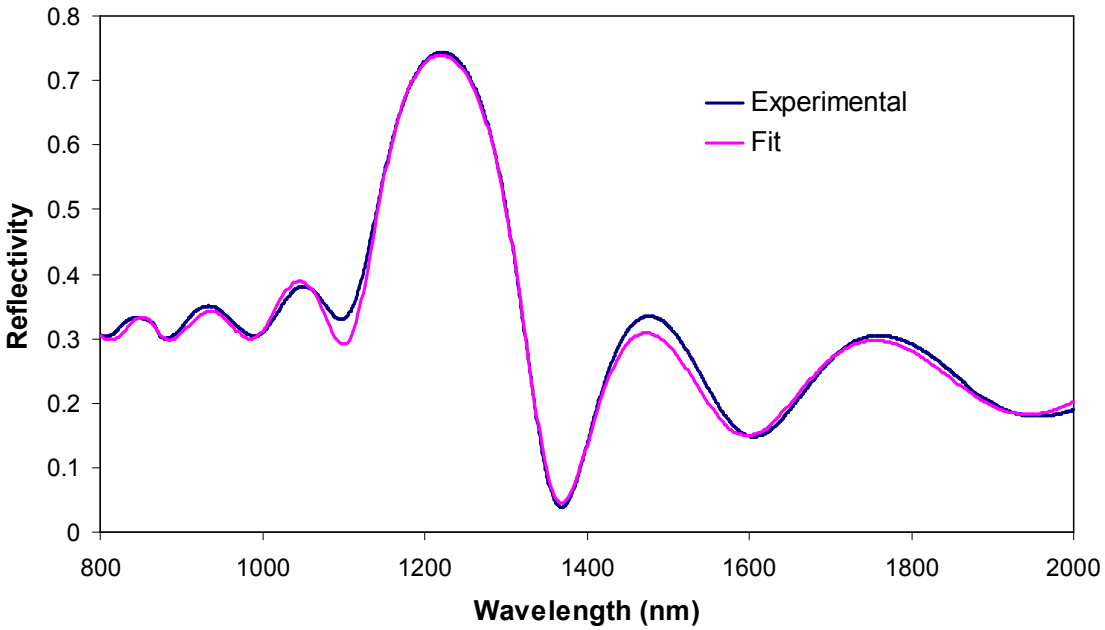

Figure E88: Measured reflectivity data for MIT-860-QW-Oxidized SESAM/SBR before oxidization. This information is kindly provided by Dr. Gale Petrich.

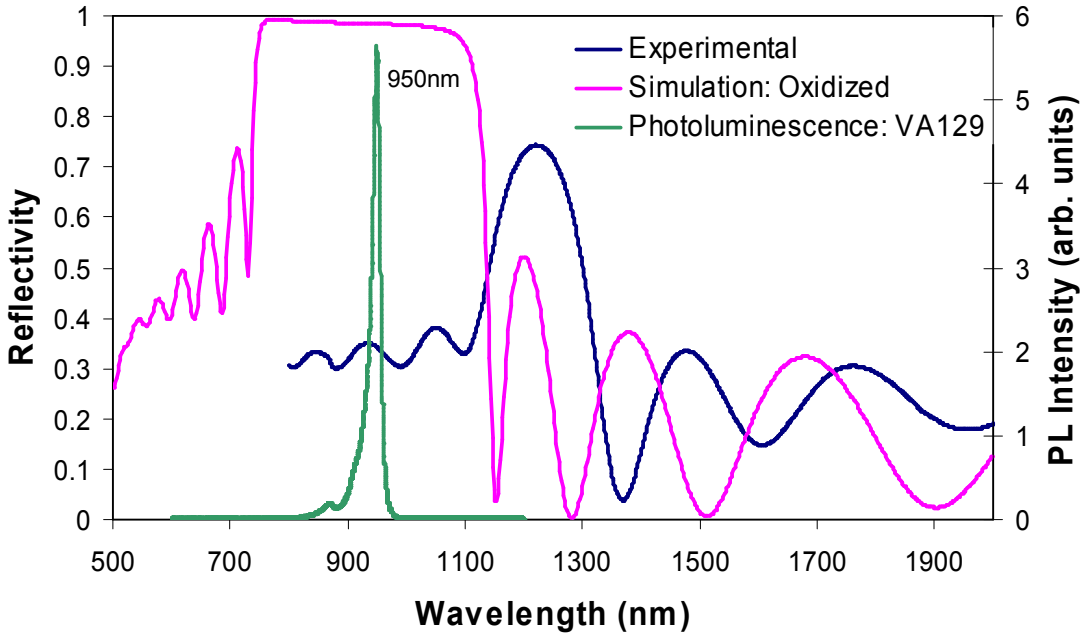

Figure E89: Measured reflectivity data for MIT-860-QW-Oxidized SESAM/SBR before oxidization is shown with the measured photoluminescence signal from the structure.. Simulated reflectivity of the oxidized structure is also shown. This information is kindly provided by Dr. Gale Petrich.

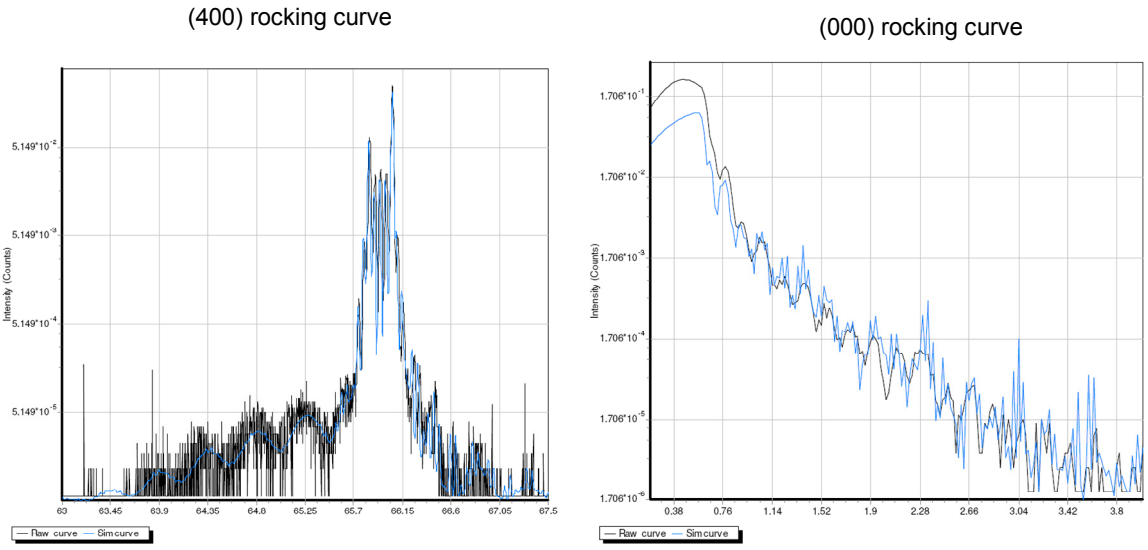

Figure E90: MIT-860-QW-Oxidized SESAM/SBR x-ray diffraction data. Notes: (i) Data is taken using both Bruker D8 systems, (ii) Fit used the (400) and the (000) data sets using the Leptos program. This information is kindly provided by Dr. Gale Petrich.

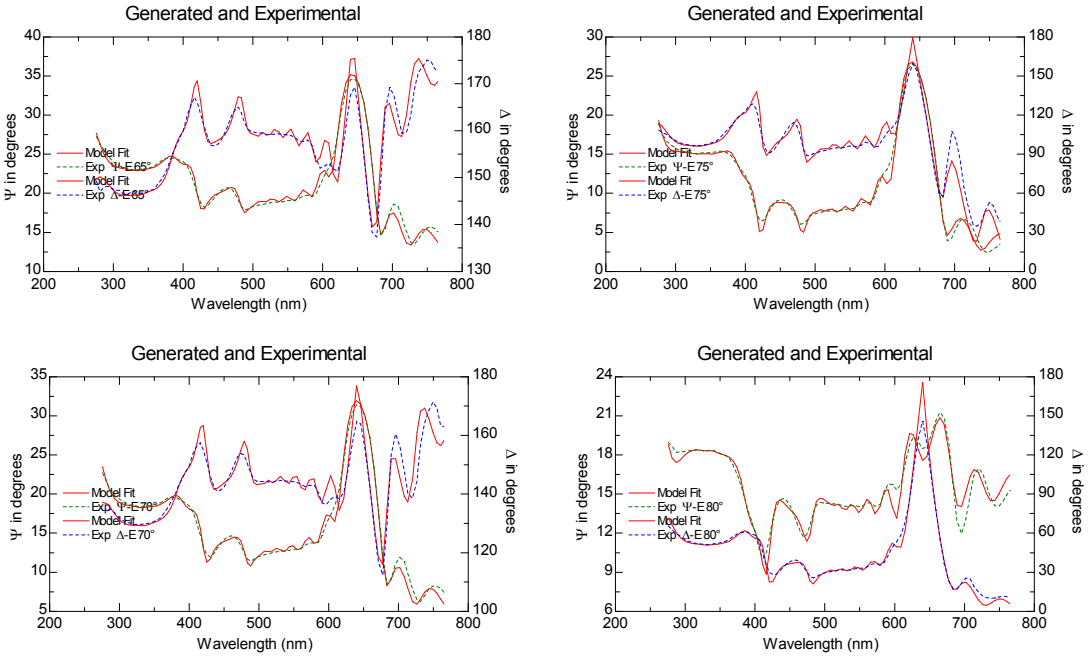

-Data taken using the J.A. Woollam M-88 Ellipsometer
-Fit calculated using all data sets assuming that the layers are uncoupled
-Relaxed Parametric InGaAs model used

Figure E91: MIT-860-QW-Oxidized SESAM/SBR WVASE (Woollam Variable Angle Spectroscopic Ellipsometer) graphs. Notes: (i) Data is taken using J.A. Woollam M-88 ellipsometer, (ii) Fit calculated using all the data sets assuming that the layers are uncoupled. This information is kindly provided by Dr. Gale Petrich.

APPENDIX F

SESAM/SBR DESIGNS FOR FUTURE PROJECTS

In this Appendix, we will provide information on several SESAM/SBR designs that might be useful for future projects. However, before growing these structures, one should carefully double-check the designs again. Especially the expected position of the band edge should be checked carefully, and it should be verified experimentally before growing the whole mirror structure.. Table F1 lists the SESAM/SBR designs that we will present in this Appendix. Note that all of the designs use a quantum well absorber based on strained InGaAs, and the modulation depth for all the designs are chosen around ~0.75%.

SESAM/SBR Name	Possible tuning range (nm)	Section
MIT 825 nm SESAM/SBR with quantum well absorber	800-855	F1
MIT 850 nm SESAM/SBR with quantum well absorber	825-880	F2
MIT 860 nm SESAM/SBR with quantum well absorber	830-890	F3
MIT 880 nm SESAM/SBR with quantum well absorber	855-915	F4
MIT 925 nm SESAM/SBR with quantum well absorber	895-960	F5

Table F1: List of SESAM/SBR designs that we will provide in this chapter. These designs have not grown yet, but we are providing them here since they might be useful in future projects.

F.1 MIT 825 nm SESAM/SBR with Quantum-Well Absorber

Layer	Material	Physical Thickness (nm)	Optical Thickness (nm)	n	Purpose
0	GaAs	-	-	-	Substrate
1	$Al_{0.95}Ga_{0.05}As$	68.12	206.25	3.03	Bragg layer
2	$Al_{0.15}Ga_{0.85}As$	57.95	206.25	3.56	Bragg layer
…	…	…	…	…	Bragg layers
49	$Al_{0.95}Ga_{0.05}As$	68.12	206.25	3.03	Bragg layer
50	$Al_{0.15}Ga_{0.85}As$	57.95	206.25	3.56	Bragg layer
51	$Al_{0.95}Ga_{0.05}As$	68.12	206.25	3.03	Bragg layer
52	$Al_{0.15}Ga_{0.85}As$	15	53.39	3.56	Barrier
53	$In_{0.05}Ga_{0.95}As$	7	25.67	3.67	Absorber
54	$Al_{0.15}Ga_{0.85}As$	35	124.58	3.56	Barrier
55	GaAs	5	18.34	3.67	Cap

Table F2: MIT 825 nm regular SESAM/SBR design with quantum well absorber. The expected band edge for $Al_{0.15}Ga_{0.85}As$ Bragg layer is around 770 nm. The expected band edge for the 7 nm thick strained $In_{0.05}Ga_{0.95}As$ quantum well absorber is around 870 nm. Note: To make this design more immune to possible growth errors one might want to increase the Al content of $Al_{0.15}Ga_{0.85}As$ that is used in the Bragg mirror (maybe to 17%). However note that, making the design safer, will narrow down the bandwidth of the Bragg mirror.

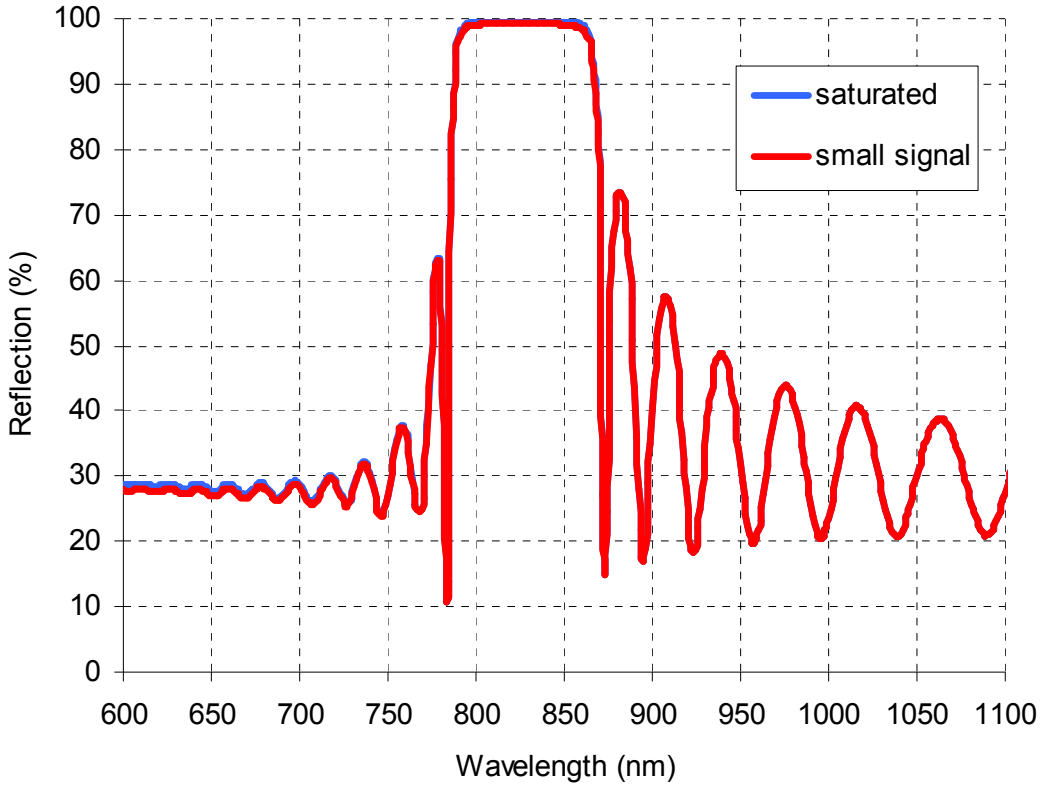

Figure F1: Calculated reflection of MIT 825 nm regular SESAM/SBR design with quantum well absorber for small signal and saturated cases.

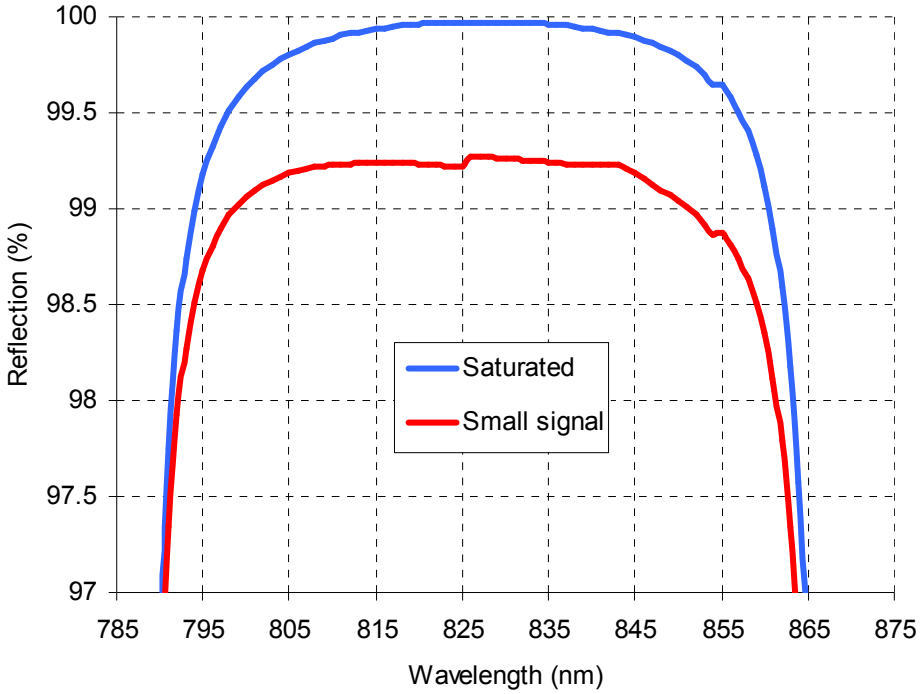

Figure F2: Calculated reflection of MIT 825 nm regular SESAM/SBR design with quantum well absorber for small signal and saturated cases (zoomed into the main reflectivity band).

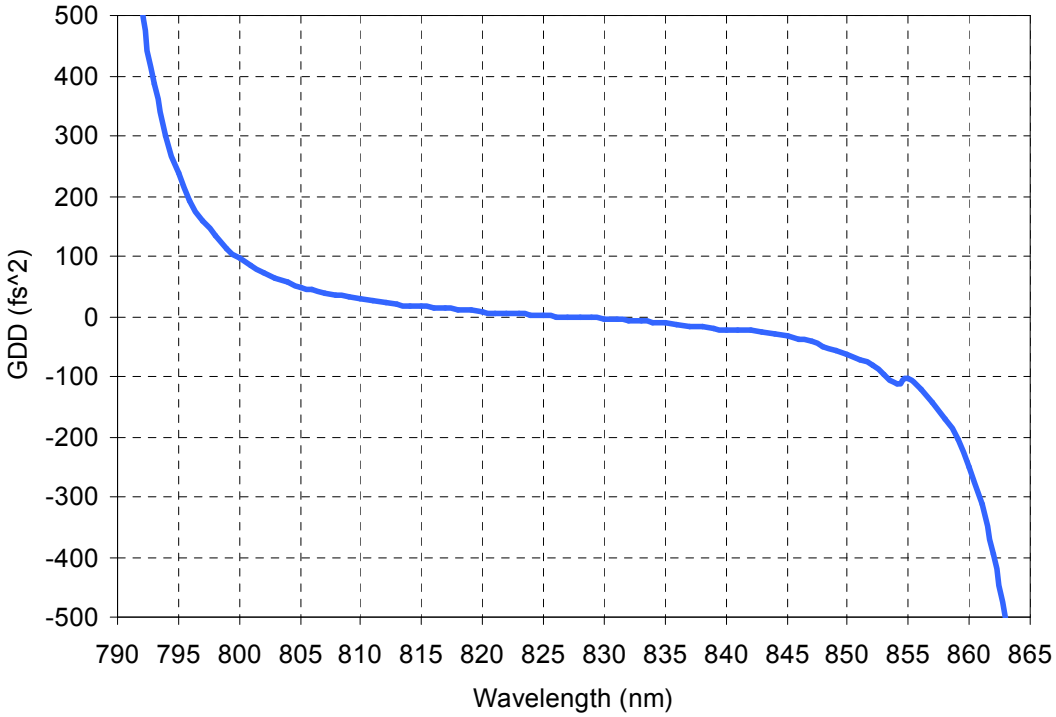

Figure F3: Calculated dispersion of MIT 825 nm regular SESAM/SBR design with quantum well absorber.

F.2 MIT 850 nm SESAM/SBR with Quantum-Well Absorber

Layer	Material	Physical thickness (nm)	Optical thickness (nm)	n	Purpose
0	GaAs	-	-	-	Substrate
1	$Al_{0.95}Ga_{0.05}As$	70.44	212.50	3.02	Bragg layer
2	$Al_{0.14}Ga_{0.86}As$	59.54	212.50	3.55	Bragg layer
…					Bragg layers
49	$Al_{0.95}Ga_{0.05}As$	70.44	212.50	3.02	Bragg layer
50	$Al_{0.14}Ga_{0.86}As$	59.54	212.50	3.55	Bragg layer
51	$Al_{0.95}Ga_{0.05}As$	70.44	212.50	3.02	Bragg layer
52	$Al_{0.14}Ga_{0.86}As$	10	35.45	3.55	Barrier
53	$In_{0.11}Ga_{0.89}As$	6	22.00	3.67	Absorber
54	$Al_{0.14}Ga_{0.86}As$	45	159.54	3.55	Barrier
55	GaAs	5	18.17	3.63	Cap

Table F2: MIT 850 nm regular SESAM/SBR design with quantum well absorber. The expected band edge for $Al_{0.14}Ga_{0.86}As$ Bragg layer is around 760 nm. The expected band edge for the 6 nm thick strained $In_{0.11}Ga_{0.89}As$ quantum well absorber is around 897 nm. Note: This design is quite immune to possible growth errors, since the margins for band edge is kept at a quite safe level.

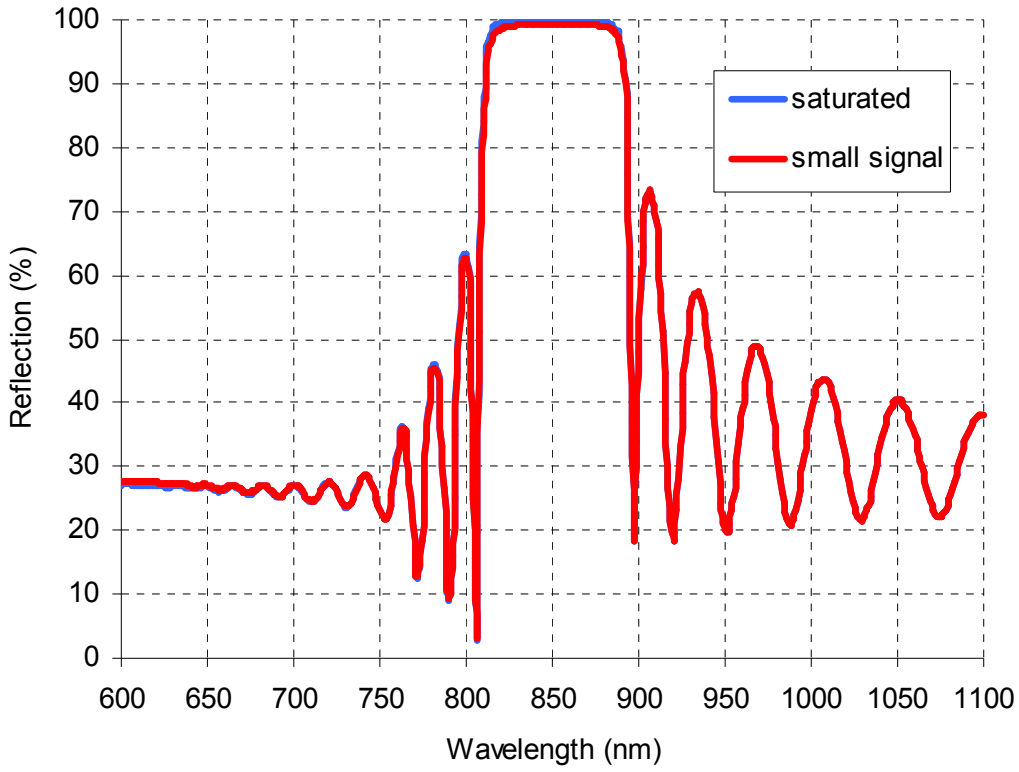

Figure F4: Calculated reflection of MIT 850 nm regular SESAM/SBR design with quantum well absorber for small signal and saturated cases.

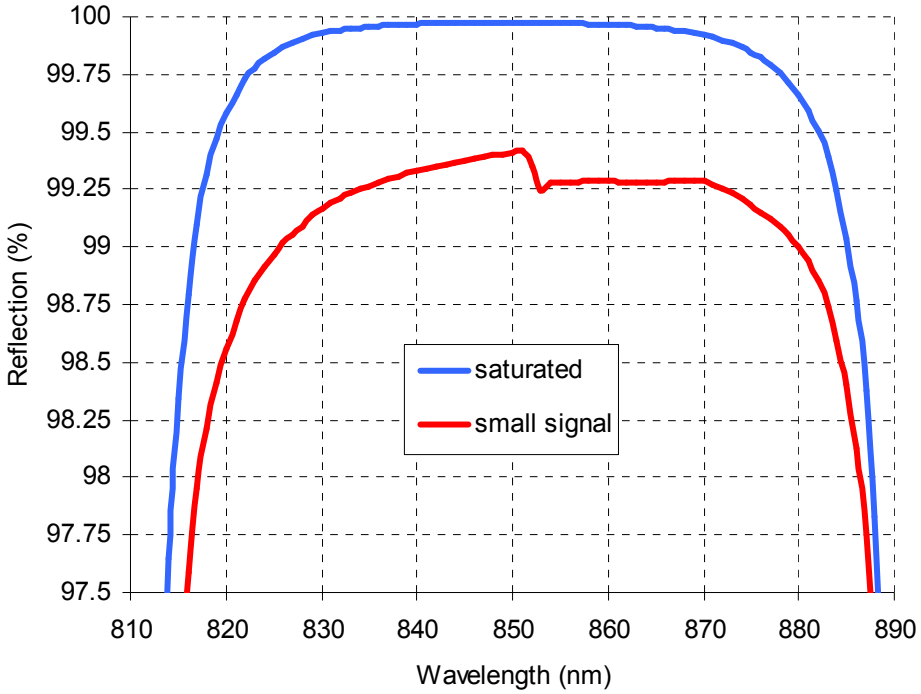

Figure F5: Calculated reflection of MIT 850 nm regular SESAM/SBR design with quantum well absorber for small signal and saturated cases (zoomed into the main reflectivity band).

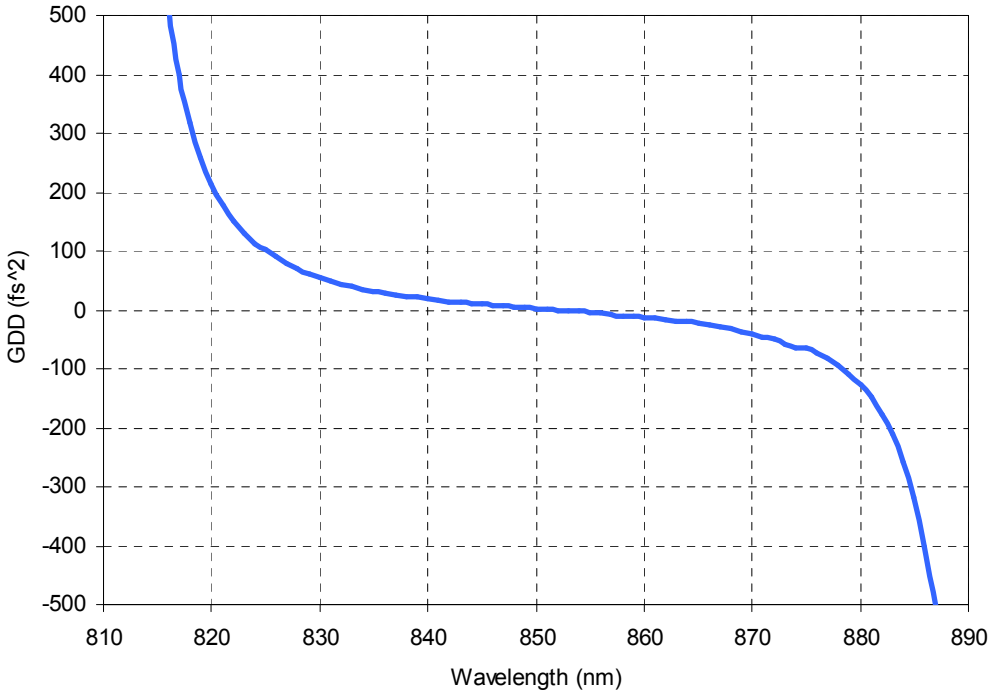

Figure F6: Calculated dispersion of MIT 850 nm regular SESAM/SBR design with quantum well absorber.

F.3 MIT 860 nm SESAM/SBR with Quantum-Well Absorber

Layer	Material	Physical thickness (nm)	Optical thickness (nm)	n	Purpose
0	GaAs	-	-	-	Substrate
1	$Al_{0.95}Ga_{0.05}As$	71.35	215	3.01	Bragg layer
2	$Al_{0.10}Ga_{0.90}As$	60.37	215	3.56	Bragg layer
…					Bragg layers
49	$Al_{0.95}Ga_{0.05}As$	71.35	215	3.01	Bragg layer
50	$Al_{0.10}Ga_{0.90}As$	60.37	215	3.56	Bragg layer
51	$Al_{0.95}Ga_{0.05}As$	71.35	215	3.01	Bragg layer
52	$Al_{0.10}Ga_{0.90}As$	15	53.42	3.56	Barrier
53	$In_{0.10}Ga_{0.90}As$	7	25.48	3.64	Absorber
54	$Al_{0.10}Ga_{0.90}As$	45	160.26	3.56	Barrier/cap

Table F4: MIT 860 nm regular SESAM/SBR design with quantum well absorber. The expected band edge for $Al_{0.10}Ga_{0.90}As$ Bragg layer is around 802 nm. The expected band edge for the 7 nm thick strained $In_{0.10}Ga_{0.90}As$ quantum well absorber is around 903 nm. Note: To make this design more immune to possible growth errors one might want to increase the Al content of $Al_{0.10}Ga_{0.90}As$ that is used in the Bragg mirror (maybe to 12%).

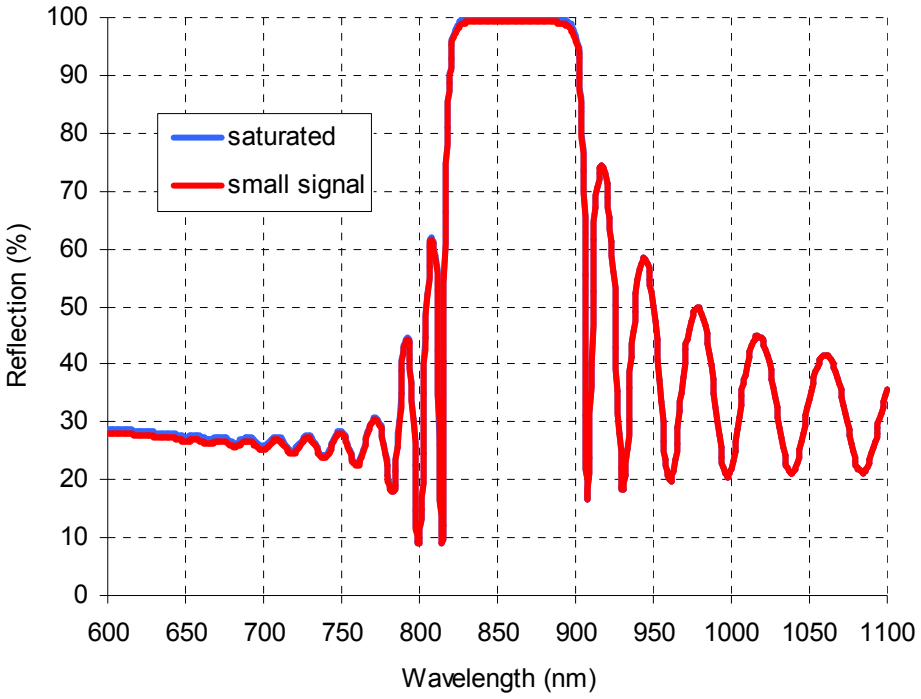

Figure F7: Calculated reflection of MIT 860 nm regular SESAM/SBR design with quantum well absorber for small signal and saturated cases.

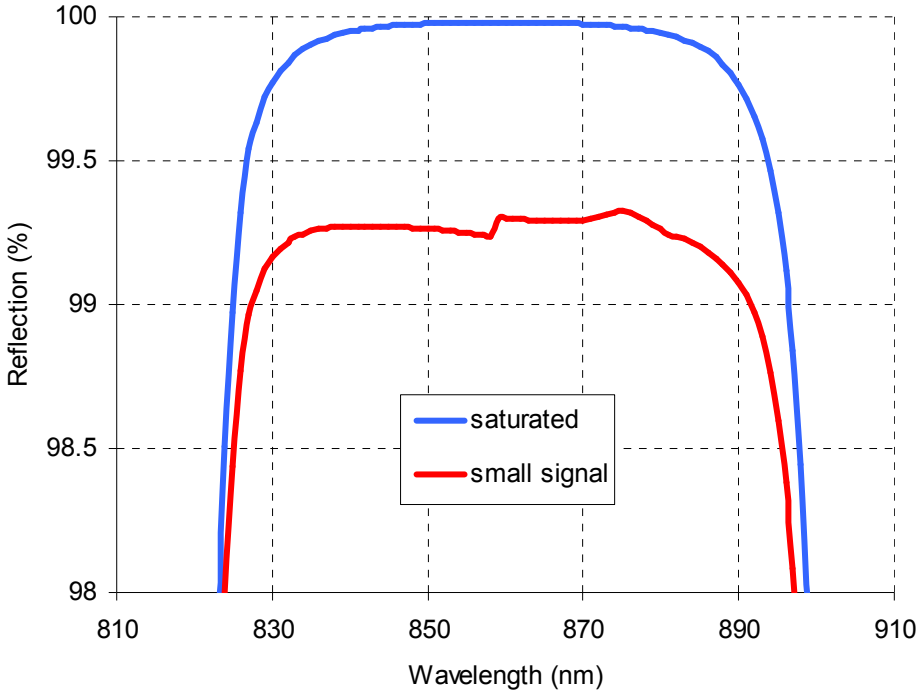

Figure F8: Calculated reflection of MIT 860 nm regular SESAM/SBR design with quantum well absorber for small signal and saturated cases (zoomed into the main reflectivity band).

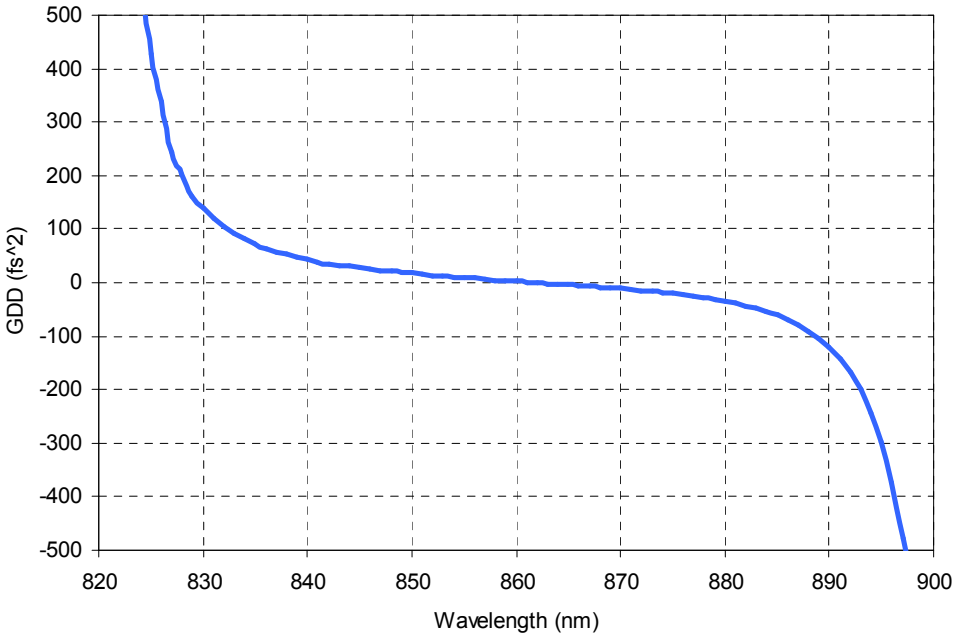

Figure F9: Calculated dispersion of MIT 860 nm regular SESAM/SBR design with quantum well absorber.

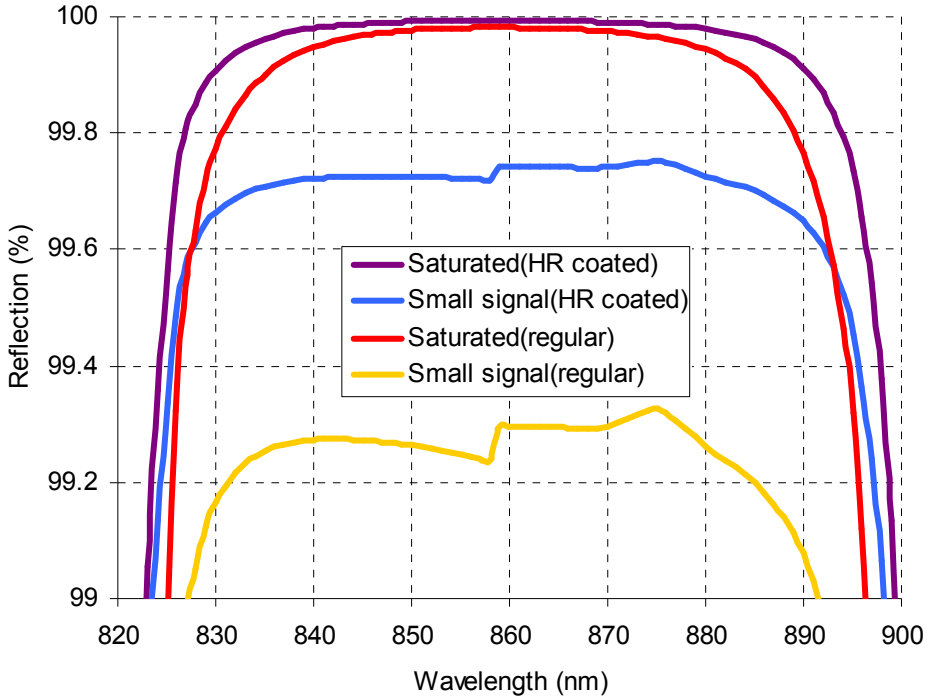

Figure F10: Effect of one pair of SiO_2/TiO_2 high reflective layer coating on the reflection of MIT 860 nm regular SESAM/SBR design with quantum well absorber (zoomed into the main reflectivity band).

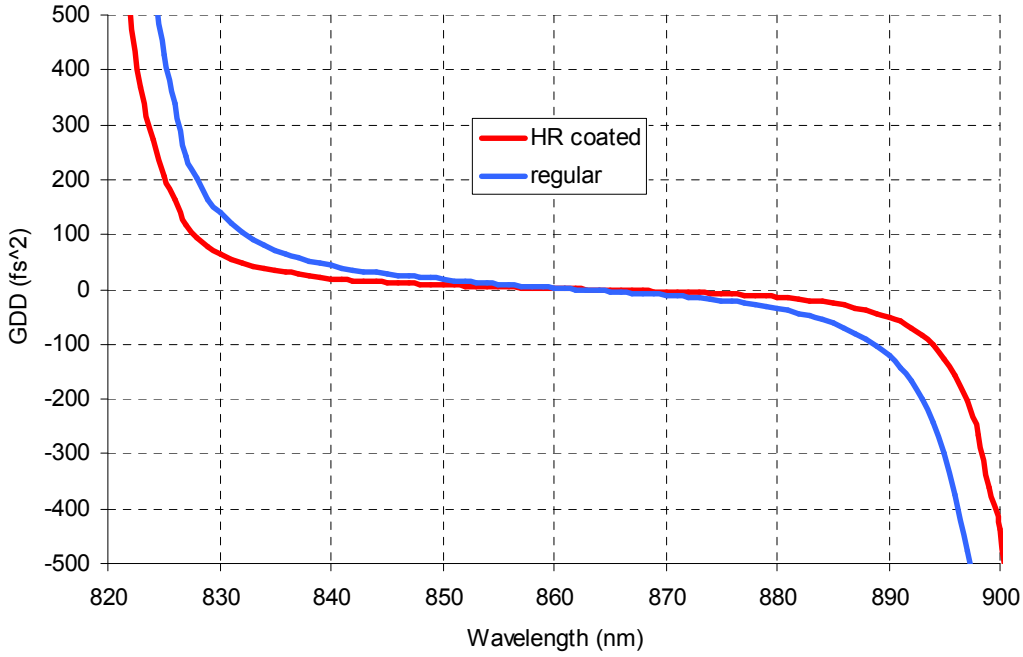

Figure F11: Effect of one pair of SiO_2/TiO_2 high reflective layer coating on the dispersion of MIT 860 nm regular SESAM/SBR design with quantum well absorber.

F.4 MIT 880 nm SESAM/SBR with Quantum Well Absorber

Layer	Material	Physical thickness (nm)	Optical thickness (nm)	n	Purpose
0	GaAs	-	-	-	Substrate
1	$Al_{0.95}Ga_{0.05}As$	73.13	220	3.01	Bragg layer
2	$Al_{0.07}Ga_{0.93}As$	61.87	220	3.56	Bragg layer
…					Bragg layers
49	$Al_{0.95}Ga_{0.05}As$	73.13	220	3.01	Bragg layer
50	$Al_{0.07}Ga_{0.93}As$	61.87	220	3.56	Bragg layer
51	$Al_{0.95}Ga_{0.05}As$	73.13	220	3.01	Bragg layer
52	$Al_{0.07}Ga_{0.93}As$	15	53.34	3.56	Barrier
53	$In_{0.14}Ga_{0.90}As$	7	25.69	3.67	Absorber
54	$Al_{0.07}Ga_{0.93}As$	50	177.80	3.56	Barrier/cap

Table F5: MIT 880 nm regular SESAM/SBR design with quantum well absorber. The expected band edge for $Al_{0.07}Ga_{0.93}As$ Bragg layer is around 822 nm. The expected band edge for the 7 nm thick strained $In_{0.14}Ga_{0.86}As$ quantum well absorber is around 930 nm. Note: To make this design more immune to possible growth errors one might want to increase the Al content of $Al_{0.07}Ga_{0.93}As$ that is used in the Bragg mirror (maybe to 9%).

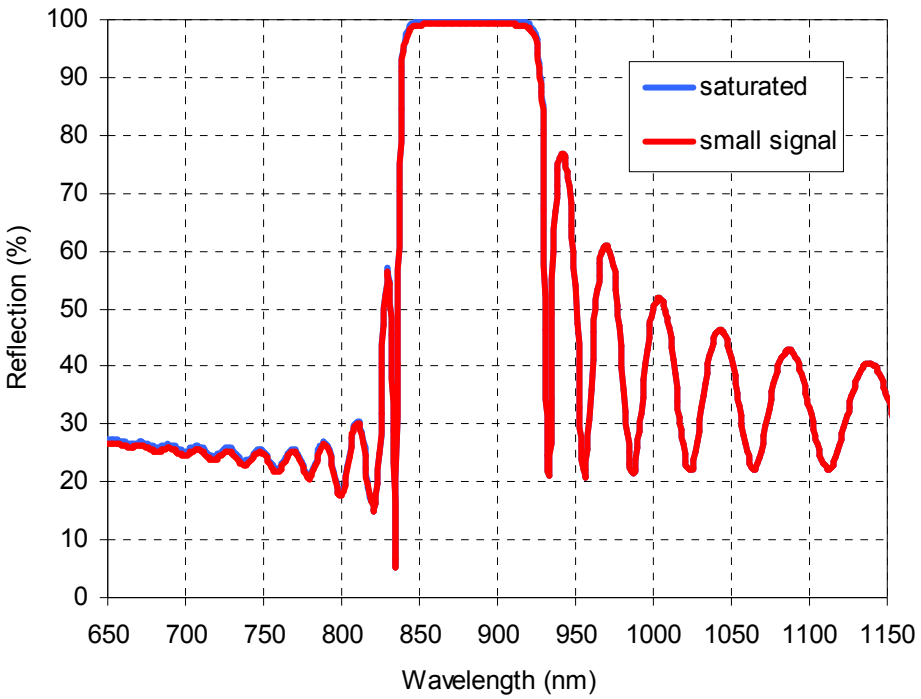

Figure F12: Calculated reflection of MIT 880 nm regular SESAM/SBR design with quantum well absorber for small signal and saturated cases.

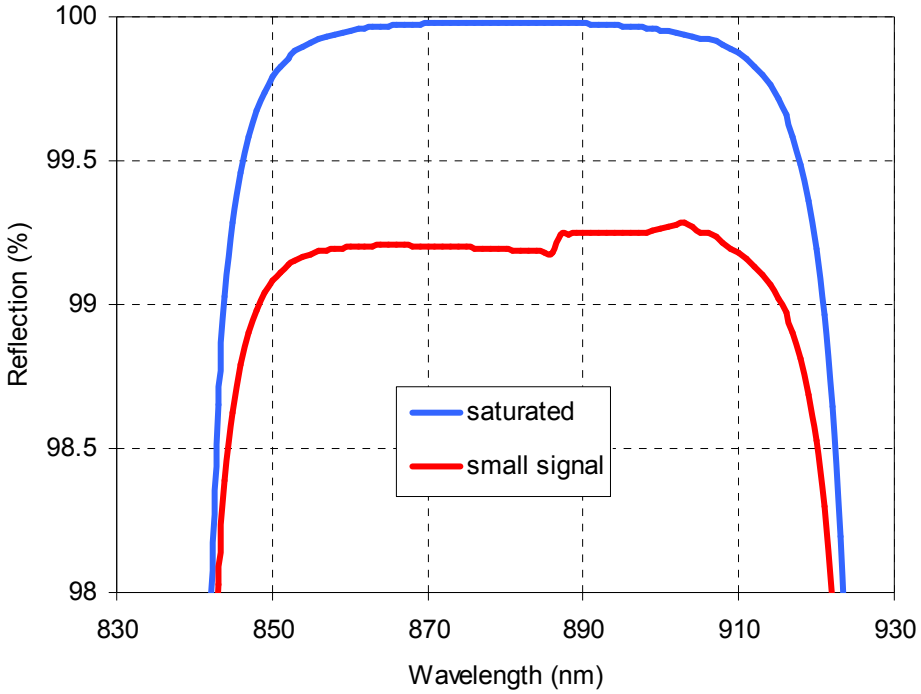

Figure F13: Calculated reflection of MIT 880 nm regular SESAM/SBR design with quantum well absorber for small signal and saturated cases (zoomed into the main reflectivity band).

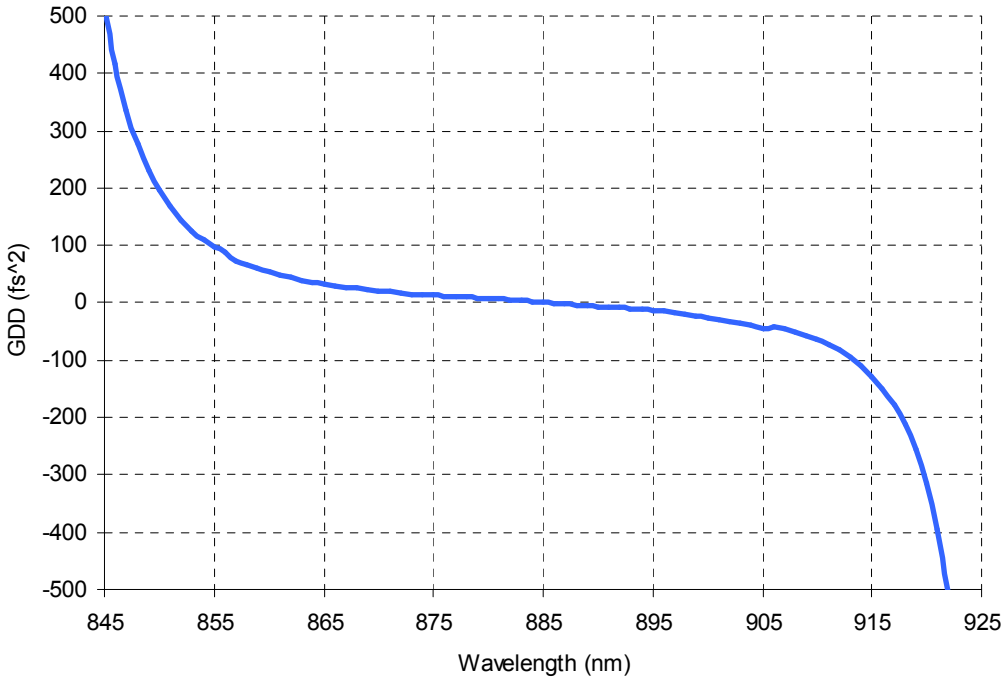

Figure F14: Calculated dispersion of MIT 880 nm regular SESAM/SBR design with quantum well absorber.

F.5 MIT 925 nm SESAM/SBR with quantum well absorber

Layer	Material	Physical thickness (nm)	Optical thickness (nm)	n	Purpose
0	GaAs	-	-	-	Substrate
1	$Al_{0.95}Ga_{0.05}As$	77.24	231.25	2.99	Bragg layer
2	GaAs	64.95	231.25	3.56	Bragg layer
…					Bragg layers
49	$Al_{0.95}Ga_{0.05}As$	77.24	231.25	2.99	Bragg layer
50	GaAs	64.95	231.25	3.56	Bragg layer
51	$Al_{0.95}Ga_{0.05}As$	77.24	231.25	2.99	Bragg layer
52	GaAs	15	53.41	3.56	Barrier
53	$In_{0.20}Ga_{0.80}As$	7	25.68	3.67	Absorber
54	GaAs	50	178.03	3.56	Barrier/cap

Table F6: MIT 925 nm regular SESAM/SBR design with quantum well absorber. The expected band edge for GaAs Bragg layer is around 872 nm. The expected band edge for the 7 nm thick strained $In_{0.20}Ga_{0.80}As$ quantum well absorber is around 977 nm.

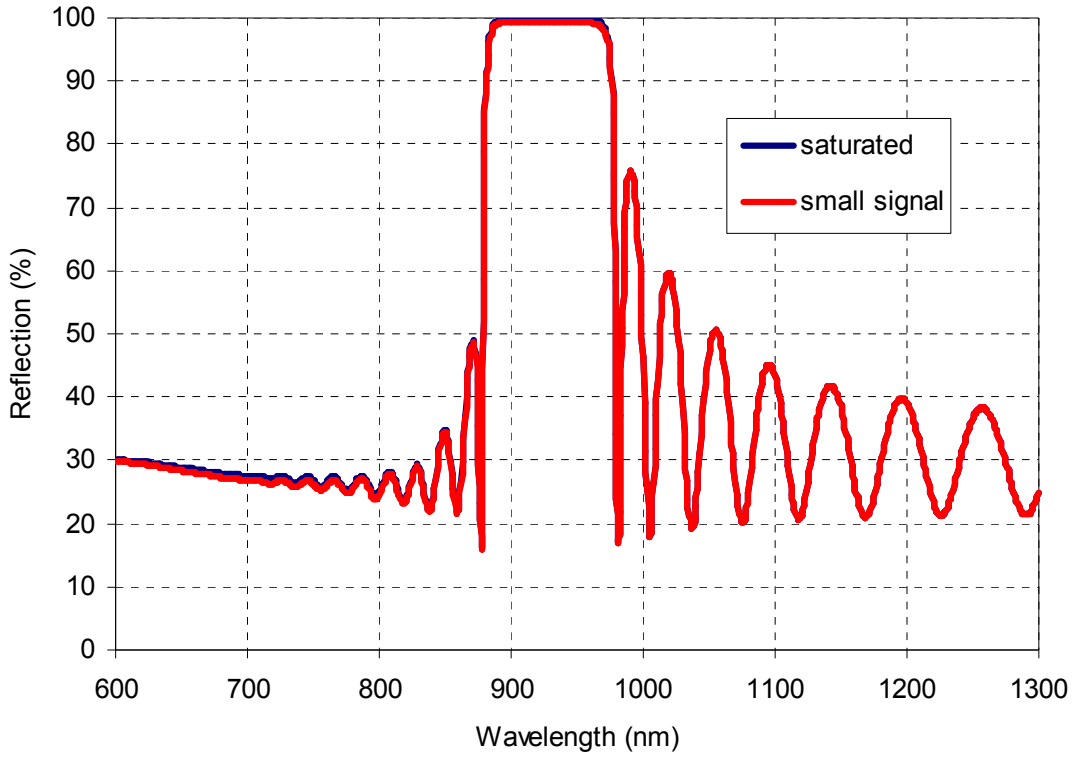

Figure F15: Calculated reflection of MIT 925 nm regular SESAM/SBR design with quantum well absorber for small signal and saturated cases.

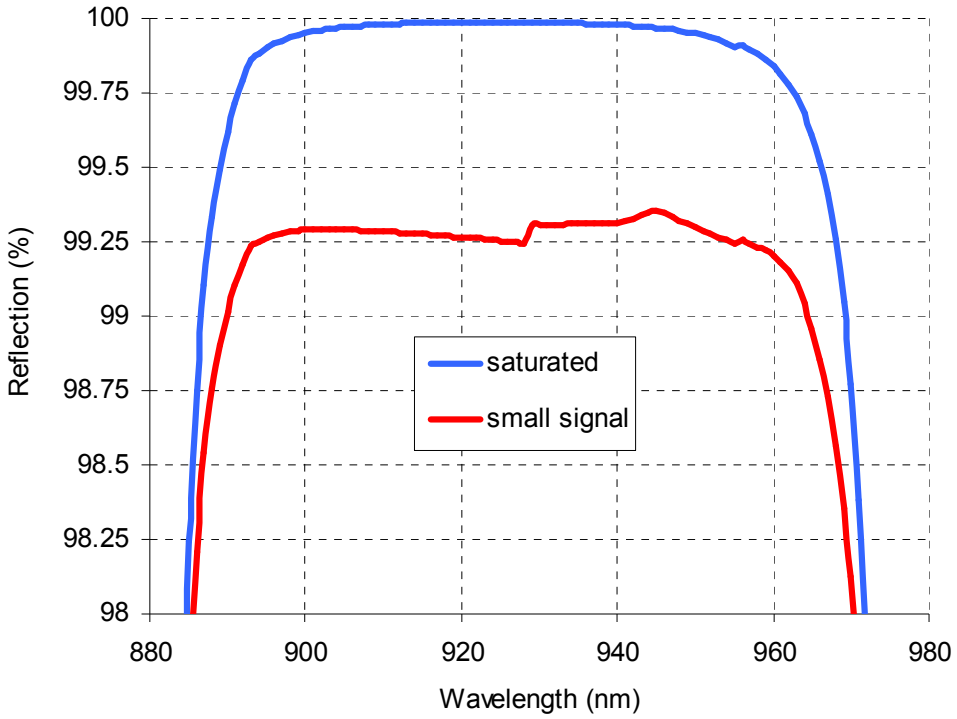

Figure F16: Calculated reflection of MIT 925 nm regular SESAM/SBR design with quantum well absorber for small signal and saturated cases (zoomed into the main reflectivity band).

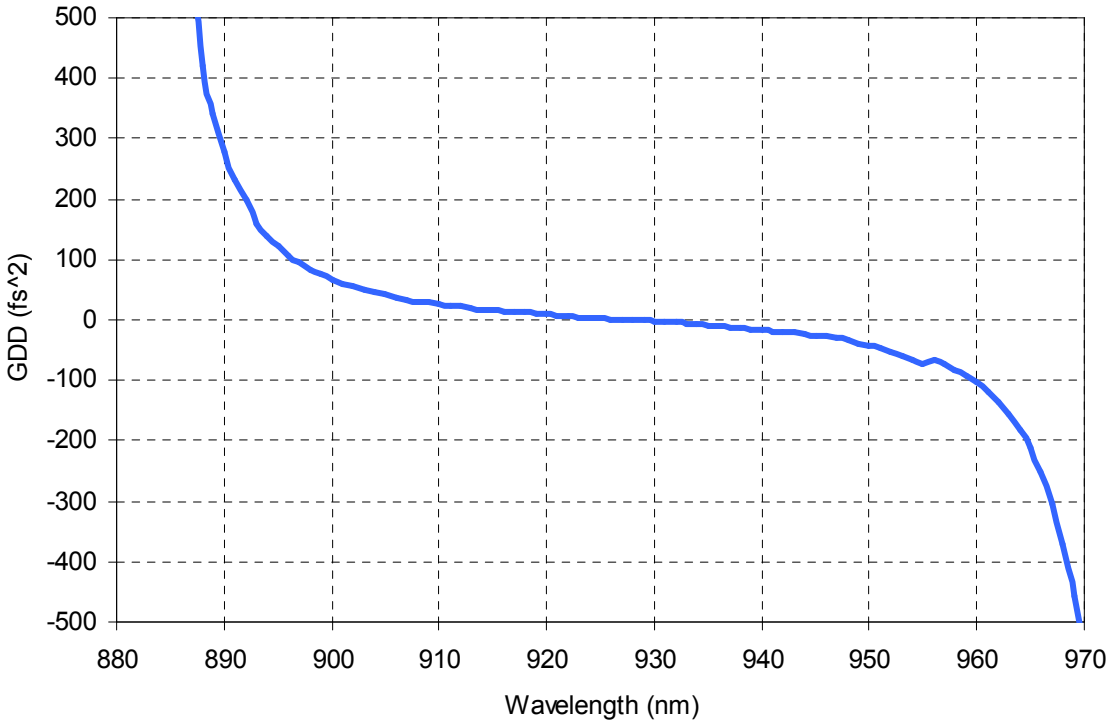

Figure F17: Calculated dispersion of MIT 925 nm regular SESAM/SBR design with quantum well absorber.

APPENDIX G

LIST OF LABORATORY NOTEBOOKS

In this Appendix, we will provide a list of lab notebooks that was used during this PhD work, for easy reference in the future.

Notebook number	Start Date	Notes
1	July 10, 2006	1-W n-light diode pumping of Cr:LiCAF
2	November 06, 2006	1-W n-light diode pumping of Cr:LiCAF
3	January 28, 2007	1-W n-light diode pumping of Cr:LiCAF
4	July 28, 2007	Repetition rate multiplication project
5	August 16, 2007	Comparative pumping of Cr:LiCAF, JOSA B article results (single mode pumping, Ti:Sapphire pumping, 1.5 W n-light diode pumping)
6	Feb 25, 2008	MPC Cr:LiCAF project
7	March 13, 2008	Cavity dumped Cr:LiCAF laser project
8	March 13, 2008	Asymmetric cavity mode Cr:LiCAF laser project
9	March 13, 2008	Multiphoton imaging project
10	May, 2008	10-20 fs Cr:LiCAF laser project
11	January 28, 2007	Notes on 5-fs Ti:Sapphire laser and pump probe setup
12	July 15, 2008	Cr:LiSAF project
13	August 13, 2008	Microwave frequency generation from Cr:Colquiriites
14	August, 2008	SESAM/SBR Design
15	December 27, 2008	Diode pumped Cr:LiSGaF project
16	May 15, 2009	TL Cr:Colquiriites project

Table G1: List of lab notebooks used by UD during this PhD work.

VITA

Umit Demirbas was born in Egirdir (Turkey) in 1979. He received his BS degrees in physics (2004) and electrical & electronics engineering (2004), and his MS degree in materials science (2006) from Koc University. He recently obtained his PhD degree in electrical engineering and computer science from MIT (2010).

During his undergraduate and MS years, Mr. Demirbas was with the Koc University Laser Research Laboratory, where he mainly worked on development of broadly-tunable Cr:ZnSe lasers under the supervision of Prof. Alphan Sennaroglu. During his PhD years he was a member of the Optics and Quantum Electronics Group at the Research Laboratory of Electronics of MIT, where he worked on the development of low-cost femtosecond Cr:Colquiriite lasers under the supervision of Prof. James Fujimoto and Prof. Franz Kärtner. His current research interests include solid-state laser development, ultrafast pulse generation, laser noise and multiphoton microscopy.

Mr. Demirbas is an author and coauthor of more than 15 journal papers. He serves as reviewer for Optics Letters, Optics Express, Applied Optics, Optics Communications, Optical & Quantum Electronics and Materials Characterization journals. He is a student member of Institute of Electrical and Electronics Engineers (IEEE) Photonics Society, Optical Society of America (OSA), The International Society for Optical Engineering (SPIE), and Optical Committee of Turkey (OCT). He is a IEEE Photonics Society Graduate Student Fellow (2009) and one of the finalists of OSA New Focus/Bookham Student Award (2008).

JOURNAL ARTICLES

1. Duo Li, **Umit Demirbas**, Jonathan R. Birge, Gale S. Petrich, Leslie A. Kolodziejski, Alphan Sennaroglu, Franz X. Kärtner, and James G. Fujimoto, "Diode-pumped passively mode-locked GHz femtosecond Cr:LiSAF laser with kW peak power", Optics Letters, 35, 1446-1449 (2010).

2. **Umit Demirbas**, Kyung-Han Hong, James G. Fujimoto, Alphan Sennaroglu and Franz X. Kärtner, "A low-cost cavity-dumped femtosecond Cr^{3+}:LiSAF laser producing >100 nJ pulses", Optics Letters, 35, 607-609, (2010).

3. **Umit Demirbas**, Duo Li, Alphan Sennaroglu, Gale S. Petrich, Leslie A. Kolodziejski, Franz X. Kärtner, and James G. Fujimoto, "Low-cost, single-mode diode-pumped Cr:Colquiriite lasers", Optics Express, 17, 14374-14388 (2009).

4. **Umit Demirbas**, Alphan Sennaroglu, Franz X. Kärtner, James G. Fujimoto, "Generation of 15-nJ pulses from a highly efficient, low-threshold, multipass-cavity Cr^{3+}:LiCAF laser", Optics Letters, 34, 497-499 (2009).

5. **Umit Demirbas**, Alphan Sennaroglu, Franz X. Kärtner, James G. Fujimoto, "Comparative investigation of diode pumping for continuous-wave and mode-locked Cr:LiCAF lasers", JOSA B, 26, 64-79 (2009).

6. Alphan Sennaroglu, Ahmet F. Coskun, **Umit Demirbas**, "Analysis of solid-state saturable absorbers with temperature-dependent absorption cross sections", Optical Materials, 31, 598-603 (2009).

7. Sava Sakadzic†, **Umit Demirbas**†, Svetlana Ruvinskaya, Thorsten R. Mempel, Anna Moore, David Boas, Alphan Sennaroglu, Franz X. Kärtner, and James G. Fujimoto, "Multiphoton microscopy with a compact, low-cost and highly-efficient Cr:LiCAF laser", Optics Express, 16, 20848-20863 (2008).
    - †Contributed equally to this work

8. Huseyin Cankaya**, Umit Demirbas**, Ahmet K. Erdamar, Alphan Sennaroglu "Absorption Saturation analysis of Cr:ZnSe and Fe:ZnSe", JOSA B, 25, 794-800 (2008).
9. **Umit Demirbas**, Alphan Sennaroglu, Franz X. Kärtner, James G. Fujimoto, "Highly efficient, low-cost femtosecond Cr^{3+}:LiCAF laser pumped by single-mode diodes", Optics Letters, 33, 590-592 (2008).
10. **Umit Demirbas**, Alphan Sennaroglu, Andrew Benedick, Aleem Siddiqui, Franz X. Kärtner, James G. Fujimoto, "Diode-pumped, high-average power femtosecond Cr^{3+}:LiCAF laser", Optics Letters, 32, 3309-3311 (2007).
11. Alphan Sennaroglu**, Umit Demirbas**, Adnan Kurt & Mehmet Somer, "Direct Experimental Determination of the Optimum Chromium Concentration in Continuous-wave Cr:ZnSe Lasers", IEEE Journal of Selected Topics in Quantum Electronics, 13, 823-830, (2007).
12. Alphan Sennaroglu, **Umit Demirbas**, Adnan Kurt & Mehmet Somer, "Concentration Dependence of Fluorescence and Lasing Efficiency in Cr:ZnSe Lasers", Optical Materials, 29, 703-708 (2007).
13. **Umit Demirbas** and Alphan Sennaroglu "Intracavity-pumped Cr^{2+}:ZnSe laser with ultrabroad tuning range between 1880 and 3100 nm ", Optics Letters, 31, 2293-2295 (2006).
14. **Umit Demirbas**, Adnan Kurt, Alphan Sennaroglu, Emel Yilgor & Iskender Yilgor "Luminescent Nd^{3+} Doped Silicone-Urea Copolymers", Polymer, 47, 982-990 (2006).
15. Alphan Sennaroglu, **Umit Demirbas**, Nathalie Vermeulen, Heidi Ottevaere & Hugo Thienpont, "Continuous-Wave Broadly Tunable Cr^{2+}:ZnSe Laser Pumped by a Thulium Fiber Laser", Optics Communications, 268, 115-120 (2006).
16. Alphan Sennaroglu, **Umit Demirbas**, Sarper Ozharar & Fatih Yaman, "Accurate Determination of Saturation Parameters for Cr^{4+}:Doped Solid-State Saturable Absorbers", JOSA B, 23, 241-249 (2006).
17. **Umit Demirbas**, Alphan Sennaroglu & Mehmet Somer, "Synthesis and Characterization of Diffusion-Doped Cr^{2+}:ZnSe and Fe^{2+}:ZnSe", Optical Materials, 28, 231-240 (2006).
18. Alphan Sennaroglu, Idris Kabalci, Adnan Kurt, **Umit Demirbas** & Gonul Ozen, "Spectroscopic Properties of Tm^{3+}:TeO_2-PbF_2 glasses", Journal of Luminescence, 116, 79-86 (2006).

MANUSCRIPTS UNDER REVIEW OR IN PREPARATION

19. **Umit Demirbas**†, Gale S. Petrich†, Sheila Nabanja, Jonathan R. Birge, Leslie A. Kolodziejski, Franz X. Kärtner, and James G. Fujimoto, "Widely-Tunable Femtosecond Operation of Cr:LiSAF Lasers using Broadband Saturable Bragg Reflectors", (2010, in preparation). Note: This work has been accepted to CLEO 2010 conference.
    - †Contributed equally to this work
20. **Umit Demirbas**†, Andrew Benedick†, Alphan Sennaroglu, Duo Li, Jungwon Kim, James G. Fujimoto and Franz X. Kärtner, "Attosecond resolution timing jitter characterization of diode pumped femtosecond Cr:LiSAF lasers", (2010, in preparation). Note: This work has been accepted to CLEO 2010 conference.
    - †Contributed equally to this work

BIBLIOGRAPHY

1. S. A. Payne, L. L. Chase, H. W. Newkirk, L. K. Smith, and W. F. Krupke, "$LiCaAlF_6:Cr^{3+}$ a promising new solid-state laser material," IEEE J. Quantum Electron. **24**, 2243-2252 (1988).
2. R. Scheps, J. F. Myers, and S. A. Payne, "Cw and Q-Switched Operation of a Low Threshold Cr+3-Licaalf6 Laser," IEEE Photonic. Tech. L. **2**, 626-628 (1990).
3. S. A. Payne, L. L. Chase, L. K. Smith, and B. H. T. Chai, "Flashlamp-Pumped Laser Performance of Licaaif6 Cr-3+," Optical and Quantum Electronics **22**, S259-S268 (1990).
4. S. A. Payne, L. L. Chase, L. K. Smith, W. L. Kway, and H. W. Newkirk, "Laser performance of $LiSAIF_6:Cr^{3+}$," J. Appl. Phys. **66**, 1051-1056 (1989).
5. S. A. Payne, L. K. Smith, R. J. Beach, B. H. T. Chai, J. H. Taasano, L. D. DeLoach, W. L. Kway, R. W. Solarz, and W. F. Krupke, "Properties of $Cr:LiSrAIF_6$ Crystals for laser operation," Appl. Opt. **33**, 5526-5536 (1994).
6. L. K. Smith, S. A. Payne, W. L. Kway, L. L. Chase, and B. H. T. Chai, "Investigation of the laser properties of $Cr^{3+}:LiSrGaF_6$," IEEE J. Quantum Electron. **28**, 2612-2618 (1992).
7. A. Einstein, "Quantum theory of radiation," Physikalische Zeitschrift **18**, 121-128 (1917).
8. http://commons.wikimedia.org/wiki/File:Townes.jpg, Accessed March 28, 2010.
9. http://en.wikipedia.org/wiki/File:Hydrogen_maser.jpg, Accessed March 28, 2010.
10. http://laserinventor.com/images/Holding_First_Laser.jpg, Accessed March 28, 2010.
11. http://en.wikipedia.org/wiki/Fair_use, Accessed March 29, 2010.
12. W. E. Lamb, and R. C. Retherford, "Fine Structure of the Hydrogen Atom by a Microwave Method," Phys. Rev. A **72**, 241 (1947).
13. J. P. Gordon, H. J. Zeiger, and C. H. Townes, "Molecular Microwave Oscillator and New Hyperfine Structure in Microwave Spectrum of NH3," Phys. Rev. **95**, 282 (1954).
14. J. P. Gordon, H. J. Zeiger, and C. H. Townes, "The Maser--New Type of Microwave Amplifier, Frequency Standard, and Spectrometer," Phys. Rev. **99**, 1264 (1955).
15. A. L. Schawlow, and C. H. Townes, "Infared and optical masers," Phys. Rev. **112**, 1940-1949 (1958).
16. W. Koechner, *Solid-state laser engineering* (Springer, New York, 2006).
17. T. H. Maiman, "Stimulated optical radiation in ruby," Nature **187**, 493-494 (1960).
18. M. J. Weber, *Handbook of Laser Wavelengths* (CRC Press, 1998).
19. M. A. Johnson, A. L. Betz, R. A. McLaren, E. C. Sutton, and C. H. Townes, "Nonthermal 10 micron CO2 emission lines in the atmospheres of Mars and Venus," Astrophys. J. **208**, L145 (1976).
20. V. Strelnitski, M. R. Haas, H. A. Smith, E. F. Erickson, S. W. J. Colgan, and D. J. Hollenbach, "Far-infrared hydrogen lasers in the peculiar star MWC 349A," Science **272**, 1459 (1996).
21. S. R. Wilk, "Defunct Lasers," OPN Optics & Photonics News **21**, 10-11 (2010).
22. E. Sorokin, "Solid-state materials for few-cycle pulse generation and amplification," in *Few-cycle laser pulse generation and its applications*, F. X. Kärtner, ed. (Springer-Verlag, Berlin, 2004), pp. 3-71.
23. http://en.wikipedia.org/wiki/File:Laser_DSC09088.JPG, Accessed March 28, 2010.
24. http://creativecommons.org/licenses/by/2.5/deed.en.
25. F. P. Schäfer, F. P. W. Schmidth, and J. Volze, "Organic Dye Solution Laser," Appl. Phys. Lett. **9**, 306-308 (1966).
26. P. P. Sorokin, and J. R. Lankard, "Stimulated Emission observed from an organic dye, cloro-aluminum phthalocyanine," IBM J. Res. Rev. **10**, 162-163 (1966).
27. J. A. Valdmanis, R. L. Fork, and J. P. Gordon, "Generation of optical pulses as short as 27 fs directly from a laser balancing self-phase modulation, group-velocity dispersion, saturable absorption, and saturable gain," Optics Lett. **10**, 131-133 (1985).
28. R. L. Fork, C. H. B. Cruz, P. C. Becker, and C. V. Shank, "Compression of optical pulses to six femtoseconds by using cubic phase compensation," Opt. Lett. **12**, 483-485 (1987).
29. R. Paschotta, *Encyclopedia of Laser Physics and Technology* (Wiley-VCH 2008).

30. R. Paschotta, and U. Keller, "Ultrafast solid-state lasers," in *Ultrafast Lasers: Technology and Applications*(Marcel Dekker, Inc., 2003).
31. http://commons.wikimedia.org/wiki/User:Hankwang, Accessed March 28, 2010.
32. http://en.wikipedia.org/wiki/File:Coherent_899_dye_laser.jpg, Accessed March 28, 2010.
33. L. K. Smith, S. A. Payne, W. F. Krupke, L. D. DeLoach, R. Morris, E. W. O'Dell, and D. J. Nelson, "Laser emission from the transition-metal compound LiSrCrF6," Opt. Lett. **18**, 200-202 (1993).
34. Y. Kalisky, *The Physics and Engineering of Solid State Lasers* (SPIE Publications, 2006).
35. W. Gellermann, "Color center lasers," J. Phys. Chem. Solids **52**, 249-297 (1991).
36. B. Fritz, and E. Menke, "Laser effect in KC1 with FA (Li) centers," Solid State Commun. **3**, 61 (1965).
37. M. N. Islam, E. R. Sunderman, C. E. Soccolich, I. Barjoseph, N. Sauer, and T. Y. Chang, "Color Center Lasers Passively Mode-Locked by Quantum Wells," IEEE J. Quantum Electron. **25**, 2454-2463 (1989).
38. H. R. Aldag, and D. H. Titterton, "From flashlamp-pumped liquid dye lasers to diode-pumped solid-state dye lasers (Invited Paper)," (SPIE 2005), p. 194.
39. D. P. Pacheco, W. H. Russell, and H. R. Aldag, "Solid state dye lasers pumped directly by diode lasers," in *Solid State Lasers XIII: Technology and Devices* (SPIE, San Jose, Ca, USA 2004), p. 180.
40. U. Kellera, and A. C. Tropper, "Passively modelocked surface-emitting semiconductor lasers," Physics Reports **429**, 67-120 (2006).
41. R. Scheps, *Introduction to Laser Diode-Pumped Solid State Lasers* (SPIE Publications, 2002).
42. http://www.blueskyresearch.com/fileupload/pdfs/vpsl/VPSL-0660-130-X-5-G.pdf.
43. http://static.howstuffworks.com/gif/periodic-table-large.jpg, Accessed March 28, 2010.
44. http://www.howstuffworks.com/, Accessed March 28, 2010.
45. http://en.wikipedia.org/wiki/Rare_earth_element, Accessed March 29, 2010.
46. http://www.britannica.com/EBchecked/topic/491579/rare-earth-element, Accessed March 28, 2010.
47. http://en.wikipedia.org/wiki/Abundance_of_elements_in_Earth%27s_crust, Accessed March 28, 2010.
48. O. Svelto, *Principles of Lasers* (Plenum Press, New York, 1989).
49. http://en.wikipedia.org/wiki/Transition_metal, Accessed March 29, 2010.
50. http://goldbook.iupac.org/T06456.html, Accessed March 29, 2010.
51. A. J. S. McGonigle, D. W. Coutts, and C. E. Webb, "530-mW 7-kHz cerium LiCAF laser pumped by the sum-frequency-mixed output of a copper-vapor laser," Opt. Lett. **24**, 232-234 (1999).
52. E. Granados, D. W. Coutts, and D. J. Spence, "Mode-locked deep ultraviolet Ce:LiCAF laser," Opt. Lett. **34**, 1660-1662 (2009).
53. J. F. Pinto, L. Esterowitz, and G. J. Quarles, "High performance Ce :LiSrAlF /LiCaAlF lasers with extended tunability," Electron. Lett.
31, 2009-2010 (1995).
54. A. J. S. McGonigle, S. Girard, D. W. Coutts, and R. Moncorgé, "10-kHz continuously tunable Ce:LiLuF laser," Electron. Lett. **35**, 1640-1641 (1999).
55. P. F. Moulton, "Spectroscopic and laser characteristics of Ti:Al_2O_3," JOSA B **3**, 125-133 (1986).
56. F. Druon, F. Balembois, and P. Georges, "New laser crystals for the generation of ultrashort pulses," Comptes Rendus Physique **8**, 153-164 (2007).
57. R. Ell, U. Morgner, F. X. Kärtner, J. G. Fujimoto, E. P. Ippen, V. Scheuer, G. Angelow, and T. Tschudi, "Generation of 5 fs pulses and octave-spanning spectra directly from a Ti:sapphire laser," Opt. Lett. **26**, 373-375 (2001).
58. J. C. Walling, O. G. Peterson, H. P. Jenssen, R. C. Morris, and E. W. O`Dell, "Tunable alexandrite lasers," IEE Journal of Quantum Electronics **16**, 1302-1315 (1980).
59. U. Demirbas, D. Li, J. R. Birge, A. Sennaroglu, G. S. Petrich, L. A. Kolodziejski, F. X. Kärtner, and J. G. Fujimoto, "Low-cost, single-mode diode-pumped Cr:Colquiriite lasers " Opt. Express **17**, 14374-14388 (2009).

60. P. Wagenblast, U. Morgner, F. Grawert, V. Scheuer, G. Angelow, M. J. Lederer, and F. X. Kärtner, "Generation of sub-10-fs pulses from a Kerr-lens modelocked Cr^{3+}:LiCAF laser oscillator using third order dispersion compensating double chirped mirrors," Opt. Lett. **27**, 1726-1729 (2002).
61. I. T. Sorokina, E. Sorokin, E. Wintner, A. Cassanho, H. P. Jenssen, and M. A. Noginov, "Efficient cw TEM00 and femtosecond Kerr-lens modelocked Cr:LiSrGaF laser," Optics Lett. **21**, 204-206 (1996).
62. I. T. Sorokina, E. Sorokin, E. Wintner, A. Cassanho, H. P. Jenssen, and R. Szipocs, "14-fs pulse generation in Kerr-lens mode-locked prismless Cr:LiSGaF and Cr:LiSAF lasers: observation of pulse self-frequency shift," Opt. Lett. **22**, 1716-1718 (1997).
63. M. Stalder, B. H. T. Chai, and M. Bass, "Flashlamp pumped Cr:$LiSrAlF_6$ laser," Appl. Phys. Lett. **58**, 216-218 (1991).
64. S. Uemura, and K. Torizuka, "Generation of 10 fs pulses from a diode-pumped Kerr-lens mode-locked Cr : LiSAF laser," Jpn. J. Appl. Phys. **39**, 3472-3473 (2000).
65. E. Sorokin, M. H. Ober, I. Sorokina, E. Wintner, A. J. Schmidt, A. I. Zagumennyi, G. B. Loutts, E. W. Zhariko, and I. A. Shcherbakov, "Femtosecond solid-state lasers using Nd3+-doped mixed scandium garnet," JOSA B **10**, 1436–1442 (1993).
66. J. A. D. Au, D. Kopf, F. MorierGenoud, M. Moser, and U. Keller, "60-fs pulses from a diode-pumped Nd:glass laser," Opt. Lett. **22**, 307-309 (1997).
67. S. Han, W. Lu, B. Y. Sheh, L. Yan, M. Wraback, H. Shen, J. Pamulapati, and P. G. Newman, "Generation of sub-40fs pulses from a mode-locked dual-gainmedia
Nd:glass laser," Appl. Phys. B **74**, 177-179 (2002).
68. V. G. Baryshevskii, M. V. Korzhik, A. E. Kimaev, M. G. Livshits, V. B. Pavlenko, M. L. Meil'man, and B. I. Minkov, "Tunable chromium forsterite laser in the near IR region," Journal of Applied Spectroscopy (USSR) **53**, 675-676 (1990).
69. C. Chudoba, J. G. Fujimoto, E. P. Ippen, H. A. Haus, U. Morgner, F. X. Kärtner, V. Scheuer, G. Angelow, and T. Tschudi, "All-solid-state Cr:forsterite laser generating 14 fs pulses at 1.3 um," Opt. Lett. **26**, 292-294 (2001).
70. S. Kuck, K. Petermann, U. Pohlmann, U. Schonhoff, and G. Huber, "Tunable room-temperature laser action of a Cr-4+-doped Y3ScxAl5-xO12," Applied Physics B **58**, 153-156 (1994).
71. D. J. Ripin, C. Chudoba, J. T. Gopinath, J. G. Fujimoto, E. P. Ippen, U. Morgner, F. X. Kartner, V. Scheuer, G. Angelow, and T. Tschudi, "Generation of 20-fs pulses by a prismless Cr4+: YAG laser," Opt. Lett. **27**, 61-63 (2002).
72. C. Honninger, F. Morier-Genoud, M. Moser, U. Keller, L. R. Brovelli, and C. Harder, "Efficient and tunable diode-pumped femtosecond Yb:glass lasers," Opt. Lett., 126-128 (1998).
73. Y. Zaouter, J. Didierjean, F. Balembois, G. Lucas-Leclin, F. Druon, P. Georges, J. Petit, P. Goldner, and B. Viana, "47-fs diode-pumped Yb3+:CaGdAlO4 laser," Opt. Lett. **31**, 119-121 (2006).
74. F. Cornacchia, E. Sani, A. Toncelli, M. Tonelli, M. Marano, S. Taccheo, G. Galzerano, and P. Laporta, "Optical spectroscopy and diode-pumped laser characteristics
of codoped Tm-Ho:YLF and Tm-Ho:BaYF: a comparative analysis," Appl. Phys. B **75**, 817-822 (2002).
75. R. C. Stoneman, and L. Esterowitz, "Efficient, broadly tunable, laser-pumped Tm:YAG and Tm:YSGG cw lasers," Opt. Lett. **15**, 486-488 (1990).
76. J. F. Pinto, L. Esterowitz, and G. H. Rosenblatt, "Continuous-wave mode-locked 2-μm Tm:YAG laser," Opt. Lett. **17**, 731-733 (1992).
77. A. Dergachev, K. Wall, and P. F. Moulton, "A CW Side-Pumped Tm:YLF Laser," in *OSA TOPS Advanced Solid State Lasers*, M. E. Fermann, and L. R. Marshall, eds. (OSA, 2002), pp. 343-346.
78. J. F. Pinto, and L. Esterowitz, "Tm^{3+}:YLF laser continuously tunable between 2.20 and 2.46 μm," Opt. Lett. **19**, 883-885 (1994).
79. D. Welford, and P. F. Moulton, "Romm-temperature operation of a Co:MgF_2 laser," Opt. Lett. **13**, 975-977 (1988).
80. I. T. Sorokina, E. Sorokin, S. Mirov, V. Fedorov, V. Badikov, V. Panyutin, and K. I.Schaffers, "Broadly tunable compact continuous-wave Cr^{2+}:ZnS laser," Opt. Lett. **27**, 1040-1042 (2002).

81. E. Sorokin, I. T. Sorokina, M. S. Mirov, V. V. Fedorov, I. S. Moskalev, and S. B. Mirov, "Ultrabroad continuous-wave tuning of ceramic Cr:ZnSe and Cr:ZnS lasers," in *OSA / ASSP/LACSEA/LS&C*(OSA, 2010).
82. J. McKay, K. L. Schepler, and G. C.Catella, "Efficient grating-tuned mid-infrared Cr^{2+}:CdSe laser," Opt. Lett. **24**, 1575-1577 (1999).
83. V. A. Akimov, M. P. Frolov, Y. V. Korostelin, V. I. Kozlovsky, A. I. Landman, Y. P. Podmar'kov, Y. K. Skasyrsky, and A. A. Voronov, "Pulsed broadly tunable room-temperature Cr2+:CdS laser," Appl. Phys. B **97**, 793-797 (2009).
84. V. A. Akimov, V. I. Kozovskii, Y. V. Korostelin, A. I. Landman, Y. P. Podmar'kov, Y. K. Skasyrskii, and M. P. Frolov, "Efficient pulsed Cr2+: CdSe laser continuously tunable in the spectral range from 2.26 to 3.61," Quantum Electronics **38**, 205-208 (2008).
85. U. Demirbas, and A. Sennaroglu, "Intracavity-pumped Cr2+: ZnSe laser with ultrabroad tuning range between 1880 and 3100 nm," Opt. Lett. **31**, 2293-2295 (2006).
86. I. T. Sorokina, E. Sorokin, and T. Carrig, "Femtosecond Pulse Generation from a SESAM Mode-Locked Cr:ZnSe Laser," in *CLEO/QELS* (Long Beach, CA, USA, 2006), pp. paper CMQ2, Technical Digest on CD.
87. I. T. Sorokina, E. Sorokin, T. J. Carrig, and K. I. Scaffers, "A SESAM passively mode-locked Cr:ZnSe laser," in *Advanced Solid-State Photonics*(Optical Society of America, Incline Village, Nevada, 2006), p. TuA4.
88. J. Kernal, V. V. Fedorov, A. Gallian, S. B. Mirov, and V. V. Badikov, "3.9-4.8 μm gain-switched lasing of Fe:ZnSe at room temperature," Optics Express **13**, 10608-10615 (2005).
89. I. T. Sorokina, "Crystalline Mid-Infrared Lasers," in *Solid-State Mid-Infrared Laser Sources*, I. T. Sorokina, and K. L. Vodopyanov, eds. (Springer, Berlin Heidelberg, 2003), pp. 255-349.
90. I. T. Sorokina, "Cr^{2+}-doped II-VI materials for lasers and nonlinear optics," Opt. Mater. **26**, 395-412 (2004).
91. A. Sennaroglu, "Broadly tunable Cr^{4+} -doped solid-state lasers in the near infrared and visible," Progress in Quantum Electronics **26**, 287-352 (2002).
92. A. A. Kaminskii, "Modern Developments in the physics of crystalline laser materials," Phys. Stat. Sol. **200**, 215-296 (2003).
93. S. Kück, "Laser-related spectroscopy of ion-doped crystals for tunable solid-state lasers," Appl. Phys. B **72**, 515-562 (2001).
94. E. Sorokin, S. Naumov, and I. T. Sorokina, "Ultrabroadband infrared solid-state lasers," IEEE J. Sel. Top. Quantum Electron. **11**, 690-712 (2005).
95. P. F. Moulton, "Tunable solid-state lasers," Proceedings of the IEEE **80**, 348-364 (1992).
96. J. C. Walling, D. F. Heller, H. Samelson, D. J. Harter, J. A. Pete, and R. C. Morris, "Tunable alexandrite lasers:development and performance," IEE Journal of Quantum Electronics **QE-21**, 1568-1581 (1985).
97. D. W. Coutts, and A. J. S. McGonigle, "Cerium-Doped Fluoride Lasers," IEEE J. Quantum Electron. **40**, 1430-1440 (2004).
98. S. Ono, Z. Liu, and N. Sarukura, "All-Solid-State Ultraviolet Cerium Lasers," in *Solid-State Lasers and Applications* A. Sennaroglu, ed. (2006), pp. 163-191.
99. Z. Liu, T. Kozeki, Y. Suzuki, N. Sarukura, K. Shimamura, T. Fukuda, M. Hirano, and H. Hosono, "Chirped-pulse amplification of ultraviolet femtosecond pulses by use of Ce3+:LiCaAlF6 as a broadband, solid-state gain medium," Opt. Lett. **26**, 301-303 (2001).
100. P. F. Moulton, "Ti-doped sapphire: tunable solid-state laser," in *Optics News*(1982), p. 9.
101. L. G. DeShazer, and K. W. Kangas, "Extended infared operation of titanium sapphire laser," Conference on Lasers and Electro Optics **14**, 296-298 (1987).
102. P. W. Roth, A. J. Maclean, D. Burns, and A. J. Kemp, "Directly diode-laser-pumped Ti:sapphire laser," Opt. Lett. **34**, 3334-3336 (2009).
103. http://www.coherent.com/Lasers/index.cfm?fuseaction=show.page&id=1851, Accessed March 29, 2010.

104. M. Arrigoni, B. Morioka, and A. Lepert, "OPTICALLY PUMPED SEMICONDUCTOR LASERS: Green OPSLs poised to enter scientific pump-laser market," Laser Focus World **45** (2009).
105. L. D. DeLoach, R. H. Page, G. D. Wilke, S. A. Payne, and W. F. Krupke, "Transition Metal-Doped Zinc Chalcogenides Spectroscopy and Laser Demonstration of a New Class of Gain Media," IEEE J. Quantum Electron. **32**, 885-895 (1996).
106. R. H. Page, K. I. Schaffers, L. D. DeLoach, G. D. Wilke, F. D. Patel, J. B. TassanoJr., S. A. Payne, W. F. Krupke, K.-T. Chen, and A. Burger, "Cr^{2+} Doped Zinc Chalcogenides as Efficient, Widely Tunable Mid-Infrared Lasers," IEEE J. Quantum Electron. **33**, 609-619 (1997).
107. J. McKay, and K. L. Schepler, "Kilohertz, 2.6-μm Cr^{2+}:CdSe laser," in *Advanced Solid-State Lasers*, M. M. Fejer, H. Injeyan, and U. Keller, eds. (OSA, 1999), pp. 420-426.
108. J. B. McKay, W. B. Roh, and K. L. Schepler, "Extended mid-IR tuning of a Cr^{2+}:CdSe laser," in *Advanced Solid State Photonics*, M. E. Fermann, and L. R. Marshall, eds. (OSA, Quebe, 2002), pp. 371-373.
109. A. G. Bluiett, U. Hommerich, R. T. Shah, S. B. Trivedi, S. W. Kutcher, and C. C. Wang, "Observation of lasing from Cr^{2+}:CdTe and compositional effects in Cr^{2+}-doped II-VI semiconductors," J. Electron. Mater. **31**, 806-810 (2002).
110. I. T. Sorokina, E. Sorokin, A. D. Lieto, M. Tonelli, B. N. Mavrin, and E. A. Vinogradov, "A new broadly tunable room temperature continuous-wave Cr^{2+}:ZnS_xSe_{1-x} laser," in *Advanced Solid State Photonics*, C. Denman, and I. T. Sorokina, eds. (OSA, Vienna, Austria, 2005), pp. 263-267.
111. U. Hommerich, X. Wu, V. R. Davis, S. B. Trivedi, K. Grasza, R. J. Chen, and S. Kutcher, "Demonstration of room-temperature laser action at 2.5 μm from Cr^{2+}:$Cd_{0.85}Mn_{0.15}Te$," Opt. Lett. **22**, 1180-1182 (1997).
112. U. Hömmerich, J. T. Seo, A. Bluiett, D. Temple, S. B. Trivedi, H. Zong, S. W. Kutcher, C. C. Wang, R. J. Chen, and B. Schumm, "Mid-infrared laser development based on transition metal doped cadmium manganese telluride," Luminescence, 1143-1145 (2000).
113. S. B. Trivedi, S. W. Kutcher, C. C. Wang, G. V. Jagannathan, U. Hommerich, A. Bluiett, M. Turner, J. T. Seo, K. L. Schepler, B. Schumm, P. R. Boyd, and G. Green, "Transition metal doped cadmium manganese telluride: a new material for tunable mid-infrared lasing," J. Electron. Mater. **30**, 728-732 (2001).
114. J. T. Seo, U. Hommerich, H. Zong, S. B. Trivedi, S. W. Kutcher, C. C. Wang, and R. J. Chen, "Mid-Infrared lasing from a novel optical material: chromium-doped $Cd_{0.55}Mn_{0.45}Te$," Phys. Stat. Sol. **175**, R3 (1999).
115. J. T. Seo, U. Hömmerich, S. B. Trivedi, R. J. Chen, and S. Kutcher, "Slope efficiency and tunability of Cr^{2+}:$Cd_{0.85}Mn_{0.15}Te$ mid-infrared laser," Opt. Commun., 267-270 (1998).
116. P. Cerny, H. Sun, D. Burns, U. N. Roy, and A. Burger, "Spectroscopic investigation and continuous wave laser demonstration utilizing single crystal Cr^{2+}:CdZnTe," in *Advanced Solid-State Photonics*, C. Denman, and I. T. Sorokina, eds. (OSA, Vienna, Austria, 2005), pp. 268-273.
117. M. Godlewski, and M. Kaminska, "The chromium impurity photogeneration transitions in ZnS, ZnSe and ZnTe," Journal of Physics C: Solid State Physics **13**, 6537-6545 (1980).
118. S. Bhaskar, P. S. Dobal, B. K. Rai, R. S. Katiyar, H. D. Bist, J.-O. Ndap, and A. Burger, "Photoluminescence study of deep levels in Cr-doped ZnSe," Applied Physics **85**, 439-443 (1998).
119. M. Godlewski, "Mechanisms of radiative and nonradiative recombination in ZnSe:Cr and ZnSe:Fe," Low Temperature Physics **30**, 891-896 (2004).
120. U. Demirbas, A. Sennaroglu, and M. Somer, "Synthesis and characterization of diffusion-doped Cr2+: ZnSe and Fe2+: ZnSe," Opt. Mater. **28**, 231-240 (2006).
121. G. J. Wagner, T. J. Carrig, R. H. Page, K. I. Schaffers, J. Ndap, X. Ma, and A. Burger, "Continuous-wave broadly tunable Cr^{2+}:ZnSe laser," Opt. Lett. **24**, 19-21 (1999).
122. R. H. Page, J. A. Skidmore, K. I. Schaffers, R. J. Beach, S. A. Payne, and W. F. Krupke, "Demonstrations of diode-pumped grating-tuned ZnSe:Cr^{+2} lasers," in *OSA TOPS, Advanced Solid-State Lasers*, C. R. Pollock, and W. R. Rosenberg, eds. (Orlando, 1997), pp. 208-210.

123. T. J. Carrig, G. J. Wagner, A. Sennaroglu, J. Y. Jeong, and C. R. Pollock, "Mode-locked Cr^{2+}:ZnSe laser," Optics Letters **25**, 168-170 (2000).
124. G. J. Wagner, B. G. Tiemann, W. J. Alford, and T. J. Carring, "Single-Frequency Cr:ZnSe Laser," in *OSA Advanced Solid-State Photonics*(New Mexico, 2004), p. WB12.
125. M. N. Cizmeciyan, H. Cankaya, A. Kurt, and A. Sennaroglu, "Kerr-lens mode-locked femtosecond Cr2+:ZnSe laser at 2420 nm," Opt. Lett. **34**, 3056-3058 (2009).
126. J. J. Adams, C. Bibeau, R. H. Page, D. M. Krol, L. H. Furu, and S. A. Payne, "4.0-4.5 μm lasing of Fe: ZnSe below 180 K, a new mid-infrared laser material," Optics Letters **24**, 1720-1722 (1999).
127. A. A. Voronov, V. I. Kozlovsky, Y. V. Korostelin, A. I. Landman, Y. P. Podmar'kov, Y. K. Skasyrsky, and M. P. Frolov, "A continuous-wave Fe2+ : ZnSe laser," Quantum Electron. **38**, 1113 (2008).
128. J. Kernal, V. V. Fedorov, A. Gallian, S. B. Mirov, and V. V. Badikov, "Room temperature 3.9-4.5 μm gain-switched lasing of Fe:ZnSe," in *Advanced Solid State Photonics*(OSA, Nevada, 2006), p. MD6.
129. A. A. Voronov, V. I. Kozlovskii, Y. V. Korostelin, A. I. Landman, Y. P. Podmar'kov, and M. P. Frolov, "Laser parameters of a Fe:ZnSe crystal in the 85-255-K temperature range," Quantum Electronics **35**, 809-812 (2005).
130. V. A. Akimov, A. A. Voronov, V. I. Kozlovsky, Y. V. Korostelin, A. I. Landman, Y. P. Podmar'kov, and M. P. Frolov, "Efficient IR Fe:ZnSe laser continuously tunable in the spectral range from 3.77 to 4.40 μm," Quantum Electronics **34**, 912-914 (2004).
131. J. J. Adams, C. Bibeau, R. H. Page, and S. A. Payne, "Tunable laser action at 4.0 microns from Fe:ZnSe," in *Advanced Solid State Lasers*, M. M. Fejer, H. Injeyan, and U. Keller, eds. (OSA, 1999), pp. 435-440.
132. A. A. Voronov, V. I. Kozlovskii, Y. V. Korostelin, A. I. Landman, Y. P. Podmar'kov, V. G. Polushkin, and M. P. Frolov, "Passive Fe^{2+}:ZnSe single-crystal Q switch for 3-μm lasers," Quantum Electronics **36**, 1-2 (2006).
133. V. A. Akimov, A. A. Voronov, V. I. Kozlovsky, Y. V. Korostelin, A. I. Landman, Y. P. Podmar'kov, and M. P. Frolov, "Efficient lasing in a Fe^{2+}:ZnSe crystal at room temperature," Quantum Electronics **36**, 299-301 (2006).
134. A. Sanchez, R. E. Fahey, A. J. Strauss, and R. L. Aggarwal, "Room-temperature continuous-wave operation of a Ti:Al_2O_3 laser," Opt. Lett. **11**, 363-364 (1986).
135. J. K. Jabczynski, W. Zendzian, Z. Mierczyk, and Z. Frukacz, "Chromium-doped LiCAF laser passively Q switched with a V^{3+}:YAG crystal," Appl. Opt. **40**, 6638-6645 (2001).
136. L. J. Atherton, S. A. Payne, and C. D. Brandle, "Oxide and fluoride laser crystals," Annual Review of Materials Science **23**, 453-502 (1993).
137. M. Stalder, M. Bass, and B. H. T. Chai, "Thermal quenching of fluoresence in chromium-doped fluoride laser crystals," J. Opt. Soc. Am. B **9**, 2271-2273 (1992).
138. J. M. Eichenholz, and M. Richardson, "Measurement of thermal lensing in Cr^{3+}-doped colquiriites," IEEE J. Quantum Electron. **34**, 910-919 (1998).
139. A. Sennaroglu, "Analysis and optimization of lifetime thermal loading in continuous-wave Cr^{4+}-doped solid-state lasers," J. Opt. Soc. Am. B **18**, 1578-1586 (2001).
140. B. W. Woods, S. A. Payne, J. E. Marion, R. S. Hughes, and L. E. Davis, "Thermomechanical and thermooptic properties of the $LiCaAlF_6$-Cr^{3+} laser material," J Opt Soc Am B **8**, 970-977 (1991).
141. J. M. Girkin, and G. McConnell, "Advances in laser sources for confocal and multiphoton microscopy," Microscopy Research and Technique **67**, 8-14 (2005).
142. D. Kopf, K. J. Weingarten, G. Zhang, M. Moser, M. A. Emanuel, R. J. Beach, J. A. Skidmore, and U. Keller, "High-average-power diode-pumped femtosecond Cr:LiSAF lasers," Appl. Phys. B **65**, 235-243 (1997).
143. U. Demirbas, A. Sennaroglu, A. Benedick, A. Siddiqui, F. X. Kärtner, and J. G. Fujimoto, "Diode-pumped, high-average power femtosecond Cr^{+3}:LiCAF laser," Opt. Lett. **32**, 3309-3311 (2007).

144. R. Scheps, J. F. Myers, H. B. Serreze, A. Rosenberg, R. C. Morris, and M. Long, "Diode-pumped Cr:LiSrAlF$_6$ laser," Opt. Lett. **16**, 820-822 (1991).
145. R. Scheps, "Cr-doped solid state lasers pumped by visible laser diodes," Opt. Mater. **1**, 1-9 (1992).
146. R. Scheps, "Laser-Diode-Pumped Cr-Lisrgaf6 Laser," IEEE Photonic. Tech. L. **4**, 548-550 (1992).
147. R. Scheps, "Cr-LiCaAlF$_6$ laser pumped by visible laser-diodes," IEEE J. Quantum Electron. **27**, 1968-1970 (1991).
148. R. Scheps, "Diode-pumping of tunable Cr-doped lasers," in *SPIE Solid State Lasers* (SPIE, 1991).
149. R. Scheps, B. M. Gately, J. F. Myers, J. S. Krasinski, and D. F. Heller, "Alexandrite Laser Pumped by Semiconductor-Lasers," Appl. Phys. Lett. **56**, 2288-2290 (1990).
150. A. Miller, P. LiKamWa, B. H. T. Chai, and E. W. V. Stryland, "Generation of 150-fs tunable pulses in Cr:LiSAF," Opt. Lett. **17**, 195-197 (1992).
151. J. M. Evans, D. E. Spence, W. Sibbett, B. H. T. Chai, and A. Miller, "50-fs pulse generation from a self-mode-locked Cr:LiSrAlF6 laser," Opt. Lett. **17**, 1447-1449 (1992).
152. P. M. W. French, R. Mellish, J. R. Taylor, P. J. Delfyett, and L. T. Florez, "All-solid-state diode-pumped modelocked Cr:LiSAF laser," Electronics Letters **29**, 1262-1263 (1993).
153. P. M. W. French, R. Mellish, J. R. Taylor, P. J. Delfyett, and L. T. Florez, "Mode-locked all-solid-state diode-pumped Cr:LiSAF Laser," Opt. Lett. **18**, 1934-1936 (1993).
154. F. Balembois, P. Georges, and A. Brun, "Quasi-continuous-wave and actively mode-locked diode-pumped Cr3+:LiSrAlF6 laser," Opt. Lett. **18**, 1730-1732 (1993).
155. G. J. Valentine, J. M. Hopkins, P. Loza-Alvarez, G. T. Kennedy, W. Sibbett, D. Burns, and A. Valster, "Ultralow-pump-threshold, femtosecond Cr^{3+}:LiSrAlF$_6$ laser pumped by a single narrow-stripe AlGaInP laser diode," Opt. Lett. **22**, 1639-1641 (1997).
156. B. Agate, B. Stormont, A. J. Kemp, C. T. A. Brown, U. Keller, and W. Sibbett, "Simplified cavity designs for efficient and compact femtosecond Cr:LiSAF lasers," Optics Communications **205**, 207-213 (2002).
157. S. Tsuda, W. H. Knox, and S. T. Cundiff, "High efficiency diode pumping of a saturable Bragg reflector-mode-locked Cr:LiSAF femtosecond laser," Appl. Phys. Lett. **69**, 1538-1540 (1996).
158. J. M. Hopkins, G. J. Valentine, B. Agate, A. J. Kemp, U. Keller, and W. Sibbett, "Highly compact and efficient femtosecond Cr : LiSAF lasers," Ieee Journal of Quantum Electronics **38**, 360-368 (2002).
159. J. M. Hopkins, G. J. Valentine, W. Sibbett, J. A. der Au, F. Morier-Genoud, U. Keller, and A. Valster, "Efficient, low-noise, SESAM-based femtosecond Cr^{3+}: LiSrAlF$_6$ laser," Opt. Comm. **154**, 54-58 (1998).
160. R. P. Prasankumar, Y. Hirakawa, A. M. J. Kowalevicz, F. X. Kärtner, J. G. Fujitimo, and W. H. Knox, "An extended cavity femtosecond Cr:LiSAF laser pumped by low cost diode lasers," Opt. Express **11**, 1265-1269 (2003).
161. D. Li, U. Demirbas, J. R. Birge, G. S. Petrich, L. A. Kolodziejski, A. Sennaroglu, F. X. Kärtner, and J. G. Fujimoto, "Diode-pumped passively mode-locked GHz femtosecond Cr:LiSAF laser with kW peak power," Opt. Lett. **35** (2010).
162. S. Uemeura, and K. Torizuka, "Generation of 12-fs pulses from a diode-pumped Kerr-lens mode-locked Cr:LiSAF laser," Opt. Lett. **24**, 780-782 (1999).
163. A. J. Kemp, B. Stormont, B. Agate, C. T. A. Brown, U. Keller, and W. Sibbett, "Gigahertz repetition-rate from directly diode-pumped femtosecond Cr : LiSAF laser," Electronics Letters **37**, 1457-1458 (2001).
164. U. Demirbas, G. S. Petrich, S. Nabanja, J. R. Birge, L. A. Kolodziejski, F. X. Kärtner, and J. G. Fujimoto, "Widely-Tunable Femtosecond Operation of Cr:LiSAF Lasers using Broadband Saturable Bragg Reflectors " (2010, in preparation (submitted to CLEO 2010)).
165. U. Demirbas, K.-H. Hong, J. G. Fujimoto, A. Sennaroglu, and F. X. Kärtner, "A low-cost cavity-dumped femtosecond Cr^{3+}:LiSAF laser producing >100 nJ pulses " Opt. Lett. **35** (2010).

166. U. Demirbas, A. Benedick, A. Sennaroglu, D. Li, J. Kim, J. G. Fujimoto, and F. X. Kärtner, "Attosecond resolution timing jitter characterization of diode pumped femtosecond Cr:LiSAF lasers," (2010, in preparation (accapted to CLEO 2010)).
167. V. P. Yanovsky, F. W. Wise, A. Cassanho, and H. P. Jenssen, "Kerr-lens mode-locked diode-pumped Cr:LiSGAF laser," Opt. Lett. **20**, 1304-1306 (1995).
168. I. T. Sorokina, E. Sorokin, and E. Wintner, "Prismless passively mode-locked femtosecond Cr:LiSGaF laser," Opt. Lett. **21**, 1165-1167 (1996).
169. I. T. Sorokina, E. Sorokin, E. Wintner, A. Cassanho, H. P. Jenssen, and R. Szipöcs, "Sub-20 fs pulse generation from the mirror dispersion controlled Cr:LiSGaF and Cr:LiSAF lasers," Appl. Phys. B **65**, 245-253 (1997).
170. K. Gabel, P. Russbuldt, R. Lebert, P. Loosen, R. Poprawe, H. Heyer, and A. Valster, "Diode pumped, chirped mirror dispersion compensated, fs-laser," Opt. Comm. **153**, 275-281 (1998).
171. I. Sorokina, E. Sorokin, E. Wintner, A. Cassanho, M. Noginov, and H. P. Jenssen, in *Conference on Lasers and Electro-Optics (Europe)*(OSA Technical Digest Series, 1994), p. CThN3.
172. V. P. Yanovsky, A. Korytin, F. Wise, A. Cassanho, and H. Jenssen, "Femtosecond diode-pumped Cr: LiSGAF lasers," IEEE J. Sel. Top. Quantum Electron. **2**, 465-472 (1996).
173. S. A. Payne, L. L. Chase, H. W. Newkirk, and W. F. Krupke, "Cr3+-Doped Colquiriite Solid State Laser Material " (1989).
174. P. Wagenblast, R. Ell, U. Morgner, F. Grawert, and F. X. Kärtner, "Diode-pumped 10-fs Cr^{3+}: LiCAF laser," Opt. Lett. **28**, 1713-1715 (2003).
175. K. M. Gabel, P. Russbuldt, R. Lebert, and A. Valster, "Diode pumped Cr3+: LiCAF fs-laser," Opt. Comm. **157**, 327-334 (1998).
176. P. LiKamWa, B. H. T. Chai, and A. Miller, "Self-mode-locked Cr^{3+}:$LiCaAlF_6$ laser," Opt. Lett. **17**, 1438-1440 (1992).
177. A. Isemann, and C. Fallnich, "High-power colquiriite laser with high slope efficiencies pumped by broad-area laser diodes.," Opt. Express **11**, 259-264 (2003).
178. U. Demirbas, A. Sennaroglu, F. X. Kärtner, and J. G. Fujimoto, "Highly efficient, low-cost femtosecond Cr^{3+}:LiCAF laser pumped by single-mode diodes," Opt. Lett. **33**, 590-592 (2008).
179. Y.-K. Kuo, M.-F. Huang, and M. Birnbaum, "Tunable Cr^{4+}:YSO Q-switched Cr:LiCAF laser," IEEE J. Quantum Electron. **31**, 657-663 (1995).
180. P. Beaud, M. C. Richardson, Y. F. Chen, and B. H. T. Chai, "Optical Amplification Characteristics of Cr-Lisaf and Cr-Licaf under Flashlamp-Pumping," IEEE J. Quantum Electron. **30**, 1259-1266 (1994).
181. Y. K. Kuo, Y. Yang, and M. Birnbaum, "Cr4+Gd3sc2ga3o12 Passive Q-Switch for the Cr3+Licaalf6 Laser," Appl. Phys. Lett. **64**, 2329-2331 (1994).
182. Y. C. Wang, C. E. Huang, L. S. Chen, and Z. Y. Fang, "Crystal growth of Cr3+:LiCaAlF6 by Bridgman technique," Journal of Crystal Growth **167**, 176-179 (1996).
183. A. Isemann, P. Wessels, and C. Fallnich, "Directly diode-pumped Colquiriite regenerative amplifiers," Opt. Comm. **260**, 211-222 (2006).
184. A. Isemann, H. Hundertmark, and C. Fallnich, "Diode-pumped Cr : LiCAF fs regenerative amplifier system seeded by an Er-doped mode-locked fiber laser," Appl. Phys. B **74**, 299-306 (2002).
185. G. Lacayo, I. Hahnert, D. Klimm, P. Reiche, and W. Neumann, "Transmission electron microscope study of secondary phases in Cr3+: LiCaAlF6 single crystals," Crystal Research and Technology **34**, 1221-1227 (1999).
186. J. J. Deyoreo, L. J. Atherton, and D. H. Roberts, "Elimination of Scattering Centers from Cr-Licaalf6," Journal of Crystal Growth **113**, 691-697 (1991).
187. D. Klimm, R. Uecker, and P. Reiche, "Melting behavior and growth of colquiriite laser crystals," Crystal Research and Technology **40**, 352-358 (2005).
188. D. Klimm, and P. Reiche, "Ternary colquiriite type fluorides as laser hosts," Crystal Research and Technology **34**, 145-152 (1999).

189. D. Klimm, and P. Reiche, "Nonstoichiometry of the new laser host LiCaAlF6," Crystal Research and Technology **33**, 409-416 (1998).
190. D. Klimm, G. Lacayo, and P. Reiche, "Growth of Cr : LiCaAlF6 and Cr : LiSrAlF6 by the Czochralski method," Journal of Crystal Growth **210**, 683-693 (2000).
191. U. Demirbas, A. Sennaroglu, F. X. Kärtner, and J. G. Fujimoto, "Generation of 15 nJ pulses from a highly efficient, low-cost multipass-cavity Cr^{3+}:LiCAF laser," Opt. Lett. **34**, 497-499 (2009).
192. M. D. Perry, D. Strickland, T. Ditmire, and F. G. Patterson, "Crlisralf6 Regenerative Amplifier," Opt. Lett. **17**, 604-606 (1992).
193. N. P. Barry, S. C. W. Hyde, R. Mellish, P. M. W. French, J. R. Taylor, C. J. Vanderpoel, and A. Valster, "All-Solid-State Femtosecond Diode-Pumped Cr-Lisaf Regenerative Amplifier," Electronics Letters **30**, 1761-1762 (1994).
194. R. Mellish, N. P. Barry, S. C. W. Hyde, R. Jones, P. M. W. French, J. R. Taylor, C. J. v. d. Poel, and A. Valster, "Diode-pumped Cr:LiSAF all-solid-state femtosecond oscillator and regenerative amplifier," Optics Lett. **20**, 2312-2314 (1995).
195. F. Falcoz, F. Balembois, P. Georges, A. Brun, and D. Rytz, "All-solid-state continuous-wave tunable blue-light source by intracavity doubling of a diode-pumped Cr:LiSAF laser," Opt. Lett. **20**, 1274-1276 (1995).
196. B. Agate, A. J. Kemp, C. T. A. Brown, and W. Sibbett, "Efficient, high repetition-rate femtosecond blue source using a compact Cr : LiSAF laser," Opt. Express **10**, 824-831 (2002).
197. B. Agate, E. U. Rafailov, W. Sibbett, S. M. Saltiel, P. Battle, T. Fry, and E. Noonan, "Highly efficient blue-light generation from a compact, diode-pumped femtosecond laser by use of a periodically poled KTP waveguide crystal," Opt. Lett. **28**, 1963-1965 (2003).
198. B. Agate, E. U. Rafailov, W. Sibbett, S. M. Saltiel, K. Koynov, M. Tiihonen, S. H. Wang, F. Laurell, P. Battle, T. Fry, T. Roberts, and E. Noonan, "Portable ultrafast blue light sources designed with frequency doubling in KTP and KNbO3," IEEE J. Sel. Top. Quantum Electron. **10**, 1268-1276 (2004).
199. R. Holzwarth, M. Zimmermann, T. Udem, T. W. Hansch, P. Russbuldt, K. Gabel, R. Poprawe, J. C. Knight, W. J. Wadsworth, and P. S. J. Russell, "White-light frequency comb generation with a diode-pumped Cr : LiSAF laser," Opt. Lett. **26**, 1376-1378 (2001).
200. P. C. Wagenblast, T. H. Ko, J. G. Fujimoto, F. X. Kaertner, and U. Morgner, "Ultrahigh-resolution optical coherence tomography with a diode-pumped broadband Cr3+: LiCAF laser," Opt. Express **12**, 3257-3263 (2004).
201. K. Svoboda, W. Denk, W. H. Knox, and S. Tsuda, "Two-photon-excitation scanning microscopy of living neurons with a saturable Bragg reflector mode-locked diode-pumped Cr:LiSrAlFl laser," Opt. Lett. **21**, 1411-1413 (1996).
202. S. Sakadžić, U. Demirbas, T. R. Mempel, A. Moore, S. Ruvinskaya, D. A. Boas, A. Sennaroglu, F. X. Kärtner, and J. G. Fujimoto, "Multi-photon microscopy with a low-cost and highly efficient Cr:LiCAF laser," Opt. Express **16**, 20848–20863 (2008).
203. H. Tsuchida, "Correlation between amplitude and phase noise in a mode-locked Cr : LiSAF laser," Opt. Lett. **23**, 1686-1688 (1998).
204. H. Tsuchida, "Pulse timing stabilization of a mode-locked Cr : LiSAF laser," Opt. Lett. **24**, 1641-1643 (1999).
205. H. Tsuchida, "Timing-jitter reduction of a mode-locked Cr : LiSAF laser by simultaneous control of cavity length and pump power," Opt. Lett. **25**, 1475-1477 (2000).
206. http://www.psicorp.com/product_service/products/hireprr.html, Accessed April 27, 2010.
207. J. C. Walling, "Tunable Cw Alexandrite Lasers," Journal of the Optical Society of America **69**, 1436-1436 (1979).
208. J. C. Walling, D. F. Heller, H. Samelson, D. J. Harter, J. A. Pete, and R. C. Morris, "Tunable Alexandrite Lasers - Development and Performance," IEEE J. Quantum Electron. **21**, 1568-1581 (1985).
209. J. C. Walling, O. G. Peterson, H. P. Jenssen, R. C. Morris, and E. W. Odell, "Tunable Alexandrite Lasers," IEEE J. Quantum Electron. **16**, 1302-1315 (1980).

210. J. C. Walling, H. P. Jenssen, R. C. Morris, E. W. O'Dell, and O. G. Peterson, "Tunable laser performance in $BeAl_2O_4Cr^{3+}$," Opt. Lett. **4**, 182-183 (1979).
211. S. Guch, and C. E. Jones, "Alexandrite-Laser Performance at High-Temperature," Opt. Lett. **7**, 608-610 (1982).
212. R. Scheps, J. F. Myers, T. R. Glesne, and H. B. Serreze, "Monochromatic End-Pumped Operation of an Alexandrite Laser," Opt. Comm. **97**, 363-366 (1993).
213. R. Frey, F. Derougemont, and C. H. Lee, "An Actively Mode-Locked Continuous Wave Alexandrite Laser," Opt. Comm. **73**, 232-234 (1989).
214. F. Volker, Q. Lu, and H. Weber, "Passive Mode-Locking of an Alexandrite Laser for Picosecond Pulse Generation," J. Appl. Phys. **69**, 3432-3439 (1991).
215. http://www.medcompare.com/details/54391/ARION-755nm-Alexandrite-Laser-formerly-WaveLight-Aesthetics.html.
216. Z. Chen, and G. Zhang, "Free-running emerald laser pumped by laser diode," CHINESE OPTICS LETTERS **4**, 649-651 (2006).
217. M. L. Shand, and J. C. Walling, "A Tunable Emerald Laser," IEEE J. Quantum Electron. **18**, 1829-1830 (1982).
218. M. L. Shand, and S. T. Lai, "Cw Laser Pumped Emerald Laser," IEEE J. Quantum Electron. **20**, 105-108 (1984).
219. S. T. Lai, "Highly Efficient Emerald Laser," J Opt Soc Am B **4**, 1286-1290 (1987).
220. U. Demirbas, A. Sennaroglu, F. X. Kärtner, and J. G. Fujimoto, "Comparative investigation of diode pumping for continuous-wave and mode-locked Cr^{3+}:LiCAF lasers " J. Opt. Soc. Am. B **26**, 64-79 (2009).
221. D. Findlay, and R. A. Clay, "The measurement of internal losses in 4-level lasers," Physics Letters **20**, 277-278 (1966).
222. J. A. Caird, L. G. DeShazer, and J. Nella, "Characteristics of room-temperature 2.3-μm laser emission from Tm^{3+} in YAG and $YAlO_3$," IEEE J. Quantum Electron. **11**, 874-881 (1975).
223. S. A. Payne, L. L. Chase, L. J. Atherton, J. A. Caird, W. L. Kway, M. D. Shinn, R. S. Hughes, and L. K. Smith, "Properties ans performance of the $LiCaAlF_6:Cr^{3+}$ laser material," in *SPIE Solid State Lasers*, G. Dube, ed. (SPIE, 1990), pp. 84-93.
224. H. W. H. Lee, S. A. Payne, and L. L. Chase, "Excited-state absorption of Cr^{+3} in $LiCaAlF_6$: Effects of asymmetric distortions and intensity selection rules," Physical Review B **39**, 8907-8914 (1989).
225. P. Beaud, Y.-F. Chen, B. H. T. Chai, and M. C. Richardson, "Gain properties of $LiSrAlF_6:Cr^{3+}$," Opt. Lett. **17**, 1064-1066 (1992).
226. P. A. Beaud, M. Richardson, and E. J. Miesak, "Multi-Terawatt Femtosecond Cr-Lisaf Laser," IEEE J. Quantum Electron. **31**, 317-325 (1995).
227. D. Kopf, U. Keller, M. A. Emanuel, R. J. Beach, and J. A. Skidmore, "1.1-W cw Cr:LiSAF laser pumped by a 1-cm diode array," Opt. Lett. **22**, 99-101 (1997).
228. D. Kopf, J. A. Derau, U. Keller, G. L. Bona, and P. Roentgen, "400-Mw Continuous-Wave Diode-Pumped Cr-Lisaf Laser-Based on a Power-Scalable Concept," Opt. Lett. **20**, 1782-1784 (1995).
229. F. Balembois, F. Falcoz, F. Kerboull, F. Druon, P. Georges, and A. Brun, "Theoretical and experimental investigations of small-signal gain for a diode-pumped Q-Switched Cr:LiSAF laser," IEEE J. Quantum Electron. **33**, 269-278 (1997).
230. S. A. Payne, L. L. Chase, and G. D. Wilke, "Optical Spectroscopy of the New Laser Materials, Lisralf6-Cr-3+ and Licaalf6-Cr-3+," J. Lumin. **44**, 167-176 (1989).
231. V. Pilla, T. Catunda, S. M. Lima, A. N. Medina, M. L. Baesso, H. P. Jenssen, and A. Cassanho, "Thermal quenching of the fluorescence quantum efficiency in colquiriite crystals measured by thermal lens spectrometry," J Opt Soc Am B **21**, 1784-1791 (2004).
232. V. Pilla, T. Catunda, H. P. Jenssen, and A. Cassanho, "Fluorescence quantum efficiency measurements in the presence of Auger upconversion by the thermal lens method," Opt. Lett. **28**, 239-241 (2003).

233. F. Balembois, F. Druon, F. Falcoz, P. Georges, and A. Brun, "Performances of Cr:LiSrAlF6 and Cr:LiSrGaF6 for continuous-wave diode-pumped Q-switched operation," Opt. Lett. **22**, 387-389 (1997).
234. S. Uemura, and K. Miyazaki, "Thermal chracteristics of a continuous-wave Cr:LiSAF laser," Jpn. J. Appl. Phys. **36**, 4312-4315 (1997).
235. H. S. Wang, P. L. K. Wa, J. L. Lefaucheur, B. H. T. Chai, and A. Miller, "Cw and self-mode-locking performance of a red pumped Cr:LiSCAF laser," Opt. Comm. **110**, 679-688 (1994).
236. V. V. Fedorov, S. B. Mirov, A. Gallian, D. V. Badikov, M. P. Frolov, Y. V. Korostelin, V. I. Kozlovsky, A. I. Landman, Y. P. Podmar'kov, V. A. Akimov, and A. A. Voronov, "3-77-5.05-μm tunable solid-state lasers based on Fe^{2+}-doped znse crystals operating at low and room temperatures," IEE Journal of Quantum Electronics **42**, 907-917 (2006).
237. M. Stalder, M. Bass, and B. H. T. Chai, "Thermal quencing of fluoresence in chromium-doped fluoride laser crystals," Journal of Optical Society of America B **9**, 2271-2273 (1992).
238. http://www.opnext.com/products/pdf/ode2_071_hl63133dg_Rev1.pdf, Accessed March 31, 2010.
239. P. Adamiec, B. Sumpf, I. Rudiger, J. Fricke, K. H. Hasler, P. Ressel, H. Wenzel, M. Zorn, G. Erbert, and G. Trankle, "Tapered lasers emitting at 650 nm with 1 W output power with nearly diffraction-limited beam quality," Opt. Lett. **34**, 2456-2458 (2009).
240. B. C. Weber, and A. Hirth, "Efficient single-pulse emission with submicrosecond duration from a Cr:LiSAF laser," Opt. Comm. **128**, 158-165 (1996).
241. B. C. Weber, and A. Hirth, "Presentation of a new and simple technique of Q-switching with a LiSrAlf(6): Cr3+ oscillator," Opt. Comm. **149**, 301-306 (1998).
242. M. Fromager, and K. A. Ameur, "Modeling of the self-Q-switching behavior of lasers based on chromium doped active material," Opt. Comm. **191**, 305-314 (2001).
243. N. Passilly, M. Fromager, K. A. Ameur, R. Moncorge, J. L. Doualan, A. Hirth, and G. Quarles, "Measurement of the index-inversion coupling contributing to the time-dependent nonlinear lens effect in a Cr-3+: USAF laser," Journal De Physique Iv **119**, 257-258 (2004).
244. N. Passilly, M. Fromager, K. Ait-Ameur, R. Moncorge, J. L. Doualan, A. Hirth, and G. Quarles, "Experimental and theoretical investigation of a rapidly varying nonlinear lensing effect observed in a Cr3+: LiSAF laser," J Opt Soc Am B **21**, 531-538 (2004).
245. N. Passilly, M. Fromager, and K. Ait-Ameur, "Improvement of the self-Q-switching behavior of a Cr : LiSrAlF6 laser by use of binary diffractive optics," Appl. Opt. **43**, 5047-5059 (2004).
246. C. Hönninger, R. Paschotta, F. Morier-Genoud, M. Moser, and U. Keller, "Q-switching stability limits of continuous-wave passive mode locking," JOSA **16**, 46-56 (1999).
247. F. X. Kärtner, L. R. Brovelli, D. Kopf, M. Kamp, I. Calasso, and U. Keller, "Control of solid-state laser dynamics by semiconductor devices," Optical Engineering **34**, 2024-2036 (1995).
248. U. Keller, "Recent developments in compact ultrafast lasers," Nature **424**, 831-838 (2003).
249. S. N. Tandon, J. T. Gopinath, H. M. Shen, G. S. Petrich, L. A. Kolodziejski, F. X. Kärtner, and E. P. Ippen, "Large-area broadband saturable Bragg reflectors by use of oxidized AlAs," Opt. Lett. **29**, 2551-2553 (2004).
250. D. Kopf, A. Prasad, G. Zhang, M. Moser, and U. Keller, "Broadly tunable femtosecond Cr:LiSAF laser," Opt. Lett. **22**, 621-623 (1997).
251. N. H. Rizvi, P. M. W. French, and J. R. Taylor, "50-fs pulse generation from a self-starting cw passively mode-locked Cr:LiSrAlF6 laser," Opt. Lett. **17**, 877-879 (1992).
252. N. H. Rizvi, P. M. W. French, and J. R. Taylor, "Generation of 33-fs pulses from a passively mode-locked Cr^{3+}:$LiSrAlF_6$ laser," Opt. Lett. **17**, 1605-1607 (1992).
253. N. H. Rizvi, P. M. W. French, J. R. Taylor, P. J. Delfyett, and L. T. Florez, "Generation of pulses as short as 93 fs from a self-starting femtosecond Cr:LiSrAlF6 lasers by exploiting multiple-quantum-well absorbers," Opt. Lett. **18**, 983-985 (1993).
254. D. Kopf, K. J. Weingarten, L. R. Brovelli, M. Kamp, and U. Keller, "Diode-Pumped 100-Fs Passively Mode-Locked Cr-Lisaf Laser with an Antiresonant Fabry-Perot Saturable Absorber," Opt. Lett. **19**, 2143-2145 (1994).

255. M. J. P. Dymott, and A. I. Ferguson, "Self-mode-locked diode-pumped Cr:LiSAF laser," Optics Lett. **19**, 1988-1990 (1994).
256. M. J. P. Dymott, I. M. Botheroyd, G. J. Hall, J. R. Lincoln, and A. I. Ferguson, "All-solid-state actively mode-locked Cr:LiSAF laser," Opt. Lett. **19**, 634-636 (1994).
257. J. R. Lincoln, M. J. P. Dymott, and A. I. Ferguson, "Femtosecond pulses from an all-solid-state Kerr-lens mode-locked Cr:LiSAF laser," Opt. Lett. **19**, 1210-1212 (1994).
258. F. Falcoz, F. Balembois, P. Georges, and A. Brun, "Self-starting self-mode-locked femtosecond diode-pumped Cr:LiSAF laser," Opt. Lett. **20**, 1874-1876 (1995).
259. M. J. P. Dymott, and A. I. Ferguson, "Self-mode-locked diode-pumped Cr:LiSAF laser producing 34-fs pulses at 42-mW average power," Opt. Lett. **20**, 1157-1159 (1995).
260. S. Tsuda, W. H. Knox, E. A. d. Souza, W. Y. Jan, and J. E. Cunningham, "Low-loss intracavity AlAs/AlGaAs saturable Bragg reflector for femtosecond mode locking in solid-state lasers," Opt. Lett. **20**, 1406-1408 (1995).
261. M. P. Critten, D. Burns, J. M. Evans, K. Lamb, C. Yelland, and W. Sibbet, "All-solid-state femtosecond Cr3+:LiSAF lasers pumped at 532nm and 670nm," Journal of Modern Optics **43**, 919-927 (1996).
262. S. Uemura, and K. Miyazaki, "Operation of a femtosecond Cr:LiSAF solitary laser near zero group-delay dispersion," Opt. Comm. **133**, 201-204 (1997).
263. S. Uemura, and K. Miyazaki, "Femtosecond Cr:LiSAF laser pumped by a single diode laser," Opt. Comm. **138**, 330-332 (1997).
264. A. Robertson, R. Knappe, and R. Wallenstein, "Diode-pumped broadly tunable (809-910 nm) femtosecond Cr : LiSAF laser," Opt. Comm. **147**, 294-298 (1998).
265. A. Sennaroglu, A. M. Kowalevicz, E. P. Ippen, and J. G. Fujimoto, "Compact femtosecond lasers based on novel multipass cavities," IEEE J. Quantum Electron. **40**, 519-528 (2004).
266. M. Ramaswamy, M. Ulman, J. Paye, and J. G. Fujimoto, "Cavity-dumped femtosecond Kerr-lens mode-locked Ti:Al_2O_3 laser," Opt. Lett. **18**, 1822-1824 (1993).
267. M. S. Pshenichnikov, W. P. d. Boeij, and D. A. Wiersma, "Generation of 13-fs, 5-MW pulses from a cavity-dumped Ti:sapphire laser," Opt. Lett. **19**, 572-574 (1994).
268. X. B. Zhou, H. Kapteyn, and M. Murnane, "Positive-dispersion cavity-dumped Ti: sapphire laser oscillator and its application to white light generation," Opt. Express **14**, 9750-9757 (2006).
269. M. Siegel, N. Pfullmann, G. Palmer, S. Rausch, T. Binhammer, M. Kovacev, and U. Morgner, "Microjoule pulse energy from a chirped-pulse Ti:sapphire oscillator with cavity dumping," Opt. Lett. **34**, 740-742 (2009).
270. A. Killi, U. Morgner, M. J. Lederer, and D. Kopf, "Diode-pumped femtosecond laser oscillator with cavity dumping," Opt. Lett. **29**, 1288-1290 (2004).
271. A. Killi, J. Dorring, U. Morgner, M. J. Lederer, J. Frei, and D. Kopf, "High speed electro-optical cavity dumping of mode-locked laser oscillators," Opt. Express **13**, 1916-1922 (2005).
272. U. Keller, K. J. Weingarten, F. X. Kärtner, D. Kopf, B. Braun, I. D. Jung, R. Fluck, C. Hönninger, N. Matuschek, and J. A. der Au, "Semiconductor saturable absorber mirrors (SESAM's) for femtosecond to nanosecond pulse generation in solid-state lasers," IEEE J. Sel. Top. Quantum Electron. **2**, 435-453 (1996).
273. S. Tsuda, W. H. Knox, S. T. Cundiff, W. Y. Jan, and J. E. Cunningham, "Mode-locking ultrafast solid-state lasers with saturable Bragg reflectors," IEEE J. Sel. Top. Quantum Electron. **2**, 454-464 (1996).
274. D. L. Wokosin, V. Centonze, J. G. White, D. Armstrong, G. Robertson, and A. I. Ferguson, "All-solid-state ultrafast lasers facilitate multiphoton excitation fluorescence imaging," Ieee Journal of Selected Topics in Quantum Electronics **2**, 1051-1065 (1996).
275. A. Diaspro, P. Bianchini, G. Vicidomini, M. Faretta, P. Ramoino, and C. Usai, "Multi-photon excitation microscopy," Biomedical Engineering Online **5**, - (2006).
276. W. R. Zipfel, R. M. Williams, and W. W. Webb, "Nonlinear magic: multiphoton microscopy in the biosciences," Nature Biotechnology **21**, 1368-1376 (2003).

277. J. M. Girkin, "Optical physics enables advances in multiphoton imaging," Journal of Physics D-Applied Physics **36**, R250-R258 (2003).
278. F. Helmchen, and W. Denk, "Deep tissue two-photon microscopy," Nature Methods **2**, 932-940 (2005).
279. J. M. Squirrell, D. L. Wokosin, J. G. White, and B. D. Bavister, "Long-term two-photon fluorescence imaging of mammalian embryos without compromising viability," Nature Biotechnology **17**, 763-767 (1999).
280. W. Denk, D. W. Piston, and W. W. Webb, "Multi-Photon Molecular Excitation in Laser Scanning Microscopy," in *Handbook of Biological Confocal Microscopy*
J. B. Pawlay, ed. (Springer, New York, 2006), pp. 535-549.
281. W. Denk, and K. Svoboda, "Photon upmanship: Why multiphoton imaging is more than a gimmick," Neuron **18**, 351-357 (1997).
282. P. T. C. So, C. Y. Dong, B. R. Masters, and K. M. Berland, "Two-photon excitation fluorescence microscopy," Annual Review of Biomedical Engineering **2**, 399-429 (2000).
283. J. N. Kerr, and W. Denk, "Imaging in vivo: watching the brain in action," Nat Rev Neurosci **9**, 195-205 (2008).
284. J. M. Squirrell, D. L. Wokosin, J. G. White, and B. D. Bavister, "Long-term two-photon fluorescence imaging of mammalian embryos without compromising viability," Nat Biotechnol **17**, 763-767 (1999).
285. P. J. Campagnola, M. D. Wei, A. Lewis, and L. M. Loew, "High-resolution nonlinear optical imaging of live cells by second harmonic generation," Biophysical Journal **77**, 3341-3349 (1999).
286. J. N. Gannaway, and C. J. R. Sheppard, "2nd-Harmonic Imaging in Scanning Optical Microscope," Optical and Quantum Electronics **10**, 435-439 (1978).
287. L. Moreaux, O. Sandre, M. Blanchard-Desce, and J. Mertz, "Membrane imaging by simultaneous second-harmonic generation and two-photon microscopy," Optics letters **25**, 320-322 (2000).
288. G. Peleg, A. Lewis, O. Bouevitch, L. Loew, D. Parnas, and M. Linial, "Gigantic optical non-linearities from nanoparticle-enhanced molecular probes with potential for selectively imaging the structure and physiology of nanometric regions in cellular systems," Bioimaging **4**, 215-224 (1996).
289. I. Freund, and M. Deutsch, "2nd-Harmonic Microscopy of Biological Tissue," Optics letters **11**, 94-96 (1986).
290. D. A. Dombeck, K. A. Kasischke, H. D. Vishwasrao, M. Ingelsson, B. T. Hyman, and W. W. Webb, "Uniform polarity microtubule assemblies imaged in native brain tissue by second-harmonic generation microscopy," Proceedings of the National Academy of Sciences of the United States of America **100**, 7081-7086 (2003).
291. A. Zoumi, A. Yeh, and B. J. Tromberg, "Imaging cells and extracellular matrix in vivo by using second-harmonic generation and two-photon excited fluorescence," Proceedings of the National Academy of Sciences of the United States of America **99**, 11014-11019 (2002).
292. A. Zumbusch, G. R. Holtom, and X. S. Xie, "Three-dimensional vibrational imaging by coherent anti-Stokes Raman scattering," Physical Review Letters **82**, 4142-4145 (1999).
293. I. Gryczynski, H. Szmacinski, and J. R. Lakowicz, "On the Possibility of Calcium Imaging Using Indo-1 with 3-Photon Excitation," Photochemistry and Photobiology **62**, 804-808 (1995).
294. J. R. Lakowicz, I. Gryczynski, H. Malak, M. Schrader, P. Engelhardt, H. Kano, and S. W. Hell, "Time-resolved fluorescence spectroscopy and imaging of DNA labeled with DAPI and hoechst 33342 using three-photon excitation," Biophysical Journal **72**, 567-578 (1997).
295. S. Maiti, J. B. Shear, R. M. Williams, W. R. Zipfel, and W. W. Webb, "Measuring serotonin distribution in live cells with three-photon excitation," Science **275**, 530-532 (1997).
296. W. R. Zipfel, R. M. Williams, R. Christie, A. Y. Nikitin, B. T. Hyman, and W. W. Webb, "Live tissue intrinsic emission microscopy using multiphoton-excited native fluorescence and second harmonic generation," Proceedings of the National Academy of Sciences of the United States of America **100**, 7075-7080 (2003).

297. L. Canioni, S. Rivet, L. Sarger, R. Barille, P. Vacher, and P. Voisin, "Imaging of Ca2+ intracellular dynamics with a third-harmonic generation microscope," Optics letters **26**, 515-517 (2001).
298. M. Muller, J. Squier, K. R. Wilson, and G. J. Brakenhoff, "3D microscopy of transparent objects using third-harmonic generation," Journal of Microscopy-Oxford **191**, 266-274 (1998).
299. D. Yelin, and Y. Silberberg, "Laser scanning third-harmonic-generation microscopy in biology," Opt. Express **5**, 169-175 (1999).
300. Y. Barad, H. Eisenberg, M. Horowitz, and Y. Silberberg, "Nonlinear scanning laser microscopy by third harmonic generation," Applied Physics Letters **70**, 922-924 (1997).
301. D. Debarre, W. Supatto, A. M. Pena, A. Fabre, T. Tordjmann, L. Combettes, M. C. Schanne-Klein, and E. Beaurepaire, "Imaging lipid bodies in cells and tissues using third-harmonic generation microscopy," Nature Methods **3**, 47-53 (2006).
302. A. Diaspro, G. Chirico, and M. Collini, "Two-photon fluorescence excitation and related techniques in biological microscopy," Quarterly Reviews of Biophysics **38**, 97-166 (2005).
303. C. Xu, and W. W. Webb, "Measurement of two-photon excitation cross sections of molecular fluorophores with data from 690 to 1050 nm," J Opt Soc Am B **13**, 481-491 (1996).
304. K. Taira, T. Hashimoto, and H. Yokoyama, "Two-photon fluorescence imaging with a pulse source based on a 980-nm gain-switched laser diode," Opt. Express **15**, 2454-2458 (2007).
305. P. Xi, Y. Andegeko, L. R. Weisel, V. V. Lozovoy, and M. Dantus, "Greater signal, increased depth, and less photobleaching in two-photon microscopy with 10 fs pulses," Opt. Comm. **281**, 1841-1849 (2008).
306. http://www.newport.com/file_store/Data_Sheet/Mai_Tai_DeepSee_Data_Sheet_(print_version_-_1_3_MB).pdf.
307. http://www.coherent.com/downloads/ChameleonUltraFamily_DS_8.pdf.
308. http://www.elliotscientific.com/pdf/Femtosource_SCI_245.pdf.
309. http://www.newport.com/file_store/Data_Sheet/Opal_BB_data_sheet_(print_version_-_2_1_MB).pdf.
310. http://www.coherent.com/downloads/MiraOPO_DSrevB_4a.pdf.
311. http://www.highqlaser.at/kms/media/uploads/www_femtotrain_yb_ndglass_062007.pdf.
312. http://www.tbwp.com/Time_Bandwidth/PDF_Docus/GLX-200.pdf.
313. G. McConnell, G. L. Smith, J. M. Girkin, A. M. Gurney, and A. I. Ferguson, "Two-photon microscopy of fura-2-loaded cardiac myocytes with an all-solid-state tunable and visible femtosecond laser source," Opt. Lett. **28**, 1742-1744 (2003).
314. G. McConnell, and E. Riis, "Photonic crystal fibre enables short-wavelength two-photon laser scanning fluorescence microscopy with fura-2," Physics in Medicine and Biology **49**, 4757-4763 (2004).
315. G. McConnell, "Nonlinear optical microscopy at wavelengths exceeding 1.4 mu m using a synchronously pumped femtosecond-pulsed optical parametric oscillator," Physics in Medicine and Biology **52**, 717-724 (2007).
316. M. Kuramoto, N. Kitajima, H. C. Guo, Y. Furushima, M. Ikeda, and H. Yokoyama, "Two-photon fluorescence bioimaging with an all-semiconductor laser picosecond pulse source," Opt. Lett. **32**, 2726-2728 (2007).
317. H. Yokoyama, H. C. Guo, T. Yoda, K. Takashima, K. Sato, H. Taniguchi, and H. Ito, "Two-photon bioimaging with picosecond optical pulses from a semiconductor laser," Opt. Express **14**, 3467-3471 (2006).
318. H. Yokoyama, H. Tsubokawa, H. C. Guo, J. Shikata, K. Sato, K. Takashima, K. Kashiwagi, N. Saito, H. Taniguchi, and H. Ito, "Two-photon bioimaging utilizing supercontinuum light generated by a high-peak-power picosecond semiconductor laser source," Journal of Biomedical Optics **12**, - (2007).
319. G. Robertson, D. Armstrong, M. J. P. Dymott, A. I. Ferguson, and G. L. Hogg, "Two-photon fluorescence microscopy with a diode-pumped Cr:LiSAF laser," Appl. Optics **36**, 2481-2483 (1997).
320. W. Denk, J. H. Strickler, and W. W. Webb, "2-Photon Laser Scanning Fluorescence Microscopy," Science **248**, 73-76 (1990).

321. P. F. Curley, A. I. Ferguson, J. G. White, and W. B. Amos, "Application of a Femtosecond Self-Sustaining Mode-Locked Ti-Sapphire Laser to the Field of Laser Scanning Confocal Microscopy," Optical and Quantum Electronics **24**, 851-859 (1992).
322. P. M. W. French, R. Mellish, and J. R. Taylor, "Modelocked all-solid-state diode-pumped Cr:LiSAF laser," Optics Letters **18**, 1934-1936 (1993).
323. L. K. Smith, S. A. Payne, W. L. Kway, L. L. Chase, and B. H. T. Chai, "Investigation of the Laser Properties of Cr3+:LiSrGaF6," IEEE J. Quantum Electron. **28**, 2612-2618 (1992).
324. S. A. Payne, L. L. Chase, H. W. Newkirk, L. K. Smith, and W. F. Krupke, "Licaalf6-Cr-3+ - a Promising New Solid-State Laser Material," Ieee Journal of Quantum Electronics **24**, 2243-2252 (1988).
325. U. Demirbas, A. Sennaroglu, A. Benedick, A. Siddiqui, F. X. Kartner, and J. G. Fujimoto, "Diode-pumped, high-average power femtosecond Cr^{+3}:LiCAF laser," Optics letters **32**, 3309-3311 (2007).
326. U. Demirbas, A. Sennaroglu, F. X. Kartner, and J. G. Fujimoto, "Highly efficient, low-cost femtosecond Cr^{3+}:LiCAF laser pumped by single-mode diodes," Optics letters **33**, 590-592 (2008).
327. W. Denk, K. R. Delaney, A. Gelperin, D. Kleinfeld, B. W. Strowbridge, D. W. Tank, and R. Yuste, "Anatomical and functional imaging of neurons using 2-photon laser scanning microscopy," J Neurosci Methods **54**, 151-162 (1994).
328. K. Svoboda, W. Denk, D. Kleinfeld, and D. W. Tank, "In vivo dendritic calcium dynamics in neocortical pyramidal neurons," Nature **385**, 161-165 (1997).
329. D. Kleinfeld, P. P. Mitra, F. Helmchen, and W. Denk, "Fluctuations and stimulus-induced changes in blood flow observed in individual capillaries in layers 2 through 4 of rat neocortex," Proc Natl Acad Sci U S A **95**, 15741-15746 (1998).
330. M. Oheim, E. Beaurepaire, E. Chaigneau, J. Mertz, and S. Charpak, "Two-photon microscopy in brain tissue: parameters influencing the imaging depth (vol 111, pg 29, 2001)," (2001), pp. 205-205.
331. P. Theer, and W. Denk, "On the fundamental imaging-depth limit in two-photon microscopy," J Opt Soc Am A Opt Image Sci Vis **23**, 3139-3149 (2006).
332. P. Theer, M. T. Hasan, and W. Denk, "Two-photon imaging to a depth of 1000 mu m in living brains by use of a Ti : Al2O3 regenerative amplifier," (2003), pp. 1022-1024.
333. E. Beaurepaire, M. Oheim, and J. Mertz, "Ultra-deep two-photon fluorescence excitation in turbid media," (2001), pp. 25-29.
334. M. Rueckel, J. A. Mack-Bucher, and W. Denk, "Adaptive wavefront correction in two-photon microscopy using coherence-gated wavefront sensing," Proc Natl Acad Sci U S A **103**, 17137-17142 (2006).
335. P. S. Tsai, B. Migliori, K. Campbell, T. N. Kim, Z. Kam, A. Groisman, and D. Kleinfeld, "Spherical aberration correction in nonlinear microscopy and optical ablation using a transparent deformable membrane," (2007), p. 3.
336. L. Sherman, J. Y. Ye, O. Albert, and T. B. Norris, "Adaptive correction of depth-induced aberrations in multiphoton scanning microscopy using a deformable mirror," J Microsc **206**, 65-71 (2002).
337. M. A. Neil, R. Juskaitis, M. J. Booth, T. Wilson, T. Tanaka, and S. Kawata, "Adaptive aberration correction in a two-photon microscope," J Microsc **200 (Pt 2)**, 105-108 (2000).
338. K. Svoboda, and R. Yasuda, "Principles of two-photon excitation microscopy and its applications to neuroscience," (2006), pp. 823-839.
339. F. Helmchen, and W. Denk, "New developments in multiphoton microscopy," Current Opinions in Neurobiology **12**, 593-601 (2002).
340. P. Verant, R. Serduc, B. Van Der Sanden, C. Remy, and J. C. Vial, "A direct method for measuring mouse capillary cortical blood volume using multiphoton laser scanning microscopy," J Cereb Blood Flow Metab **27**, 1072-1081 (2007).
341. E. J. Yoder, and D. Kleinfeld, "Cortical imaging through the intact mouse skull using two-photon excitation laser scanning microscopy," Microsc Res Tech **56**, 304-305 (2002).

342. J. Schummers, H. Yu, and M. Sur, "Tuned responses of astrocytes and their influence on hemodynamic signals in the visual cortex," Science **320**, 1638-1643 (2008).
343. M. J. Pittet, and T. R. Mempel, "Regulation of T-cell migration and effector functions: insights from in vivo imaging studies," Immunol. Rev. **221**, 107-129 (2008).
344. A. Isemann, and C. Fallnich, "High-power Colquiriite lasers with high slope efficiencies pumped by broad-area laser diodes," Opt. Express **11**, 259-264 (2003).
345. S. N. Tandon, J. T. Gopinath, A. A. Erchak, G. S. Petrich, L. A. Kolodziejski, and E. P. Ippen, "Large-area oxidation of AlAs layers for dielectric stacks and thick buried oxides," J. Electron. Mater. **33**, 774-779 (2004).
346. S. N. Tandon, J. T. Gopinath, H. M. Shen, G. S. Petrich, L. A. Kolodziejski, F. X. Kartner, and E. P. Ippen, "Large-area broadband saturable Bragg reflectors by use of oxidized AlAs," Optics letters **29**, 2551-2553 (2004).
347. F. Bestvater, E. Spiess, G. Stobrawa, M. Hacker, T. Feurer, T. Porwol, U. Berchner-Pfannschmidt, C. Wotzlaw, and H. Acker, "Two-photon fluorescence absorption and emission spectra of dyes relevant for cell imaging," Journal of Microscopy-Oxford **208**, 108-115 (2002).
348. M. E. Dickinson, E. Simbuerger, B. Zimmermann, C. W. Waters, and S. E. Fraser, "Multiphoton excitation spectra in biological samples," Journal of Biomedical Optics **8**, 329-338 (2003).
349. I. D. Johnson, "Practical Considerations in the Selection and Application of Fluorescent Probes," in *Handbook of Biological Confocal Microscopy*
J. B. Pawlay, ed. (Springer, New York, 2006), pp. 353-367.
350. C. Xu, R. M. Williams, W. Zipfel, and W. W. Webb, "Multiphoton excitation cross-sections of molecular fluorophores," Bioimaging **4**, 198-207 (1996).
351. C. Xu, W. Zipfel, J. B. Shear, R. M. Williams, and W. W. Webb, "Multiphoton fluorescence excitation: New spectral windows for biological nonlinear microscopy," Proceedings of the National Academy of Sciences of the United States of America **93**, 10763-10768 (1996).
352. M. A. Albota, C. Xu, and W. W. Webb, "Two-photon fluorescence excitation cross sections of biomolecular probes from 690 to 960 nm," Appl. Optics **37**, 7352-7356 (1998).
353. D. R. Larson, W. R. Zipfel, R. M. Williams, S. W. Clark, M. P. Bruchez, F. W. Wise, and W. W. Webb, "Water-soluble quantum dots for multiphoton fluorescence imaging in vivo," Science **300**, 1434-1436 (2003).
354. N. S. Makarov, M. Drobizhev, and A. Rebane, "Two-photon absorption standards in the 550-1600 nm excitation wavelength range," Opt. Express **16**, 4029-4047 (2008).
355. S. Namiki, and H. A. Haus, "Noise of the stretched pulse fiber laser .1. Theory," IEEE J. Quantum Electron. **33**, 649-659 (1997).
356. R. Paschotta, "Noise of mode-locked lasers (Part II): timing jitter and other fluctuations," Appl. Phys. B **79**, 163-173 (2004).
357. R. P. Scott, C. Langrock, and B. H. Kolner, "High-dynamic-range laser amplitude and phase noise measurement techniques," IEEE J. Sel. Top. Quantum Electron. **7**, 641-655 (2001).
358. J. Kim, J. Chen, J. Cox, and F. X. Kärtner, "Attosecond-resolution timing jitter characterization of free-running mode-locked lasers," Opt. Lett. **32**, 3519-3521 (2007).
359. Y. F. Chen, J. Jiang, and D. J. Jones, "Remote distribution of a mode-locked pulse train with sub 40-as jitter," Opt. Express **14**, 12134-12144 (2006).
360. T. R. Schibli, J. Kim, O. Kuzucu, J. T. Gopinath, S. N. Tandon, G. S. Petrich, L. A. Kolodziejski, J. G. Fujimoto, E. P. Ippen, and F. X. Kaertner, "Attosecond active synchronization of passively mode-locked lasers using balanced cross-correlation," Opt. Lett. **28**, 947-949 (2003).
361. http://www.layertec.de/, Accessed March 30, 2010.
362. J. R. Birge, (2010), http://www.mit.edu/~birge/, Accessed March 20, 2010.
363. J. R. Birge, and F. X. Kärtner, "Efficient optimization of multilayer coatings for ultrafast optics using analytic gradients of dispersion," Appl. Opt. **46**, 2656-2662 (2007).
364. http://www.layertec.de/fileadmin/scripts/shop_info.php?arnr=101121, Accessed March 29, 2010.
365. http://www.layertec.de/fileadmin/scripts/shop_info.php?arnr=101122, Accessed March 30, 2010.

366. http://www.layertec.de/fileadmin/scripts/shop_info.php?arnr=104146, Accessed March 30, 2010.
367. http://www.layertec.de/fileadmin/scripts/shop_info.php?arnr=104147, Accessed March 30, 2010.
368. http://www.layertec.de/fileadmin/scripts/shop_info.php?arnr=103287, Accessed March 30, 2010.
369. http://www.layertec.de/fileadmin/scripts/shop_info.php?arnr=100471, Accessed March 30, 2010.
370. http://www.layertec.de/fileadmin/scripts/shop_info.php?arnr=100465, Accessed March 30, 2010.
371. http://www.layertec.de/fileadmin/scripts/shop_info.php?arnr=104189, Accessed March 30, 2010.
372. http://www.layertec.de/fileadmin/scripts/shop_info.php?arnr=108487, Accessed March 30, 2010.
373. http://www.opnext.com/products/pdf/ode2_036_hl6545mg2.pdf, Accessed March 31, 2010.
374. http://www.opnext.com/products/pdf/ode2_001_hl6385dg.pdf, Accessed March 31, 2010.
375. http://www.blueskyresearch.com/c/b/posts/view/37, Accessed March 31, 2010.
376. http://www.blueskyresearch.com/fileupload/pdfs/vpsl/VPSL-0660-130-X-5-G.pdf, Accessed March 31, 2010.
377. http://www.thorlabs.com/thorproduct.cfm?partnumber=HL6545MG, Accessed March 31, 2010.
378. http://www.thorlabs.com/thorProduct.cfm?partNumber=LT230P-B, Accessed March 31, 2010.
379. http://www.thorlabs.com/thorProduct.cfm?partNumber=A230TM-B, Accessed March 31, 2010.
380. http://www.teamwavelength.com/, Accessed March 31, 2010.
381. http://www.thorlabs.com/Thorcat/0800/0897-E0W.pdf, Accessed March 31, 2010.
382. http://www.thorlabs.com/NewGroupPage9.cfm?ObjectGroup_ID=1378, Accessed March 31, 2010.
383. https://www.thorlabs.com/thorProduct.cfm?partNumber=ITC8052, Accessed March 31, 2010.
384. http://www.thorlabs.com/thorProduct.cfm?partNumber=PRO8000, Accessed March 31, 2010.
385. http://www.nlight.net/diodes/details/4~Single-Emitter-Diode-Laser-Devices-visible, "SINGLE EMITTER DIODE LASER DEVICES (VISIBLE)," (2009).
386. http://www.ldxoptronics.com/pkagedraw/C-mount_Packag_handling.pdf, "LASER DIODES IN THE C-MOUNT PACKAGE."
387. http://www.ilxlightwave.com/selection-guide/laser-diode-mounts-selection-guide.html, "Laser Diode Mounting Fixtures."
388. http://www.ilxlightwave.com/propgs/temperature-controlled-c-mount-fixture-4409.html, "LDM-4409, Temperature Controlled C-Mount Fixture."
389. http://www.nlight.net/nlight-files/file/datasheets/Single%20emitters/nLIGHT_Single-Emitters-Visible_081025.pdf, Accessed March 31, 2010.
390. http://www.ikz-berlin.de/index.php, Accessed April 04, 2010.
391. http://www.vloc.com/, Accessed April 4, 2010.
392. U. Keller, "Recent developments in compact ultrafast lasers," Nature **424**, 831-838 (2003).
393. J. Kleinbauer, R. Knappe, and R. Wallenstein, "Principles of ultrashort pulse generation," in *Femtosecond Technology for Technical and Medical Applications*(2004), pp. 9-16.
394. F. X. Kartner, U. Morgner, T. Schibli, R. Ell, H. A. Haus, J. G. Fujimoto, and E. P. Ippen, "Few-cycle pulses directly from a laser," in *Few-Cycle Laser Pulse Generation and Its Applications*(2004), pp. 73-135.
395. I. D. Jung, F. X. Kartner, N. Matuschek, D. H. Sutter, F. MorierGenoud, Z. Shi, V. Scheuer, M. Tilsch, T. Tschudi, and U. Keller, "Semiconductor saturable absorber mirrors supporting sub-10-fs pulses," Applied Physics B-Lasers and Optics **65**, 137-150 (1997).
396. D. H. Sutter, G. Steinmeyer, L. Gallmann, N. Matuschek, F. Morier-Genoud, U. Keller, V. Scheuer, G. Angelow, and T. Tschudi, "Semiconductor saturable-absorbermirrorassisted Kerr-lensmode-locked Tisapphire laser producing pulses inthe two-cycle regime," Opt. Lett. **24** (1999).
397. D. H. Sutter, L. Gallmann, N. Matuschek, F. Morier-Genoud, V. Scheuer, G. Angelow, T. Tschudi, G. Steinmeyer, and U. Keller, "Sub-6-fs pulses from a SESAM-assisted Kerr-lens modelocked Ti : sapphire laser: at the frontiers of ultrashort pulse generation," Applied Physics B-Lasers and Optics **70**, S5-S12 (2000).
398. http://www.ila.org.in/lasernews/ln992/ln992a01.html, Accessed March 05, 2010.

399. S. Adachi, "Optical properties of AlGaAs: Interband-transition region," in *Properties of Aluminium Gallium Arsenide*, S. Adachi, ed. (The Institution of Engineering and Technology 1993), pp. 118-148.
400. R. E. Fern, and A. Onton, "Refractive Index of AlAs," J. Appl. Phys. **42**, 3499-3500 (1971).
401. M. Garriga, P. Lautenschlager, M. Cardona, and K. Ploog, "Optical properties of AlAs " Solid State Communications **61**, 157-160 (1987).
402. D. D. Nolte, "Optical functions of GaAs," in *PROPERTIES OF Gallium Arsenide*, M. R. BROZEL, and C. E. STILLMAN, eds. (INSPEC, The Institution of Electrical Engineers, 1995), pp. 199-213.
403. A. N. Pikhtin, and A. D. Yaskov, " DISPERSION OF REFRACTIVE-INDEX OF SEMICONDUCTORS WITH DIAMOND AND ZINCBLENDE STRUCTURES," SOVIET PHYSICS SEMICONDUCTORS-USSR **12**, 622-626 (1978).
404. D. E. Aspnes, S. M. Kelso, R. A. Logan, and R. Bhat, "Optical properties of AlxGa1−x As," J. Appl. Phys. **60**, 754-767 (1986).
405. H. C. Casey, D. D. Sell, and K. W. Wecht, "CONCENTRATION-DEPENDENCE OF ABSORPTION-COEFFICIENT FOR N-TYPE AND P-TYPE GAAS BETWEEN 1.3 AND 1.6 EV " J. Appl. Phys. **46**, 250-257 (1975).
406. H. C. Casey, D. D. Sell, and K. W. Wecht, "CONCENTRATION-DEPENDENCE OF REFRACTIVE-INDEX FOR N-TYPE AND P-TYPE GAAS BETWEEN 1.2 AND 1.8 EV " J. Appl. Phys. **45**, 2650-2657 (1974).
407. http://www.batop.de/information/Eg_AlGaAs.html, Accessed April 5, 2010.
408. S. W. Corzine, "Design of vertical-cavity surface-emitting lasers with strained and unstrained quantum well active regions," in *Electrical and Computer Engineering*(University of California, Santa Barbara, 1993).
409. http://www.batop.de/information/Eg_AlGaAs.html, Accessed April 05, 2010.
410. S. Adachi, *Gaas and Related Materials: Bulk Semiconducting and Superlattice Properties* (World Scientific Publishing Company 1994).
411. http://www.batop.de/information/Eg_GaAs.html, Accessed April 05, 2010.
412. J. S. Blakemore, "Semiconducting and other major properties of gallium arsenide," J. Appl. Phys. **53**, R123-R181 (1982).
413. http://www.batop.de/information/r_Bragg.html, Accessed April 6, 2010.
414. S. Tandon, "Engineering Light Using Large Area Photonic Crystal Devices," in *Electrical Engineering and Computer Science*(Massachusetts Institute of Technology, 2005), p. 172.
415. P. S. Zory, *Quantum well lasers* (1993).
416. N. E. Nahory, M. A. Pollack, J. W. D. Johnston, and R. L. Barns, "Band gap versus composition and demonstration of Vegard's law for In1−xGaxAsyP1−y lattice matched to InP," Appl. Phys. Lett. **33**, 659-661 (1978).